

EAI/Springer Innovations in Communication and Computing

Chika Sugimoto
Hamed Farhadi
Matti Hämäläinen *Editors*

13th EAI International Conference on Body Area Networks

 **EAI**
RESEARCH MEETS INNOVATION

 Springer

EAI/Springer Innovations in Communication and Computing

Series editor

Imrich Chlamtac, European Alliance for Innovation, Ghent, Belgium

Editor's Note

The impact of information technologies is creating a new world yet not fully understood. The extent and speed of economic, life style and social changes already perceived in everyday life is hard to estimate without understanding the technological driving forces behind it. This series presents contributed volumes featuring the latest research and development in the various information engineering technologies that play a key role in this process.

The range of topics, focusing primarily on communications and computing engineering include, but are not limited to, wireless networks; mobile communication; design and learning; gaming; interaction; e-health and pervasive healthcare; energy management; smart grids; internet of things; cognitive radio networks; computation; cloud computing; ubiquitous connectivity, and in mode general smart living, smart cities, Internet of Things and more. The series publishes a combination of expanded papers selected from hosted and sponsored European Alliance for Innovation (EAI) conferences that present cutting edge, global research as well as provide new perspectives on traditional related engineering fields. This content, complemented with open calls for contribution of book titles and individual chapters, together maintain Springer's and EAI's high standards of academic excellence. The audience for the books consists of researchers, industry professionals, advanced level students as well as practitioners in related fields of activity include information and communication specialists, security experts, economists, urban planners, doctors, and in general representatives in all those walks of life affected ad contributing to the information revolution.

About EAI

EAI is a grassroots member organization initiated through cooperation between businesses, public, private and government organizations to address the global challenges of Europe's future competitiveness and link the European Research community with its counterparts around the globe. EAI reaches out to hundreds of thousands of individual subscribers on all continents and collaborates with an institutional member base including Fortune 500 companies, government organizations, and educational institutions, provide a free research and innovation platform.

Through its open free membership model EAI promotes a new research and innovation culture based on collaboration, connectivity and recognition of excellence by community.

More information about this series at <http://www.springer.com/series/15427>

Chika Sugimoto • Hamed Farhadi
Matti Hämäläinen
Editors

13th EAI International Conference on Body Area Networks

 Springer

 **EAI**
RESEARCH MEETS INNOVATION

Editors

Chika Sugimoto
Yokohama National University
Yokohama, Kanagawa, Japan

Hamed Farhadi
KTH Royal Institute of Technology
Stockholm, Stockholms Län, Sweden

Matti Hämäläinen 
Centre for Wireless Communications
University of Oulu
Oulu, Finland

ISSN 2522-8595 ISSN 2522-8609 (electronic)
EAI/Springer Innovations in Communication and Computing
ISBN 978-3-030-29896-8 ISBN 978-3-030-29897-5 (eBook)
<https://doi.org/10.1007/978-3-030-29897-5>

© Springer Nature Switzerland AG 2020

This work is subject to copyright. All rights are reserved by the Publisher, whether the whole or part of the material is concerned, specifically the rights of translation, reprinting, reuse of illustrations, recitation, broadcasting, reproduction on microfilms or in any other physical way, and transmission or information storage and retrieval, electronic adaptation, computer software, or by similar or dissimilar methodology now known or hereafter developed.

The use of general descriptive names, registered names, trademarks, service marks, etc. in this publication does not imply, even in the absence of a specific statement, that such names are exempt from the relevant protective laws and regulations and therefore free for general use.

The publisher, the authors, and the editors are safe to assume that the advice and information in this book are believed to be true and accurate at the date of publication. Neither the publisher nor the authors or the editors give a warranty, expressed or implied, with respect to the material contained herein or for any errors or omissions that may have been made. The publisher remains neutral with regard to jurisdictional claims in published maps and institutional affiliations.

This Springer imprint is published by the registered company Springer Nature Switzerland AG.
The registered company address is: Gewerbestrasse 11, 6330 Cham, Switzerland

Preface

We are delighted to introduce the proceedings of the first edition of the 2018 European Alliance for Innovation (EAI) International Conference on Body Area Networks (BODYNETS). This conference has brought researchers, developers and practitioners around the world who are leveraging and developing WBAN technology for wearable communications and personal health management. The theme of BODYNETS 2018 was “Technologies providing information from inside a body as well as on- and off-body devices.”

The technical program of BODYNETS 2018 consisted of 39 full papers. The conference had a main track and four special tracks. The special tracks were Track 1—Ultra Wide Band for Body Area Networks (UWBAN); Track 2—Smart Body Area Networks (SmartBAN); and Track 3—Antenna/Propagation and WiBEC project (APWiBEC). Aside from the high-quality technical paper presentations, the technical program also featured two keynote speeches, three invited speeches, and one panel. The two keynote speeches were given by Prof. Emil Jovanov from the University of Alabama, USA, and Prof. William Scanlon from Queen’s University Belfast, United Kingdom. The invited speeches were presented by Prof. DK Arvind from the University of Edinburgh, United Kingdom, Prof. Ryuji Kohno from Yokohama National University, Japan, and Dr. John Farserotu from CSEM, Switzerland. The title of the panel was “Technological Trends and Challenges for Future Healthcare.” The panel aimed to enrich our understanding of future trends the healthcare procedures are nowadays going to, and give insights into their key challenges.

Coordination with the steering chair, Imrich Chlamtac, and the general chair, Matti Hämäläinen, was essential for the success of the conference. We sincerely appreciate their constant support and guidance. It was also a great pleasure to work with such an excellent organizing committee for their hard work in organizing and supporting the conference: in particular, the Technical Program Committee, led by our TPC Co-Chairs, Prof. Jari Iinatti, Prof. Lorenzo Mucchi, Prof. Carlos Pomalaza-Raez, and Prof. Daisuke Anzai who have completed the peer-review process of technical papers. We are also grateful to the conference manager, Radka Pincakova,

for her support and all the authors who submitted their papers to the BODYNETS 2018 conference and workshops.

We strongly believe that the BODYNETS conference provides a good forum for all researchers, developers, and practitioners to discuss all science and technology aspects that are relevant to Wireless BAN. We also expect that the future BODYNETS conference will be as successful and stimulating as indicated by the contributions presented in this volume.

Yokohama, Japan
Stockholm, Sweden

Chika Sugimoto
Hamed Farhadi

Contents

Part I Ultra Wide Band for Body Area Networks

1 Ultra-Wide Band Positioning in Sport: How the On-Body Tag Location Affects the System Performance	3
Alessio Martinelli, Marco Dolfi, Simone Morosi, Lorenzo Mucchi, Matteo Paoli, and Andrea Agili	
2 Human Body Effect on Static UWB WBAN Off-Body Radio Channels	17
Timo Kumpulniemi, Juha-Pekka Mäkelä, Matti Hämäläinen, Kanya Yekeh Yazdandoost, and Jari Iinatti	
3 Reliable and High-Speed Implant Ultra-Wideband Communications with Transmit–Receive Diversity	27
Daisuke Anzai, Ilangko Balasingham, Georg Fischer, and Jainqing Wang	
4 A Finite Integration Technique-Based Simulation Study on the Impact of the Sternotomy Wires on the UWB Channel Characteristics	33
Mariella Särestöniemi, Carlos Pomalaza-Raez, Timo Kumpulniemi, Matti Hämäläinen, and Jari Iinatti	

Part II Smart Body Area Networks

5 Joint Throughput and Channel Aware MAC Scheduling for SmartBAN	49
Rida Khan and Muhammad Mahtab Alam	
6 Neighbour Wireless Body Area Network Discovery Mechanism for ETSI SmartBAN	65
Tuomas Paso and Jussi Haapola	

7	Evaluation of Preamble Detection in ETSI SmartBAN PHY	79
	Kento Takabayashi, Hirokazu Tanaka, and Katsumi Sakakibara	
Part III Security and Safety		
8	Security in Body Networks: Watermark-Based Communications on Air-Gap Acoustic Channel	89
	Simone Soderi	
9	Secrecy Capacity of Diffusion-Based Molecular Communication Systems	103
	Lorenzo Mucchi, Alessio Martinelli, Stefano Caputo, Sara Jayousi, and Massimiliano Pierobon	
10	Towards Efficient and Real-Time Human Activity Recognition Using Wearable Sensors: A Shapelet-Based Pattern Matching Approach	115
	Delaram Yazdansepas, Nitin Saroha, Lakshmesh Ramaswamy, and Khaled Rasheed	
11	Opportunistic IoT Service to Support Safety Driving from Heterogeneous Data Sources	131
	Giancarlo Fortino, Raffaele Gravina, Qimeng Li, and Claudio Savaglio	
Part IV Communications and Networking		
12	Performance Evaluation of Bluetooth Low Energy Technology Under Interference	147
	Heikki Karvonen, Konstantin Mikhaylov, Dinesh Acharya, and Md. Moklesur Rahman	
13	A Hybrid Optical-Radio Wireless Network Concept for the Hospital of the Future	157
	Iqrar Ahmed, Timo Kumpuniemi, and Marcos Katz	
14	Signal Transmission with Intra-Body and Inter-Body Communications: Simulation-Based Models	171
	Doaa Ahmed, Jens Kirchner, and Georg Fischer	
15	Indoor Energy Harvesting for WE-Safe Wearable IoT Sensor Nodes	185
	Fan Wu, Jean-Michel Redouté, and Mehmet Rasit Yuce	
16	Learning and Recognition with Neural Network of Heart Beats Sensed by WBAN for Patient Stress Estimate for Rehabilitation	195
	Yukihiro Kinjo, Yoshitomo Sakuma, and Ryuji Kohno	
17	A Machine Learning Based Method for Coexistence State Prediction in Multiple Wireless Body Area Networks	203
	Yongmei Sun, Tingshuo Chen, Jingxian Wang, and Yuefeng Ji	

Part V Systems and Applications

18 Private Audio-Based Cough Sensing for In-Home Pulmonary Assessment Using Mobile Devices 221
 Ebrahim Nemati, Md. Mahbubur Rahman, Viswam Nathan, and Jilong Kuang

19 Using an Indoor Localization System for Activity Recognition 233
 Andrea Aliperti, José Corcuera, Chiara Fruzzetti, Gianluca Marchini, Francesco Miliani, Simone Musetti, Andrea Primaverili, Riccardo Rocchi, Davide Ruisi, and Alessio Vecchio

20 Indoor-Outdoor Detection Using Head-Mounted Lightweight Sensors 245
 Tommaso Martire, Payam Nazemzadeh, Alberto Sanna, and Diana Trojaniello

21 Analysis of Walking Body Using Kinect2 and Application of Integer Code to WBAN 255
 Hirohisa Kitahara, Hiroyoshi Morita, and Akiko Manada

Part VI Medical Applications

22 InstantRR: Instantaneous Respiratory Rate Estimation on Context-Aware Mobile Devices 267
 Md. Mahbubur Rahman, Ebrahim Nemati, Viswam Nathan, and Jilong Kuang

23 Pre-Ejection Period (PEP) Estimation Based on R-Wave in ECG and On-Body Continuous Wave Radar Signal During Daily Activities 283
 Malikeh Pour Ebrahim, Fatemeh Heydari, Jean-Michel Redouté, and Mehmet Rasit Yuce

24 Wearable Continuous Blood Pressure Estimation with Photoplethysmography Sensors Array on the Arm 293
 Chunkai Qiu, Taiyang Wu, Jean-Michel Redouté, and Mehmet Rasit Yuce

25 Cuffless Blood Pressure Estimation Based on Pulse Arrival Time Using Bio-impedance During Different Postures and Physical Exercises 301
 Fatemeh Heydari, Malikeh Pour Ebrahim, Taiyang Wu, Katie Walker, Keith Joe, Jean-Michel Redouté, and Mehmet Rasit Yuce

26 Estimation Method of Abdominal Fat Thickness by Microwave 309
 Nobuaki Tanaka and Takahiro Aoyagi

27 Exposure to RF EMF from 5G Handheld Devices 317
 Kamyā Yekeh Yazdandoost and Ilkka Laakso

Part VII Case Studies and Wearable Devices

- 28 Driving Operation Recognition Using Smart Cushion Based on Deep Neural Network** 325
Xiong Li, Meng Yu, Wenfeng Li, Congcong Ma, Raffaele Gravina, and Giancarlo Fortino
- 29 A Wearable Device for Brain–Machine Interaction with Augmented Reality Head-Mounted Display** 339
Mattia Salvaro, Simone Benatti, Victor Kartsch, Marco Guermandi, and Luca Benini
- 30 A Cost-Effective Embedded Platform for Scalable Multichannel Biopotential Acquisition** 353
Simone Benatti, Marco Guermandi, and Luca Benini
- 31 A Pilot Study on Electrode–Skin Impedance Analysis of Embroidered EMG Electrodes** 365
Bilge Guvenc Tuna, Gozde Goncu Berk, Nese Topcuoglu, and Umit Ozorhan
- 32 Toward a Wearable Epileptic Seizure Monitoring: A Case Study** 373
Javad Birjandtalab, Diana Cogan, Mehrdad Nourani, and Jay Harvey
- 33 Virtual Machine Execution for Wearables Based on WebAssembly** 381
Martin Jacobsson and Jonas Willén

Part VIII Antenna/Propagation and WiBEC Project

- 34 Biometallic Orthopedic Implant with Printed Antenna** 393
Ildiko Peter and Ladislau Matekovits
- 35 EM Imaging-Based Capsule Endoscope Localization with Peak-Formed Incident Electric Fields** 399
Hisato Kobayashi, Daisuke Anzai, and Jainqing Wang
- 36 Information Theoretic Analysis for Securing Next Generation Leadless Cardiac Pacemaker** 407
Muhammad Faheem Awan, Kimmo Kansanen, and Deepak Palaksha
- 37 Feasibility Analysis for Pulse-Based Synchronization in a Dual Chamber Leadless Pacemaker System** 419
Deepak Palaksha, Kimmo Kansanen, and Muhammad Faheem Awan
- 38 Low-UWB Directive Antenna for Wireless Capsule Endoscopy Localization** 431
Chaima Kissi, Mariella Särestöniemi, Carlos Pomalaza-Raez, Marko Sonkki, and Mohamed Nabil Srifi

- 39 Experimental Path Loss Models Comparison and Localization of Wireless Endoscopic Capsule in the Ultra-Wideband Frequency Band** 443
Sofia Perez-Simbor, Martina Barbi, Mehrab Ramzan, Xiao Fang, Concepcion Garcia-Pardo, Narcis Cardona, Qiong Wang, Niels Neumann, and Dirk Plettemeier
- 40 Planar Elliptical Ring Implanted Antennas for UWB Body Area Communication** 455
Qiangbo Zhang, Xiao Fang, Qiong Wang, and Dirk Plettemeier
- 41 Motion Artifact Reduction in Electrocardiogram Using Adaptive Filtering Based on Skin-Potential Variation Monitoring ...** 465
Shumei Dai, Dongyi Chen, Fan Xiong, and Zhenghao Chen
- Index**..... 473

Part I
Ultra Wide Band for Body Area Networks

Chapter 1

Ultra-Wide Band Positioning in Sport: How the On-Body Tag Location Affects the System Performance



Alessio Martinelli, Marco Dolfi, Simone Morosi, Lorenzo Mucchi,
Matteo Paoli, and Andrea Agili

1.1 Introduction

The increasing spread of location-based services (LBSs) [7] has encouraged the collaboration between academics and industry to define innovative positioning and navigation solutions. The pedestrian position-based services rely on those technologies which primarily implement two positioning techniques: position fixing and pedestrian dead reckoning [4]. In a remote positioning configuration, position fixing aims to determine the pedestrian position exploiting the ranging signals transmitted by a wearable device and received by an external infrastructure; alternatively, pedestrian dead reckoning relies only on wearable sensors to measure the distance and direction traveled from a previous position, in order to determine the current one [9].

LBSs mainly involve sectors like military, emergency, and commercial [7]. The latter, in particular, includes many specific contexts such as wellness and sport [8, 13], in which the pedestrian position-based services have become very popular. Tens of applications for smartphones or wearable devices hit the market with the aim of providing position tracking information, mostly in outdoor environment through satellite positioning technologies. Many professional sport teams have adopted positioning system to carry out, e.g., analysis of physiological factors such as the physical overload of the players or analysis of technical-tactical behaviors [11].

A. Martinelli (✉) · M. Dolfi · S. Morosi · L. Mucchi
Information Engineering Department, University of Florence, Florence, Italy
e-mail: alessio.martinelli@unifi.it; marco.dolfi@unifi.it; simone.morosi@unifi.it;
lorenzo.mucchi@unifi.it

M. Paoli · A. Agili
Tracking4Fun, Florence, Italy
e-mail: matteo.paoli@tracking4fun.com; andrea.agili@tracking4fun.com

However, the positioning technologies that are currently used in sports are primarily based on the Global Positioning System (GPS) [6, 12]. The latter provides a reliable position solution only in the presence of open-sky environment and low human motion dynamics, i.e., when the line-of-sight to the satellite is not obstructed and the player is not performing short, high-speed straight line running and fast change of directions [5].

Ultra-wide band (UWB) positioning can be considered a valid solution for position tracking in sports. It can support high human dynamics being able to determine the target position with centimeter-level positioning accuracy [1]. A UWB positioning system relies on an external infrastructure, which can be arranged either indoor or outdoor, and it aims to determine the position of wearable tags. Since the UWB communication link between the tag and the positioning infrastructure can be affected by the on-body tag location, the latter becomes a crucial aspect for achieving the best positioning performance.

This paper introduces an UWB positioning system [14] whose proposal is subject to patenting and that is based on the architecture illustrated in Fig. 1.1. This system has been considered in a particular sport such as five-a-side football. Four static UWB receivers are placed at the corners of a five-a-side pitch, while a mobile player is equipped with four UWB transmitters arranged on different body locations: left arm, right arm, upper back, and lower back, as shown in Fig. 1.2. The objective of this work is to evaluate how different on-body sensor locations may affect the system performance. The player's body influences the UWB communication link defined between the on-body transmitter and the receiver located on the sideline. The line-of-sight (LOS) and non-light-of-sight (NLOS) propagation conditions, depending on the location of the body-worn transmitter and the orientation of the player's body with respect to the receivers, affect the system performance. In order to assess the performance of the positioning system, on-field tests have been performed with a

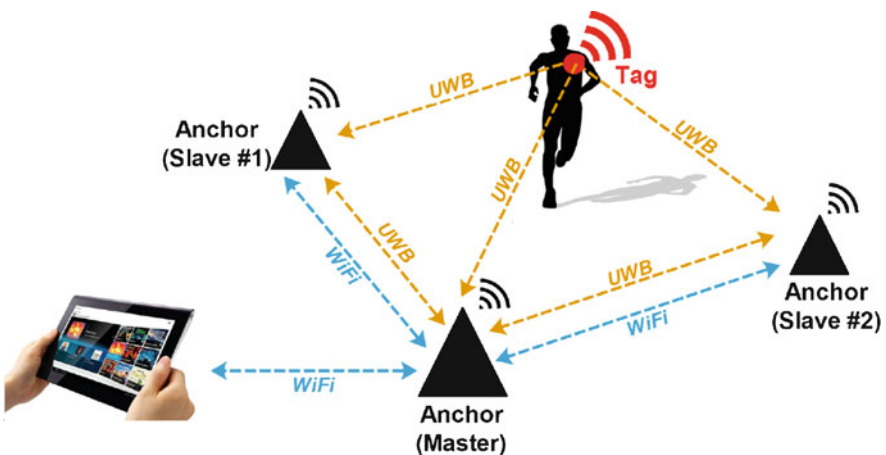


Fig. 1.1 The UWB positioning system architecture



Fig. 1.2 On-body locations of the tags: left arm, right arm, lower back, and upper back

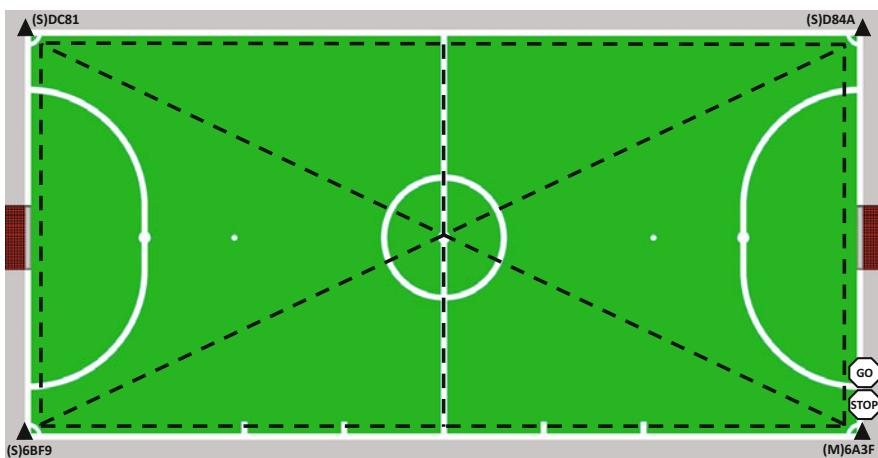


Fig. 1.3 The five-a-side football pitch with the size of 39.30 m × 17.95 m. The black dashed line represents the experimental test path, which has been traveled by the player in both directions. The black cones represent the static UWB receivers: the master anchor and the three slave ones

player. The latter was asked to run at a variable speed while traveling a predefined path inside pitch, as depicted in Fig. 1.3. The path has been devised to better represent a prospective motion that a player might perform during a real five-a-side football match. Three metrics have been considered to compare the system performance for the different on-body transmitter locations: the position accuracy of each UWB transmitter, the percentage of packets lost by the receivers with respect to

the transmitted packets, and the percentage of packets transmitted and, respectively, received by one, two, three, or four receivers.

The remainder of this paper is organized as follows: Sect. 1.2 describes the positioning system architecture, while Sect. 1.3 explains the positioning process which includes the procedures of time synchronization and time differential of arrival (TDOA) positioning; Sect. 1.4 characterizes the experimental setup and Sect. 1.5 reports the experimental results. Finally, Sect. 1.6 presents the conclusions of the work.

1.2 The Positioning System Architecture

The proposed system architecture consists of three components: a mobile tablet/smartphone, tags, and anchors [14], as illustrated in Fig. 1.1. The tags are mobile devices which transmit UWB signals to the anchors. The anchors are static UWB receivers positioned on the sides of the reference scenario. They represent the positioning system infrastructure, coordinated by the master anchor, which transmits UWB signals to the other slave anchors and establishes the local Wi-Fi network used to share the positioning process data among the anchors and the connected tablet/smartphone [14].

The positioning system that is described in Sect. 1.4 has been implemented over this architecture, which can be considered multi-context and scalable: as a matter of facts a larger number of anchors may increase the coverage of the positioning service.

1.3 The Positioning Process

In the system that is described in this paper, the positioning process involves two primary procedures: time synchronization and TDOA positioning, as depicted in Fig. 1.4.

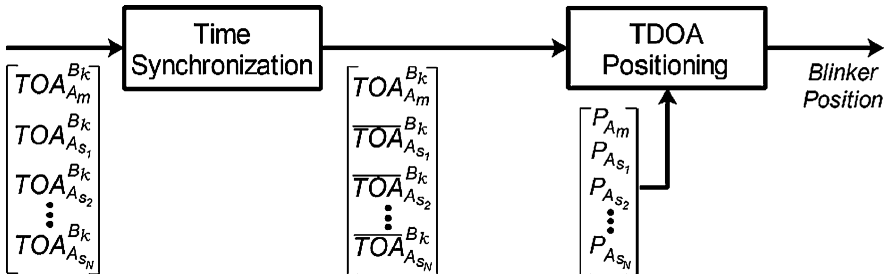
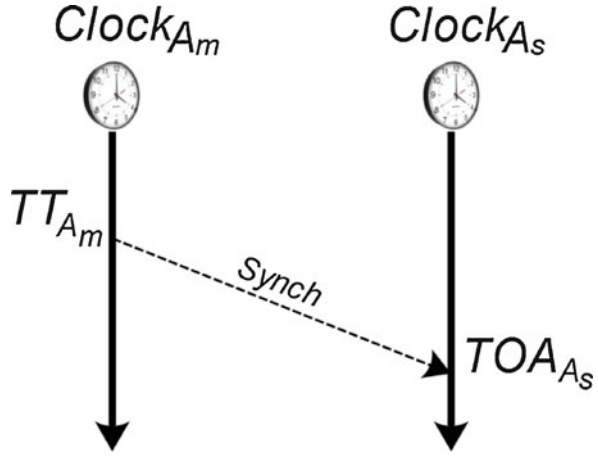


Fig. 1.4 The positioning process

Fig. 1.5 Representation of the time synchronization routine between the clock of the master anchor A_m and the clock of the slave anchor A_s : the master anchor sends a synchronization signal at transmitting time TT_{A_m} to the slave anchor, which receives the signal at the time of arrival TOA_{A_s} .



Clock Synchronization

The TDOA positioning algorithm (described in Sect. 1.3) is based on the time of flight, i.e., the time the signal takes to travel from the tag to the anchors. In order to apply a positioning algorithm based on the time of flight, the anchors must be synchronized among them [4, 10]. As depicted in Fig. 1.5, the master anchor A_m transmits a synchronization UWB signal at the time TT_{A_m} ; then, the slave anchor A_s receives the signal at the time of arrival TOA_{A_s} . The times TT_{A_m} and TOA_{A_s} refer to different time scales, which, respectively, correspond to the master clock and the slave one. The time offset between the two clocks is defined as follows:

$$\Delta T = TOA_{A_s} - TT_{A_m} - TOF_{A_s}^{A_m}, \quad (1.1)$$

where $TOF_{A_s}^{A_m}$ is the time of flight the signal takes to travel from the master anchor to the slave one. The TOA_{A_s} can be synchronized to the master clock as follows:

$$\overline{TOA}_{A_s} = TOA_{A_s} - \Delta T. \quad (1.2)$$

Once the time synchronization procedure has been carried out, the TOAs received by all anchors will refer to the time scale of the master clock.

TDOA Positioning

The TDOA positioning algorithm [6, 15] aims to determine the tag position given two pieces of information as inputs (Fig. 1.4): the first one is a vector which includes the positions of the anchors:

$$\mathbf{P}_A = [P_{A_m}, P_{A_{s_1}}, P_{A_{s_2}}, \dots, P_{A_{s_N}}]^T, \quad (1.3)$$

where P_{A_m} is the position of the master anchor A_m and $P_{A_{s_i}}$ is the position of the i -th slave anchor A_{s_i} , with $i=1, 2, \dots, N$ and N the total number of the slave anchors; the second one is a vector of the TOAs:

$$\mathbf{TOA}_A^{B_k} = [TOA_{A_m}^{B_k}, \overline{TOA}_{A_{s_1}}^{B_k}, \overline{TOA}_{A_{s_2}}^{B_k}, \dots, \overline{TOA}_{A_{s_N}}^{B_k}]^T, \quad (1.4)$$

where $TOA_{A_m}^{B_k}$ is the TOA of the signal transmitted by the tag B_k and received by the master anchor, and $\overline{TOA}_{A_{s_i}}^{B_k}$ is the TOA received by the i -th slave anchor.

Assuming the master anchor as the first one hit by the transmitted signal, the vector of the time difference of arrivals is defined as follows:

$$\mathbf{TDOA}_A^{B_k} = \begin{bmatrix} TDOA_{A_{s_1}}^{A_m} \\ TDOA_{A_{s_2}}^{A_m} \\ \vdots \\ TDOA_{A_{s_N}}^{A_m} \end{bmatrix} = \begin{bmatrix} \overline{TOA}_{A_{s_1}}^{B_k} - TOA_{A_m}^{B_k} \\ \overline{TOA}_{A_{s_2}}^{B_k} - TOA_{A_m}^{B_k} \\ \vdots \\ \overline{TOA}_{A_{s_N}}^{B_k} - TOA_{A_m}^{B_k} \end{bmatrix}, \quad (1.5)$$

where $TDOA_{A_{s_i}}^{A_m}$ is the TDOA between the master anchor and the i -th slave anchor.

In a 2D scenario, the i -th range difference can be defined as follows:

$$\begin{aligned} R_{i,m} &= c TDOA_{A_{s_i}}^{A_m} = R_i - R_m \\ &= \sqrt{(X_i - x)^2 + (Y_i - y)^2} - \sqrt{(X_m - x)^2 + (Y_m - y)^2}, \end{aligned} \quad (1.6)$$

where (X_i, Y_i) is the i -th slave anchor position, (X_m, Y_m) is the position of the master anchor, c is the speed of light in vacuum, and (x, y) is the unknown position solution of the tag.

The 2D tag position can be precisely determined by solving for a system of equations which contain at least two equations expressed in (1.6); therefore, at least three anchors must receive the signal transmitted by the tag. The Newton–Raphson method for non-linear least squares problems has been used to solve for a system of equations which comprises the range difference measurements described in (1.6). This is an iterative approach which linearizes the set of equations and begins with an initial position guess and then improves the estimate at each iteration by determining the local linear least-square (LS) solution. Starting with an initial guess (x_0, y_0) of the tag position, the iterative method computes the deviations vector $[\Delta x, \Delta y]^T$ of the position estimation:

$$\begin{bmatrix} \Delta x \\ \Delta y \end{bmatrix} = (G_t^T G_t)^{-1} G_t^T h_t, \quad (1.7)$$

where

$$h_t = \begin{bmatrix} R_{1,m} - (R_1 - R_m) \\ R_{2,m} - (R_2 - R_m) \\ \vdots \\ R_{N,m} - (R_N - R_m) \end{bmatrix}, \quad (1.8)$$

$$G_t = \begin{bmatrix} [(X_m - x)/R_m] - [(X_1 - x)/R_1] & [(Y_m - x)/R_m] - [(Y_1 - x)/R_1] \\ [(X_m - x)/R_m] - [(X_2 - x)/R_2] & [(Y_m - x)/R_m] - [(Y_2 - x)/R_2] \\ & \vdots \\ [(X_m - x)/R_m] - [(X_N - x)/R_N] & [(Y_m - x)/R_m] - [(Y_N - x)/R_N] \end{bmatrix}, \quad (1.9)$$

where $R_{i,m}$ is the range difference between the master anchor and the i -th slave anchor, with $i = 1, 2, \dots, N$; R_m is the range between the tag and the master anchor referred to the previous estimation of the tag position; and R_i is the range between the tag and the i -th slave anchor. In the next iteration, x_0 and y_0 are updated to $x_0 + \Delta x$ and $y_0 + \Delta y$. The whole process is repeated until Δx and Δy are sufficiently small: in our case, until the following condition is satisfied:

$$\sqrt{\Delta x^2 + \Delta y^2} < 0.01 \text{ m}. \quad (1.10)$$

The Newton–Raphson method achieves a precise position estimate at reasonable noise level; however, it requires a close initial guess (x_0, y_0) to guarantee convergence.

1.4 Experiment Setup

In this paper, the proposed UWB positioning system [14] has been considered in a particular sport such as five-a-side football. Referring to the architecture illustrated in Fig. 1.1, the static UWB receivers (anchors) were positioned at the four corners of the field illustrated in Fig. 1.3, while a mobile player is equipped with four UWB transmitters arranged on different body locations: left arm, right arm, upper back, and lower back, as shown in Fig. 1.2. Note that the vertical arrangement of the DWM1000 on the player's body (Fig. 1.2) leads to a quasi-omnidirectional radiation pattern of the UWB antenna in the azimuth plane [2]. In this way, the orientation changes of the player along the football pitch do not significantly affect the radiation pattern of the antenna.

Both the anchors and the tag are provided with a Decawave DWM1000 UWB transceiver [2] and are powered by a Li-Po battery. The anchors are also equipped

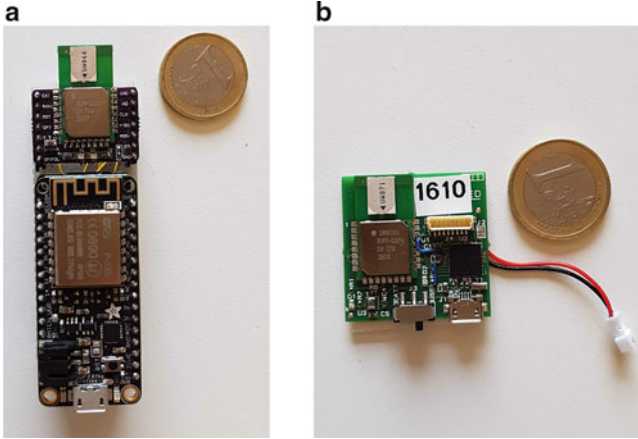


Fig. 1.6 Hardware devices used in the on-field experimental tests: (a) anchor; (b) tag

with a Wi-Fi module [3], as depicted in Fig. 1.6. The Decawave DWM1000 is a UWB transceiver compliant with the IEEE 802.15.4-2011 standard and allows very accurate proximity detection using two-way ranging time-of-flight (TOF) measurements. It spans 6 RF bands from 3.5 to 6.5 GHz, with a bandwidth of 500 or 900 MHz. The accuracy of the ranging measurements goes down to a few centimeters in LOS conditions, thanks to the high temporal resolution required to perform UWB communication. Because of its high bandwidth and spectrum usage, to avoid inter-system interference the transmit power density of the UWB transceivers is limited to -41.3 dBm/MHz. Due to this restriction, the operational range of the UWB transceivers is limited up to 300 m in LOS and 40 m in NLOS conditions [2]. In this work, the configuration of DWM1000 UWB transceivers is designed to operate on channel 4 (bandwidth of 900 MHz with a center frequency of 3993.6 MHz), with a data rate of 850 kbps and a preamble length of 2048 symbols. Both the tag and the anchors are supplied with a Decawave DWM1000 UWB transceiver [2] and a Li-Po battery-powered, whereas the anchors include also a Wi-Fi module [3], as illustrated in Fig. 1.6. The DWM1000 transceiver can transmit pulses that are few nanoseconds long with a bandwidth of 500 or 900 MHz and a frequency center that spans from 3.5 to 6.5 GHz. The high temporal resolution required to perform UWB communication allows an accuracy of the ranging measurements down to a few centimeters in LOS conditions. In this work, the DWM1000 UWB transceivers are configured to operate on channel 4 (900 MHz bandwidth with a center frequency of 3993.6 MHz), with a preamble length of 2048 symbols and a data rate of 850 kbps.

The objective of this work is to evaluate how different on-body sensor locations may affect the positioning system performance in the game. The player's body influences the UWB communication link defined between the on-body transmitter and the receiver located on the sideline. The LOS and NLOS propagation conditions,

depending on the location of the body-worn transmitter and on the orientation of the player's body with respect to the receivers, affect the positioning performance.

In order to evaluate the performance of the positioning system, a player was asked to perform a test which consisted in traveling the path illustrated in Fig. 1.3, in both directions and by running at variable speed. The black cones represent the location of the anchor nodes on the field test, while the black dashed line represents the path performed by the player. During the test, the anchors have been located at the height of 60 cm off the ground and the tag transmission rate has been set equal to 2 packets/s. To keep the complexity of the localization process low, the tag's height is not computed by the localization algorithm. The main goal of considering symmetric trajectories on the field is to assess how different body locations of the tag affect the performance of the positioning system, evaluated in a dynamic scenario with device-related consequences and impairments (e.g., clock drift, antenna placement, and radiation pattern) and body effects.

1.5 Experiment Results

In this section, the performance of the UWB positioning system for the different on-body tag locations is evaluated and discussed. Table 1.1 represents the percentage of packets lost by each anchor with respect to the packets transmitted by each tag. It can be observed that the lower back location suffers the greater loss of packets compared to the other tag locations, with on average more than half of the transmitted packets lost by the anchors. As expected, given the symmetry with the bust, left arm and right arm locations determine similar results, while the upper back location guarantees the best result, with an average of 40% of the transmitted packets lost by the anchors. The number of packets lost by an anchor may be influenced by the asymmetry of the pitch with respect to the diagonal. Since the anchors are placed at the corner of the pitch and the pair of anchors arranged in a diagonal is not symmetric with respect to the other diagonal, different anchors may experience different packet loss for the same tag arrangement. In terms of packet loss, it can

Table 1.1 Percentage of packets lost by the anchors with respect to the packets transmitted by each tag

Anchor ID	Left arm	Right arm	Lower back	Upper back
(M)6A3F	69%	60%	68%	53%
(S)6BF9	35%	35%	48%	40%
(S)D84A	32%	33%	50%	28%
(S)DC81	42%	45%	59%	38%

Table 1.2 Percentage of packets transmitted by the tag and received by one, two, three, or four anchors (%)

Received by	Left arm	Right arm	Lower back	Upper back
1 Anchor	19%	15%	29%	11%
2 Anchors	41%	45%	47%	44%
3 Anchors	27%	26%	12%	28%
4 Anchors	8%	8%	2%	14%

be basically observed that the performance of the anchors (M)6A3F and (S)DC81, organized in a particular diagonal, is worse with respect to the other pair of anchors, i.e., the (S)6BF9 and the (S)D84A.

As stated above, in order to estimate the actual position of the player during the dynamic test, the proposed positioning algorithm needs at least three anchors to determine the tag position solution. In Table 1.2, the percentage of packets transmitted by the tag and received by one, two, three, or four anchors is presented. Once again, the best results are guaranteed by the upper back-worn tag. As a consequence, this positive behavior determines a greater number of position estimates with respect to the other body locations, as shown in Figs. 1.7 and 1.8. From the analysis of both pictures, it is possible to confirm the best performance of the upper back tag location, when compared with the other body locations. In particular, the 42% of the packets that are transmitted by the upper back tag reach at least three anchors: to be more specific 28% is received by three anchors, while 14% by four, as shown in Table 1.2. Another interesting observation is the concentration at the center of the field of the missing position estimates, both for arms and lower back locations. The lateral position of the arm-worn tags may explain the poor rate of packets received by at least three anchors, especially during the crossing of the midfield line performed by the player. Regarding the lower back tag location, the number of position estimates further degrades. This behavior could be explained by the different height of the worn tag, which suffers more from NLOS condition caused by the human body influence during the dynamic test.

Finally, the root mean square error (RMSE) of the accuracy performance of the positioning system with different on-body tag locations is compared; the RMSE metric allows computing the positioning error in the Cartesian coordinates of the system in Figs. 1.7 and 1.8: it represents the mean difference between the true position and the estimated position of the tag. This metric is generally measured as the average of the Euclidean distance between the estimated position and the true position, as defined by the following equation:

$$RMSE = \sqrt{\sum_{k=1}^N \frac{(x_k - x_{actual})^2 + (y_k - y_{actual})^2}{N}} \quad (1.11)$$

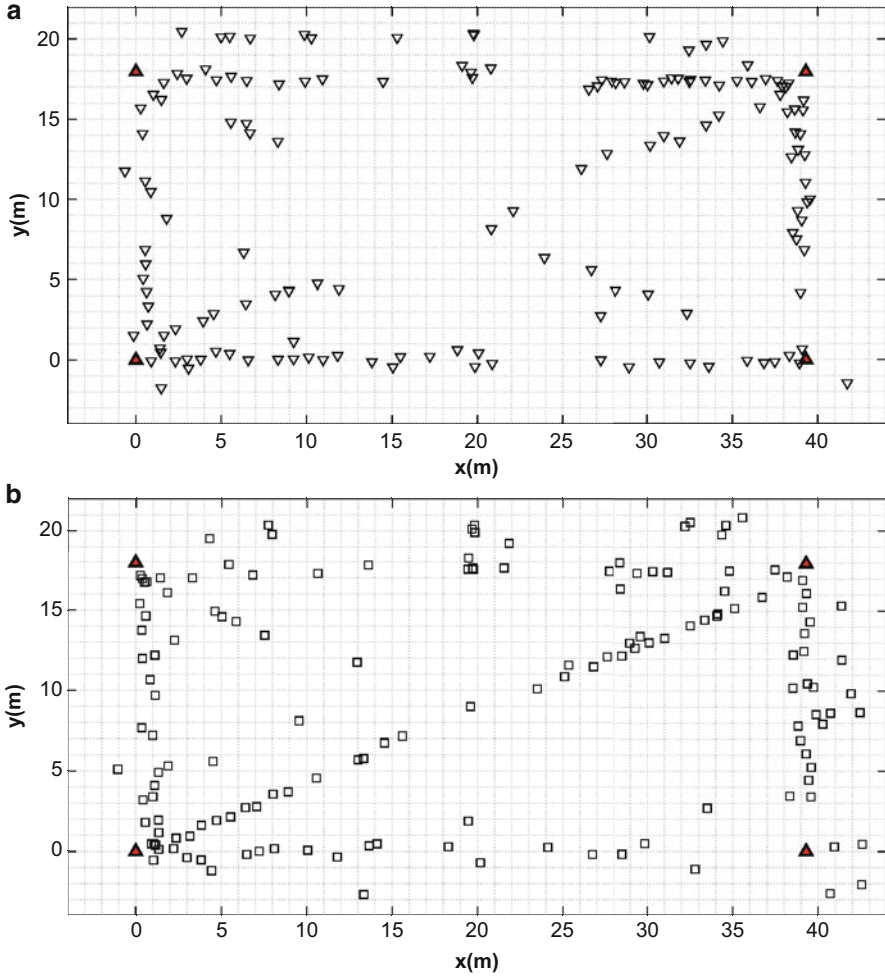


Fig. 1.7 Experiment results: (a) position solutions of the left arm-worn tag; (b) position solutions of the right arm-worn tag

where (x_k, y_k) are the k -th Cartesian coordinates estimated by the localization algorithm, (x_{actual}, y_{actual}) are the true Cartesian coordinates and N is the number of the position estimates. The true position (x_{actual}, y_{actual}) is defined as the point (x, y) which is closest to the estimated position (x_k, y_k) and belongs to the experimental path. Table 1.3 represents the accuracy performance of the tag position estimates in terms of RMSE. The upper back location performs better than the other tag locations, with a RMSE equal to 0.70 m. Moreover, the gain in accuracy is more evident for the central body locations (upper and lower back) compared to the lateral ones (right and left arm). This different accuracy performance could be explained by

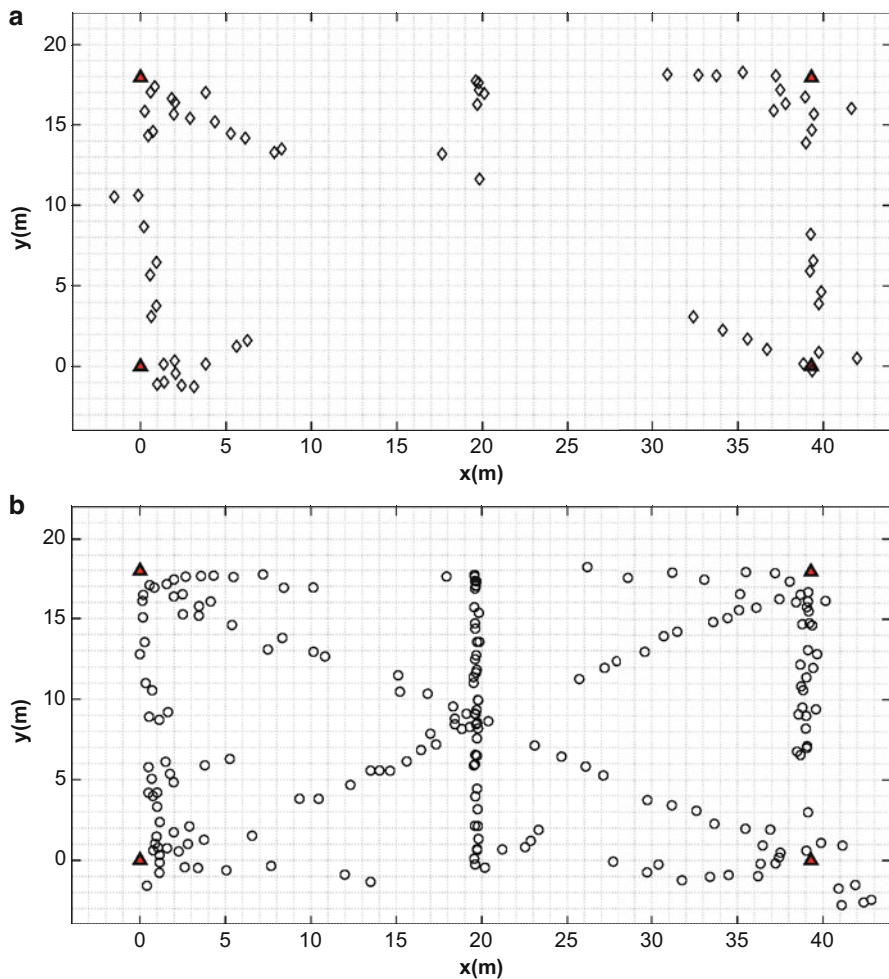


Fig. 1.8 Experiment results: (a) position solutions of the lower back-worn tag; (b) position solutions of the upper back-worn tag

Table 1.3 Root mean square error (RMSE) of the tag position solutions

Body tag	RMSE [m]
Left arm	0.83
Right arm	1.00
Lower back	0.71
Upper back	0.70

the distance of the arm-worn tag from the central axis of the body, while the player travels along the planned path at variable speed.

It is important to note that although the lower back tag location has experienced the greatest loss of packets between all tags, this behavior does not affect the

accuracy performance, and, what is even more important, the reliability of the positioning algorithm. This means that the packet loss and the tag position accuracy are not directly related to each other.

1.6 Conclusion

In this paper, the results of a measurement campaign of a UWB positioning system for monitoring of sport players have been reported and discussed. The positioning system based on the architecture illustrated in Fig. 1.1 [1, 14] has been considered in a five-a-side football scenario. Four static UWB receivers are placed at the corners of a five-a-side pitch, while a mobile player is equipped with four UWB transmitters arranged on different body locations: left arm, right arm, upper back, and lower back, as shown in Fig. 1.2. The objective of this work is to evaluate how different on-body sensor locations may affect the system performance. In order to evaluate the performance of the positioning system, the player was asked to perform a test which consisted in traveling the path illustrated in Fig. 1.3, in both directions and by running at variable speed. Three metrics have been considered to compare the system performance for the different on-body tag locations: the RMSE of the position solutions for each tag, the packet lost by the anchors with respect to the packet transmitted by each tag, the percentage of packets transmitted by each tag and, respectively, received by one, two, three, or four anchors.

The experimental results show the upper back as the on-body tag location that presents the best results: the lowest position RMSE equal to 0.70 m, an average of 40% of the transmitted packets lost by the anchors, and the 42% of the transmitted packets that reach at least 3 anchors (28% received by three anchors, while 14% received by four anchors). With the aim to expand the statistical results, the influence of the anchor antenna height on the system performance and the involvement of several players in the test will be considered in future works.

References


1. Alarifi, A., Al-Salman, A., Alsaleh, M., Alnafessah, A., Al-Hadhrami, S., Al-Ammar, M.A., Al-Khalifa, H.S.: Ultra wideband indoor positioning technologies: analysis and recent advances. *Sensors* **16**, 707 (2016)
2. Decawave Company. <https://www.decawave.com/>
3. Espressif Systems Company. <https://www.espressif.com>
4. Groves, P.: *Principles of GNSS, Inertial, and Multisensor Integrated Navigation Systems*, 2nd edn. Artech House, Boston (2013)
5. Jennings, D., Cormack, S., Coutts, A., Boyd, L., Aughey, R.: The validity and reliability of GPS units for measuring distance in team sport specific running patterns. *Int. J. Sport Physiol. Performance* **5**, 328–341 (2010)
6. Kaplan, E., Hegarty, C.: *Understanding GPS/GNSS: Principles and Applications*, 3rd edn. Artech House, Boston (2017)

7. Küpper, A.: Location-Based Services: Fundamentals and Operation. marketsandmarkets.com **TC 2371** (2005)
8. Leser, R., Baca, A., Ogris, G.: Local Positioning Systems in (Game) Sports. *Sensors* **11**, 9778–9797 (2011)
9. Martinelli, A., Gao, H., Groves, P., Morosi, S.: Probabilistic Context-Aware Step Length Estimation for Pedestrian Dead Reckoning. *IEEE Sensors* **18**, 1600–1611 (2018)
10. McElroy, C., Neiryneck, D., McLaughlin, M.: Comparison of wireless clock synchronization algorithms for indoor location systems. In: *Proceedings of the International Conference on Communications Workshops (ICC)* (2014)
11. Memmert, D., Lemmink, K., Sampaio, J.: Current approaches to tactical performance analyses in soccer using position data. *Sports Med.* **47**, 1–10 (2017)
12. Morosi, S., Martinelli, A., Re, E.D.: Peer-to-peer cooperation for GPS positioning. *Int. J. Satell. Commun. Netw.* **35**, 323–341 (2017)
13. Mucchi, L., Trippi, F., Carpini, A.: Ultra wide band real-time location system for cinematic survey in sports. In: *Proceedings of the 3rd International Symposium on Applied Sciences in Biomedical and Communication Technologies (ISABEL)*, Rome (2010)
14. Paoli, M., et al.: Individual Tracking Method and System. Italy Patent Pending, No 102017000062080 (UA2017A004096) (June 2017)
15. Stefanski, J.: Hyperbolic Position Location Estimation in the Multipath Propagation Environment. *Wireless and Mobile Networking*, pp. 232–239. Springer, Berlin (2009)

Chapter 2

Human Body Effect on Static UWB WBAN Off-Body Radio Channels



Timo Kumpuniemi, Juha-Pekka Mäkelä, Matti Hämäläinen , Kanya Yekeh Yazdandoost, and Jari Iinatti

2.1 Introduction

The development in computing power of electronic devices together with their decreasing sizes and energy efficiency has enabled the birth of new application areas to wireless appliances. Currently, one key focal area in wireless communications is the fifth-generation (5G) systems and its implementation into reality. One vertical in 5G systems is the concept of Internet of Things (IoT) where the number of different kind of sensors utilized in new environments is expected to explode. If the sensors are operating wirelessly, one or several of them are usually planned to be in contact to an access point. IoT sensors can be installed into, e.g., vehicles, buildings, house appliances, industrial plants, and machines. Furthermore, IoT sensors can be utilized with humans, thus forming a wireless body area network (WBAN). With persons, WBANs can be constructed by applying sensors on human bodies (on-body), in the close vicinity of them (off-body), or even inside the bodies (in-body). In body-to-body communications, the sensors are exchanging information between two or more individuals [1].

WBANs can be applied in various applications. They can be used in sports to monitor the body parameters providing information on the effectiveness of the exercise. In the well-being sector, the daily activity can be monitored as well as, e.g., the quality of the sleep. Authorities, as fire and police departments or the military, can utilize WBANs in their daily work to increase their own safety.

One of the most enhancing and promising areas is however the medical field. A practical reason to this is the constant aging of population in many nations around the world forcing to search for new more effective and economical solutions to pro-

T. Kumpuniemi (✉) · J.-P. Mäkelä · M. Hämäläinen · K. Yekeh Yazdandoost · J. Iinatti
Centre for Wireless Communications, University of Oulu, Oulu, Finland
e-mail: timo.kumpuniemi@oulu.fi

vide healthcare services to the growing number of patients. Different technological solutions are one answer to this question, among them belonging also WBANs. The wireless characteristics of WBANs enable better working comfortability and effectiveness for the medical staff. The patients will have a more pleasant treatment experience as they can move freely. They may even live their lives during the recovery phase at homes through remote monitoring the vital parameters from the hospital or other medical unit.

The ultra-wideband (UWB) technology is a very suitable solution for wireless communications to use in the WBANs for many reasons. The wide bandwidth of the UWB signals facilitates an accurate positioning and provides a good performance in difficult radio channel conditions with a large number of multipath components. The transmission power of UWB signals is low minimizing the interference caused to other systems. In practice, the UWB transmission power spectral densities often remain below the existing noise power density. On the other hand, UWB is robust against interferences from other transmissions originating nearby. The transceiver structures are simple providing a low unit price, a small size, and a low power consumption providing excellent battery life [2, 3].

The adoption of UWB technology in WBANs has been under investigation for over a decade [4]. Most of published articles in the field of radio channels are related to on-body communications [5–7] both in static and dynamic cases. Off-body WBANs are often covered in narrowband cases [8, 9], but for UWB signals, references are found as well [10–13].

This paper reports static UWB off-body radio channel measurements with the focus on the effect of the human body on the channels. The measurements are conducted in an anechoic chamber to exclude the radio channel responses originating beyond the human body. A vector network analyzer (VNA) is applied in the frequency sweeping mode to examine the 2–8 GHz frequency band. The results extend the knowledge on the off-body UWB channels beyond the ones reported in [13] to the direction of static UWB channels. The work is a part of a larger measurement campaign reported, e.g., in [6, 7, 14, 15].

The structure of the paper is the following. In Sect. 2.2, the measurement setup is explained. Section 2.3 describes the measurement scenario with antenna locations and practical arrangements of the measurements. Section 2.4 explains the data processing methods together with the presentation of the results. Conclusions and future work plans are covered in Sect. 2.5.

2.2 Measurement Setup

Test Person and Anechoic Chamber

A 183 cm tall male test person with a 95 kg body weight was standing still in an anechoic chamber facing toward the off-body antenna pole. The chamber had a floor

size of 245 cm by 365 cm, and it was assembled by using movable absorber blocks. The test person was wearing a cotton T-shirt and jeans. All metal-containing items and shoes were absent during the measurements.

Equipment

A four-port VNA (Rohde & Schwarz ZVA-8, upper frequency limit 8 GHz) was located outside the anechoic chamber, and four 8 m long measurement cables were led into the chamber. The VNA was sweeping the 2–8 GHz frequency band 100 times with 1601 points within the band in each measurement. A more detailed list of the VNA settings can be found in [14].

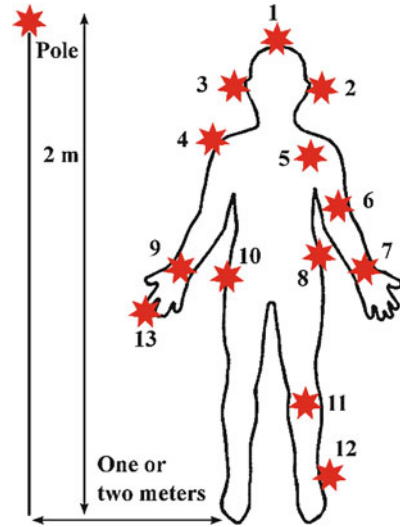
Two planar prototype antenna types were utilized in the measurements: dipole and double loop. The maximum total free space gain of the antennas is 6 dBi. The operational frequency band for the antennas is 2–12 GHz. The detailed description of the structures and the performance of the antennas, as well as the measured free space radiation patterns, are found in [16–18].

2.3 Measurement Scenario

Thirteen antenna locations were selected in different parts of the human body: the locations represent either existing or very probable sites for the on-body sensors. The off-body antenna was located on a pole at the height of 2 m. The measurements were repeated with the human-pole distances of 1 and 2 m and with both antenna types, respectively.

As depicted in Fig. 2.1, three antenna spots (1–3) are situated at the head, six at the limbs (6, 7, 9, 11–13), and four on the torso (4, 5, 8, 10). The antennas were attached three at a time on the body—due to the four-port VNA—by using elastic bands and paper tape, while the fourth one remained at the pole. A 20 mm piece of ROHACELL HF31 material was inserted to keep the antenna-body distance constant between the antennas and the body. In [17], this distance was noted to be a proper choice providing good antenna matching and channel gain characteristics close to the free space performance of the antennas.

Fig. 2.1 The antenna locations used in the measurements. The case is measured with two human-pole distances: 1 and 2 m



2.4 Results

Data Processing

The results are extracted from the channel impulse responses (CIRs) in the time domain. By this manner, the possible reflection components due to the un-idealities of the anechoic chambers can be filtered out. The CIRs are obtained from the frequency domain measurement data by applying the inverse fast Fourier transform. No windowing is applied in the transform. From the CIRs, the first arriving paths (FAPs) are considered in the calculations, i.e., considering the first multipath component. In the measurement scenario, it was noted that other multipaths are weak compared to FAP originating mainly from reflections from the body. As an anechoic chamber is used, the reflections from other sources than the body were also noted to be minor. However, utilizing more multipaths in a RAKE-type receiver would be beneficial in real-life situations, where FAP may not be necessarily the strongest CIR component. The FAPs are found out by detecting all arriving multipath components above a threshold and selecting the first component. The threshold is set to be 10 dB lower than the strongest signal component, since this value was noted to be a suitable choice to block the noise and rising edge spikes of the CIRs.

The full band of the measurements was selected for the data processing, as the division for high and low bands in the standard IEEE 802.15.6 [19] was not feasible due to the frequency band limitation of the applied VNA.

Path Loss Models Between the Antenna Sites

At first, the path losses (PLs) are compared between the different antenna sites. The PL can be expressed as

$$PL(d) = PL(d_0) + 10n \log_{10}(d/d_0) + S \quad (2.1)$$

where $PL(d)$ is the path loss in decibels at the distance of d , $PL(d_0)$ is the path loss at the used reference distance d_0 (50 mm), n is the path loss exponent, and S is a random scattering term. In the measurements in the paper, the effect of S is minor as the case is a static one measured in an anechoic chamber. The path distances d are solved from the CIRs based on the arrival time of the FAPs. The signal propagation speed in the antennas and the physical dimensions of the antennas cause delay bringing out inaccurate distance values. The explanation is as follows. After calibrating the VNA, it is assumed that the zero-delay plane is at the open ends of the measurement cables, i.e., if the cables are connected together, they show a zero delay in the time domain. When antennas are applied, two phenomena occur. Firstly, the distance between the cable ends and the phase center of the antennas causes delay, both in transmit and receive side. Secondly, the electrical parameters of the antenna parameters have an effect on the signal propagation speed v . In a lossless case, it can be stated with the well-known classical equation as

$$v = c/\sqrt{\varepsilon_r} \quad (2.2)$$

where c is the propagation of light in vacuum and ε_r is the relative permittivity of the media, i.e., in this case, the substrate material of the antenna structures. Also this effect takes place both in transmit and receive antennas.

Therefore, a correction factor is needed for this reason: the correction factors of 90 and 109 mm in distance are applied for the dipole and double loop cases, respectively. They were obtained by inserting the antennas to a carefully measured fixed distance, and the measured distance error in six relative positions to each other, for both antenna types. The correction factors are the mean values of the noted error distances in the measured positions. The effect is described in more detail in [14].

Table 2.1 presents the numerical values of n and $PL(d_0)$ based on the first-order least squares data fitting. The results are shown for the antenna sites separately and for both antenna types. The case “all” depicts the general case with all antenna locations considered jointly in the analysis. The path loss exponent is on the average 1.7 for the dipole antenna varying between the values $-0.7 \dots 4.7$. For the double loops, the path loss exponent reaches the value 1.4 on the average. The range of variation is $-4.2 \dots 1.6$. The negative values originate from firstly the shadowing effect caused by the human body. In different measurements, the test person may be situated slightly differently with respect to the off-body antenna on the pole.

Table 2.1 Path loss model values of the antenna sites

Site	Dipole		Double loop	
	n	PL(d_0) [dB]	n	PL(d_0) [dB]
1	1.65	32.8	0.9	50.3
2	2.5	16.7	1.6	29.6
3	1.4	40.4	1.4	34.5
4	2.0	25.9	1.5	30.4
5	2.3	27.8	1.4	30.4
6	1.6	28.8	0.8	38.9
7	4.7	-16.3	0.9	39.1
8	-0.7	66.9	-0.7	67.1
9	1.5	40.8	-0.9	68.9
10	1.7	29.5	0.5	45.6
11	2.9	17.5	-2.4	101.4
12	-0.4	66.8	-4.2	138.0
13	2.8	10.6	-2.4	97.0
All	1.7	32.4	1.4	35.3

Therefore, the path loss is more dependent on the degree of shadowing instead of the distance. Secondly, the antennas have been reported to have up to 30 dB variation in gain depending on the direction of radiation and the frequency [18] having a strong impact on the received signal power with only a minor change of antenna position. The effect of body shadowing and antenna radiation pattern on the classical path loss model (1) is noted earlier in [6]. The suitability of classical path loss model in WBAN cases is questioned also in [20].

Path loss exponent values between 1.28 and 3.90 have been reported in [12] for an off-body UWB case in an echoic surroundings. Therefore, the average results in Table 2.1 are in line with the ones in [12]. The path loss exponent values below two are due to the human body acting as a directing element for the electromagnetic radiation.

Absolute Path Loss

Next, the absolute path loss values are examined. Table 2.2 gathers together the obtained results for all antenna locations, both antenna types and for both measured distances. The values are extracted by averaging measured sweeps for each measurement separately. The PLs range between 50.6...66.5 dB and 49.9...68.2 dB for the dipole and double loop antenna cases, respectively. When comparing the 13 antenna location cases and both measured distances between the antennas, in 17 cases out of 26, the double loop antenna results in lower PL than the dipole. At the locations 3, 4, 5, 6, 7, 9, and 10, the double loop performs better at both distances. At the sites 1, 8, and 12, the dipole antenna shows lower PL values. Based on the

Table 2.2 Absolute measured path losses [dB]

Site	Dipole		Double loop	
	1 m	2 m	1 m	2 m
1	54.9	59.5	61.3	64.5
2	50.6	57.2	51.8	56.1
3	59.7	63.4	53.9	57.6
4	54.7	59.3	51.4	54.9
5	60.0	65.4	49.9	53.3
6	52.2	55.7	49.9	51.7
7	54.7	62.0	53.1	54.8
8	57.0	55.7	57.1	55.9
9	63.1	66.5	56.3	54.7
10	54.8	57.7	53.4	54.4
11	62.5	66.2	64.3	61.1
12	60.5	60.0	68.2	63.5
13	53.4	57.7	60.6	56.8

Table 2.3 Mean and standard deviations of the path losses [dB]

		μ	σ
Dipole	1 m	57.6	4.0
	2 m	61.3	3.9
	Both distances	59.6	4.3
Double loop	1 m	58.2	4.8
	2 m	57.8	3.9
	Both distances	58.0	4.8
Both antennas	1 m	57.9	4.9
	2 m	59.7	4.2
	Both distances	58.9	4.6

comparison, it can be stated that the double loop antenna outperforms statistically in most cases the dipole.

Table 2.3 reports the mean (μ) values of the PLs and their standard deviation (σ) in decibels. The results are shown for both antennas and distances. Also the cases where both distances are joined and both antenna data are joined are presented. The mean value is calculated from the data in Table 2.2 by averaging the PLs in linear scale and converting the result in dB. The standard deviations are obtained from the decibel-valued PLs.

The mean values lie between 57.6 and 61.3 dB. The standard deviations vary approximately between 4 and 5 dB. When both distances are examined, the double loop performs slightly better confirming the observation noted from Table 2.2. The PL for the double loop is lower at 2 m compared with the 1 m case, which is due to the dominating body shadowing and antenna radiation pattern effect over the distance dependence as discussed in the subsection “Path Loss Models Between the Antenna Sites.”

2.5 Conclusion and Future Work

The human body effects on the UWB WBAN off-body radio channels are discussed. The work is based on static measurements with a VNA set to the frequency sweeping mode at 2–8 GHz. To limit the examination on the effects originating from the human body, the measurements are conducted in an anechoic chamber. Thirteen antenna locations are selected on the body while the off-body antenna is attached to a pole at 1 or 2 m distances. The experiment is repeated with prototype dipole and double loop antennas.

By applying the classical path loss model, the average path loss exponent is found to be 1.7 (dipole) and 1.4 (double loop). The obtained path loss exponents are noted to vary largely depending on the antenna site under study. The negative exponents in some cases are a result of the dominance of the body shadowing together with the antenna pattern variation over the distance. The classical path loss model is thus found to be not always unconditionally suitable in the WBAN cases where the channel model may be rather shadowing and radiation pattern dependent than distance dependent.

The absolute path losses reach numerical values between 50.6...66.5 dB (dipole) and 49.9...68.2 dB (double loop). In the majority of cases, when examining individually the antenna spots and distances, the double loop performs slightly better than the dipole. When examining the antenna sites jointly, and/or the different distances and antenna types together, the mean values of the path losses are found to be between 57.6 and 61.3 dB and the standard deviation approximately 4...5 dB.

As a future work, it would be interesting to extend the measurements into echoic environments as well as to increase the number of measured distances and antenna sites in order to obtain more data for the data analysis. The frequency range could be extended to cover the full frequency range defined by the IEEE 802.15.6 standard for UWB by adopting a VNA with higher upper frequency limit. Furthermore, a larger set of test persons could be applied in order to investigate, e.g., the effect of the test person age, gender, and the different body parameters.

Acknowledgment This research has been financially supported in part by Academy of Finland 6Genesis Flagship (grant 318927).

References

1. Hall, P.S., Hao, Y.: *Antennas and Propagation for Body-Centric Wireless Communications*, 2nd edn. Artech House, Norwood, MA (2012)
2. Oppermann, I., Hämmäläinen, M., Iinatti, J. (eds.): *UWB Theory and Applications*. Wiley, West Sussex, England (2004)
3. Ghawami, M., Michael, L.B., Kohno, R.: *Ultra Wideband Signals and Systems in Communication Engineering*, 2nd edn. Wiley, West Sussex, England (2007)

4. Fort, A., Dessel, C., De Doncker, P., Wambacq, P., Van Biesen, L.: An ultra-wideband body area propagation channel model—from statistics to implementation. *IEEE Trans. Microwave Theory Tech.* **54**(4), 1820–1826 (2006)
5. Di Bari, R., Abbasi, Q.H., Alomainy, A., Hao, Y.: An advanced UWB channel model for body-centric wireless networks. *Prog. Electromagn. Res.* **136**, 79–99 (2013)
6. Kumpuniemi, T., Hämäläinen, M., Yekeh Yazdandoost, K., Iinatti, J.: Categorized UWB on-body radio channel modeling for WBANs. *Prog. Electromagn. Res. B.* **67**, 1–16 (2016)
7. Kumpuniemi, T., Hämäläinen, M., Yekeh Yazdandoost, K., Iinatti, J.: Human body shadowing effect on dynamic UWB on-body radio channels. *IEEE Antennas Wirel. Propag. Lett.* **16**, 1871–1874 (2017)
8. Rosini, R., D’Errico, R.: Off-body channel modelling at 2.45 GHz for two different antennas. In: *Proceedings of the 6th European Conference on Antennas and Propagation (EUCAP)*, pp. 3378–3382. IEEE, Prague, Czech Republic (2011)
9. Yoo, S.K., Cotton, S.L.: Shadowed fading in indoor off-body communications channels: a statistical characterization using the κ - μ /gamma composite fading model. *IEEE Trans. Wirel. Commun.* **17**(8), 5231–5244 (2016)
10. Ali, A.J., Scanlon, W.G., Cotton, S.L.: Pedestrian effects in indoor UWB off-body communication channels. In: *Proceedings of. 2010 Loughborough Antennas & Propagation Conference*, pp. 57–60. IEEE, Loughborough, UK (2010)
11. Catherwood, P.A., Scanlon, W.G.: Body-centric antenna positioning effects for off-body UWB communications in a contemporary learning environment. In: *Proceedings of the 8th European Conference on Antennas and Propagation (EUCAP)*, pp. 1571–1574. IEEE, The Hague, Netherlands (2014)
12. Garcia-Serna, R.-G., Garcia-Pardo, C., Molina-Garcia-Pardo, J.: Effect of the receiver attachment position on ultrawideband off-body channels. *IEEE Antennas Wirel. Propag. Lett.* **14**, 1101–1104 (2015)
13. Kumpuniemi, T., Mäkelä, J.-P., Hämäläinen, M., Yekeh Yazdandoost, K., Iinatti, J.: Dynamic UWB off-body radio channels—human body shadowing effect. In: *Proceedings of the 28th Annual IEEE International Symposium on Personal, Indoor and Mobile Radio Communications (IEEE PIMRC 2017)*, pp. 1–7. IEEE, Montreal, Canada (2017)
14. Kumpuniemi, T., Tuovinen, T., Hämäläinen, M., Yekeh Yazdandoost, K., Vuohtoniemi, R., Iinatti, J.: Measurement-based on-body path loss modelling for UWB WBAN communications. In: *Proceedings of the 7th International Symposium on Medical Information and Communication Technology (ISMICT)*, pp. 233–237. IEEE, Tokyo, Japan (2013)
15. Kumpuniemi, T., Hämäläinen, M., Tuovinen, T., Yekeh Yazdandoost, K., Iinatti, J.: Generic small scale channel model for on-body UWB WBAN communications. In: *Proceedings of the Second Ultra Wideband for Body Area Networking Workshop (UWBAN-2013) co-located with the 8th International Conference on Body Area Networks (BodyNets-2013)*, pp. 370–374. ACM, Boston, MA (2013)
16. Tuovinen, T., Kumpuniemi, T., Yekeh Yazdandoost, K., Hämäläinen, M., Iinatti, J.: Effect of the antenna-human body distance on the antenna matching in UWB WBAN applications. In: *Proceedings of the 7th International Symposium on Medical Information and Communication Technology (ISMICT)*, pp. 193–197. IEEE, Tokyo, Japan (2013)
17. Tuovinen, T., Kumpuniemi, T., Hämäläinen, M., Yekeh Yazdandoost, K., Iinatti, J.: Effect of the antenna-body distance on the on-ext and on-on channel link path gain in UWB WBAN applications. In: *Proceedings of the 35th Annual International Conference of IEEE Engineering in Medicine and Biology Society (EMBC)*, pp. 1242–1245. IEEE, Osaka, Japan (2013)
18. Kumpuniemi, T., Hämäläinen, M., Yekeh Yazdandoost, K., Iinatti, J.: Measurements for body-to-body UWB WBAN radio channels. In: *Proceedings of the 9th European Conference on Antennas and Propagation (EUCAP)*, pp. 1–5. IEEE, Lisbon, Portugal (2015)
19. IEEE Standard for Local and Metropolitan Area Networks, IEEE 802.15.6-2012—Part 15.6: Wireless Body Area networks (2012)
20. Smith, D.B., Miniutti, D., Lamahewa, T.A., Hanlen, L.W.: Propagation models for body-area networks: a survey and new outlook. *IEEE Antennas Propag. Mag.* **55**(5), 97–117 (2013)

Chapter 3

Reliable and High-Speed Implant Ultra-Wideband Communications with Transmit–Receive Diversity



Daisuke Anzai , Ilango Balasingham, Georg Fischer , and Jainqing Wang

3.1 Introduction

Nowadays, implant communications have gathered much attention in medical and healthcare applications [1]. As an example of implant communication applied applications, capsule endoscopy transmits high-quality image data from inside of a human body to outside receivers [2].

Although the data rate of the current narrow band implant communications at 400 MHz MICS and 2.4 GHz ISM bands is limited, an ultra-wideband (UWB) technology allows us to realize high-speed and reliable implant communications [3]. However, due to large attenuation of the UWB signal inside the human body, the communication performance may be significantly degraded in the case of implant transmission. For example, in the related work [4], it is reported that a communication distance of 12 cm at maximum with a data rate of 1 Mbps is achieved by UWB impulse radio (UWB-IR) transmission. However, further communication performance improvement is required to realize high-resolution image data transmission for a capsule endoscope [5].

First we develop a polarization diversity transmit antenna for implant communications. This paper then carries out a performance evaluation experiment where the developed antenna is put inside a living animal in order to investigate

D. Anzai (✉) · J. Wang
Nagoya Institute of Technology, Nagoya, Japan
e-mail: anzai@nitech.ac.jp

I. Balasingham
Oslo University Hospital, University of Oslo, Oslo, Norway

G. Fischer
Friedrich-Alexander-Universität Erlangen-Nürnberg, Erlangen, Germany

a feasibility of implant side transmit diversity experimentally. Consequently, this paper evaluates the improvement of the communication performance with the living animal experiment results.

3.2 Antenna Development for Implant Side Polarization Diversity

This paper assumes a polarization diversity at an implant transmitter as a diversity technique. In order to accomplish the polarization diversity at the implant transmitter, two planar loop antennas were combined to develop an implant-side diversity antenna [6]. Additionally, low reflection coefficient and low coupling effect between each antenna element are required to realize the polarization diversity in the UWB low band. Fig. 3.1a shows one antenna element of the developed antenna, where we used a dielectric substrate with a thickness of 1.6 mm and a relative permittivity of 4.0. Also, Fig. 3.1b demonstrates the bird's-eye view of the dual-polarized implant antenna. For the elliptical loop shown in Fig. 3.1a, the major and minor axes were set to 4.8 and 3.2 mm, respectively. Copper with a thickness of 0.1 mm was used for the loop antenna. We can see from Fig. 3.1b that one loop is arranged along a horizontal direction (on x - y plane) and the other one is arranged along a vertical direction (on y - z plane) without touching each other.

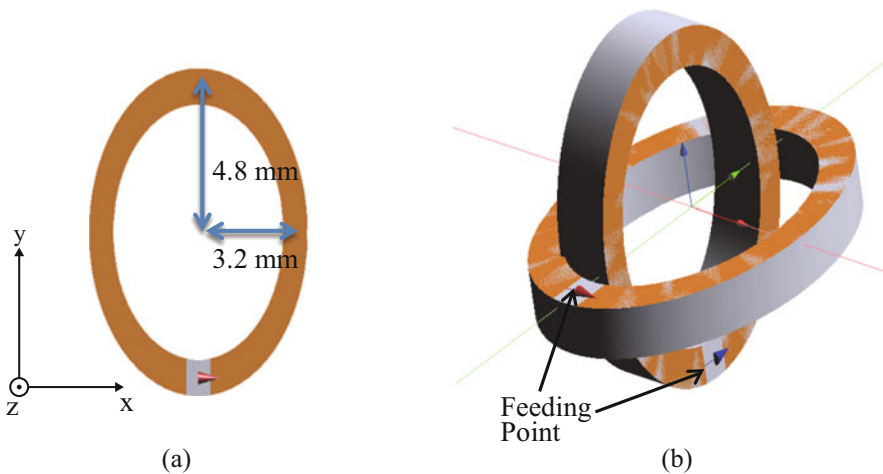


Fig. 3.1 Developed diversity antenna for implant UWB communication. (a) Planar elliptical loop antenna. (b) Bird's-eye view of the dual-polarized diversity antenna

3.3 Experimental Evaluation with a Living Animal

The developed diversity antenna was evaluated in a living animal experiment in terms of fundamental performance including the path loss characteristics. We set up the environment of the living animal experiment as shown in Fig. 3.2. As shown in the cross-sectional overview of the living animal experiment in Fig. 3.2, the developed diversity antenna was implanted to the animal body, and the receive antenna was put on the surface of the body. Laparotomy surgery was done to allow implantation of the implant-side diversity antenna at various depths within the abdominal cavity. It is important to avoid the antenna coupling through creeping waves, so we used ferrite cores on the cable entering the pig and also the point of insert was covered with electromagnetic insulator. The distance between the transmit and receive antennas was measured by using an electromagnetic tracking system, which can estimate the distance with the accuracy of 0.7 mm. To measure the path loss and coupling characteristics between the transmit and receive antennas, a vector network analyzer (Rohde & Schwarz TM ZVA67) was employed, whose ports were connected to both antennas with shielded coaxial cables. For avoiding touching with abdominal fluids and the skin of the pig, both transmit and receive antennas were covered with a layer of nitrile butadiene rubber.

Let us show the distance dependency of the average path loss characteristics at UWB low band (from 3.4 to 4.8 GHz) measured in the living animal experiment in Fig. 3.3. Figure 3.3 shows the path loss characteristics in two cases of excitation at either port one or two shown in Fig. 3.1b. The path loss characteristics on the distance between the transmit and receive antennas $PL_{\text{dB}}(d)$ can be calculated by [7]

$$PL_{\text{dB}}(d) = PL_{0,\text{dB}} + 10n \log_{10} \left(\frac{d}{d_0} \right) + S_{\text{dB}} \quad (3.1)$$

where $PL_{0,\text{dB}}$, n , and S_{dB} are the path loss at a reference distance, the path loss exponent, and the shadow fading component in dB domain, respectively. Also, d and d_0 express the communication distance and the reference communication distance, respectively. In (3.1), the former two terms represent the average characteristics

Fig. 3.2 Overview of experimental environment with a living animal

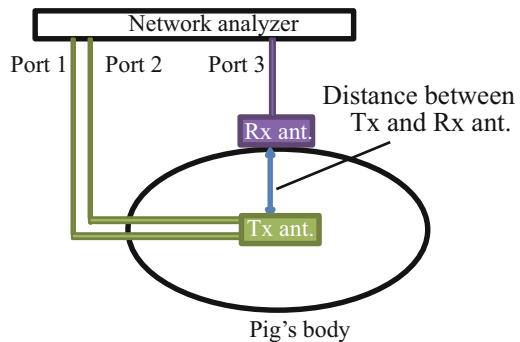


Fig. 3.3 Measured path loss performance in the experiment with the living animal

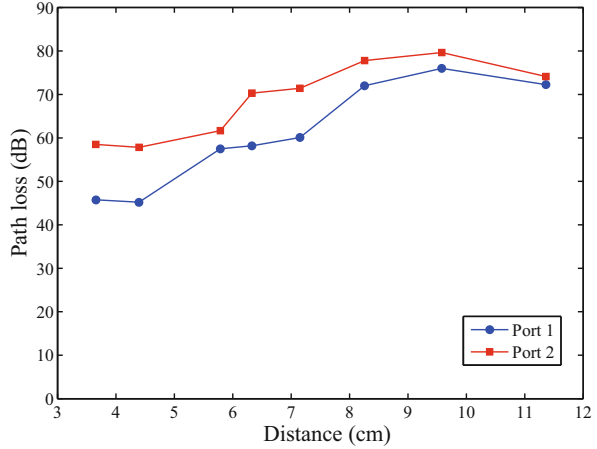


Table 3.1 Path loss characteristics obtained in the living animal experiment

	Port 1	Port 2
n (path loss exponent)	6.8	4.6
$PL_{0,\text{dB}}$ (path loss at the reference distance)	52.5 dB	63.2 dB
d_0 (reference distance)	0.05 m	0.05 m

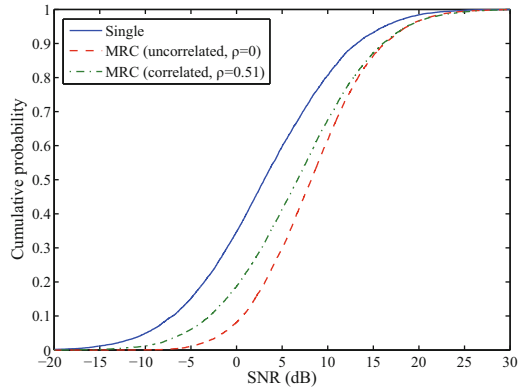
on the path loss, on the other hand, the latter term denotes the variation of the average path loss, which is affected by different internal organs inside the body. Figure 3.3 shows the measurement results of the parameters of $PL_{0,\text{dB}}$ and n . Table 3.1 summarizes the fitted parameters in (3.1). It should be noted that we achieved an acceptable level of the path loss performance because the channel parameters obtained in the living animal experiment are almost the same as the simulation results in the existing literature [7].

Improvement of Communication Performance

Then, the improvement of the communication performance by the implant side diversity system was evaluated. In this paper, the communication performance was discussed in a viewpoint of signal-to-noise power ratio (SNR). In order to perform the performance evaluation, we assume not only a case of transmit diversity with maximum ratio combining (MRC) model but also a case of single transmit antenna (namely a case without transmit diversity). In the evaluation, it was assumed that two transmit antennas were alternately used for signal transmission. For investigating the communication performance with the transmit diversity, it is important to take into consideration correlation coefficient between the two channel from each transmit

Table 3.2 Parameters of communication performance evaluation

Number of trials	1,000,000
Shadow fading model	log-normal distribution
σ (parameter of shadow fading)	1.80 [7]
n (path loss exponent)	6.8
$PL_{0,\text{dB}}$ (path loss at the reference distance)	52.5 dB
d_0 (reference distance)	0.05 m
ρ (correlation coefficient)	0, 0.51
Threshold for outage rate	-90 dBm
Transmit diversity scheme	MRC with two branches

Fig. 3.4 Cumulative distribution function of the SNR characteristics

antenna to the receive antenna. Here, we set the correlation coefficient ρ to 0.51 based on the measurement in the living animal experiment at 3.4–3.6 GHz UWB low band. Finally, Table 3.2 summarizes the simulation parameters.

The cumulative distribution function (c.d.f) on the SNR characteristics at the receiver side is demonstrated in Fig. 3.4. From the results in Fig. 3.4, the transmit diversity with the developed antenna improved the SNR by around 4 dB as compared with the single antenna case when the cumulative probability is 0.8. Furthermore, we accomplished similar SNR improvement in the two cases for the correlated and perfectly uncorrelated cases, which means that the correlation coefficient obtained in the developed transmit antenna is acceptable for the polarization diversity.

Finally, we discuss SNR performance improvement with transmit–receive diversity technique. In the case of the receive diversity, the SNR improvement of 3 dB was reported in the literature [8]. In addition, the transmit–receive diversity can independently accomplish the diversity gains of the transmit and receive diversities. Hence, if we introduce the receive diversity technique to the implant side transmit polarization diversity with the developed antenna, the total improvement of the SNR performance should be achieved to around 7 dB.

3.4 Conclusions

In this paper, for realizing the implant side diversity, we have developed a dual-polarization antenna for implant communications. Also, an experiment with a living animal experiment has been carried out to evaluate the performance improvement with the transmit–receive diversity system. We have evaluated the improvement of the communication performance with the dual-polarization diversity based on the correlation coefficient obtained from the experiment. Consequently, the transmit–receive diversity has accomplished 7 dB improvement in the SNR characteristics from the case with a single antenna.

Acknowledgement This research is supported in part by the MIC/SCOPE #185106002, Japan.

References

1. Wang, J., Wang, Q.: *Body Area Communications*. Wiley/IEEE, Singapore/Piscataway (2012)
2. Iddan, G., Meron, G., Glukhovsky, A., Swain, P.: Wireless capsule endoscopy. *Nature* **405**, 417 (2000)
3. Yuce, M.R., Dissanayake, T.: Easy-to-swallow wireless telemetry. *IEEE Microw. Mag.* **13**(6), 90–101 (2012)
4. Anzai, D., Katsu, K., Chavez-Santiago, R., Wang, Q., Plettemeier, D., Wang, J., Balasingham, I.: Experimental evaluation of implant UWB-IR transmission with living animal for body area networks. *IEEE Trans. Microw. Theory Tech.* **62**(1), 183–192 (2014)
5. Chavez-Santiago, R., Balasingham, I., Bergsland, J., Zahid, W., Takizawa, K., Miura, R., Li, H.: Experimental implant communication of high data rate video using an ultra wideband radio link. In: *Proceedings of the IEEE Conference on Engineering in Medicine and Biology Society (EMBC) 2013, Osaka, Jul. 2013*, pp. 5175–5178
6. Shimizu, Y., Anzai, D., Santiago, R.C., Floor, P., Balasingham, I., Wang, J.: Performance evaluation of an ultra-wideband transmit diversity in a living animal experiment. *IEEE Trans. Microw. Theory Tech.* **65**(7), 2596–2606 (2017)
7. Shi, J., Anzai, D., Wang, J.: Channel modeling and performance analysis of diversity reception for implant UWB wireless link. *IEICE Trans. Commun.* **E95-B**(10), 3197–3205 (2012)
8. Takizawa, K., Aoyagi, T., Hamaguchi, K., Kohno, R.: Performance evaluation of wireless communications through capsule endoscope. In: *Proceedings of the IEEE Conference on Engineering in Medicine and Biology Society (EMBC) 2009, Minneapolis, Sept. 2009*, pp. 6897–6900

Chapter 4

A Finite Integration Technique-Based Simulation Study on the Impact of the Sternotomy Wires on the UWB Channel Characteristics



Mariella Särestöniemi, Carlos Pomalaza-Raez, Timo Kumponiemi, Matti Hämäläinen , and Jari Iinatti

4.1 Introduction

Recently, in-body, or also called intra-body, communication has become an intensively studied topic in the field on wireless body area networks (WBAN). Numerous channel models have been presented to describe the in-body channel characteristics [1–4]. Implant communication has also raised interest recently. Studies relating to the channel between the on-body antenna and the implant or between the implants have been under the scope [5, 6]. However, the impact of the medical implants on the radio channel characteristics is scarcely studied topic. A study on the impact of the aortic valve implant on the channel characteristics was a pioneering work in this field, as shown in [7], which was later continued in [8–10].

Furthermore, medical wires, staples, and bands, which are used for the closure after the operation [11], can have significant impact since usually they are located close to the skin and hence close to the on-body antennas and sensor nodes. Besides, they usually contain titanium, steel, and other highly conductive material.

The impact of sternotomy wires on the UWB on-body channel characteristics was studied first time in [10] using measurement data-based evaluations. It was shown that the sternotomy wires may cause additional peaks in the impulse response since the wires form like loops which store and release energy to different directions. Besides, the signal may propagate faster via the wires.

The main contribution of this paper is to present, for the first time, a simulation-based study on the impact of the sternotomy wires on the UWB radio channel

M. Särestöniemi (✉) · T. Kumponiemi · M. Hämäläinen · J. Iinatti
Centre for Wireless Communications, University of Oulu, Oulu, Finland
e-mail: mariella.sarestoniemi@oulu.fi

C. Pomalaza-Raez
Department of Electrical and Computer Engineering, Purdue University, West Lafayette, IN, USA

characteristics and verify the simulation results with the measurement data and propagation calculations. The simulator is based on the finite integration technique (FIT), which is known to be among the best techniques in the propagation prediction in the vicinity of the human body [12, 13]. After we can verify that the simulation is possible and model is satisfactory, it is possible to develop and investigate the transceiver's structures for in-body communications.

This paper is organized as follows: Sect. 4.2 describes the study case. Section 4.3 summarizes the calculated propagation paths. Section 4.4 presents the numerical results. The summary and conclusion are given in Sect. 4.5.

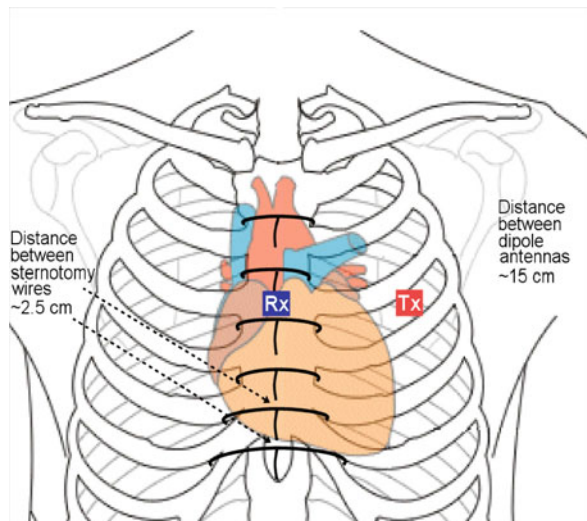
4.2 Study Case

Sternotomy Wires

Sternotomy wiring is the most commonly used technique in the sternum closing after the operation that requires opening the sternum. The sternotomy wires are 1 mm wide, made from steel, and they are wrapped around the sternum, as shown in Fig. 4.1. The distance between the sternotomy wires is approximately 2.5 cm, but it depends on the area of the sternum where the wires are located [11].

Figure 4.1 illustrates also the location of the on-body antennas in this study. The transmitter antenna, Tx, is located in the left side of the sternum, whereas the receiver antenna, Rx, is located in the middle of the sternum. The distance between the antennas is 15 cm. The distance between the antenna and the skin surface is 4 mm.

Fig. 4.1 Location of the sternotomy wires in the sternum



Simulation Model

In this study, a simplified layered human body tissue model has been used to evaluate the radio propagation in the vicinity and inside the human body. The layer model, presented in Fig. 4.2, consists of the following tissues: skin, fat, muscle, bone, cartilage (cart.), heart, blood vessel, lung, and anterior mediastinum (ant. med). Due to simplicity, tissues are modeled as rectangular blocks. The dimensions of the tissues are designed according to [4], as well as according to the X-ray figure of the implanted volunteer assisted in this study. The dielectric properties for different tissues were found in [16].

Furthermore, the sternotomy are modeled in the layer model. The layer model without the sternotomy wires is used as a reference study case. Dipole antennas, which were presented for on- and off-body communication in [14], were used in this study. The details of the antenna structure and radiation patterns are found in [14].

Simulations were conducted using the CST MicrowaveStudio (MWS) simulation software (CST) [15] for frequency bandwidth 0–10 GHz. The number of the samples within the simulated bandwidth was 2134. In this case, TX antenna is noted as Antenna 1 and RX antenna as Antenna 2. The simulator provides reflection coefficients $S_{1,1}$ and $S_{2,2}$, as well as channel responses $S_{2,1}$ and $S_{1,2}$ as an output. These results are then compared in the wire and non-wire cases, as well as verified with the measurement data.

Measurement Data

The aim of this study is to verify simulation results with measurement data presented in [10]. The details of the measurement scenario are explained in [10], and thus this section only briefly summarizes the measurement setup.

The measurements were taken in an anechoic chamber with two volunteers. One of them has sternotomy wires in his sternum. Besides, this volunteer has a titanium-based aortic valve implant, which also has an impact on the channel characteristics as shown in [7, 10]. However, the time window, in which the impact of the aortic valve implant is visible (>5 ns), is out of the scope of this study, and we merely focus on the time window where impact of the sternotomy wires is visible.

The measurements were conducted with Vector Network Analyzer (VNA) 8720ES in frequency domain to obtain channel frequency response (S_{21}) and reflection coefficients S_{11} and S_{22} . Frequency bandwidth used in the measurements was 3.1–10.6 GHz. Number of frequency points per sweep was set to 1601. Radio channel frequency response was then later transformed into time domain in Matlab using inverse fast Fourier transform (IFFT) to get impulse response.

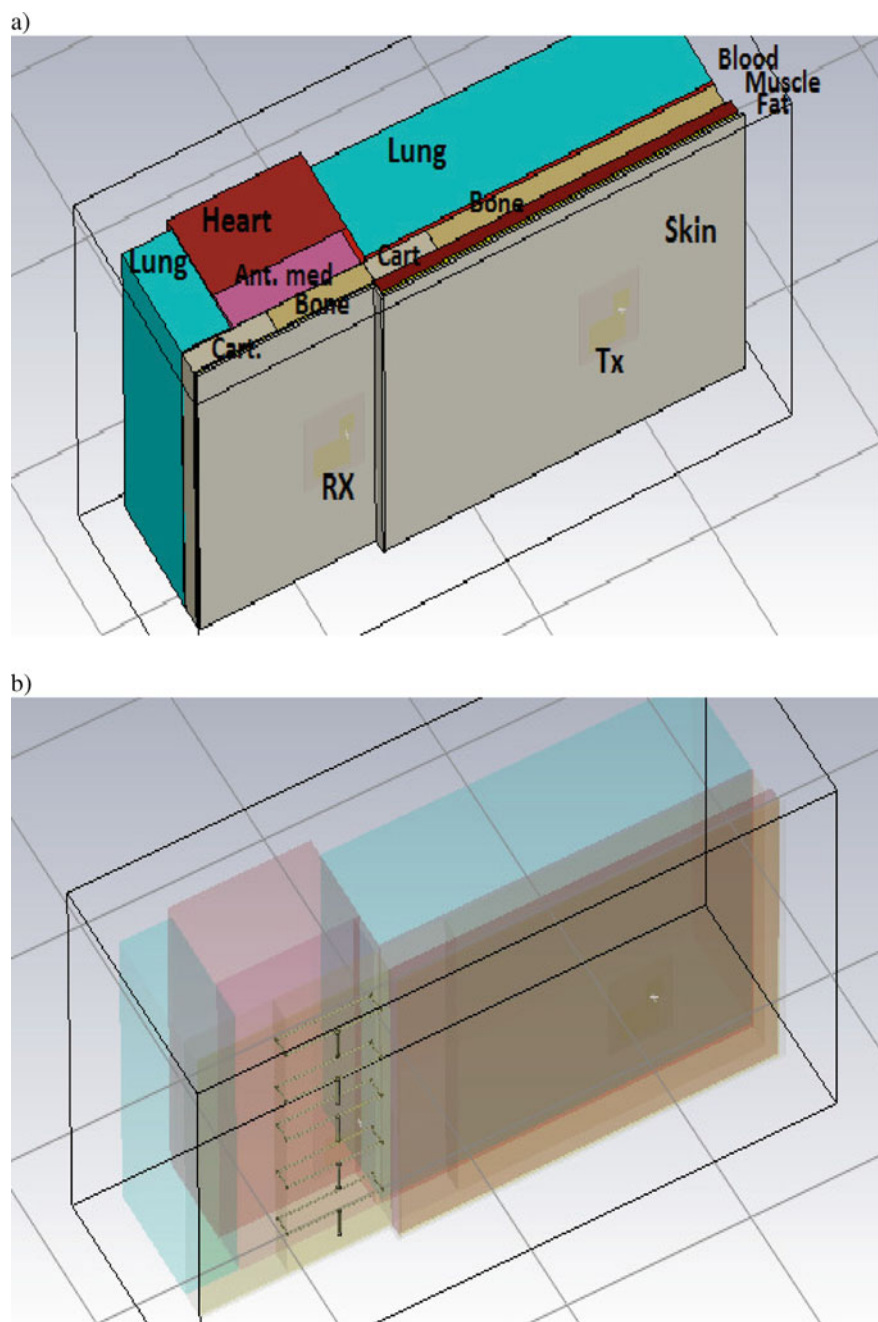


Fig. 4.2 Tissue layer models without (a) and with (b) the sternotomy wires

4.3 Propagation Paths

In this section, different propagation path options are presented. The path options are calculated similar to [10] taking account the frequency, dielectric properties of the tissue, and the distance travelled through the tissue. First, the velocity of the propagation signal in the i th tissue is calculated as

$$v_{i,f} = \frac{c}{\sqrt{\varepsilon_{i,f}}}, \quad (4.1)$$

where $\varepsilon_{i,f}$ is the relative permittivity of a tissue at frequency f . This value, and also other dielectric properties of different tissues, can be found, e.g., in [16]. Table 4.1 summarizes $\varepsilon_{i,f}$ for the tissues used in the model. Once we know the velocity, we can easily calculate the propagation time in each of the tissues having a length of d_i using

$$t_{i,f} = \frac{d_i}{v_{i,f}}, \quad (4.2)$$

which are then summed up to obtain overall propagation time.

The propagation distance d_i may vary for tissues depending if it goes along the tissue or through the tissue. Propagation distance $d_{i:s}$ is marked in the brackets for each propagation path options when it differs from the previous path's case.

In the presence of the wires, part of the signal may travel through wires which makes the propagation much faster. Besides, due their loop form, the wires absorb the energy and then release it afterward in several directions. As explained in [10], this can be seen as additional or stronger peaks in the impulse responses. Furthermore, the sternotomy wires, which are located above or below the antenna, can have some impact as well since the propagating signal can be diffracted from the above-/below-located wires toward the Rx antenna. Besides, the signal travels

Table 4.1 Relative permittivity for the tissues used in the layer model [16]

Tissue	2 GHz	4 GHz	6 GHz	8 GHz	10 GHz
Skin	38.6	36.6	34.9	33.2	37.5
Fat	5.32	5.12	4.94	4.76	4.6
Muscle	53.3	50.8	48.4	45.5	42.8
Lung	31.2	32.3	30.95	29.0	27.4
Anterior mediastinum	57.87	54.91	51.72	48.42	45.15
Blood vessel	59.0	55.7	52.5	48.61	45.11
Bone	19.6	16.95	15.2	13.83	12.61
Heart	58.8	52.0	52.2	45.37	42.24
Cartilage	39.8	35.6	31.8	28.47	25.63

easily through the wires and their twisted ends so there will be summed up more signal energy than in the reference case.

The expected propagation paths within the tissue layer model are presented in Table 4.2. Since the idea of calculating the propagation paths is presented in [10], this paper just summarizes the path options.

Denotation bone/wire means that the signal travels through the bone and sternotomy wires in the simulation layer model with sternotomy wires. In the reference case, the signal travels through the bone. The calculated propagation times are summarized in Table 4.3. Denotations Path 2 and Path 2w refer to the propagation path 2 in the reference case without sternotomy wires and with sternotomy wires, respectively.

Table 4.2 Propagation path options

Path	Tissues and their dimensions within the path
Path 1a	Skin (15 cm)
Path 1b	Skin (0.2 cm)-fat (15 cm)-skin(0.2 cm)
Path 2	Skin (0.2 cm)-fat (0.1 cm)-muscle (0.6 cm)-bone (rib, 10.5 cm)-cartilage (2 cm)-bone (sternum, 1.5 cm)/wire-fat (0.1 cm)-skin (0.2 cm)
Path 3	Skin-fat-muscle-bone (rib, 1 cm)-blood (13.5 cm)-bone (sternum, 1.5 cm)/wire-fat-skin
Path 4	Skin-fat-muscle (13.5 cm)-bone sternum (1.5 cm)wire-fat-skin
Path 5	Skin-fat-muscle (11.5 cm)-cartilage (2 cm)-sternum bone/wire-fat-skin
Path 6	Skin-fat-muscle-bone-lung (13.5 cm)-anterior mediastinum (2 cm)-bone (sternum)/wire-fat-skin
Path 7	Skin-fat-muscle-bone-lung (13.7 cm)-heart (2 cm)-anterior mediastinum-bone (sternum)/wire-fat-skin

Table 4.3 Propagation times for propagation paths

Path/frequency	2 GHz	4 GHz	6 GHz	8 GHz	10 GHz
Path 1a	3.14 ns	3.06 ns	2.99 ns	2.94 ns	2.94 ns
Path 1b	1.18 ns	1.21 ns	1.14 ns	1.10 ns	1.08 ns
Path 2	2.81 ns	2.73 ns	2.71 ns	2.54 ns	2.48 ns
Path 2w	2.64 ns	2.55 ns	2.51 ns	2.38 ns	2.31 ns
Path 3	3.30 ns	3.20 ns	3.20 ns	3.02 ns	2.94 ns
Path 3w	3.20 ns	3.12 ns	3.17 ns	2.95 ns	2.86 ns
Path 4	3.527 ns	3.45 ns	3.507 ns	3.294 ns	3.22 ns
Path 4w	3.411 ns	3.34 ns	3.34 ns	3.184 ns	3.11 ns
Path 5	3.462 ns	3.34 ns	3.424 ns	3.205 ns	3.12 ns
Path 5w	3.346 ns	3.26 ns	3.311 ns	3.095 ns	3.01 ns
Path 6	3.501 ns	3.40 ns	3.458 ns	3.235 ns	3.15 ns
Path 6w	3.385 ns	3.29 ns	3.345 ns	3.126 ns	3.04 ns
Path 7	4.0 ns	3.84 ns	3.88 ns	3.64 ns	3.55 ns
Path 7w	3.8 ns	3.68 ns	3.73 ns	3.5 ns	3.51 ns

Path 2 = reference, Path 2w = wire case, etc.

4.4 Numerical Results

In this section, the simulation results are examined by comparing the wired and non-wired simulation model cases. The results are reflected to the propagation path options presented in the previous section. Furthermore, the results are verified with the measurement data.

At first, we compare the results in frequency domain. Figure 4.3a, b presents reflection coefficients $S_{1,1}$ for antenna 1 (on the left side of the chest) and $S_{2,2}$ for

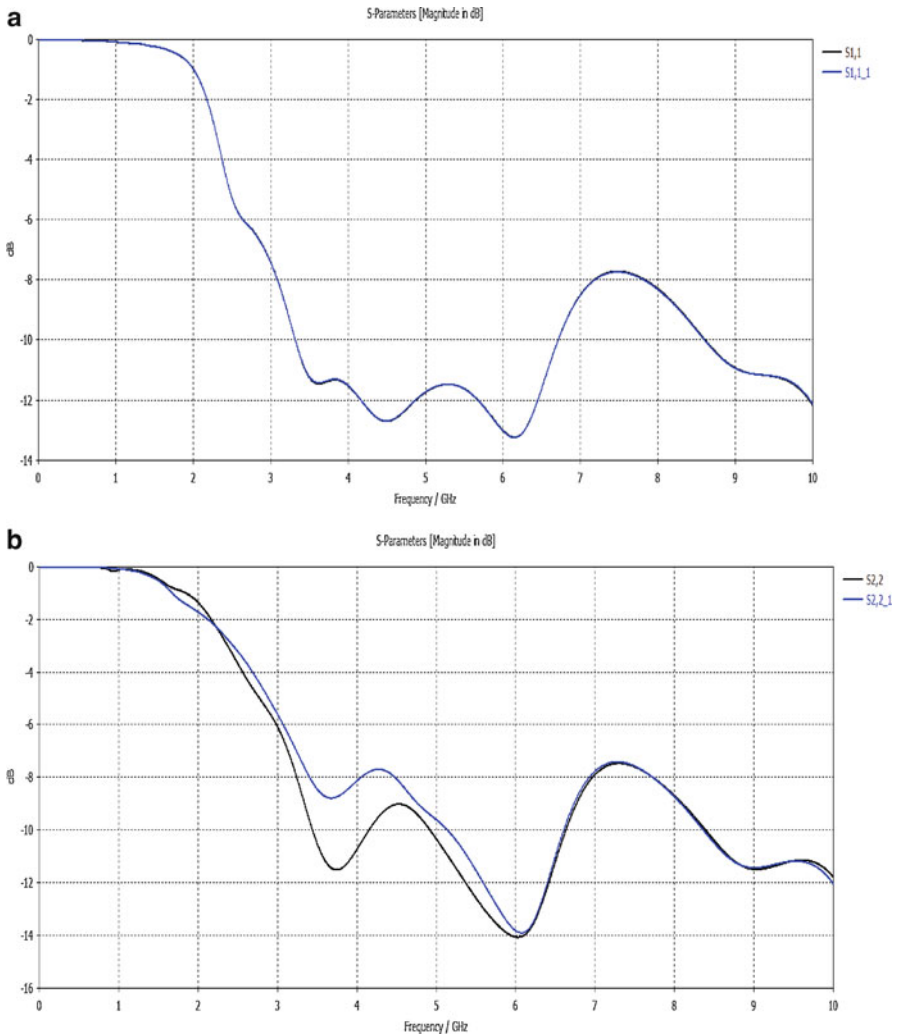


Fig. 4.3 (a) Simulated reflection coefficients for antenna 1 with sternotomy wires ($S_{1,1}$) and without the sternotomy wires ($S_{1,1,1}$) and (b) for antenna 2 with sternotomy wires ($S_{2,2}$) and without the sternotomy wires ($S_{2,2,1}$)

antenna 2 (in the middle of the sternum), respectively. The results obtained with the simulation model with sternotomy wires are marked as S1,1 or S2,2, and they are plotted as black curves. The reference case, i.e., the results obtained with the layer model without the sternotomy wires, is denoted as S1,1_1 and S2,2_1 and plotted as blue curves.

As it can be noticed from Fig. 4.3a, there is no difference between the reflection coefficients S1,1 and S1,1_1, since the sternotomy wires are enough far away from the antenna 1 to have any impact on the reflection coefficient. Thus, the S1,1 and S1,1_1 curves are equal, and they are completely overlapping. Instead, in the reflection coefficients of antenna 2, which is exactly above the sternotomy wires, one can notice a difference clearly, especially at frequency range 3–6 GHz.

Figure 4.4 presents the channel response for the wired (S2,1) and non-wired cases (S2,1_1). There is only some small differences in the lower part of the frequency range. However, despite of small changes in frequency domain, we can see more differences in time domain results presented in Figs. 4.5, 4.6, and 4.7. Figures 4.5 and 4.6 present the impulse response obtained by performing IFFT for the whole frequency bandwidth 0–10 GHz, up to 5 ns and up to 16 ns, respectively. Figure 4.7 presents the impulse response obtained by performing IFFT for the bandwidth 3.1–10.6 GHz, which corresponds to the bandwidth used in the measurements.

When comparing the impulse responses in Fig. 4.5, we can notice that the main peaks are at the same level, but there are changes in the following side peaks. The

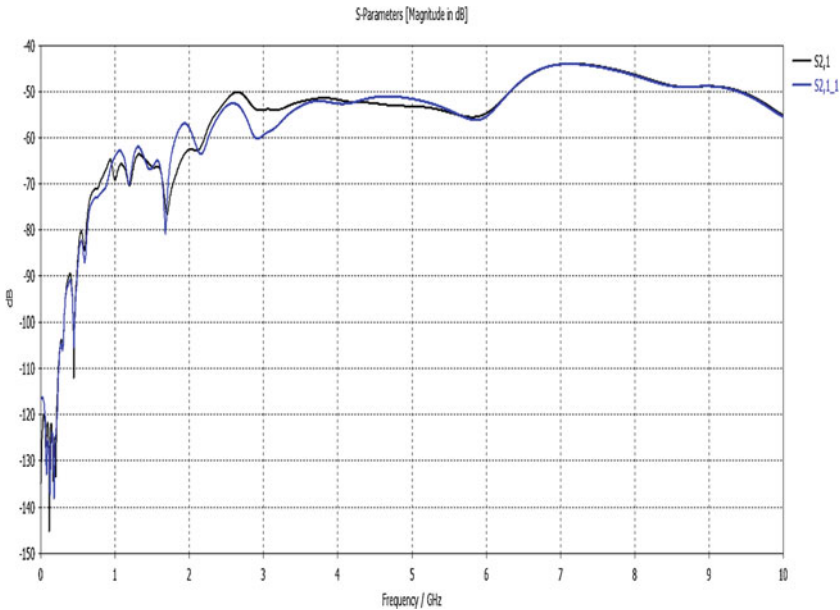


Fig. 4.4 Simulated channel parameter with sternotomy wires (S2,1) and without the sternotomy wires (S2,1_1)

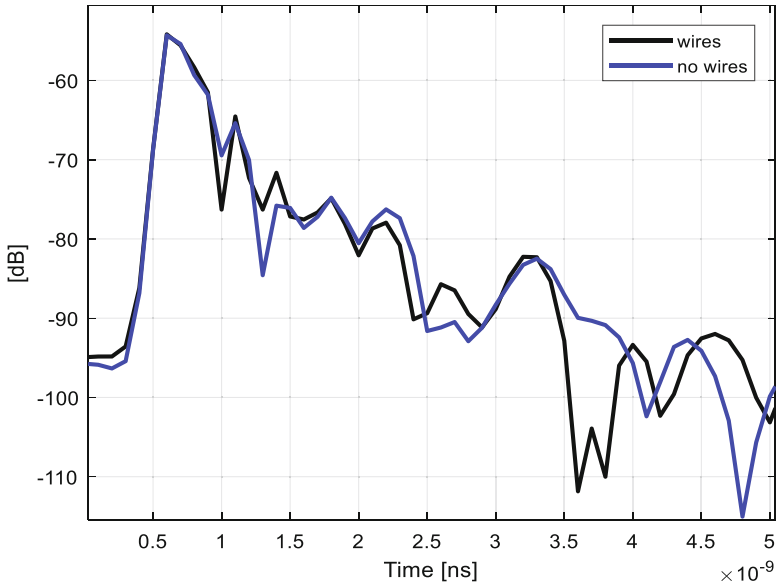


Fig. 4.5 Simulated impulse responses for wired and non-wired cases as the IFFT is performed for 0–10 GHz, presented up to 5 ns

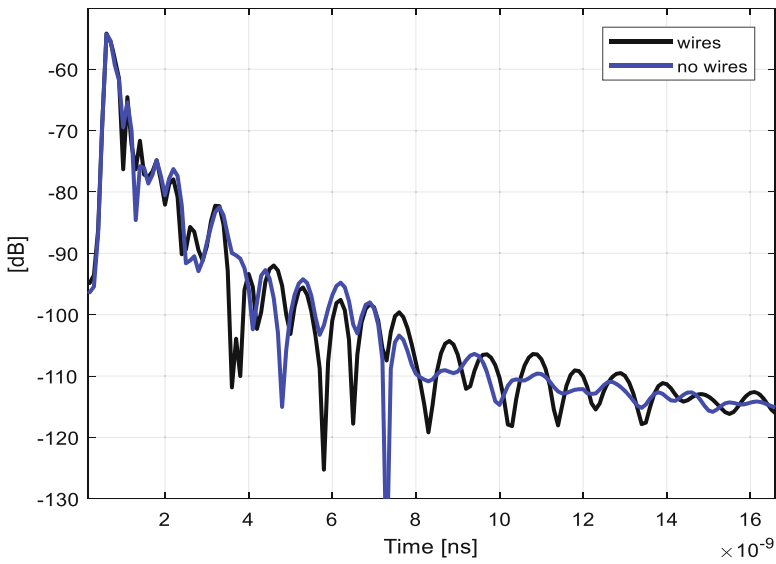


Fig. 4.6 Simulated impulse responses for wired and non-wired cases as the IFFT is performed for 0–10 GHz bandwidth, presented up to 16 ns

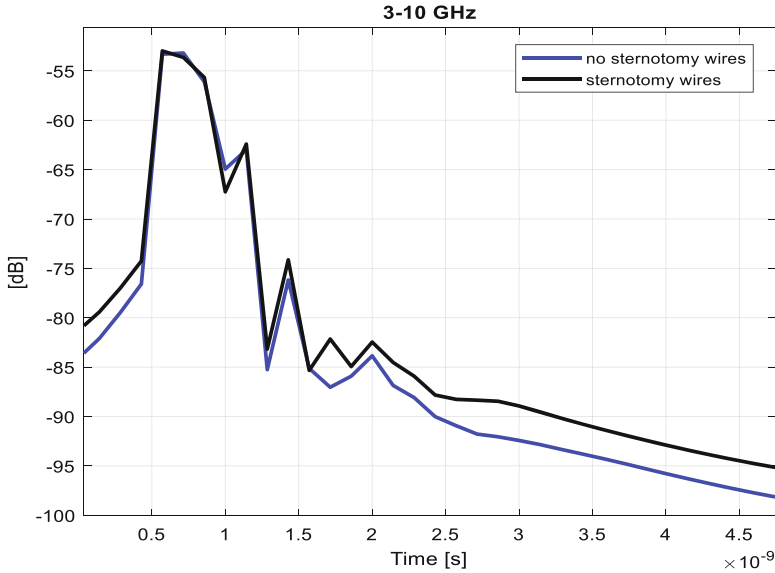
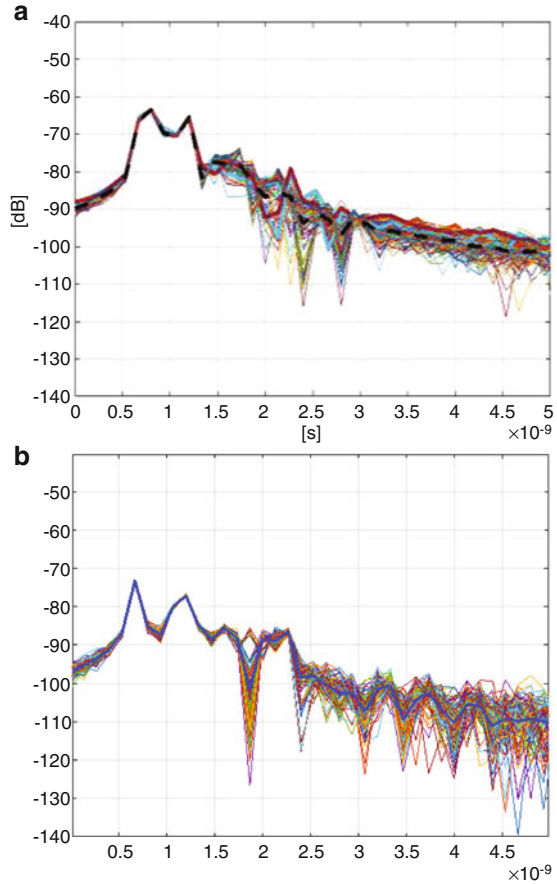


Fig. 4.7 Simulated impulse responses for wired and non-wired cases as the IFFT is performed for 3–10 GHz bandwidth

location of the peaks match well with the propagation path calculations presented in Table 4.2. According to the calculations, the impact of the wires should be seen at time instants 1.0–1.2 ns (Path 1b), 2.5–2.8 ns (Path 2), and 3.5–4.0 ns (rest of the paths). In the impulse responses, the difference between the wired and non-wired cases appears slightly earlier than expected from the propagation path calculations, starting before 1 ns. Besides, at this early time instant the impulse response of the wired case is at lower level than that of the non-wired case. This can be due to the wires' tendency to store energy and later release it like a solenoid as explained earlier. We can note an additional peak at the time instant 1.4 ns in the IR of the wired case. This additional peak occurs 0.2 ns later than the peak of the propagation path through the fat layer (Path 1b, 1.2 ns). The additional peak is due to signal reflected from the sternotomy wires located 2.5 cm above and below the Rx antenna. After the reflection, the signal further travels through the fat layer to the Rx antenna. Propagation time for the signal travelling the distance of 2.5 cm in the fat tissue is approximately 0.2 ns, resulting in 1.4 ns overall propagation time for the reflected signal.

The time window 3.5–4.0 ns, which corresponds to Path option 7, is interesting: we can notice that there is a clear peak at this time range, much stronger than in the wired model case. Normally the peaks are stronger when the wires are influencing. This may be due to the fact that the signal propagating through the lungs until the heart and then to anterior mediastinum is already strongly attenuated when reaching the wires. There might not be enough energy they could accumulate to release it afterward, like in the Path 2's case. As explained earlier, the wired loops absorb

Fig. 4.8 Measured impulse responses (a) with and (b) without the wires [10]



the energy and then release it afterward in several directions. In the case of Path 7, the released energy that is in the direction of the antenna might be too weak to be recognized in the channel response. Figure 4.6 presents the impulse responses for the larger time range, up to 16 ns. There we can see the oscillating effect due to the wires at the lower dB levels.

Next, we compare the results with the measurement data. The impulse responses obtained from the measurements are presented in Fig. 4.8a, b, for wire case and non-wire case, respectively. These two measured impulse response figures have already been presented in [10], but they are repeated in this paper to enable smooth comparison between the measurement and simulation results. One should note that the measurement data is obtained with the volunteer having also an aortic valve implant besides of the sternotomy wires. However, based on the propagation calculations presented in [10], we know the time window at which aortic valve effect appears, and thus we focus only on the time window up to the aortic valve effect.

When comparing simulated IRs in Fig. 4.5 to measured IRs in Figs. 4.8a, b, one can note the clear similarity in the shapes of the simulated and measured impulse responses since the locations of the side peaks with respect to the main peak are similar. However, the delays due to the unidealities in the measurements, such as the delays due to the antennas, etc. [17], should be taken into account. Instead, there are clear differences in the level of the peaks, especially in the main peaks. In the simulated impulse responses, the main peak level is approximately at 55 dB, and there is no difference between the wired and non-wired case. With the measurement data, the level with wired model is around -62 dB and non-wired model -72 dB. The level difference is surprisingly high. Level differences may be due to different body shapes, different antenna attachments, different clothing, unidealities in the antenna prototyping, etc.

As explained in the Sect. 4.2, the measurement was conducted for the frequency band 3.1–10.6 GHz. Thus, it is relevant to compare measured impulse responses with Fig. 4.7, in which IFFT was performed for the simulated channel response within the frequency range 3.1–10.6 GHz. We notice that in this case, the shapes of the simulated and measured impulse responses are even more similar but only until 2 ns, after which the simulated impulse responses fade completely. Apparently, the resolution of the 7.5 GHz bandwidth with the selected simulation settings is not enough to show the peaks after 2 ns.

4.5 Summary and Discussion

In this paper, we have presented FIT-based simulation study on the impact of the sternotomy wires on the UWB on-body channel characteristics. The results are verified with the measurement data and propagation path calculations. In the simulations, we used human tissue layer model, whose dimensions were designed taking into account the volunteer's body size. It was found that there is a clear correspondence between simulated and measurement results. Besides, the location of the peaks in the simulated impulse response matches well with the propagation path calculations.

The benefit of using a human tissue layer model in this kind of study is that we can design the layer model according to the dimensions of the volunteer. The implanted volunteer who assisted in our measurements is lean; hence his fat tissue is very thin. Since the propagation loss in the fat tissue is high, the impact of the sternotomy wires is assumed to be clearer in the cases of lean people. Our next target is to study the impact of the body structure on sternotomy wire effect.

The knowledge about the impact of sternotomy wires on the channel characteristics is important because the additional peaks or stronger side peaks may cause some interference on the monitoring devices. It should be noted that in this study, we used antennas designed for on- and off-body communication. With antennas designed for in-body communication (used, for instance, in the capsule endoscopy localization),

the impact of the sternotomy wires is presumably even more significant, which belongs to our next research plan as well.

Acknowledgments This research has been financially supported by the project WBAN Communications in the Congested Environments and in part by Academy of Finland 6GGenesis Flagship (grant 318927).

References

1. Turalchuk, P., Munina, I., Pleskachev, V., Kirillov, V., Vendik, O., Vendik, I.: In-body and on-body wave propagation: modeling and measurements. In: International Workshop on Antenna Technology: Small Antennas, Innovative Structures, and Applications (iWAT), 2017
2. Amon, N.R., Mahbub, I., Saha, P.K.: Propagation characteristics of ultra-wideband pulse in multilayered human chest tissue. In: International Conference on Electrical Engineering and Information Communication Technology (ICEEICT), 2016
3. Dove, I.: Analysis of Radio Propagation Inside the Human Body for in-Body Localization Purposes. University of Twente, Netherland (2014)
4. Sahu, K.N., Naidu, C.D., Satyam, M., Jaya Sankar, K.: Study of RF signal attenuation of human heart. *Hindawi J. Eng.* **2015**, 484686 (2015)
5. Li, J., Nie, Z., Liu, Y., Wang, L., Hao, Y.: Characterization of in-body radio channels for wireless implants. *IEEE Sensors J.* **17**(5), 1528–1537 (2017)
6. Garcia-Pardo, C., Fornes-Leal, A., Cardona, N., Brovoll, S., Aardal, O., Hamran, S.-E., Chavez-Santiago, R., Berland, J., Balasingham, I., Palomar, R.: Experimental ultra wideband path loss model for implant communication. In: IEEE International Symposium on Personal Indoor and Mobile Radio Communications (PIMRC), 2016
7. Taparugssanagorn, A., Pomalaza-Ráez, C., Isola, A., Tesi, R., Hämäläinen, M., Iinatti, J.: UWB channel modeling for wireless body area networks in medical applications. In: Applied Sciences in Biomedical and Communication Technologies (ISABEL), 2009
8. Taparugssanagorn, A., Pomalaza-Ráez, C., Isola, A., Tesi, R., Hämäläinen, M., Iinatti, J.: Preliminary UWB channel study for wireless body area networks in medical applications. *Int. J. Ultra Wideband Commun. Syst.* **2**(1), 14–22 (2011)
9. Yang, W.-B., Sayrafian-Pour, K., Hagedorn, J., Terrill, J., Yazdandoost, K.Y., Taparugssanagorn, A., Hämäläinen, M., Iinatti, J.: Impact of an aortic valve implant on body surface UWB propagation: a preliminary study. In: Proceedings of the 5th International Symposium on Medical Information and Communication Technology, 2011
10. Särestöniemi, M., Kumpuniemi, T., Hämäläinen, M., Pomalaza-Raez, C., Iinatti, J.: Impact of the sternotomy wires and aortic valve implant on the on-body UWB radio channel. In: Publish in ISMICT 2018, March 2018
11. Elfström, A., Grunditz, A.: Evaluation of sternum closure techniques using finite element analysis. Master thesis, Medical Engineering, The Royal Institute of Technology, Sweden (2013)
12. Särestöniemi, M., Hämäläinen, M., Iinatti, J.: An overview of electromagnetic propagation based channel modeling techniques for wireless body area network applications. In: IEEE Access, 2017
13. Pellegrini, A., Brizzi, A., Zhang, L., Ali, K., Hao, Y., Wu, X., Constantinou, C.C., Nechayev, Y., Hall, P.S., Chahat, N., Zhadobov, M., Sauleau, R.: Antennas and propagation for body-centric wireless communications at millimeter-wave frequencies: a review [wireless corner]. *Antennas Propag. Mag. IEEE.* **55**, (2013)

14. Tuovinen, T., Yekeh Yazdandoost, K., Iinatti, J.: Comparison of the performance of two different UWB antennas for the use in WBAN on-body communications. In: 6th European Conference on Antennas and Propagation (EUCAP), 2012
15. CST Microwave Studio, [Online]. <http://www.cst.com>
16. <https://www.itis.ethz.ch/virtual-population/tissue-properties/database/dielectric-properties>
17. Kumpuniemi, T., Tuovinen, T., Hämäläinen, M., Yekeh Yazdandoost, K., Vuohoniemi, R., Iinatti, J.: Measurement-based on-body path loss modelling for UWB WBAN communications. In: The 7th International Symposium on Medical Information and Communication Technology (ISMICT2013), Tokyo, Japan, 6–8 March 2013

Part II
Smart Body Area Networks

Chapter 5

Joint Throughput and Channel Aware MAC Scheduling for SmartBAN



Rida Khan and Muhammad Mahtab Alam

5.1 Introduction

Wireless body area networks (WBANs) are becoming self-evident and a well-known research discipline due to numerous potential applications in future, ranging from health-care environments to mission critical operations [1]. A typical WBAN consists of various sensor nodes for measuring diverse set of biomedical data and a coordinator or hub node to monitor and regulate those sensor nodes. Standardized protocols are required to ensure proper functionality at the desired quality level in WBANs as well. Among several standards dedicated to WBANs, such as IEEE 802.15.4 [2, 3], was the first officially recognized standard to provide guidelines about WBAN operation [4]. However, European Telecommunications Standards Institute (ETSI) introduced another WBAN specific standard termed as Smart Body Area Network (SmartBAN) [5] with a comparatively simplified and efficient physical (PHY) and medium access control (MAC) structure [6].

SmartBAN supports a significantly high symbol rate of 1 MSymbols/s [7] with many different options for payload sizes that are pre-defined in control channel beacon by hub [8]. However, the packet reception rate (PRR) performance starts degrading for transmission power levels below -5 dBm and increased packet sizes as the WBAN links are shadowed by human body [9]. In order to provide PHY-MAC performance gain, the provision of data packet repetition is supported at the SmartBAN PHY layer [7]. The importance of this repetition is highlighted in [10] in which data repetition is deemed necessary to get the acceptable 1% frame error rate under high interference scenario.

R. Khan (✉) · M. M. Alam
Thomas Johann Seebeck Department of Electronics, Tallinn University
of Technology, Tallinn, Estonia
e-mail: rikhan@ttu.ee; muhammad.alam@ttu.ee

One of the most common MAC approach in WBAN is scheduled access mechanism in which every sensor node is assigned a dedicated time slot for data transmission to the BAN coordinator. But, for any given application, every sensor node requires different data transmission rate [11]; therefore, the slot allocation to WBAN sensor nodes should be adapted according to their prescribed data transmission intervals. Moreover, an average difference of 10 dBs is reported in the pathloss measurements of a space-time varying WBAN communication link [12], leading to the conclusion that variations in radio link quality can have a considerable effect on PRR performance. These phenomena motivate the research on dynamic slot scheduling to enhance the effective throughput, energy efficiency, and PHY-MAC performance. Many noteworthy research contributions have been made in this domain but most of them focus on either minimizing energy consumption while keeping higher PRR or proposing channel estimation techniques to enhance PRR under dynamic environments. Addressing the throughput, energy efficiency, and PRR performance requirements of emerging wearable applications, a joint throughput and channel aware dynamic scheduling algorithm was proposed in [13] in compliance with the IEEE 802.15.6 scheduled access mechanism. The algorithm was demonstrated to be successful in providing better PRR performance keeping the transmission power, and hence the energy consumption levels substantially low. Our initial simulation results on SmartBAN indicated that even the repetition was not able to achieve above 90 % PRR at lower transmission power, which is often favored in WBAN communications for energy efficiency and reduced interference for multiple co-located BANs. Therefore this study is dedicated to the performance analysis of SmartBAN in the context of required throughput and channel aware scheduling for prospective WBAN applications.

This paper addresses the effective throughput, energy consumption, and reliability concern of potential WBAN applications under dynamic and realistic conditions in SmartBAN. A joint throughput and channel aware dynamic MAC scheduling algorithm is presented incorporating the SmartBAN proposed scheduled access technique. Various mobility patterns, including walking, sitting, standing, and running, are generated using bio-mechanical mobility modeling to analyze the performance at different channel conditions for several sensor-hub links. The primary contributions of this paper are: (1) Enhancing the throughput and channel aware MAC scheduling algorithm for SmartBAN complaint scheduled access method. (2) Evaluating the reference SmartBAN MAC scheduled access mechanism with and without repetitions for performance comparison. (3) Providing performance gain in terms of PRR and energy consumption, with possible effects on latency.

The remainder of this paper is organized in the following way: Sect. 5.2 provides an overview of the mobility and radio link modeling, while Sect. 5.3 explains SmartBAN MAC superframe format considered in simulations. Section 5.4 elaborates the reference SmartBAN MAC scheduling with and without repetitions as well as throughput and channel aware MAC scheduling for SmartBAN. In Sect. 5.5, performance results are presented and discussed comprehensively, whereas Sect. 5.6 concludes this paper.

5.2 Mobility and Radio Link Modeling

The underlying mobility and radio link modeling for PHY-MAC performance analysis is presented in this section.

Channel Model

We use IEEE 802.15.6 proposed CM3-B channel model in order to compute pathloss values for space-time varying distances and link types, as shown

$$PL_{\text{dB}} = -10\log_{10}(P_0e^{-m_0d} + P_1) + \sigma_P n_P [\text{dB}], \quad (5.1)$$

where $P_0 = -25.8$ dB, $m_0 = 2.0$ dB/cm, $P_1 = -71.3$ dB, $\sigma_P = 3.6$ dB, n_P is the Gaussian random variable with zero mean and unity variance, d is the distance in cm, and PL_{dB} is the pathloss in dBs [14].

Mobility Modeling

Bio-mechanical mobility modeling, as proposed in [15], is used to generate dynamic distances and link types for various on-body links between sensor nodes and coordinator. The dynamic distances serve as input distances in the CM3-B model to provide pathlosses for dynamic mobility scenarios. Furthermore, the space-time varying link types are used to characterize the given link as line of sight (LOS) or non-line of sight (NLOS). In case of NLOS link status, an additional NLOS factor of 13% is added to the calculated pathloss [16]; otherwise, the pathloss remains the same.

Radio Link Modeling

The precise mobility and channel modeling of dynamic links is followed by accurate radio link modeling. This modeling consists of SNR, bit error rate (BER), and packet error rate (PER) computations. We utilize the similar approach as performed in [15] for radio link modeling with few modifications in BER calculations for SmartBAN.

BER with No Repetition

SmartBAN standard proposes Gaussian frequency shift keying (GFSK) modulation technique at the physical layer with the bandwidth-bit period product BT and modulation index h of 0.5 [7]. According to [17], for $h = 0.5$ frequency shift keying modulation becomes minimum shift keying modulation, and therefore, the corresponding BER expression becomes

$$P_e \left(\frac{E_b}{N_0} \right) = Q \left(\sqrt{2\epsilon \frac{E_b}{N_0}} \right), \quad (5.2)$$

where $\frac{E_b}{N_0}$ is the signal-to-noise ratio for a bit, ϵ is a constant [18] and for BT of 0.5, is equal to 0.79 [19]. The detailed calculation of $\frac{E_b}{N_0}$ using pathloss and SNR values can be found in [15].

BER with Repetition

BER for this case is computed using the similar BER expression as provided in the previous subsection but SNR calculations are made in accordance with the diversity technique used for evaluating the repetition gain. Since maximal ratio combining (MRC) provides the best performance over all diversity combining techniques, we assume MRC diversity scheme for evaluating the best case scenario performance that SmartBAN can provide with repetition. In MRC with statistically independent transmission channels, the output SNR is equal to the addition of instantaneous SNRs at the individual links [17].

5.3 SmartBAN MAC Superframe Format

This section provides a detailed explanation about the SmartBAN MAC superframe format that is considered for MAC scheduling in this paper, as illustrated in Fig. 5.1. The transmissions between node and hub take place on data channels and the data channel used for transmission is partitioned into inter-beacon intervals or superframe durations. The beginning of each superframe is marked by a data channel beacon (D-Beacon), followed by scheduled access period for data transmissions by sensor nodes and corresponding acknowledgements. Control and management period is used for management and control signaling by hub and/or sensor nodes and the entire superframe duration ends with an inactive period [8]. Each scheduled access slot is made of physical-layer protocol data unit (PPDU) transmissions and PPDU acknowledgements separated by interframe spacing (IFS). The actual payload is found in MAC frame body that along with MAC header and frame parity constitutes a MAC protocol data unit (MPDU). Since, we assume uncoded MPDU

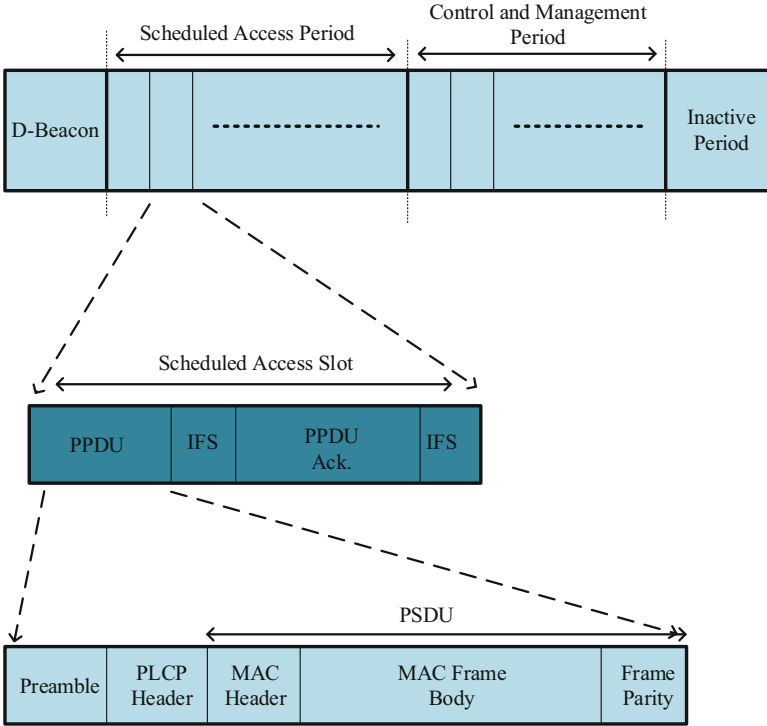


Fig. 5.1 SmartBAN MAC superframe format

in our case, the resultant MPDU becomes physical-layer service data unit (PSDU). PSDU, after the addition of physical-layer convergence protocol (PLCP) header and preamble, creates a complete PPDU [7], as depicted in Fig. 5.1.

For superframe duration computation, it is necessary to first calculate the beacon duration, time slot duration and the number of time slots in scheduled access period, time slot duration and the number of time slots in control and management period, and the duration of inactive period. D-beacon duration is found as

$$T_{Beacon} = \frac{N_{Beacon}}{R_{Sym}}, \quad (5.3)$$

where N_{Beacon} is the number of bits in D-beacon and R_{Sym} is the symbol rate. The duration of each time slot in scheduled access period is found according to a predefined parameter L_{SLOT} [8], as under

$$T_{SLOT} = T_{min} \times L_{SLOT}, \quad (5.4)$$

where T_{min} is the minimum duration for any scheduled access slot. We do not assume any inactive period in our simulations, while the calculations for control and management period will be provided in the later sections for each case of SmartBAN MAC scheduling.

Within a single time slot during scheduled access period, there is acknowledgement and IFS duration as well. IFS duration is fixed and the duration for acknowledgement is written as

$$T_{ACK} = \frac{N_{preamble} + N_{PLCPheader} + N_{parity} + N_{MACheader}}{R_{Sym}}, \quad (5.5)$$

where $N_{preamble}$, $N_{PLCPheader}$, N_{parity} , and $N_{MACheader}$ are the number of bits in physical-layer preamble, PLCP header, MAC frame parity, and MAC frame header, respectively. After the computation of T_{ACK} , the effective duration for PPDU transmission is given as

$$T_{TX} = \frac{T_{SLOT} - T_{ACK} - 2 \times T_{IFS}}{REP}, \quad (5.6)$$

where REP is the number of PPDU repetitions. The calculation of T_{TX} is followed by the computation of maximum allowed MAC frame body size for uncoded MPDU, as under

$$Payload = T_{TX} \times R_{Sym} - N_{preamble} - N_{PLCPheader} - N_{parity} - N_{MACheader}. \quad (5.7)$$

5.4 MAC Scheduling with m-Periodicity

This section discusses SmartBAN MAC scheduling with m-periodic slot assignment for reference MAC with and without repetition as well for traffic and channel aware MAC.

SmartBAN MAC Scheduling without Repetition

For applications with sensor nodes having a variety of data generation rates, it becomes unnecessary to allocate a fixed time slot for every node inside MAC superframe. Therefore, the time slots inside the scheduled access period are assigned based on their data generation rates. The m-periodic slot assignment considered in this case is depicted in Fig. 5.2. In the given scheme, the priority node P, based on high data generation rate and/or emergency traffic, is assigned time slot in consecutive superframes, while the other low traffic nodes periodically wake up

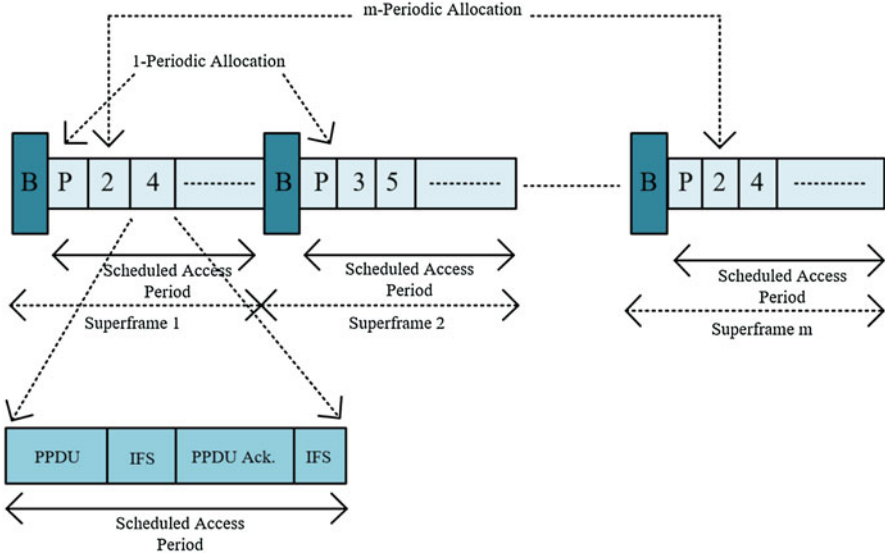


Fig. 5.2 m-Periodic MAC scheduling and scheduled access slot without repetition for SmartBAN

to send their data after a fixed number of m superframes, defined by their required data rate. As shown in Fig. 5.2, we assume only scheduled access period along with data beacons in superframe duration, unless stated otherwise, in order to evaluate the performance for transmitted data packets only. It should be noted that all the sensor nodes are assumed to have their respective time slots pre-assigned by coordinator based on the packet generation rates. Therefore, under reference SmartBAN m-periodic MAC scheduling without repetitions, each time slot consists of PPDU transmission followed by PPDU acknowledgement and both separated by IFS. Each inter-beacon duration comprises of time slots assigned on the basis of m-periodicity principle.

Scheduled Access Slot with Repetition for SmartBAN

In this scenario, the transmitted PPDU is repeated within the assigned time slot for each node, so the effective payload size for a given slot length is reduced. Consequently, for sending the same amount of data, sensor nodes would be required to assign time slots more often with reduced payload sizes. At reception, the repeated PPDUs are combined using MRC technique. Figure 5.3 illustrates the scheduled access time slot structure with repetition for SmartBAN. The remaining m-periodic scheduled access method is the same as described in section “SmartBAN MAC Scheduling Without Repetition.”

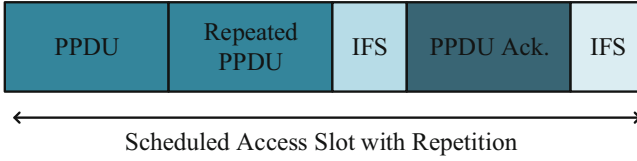


Fig. 5.3 Scheduled access slot with 2 repetitions for SmartBAN

Throughput and Channel Aware MAC Scheduling for SmartBAN

This scheduled access mechanism has slightly different superframe structure from the previous scheduling strategies since the time slots are dynamically assigned based on the SNR level and the availability of data packet. As indicated in Fig. 5.4, superframe now includes control and management period as well in which hub dynamically assigns time slots to sensor nodes for data transmission during scheduled access period in the next superframe. Every sensor node periodically wakes up during the control and management period which contains the slot re-assignments for every node. The slot goes to sleep mode for energy conservation if it is not assigned any slot; otherwise, the node remains in low power mode and wakes up for data transmission just before the start of the slot. The flow chart of the algorithm for slot assignment is given in Fig. 5.5. During the first step, each time slot is checked for the SNR conditions of every node-hub link and a set of sensor nodes is defined for which the link SNR is greater than a pre-defined threshold value. In the second step, the set of sensor nodes with good links is checked for priority node. If priority node is among the candidate sensor nodes and it has data packet to send, it is assigned the time slot, else other low priority nodes are assigned the given slot based on their data packet status. In order to define the SNR threshold for the first phase, a PER value of 0.1 is considered to obtain the PRR above 90% and reverse radio link computations are performed to acquire the corresponding SNR threshold. The required PER value of 0.1 gives the resultant BER value using the relation $PER = 1 - \left(1 - P_e \left(\frac{E_b}{N_0}\right)\right)^N$, where N is the packet size in bits, which in turn provides $\frac{E_b}{N_0}$ after evaluation in (2). The required SNR can be obtained using the equation $\frac{E_b}{N_0}[\text{dB}] = \text{SNR}[\text{dB}] + 10 \times \log_{10}\left(\frac{BW}{R}\right)$, where BW is the channel bandwidth which is 2 MHz and R is the information rate which is 1M Symbols/s for SmartBAN. The appropriate SNR threshold found for SmartBAN standard using this method is 7 dB or higher to get a resulting PRR above 90%.

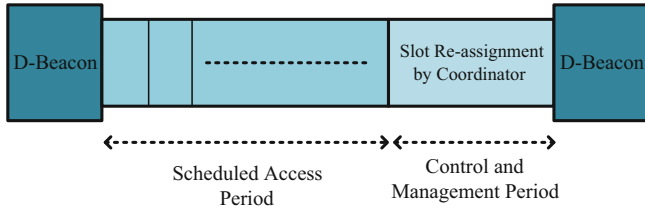
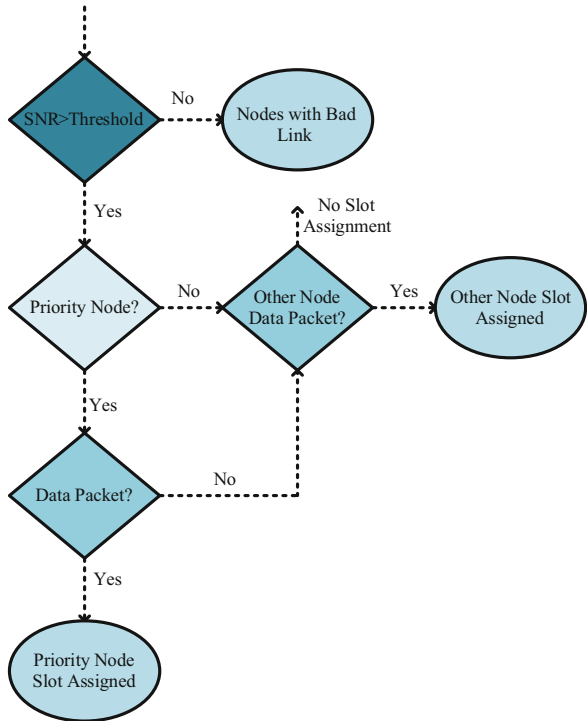


Fig. 5.4 Superframe format for joint throughput and channel aware scheduled access MAC

Fig. 5.5 Throughput and channel aware MAC scheduling algorithm



5.5 Performance Evaluation

This section analyzes the performance results of the reference SmartBAN MAC scheduling with and without repetition and the presented throughput and channel aware MAC scheduling in terms of PRR, energy consumption, and latency.

Simulation Setup

For the performance assessment of the above mentioned scheduled access mechanisms, we consider a rescue and emergency management application scenario [20] with six sensors and a coordinator node located on chest. Each sensor collects information about different parameters which include body temperature, pulse rate, GPS coordinates, blood pressure, user mobility, and voice commands, with their corresponding data rate requirements of 2.4 bps, 48 bps, 96 bps, 1.2 kbps, 4.8 kbps, and 100 kbps [16]. These sensors are, respectively, placed on the right wrist, left wrist, right knee, left elbow, left knee, and right shoulder, as shown in Fig. 5.6. In order to have better energy efficiency and reduced interference over the surrounding WBANs, we consider rather low transmission power levels of -10.9 dBm, defined for RN4020 Bluetooth low energy (BLE) devices [21]. Three mobility patterns (walking, sit-stand, and running) are assumed in all simulations and $L_{SLOT} = 4$ is taken to define T_{SLOT} . According to the calculations made in Sect. 5.3, T_{SLOT} is found to be equal to 2.5 ms, while T_{Beacon} is 128 μ s. Since the reference SmartBAN MAC scheme is not assumed to have control and management period, 66 superframes can be transmitted every second while for throughput and channel aware SmartBAN MAC scheduling scheme, 65 superframes are sent every second. Table 5.1 summarizes all the major simulation setup parameters. The voice communication node is given priority status because of its higher data generation rate and assigned time slot in every consecutive superframe for all scheduling scenarios. For reference SmartBAN MAC, body temperature, pulse rate, blood pressure, and GPS sensor nodes are allocated time slot after every 65 superframes, while the motion sensor node is provided time slot after every 21 superframes. For reference SmartBAN MAC scheduling with 2 repetitions ($REP = 2$), the maximum allowed payload size is reduced and body temperature, pulse rate, and GPS sensor nodes send their packets after every 65 superframes. Blood pressure node is allocated time slot after every 32 superframes, whereas the motion sensor node is assigned a time slot after every 10 superframes. For reference SmartBAN MAC with 4 repetitions ($REP = 4$), body temperature, pulse rate, and GPS sensor nodes are given time slots after every 65 superframes, blood pressure sensor node is assigned a time slot after every 15 superframes, and motion sensor node can send data after every 4 superframes. Finally, for throughput and channel aware SmartBAN MAC, body temperature, pulse rate, blood pressure, and GPS sensor nodes have slot allocation after every 64 superframes, while the motion sensor node sends data after every 20 superframes.

Fig. 5.6 Coordinator and sensor nodes placements

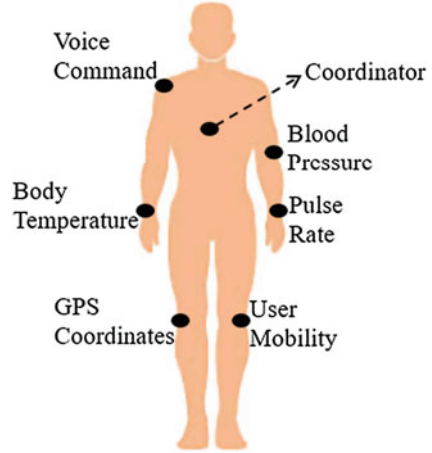


Table 5.1 Simulation setup parameters

<i>RF parameters</i>	
Transmitter power (dBm)	-10.9
Receiver sensitivity (dBm)	-92.5
Current consumption Tx (mA)	15
Current consumption Rx (mA)	16
Bandwidth per channel (MHz)	2
<i>PHY/MAC parameters</i>	
Minimum slot length (T_{min})	625 μ s
Slot duration (T_{SLOT})	2.5 ms
Beacon duration (T_{Beacon})	128 μ s
Interframe spacing (IFS)	150 μ s
Symbol rate (R_{Sym})	10^6

Simulation Results

Packet Reception Rate (PRR)

Figure 5.7 summarizes the PRR results for each link between different sensor nodes and the coordinator node, under walking, sit-stand, and running mobility scenarios. In this scenario, links corresponding to the voice communication, pulse rate, body temperature, motion detection, positioning, and blood pressure are, respectively, identified as Link1, Link2, Link3, Link4, Link5, and Link6. It can be observed that throughput and channel aware MAC scheduling in SmartBAN outperforms the reference SmartBAN MAC schemes with and without repetition due to appropriate slot assignment. Despite using packet repetitions with MRC technique, a significant improvement in performance is not observed because of data transmission under poor channel conditions. Moreover, SmartBAN reference MAC scheduling gives severely degraded PRR performance for some links under certain mobility patterns

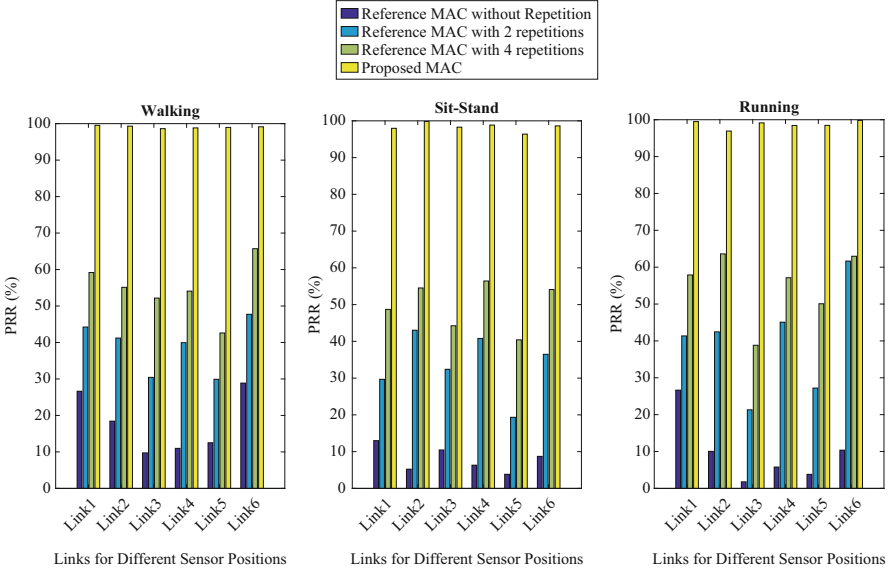


Fig. 5.7 Packet Reception Rate (PRR) in % under: walking, sit-stand, and running mobility profiles

primarily because of shadowing by body posture. For example, Link4 and Link5 in which sensor nodes are placed on left and right knees experience the worst performance in sit-stand posture as they are shadowed by human torso most of the time. Also, in running scenario, the links corresponding to wrists and knees have lower PRR for reference SmartBAN MAC without any repetition and with 2 repetitions because of the higher pathloss associated with higher mobility.

Energy Consumption

The energy consumption in joules for each transmitted packet by a sensor node is given as

$$E_J = T_{TX} \times 3_{Volts} \times I_{mA}, \quad (5.8)$$

where I_{mA} is the current consumption in mA. Figure 5.8 illustrates the energy consumption profile for various links under the given mobility scenarios. These results are computed for the total number of packets transmitted in a given duration for all links, mobility profiles, and the previously discussed MAC-layer scheduling schemes, as given in Table 5.2. The energy consumption is generally the highest for priority node-hub link since this node sends data packet the most often; however, the implementation of throughput and channel aware scheduling leads to better

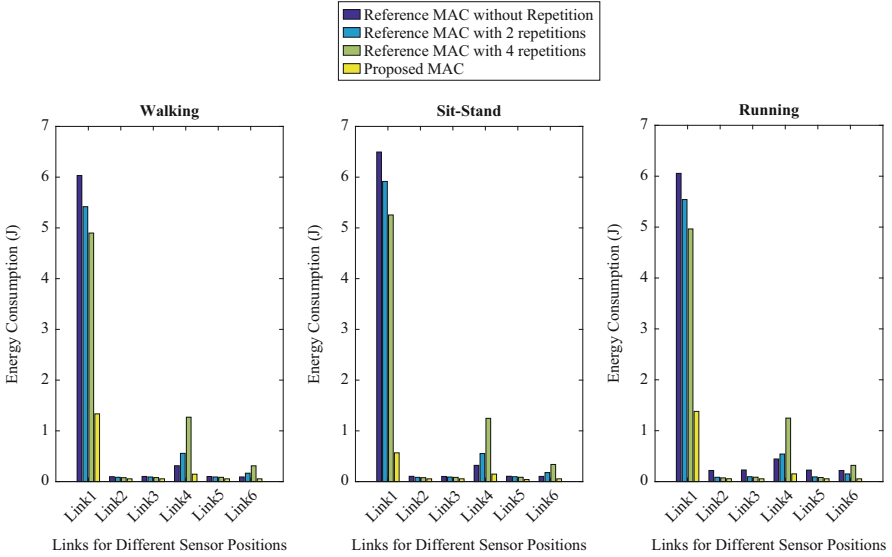


Fig. 5.8 Energy Consumption in joules under: walking, sit-stand, and running mobility profiles

energy efficiency because of opportunistic data transmission over good links. The energy consumption observations for reference SmartBAN MAC with and without repetition do not have any noticeable dissimilarities, except for Link1 which has an average energy consumption difference of 1.2J between reference MAC without repetition and reference MAC with 4 repetitions scheduling schemes. Also, the energy consumption with repetitions is slightly increased for the links having higher data rates as their related nodes send data more frequently.

Latency

The packet latency is found as the time difference between the generated and the received data packet. Figure 5.9 provides latency results for each link considering the given MAC scheduling schemes. Link1 has the lowest latency in all mobility profiles since it is associated with the priority node which sends data in consecutive superframes. In addition, the links having lower data generation rates generally seem to have higher latencies in all mobility scenarios. Latency is also dependent on the link quality as the links having poor SNR usually do not lead to successful packet receptions, resulting in higher latencies. Therefore, the links with lower PRRs for reference SmartBAN MAC schemes are observed to have higher latencies as well. For example, Link3 has the worst PRR performance in running posture which is reflected in its associated latency result as well. The latency for throughput and channel aware SmartBAN MAC is also noticeably higher for Link2, Link3,

Table 5.2 Number of packets transmitted

	Walking	Sit-stand	Running
<i>SmartBAN reference MAC without repetition</i>			
Link1	37,312	37,250	37,464
Link2	575	574	1235
Link3	575	574	1235
Link4	1777	1774	2453
Link5	575	574	1235
Link6	575	574	1235
<i>SmartBAN reference MAC with 2 repetitions</i>			
Link1	37,312	37,250	37,464
Link2	575	574	577
Link3	575	574	577
Link4	3732	3726	3747
Link5	575	574	577
Link6	1167	1165	1171
<i>SmartBAN reference MAC with 4 repetitions</i>			
Link1	37,312	37,250	37,464
Link2	575	574	577
Link3	575	574	577
Link4	9328	9313	9366
Link5	575	574	577
Link6	2488	2484	2498
<i>Throughput and channel aware SmartBAN MAC</i>			
Link1	14,256	5960	14,718
Link2	583	583	586
Link3	583	582	586
Link4	1548	1565	1606
Link5	583	415	586
Link6	583	582	586

Link5, and Link6 in sit-stand mobility scenario which can be traced back to their corresponding lower PRR values and lower data generation rates.

5.6 Conclusion

This paper provides an overview about the effectiveness of different SmartBAN MAC scheduling strategies considering PRR, energy consumption, and latency as criteria. The conventional SmartBAN scheduled access MAC schemes with and without repetition as well as a throughput and channel aware dynamic MAC scheduling scheme are evaluated in this context for multiple on-body links. The simulation results in terms of PRR and energy consumption certainly recommend

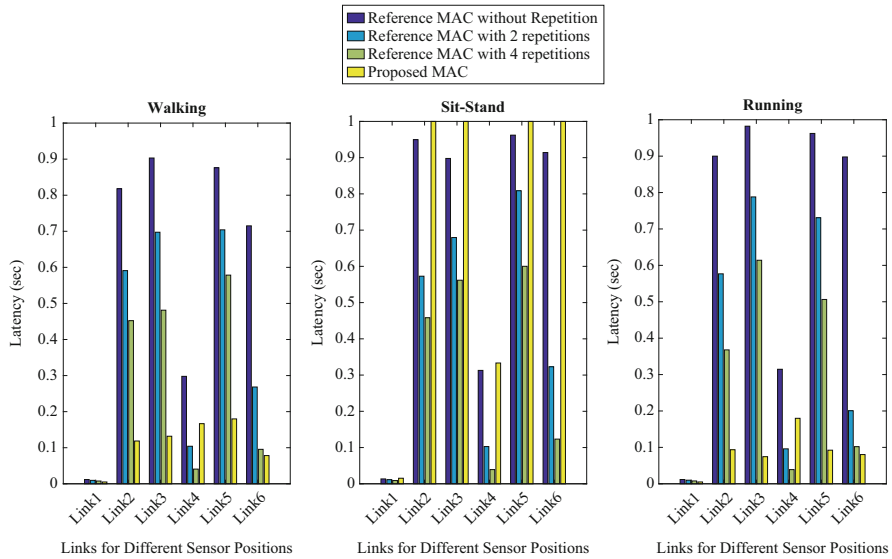


Fig. 5.9 Latency in seconds under: walking, sit-stand, and running mobility profiles

the dynamic scheduling, based on channel and data packet availability, for reliable and energy efficient data transmission.

Acknowledgements This research was supported by the Estonian Research Council through the Institutional Research Project IUT19-11, and by the Horizon 2020 ERA-chair Grant “Cognitive Electronics COEL” H2020-WIDESPREAD-2014-2 (Agreement number: 668995; project TTU code VFP15051).

References

1. Movassaghi, S., Abolhasan, M., Lipman, J., Smith, D., Jamalipour, A.: Wireless body area networks: a survey. *IEEE Commun. Surv. Tutorials* **16**(3), 1658–1686 (2014)
2. Scazzoli, D., Kumar, A., Sharma, N., Magarini, M., Verticale, G.: Fault recovery in time-synchronized mission critical ZigBee-based wireless sensor networks. *Int. J. Wireless Inform. Netw.* **24**(3), 268–277 (2017)
3. Scazzoli, D., Kumar, A., Sharma, N., Magarini, M., Verticale, G.: A novel technique for ZigBee coordinator failure recovery and its impact on timing synchronization. In: *Proceedings of the IEEE 27th Annual International Symposium on Personal, Indoor, and Mobile Radio Communications (PIMRC)*, pp. 1–5. IEEE, Valencia (2016)
4. IEEE Xplore Digital Library Homepage. <https://ieeexplore.ieee.org/document/6161600>. Last accessed 26 May 2018
5. Hamalainen, M., Paso, T., Mucchi, L., Girod-Genet, M., Farserotu, J., Tanaka, H., Chin, W.H., Ismail, L.N.: ETSI TC SmartBAN: overview of the wireless body area network standard. In: *Proceedings of the IEEE 9th International Symposium on Medical Information and Communication Technology*, pp. 1–5. IEEE, Piscataway (2015)

6. ETSI SmartBAN Homepage. http://www.etsi.org/deliver/etsi_tr/103300_103399/103394/01_01_01_60/tr_103394v010101p.pdf. Last accessed 26 May 2018
7. ETSI SmartBAN Homepage. http://www.etsi.org/deliver/etsi_ts/103300_103399/103326/01_01_01_60/ts_103326v010101p.pdf. Last accessed 26 May 2018
8. ETSI SmartBAN Homepage. http://www.etsi.org/deliver/etsi_ts/103300_103399/103325/01_01_01_60/ts_103325v010101p.pdf. Last accessed 26 May 2018
9. Khan, R., Alam, M.M.: Joint PHY-MAC realistic performance evaluation of body-to-body communication in IEEE 802.15.6 and SmartBAN. In: Proceedings of the IEEE 12th International Symposium on Medical Information and Communication Technology. IEEE, Australia (2018)
10. Viittala, H., Mucchi, T., Hamalainen, M.: Performance of the ETSI SmartBAN System in the Interfered IEEE 802.15.6 Channel. In: Proceedings of the IEEE 11th International Symposium on Medical Information and Communication Technology, pp. 15–18. IEEE, Portugal (2017)
11. Alam, M.M., Hamida, E.B.: Strategies for optimal MAC parameters tuning in IEEE 802.15.6 wearable wireless sensor networks. *J. Med. Syst.* **39**(9), 1–16 (2015)
12. Alam, M.M., Hamida, E.B.: Performance evaluation of IEEE 802.15.6 MAC for wearable body sensor networks using a space-time dependent radio link model. In: Proceedings of the IEEE/ACS 11th International Conference on Computer Systems and Applications (AICCSA), pp. 441–448. IEEE, Qatar (2014)
13. Alam, M.M., Arbia, D.B., Hamida, E.B.: Joint throughput and channel aware (TCA) dynamic scheduling algorithm for emerging wearable applications. In: Proceedings of the IEEE Wireless Communication and Networking Conference (WCNC), pp. 1–6. IEEE, Qatar (2016)
14. Martelli, F., Buratti, C., Verdone, R.: On the performance of an IEEE 802.15.6 Wireless Body Area Network. In: Proceedings of the 11th European Wireless Conference, pp. 1–6. IEEE, Austria (2011)
15. Alam, M.M., Hamida, E.B.: Towards accurate mobility and radio link modeling for IEEE 802.15.6 wearable body sensor networks. In: Proceedings of the 10th WiMob Conference, pp. 298–305. IEEE, Cyprus (2014)
16. Alam, M.M., Hamida, E.B., Arbia, D.B., Maman, M., Mani, F., Denis, B., D’Errico, R.: Realistic simulation for body area and body-to-body networks. *Sensors* **16**(4), art. 561 (2016)
17. Simon, M.K., Alouini, M.S.: *Digital Communication over Fading Channel*, 2nd edn. Wiley, New York (2005)
18. Ziong, F.: *Digital Modulation Techniques*, 2nd edn. Artech House, London (2006)
19. Anane, R., Bouallegue, M., Raouf, K., Bouallegue, R.: Achieving energy efficient and reliable communication in WSN with coded GMSK system under various channel conditions. In: Proceedings of the IEEE International Conference on Wireless Communication and Mobile Computing, pp. 769–775. IEEE, Croatia (2015)
20. Alam, M.M., Hamida, E.B.: Surveying wearable human assistive technology for life and safety critical applications: standards, challenges and opportunities. *Sensors* **14**(5), 9153–9209 (2014)
21. Microchip Homepage. <https://www.mouser.com/ds/2/268/50002279A-515512.pdf>. Last accessed 29 May 2018

Chapter 6

Neighbour Wireless Body Area Network Discovery Mechanism for ETSI SmartBAN



Tuomas Paso and Jussi Haapola

6.1 Introduction

The Institute of Electrical and Electronics Engineers (IEEE) standard 802.15.6 [1] and the European Telecommunications Standards Institute (ETSI) technical committee SmartBAN [2, 3] define physical (PHY) and medium access control (MAC) specifications for packet-based short-range communications in wireless body area networks (WBANs). WBANs target, e.g. medical and healthcare monitoring systems in the vicinity of, or inside a human body.

The discovery of neighbour WBAN networks is the first step in enabling inter-WBAN communications. However, the aforementioned IEEE and the ETSI standards provide only hooks to implement provider-specific means for detection of existence and coexistence with other neighbour networks but do not specify mechanisms for discovery using the same standard specifications in near vicinity. Wireless sensor network research has identified over the years various mechanisms for neighbour network discovery. Such mechanisms can roughly be classified in four underlying principles: randomness, over-half occupation, rotation-resistant intersection, and coprime cycles [4]. For Bluetooth Low Energy devices, a precision mechanism has been proposed in [5, 6], in which the devices can operate in three different modes, i.e. advertising, scanning and initiating. However, the proposed mechanisms focus on the case where a new device initialises and attempts to discover an existing network.

The contribution of this paper is the proposal of a mechanism for the case where a WBAN is already operational and attempts to discover another operational WBAN without interrupting either WBAN operations already being carried out. The

T. Paso (✉) · J. Haapola
Centre for Wireless Communications, University of Oulu, Oulu, Finland
e-mail: tuomas.paso@oulu.fi; jussi.haapola@oulu.fi

mechanism is SmartBAN compliant, and currently it is under consideration to be included in the ongoing revision of the SmartBAN MAC specifications. In addition, the discovery mechanism is further applicable to other similar types of networks for the discovery of their corresponding neighbour networks.

The rest of the paper is organised as follows. Section 6.2 provides a short introduction to the SmartBAN network and details the description on the system model for the proposed neighbour WBAN discovery mechanism. In Sect. 6.3, neighbour WBAN discovery probability and discovery time are analytically derived. Results are presented in Sect. 6.4, and Sect. 6.5 concludes the paper.

6.2 System Model

Firstly, the ETSI SmartBAN network is introduced in this section. Secondly, we provide a detailed description of the proposed neighbour wireless body area network discovery mechanism.

ETSI SmartBAN Network

A SmartBAN network operates in two physical channels: a control channel (CCH) and a data channel (DCH). The frequency of operation falls within 2401–2481 MHz in the industrial, scientific and medical (ISM) band. Using 2 MHz channels, the system has 3 CCHs and 37 DCHs, from which the utilised channels can be selected based on interference and other possible restrictions.

The CCH is only utilised for network initialisation and transmitting periodic control channel beacons (C-Beacons) by the coordinator of a SmartBAN, called Hub. Data transmissions are carried out in the DCH, where the Hub transmits a periodic data channel beacon (D-Beacon). The period between two consecutive D-Beacons is termed as Inter-Beacon Interval (IBI), which is conceptually divided into three parts: Scheduled Access Period, Control and Management Period, and Inactive Period. Each of the periods is further divided into time slots (T_s) of equal duration, as depicted in Fig. 6.1. The Scheduled Access Period and the Control and Management Period together form the Active Period, during which devices other than the Hub of the SmartBAN network are allowed to transmit.

Detailed specifications of the SmartBAN network are defined in [2, 3]. An overview of the SmartBAN PHY and MAC specifications are provided in [7, 8], respectively, and an overview of the SmartBAN standardisation activities is carried out in [9].

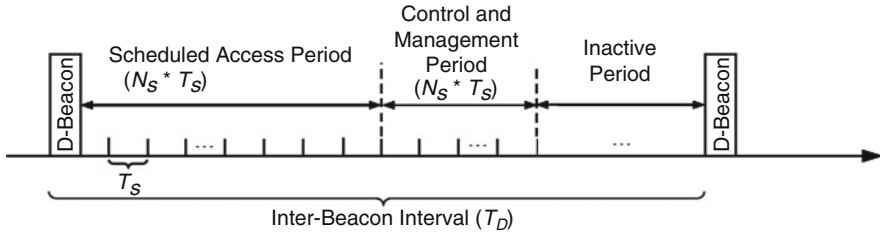


Fig. 6.1 Inter-Beacon Interval structure of the SmartBAN

Neighbour Wireless Sensor Network Discovery Mechanism

The operation of the neighbour WBAN discovery mechanism is based on channel scan performed by the Hub. The scan is executed during the Inactive Periods of the discovering SmartBAN, and the aim of the scan is to capture a C-Beacon of a neighbouring SmartBAN. A key factor in the proposed mechanism is the alternation of the Inactive Period durations of the SmartBAN conducting the discovery.

A flowchart of the proposed neighbour wireless body area network discovery mechanism is proposed in Fig. 6.2. The flowchart includes the following steps in the discovery process.

1. A Hub initiates the discovery mechanism by a higher layer protocol entity issuing hub-to-hub (H2H) discovery start. A Hub actively supporting H2H communications increases its C-Beacon rate to at least the rate of D-beacon interval (T_D)/2.
2. The Hub begins issuing an alternating Inactive Period duration in every forthcoming IBI. Note that T_D alternates correspondingly in every IBI.
3. During the first Inactive Period following commencement of the neighbour discovery mechanism, the Hub initiates a timer. While the timer has not expired, the Hub scans for C-Beacons of other networks during the Inactive Periods. If the timer has expired after the end of Inactive Period j , the Hub resets the timer and starts scanning C-Beacons on the next CCH of the applicable CCH list. Once the CCH list has been exhausted, the Hub stops scanning for C-Beacons and reports the list of neighbour C-Beacons found to the higher layer. If the list is empty, the report indicates a failure.
4. If a C-Beacon or C-Beacons are successfully received during an Inactive Period j , the Hub appends those beacons to the neighbour Hub list. Once such an event occurs, the Hub may terminate the neighbour network discovery mechanism early (e.g. if all predefined C-Beacons have been found) and report the list to the higher layer.

An example on the effect of alternating the Inactive Period and the T_D on C-Beacon discovery is illustrated in Fig. 6.3. C-Beacon scans in constant length Inactive Periods may not be able to receive transmitted C-Beacons since a neighbour

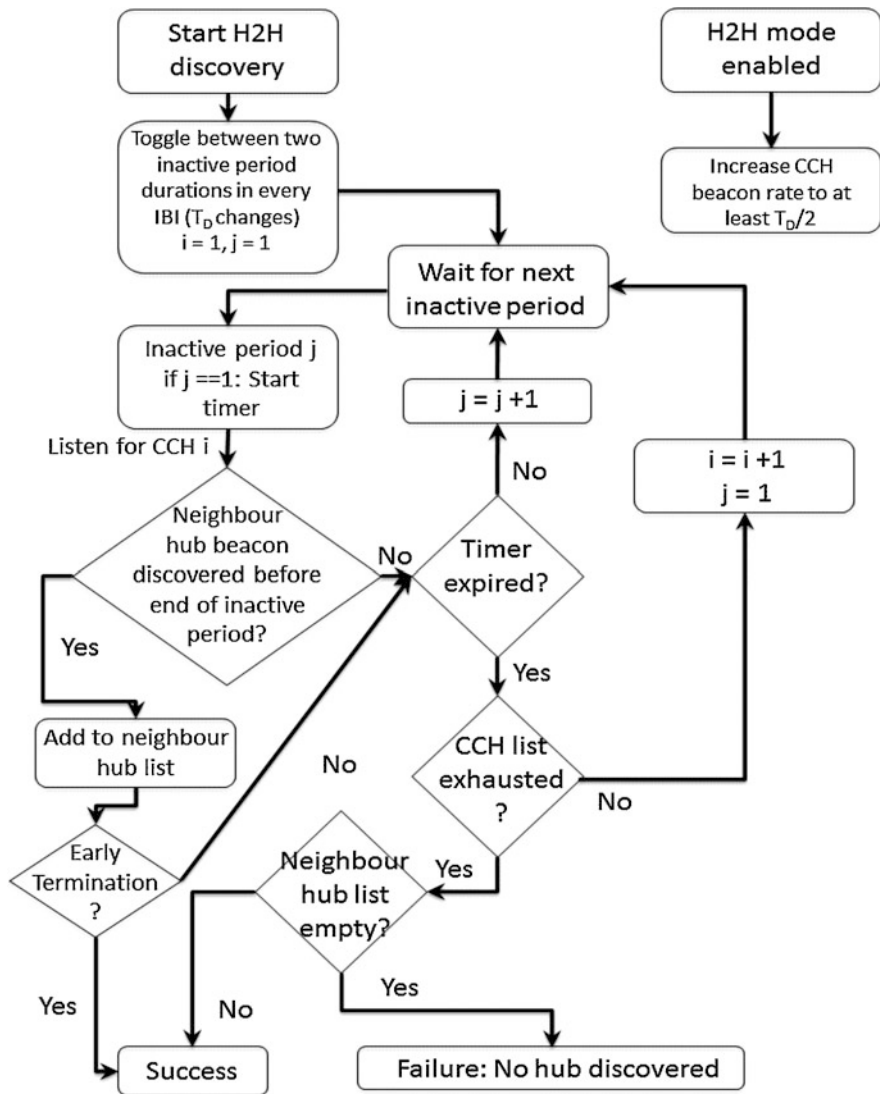


Fig. 6.2 Flowchart of neighbour wireless body area network discovery mechanism

SmartBAN C-Beacon period is unknown to the Hub before discovery. Alternating the Inactive Period improves the probability of receiving any periodic C-Beacon transmissions as the varying length of the T_D disrupts the constant cyclic transmission of D-Beacons and shifts the relative occurrence of the Inactive Period scans with respect to the constant cyclical C-Beacon transmissions.

It should also be noted that the proposed model provides a mechanism for the discovery of other neighbouring networks without interrupting the ongoing

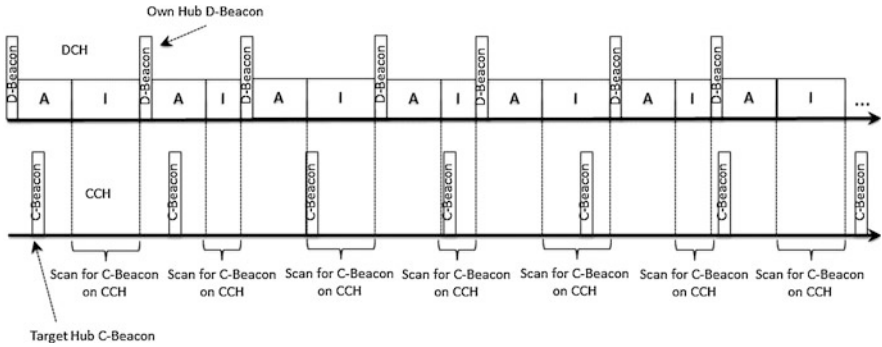


Fig. 6.3 Example of the effect of alternating Inactive Period and T_D duration for C-Beacon discovery

operations of either the wireless network carrying out the discovery or the wireless networks to be discovered. Current methods either do not provide for such a mechanism or they require the shutdown of the existing discovering network and its re-establishment as a child network of another wireless network after such network's discovery and association to it. The discovery mechanism is originally presented in [10].

6.3 Analysis

This section proposes a mathematical analysis for the proposed neighbour WBAN discovery mechanism. The analysis is carried out in terms of probability of discovery and discovery time for both the non-alternating and the alternating Inactive Periods.

Probability of Discovery

Firstly, we define the probability of discovery in a case where non-alternating Inactive Period durations are utilised, i.e. Inter-Beacon Interval remains constant. Secondly, the probability of discovery is defined for the proposed mechanism having alternating Inactive Period durations.

Non-alternating Inter-Beacon Interval

We define a maximum time, T_{Scan} , for the CCH scan. Based on T_{Scan} , the number of Inter-Beacon Intervals during the maximum CCH scan time is

$$N_{\text{IBI}} = \left\lfloor \frac{T_{\text{Scan}}}{T_{\text{D}}} \right\rfloor. \quad (6.1)$$

The probability of a C-Beacon transmission of a neighbouring SmartBAN during a single time slot is

$$P_{\text{CB}|T_S} = \frac{T_S}{T_C}, \quad (6.2)$$

where T_S is time slot duration and T_C is the C-Beacon interval. Correspondingly, the probability of not having a C-Beacon transmission during a single time slot is

$$P_{\text{NoCB}|T_S} = 1 - \frac{T_S}{T_C}. \quad (6.3)$$

The probability of being in an Inactive Period of the discovering SmartBAN is

$$P_1 = \frac{N_{\text{Slot}_{\text{IBI}}} - N_{\text{Slot}_{\text{A}}} - 1}{N_{\text{slot}_{\text{IBI}}}}, \quad (6.4)$$

where $N_{\text{Slot}_{\text{IBI}}}$ is the number of slots in the IBI, $N_{\text{Slot}_{\text{A}}}$ is the number of slots in the Active Period, and -1 represents the Beacon slot. Based on (6.3) and (6.4), the probability of not having at least a single C-Beacon during a single Inactive Period is

$$P_{\text{NoCB|I}} = \left(1 - \frac{T_S}{T_C}\right)^{N_{\text{Slot}_{\text{IBI}}} - N_{\text{Slot}_{\text{A}}} - 1}. \quad (6.5)$$

Therefore, the probability of having at least a single C-Beacon during the Inactive Period is

$$P_{\text{CB|I}} = 1 - \left(1 - \frac{T_S}{T_C}\right)^{N_{\text{Slot}_{\text{IBI}}} - N_{\text{Slot}_{\text{A}}} - 1}. \quad (6.6)$$

Finally, the probability of having a C-Beacon during one of the Inactive Periods during the maximum CCH scan time is

$$P_C = 1 - (1 - P_1 P_{\text{CB|I}})^{N_{\text{IBI}}}. \quad (6.7)$$

Alternating Inter-Beacon Interval

The probability of discovery for the proposed mechanism using alternating Inactive Period durations is calculated similarly. The number of alternating tuple Inter-Beacon Intervals during the maximum CCH scan time is

$$N_{\text{IBI_Alt}} = \left\lfloor \frac{T_{\text{Scan}}}{T_{\text{D}} + T_{\text{D2}}} \right\rfloor, \quad (6.8)$$

where T_{D2} is the length of the increased Inter-Beacon Interval, IBI_2 . The number of either normal or increased IBIs during the maximum CCH scan time is

$$N_{\text{IBI_Comb}} = \left\lfloor \frac{T_{\text{Scan}}}{\frac{T_{\text{D}}}{T_{\text{D}}+T_{\text{D2}}} T_{\text{D}} + \frac{T_{\text{D2}}}{T_{\text{D}}+T_{\text{D2}}} T_{\text{D2}}} \right\rfloor. \quad (6.9)$$

The probability of being in an increased Inactive Period during IBI_2 of the discovering SmartBAN is

$$P_{\text{I2}} = \frac{N_{\text{Slot}_{\text{IBI2}}} - N_{\text{Slot}_{\text{A}}} - 1}{N_{\text{slot}_{\text{IBI2}}}}, \quad (6.10)$$

where $N_{\text{Slot}_{\text{IBI2}}}$ is the number of slots in IBI_2 . The probability of having a C-Beacon during the increased Inactive Period is

$$P_{\text{CB|I2}} = \left(1 - \frac{T_{\text{S}}}{T_{\text{C}}}\right)^{N_{\text{Slot}_{\text{IBI2}}} - N_{\text{Slot}_{\text{A}}} - 1}. \quad (6.11)$$

Based on (6.7)–(6.11), the probability of having a C-Beacon during one of the Inactive Periods (normal or increased) during the maximum CCH scan time is

$$P_{\text{C2}} = 1 - \left(1 - \frac{T_{\text{D}}}{T_{\text{D}} + T_{\text{D2}}} P_{\text{I}} P_{\text{CB|I}} + \frac{T_{\text{D2}}}{T_{\text{D}} + T_{\text{D2}}} P_{\text{I2}} P_{\text{CB|I2}}\right)^{N_{\text{IBI_Comb}}}. \quad (6.12)$$

Discovery Time

Non-alternating Inter-Beacon Interval

The C-Beacon discovery time for non-alternating Inter-Beacon Interval scan is derived from Fig. 6.4, where T_{A} and T_{I} are the durations of Active Period and Inactive Period, respectively. $T_{\text{C_Offset}}$ is the offset between a D-Beacon of the discovering SmartBAN and a C-Beacon of the target SmartBAN. The C-Beacon is discovered if the inequality

$$nT_{\text{A}} + (n-1)T_{\text{I}} \leq T_{\text{C_Offset}} + kT_{\text{C}} < nT_{\text{D}}, \quad \forall n \in 1, 2, 3, \dots, \quad \forall k \in 0, 1, 2, \dots \quad (6.13)$$

holds, where the maximum value of $n = N_{\text{IBI}}$ and k is an integer with a maximum value of

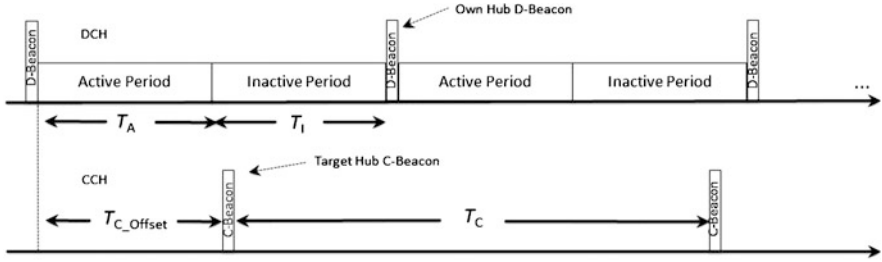


Fig. 6.4 C-Beacon discovery time for non-alternating Inter-Beacon Interval

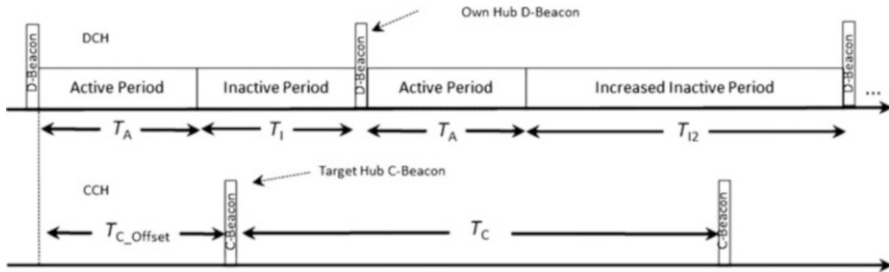


Fig. 6.5 C-Beacon discovery time for alternating Inter-Beacon Interval

$$k = \left\lceil \frac{T_{Scan}}{T_C} \right\rceil. \tag{6.14}$$

Alternating Inter-Beacon Interval

The C-Beacon discovery time for alternating Inter-Beacon Interval scan is derived from Fig. 6.5, where T_{I2} is the duration of the Increased Inactive Period. The C-Beacon is discovered if either of the inequalities

$$nT_A + (n - 1)(T_I + T_{I2}) \leq T_{C_Offset} + kT_C < n(T_A + T_I) + (n - 1)(T_A + T_{I2}), \quad \forall n \in 1, 2, 3 \dots, \quad \forall k \in 0, 1, 2 \dots \tag{6.15}$$

or

$$n(2T_A + T_I) + (n - 1)T_{I2} \leq T_{C_Offset} + kT_C < n(2T_A + T_I + T_{I2}), \quad \forall n 1, 2, 3 \dots, \quad \forall k \in 0, 1, 2 \dots \tag{6.16}$$

hold, where the maximum value of $n = N_{IBI_Alt}$.

6.4 Results

The most relevant SmartBAN network parameters utilised in the performance analysis are presented in Table 6.1.

Control Channel Beacon discovery probability as a function of Data Channel Inter-Beacon Interval and Control Channel Inter-Beacon Interval is presented in Fig. 6.6. The proposed discovery mechanism utilising alternating Inter-Beacon Interval durations outperforms the reference mechanism using non-alternating Inter-

Table 6.1 SmartBAN network parameters

Parameter	Value
Time slot length (T_S)	0.00125 s
D-Beacon Interval (T_D)	0.1, 0.2, 0.5, 0.8, 1.0, 1.5, 2.0, 2.5, 3.0, 5.0 s
C-Beacon Interval (T_C)	0.01, 0.1, 0.2, 0.5, 0.8, 1.0, 1.5, 2.0, 2.5, 3.0 s
Control Channel Beacon offset as fraction of T_C (CCH_{Offset})	0, $0.2T_C$, $0.5T_C$, $0.8T_C$
Inactive Period increase factor	2
Maximum scan time (T_{Scan})	5.0 s

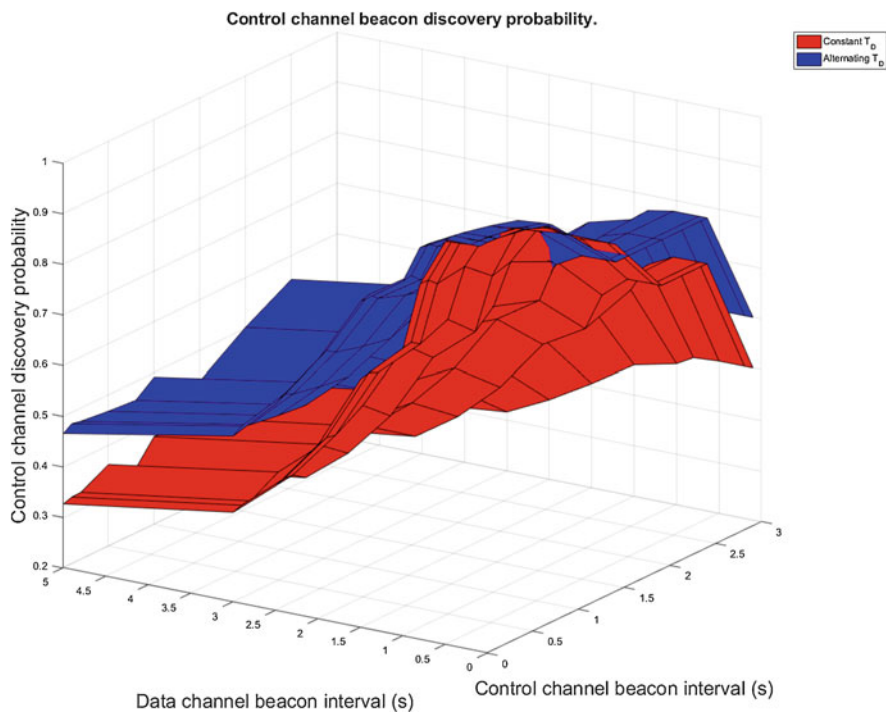


Fig. 6.6 Control Channel Beacon discovery probability as a function of Data Channel Inter-Beacon Interval and Control Channel Inter-Beacon Interval

Beacon Interval durations in almost all cases. The discovery probability is 1 for the proposed mechanism when Data Channel Inter-Beacon Interval is 0.5 s or less and Control Channel Inter-Beacon Interval is 0.2 s or less. Since the current SmartBAN specifications support up to 16 nodes in a SmartBAN network, the above-mentioned limit for the Data Channel Inter-Beacon Interval can be considered feasible. With the utilised 0.00125 s time slot length, and 50% duty cycle of the network, one time slot can be allocated to 16 nodes in every Inter-Beacon Interval, and still nine time slots remain to be used by the Control and Management Period of the Inter-Beacon Interval.

When averaged over the entire data set, the alternating mechanism provides, on average, 18% higher C-Beacon discovery probability as compared to the non-alternating mechanism. At best, alternating mechanism provides 61% higher discovery probability (Data Channel Inter-Beacon Interval = 5 s, Control Channel Inter-Beacon Interval = 2 s). In addition, in 89% of the cases, the alternating mechanism provides better discovery probability as compared to the non-alternating version and in 3% of the cases equal probability.

When the Data Channel Inter-Beacon Interval and/or the Control Channel Inter-Beacon Interval increases, the discovery probability decreases. The results are expected, since in those cases there are less Inactive Periods (i.e. less individual

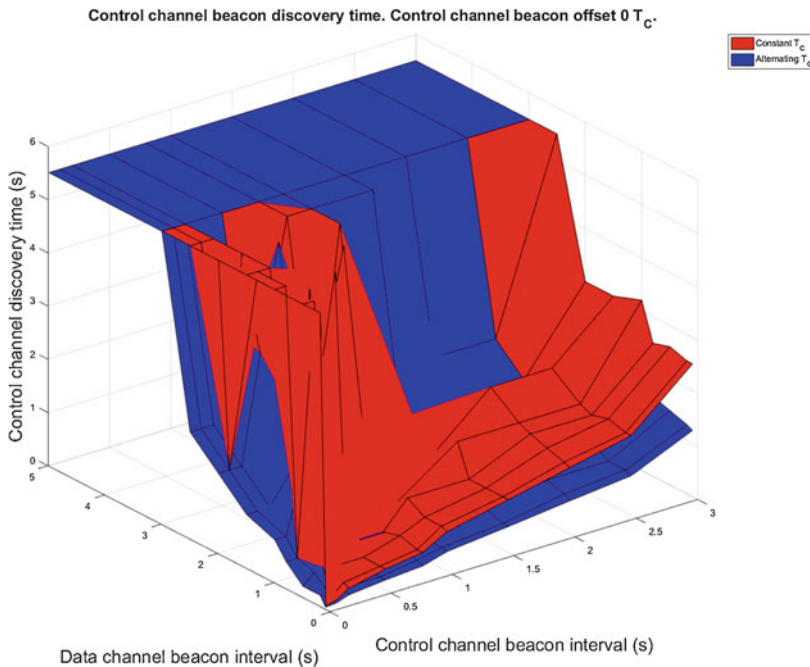


Fig. 6.7 Control Channel Beacon discovery time as a function of Data Channel Inter-Beacon Interval and Control Channel Inter-Beacon Interval. Control Channel Beacon offset = 0. A value of 5.5 s indicates failure to discover a C-Beacon

scans) and less Control Channel Beacon transmissions. Therefore, the discovery probability becomes heavily dependent on the timings of the neighbouring networks. In a worst-case scenario, the Data Channel Inter-Beacon Interval duration of the discovering network and the Control Channel Inter-Beacon Interval duration of the neighbouring network are the same, and beacon transmissions occur at the same time. In this case, the discovery probability would be zero with the reference mechanism.

The Control Channel Beacon discovery time as a function of Data Channel Inter-Beacon Interval and Control Channel Inter-Beacon Interval with Control Channel Beacon offset = 0, 0.2, 0.5, and 0.8 is presented in Figs. 6.7, 6.8, 6.9, and 6.10, respectively. In the figures a value of 5.5 s on the discovery time indicates the Control Channel Beacon could not be found during the maximum scan time. Based on the figures, it can be stated that the proposed discovery mechanism utilising alternating Inter-Beacon Interval durations outperforms the reference mechanism using non-alternating Inter-Beacon Interval durations in almost all cases in terms of discovery time as well. When considering Data Channel Inter-Beacon Interval and Control Channel Inter-Beacon Interval durations of 0.5 s or less, and Control Chan-

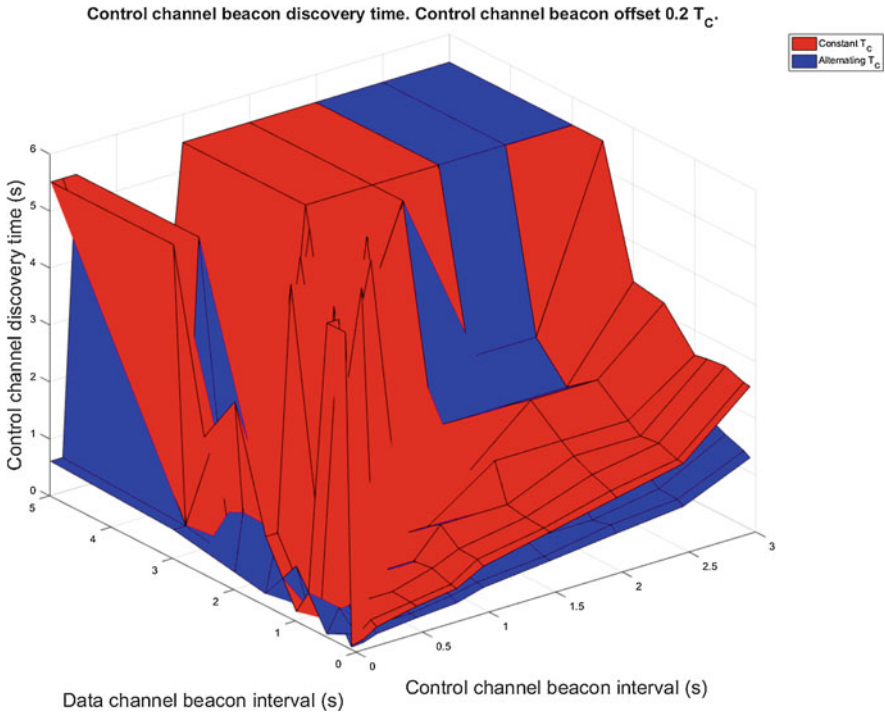


Fig. 6.8 Control Channel Beacon discovery time as a function of Data Channel Inter-Beacon Interval and Control Channel Inter-Beacon Interval. Control Channel Beacon offset = 0.2. A value of 5.5 s indicates failure to discover a C-Beacon

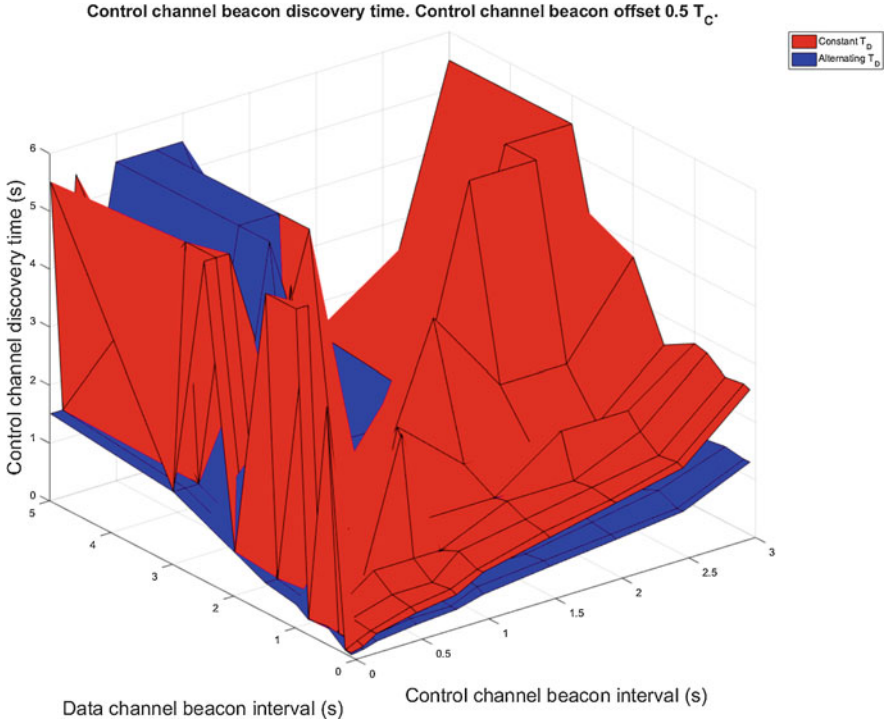


Fig. 6.9 Control Channel Beacon discovery time as a function of Data Channel Inter-Beacon Interval and Control Channel Inter-Beacon Interval. Control Channel Beacon offset = 0.5. A value of 5.5 s indicates failure to discover a C-Beacon

nel Beacon offset 0, the proposed mechanism captures Control Channel Beacon approximately in 0.2 s, whereas the reference mechanism captures it approximately in 0.4 s. The effect of Control Channel Beacon offset on the discovery is clearly visible, when utilising the reference discovery mechanism. Even with short Data Channel Inter-Beacon Interval and Control Channel Inter-Beacon Interval durations, there are cases in which the Control Channel Beacon cannot be discovered. Since the relative occurrence of the Inactive Period, i.e. the scan, remains constant in this case, the result is expected. When utilising the proposed mechanism, the aforementioned phenomenon is mostly avoided.

6.5 Conclusion

In this paper, we introduced a novel neighbour network discovery mechanism for WBANs. The mechanism is based on the utilisation of the Inactive Periods of the discovering WBAN by alternating the Inactive Period durations for scanning

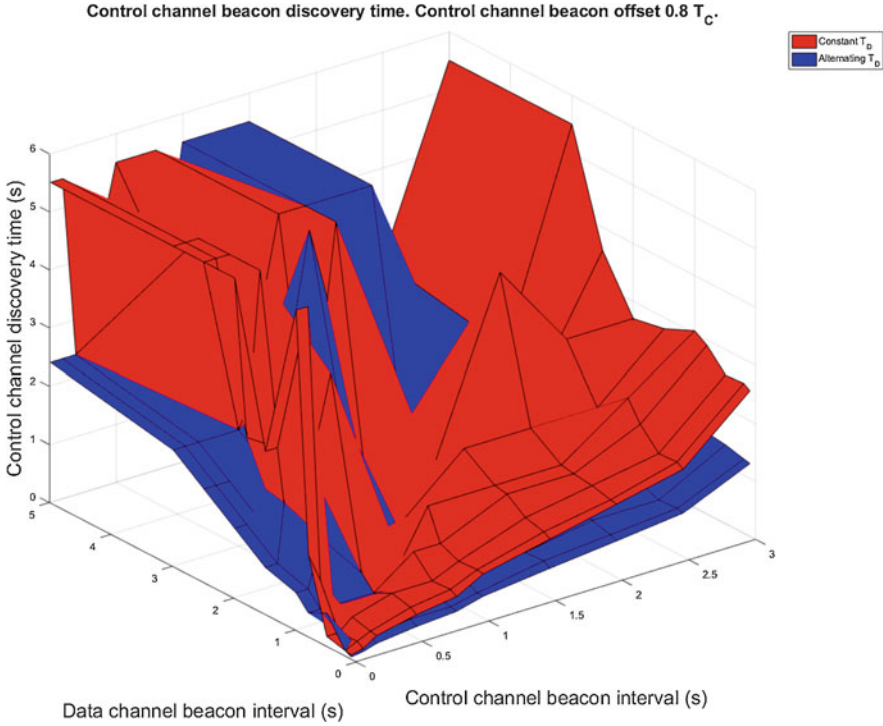


Fig. 6.10 Control Channel Beacon discovery time as a function of Data Channel Inter-Beacon Interval and Control Channel Inter-Beacon Interval. Control Channel Beacon offset = 0.8. A value of 5.5 s indicates failure to discover a C-Beacon

neighbouring WBANs. The key advantage of the mechanism is that it is defined for the case where a WBAN is already operational and attempts to discover another operational WBAN without interrupting either WBAN operations already being carried out. Furthermore, the mechanism is SmartBAN compliant, and currently it is under consideration to be included in the ongoing revision of SmartBAN MAC specifications.

We have analytically derived the performance of the proposed mechanism in terms of discovery probability and discovery time. Based on the results, it can be concluded that the proposed mechanism outperforms a reference mechanism using non-alternating Inactive Period durations for the discovery in almost all cases. The main reason for better performance is that alternating the Inactive Period improves the probability of receiving any periodic C-Beacon transmissions, since the varying length of the Inter-Beacon Interval disrupts the constant cyclic transmission of D-Beacons. Therefore, it shifts the relative occurrence of the Inactive Period scans with respect to the constant cyclical C-Beacon transmissions.

Based on the results, it can also be stated that in certain special cases, neighbour network cannot be discovered. However, these cases can be solved by provider-specific implementation in defining network parameters.

Acknowledgements This research has been financially supported in part by Academy of Finland 6Genesis Flagship (grant 318927).

References

1. IEEE Computer Society, LAN/MAN Standards Committee: IEEE Std 802.15.6-2012, IEEE Standard for Local and metropolitan area networks—Part 15.6: Wireless Body Area Networks. IEEE (2012)
2. ETSI TC SmartBAN: Smart Body Area Network (SmartBAN), Enhanced Ultra-Low Power Physical Layer, ETSI TS 103 326 V1.1.1. ETSI (2015)
3. ETSI TC SmartBAN: Smart Body Area Network (SmartBAN), Low Complexity Medium Access Control (MAC) for SmartBAN, ETSI TS 103 325 V1.1.1. ETSI (2015)
4. Sun, W., Yang, Z., Zhang, X., Liu, Y.: Energy-efficient neighbor discovery in mobile ad hoc and wireless sensor networks: a survey. *IEEE Commun. Surv. Tutorials.* **16**(3), 1448–1459 (2014)
5. Liu, J., Chen, C., Ma, Y.: Modeling neighbor discovery in Bluetooth low energy networks. *IEEE Commun. Lett.* **6**(9), 1439–1441 (2012)
6. Jeon, W.S., Wwijaksara, M.H., Jeong, D.G.: Performance analysis of neighbor discovery process in Bluetooth low-energy networks. *IEEE Trans. Veh. Technol.* **66**(2), 1865–1871 (2017)
7. Chin, W.H., Tanaka, H., Nakanishi, T., Paso, T., Hämäläinen, M.: An overview of ETSI TC SmartBAN's ultra low power physical layer. In: 9th International Symposium on Medical Information and Communication Technology, IEEE, Kamakura, Japan (2015)
8. Paso, T., Tanaka, H., Hämäläinen, M., Chin, W.H., Matsuo, R., Subramani, S., Haapola, J.: An overview of ETSI TC SmartBAN MAC protocol. In: 9th International Symposium on Medical Information and Communication Technology, IEEE, Kamakura, Japan (2015)
9. Hämäläinen, M., Paso, T., Mucchi, L., Girod-Genet, M., Farserotu, J., Tanaka, H., Chin, W.H., Nachabe Ismail, L.: ETSI TC SmartBAN—overview of the wireless body area network standard. In: 9th International Symposium on Medical Information and Communication Technology, IEEE, Kamakura, Japan (2015)
10. Paso, T., Haapola, J.: Neighbour wireless sensor network discovery mechanism. Patent Application FI 20175994 (2017)

Chapter 7

Evaluation of Preamble Detection in ETSI SmartBAN PHY



Kento Takabayashi, Hirokazu Tanaka, and Katsumi Sakakibara

7.1 Introduction

In recent years, a medical and healthcare IoT (Internet of Things) system has attracted attention as a means of building home medical care or remote medical care system using wearable wireless vital sign sensors or medical robots [1–6]. For example, IEEE 802.15.6 which is one of the standards of wireless body area networks (WBAN) known as one of the systems was issued in 2012 [7]. Then, system specifications for a physical layer (PHY) and a media access control layer (MAC) in smart body area networks (SmartBAN), which is a standard for medical and health care advanced by the European Telecommunications Standards Organization (ETSI), were issued in April 2015 [8, 9].

Our previous work provided performance evaluations of an error control scheme in ETSI SmartBAN PHY under several conditions [10]. In particular, we evaluated the performance in case that Bose–Chaudhuri–Hocquenghem (BCH) codes with almost the same redundancy as the packet repetition was applied, and then compared with the standard scheme. In addition, the performance when retransmission was performed was also evaluated. Numerical results showed that retransmission greatly improved the packet error ratio and energy efficiency under the IEEE model CM3 [11].

K. Takabayashi (✉) · K. Sakakibara

Department of Information and Communication Engineering, Faculty of Computer Science and Systems Engineering, Okayama Prefectural University, Okayama, Japan
e-mail: sakaki@c.oka-pu.ac.jp

H. Tanaka

Graduate School of Information Sciences, Hiroshima City University, Hiroshima, Japan
e-mail: hi.tanaka@m.ieice.org

© Springer Nature Switzerland AG 2020

C. Sugimoto et al. (eds.), *13th EAI International Conference on Body Area Networks*, EAI/Springer Innovations in Communication and Computing,
https://doi.org/10.1007/978-3-030-29897-5_7

In this research, preamble detection in ETSI SmartBAN PHY was evaluated. This is because other researches about ETSI SmartBAN PHY including our previous work did not consider that [10, 12, 13]. In the SmartBAN PHY, the packet structure has a two-octet preamble used for timing synchronization and so on. However, the preamble detection cannot be sufficiently performed except in a very good channel condition because the preamble structure is too simple. Hence, there is concern that reliable communication for medical use can only be performed under such conditions. For that reason, we proposed a preamble structure which added a Start Frame Delimiter (SFD) in order to correctly detect the position of the header. Several SFD candidates were selected and their preamble detection performances were evaluated by computer simulations. As a result of them, the best performance was obtained when an orthogonal M-sequence was used as the SFD under the additive white Gaussian noise (AWGN) channel and IEEE model CM3.

7.2 Summary of SmartBAN PHY

Frequency Spectrum

In the SmartBAN, a frequency band within 2401 MHz to 2481 MHz is used, and each channel has a bandwidth of 2 MHz. In addition, each center frequency is defined as the following equation:

$$f_c = 2402 + 2n \text{ MHz}, \quad \text{for } n = 0 \text{ to } 39. \quad (7.1)$$

Here, n is the channel number.

Packet Structure

Figure 7.1 shows a structure of a packet in the physical layer (PPDU: Physical-Layer Protocol Data Unit). PPDU has a sixteen-bit preamble “1010101010101010” used for frequency synchronization, timing synchronization, and automatic gain control. The Physical Layer Convergence Protocol (PLCP) header consists of the packet length, PHY scheme, and so on. The Physical-Layer Service Data Unit (PSDU) is either an encoded or uncoded MAC Protocol Data Unit (MPDU) [8, 9].

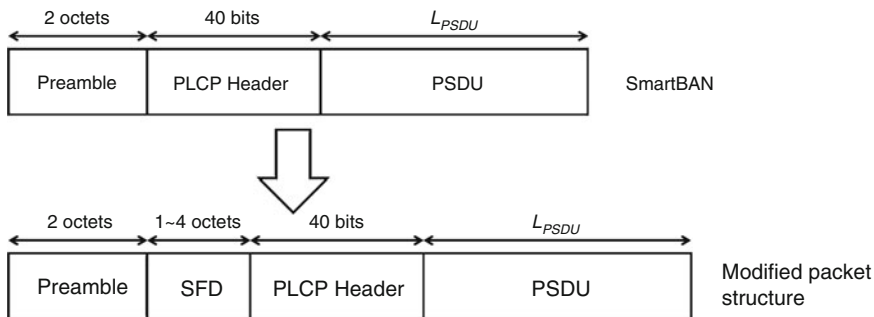


Fig. 7.1 Proposed packet structure. The above one is the packet structure of SmartBAN. The proposed one is below

Modulation and Error Controlling

In the SmartBAN PHY, Gaussian Frequency Shift Keying (GFSK) with a bandwidth-bit period product $BT = 0.5$ and modulation index $h = 0.5$ is applied as a modulation scheme. On the other hand, as an error controlling in the SmartBAN PHY, we can use two schemes. The first one is a scheme of repeatedly transmitting PPDU. It is possible to set with the number of repetitions $N_R = 2, 4$. Another one is a scheme of encoding the MPDU by using the (127, 113) BCH code.

7.3 Proposed Preamble Structure

We propose to modify the preamble structure in ETSI SmartBAN. The reason is that the current preamble structure is too simple, and the preamble detection cannot be sufficiently performed except in a very good channel condition. To correctly detect the position of the PLCP header, in particular, a SFD is added between the two-octet preamble and the PLCP header as shown in Fig. 7.1. When detecting the position of the header, cross-correlation is performed on the known modulated SFD symbol. The advantage of this proposal is that it can be realized without changing the standards drastically. Hence, the part of two-octet preamble can also play a conventional role.

7.4 Result of Computer Simulation

In this section, we describe the performance evaluation by computer simulations on the preamble detection in the SmartBAN PHY and our proposed method. Table 7.1 shows the simulation parameters. The computer simulator was built by

MATLAB. Then, the comm.PreambleDetector System object in MATLAB was used for preamble detection, and the detection threshold was set to the length of each SFD minus one ($L_{\text{SFD}} - 1$). In the only case of SmartBAN, all of the two-octet preambles were correlated, and the threshold was set to the length of the preamble minus one ($L_{\text{preamble}} - 1$). In this computer simulation, the AWGN channel and IEEE model CM3 which is one of the channel models of wearable WBAN were used [11]. Similarly, IEEE model CM3 was applied to the path loss model. Table 7.2 summarizes SFD used in the computer simulations. The reason for choosing these sequences is that they can be handled in units of octets.

Figures 7.2 and 7.3 show performances of failure detection ratio under the AWGN channel and IEEE model CM3 respectively as function of energy per

Table 7.1 Simulation parameters

Channel model	AWGN and IEEE model CM3
Pass loss model	IEEE model CM3
Frequency Spectrum	2401–2481 MHz
Bandwidth (BW)	2 MHz
Modulation	GFSK
Bandwidth-Time product (BT)	0.5
Modulation index (h)	0.5
Transmission power (P_{tr})	0 dBm $\geq P_{\text{tr}}$
Thermal noise density (N_0)	–174 dBm/Hz
Implementation losses (I)	5 dB
Receiver noise figure (NF)	10 dB
Information bit length (L_{info})	150 bits
Symbol rate	1.0 Msps

Table 7.2 SFD used in computer simulations

Type of sequence		Bit sequence (Hexadecimal)
Additional SFD 1		“01010101” (0x55)
Additional SFD 2		“10101011” (0xAB)
Hadamard seq. [14]	1 octet	“11001100” (0xCC)
	2 octets	“1100001111000011” (0xC3C3)
	4 octets	“11000011110000111100001111000011” (0xC3C3C3C3)
Orthogonal M-seq. [15]	1 octet	“11101000” (0xE8)
	2 octets	“1111010110010000” (0xF590)
	4 octets	“11111001101001000010101110110000” (0xF9A42BB0)
Manchester- coded Orthogonal M-seq. [15]	1 octet	“10100101” (0xA5)
	2 octets	“1010100101100101” (0xA965)
	4 octets	“10101010011001101001011001010101” (0xAA669655)

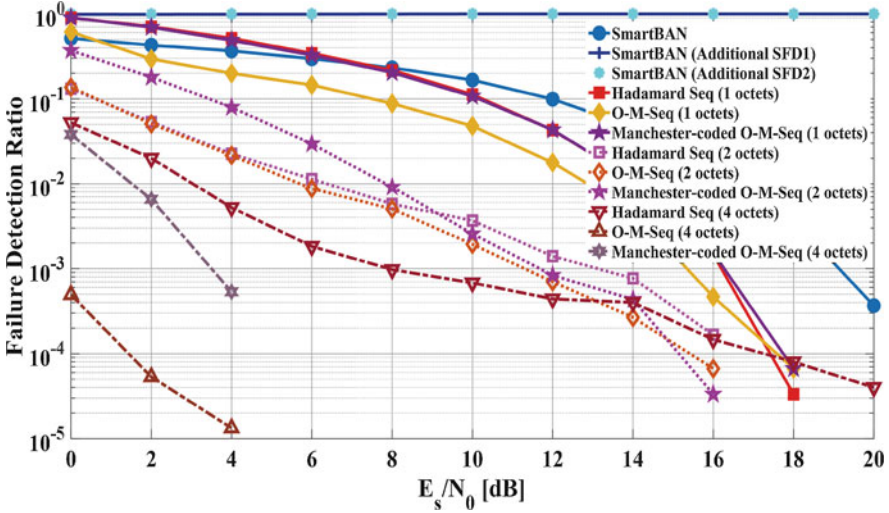


Fig. 7.2 Failure detection ratio under the AWGN channel as function of E_s/N_0

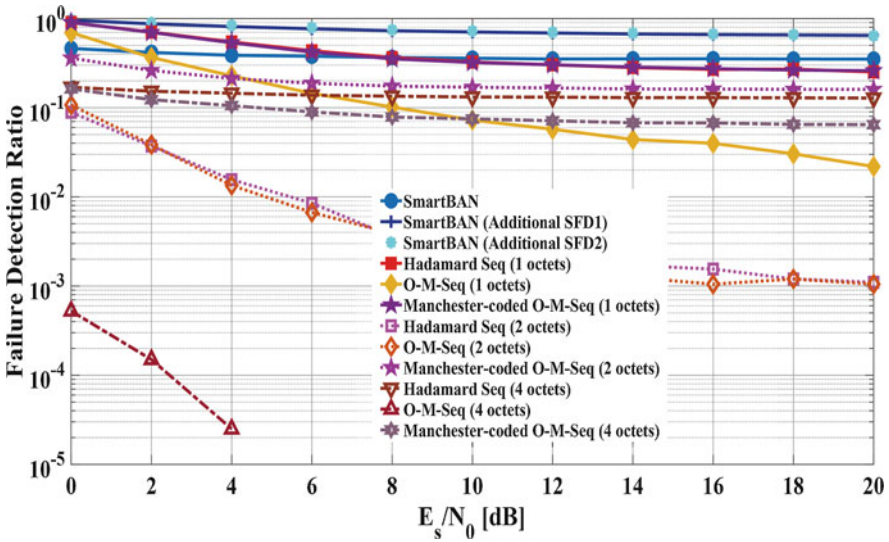


Fig. 7.3 Failure detection ratio under IEEE model CM3 as function of E_s/N_0

symbol to noise power spectral density (E_s/N_0). In addition, Fig. 7.4 shows that under IEEE model CM3 as function of communication distance between a transmitter and a receiver. Here, “failure detection” includes false detection and not detection. False detection is to detect the erroneous position as the correct PLCP header position. On the other hand, not detection is to miss detection of peaks by cross-correlation. As shown in these figures, the preamble of SmartBAN had good

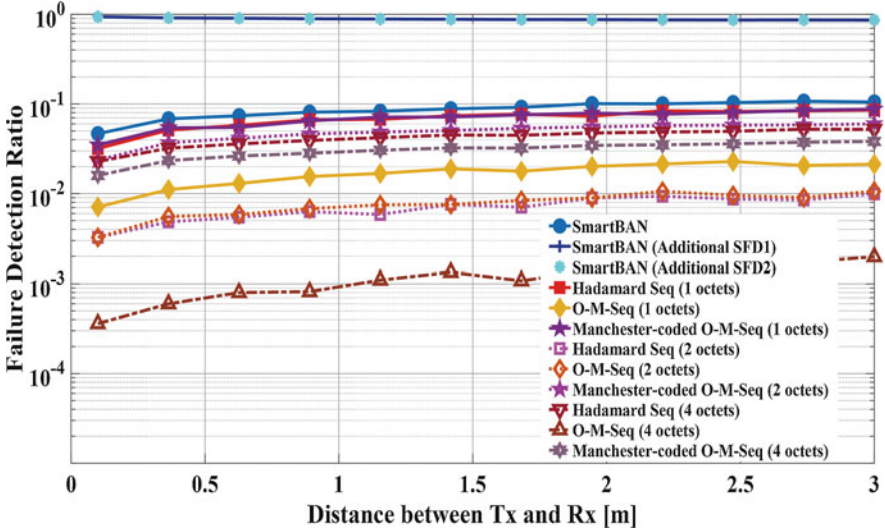


Fig. 7.4 Failure detection ratio under IEEE model CM3 as a function of communication distance

performance only under the AWGN channel and very good channel conditions. On other words, its performance was very bad in other conditions. Additional SFDs were not able to detect correctly each preamble because they were very similar to part of the two-octet preamble. Of the other sequences, orthogonal M-sequences obtained better performances than others. Particularly, the four-octet orthogonal M-sequence gained good results even in very poor channel conditions. The reason for that is considered to be that the autocorrelation characteristic is higher than other sequences.

7.5 Conclusion

In this research, we have evaluated preamble detection in ETSI SmartBAN PHY and proposed to modify the preamble structure. Specifically, a SFD has been added between the two-octet preamble and the PLCP header. Computer simulations have shown that the preamble with SFD consisting of the four-octet orthogonal M-sequence has better detection performance than that of SmartBAN and so on, in particular, under poor channel conditions of IEEE model CM3.

As for the future work, we need to consider changing the preamble itself. In addition, performance evaluation of the PHY should also be performed in consideration of preamble detection performance. At that time, it is necessary to consider the influence of overhead caused by adding SFD.

References

1. Costa, C.R., Anido-Rifón, L.E., Fernández-Iglesias, M.J.: An open architecture to support social and health services in a smart TV environment. *IEEE J. Biomed. Health Inform.* **21**(2), 549–560 (2017)
2. Chen, M., Gonzalez, S., Vasilakos, A., Cao, H., Leung, V.C.M.: Body area networks: a survey. *Mobile Netw. Appl.* **16**(2), 171–193 (2010)
3. Cao, H., Leung, V., Chow, C., Chan, H.: Enabling technologies for wireless body area networks: a survey and outlook. *IEEE Commun. Mag.* **47**(12), 84–93 (2009)
4. Caldeira, J.M.L.P., Rodrigues, J.J.P.C., Lorenz, P.: Toward ubiquitous mobility solutions for body sensor networks on healthcare. *IEEE Commun. Mag.* **50**(5), 108–115 (2012)
5. Cavallari, R., Martelli, F., Rosini, R., Buratti, C., Verdone, R.: A survey on wireless body area networks: technologies and design challenges. *IEEE Commun. Surv. Tuts.* **16**(3), 1635–1657 (2014)
6. Movassaghi, S., Abolhasan, M., Lipman, J., Smith, D., Jamalipour, A.: Wireless body area networks: a survey. *IEEE Commun. Surv. Tuts.* **16**(3), 1658–1686 (2014)
7. Wireless Medium Access Control (MAC) and Physical Layer (PHY) specifications for Wireless Personal Area Networks (WPANs) used in or 12 around a body. *IEEE Standard for Information technology—telecommunications and information exchange between systems—local and metropolitan area networks—specific requirements: Part 15.6* (2012)
8. Smart Body Area Network (SmartBAN), Low Complexity Medium Access Control (MAC) for SmartBAN. ETSI TC Smart BAN TS 103 325 V1.1.1 (2015)
9. Smart Body Area Network (SmartBAN), Enhanced Ultra-Low Power Physical Layer. ETSI TC Smart BAN TS 103 326 V1.1.1 (2015)
10. Takabayashi, K., Tanaka, H., Sakakibara, K.: Performance evaluation of error control scheme in ETSI SmartBAN PHY. In: *The 2018 Global IoT Summit (GIoTS 2018)*, Bilbao, Spain (2018)
11. Yazdandoost, K.Y., Sayrafi-an-Pour, K.: Channel model for Body Area Network (BAN). *IEEE P802.15 Working Group for Wireless Personal Area Networks (WPANs)*, IEEE P802.15-08-0780-10-0006 (2009)
12. Khan, R., Alam, M.M.: Joint PHY-MAC realistic performance evaluation of body-to-body communication in IEEE 802.15.6 and SmartBAN. In: *The 12th International Symposium on Medical Information and Communication Technology (ISMICT 2018)*, pp. 137–142, Sydney, Australia, (2018)
13. D’Souza, A., Viittala, H., Hämäläinen, M., Mucci, L.: Performance comparison between ETSI SmartBAN and Bluetooth. In: *The 12th International Symposium on Medical Information and Communication Technology (ISMICT 2018)*, pp. 143–147, Sydney, Australia (2018)
14. Seberry, J., Yamada, M.: Hadamard matrices, sequences, and block designs. In: Stinson, D.J., Dinitz, J. (eds.) *Contemporary Design Theory—A Collection of Surveys*, pp. 431–560. Wiley, New Jersey (1992)
15. Habuchi, H.: Pseudo-noise sequences based on M-sequence and its application for communications. *IEICE Fundam. Rev.* **3**(1), 32–42 (2009). in Japanese

Part III
Security and Safety

Chapter 8

Security in Body Networks: Watermark-Based Communications on Air-Gap Acoustic Channel



Simone Soderi

8.1 Introduction

We live in a hyper-connected society where communications infiltrated our lives. This technological evolution changed positively the daily life making several things easier. On the other hand, the wide utilization of communications imposed the development of security engineering as a multidisciplinary field ranging from cryptography and computer science to hardware and embedded systems [1]. Cybersecurity is now a fundamental fact of global life. It impacts political, economic, and military affairs. The rapid evolution of the information communications and technology (ICT) industry has disadvantages, for example, sometimes ICT players are not responsive to new security issues. On the other hand, each country elaborates strategies to mitigate security threats that could affect the national security. In United States (US), the National Defense University (NDU) defined the *cyberspace* as an operational domain framed by the use of electronics and the electromagnetic spectrum to create, store, modify, exchange, and exploit information via interconnected information systems and their associated infrastructures. The structure of the cyberspace changes with the technology evolution. Today, its structure consists of sub-domains represented as follows [12]:

Communication infrastructures: networks, protocols/packets in accordance with the open systems' interconnection (OSI), and transmission control protocol/Internet protocol (TCP/IP) models;

Contents and applications: software that exploits hierarchical file systems and relational databases to process data;

S. Soderi (✉)
IEEE Senior Member, Firenze, Italy
e-mail: soderi@ieee.com

People and social: on-line communities such as mailing list, blog, social networks, health-care oriented communities, etc.

Wireless body area networks (WBANs) are part of the cyberspace supporting people in many daily activities and collecting humans' information. Nowadays, we should consider that the global transformation of the industry to a renewed digital industry has given rise to unexpected consequences. Many people, such as terrorist, hacktivist, and hackers are making life more dangerous the life for those uses digital products such as body sensors.

One of the field with the greater impact of this situation is undoubtedly the health-care system. For many years, the adoption of electronic medical record (EMR) and the wide utilization of highly interconnected medical devices created a large database of health data. With growing reports of ransomware and other hacking-related incidents, the cybersecurity in health-care systems has become a priority [18]. In this study, the author provides a method for the security hardening in WBAN scenarios. The rest of this paper is organized as follows: Section 8.2 overviews the related work and the motivation behind this study. Section 8.3 describes the physical layer security system model applied to audio communication scenario. Then, this paper continues with the results achieved in the test-bed. Finally, the conclusions are presented in Sect. 8.5.

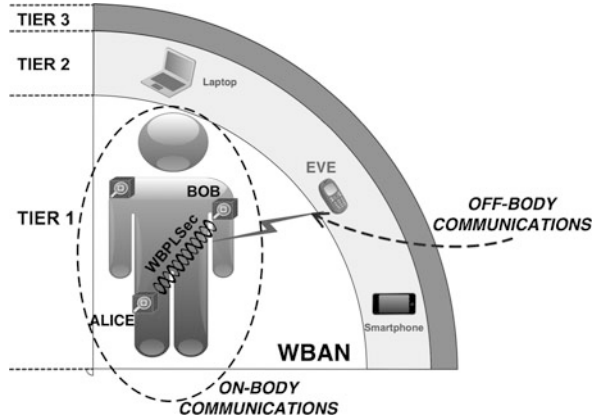
8.2 Related Work

WBANs collect humans' information through low energy sensors nodes. Bluetooth Low Energy (BLE) is the dominant technology to convey efficiently data in body networks. Other wireless short-range technologies available on the market, such as ZigBee and IEEE802.15.6, implement WBANs. In addition, the European Telecommunications Standards Institute (ETSI) under the Technical Committee SmartBAN is also developing its own standard for smart body area networks (SmartBAN) [6]. In particular, this new standard is developed to support health-care applications.

In accordance with the tier model, WBAN and more in general wearable wireless networks (WWNs) include three levels of communication [2, 16]. Wearable sensors collect data within the *tier 1* and convey this information to *tier 2* for aggregation purposes and data processing. Finally, data are transmitted to *tier 3* making them available for remote access. As shown in Fig. 8.1, the classical WBAN can be classified as *on-body* communications. Instead, all the communications that occur in *tier 2* are *off-body* [2].

In this transmission chain, the security is one of the major concerns because an adversary, i.e., Eve in Fig. 8.1 can perform several attacks. The wireless link between nodes in the WBAN can be attacked. The severity of these attacks changes with the application scenario. For instance, in health-care WWNs we could have a high risk for patient's safety [17]. Usually, WWNs operate in a public environment,

Fig. 8.1 Architecture of the WBAN: tiers model and on-body/off-body communications



e.g., hospitals, in which people, including an attacker, has access without restriction. Moreover, the utilization of wireless technology makes the data prone to being eavesdropped, modified, and injected. This raises concerns about the privacy of the information managed in WBANs. On the other hand, the security hardening of the wireless nodes within WBAN is challenging. These nodes have limited resources and require the security mechanisms to be as lightweight as possible [14].

Motivation

The design of security solutions for WBANs shall overcome the resources limitations in each wireless device. The balance between security, usability, and efficiency are aspects that shall be taken into account. IEEE802.15.6 defines different levels of security throughout encryption and authentication of the data [10]. Moreover, ETSI takes into account the security in the SmartBAN standard [21]. So far, although there are security solutions, in several applications security is implemented through cryptography at upper layers in the open system interconnection (OSI) model [1]. However, in the past few years, several techniques based on signal processing have been utilized to secure communications at the physical layer, and they have been shown to be promising methods where standalone security solution is needed. Undoubtedly, nodes of a WBAN fall in this case. Since 1949, when Shannon developed the metric for the information theory for secrecy systems [20]. In the literature, there are several contributions that deal with the *physical layer security* in which secure communications are developed exploiting wireless channel imperfections, multipath, and even interference. In 1973, Lampton defined the *covert channel* as a communication channel that is not intended for information transfer at all [13]. Recently, the utilization of covert channels is proposed to circumvent network security policies by establishing new communication paths [7]. In this paper, the author extends to *acoustical communications*, the watermark-

based blind physical layer security (WBPLSec) protocol that utilizes a jamming receiver in conjunction with spread-spectrum (SS) watermarking technique [23]. At the time of writing, there was no literature describing a similar technique in which the watermark-based communication exploits acoustical emanations to secure a wireless communication in WBANs.

8.3 Scenario

Acoustic Covert Channel

Two electronic devices in the same room, without any physical connection, between them, are separated by an *air-gap*. This scenario cannot guarantee the isolation between two computers [5]. *Acoustical emanations* produced by electronic devices can bridge the air-gap. The idea proposed in this paper addresses countermeasures against confidentiality and integrity attacks exploiting acoustic covert channel. WBANs have high dynamics by their nature. Nodes join and leave the network continuously. In that scenario, WBANs are subject to threats from network dynamics. Building new sensors with physical layer capability to secure a wireless communication through acoustic channel makes the entire WWN stronger.

Humans can perceive sound frequencies within the range of 20 Hz to 20 kHz, whereas ultrasounds are defined as those frequencies above 20 kHz. Sound-based covert channels can stealthily bypass many information flow control mechanisms. In literature, there are contributions in which covert mesh networks are implemented over the air [7]. Ultrasonic communications are feasible with good accuracy utilizing standard microphones and loudspeakers [4, 9].

On the other hand, from the security point of view, ultrasonic sound does not require a permission and a computer can emit sounds to anything that can hear them bypassing network security policies restriction. This mechanism was exploited by malware to infect other devices [5, 9]. Only military devices mitigate this kind of security issue disabling the sound-card driver when it is not needed.

WBPLSec System Model in Acoustical Communications

This paper proposes the application of the WBPLSec over an acoustic channel by utilizing the near ultrasonic frequency range. WBPLSec transmits the information through two independent paths implementing *data decomposition policy*. The information is sent via a narrow-band signal and through the SS watermarked signal. The narrow-band signal is partially jammed by Bob, but the watermark into the SS signal is utilized to re-compose the entire symbol [23]. Figure 8.2 illustrates the main idea underlying the WBPLSec when it is applied to the acoustic air-gap channel.

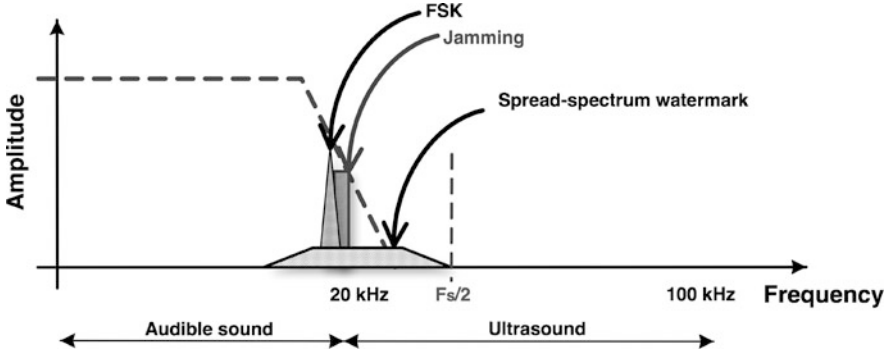


Fig. 8.2 Spectrum of the WBPLSec in acoustic air-gap channel

In accordance with the framework presented by Cox et al. [3], transmitter combines the original modulated signal with an SS watermark, with an embedding rule defined as

$$x'_S(i) = x_S(i) + \mu w(i), \quad (8.1)$$

where $x_S(i)$ is the i -th sample of the frequency shift keying (FSK) transmitted signal, μ is the scaling parameter, and $w(i)$ is the SS watermark. The direct sequence spread spectrum (DSSS) technique is selected for the signal watermarking implementation.

The host FSK modulated signal x_S can be expressed as

$$x_S(i) = \begin{cases} A_a \sqrt{\frac{2}{T_{hs}}} \cdot \cos(2\pi(f_c + \Delta f)i), & \text{for } 0 \leq i \leq T_{hs}(\text{binary}1), \\ A_a \sqrt{\frac{2}{T_{hs}}} \cdot \cos(2\pi(f_c - \Delta f)i), & \text{for } 0 \leq i \leq T_{hs}(\text{binary}0), \end{cases} \quad (8.2)$$

where A_a is the amplitude, T_{hs} is the symbol time, f_c is the carrier frequency of the modulated signal, and the Δf is the frequency offset needed to transmit two binary digits.

The DSSS watermark signal can be expressed as

$$w(i) = \sum_{k=-\infty}^{+\infty} \sum_{j=0}^{N_c-1} g(i - kT_b - jT_c)(c_W(i))_j (x_W(i))_k, \quad (8.3)$$

where $(x_W(i))_k$ is the k -th data bit of the watermark signal. $(c_W(i))_j$ represents the j -th chip of the orthogonal pseudo-noise (PN) sequence. $g(i)$ is the pulse waveform, T_c is the chip length, and $T_b = N_c T_c$ is the bit length. Then, w modulates a carrier frequency close to the range of the f_c utilized by FSK.

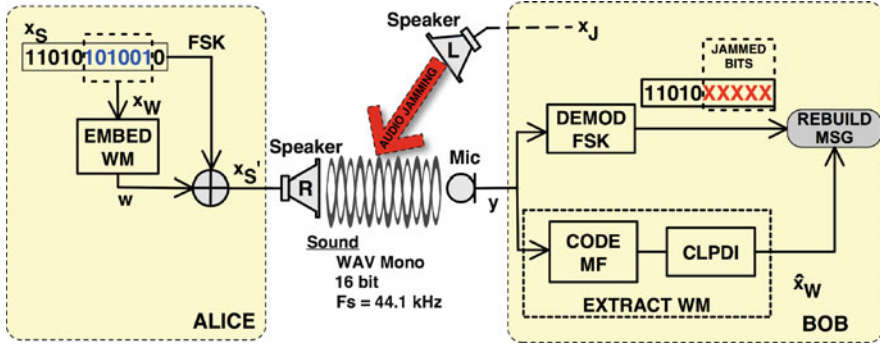


Fig. 8.3 WBPLSec system model in air-gap acoustic channel

Figure 8.3 shows the embedding stage of the watermark into the FSK, in which the information x_w is spread and then added in the host signal. In order to maintain the versatility, the watermarked signal x'_S is encoded into a waveform audio file format (WAV). Alice transmits the x'_S to Bob playing the WAV file through her loudspeaker. While Bob is recording, i.e., receiving, the message he jams it playing the jamming signal encoded into another WAV file. In this scheme, only the legitimate receiver, i.e., Bob, knows which part of the WAV file he jammed. Later, Bob is able to get a clean signal by replacing corrupted samples with the information conveyed by the SS watermark that it is immune to jamming interference. In contrast, the eavesdropper cannot remove the interference because he does not have any information on the jamming characteristics.

The physical layer security mechanism implemented by the WBPLSec consists of steps shown in Algorithm 1. In this model each sensor is equipped with a microphone and a loudspeaker; therefore, nodes in the WBAN convey humans' vital signal over the acoustic air-gap covert channel. Figure 8.1 shows the operating scenario of the WBPLSec inside the three network tiers model, in which the proposed solution can mitigate threats, such as man-in-the-middle (MitM) and eavesdropping, within off-body communications.

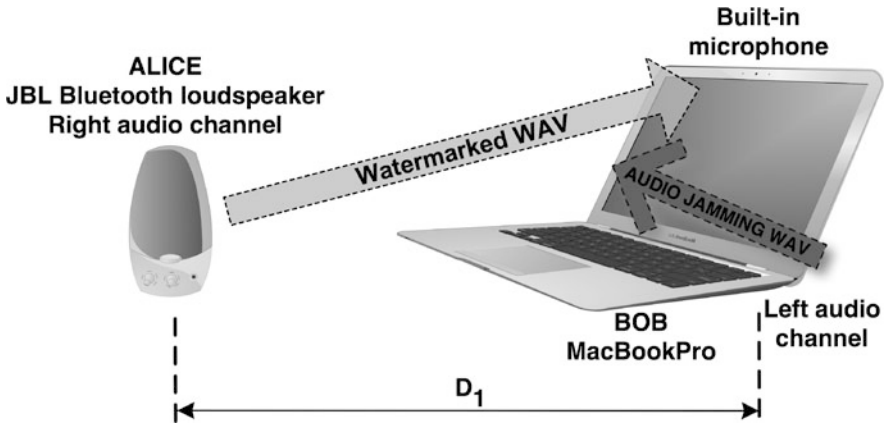
8.4 Experiments and Measurements

Experiment Setup

Experiments have been performed on a real test-bed to investigate the performance of the WBPLSec over the acoustic air-gap channel. The test-bed consisted of an Apple MacBook Pro and a JBL Flip Bluetooth speaker as shown in Fig. 8.4. The wireless speaker was necessary to vary the relative distance D_1 between Alice and Bob. The MacBook Pro is utilized as the main processing unit. Alice is emulated

Algorithm 1 WBPLSec protocol in acoustic air-gap channel

-
- 1: **procedure** PHYSICAL LAYER SECURITY
 - 2: *SS Watermarking (ALICE)*:
 A message is first modulated with DSSS and then embedded into the host FSK signal.
 The FSK watermarked message is encoded in a WAV file, then is played, i.e. transmitted, through the loudspeaker.
 - 3: *Jamming Receiver (BOB)*:
 The receiver jams N_W samples for each symbol transmitted by Alice.
 The jamming signal is encoded into a WAV file and played through BOB's loudspeaker while he is recording ALICE's message with his microphone.
 - 4: *Watermark Extraction (BOB)*:
 The receiver extracts the watermark utilizing a code matched filter.
 - 5: *Symbol Rebuild (BOB)*:
 Knowing which samples are jammed the receiver, i.e. Bob, is able to rebuild a clean symbol using information contained into the watermark.
 - 6: **end procedure**
-

**Fig. 8.4** Test-bed setup

with the Bluetooth speaker which plays only the *right* audio channel. Instead, Bob is emulated by the MacBook Pro and it plays only the *left* audio channel. The decision to play WAV files as a mono channel, i.e., only right for Alice and only left to jam, is due to the opportunity to split the communication and utilize one main processing unit, i.e., the MacBook Pro.

As output devices, MacBook Pro and JBL Flip have a frequency response that spans from 20 Hz to 20 kHz. Moreover, the internal speakers support a stereo data stream at bit depths of 16 bits per sample and at sample rates of 44.1 kHz. By the Nyquist–Shannon Sampling theorem [19], this means that the highest frequency

Table 8.1 Experiment scenario parameters

Parameter	Value
D_1	0.3 m, 0.5 m
FSK frequencies	17.5 kHz, 18.5 kHz
DSSS carrier frequency	19.5 kHz
Jamming frequency	17.5 kHz
FSK bit-rate ^a	8 bps
Number of bits FSK payload (N)	128
Number of bits FSK preamble ^b	256
Number of jammed bits (M)	40
Number of bits to create the watermark (N_W)	40
Watermarking scaling parameter (μ)	0.3, 0.5
DSSS Processing Gain (G_p) ^c	128, 256
Alice's WAV file ^d	Mono—right channel
Bob's jamming WAV file ^d	Mono—left channel
WAV file depth	16 bit
Input/output sampling frequency (F_s)	44.1 kHz
Input/output frequency response	20 Hz–20 kHz

^aThe low bit-rate is due to the oversampling, 5120 samples for each bit

^bIt consists of the preamble and a synchronization sequence

^cUsing Hadamard PN code

^dAuthor assumed perfect synchronization between Alice and Bob

signal that can be perfectly reconstructed without aliasing is a little over 22 kHz. On the other hand, as input device, the internal microphone of the MacBook Pro supports recording at bit depths of 16 bits per sample and at sample rates of 44.1 kHz (F_s). Table 8.1 lists the parameters used for experiments in the test-bed.

Experiments Over the Acoustic Air-Gap Channel

The FSK transmitter is a Matlab function that encodes binary 1's and 0's as two frequencies in the near range of ultrasound as shown in Fig. 8.2. The first part of the Alice's message consists of a preamble plus a synchronization sequence. The message payload consists of 128 bits. From this payload, only 40 bits (i.e., x_W) are utilized to create the SS watermark. The script creates a mono WAV right channel file (the left channel is silent) ready to be transmitted through the Bluetooth speaker. The amplitude of the watermarked signal is scaled up in order to maximize the volume of a 16 bit audio signal. The script creates also a continuous wave (CW) jamming signal. This signal uses a set amount of time to jam 40 bits over one frequency utilized by FSK. A second mono WAV left channel file is created with jamming information. The author assumed a perfect synchronization of these two WAV files.

Bob records the jammed WAV file through the MacBook Pro internal microphone as shown in Fig. 8.4. In accordance with the WBPLSec Algorithm 1, the receiver demodulates the FSK and extracts the watermark to rebuild the original message. The watermark extraction is performed with the use of a code matched filter (CMF). The watermark extraction is performed by computing the normalized statistics as [15, 23]

$$r \triangleq \frac{\langle \mathbf{y}_M, \mathbf{c}_W \rangle}{\langle \mathbf{c}_W, \mathbf{c}_W \rangle}, \quad (8.4)$$

where the \mathbf{y}_M is the received signal by Bob as shown in Fig. 8.3, \mathbf{c}_W represents the PN sequence. The author assumed $\langle \mathbf{c}_W, \mathbf{c}_W \rangle = 1$, i.e., PN sequences have unit energy. To speed up the process the author utilized the chip level post-detection integration (CLPDI) [11, 22]. CLPDI combines multiple outputs of the CMF reducing the time needed for the SS code synchronization. After the code synchronization, the receiver despreads the signal and then extracts the watermark.

The detector is the same introduced with the traditional spread spectrum watermarking [15, 23] and the estimation of the embedded bit is given by

$$\hat{x}_W = \text{sign}(r). \quad (8.5)$$

The transition between frequencies in the close range of ultrasound produces highly audible clicking noise. To mitigate this effect the Matlab script applies a fade-in and fade-out for each tone [4, 9]. One drawback of the usage of this medium is the low bit-rate achievable. Actually, the receiver needs a sufficient number of samples per symbol to detect the signal power. The oversampling of each symbol reduces the bit-rate but improves the communication reliability.

Results

The experiment described in the previous section was carried out arranging the test-bed in a room. The main objective was to verify the reliability of the WBPLSec over an acoustic air-gap channel. The acoustic communication between Alice and Bob was evaluated using the bit error rate (BER) as metric. The laptop (i.e., MacBook Pro) and the wireless loudspeaker (i.e., JBL Flip) were placed face to face at different distances up to 0.5 m. Due to hardware and firmware limitations, experiments showed that at wider distances BER increases, and hence, the wireless communication might not be feasible in those cases. The author assumed that the maximum distance is comparable with WBAN layout. Figure 8.5 illustrates the transmitted signal in the acoustic air-gap covert channel, i.e., the watermarked FSK signal and the CW jamming as well.

Bob and the adversary, i.e., Eve, receive the acoustic signal through the microphone. The microphone records signal up to 20 kHz. In that frequency range, it is

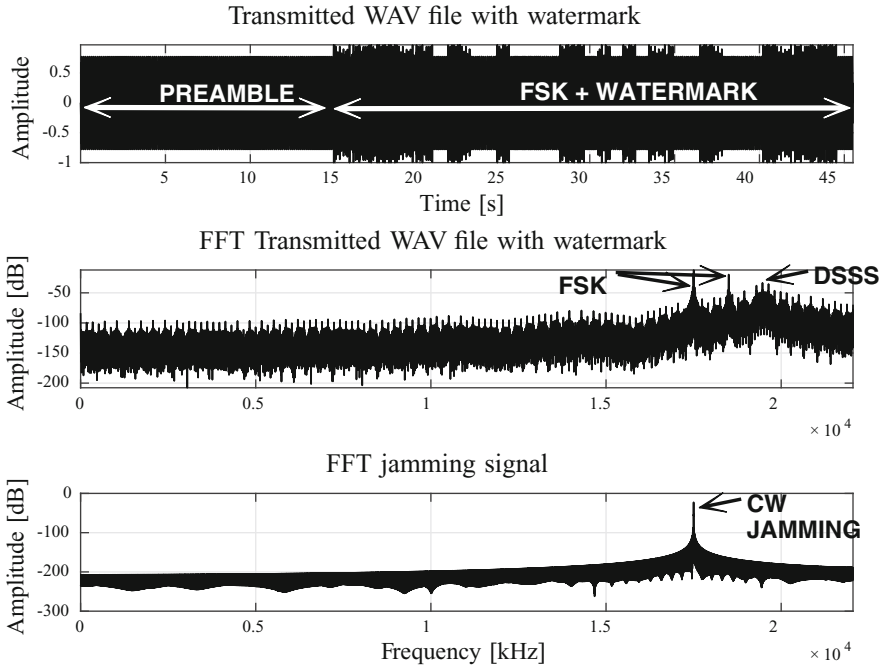


Fig. 8.5 Signals transmitted in the acoustic air-gap channel

a linear system that utilizes an automatic gain control (AGC) to adjust the signal amplitude and use the internal analog to digital converter (ADC) in its whole range. In this architecture, Bob selected a 17.5 kHz CW jamming to suppress up to 40 bits of the payload transmitted by Alice. The jamming effectiveness depends on the distance between Alice and Bob. The idea utilized for the jamming was to increase its intensity by altering the dynamic of the microphone and weakening part of the wanted Alice’s signal. Figure 8.6 shows the signal recorded by the legitimate receiver in which a segment of the payload is jammed. Only Bob knows which bits are jammed.

During the experiments, the ambient noise reduction feature was turned off on the laptop and the energy saving on the external loudspeaker as well. These features might alter the transmitted and received acoustic signals. In acoustic communications, ambient noise and distance are the greatest limitations. Environmental noise usually creates audio clipping because the microphone is driven to its maximum excitation [9]. The results confirmed these limitations, and therefore, experiments occurred in a quiet room. In order to have a reliable wireless communication over the air-gap acoustic channel, Bob needs enough samples per bit. The trade-off between the bit oversampling and the communication reliability sets the bit-rate in the range defined in Table 8.1. Currently, this implementation supports only low bit-rate, e.g., 8 bps.

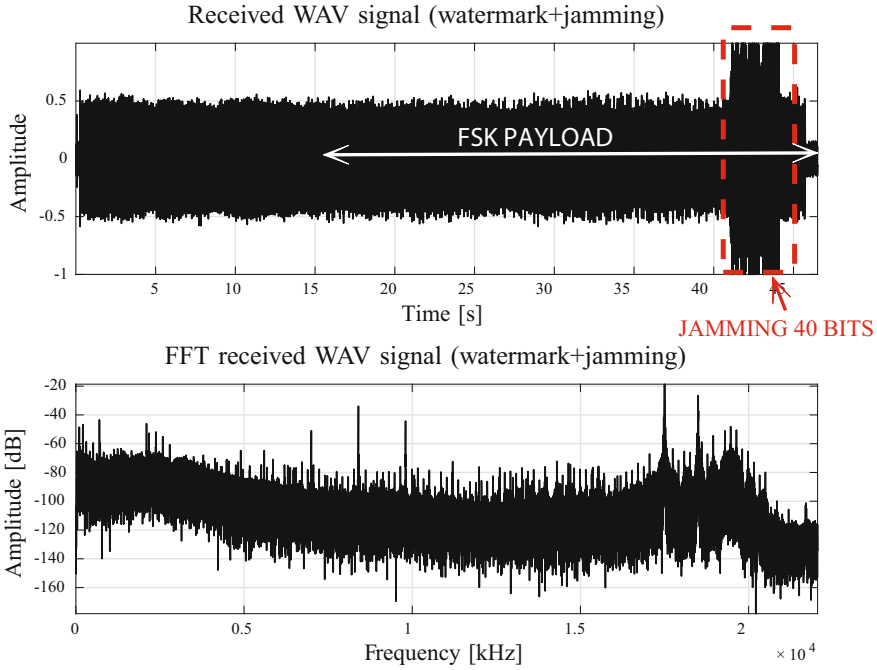


Fig. 8.6 Signal received by the legitimate receiver, i.e., Bob

Figure 8.7 shows as using the CLPDI technique, the receiver reduces the uncertainty region by a factor of 16, i.e., m , improving the performance of the watermark code detection.

Figure 8.8 illustrates the BER of the payload (i.e., 128 bits) at the legitimate receiver. During the measurement campaign, the author modified the distance between Alice and Bob, the DSSS processing gain (G_p), and the intensity of the watermark μ as defined in (8.1). Varying the distance between Alice and Bob, the higher is the G_p , the lower is the BER that yields to increase the performance of the proposed protocol. The SS watermark was not affected by the jamming as its bit error rate (BER_{WM}) was 0 for each communication.

The WBPLSec is a promising technique for low-power sensor network. This algorithm secures the wireless communication utilizing lower energy than other jamming techniques [23]. Table 8.2 shows the evaluation of energy cost for each packet transmitted by Alice and jammed by Bob. The implementation of WBPLSec requires more energy but the author expects to save computation when compared to encryption [8]. Furthermore, the extra energy might be tuned changing the length of the watermark, i.e., N_W , and the number of jammed bits, i.e., M .

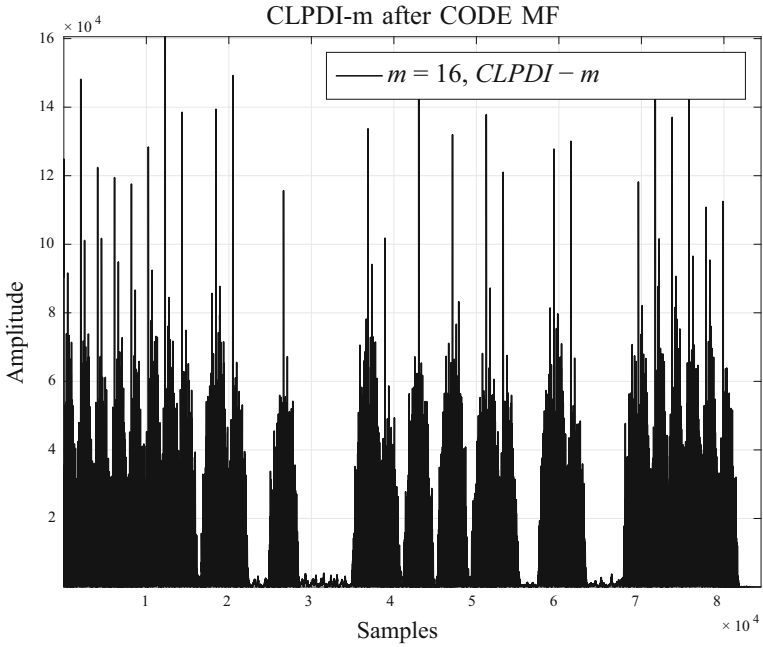


Fig. 8.7 Output of the CLPDI block after the CMF

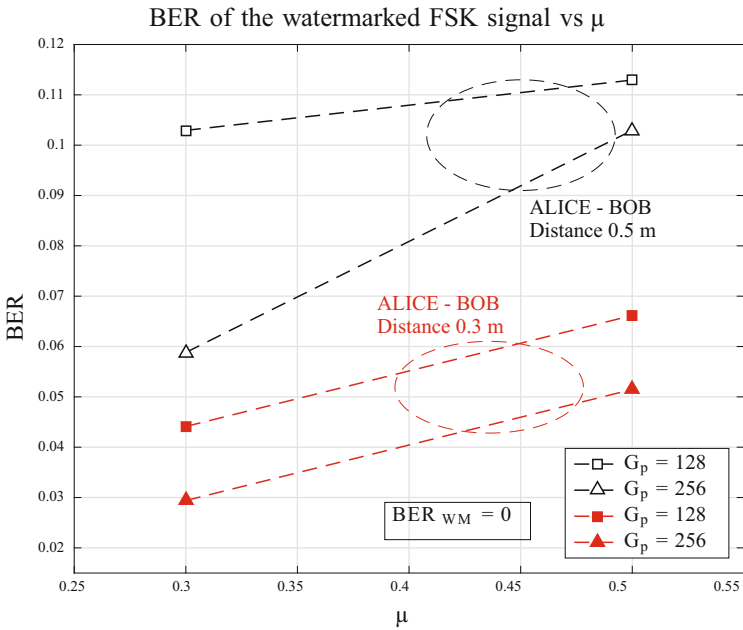


Fig. 8.8 BER of the FSK watermarked and jammed signal received by Bob

Table 8.2 Energy cost for each packet

ALICE energy Tx	BOB energy Tx	WBPLSec total energy	$N = 128, N_W = 40, M = 40$
$E_{pkt} \left(1 + \frac{N_W}{N}\right)$	$\frac{3}{2} E_{pkt}$	$E_{pkt} \left(1 + \frac{N_W}{N} + \frac{M}{N}\right)$	$1.625 \cdot E_{pkt}^a$

^a E_{pkt} is the energy for each packet

8.5 Conclusions

Due to their nature WBANs are vulnerable to eavesdropping attacks. Furthermore, WBANs are subject to security threats from network dynamics. The idea proposed in this paper shall support the design of new sensors with physical layer capability to secure a wireless communication through acoustic channel gets stronger the whole WWN.

The watermark-based communication with a jamming receiver needs multiple wireless interfaces. Today, wireless sensors are equipped with several air interfaces, e.g., audio inputs/outputs, BLE, and Wi-Fi. The author successfully demonstrated that the WBPLSec algorithm is applicable to acoustic air-gap covert channels to exchange a secret shared key. The results demonstrated that this method is a valuable technique for deploying physical layer security by creating a *secure region* around the receiver up to 50 cm.

The utilization of consumer electronics during experiments showed some drawbacks of this medium. This medium has some limitations in the communication range on how even the maximum achievable bit-rate is. It does not mean that acoustic communications are useless. The WBAN use case, in which wireless few nodes are in proximity can benefit from the WBPLSec over an acoustic channel to exchange secret shared keys. Hence, there are scenarios which might be convenient for exploiting existing low power air interface instead to re-design the whole wireless sensors. This study supports such strategy.

References

1. Anderson, R.J.: Security Engineering - A Guide to Building Dependable Distributed Systems, 2nd edn. Wiley, New York (2008)
2. Arbia, D.B., Alam, M.M., Moullec, Y.L., Hamida, E.B.: Communication challenges in on-body and body-to-body wearable wireless networks — a connectivity perspective **5** (7 2017). <https://doi.org/10.3390/technologies5030043>
3. Cox, I.J., Kilian, J., Leighton, F., Shamoon, T.: Secure spread spectrum watermarking for multimedia. *IEEE Trans. Image Process.* **6**(12), 1673–1687 (1997). <https://doi.org/10.1109/83.650120>
4. Deshotels, L.: Inaudible sound as a covert channel in mobile devices. In: 8th USENIX Workshop on Offensive Technologies (WOOT 14). USENIX Association, San Diego (2014). <https://www.usenix.org/conference/woot14/workshop-program/presentation/deshotels>

5. Guri, M., Solewicz, Y.A., Daidakulov, A., Elovici, Y.: MOSQUITO: covert ultrasonic transmissions between two air-gapped computers using speaker-to-speaker communication. CoRR abs/1803.03422 (2018). <http://arxiv.org/abs/1803.03422>
6. Hämäläinen, M., Li, X.: Recent advances in body area network technology and applications. *Int. J. Wirel. Inf. Netw.* **24**, 63–64 (2017)
7. Hanspach, M., Goetz, M.: On covert acoustical mesh networks in air. CoRR abs/1406.1213 (2014). <http://arxiv.org/abs/1406.1213>
8. Harrison, W., Almeida, J., Bloch, M., McLaughlin, S., Barros, J.: Coding for secrecy: an overview of error-control coding techniques for physical-layer security. *IEEE Signal Process. Mag.* **30**(5), 41–50 (2013). <https://doi.org/10.1109/MSP.2013.2265141>
9. Harvest, Z., Bonnie, E.: SqueakyChat: ultrasonic communication using commercial notebook computers (2014). <https://github.com/bonniee/ultrasonic/blob/master/SqueakyChat.pdf>
10. IEEE Standard for Local and metropolitan area networks - Part 15.6: Wireless Body Area Networks (Feb 2012). <https://doi.org/10.1109/IEEESTD.2012.6161600>
11. Iinatti, J., Latva-aho, M.: A modified CLPDI for code acquisition in multipath channel. In: 12th IEEE International Symposium on Personal, Indoor and Mobile Radio Communications. PIMRC 2001. Proceedings (Cat. No.01TH8598), vol. 2, pp. F–6–F–10 vol.2 (Sep 2001). <https://doi.org/10.1109/PIMRC.2001.965284>
12. Kramer, F., Starr, S., Wentz, L., National Defense University Press for Technology, National Security Policy: Cyberpower and National Security. Potomac Books, Washington (2009)
13. Lampson, B.W.: A note on the confinement problem. *Commun. ACM* **16**(10), 613–615 (1973). <http://doi.acm.org/10.1145/362375.362389>
14. Li, M., Lou, W., Ren, K.: Data security and privacy in wireless body area networks. *Wirel. Commun.* **17**(1), 51–58 (2010). <https://doi.org/10.1109/MWC.2010.5416350>
15. Malvar, H., Florencio, D.: Improved spread spectrum: a new modulation technique for robust watermarking. *IEEE Transactions on Signal Processing* **51**(4), 898–905 (2003). <https://doi.org/10.1109/TSP.2003.809385>
16. Otto, C., Milenković, A., Sanders, C., Jovanov, E.: System architecture of a wireless body area sensor network for ubiquitous health monitoring. *J. Mob. Multimed.* **1**(4), 307–326 (2005). <http://dl.acm.org/citation.cfm?id=2010498.2010502>
17. Partala, J., Keränen, N., Särestöniemi, M., Hämäläinen, M., Iinatti, J., Jämsä, T., Reponen, J., Seppänen, T.: Security threats against the transmission chain of a medical health monitoring system. In: 2013 IEEE 15th International Conference on e-Health Networking, Applications Services (Healthcom), October 2013, pp. 243–248 (2013). <https://doi.org/10.1109/HealthCom.2013.6720675>
18. Ronquillo, J., Winterholler, J., Cwikla, K., Szymanski, R., Levy, C.: Data from: health it, hacking, and cybersecurity: national trends in data breaches of protected health information (2018). <https://doi.org/10.5061/dryad.24275c6>
19. Shannon, C.E.: Communication in the presence of noise. *Proc. IRE* **37**(1), 10–21 (1949). <https://doi.org/10.1109/JRPROC.1949.232969>
20. Shannon, C.: Communication theory of secrecy systems. *Bell Syst. Tech. J.* **28**(4), 656–715 (1949). <https://doi.org/10.1002/j.1538-7305.1949.tb00928.x>
21. Smart body area networks (SmartBAN); system description. Tech. Rep. ETSI TR 103 394 V1.1.1, European Telecommunication Standard Institute (ETSI) (1 2018). http://www.etsi.org/deliver/etsi_tr/103300_103399/103394/01.01.01_60/tr_103394v010101p.pdf
22. Soderi, S., Iinatti, J., Hämäläinen, M.: CLPDI algorithm in UWB synchronization. In: Proceedings of the 2003 International Workshop on UWB Systems, pp. 759–763 (2003)
23. Soderi, S., Mucchi, L., Hämäläinen, M., Piva, A., Iinatti, J.H.: Physical layer security based on spread-spectrum watermarking and jamming receiver. *Trans. Emerg. Telecommun. Technol.* **28**(7) (2017). <http://dblp.uni-trier.de/db/journals/ett/ett28.html#SoderiMHPI17>

Chapter 9

Secrecy Capacity of Diffusion-Based Molecular Communication Systems



Lorenzo Mucchi, Alessio Martinelli, Stefano Caputo, Sara Jayousi, and Massimiliano Pierobon

9.1 Introduction

Molecular communication (MC) is a recent inter-disciplinary research topic between telecommunications, computer science, and biology [1]. The basic concept under this research area is that in biological systems, which include the human body, the transmitters and receivers communicate each other by using chemical signals or molecules. Molecular communication is seen by telecommunication engineers as a new paradigm where the information flows through chemical reactions and molecules transportation, as opposed to radio or optical signals. For biologists, MC is an abstraction of how biological cells and their components communicate. During the last decade, researchers devoted a lot of efforts in investigating and developing MC-based nano-(bio)-devices and nano-(bio)-networks, and MC is now considered a future (potentially disruptive) communication technology. Communications at molecular/nano-scale level have very different rules and objectives compared to the traditional radio communications.

Healthcare is one of the most promising application fields of MC [2]. In particular, MC for health studies how biological and artificial components (nano-sensors, nano-reactors) communicate with each other using molecules. The impacts of this research study could enable a wide number of future applications such as lab-on-a-chip, drug/DNA delivery systems, and human body monitoring using

L. Mucchi (✉) · A. Martinelli · S. Caputo · S. Jayousi
Department of Information Engineering, University of Florence, Firenze, Italy
e-mail: lorenzo.mucchi@unifi.it

M. Pierobon
Department of Computer Science & Engineering, University of Nebraska-Lincoln,
Lincoln, NE, USA
e-mail: pierobon@cse.unl.edu

implanted biochemical sensors [3]. Recently biological cells have been proposed to be as programmable computing systems, and the interaction between cells as a biological computer network. This new vision of biological cells as a network led to use information theory tools to define the performance of an MC system composed of biological or engineered cells [4]. Although much effort has been already devoted to the study of MC systems, most of the research has been focused on the information theoretical foundation.

Security has always been an important feature of every communication systems, in particular where information is privacy-sensitive, such as human health data. Molecular communications are expected to be particularly sensitive to security. Security issues related to this novel communication paradigm have been only partially considered. Existing papers focus basically on providing some first insights about security aspects of MC systems, by highlighting the open issues and directions of potential solutions [5]. It is important that security in this new communication paradigm is investigated from the very beginning of its practical development (security by design). Adding security features when the MC systems are ready to be deployed could be a serious problem, which could lead to a decrease in the interest for this promising technology.

This paper focuses on the theoretical derivation of the information leakage and secrecy capacity [6, 7] of a diffusion-based MC system. In particular, a closed-form mathematical expression of the secrecy capacity of a diffusion-based MC system is derived. This metric is useful to define how secure is a communication link, when information flows by molecules diffusion. The numerical results show the secrecy capacity as a function of the distance between transmitter–receiver (Alice–Bob) and transmitter–eavesdropper (Alice–Eve). The MC secrecy capacity is also drawn as a function of the transmitter bandwidth, the average thermodynamic power, and the receiver radius, which are important parameters to be considered when designing an MC system.

The rest of this paper is organized as follows: In Sects. 9.2 and 9.3 we review the main processes, components, and information-theoretical results at the basis of a diffusion-based MC system, respectively. In Sect. 9.4 we detail our main contribution in terms of closed-form expressions for the information leakage and secrecy capacity of such a system, while in Sect. 9.5 we present a study on the MC secrecy with numerical results based on these expressions. Finally, in Sect. 9.6 we conclude this paper.

9.2 Diffusion-Based Molecular Communication System

The processes of molecule emission, diffusion, and reception can be abstracted to be the transmitter, the channel, and the receiver of a molecular communication system, respectively. These components are located in the physical system, which is the space volume where the communication takes place, as shown in Fig. 9.1. The physical system follows laws and is influenced by parameters that depend on

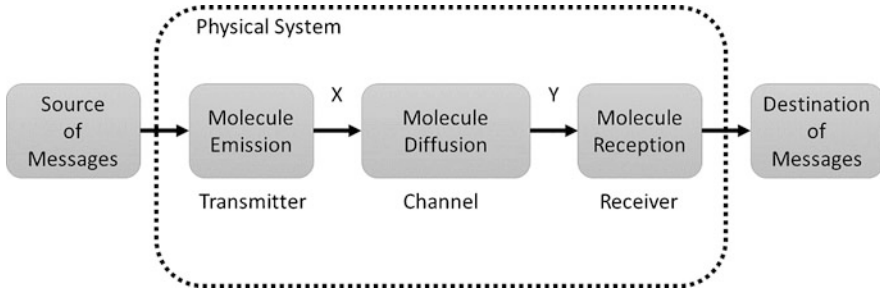


Fig. 9.1 Information-theoretical diagram of a diffusion-based MC system

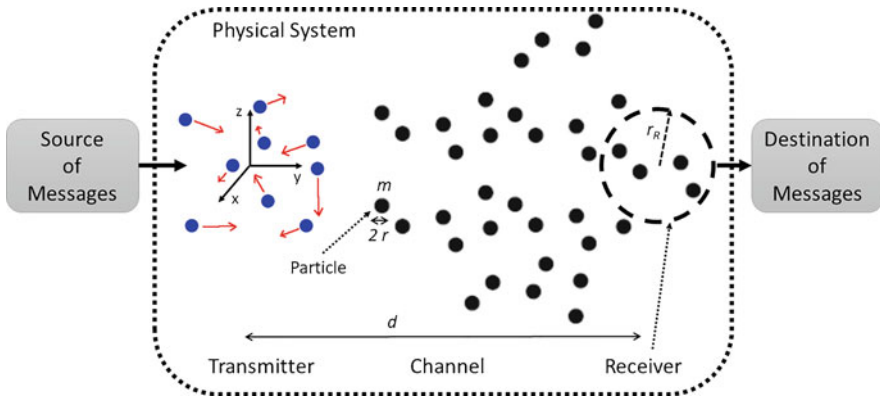


Fig. 9.2 Physical scheme of the diffusion-based MC system

how these components are physically realized. For example, in a drug delivery application inside the human body, once the reception of a specific concentration of molecules is detected by the destination, it can start chemical reactions to synthesize drug molecules.

The physical system considered in this paper is reported in Fig. 9.2 and it is based on the following assumptions:

- The diffusion-based MC channel extends infinitely in all three dimensions (x, y, z) . A fluid with viscosity μ fills the space. The fluid is assumed not to have flow currents or turbulence, i.e., the propagation is solely due to the Brownian motion;
- The transmitter emits indistinguishable molecules, equivalent to spherical particles of radius r and mass m ;
- The transmitter is considered point-wise and located in $(0, 0, 0)$;
- Each particle, once emitted, follows a movement that is independent from the others and according to its Brownian motion in the fluid. The Brownian motion of a molecule in a fluid is a random motion according to the Langevin equation [8];

- The (legitimate) receiver, located at distance d from the transmitter, aims to detect a signal proportional to the concentration of the incoming particles.

As depicted in Fig. 9.2, the transmitter receives the messages from the source and produces a signal suitable for the transmission over the channel. The transmitted signal X is represented by the number of particles $n_T(t)$ emitted into the fluid over the time t .

Molecules diffusion process is the channel that propagates the signal from the transmitter to the receiver. Diffusion is the result of the collective Brownian motion of many particles from a more dense area to an area with lower density. Brownian motion represents the propagation of the particles emitted by the transmitter in the 3D space and it can be expressed as the translation of the (x, y, z) coordinates from the location of the transmitter to a general location at time t . This location can be computed by applying the well-known Langevin equation [8] to each particle:

$$m \frac{\partial^2 \mathbf{P}^{[n]}(t)}{\partial t^2} = -6\pi\mu r \frac{\partial \mathbf{P}^{[n]}(t)}{\partial t} + \mathbf{F}(t), \quad (9.1)$$

where $\mathbf{P}^{[n]} = (P_x^{[n]}, P_y^{[n]}, P_z^{[n]})$ is the position of the particle in the 3D space, m is the mass, and r is the radius of the particle. μ is the viscosity of the fluid and $\mathbf{F}(t)$ is a random process whose probability density function is Gaussian with

$$E\{F_i(t), F_j(t')\} = 12\pi\mu r K_b T \delta(i - j) \delta(t - t'),$$

where K_b is the Boltzmann constant, T is the absolute temperature of the fluid, and $\delta(\cdot)$ is the Dirac function [9].

The message is reconstructed by the receiver from the observed signal Y that is proportional to the concentration of the incoming particles. The received signal is represented by the time-varying number of particles that are located inside a spherical volume V_R centered at the receiver location. The following statement should hold: $r_R \ll d$, where r_R is the radius of the receiver and d is the distance between the transmitter and the receiver. The above statement makes the results not dependent on a specific technique for the reception. Thus, the received signal Y can be defined as the number of particles emitted by the transmitter in the time interval $(0, t)$ whose position $\mathbf{P}^{[n]}(t)$ at time t is inside the volume V_R .

9.3 Capacity of a Molecular Communication System

The information capacity of a communication system is defined by the well-known equation by Claude Shannon [7]. The Shannon capacity formula

$$C = \max_{f_X(x)} I(X; Y) = \max_{f_X(x)} \{H(X) - H(X|Y)\} \quad (9.2)$$

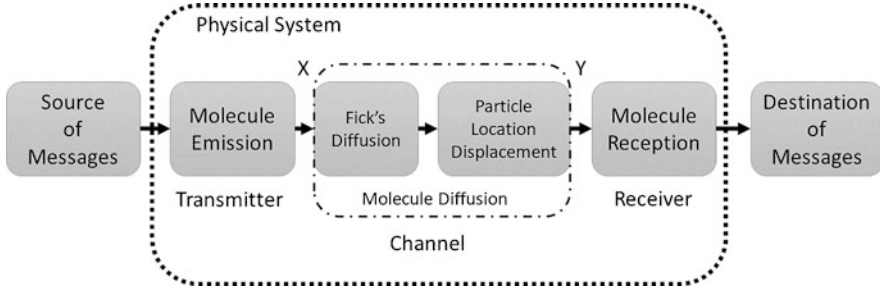


Fig. 9.3 Scheme of the diffusion-based MC system: the channel is divided into two effects: Fick's diffusion and particle location displacement

defines the information capacity C as the maximum (over all possible signals emitted by the source) difference between the entropy $H(X)$ of the signal X in input to the channel and the equivocation rate $H(X|Y)$. The equivocation rate represents the entropy of X conditioned to the observation signal Y at destination. The difference between the entropy $H(X)$ and the equivocation $H(X|Y)$ is called mutual information $I(X; Y)$.

Taking in mind the physical system defined in Sect. 9.2, two effects have to be characterized to derive the mutual information $I(X; Y)$: the channel memory and the molecular noise. In [4] the computation of the mutual information is divided into two processes: the Fick's diffusion and the particle location displacement (Fig. 9.3). The former takes into account solely the effects of the channel memory, while the latter the effects of the molecular noise.

The mutual information of a diffusion-based MC system is analytically derived in [4]

$$I(x; y) = 2W H(\bar{n}_T) - \log_2 \left[(\pi d D)^2 \right] - \frac{4d}{3 \ln 2} \sqrt{\frac{\pi W}{D}} - 2W \eta - 2W \ln(W \tau_p) - 2W \ln(\Gamma(\eta)) - 2W(1 - \eta)\psi(\eta), \quad (9.3)$$

where

$$\eta = \frac{2E[\bar{n}_T]R_{V_R}}{3Wd},$$

$$E[\bar{n}_T] = \frac{\bar{P}_H}{3W K_b T},$$

$$H(\bar{n}_T) = 1 + \log_2 E[\bar{n}_T],$$

and

- W is the bandwidth of the transmitted signal X ,
- $\tau_p = \frac{r_R^2}{D}$ is the time interval in which we consider a quasi-constant particle distribution,

- $\Gamma(\cdot)$ is the gamma function and $\psi(\cdot)$ is the digamma function,
- $D = \frac{K_b T}{6\pi\mu r}$ is the diffusion coefficient,
- d is the distance between the transmitter and the receiver,
- r_R is the radius of the spherical receiver volume,
- \bar{P}_H is the average thermodynamic power,
- \bar{n}_T is the discrete-time version of the particle concentration $n_T(t)$.

From (9.2) and (9.3), the capacity C of the diffusion-based MC system can be derived [4]

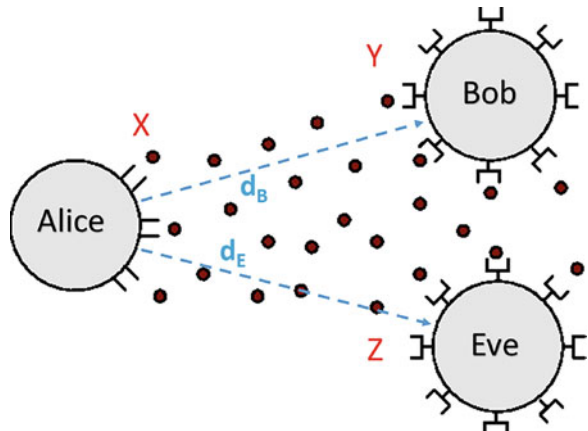
$$C = 2W \left(1 + \log_2 \frac{\bar{P}_H}{3W K_b T} \right) - \log_2 \left[(\pi d D)^2 \right] - \frac{4d}{3 \ln 2} \sqrt{\frac{\pi W}{D}} - 2W\eta - 2W \ln \left(W \frac{r_R^2}{D} \right) - 2W \ln(\Gamma(\eta)) - 2W(1 - \eta)\psi(\eta). \quad (9.4)$$

9.4 Information Leakage and Secrecy Capacity

The information-theoretical security computes exactly the amount of information that an eavesdropper (Eve) can get by observing the channel while the legitimate communication is on. The generic reference scheme for evaluating the information-theoretical security of an MC system is reported in Fig. 9.4. Alice is the cell that transmits the particles, Bob is the intended legitimate receiver-cell, and Eve is the eavesdropping receiver-cell.

The amount of information that is exchanged by Alice and Bob is given by (9.3), while the amount of information “stolen” by Eve is called information leakage.

Fig. 9.4 Scheme for the evaluation of the information-theoretical security of a diffusion-based MC system



In information-theoretical security, the information leakage can be written as [6]

$$I(X; Z) = H(X) - H(X|Z), \quad (9.5)$$

where Z is the signal observed by Eve. The eavesdropper receiving particle is supposed to be at distance d_E from the transmitter.

The secrecy capacity of the diffusion-based channel can be derived as the difference between the mutual information of the legitimate communication link and the information leakage [6]. It is important to note that the secrecy capacity has to be intended as an upper bound of the security performance of a diffusion-based MC system.

$$C_s = \max_{f_X(x)} \{I(X; Y) - I(X; Z)\} \geq \max\{I(X; Y)\} - \max\{I(X; Z)\} = C_B - C_E, \quad (9.6)$$

where C_B is the capacity of the legitimate channel and C_E is the capacity of Eve's channel. Since the secrecy capacity cannot be less than zero, (9.6) is usually written as

$$C_s = \max\{0, C_B - C_E\}. \quad (9.7)$$

Both C_B and C_E can be computed by using (9.4). The secrecy capacity in (9.7) represents the amount of information that can be securely exchanged between two legitimate particles (transmitter and receiver) while an eavesdropping particle is "overhearing" the channel.

The capacity of the legitimate receiver (Bob) is

$$\begin{aligned} C_B = 2W \left(1 + \log_2 \frac{\bar{P}_H}{3W K_b T} \right) - \log_2 \left[(\pi d_B D)^2 \right] - \frac{4d_B}{3 \ln 2} \sqrt{\frac{\pi W}{D}} \\ - 2W \eta_B - 2W \ln \left(W \frac{r_{R_B}^2}{D} \right) - 2W \ln(\Gamma(\eta_B)) - 2W(1 - \eta_B)\psi(\eta_B), \end{aligned} \quad (9.8)$$

where

$$\eta_B = \frac{2\bar{P}_H r_{R_B}}{9W^2 K_b T d_B}. \quad (9.9)$$

The capacity of Eve's receiver can be computed by substituting d_B and r_{R_B} with d_E and r_{R_E} , respectively, into (9.8) and (9.9).

The secrecy capacity of an MC diffusion-based system is

$$\begin{aligned}
 C_s = & \log_2 \left[\left(\frac{d_E}{d_B} \right)^2 \right] + \frac{4}{3 \ln 2} \sqrt{\frac{\pi W}{D}} (d_E - d_B) + 2W(\eta_E - \eta_B) \\
 & + 2W \ln \left[\left(\frac{r_{R_E}}{r_{R_B}} \right)^2 \right] + 2W \ln \left[\frac{\Gamma(\eta_E)}{\Gamma(\eta_B)} \right] + 2W [(1 - \eta_E) \psi(\eta_E) \\
 & - (1 - \eta_B) \psi(\eta_B)]. \tag{9.10}
 \end{aligned}$$

9.5 Numerical Results

In this section, a numerical evaluation of the closed-form mathematical expression of the secrecy capacity of the diffusion-based MC system is provided. A common set of parameters have been used for the numerical evaluation:

- the radius of the receiver volume, assumed to be spherical, is $r_{R_B} = r_{R_E} = 10 \times 10^{-9}$ m [10];
- the temperature of the system is set to a standard room temperature $T = 298.15$ °K;
- the diffusion coefficient $D = 10^{-9}$ m²/s [10];
- the Boltzmann constant $K_b = 1.380650424 \times 10^{-23}$ J/K.

Figure 9.5 shows the secrecy capacity as a function of Eve’s distance for different values of the bandwidth of the transmitted signal. The distance of the legitimate receiver is 150 μm. While the distance of the Eve is lower than the distance of Bob, the C_s is zero. As the distance of Eve increases, the secrecy capacity grows. The slope of the C_s is lower for high values of the bandwidth.

Figure 9.6 shows the secrecy capacity as a function of the bandwidth, for different distances of the eavesdropper. The distance of the legitimate receiver is 150 μm. While the distance of the Eve is lower than the distance of Bob, the C_s is zero, for any value of bandwidth. As the distance of Eve increases, the C_s grows up to $B = 30$ Hz and then it starts decreasing. For high bandwidth $B = 60$ Hz, a greater distance of Eve does not yield a much larger secrecy capacity.

The bandwidth has been limited to the interval $B \in [20, 60]$ Hz. A natural diffusion-based MC system is the communication between human brain neurons. According to [11], 20 Hz and 60 Hz are the frequencies of diffusion of molecules between the synapses of the human brain neurons for the processing of general information and for visual images, respectively.

Figure 9.7 shows the 2D map of the secrecy capacity. The secrecy map is calculated by assuming Eve located in a generic point (x, y) of the surface and computing the C_s [12]. The transmitter (Alice) is positioned in $(0, 0)$, while the legitimate receiver (Bob) is located in $(100, 100)$ μm. For the sake of clarity, we

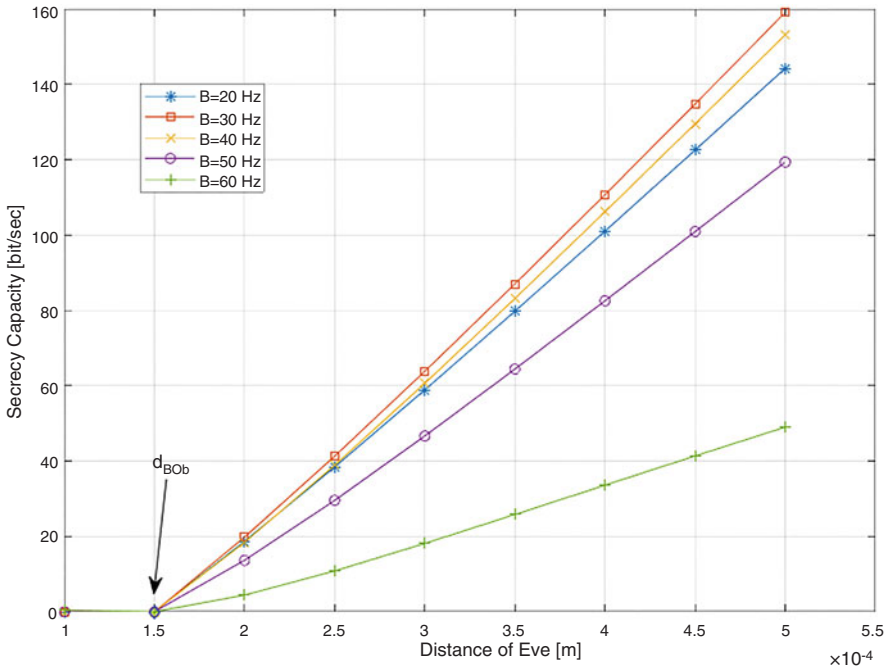


Fig. 9.5 Secrecy capacity as a function of the distance of the eavesdropper, for several values of the bandwidth. The distance of the legitimate receiver (Bob) is 150 μm

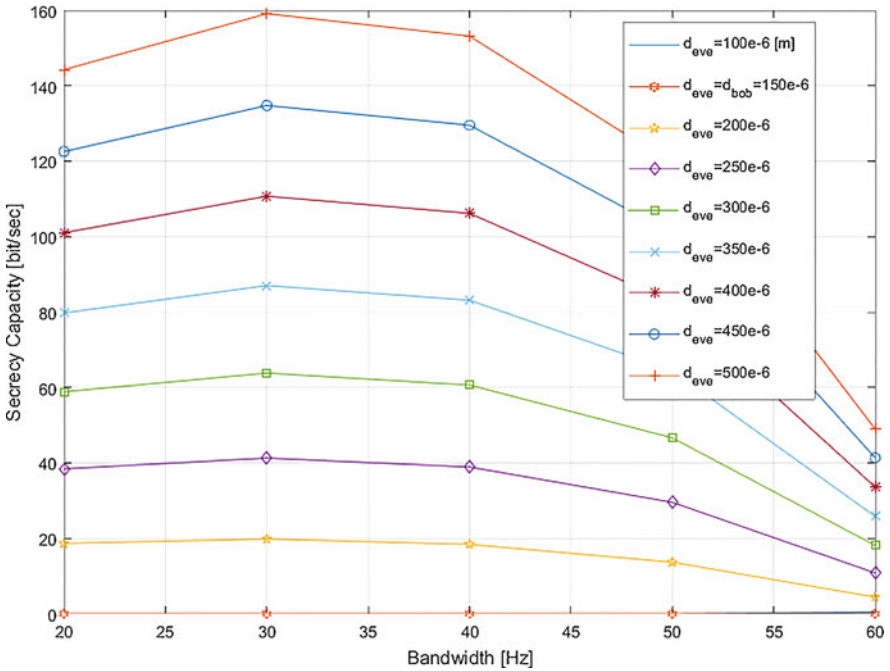


Fig. 9.6 Secrecy capacity as a function of the bandwidth of the transmitter, for several values of the eavesdropper's distance. The distance of the legitimate receiver (Bob) is 150 μm

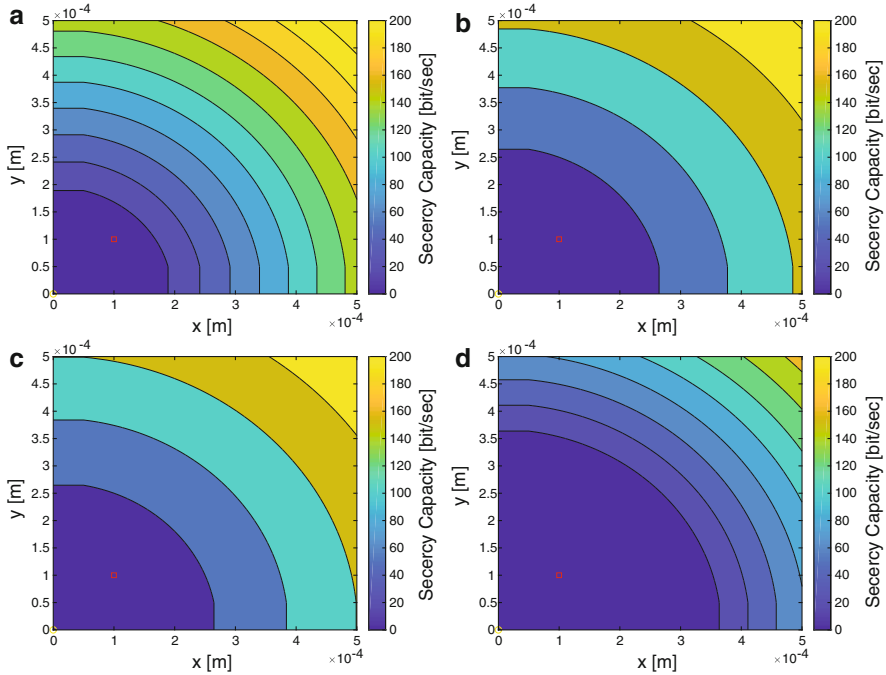


Fig. 9.7 2D map of the secrecy capacity. The transmitter (Alice) is positioned in $(0, 0)$, while the legitimate receiver (Bob) is located in $(100, 100) \mu\text{m}$ (red point). (a) Secrecy map with: $B = 20 \text{ Hz}$, $\bar{P}_H = 1 \times 10^{-12} \text{ W}$, $r_{R_B} = r_{R_E} = 10 \times 10^{-9} \text{ m}$. (b) Secrecy map with: $B = 40 \text{ Hz}$, $\bar{P}_H = 1 \times 10^{-12} \text{ W}$, $r_{R_B} = r_{R_E} = 10 \times 10^{-9} \text{ m}$. (c) Secrecy map with: $B = 20 \text{ Hz}$, $\bar{P}_H = 2 \times 10^{-12} \text{ W}$, $r_{R_B} = r_{R_E} = 10 \times 10^{-9} \text{ m}$. (d) Secrecy map with: $B = 20 \text{ Hz}$, $\bar{P}_H = 1 \times 10^{-12} \text{ W}$, $r_{R_B} = 20 \times 10^{-9} \text{ m}$, $r_{R_E} = 10 \times 10^{-9} \text{ m}$

decided to show only the first quadrant, but the C_s is spherical. In other words, the expression of the secrecy capacity considers (and it is valid for) a 3D spherical system; the 2D representation has been selected only for easier display of the results. The four secrecy maps in Fig. 9.7 have been selected to highlight the dependence of the C_s on the transmit bandwidth, on the average thermodynamic power, and on the receiver radius. Analyzing Fig. 9.7a and b we can appreciate the effect of doubling the bandwidth. As expected, a greater bandwidth at the transmitter results into a larger portion of space where the secrecy capacity is zero. In general, doubling the bandwidth makes the “strips” of the secrecy map larger.

The same effect is provided if the average thermodynamic power is increased. In fact, by observing Fig. 9.7a and c we can conclude that increasing \bar{P}_H yields larger “strips” in the secrecy capacity map. In other words, a higher transmitting power produces lower secrecy capacity, since Eve can be located in more points of the surface where it can receive information.

Observing Fig. 9.7a and d we can appreciate the effect of doubling the radius of Bob’s receiver. This produces a drastic decrease of the C_s , since the ligand–receptor

binding noise increases with the receiver's radius [13]. The ligand–receptor binding noise is a model which allows to simulate the random perturbations in the chemical processes of the reception.

9.6 Conclusion

In this paper we derived the closed-form mathematical expressions for the information leakage and the secrecy capacity of an MC system based on molecules diffusion. These metrics are useful to define how much secure is a communication link, when the information flows by molecules diffusion. The secrecy capacity depends on several physical parameters, such as the medium diffusion coefficient, the system temperature, and, in particular, the distance Alice–Bob and Alice–Eve. The MC secrecy capacity is also function of the bandwidth, average thermodynamic power, and receiver radius. Numerical results presented in this paper show the dependencies of the MC secrecy capacity with respect to all these parameters. In addition, a secrecy map has been also drawn to graphically show where the secure–insecure areas are located around the transmitter and receiver.

According to results, a secrecy rate of 60 bit/s can be reached if Eve's distance is twice the distance of the legitimate transmitter–receiver, for an average transmitted power of 1 pW and a bandwidth of 20 Hz. The numerical results have to be intended as an upper bound to the security performance of a diffusion-based MC system. Further investigations will be carried out in the future, e.g., on evaluating the effect of a secure coding scheme at the transmitter.

References

1. Nakano, T.: Molecular communication: a 10 year retrospective. *IEEE Tran. Mol. Biol. Multi-Scale Commun.* **3**(2), 71–78 (2017)
2. Moritani, Y., Hiyama, S., Suda, T.: Molecular communication for health care applications. In: *Fourth Annual IEEE International Conference on Pervasive Computing and Communications Workshops (PERCOMW'06)*, pp. 549–553 (Pisa, 2006)
3. Oosterbroek, E., van den Berg, A.: *Lab-on-a-Chip: Miniaturized systems for (Bio) Chemical Analysis and Synthesis*. Elsevier, Amsterdam (2003)
4. Pierobon, M., Akyildiz, I.F.: Capacity of a diffusion-based molecular communication system with channel memory and molecular noise. *IEEE Trans. Inform. Theory* **59**(2), 942–954 (2013)
5. Loscrí, V., Marchal, C., Mitton, N., Fortino, G., Vasilakos, A.V.: Security and privacy in molecular communication and networking: opportunities and challenges. *IEEE Trans. NanoBiosci.* **13**(3), 198–207 (2014)
6. M. Bloch, J. Barros, M.R.D. Rodrigues, S.W. McLaughlin, *Wireless information-theoretical security*. *IEEE Trans. Inform. Theory* **54**(6), 2515–2534 (2008)
7. Cover, T.M., Thomas, J.A.: *Elements of Information Theory*, 2nd edn. Wiley, New York (2006)
8. Langevin, M.P.: Paul Langevin's 1908 paper on the theory of Brownian motion. *Am. J. Phys.* **65**(11), 1079–1081 (1997)

9. Hassani, S.: *Mathematical Methods: For Students of Physics and Related Fields*. Springer, Berlin (2009)
10. Pierobon, M., Akyildiz, I.F.: A physical end-to-end model for molecular communication in nanonetworks. *IEEE J. Sel. Areas Commun.* **28**(4), 602–611 (2010)
11. Nelson, D.L., Cox, M.M.: *Lehninger Principles of Biochemistry*. Freeman, New York (2005)
12. Mucchi, L., Ronga, L., Zhou, X., Huang, K., Chen, Y., Wang, R.: A new metric for measuring the security of an environment: the secrecy pressure. *IEEE Trans. Wirel. Commun.* **16**(5), 3416–3430 (2017)
13. Pierobon, M., Akyildiz, I.F.: Noise analysis in ligand-binding reception for molecular communication in nanonetworks. *IEEE Trans. Signal Process.* **59**(9), 4168–4182 (2011)

Chapter 10

Towards Efficient and Real-Time Human Activity Recognition Using Wearable Sensors: A Shapelet-Based Pattern Matching Approach



Delaram Yazdansepas, Nitin Saroha, Lakshmish Ramaswamy,
and Khaled Rasheed

10.1 Introduction

Mobile phones, activity trackers, and many other current mobile devices incorporate various sensors such as GPS, accelerometer, and gyroscope. These sensors can be used to study and analyze human physical activities. In recent years, there is growing research interest in Human Activity Recognition. HAR has many applications particularly in health care, city planning, sport coaching, fitness assessment, and smart homes domains [3–5, 14]. Many of these domains demand an online robust HAR system that can distinguish various human activities in real-time. Most approaches on human activity recognition are offline or in batch-processing mode. Offline HAR systems have significant limitations with certain applications such as continuously monitoring patients with physical or mental difficulties for their safety and recovery and elder fall detection [2]. HAR systems are effective in such applications when they can recognize and detect human activities in a reasonable time. Many offline HAR systems are based on employing machine learning techniques on motion data on powerful servers. This requires the system to record data and send it to a server for analyzing and detecting the subjects' activities, and thus cannot be achieved in real-time. Furthermore, most current research in this field focuses on extracting complex features to achieve high classification accuracy. HAR systems based on complex feature extraction cannot be deployed in real-time scenarios because of the high time complexity of feature extraction and feature selection algorithms.

Towards designing an effective real-time HAR system, this paper explores a waveform pattern matching approach. Our framework extracts a representative

D. Yazdansepas (✉) · N. Saroha · L. Ramaswamy · K. Rasheed
Department of Computer Science, University of Georgia, Athens, GA, USA
e-mail: delaram@cs.uga.edu; nitin@cs.uga.edu; laks@cs.uga.edu; khaled@cs.uga.edu

waveform pattern called “Activity Shapelet” (“A-Shapelet,” for short) for each activity. Incoming data from the accelerometer sensor is classified in real-time by matching against a library of A-Shapelets. In designing our framework we make the following novel contributions:

- We propose a unique technique to compute the A-Shapelet that best represents each activity. Our technique extracts repetitive patterns from waveforms and computes the distance between the extracted pattern and the original accelerometer waveforms. Furthermore, we use dynamic time warping (DTW) to ameliorate the sensitivity of the distance metric towards misalignment in between the waveforms.
- We generate a personalized library of A-Shapelet with each shapelet representing a distinct activity. Using the A-Shapelets in the personalized library, we build decision tree models which are used for efficient matching and classification of incoming accelerometer data stream.
- We perform detailed evaluation of the proposed framework on a heterogeneous dataset consisting of subjects performing daily activities. Our evaluations show that our framework results in the same accuracy of activity classification regardless of the kind or model of the wearable accelerometer sensors or its orientation and placement. We also observe that some ambulatory activities are classified with higher accuracy due to their distinguishable waveform patterns.

In this paper, we present background and motivation for Human Activity Recognition Systems (Sect. 10.2), provide an overview of our online HAR system (Sect. 10.3), demonstrate how time series are matched to shapelets (Sect. 10.4), describe the framework’s implementation details (Sect. 10.5), and demonstrate the experimental study and detailed empirical evaluations of our system (Sect. 10.6) followed by a conclusion (Sect. 10.7).

10.2 Background

Most existing wearable sensor-based HAR systems work in an offline or batch-processing mode. Typically, these systems extract statistical features from accelerometer data such as mean, maximum, minimum values, standard deviations, median crossings, and the 10th, 25th, 50th, 75th, 90th percentiles [8]. Machine learning methods such as SVM, K-Nearest Neighbor, and Clustering are trained on the extracted features from training data batches. The trained models are then used to classify the test data batches. In a previous experimental study on offline HAR systems, we applied different machine learning algorithms on a heterogeneous dataset consisting activity data for 77 subjects. A total of 176 features were extracted from the combination of time and frequency domain and the most effective features for discriminating different activities were selected. It was found that a combination of time domain and frequency domain features yields the highest accuracy on most classifiers [15]. One reason that HAR systems are generally offline is because they

are based on extracting features from the dataset and the training process becomes computationally expensive. There is a limited number of studies on Online HAR systems which can classify activities on wearable devices in real-time compared to offline HAR systems.

In offline HAR systems data is transmitted to a server where the activities are classified. Offline HAR systems are not suitable for various applications such as those that require immediate feedback. Contrary to offline systems, online HAR systems classify activities in real-time mostly locally on the device. In designing online HAR systems there are a number of challenges which need to be addressed. First, in real-time systems it is crucial that activities be classified in a short time frame, usually within 3 s of the activity happening. This requires that the system not be dependent on heavy computations and complex features. Second, online HAR systems should classify activities based on a short period of data readings; therefore, the system should rely on a small set of data readings to classify the activity.

10.3 Overview

Our method is based on extracting representative patterns from accelerometer data. The extracted waveforms are used to classify the activities time series. The representative patterns are called “A-Shapelets” short for activity shapelets, and each A-Shapelet is a representation of each activity class. By using several distance metrics we compare the time series to the A-Shapelets, each time series that exhibits similar patterns to the shapelet will be labeled as same class. The ultimate purpose of our proposed method is to classify activities using raw data; therefore, there is no need to define or extract features that separate different activities. Using raw data makes the method more general for applying to other sets of activities. This method raises a number of questions as follows: (1) how to compute the waveforms in activity time series? (2) How to find the best A-Shapelet representing an activity class? (3) What method should be used efficiently to match A-Shapelets with activities? And (4) which metric can be used to efficiently calculate the distance between the activity time series and the A-Shapelet?

The main component of our proposed method is extracting and selecting A-Shapelets from activity time series. Ideally, each shapelet is a representation of each activity class capturing the dominant pattern of the activity. We evaluate all sub-patterns in the time series and select those of which are representative of the activity. Finding the best of such patterns requires examining every single sub-pattern of a particular size. With the recent improvements in CPU time and parallelization techniques the proposed algorithm for discovering time series sub-patterns is achievable in a reasonable time. We then select the activity class shapelets by finding the most representative shapelet for each activity which captures the dominant pattern in that activity time series. We then classify time series based on distance or similarity to the shapelet of each class (Fig. 10.1).

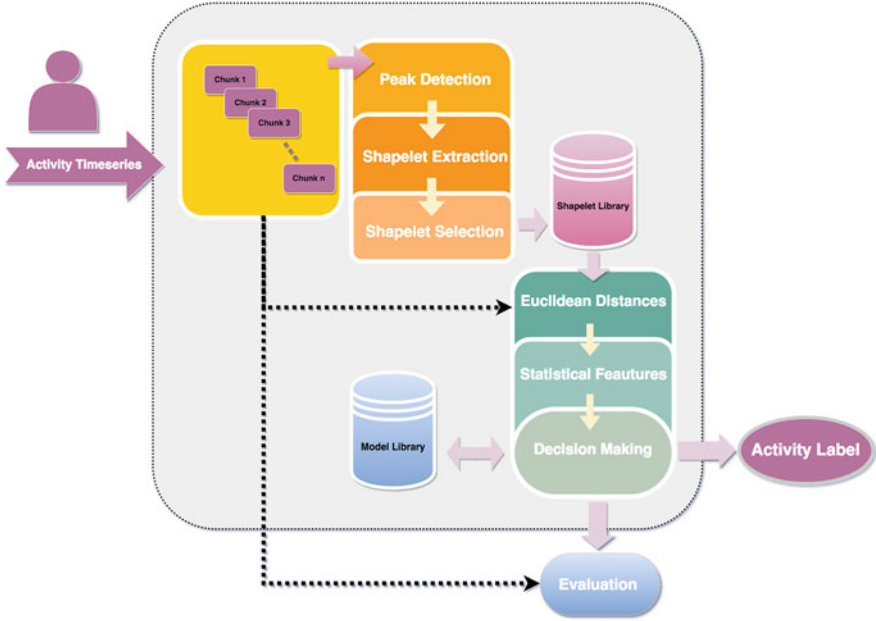


Fig. 10.1 Online HAR system overview

We generate a personalized shapelet library database driven from subjects' activity time series for a shapelet-based online implementation of human activity classification. This database is small regarding the size and can be stored on mobile phones and wearable devices. To build this library, in the training phase each individual's activity time series goes through the different components in our method defined below:

- **Average Peak Distance.** Given a time series, P is the average number of data points between two consecutive local peaks. We find the local upper and lower peaks and denote the average distance of the upper peaks with P_{upper} and the lower peak distance with P_{lower} .
- **Shapelet Extraction.** We extract all shapelets of a certain length l_{sh} using a sliding window. The size of the sliding window is set based on the P_{lower} and P_{upper} of the activity times series. We call the set of all shapelets of a time series the candidate shapelets. The total number of possible candidate shapelets for all the time series in the dataset are

$$\sum_{TS_i \in D} (n_i - l_i + 1)$$

where n_i is the length of TS_i , D is the set of all time series, and l is the length of the shapelets for the i th time series.

- **Distance Metric.** The distance between each time series and a shapelet is represented with *dist*. The distance function takes *TS* and *Shapelet* as inputs and returns a total distance value. In this study, we measure distance using Euclidean distance and DTW.
- **Class Shapelet Representative.** Given a set of candidate shapelets, we find the single best shapelet which is representative of the activity class from the set of candidate shapelets. There are several methods used to select the single best shapelet that would represent an activity class, and we discuss this further in Sect. 10.4.

We propose a procedure to find the best shapelet which represents an activity class based on time series distance metrics and DTW. For demonstration, we use real human activity data and show our system is independent of the sensor device.

We refer to time series $TS = t_1 t_2 t_3, \dots, t_n$ as an ordered set of accelerometer sensor recordings measured in meters per second squared (m/s^2). Each value t_k in the time series represents the rate of change of the velocity of the subject wearing the sensor. Given an activity time series *TS* a shapelet is a partition of the time series. A shapelet is a continuous set of sensor readings that are spaced at the same rate of the time series. Data points in activity time series are arranged in temporal order spaced at equal time intervals $1/r$.

10.4 Shapelet Library Creation

In this step, we will define the necessary steps to create a library of “A-Shapelets.” Creating the A-Shapelet library is done offline, and the system builds a personalized library of A-Shapelets for each subject. A-Shapelets are representative patterns that are repeatedly observed in each activity time series. A-Shapelets are extracted from subject’s activity time series in the training phase, and a personalized shapelet library is built by finding such shapelets. In the remainder of this section, we describe the steps involved in the creation of the shapelet library.

Time Series Normalization

Normalizing activity time series is a necessary step in extracting and selecting A-Shapelets. In selecting A-Shapelets, we need to measure the distance of the extracted shapelets and the time series. Normalizing time series eliminates differences in the overall magnitude of two time series. Therefore, with normalization, we can correctly measure the true similarity of a shapelet and a segment of an activity time series that may be similar in shape but have different offsets along the accelerometer axis. There are various methods of normalization techniques. Our method is based on simple moving average smoothing (SMA) technique. SMA avoids noise and smoothens the pattern in the times series. The formula is shown below.

$$SMA_t = \sum_{i=t-N+1}^t \frac{x_i}{N}$$

SMA_t is the simple moving average for the t th data point, x_i is the i th time series data point, and N is the length of the moving average window.

Peak Detection

The nature of human motion is based on repetition of movement phases [6]. This is an essential feature of human motion data which helps us analyze and classify activities. The data point values that are recorded by the accelerometer signal in every point of time may change in each cycle, but the general shape of the pattern in the time series stays the same. For example, when a person is walking, each leg goes through a stance phase, a swing phase, and then returns to the stance phase again [13]. When a person is performing a non-ambulatory activity, such as brushing teeth, the repetition phase in the time series data is less visible. Usually, in non-ambulatory activities, repetition is connected with respiration phases [6]. We can find the repetition pattern in activity time series signals and based on the average length of these patterns we measure *repetition periods*. We denote the average number of data points in the repetition period with P . Repetition period is a segment of time series, measured during one cycle of motion [6], such as a step. Figure 10.2 shows that finding peaks can help us segment the time series into individual steps or pattern repetitions. Every peak in the accelerometer time series denotes that there has been a sudden increase in acceleration, followed by a sudden drop. In every step when the lower limb goes through a swing phase we can see a sudden rise in the accelerometer value. We can, therefore, use such peaks to determine the step size (number of data points in each step). In our method, we use a common peak detection algorithm to detect the peaks. We use Python¹ PeakUtils [7] package to identify peaks and find their indexes as illustrated in Fig. 10.2. Once we have

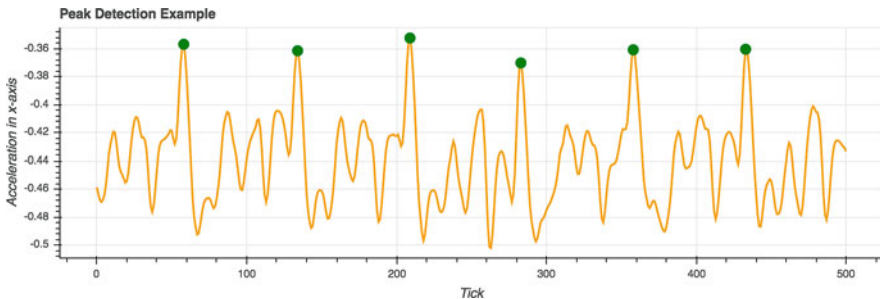


Fig. 10.2 Detecting peaks on “walking” time series

¹<https://www.python.org/>.

detected all peaks, we find the median number of data points between every two consecutive peaks in the time series. Using median instead of average enables us to eliminate any outlier peak distances. We apply peak detection algorithm to the data for finding positive peaks, called *upper* peaks, and negative peaks, called *lower* peaks. P_{upper} and P_{lower} denote the median of the number of data points in between upper and lower peaks, respectively.

Shapelet Extraction

Given a time series TS with a median peak distance of P , we extract candidate shapelets from the time series. Candidate shapelets are the set of all overlapping time series subsequences. Candidate shapelet sizes are the same length of P . We start from the first data point of the time series and select the first P data points as our first candidate shapelet, we move to the next data point and select the next P points. These steps are repeatedly continued to the $(||TS|| - P)$ th data point of the time series, every time moving to the next data point. All these time series subsequences will be stored in an unordered list called the Candidate Shapelets Dataset. We then select the best shapelet among the candidate shapelets.

Shapelet Selection

In this section, we present our proposed algorithm to select a single shapelet that has the closest pattern to the time series from the list of candidate shapelets. In other words, we select the shapelet that is most similar to the dominant pattern in the times series. The proposed algorithm compares each shapelet against the entire time series using a sliding window and computes a similarity value. We use this similarity value as a metric to select the shapelet that is most similar to the fundamental or dominant pattern in the time series. This brute force algorithm along with the sliding window guarantees that every single segment of the time series will be compared to the candidate shapelet and its similarity measure is accumulated. This value denotes the similarity of a particular shapelet and the activity time series. However, the brute force method takes a long time and is a computationally expensive operation. Therefore, we parallelized the algorithm using PySpark² which is the Python API for Apache Spark [16]. Parallelizing the brute force method enables us to run the main function and execute various parallel operations on a cluster. We reduced the run time of the brute force shapelet selection method by 75%.

10.5 Matching Time Series with Shapelets

An essential task in time series analysis is the estimation of similarity among different time series [1]. In activity time series the similarity measure is a relation between a shapelet and a time series. The algorithm requires comparing the time series to each candidate shapelet by evaluating the distance function and keeping

²<http://spark.apache.org/docs/latest/api/python/pyspark.html>

track of the shapelet with the lowest distance to the time series. Shapelet matching requires that the shapelet SH be placed at every possible offset within the time series. In the next section, we describe two experimented methods in this study to estimate the similarity between a shapelet and a time series.

Euclidean Distance

A common way to compare time series data involves the concept of distance measures. Let two time series x and y be the length of n , and x_i and y_i the i th values of x and y , respectively. Euclidean Distance of the two time series is the sum of the point-to-point distances along all the time series data points.

$$\|\bar{x} - \bar{y}\|^2 = \sqrt{\sum_{i=1}^n |x_i - y_i|^2}$$

Shapelets have smaller lengths compared to time series; therefore, when we compare a shapelet to a time series, we use a sliding window in the time series that is the same length of the shapelet. We compute the Euclidean distance of the shapelet to the time series within the sliding window, store the distance in a variable, and shift the sliding window to the next data point. As the sliding window goes through all the data points in the time series, the total distance gets accumulated each time. The total Euclidean distance is a single value representing the distance between the shapelet and the entire time series. Once every candidate shapelet is compared to the activity time series, and a total Euclidean distance is computed for each shapelet, we will select a single or a set of shapelets as our final representatives for each activity class. We experiment two approaches to select a final shapelet. In the first approach, we choose a single shapelet based on the least Euclidean distance measure. The shapelet which has a corresponding Euclidean distance of the median of the first decile is selected. The median of the first decile of Euclidean distances is selected instead of the shapelet with the least Euclidean distance because after performing many experiments we observed that the shapelets with the least Euclidean distances were not expressing any visible pattern. Usually, such shapelets resembled vertical lines with no trend or pattern, which are not a realistic representation of the time series. In light of these findings, we explored another approach for selecting a shapelet. This approach selects a set of 10 shapelets instead of a single shapelet, aligns and averages the shapelets to generate a new shapelet. This approach also returns a single shapelet, but the shapelet is built upon ten shapelets that had minimum Euclidean distance with the time series. Figure 10.3 presents our second approach to select a shapelet. We perform simple averaging on the shapelets to create the new shapelet.

Euclidean distance is a simple and commonly used method for finding the similarity of time series. However, it has several drawbacks. Activity time series may be similar in pattern, but they may not be aligned in the time phase. This will cause the Euclidean distance to measure the similarity incorrectly. To reduce the error associated with the Euclidean distance metric, we study another similarity measure explained in the next section.

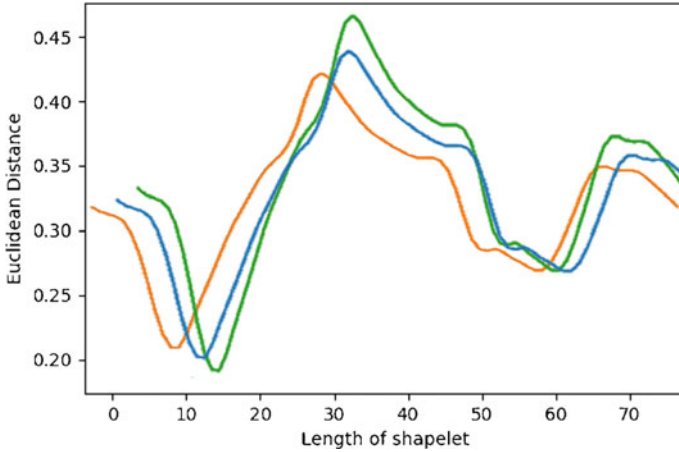


Fig. 10.3 Aligning and averaging multiple shapelets to generate a new shapelet representing an activity class. Blue shapelet is the result of aligning and averaging the green and orange shapelets

Dynamic Time Warping

As mentioned in the previous section one of the disadvantages of Euclidean distance is that if two time series are identical, but one is slightly shifted along the time axis, then their Euclidean distance will show them being different or distant from each other. Most algorithms used to compare time series use the Euclidean distance or some variation of this technique. However, since Euclidean distance is sensitive to distortion [10] we need another method for calculating the distance between time series that would ignore the shifts in the time dimensions of the time series. Dynamic Time Warping (DTW) is a widely used algorithm for computing the distance and alignment of time series [12]. DTW is less sensitive to time series shiftings, thus allows us to measure the similarity of time series even if they are out of phase in time. Although DTW has a time complexity of $O(n^2)$, it is still the best solution known for time series problems in a variety of domains [11]. This method is more robust compared to other similarity measures such as Euclidean distance. It finds the best alignment between time series by finding the path through the grid that minimizes the total distance between them. Our evaluations show that DTW yields the most precise similarity between activity time series and shapelets.

10.6 Implementation Details

Training Phase

In this phase we extract shapelets from activity time series of each subject, using methods described in Sect. 10.4 and select the A-Shapelet which is the most representative shapelet of the subject's activity among all other candidate shapelets

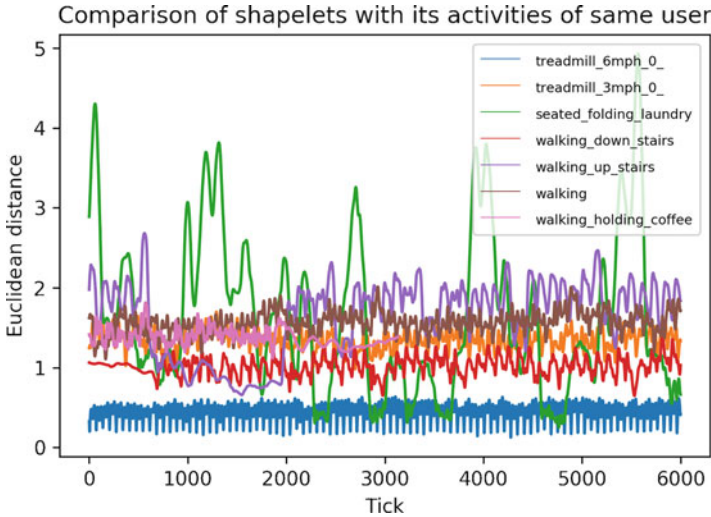


Fig. 10.4 Euclidean distances of “jogging on treadmill” time series and different shapelets of the same subject. Comparing the time series to “jogging on treadmill” shapelet (blue line) results in lower Euclidean distances

based on similarity measure metrics. Each activity shapelet will be stored in a local database for a specific subject. Figure 10.4 shows a graph of Euclidean distances when comparing different A-Shapelets of a particular subject to treadmill jogging time series of the same subject. When the activity time series is compared to a shapelet of the same activity—in this example jogging on a treadmill—the Euclidean distances are relatively lower than distances of time series compared to shapelets of other activities. This is a critical component for classifying the time series class.

Activity time series are compared against each A-Shapelet, while the distances are recorded. For each shapelet, we have a set of Euclidean distance values for which we find the *five number summary* statistics in addition to variance and standard deviation. These statistic summaries provide the baseline to compare how the time series are being matched to each shapelet. When comparing an activity time series to the shapelet of the same activity, the summary statistics are significantly distinguishable from other shapelets. Based on these summary statistics we train a decision tree to classify the time series. We create a model for each shapelet to predict the class of a time series by learning simple decision rules inferred from the statistic summaries. The Decision Tree Classifier is implemented using the well-known Python machine learning library, scikit-Learn [9]. After fitting the tree, the model is used to classify the class of activities of time series which are not labeled yet. We use decision tree model because they have features which make them favorable over other classifiers. First, because the trees do not require much of data preparation. Second, because the cost of using the tree is logarithmic in the number of data points used to train the tree.

Labeling New Activities

As a subject is performing an activity, the accelerometer sensor data is buffered in chunks of 300 data points (3 s). We set chunk sizes to three seconds because after studying daily human activities time series we observed that normally activities are performed at least 3 s, or have a recurring pattern length less than 3 s. After two chunks of the activity time series are buffered in the system, they will be compared to all the shapelets in the shapelet library of that subject. As the sliding window goes over the time series and gets compared to a shapelet Euclidean distance statistics are created. These statistics include the minimum, maximum, median, standard deviation, variance, the first and third percentile of the Euclidean distances. The statistics for each shapelet along with the shapelet decision tree models predict the class of each chunk of the time series. The system will behave similar to a binary classifier on each model, outputting a label of yes or no for each shapelet. Since there are multiple classes of activities, we need a multi-classifier to detect and label activities. We decompose the multi-classification problem to n binary classification problems where n is the number of activity classes. When an activity time series chunk is presented to each one of the binary classifiers, the classifier which gives a positive output (“yes”) indicates the output class. If more than one of the classifiers outputs a positive label for a chunk of activity a tie-breaking technique is required to decide on the activity label. In such cases, we use the common approach of maximum confidence. The classifier determines the output class with the largest confidence score.

10.7 Experimental Evaluation

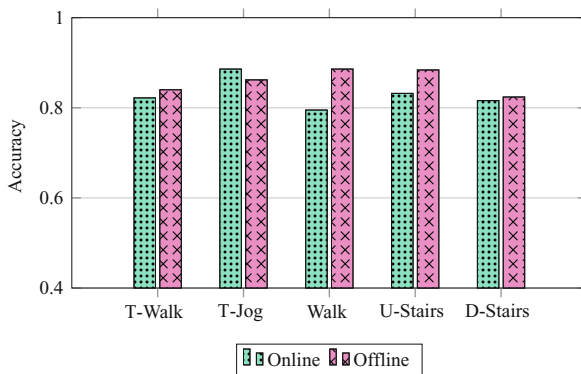
Dataset

Participants and Procedures Participants were selected from a broad age range of 18–64 years old and are all free of any contraindications for exercise. Participants were fitted with a single hip-worn accelerometer and completed a series of activities for 3 min in duration. Time stamps for the beginning and end of activities were captured using a custom-built Android application which was synced to the same server as the activity monitor. We use a subset of ambulatory activities performed by subjects in this study (see Table 10.1). We select activities that are similar but are performed in different environments to show that shapelets can capture the differences in activities that may appear similar. For instance, walking on a treadmill may seem to have a similar pattern of walking on a normal surface. However, we show the shapelets that represent each activity class have different patterns.

Activity Monitor Device Participants were fitted with the ActiGraph GT3X+ (ActiGraph, LLC, Pensacola, FL) activity monitor positioned along the anterior axillary line of the non-dominant hip. For more details about the procedure and device, please refer to [15].

Table 10.1 Summary of activities

Activity description	No. of subjects	Duration/distance
Treadmill at 1 mph @ 0% grade	29	3 min
Treadmill at 3 mph @ 0% grade	28	3 min
Treadmill at 6 mph @ 0% grade	34	3 min
Hard surface walking w/sneakers	76	400 m
Walking up stairs (5 floors)	77	5 floors \times 2 times
Walking down stairs (5 floors)	77	5 floors \times 2 times

Fig. 10.5 Performance comparison of online and offline systems

Results

Once activities are classified by the system, we evaluate the results using an automated program. The program checks each chunk and its label against the ground truth and provides performance metrics.

Comparison with Offline HAR We compare the results of the online HAR system to an offline system that is based on feature extraction, feature selection, and Machine Learning Classifiers. The same dataset is used in the offline system. It can be observed by Fig. 10.5 that in most activities the offline system has slightly better accuracy. However, the improvement in accuracy is about 5% and is negligible because an online system has many more applications and uses fewer resources.

Effect of Training Dataset Figure 10.6 provides the summary of classification performance metrics per activity when the system is trained on one chunk, four chunks, and eight chunks. Activities such as Treadmill jogging have better classification performance metrics compared to other activities. This is because such activities, which involve several singular moving components, have a defined pattern which is much more visible and dominant than other patterns in the time series. Compare jogging to an activity that does not have many moving components, such as brushing teeth; it would be a far more difficult task to extract patterns from such an activity, and therefore extracted shapelets would not contain valuable information about the pattern of the activity. Shapelets of non-ambulatory activities resemble a horizontal line. These shapelets would not be effective in finding a common pattern in the time

Fig. 10.6 Performance comparison of activities trained on different chunk sizes

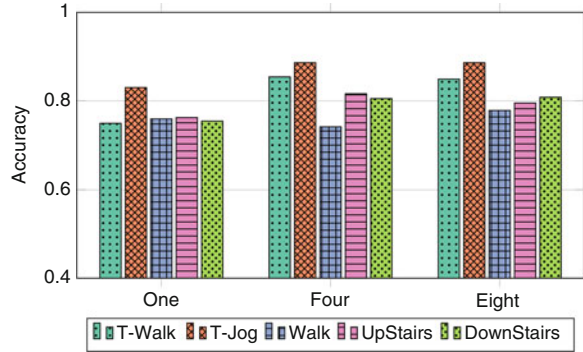
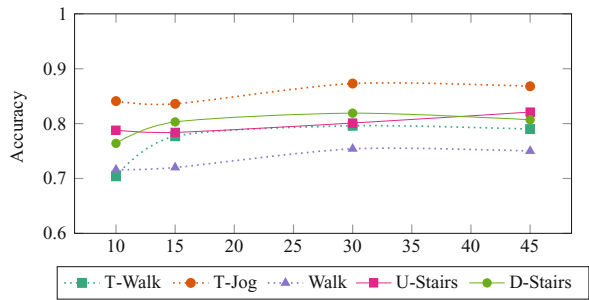


Fig. 10.7 Accuracy of online HAR system on varying test durations (chunks)



series; therefore, our proposed system has low accuracy rates when recognizing non-ambulatory activities. We also observe that there is a very slight difference in accuracy when the system is trained on more data chunks. This means we can train the data on a small number of chunks and still obtain a comparable accuracy. This is in contrast to generic Machine Learning based HAR techniques which require large amounts of training data for providing reasonable performance.

Effect of Test Duration We test our Online HAR system on stream sensor data in different durations to show that the accuracy stays consistent as the duration of the test increases. The steady accuracy rates in Fig. 10.7 prove the fact that the system’s accuracy is not dependent on the amount of data or duration it is being tested on.

Subject-Based Analysis Table 10.2 summarizes the performance metrics of our system for each subject. These metrics are the result of the average performance metrics over all the activities performed by the subject. For each subject, we have noted gender and age (e.g., subject 1 is a 40 year old female). The results in Table 10.2 present that the accuracy of the system can be variable between different subjects. Subjects who have higher accuracy in activity detection have shapelets that are more representative of an activity class. The system can improve by retraining shapelets for a subject who has low accuracy. Different real-life situations may affect the subjects time series and shapelet. As an example, a subject may be wearing uncomfortable shoes when training data was being collected. This will change

Table 10.2 Summary of classification performance metrics for random subjects

Subject ID	Sensitivity	Specificity	Precision	False positive rate	False discovery rate	Accuracy	F1 score
Subject 1 [F, 40]	0.77	0.94	0.68	0.06	0.32	0.92	0.72
Subject 2 [F, 26]	0.20	0.88	0.20	0.12	0.80	0.79	0.20
Subject 3 [F, 27]	0.59	0.95	0.65	0.05	0.35	0.90	0.62
Subject 4 [M, 49]	0.40	0.97	0.73	0.03	0.27	0.88	0.52
Subject 5 [M, 28]	0.25	0.91	0.31	0.09	0.69	0.83	0.28
Average	0.44	0.93	0.51	0.07	0.47	0.87	0.47

their normal movement patterns, and shapelets would not be representative of their normal movement signature. Therefore an essential step in the system would be to repeat the training phase for subjects who show low accuracy rates.

Sensor Independency We show our method is sensor-type independent, by testing the system on data collected from different accelerometer sensor types. We have used an iPhone 6s and Samsung Galaxy S8+ to gather motion data. We observe comparable performance rates when we use a new dataset, which indicates that our framework can perform very good regardless of the sensor type used to collect or sense the data.

10.8 Conclusion

We propose a real-time HAR framework to detect human activities based on a waveform pattern matching approach. Our scheme extracts the most distinctive A-Shapelet for each activity from waveforms and uses Dynamic Time Warping (DTW) for overcoming the misalignment problem when comparing the distance of waveforms. We build personalized decision tree models using the library of A-Shapelets for each subject. Our framework can detect and classify incoming activity accelerometer data in real-time with a low-overhead pattern matching algorithm. Our results validate the effectiveness of our framework for recognizing human activity in real-time with a high performance rate. The results obtained were promising for the following reasons. Firstly, they represent a baseline for practical real-time activity recognition using a device with a single accelerometer sensor. Secondly, our empirical evaluations demonstrate that the performance of our framework is comparable with offline HAR systems. And thirdly, the results suggest that we can train the data on a small number of data chunks and still obtain a comparable accuracy to other HAR systems. This is in contrast with generic ML-based HAR techniques which require large amounts of training data to provide acceptable performance. We also observed that some activities have better performance rates than others; in general, better performance rates are associated with the more distinct A-Shapelet of the activities with more definite patterns. Finally, we were able to replicate our results using more than one type of sensor, indicating that our framework is sensor-type independent. Our proposed human activity recognition framework using A-Shapelets overcomes some of the challenges of online HAR systems, and is especially promising for applications where fast and efficient human activity recognition is necessary.

Acknowledgements The authors would like to thank Paula Capece, Grant Cooksey, Dr. Jennifer Gay, Dr. Fredrick Maier for their contributions and help in this project. Also we would like to thank Dr. Matthew Buman for providing us the dataset. This research has been partially funded by the National Science Foundation (NSF) under grant numbers CCF-1442672 and SES- 1637277. Any opinions, findings, conclusions, or recommendations expressed in this material are those of the authors, and do not necessarily reflect the views of the NSF.

References

1. Cassisi, C., Montalto, P., Aliotta, M., Cannata, A., Pulvirenti, A.: Similarity measures and dimensionality reduction techniques for time series data mining. In: *Advances in data mining knowledge discovery and applications*. InTech (2012)
2. Castillo, J.C., Carneiro, D., Serrano-Cuerda, J., Novais, P., Fernández-Caballero, A., Neves, J.: A multi-modal approach for activity classification and fall detection. *Int. J. Syst. Sci.* **45**(4), 810–824 (2014)
3. Das, B., Seelye, A.M., Thomas, B.L., Cook, D.J., Holder, L.B., Schmitter-Edgecombe, M.: Using smart phones for context-aware prompting in smart environments. In: *Consumer Communications and Networking Conference (CCNC)*, pp. 399–403. IEEE, Piscataway (2012)
4. Ermes, M., Parkka, J., Mantyjarvi, J., Korhonen, I.: Detection of daily activities and sports with wearable sensors in controlled and uncontrolled conditions. *IEEE Trans. Inf. Technol. Biomed.* **12**(1), 20–26 (2008)
5. Feng, T., Timmermans, H.J.: Transportation mode recognition using {GPS} and accelerometer data. *Transp. Res. C Emerg. Technol.* **37**, 118–130 (2013)
6. Ignatov, A.D., Strijov, V.V.: Human activity recognition using quasiperiodic time series collected from a single tri-axial accelerometer. *Multimed. Tools Appl.* **75**(12), 7257–7270 (2016). <https://doi.org/10.1007/s11042-015-2643-0>
7. Negri, L.H.: Peakutils (2014). <http://pythonhosted.org/PeakUtils>
8. Niazi, A.H., Yazdansepar, D., Gay, J.L., Maier, F.W., Ramaswamy, L., Rasheed, K., Buman, M.P.: A hierarchical meta-classifier for human activity recognition. In: *2016 15th IEEE International Conference on Machine Learning and Applications (ICMLA)*, pp. 81–86. IEEE, Piscataway (2016). <https://doi.org/10.1109/ICMLA.2016.0022>
9. Pedregosa, F., Varoquaux, G., Gramfort, A., Michel, V., Thirion, B., Grisel, O., Blondel, M., Prettenhofer, P., Weiss, R., Dubourg, V., Vanderplas, J., Passos, A., Cournapeau, D., Brucher, M., Perrot, M., Duchesnay, E.: Scikit-learn: machine learning in python. *J. Mach. Learn. Res.* **12**, 2825–2830 (2011). <http://dl.acm.org/citation.cfm?id=1953048.2078195>
10. Ratanamahatana, C.A., Keogh, E.: Making time-series classification more accurate using learned constraints. In: *Proceedings of the 2004 SIAM International Conference on Data Mining*, pp. 11–22. SIAM (2004)
11. Ratanamahatana, C.A., Keogh, E.: Three myths about dynamic time warping data mining. In: *Proceedings of the 2005 SIAM International Conference on Data Mining*, pp. 506–510. SIAM (2005)
12. Seto, S., Zhang, W., Zhou, Y.: Multivariate time series classification using dynamic time warping template selection for human activity recognition. In: *2015 IEEE Symposium Series on Computational Intelligence*, pp. 1399–1406. IEEE, Piscataway (2015)
13. Shultz, S., Houghlum, P., Perrin, D.: *Examination of Musculoskeletal Injuries with Web Resource*, 3rd edn. Human Kinetics Publishers, Champaign (2009)
14. Wu, W.H., Bui, A.A.T., Batalin, M.A., Au, L.K., Binney, J.D., Kaiser, W.J.: MEDIC: medical embedded device for individualized care. *Artif. Intell. Med.* **42**(2), 137–152 (2008)
15. Yazdansepar, D., Niazi, A.H., Gay, J.L., Maier, F.W., Ramaswamy, L., Rasheed, K., Buman, M.P.: A multi-featured approach for wearable sensor-based human activity recognition. In: *2016 IEEE International Conference on Healthcare Informatics, ICHI 2016*, pp. 423–431. Chicago (2016). <https://doi.org/10.1109/ICHI.2016.81>
16. Zaharia, M., Xin, R.S., Wendell, P., Das, T., Armbrust, M., Dave, A., Meng, X., Rosen, J., Venkataraman, S., Franklin, M.J., Ghodsi, A., Gonzalez, J., Shenker, S., Stoica, I.: Apache spark: a unified engine for big data processing. *Commun. ACM* **59**(11), 56–65 (2016)

Chapter 11

Opportunistic IoT Service to Support Safety Driving from Heterogeneous Data Sources



Giancarlo Fortino , Raffaele Gravina , Qimeng Li ,
and Claudio Savaglio 

11.1 Introduction

The Internet of Things (IoT) represents an ecosystem where different systems (e.g., Smart Buildings, Smart Grids, Body Area Networks) and their heterogeneous components (e.g., PCs, smartphones, wearable devices, smart meters) seamlessly interoperate, sharing the same environment and resources [9]. In such a way, through contextualized and dynamic interactions, advanced cyberphysical IoT services can be provided, thus opening a broad range of novel opportunities in any application scenario, like healthcare, logistics, and smart automotive. Among the factors currently hindering the provision of IoT services, the marked heterogeneity featuring IoT technology (802.15.4, Bluetooth, Wi-Fi, NFC, etc.), communication protocols (CoAP, MQTT, IPv6, etc.), and data formats (including structured, semi-structured, and unstructured data) is one of the major. However, while gateway-based solutions are widely adopted to support both multi-technology and multi-protocol interaction [1], the integration of cyberphysical services of different providers, described through heterogeneous data models, remains an open issue. Indeed, if gateways basically perform the syntactical translation and forwarding of the messages received on their several interfaces, realizing an integrated IoT service is a complex task which consists in combining IoT devices' functionalities and available data, abstracting from their specific format and focusing on their high-level description and opportunistic exploitation.

In this paper, the IoT domain and Opportunistic IoT Service models presented in [3, 8, 9] are reported and applied in the context of safety driving assistance. In

G. Fortino · R. Gravina · Q. Li · C. Savaglio (✉)
Department of Informatics, Modeling, Electronics and Systems, University of Calabria,
Rende, Italy
e-mail: g.fortino@unical.it; r.gravina@dimes.unical.it; csavaglio@dimes.unical.it

particular, heterogeneous Smart Objects (SOs, i.e., Smart Bracelet, Smartphone, Raspberry-based Smart Safety Unit, Smart Cushion) interact within the vehicle to retrieve information about driver psycho-physical status and alert if dangerous conditions (boredom, fatigue, drowsiness, stress, agitation) are detected. In addition to distraction, fatigue, and drowsiness, studies have shown that emotional driver's status (e.g., stress, impatience) may also endanger driving safety [17, 20]. High stress level or aggressive behavior can reduce self-confidence, attention and, as a consequence, driver concentration. In terms of relevant physiological signals, while facial expressions and eye movements can effectively support distraction and drowsiness detection, it has been found that heart rate indicators are strongly correlated with driver stress level [14].

The outlined "Driving Assistance Service" is expected to perform (1) data retrieving from the aforementioned heterogeneous SOs, not purposely designed for implementing such service nor for interoperating; (2) data fusion, for example, by combining Smart Cushion and Smart Bracelet data to detect driver's posture and gesture; (3) inference, by correlating information about driver's eye blinks, postural and gestural behavior with related psycho-physical conditions; (4) risk evaluation, by outlining a risk index according to both driver's psycho-physical conditions and factors such as the driving time or road type; (5) actuation, by means of notifications sent to driver's smartphone if risky conditions are detected. The goal of this work, indeed, is to show that the implementation of such an integrated IoT service is facilitated by the proposed metamodel-based approach, focused on those important features and data which enable the accurate IoT service description, automatic discovery, provision, and composition.

The reminder of this paper is structured as follows: Section 11.2 surveys some related work on driving assistance services and Sect. 11.3 presents the proposed system architecture. Section 11.4 reports the IoT domain model and the Opportunistic IoT service model, while their exemplification on the driving assistance case study finds place in Sect. 11.5. Final remarks conclude this paper.

11.2 Related Work

There is established literature on advanced driver assistance systems (ADASs) which focus on diversified aspects of driving. Collision avoidance systems involve active technology such as automatic emergency brake (include pedestrian and obstacle detection), safety distance control, and unintended lane crossing avoidance. Other assistive systems provide visual, passive feedbacks based on the detection of road signs (e.g., speed limit), road conditions, approaching corners, and traffic lights. This paper, in particular, focuses on a specific category of ADAS for driver conditions monitoring. In this specific context, most of the literature studies focused on detecting attention/distraction, activity/behavior drowsiness, fatigue, stress, and aggressiveness level of the driver, which are conditions with high correlation and influence on car accidents [7]. In [22] the authors propose a system

for detecting driver distraction based on image data from an inward dashboard-mounted facing camera and inertial data from a mobile device. Driver behavior is categorized in terms of activities (Normal Driving, Talking, Texting Image, Eating/Drinking Image, Hair and Makeup, Reaching objects) which are classified using Convolutional Neural Networks (CNN) and Support Vector Machines (SVM). The authors in [5] focused on both attention and drowsiness detection using Viola–Jones algorithm associated with SVM. Facial images are used to recognize mouth yawning and eye movements for drowsiness detection and head movements and pupil detection for distraction. In [19], a system with similar goal is proposed. The authors monitor the attention of the driver using a camera for head posture and eye tracking. Binary classifiers and iconic data reduction based on Sanger neural networks are used to analyze head pose for drowsiness and visual distraction, while eyes blink are used as a measure related to fatigue. Facial and eye features are also used in [11, 21] to detect driver drowsiness with a trained classifier based on local Haar features and dynamic global Haar features (PPD +DGHaar). In [6, 23], the authors propose sensor fusion approaches to take into account, in addition to eye-related indicators, vehicle-based signals including vehicle speed, braking, and acceleration, lateral position, and steering wheel angle. A different driver monitoring approach is proposed in [4] based on the concept of scoring function to obtain driver behavior profiling. Multiple sensors (magnetometer, gravity sensor, accelerometer, GPS) of the driver’s smartphone are used for event detection and feature level fusion is applied to combine them with weather information and time of day (day/night). Facial expression analysis based on inward near-infrared (NIR) camera is used in [12] with the different aim of detecting emotional states—stress in particular—of the driver. Although most state-of-the-art driver monitoring systems are based on cameras facing driver’s face, interesting research efforts analyze specific physiological signals to detect drowsiness, fatigue, and stress level. A smartwatch-enabled Bluetooth Electroencephalogram (EEG)-headband proposed in [16] uses SVM-based posterior probabilistic model to estimate the severity of drowsy driving. A similar EEG-based [24] driver fatigue detection method uses wavelet entropy and pulse coupled neural network (PCNN). An interesting study [15] suggests the use of Heart Rate Variability (HRV) signal as an indicator of autonomous nervous system activation for normal, fatigued, and drowsy states by embedding an ECG sensor on the steering wheel. Truly wearable sensing is proposed by the authors of [10] to detect driver fatigue. EEG, Electromyogram (EMG), and respiration signals were simultaneously recorded and sent to a notebook via Bluetooth.

11.3 System Architecture

The proposed system includes a Smart Cushion (deployed on the driver’s seat), a Smart Bracelet (worn at the driver’s wrist), a Smart Safety Unit (based on Raspberry Pi connecting a Camera, a Temperature module, and a Global Positioning System



Fig. 11.1 System deployment of driver assistance system

GPS), and a Smartphone, as shown in Fig. 11.1. System components and related functionalities are explained in the following:

Smart Cushion—the smart cushion developed in our previous research [13, 18] is composed of a pressure sensor array, a processing unit, and a communication module:

- six Force Sensing Resistors 406 (FSR-406), arranged as a sensor array, measure pressure changes due to driver's posture transitions;
- processing unit (i.e., Arduino Mini Pro) collects pressure analog signals to recognize five different sitting postures (Proper Sitting, Leaning Left, Leaning Right, Leaning Forward, and Leaning Backward) through an embedded J-48 decision tree classifier; sensor data were acquired at a sampling frequency of 100 Hz;
- Bluetooth-based communication module transmits raw data and the recognized postures to the Smart Safety Unit.

Smart Bracelet—the XIAOMI mi Band 2 smart bracelet collects wrist acceleration and heartbeat. The wrist acceleration can be used to identify driver's gestures, while heartbeat to detect driver's stress.

Smart Safety Unit—a Raspberry Pi 3.0 is equipped with the following augmentation devices:

- Camera, to detect eye blinking;
- Temperature sensor, to measure vehicle cabin temperature;
- GPS, to retrieve vehicle position and actual time.

Smart Safety Unit is used as a base station to receive, send, and process data. All types of data will be synchronized with global timestamps as shown in previous research [13]. In particular, it performs data fusion and contextualization (i.e., combining recognized driver’s posture and gesture and correlating them with information about driver’s eye blink, time of day, weather info), and estimates a risk index according to factors such as the driving time or road type. A compelling index risk is associated with situations in which risky conditions are detected at high-speed or night time, on highways or in adverse weather conditions. A severe index risk refers to risky conditions detected when driving in urban contexts at reduced speed or at diurnal hours, or during a long driving time. Finally, moderate index risk refers to risky conditions detected when vehicle is not moving, e.g., driver stuck in traffic. Once estimated the index risk, the related alert command is sent to the driver’s smartphone.

Smartphone—the smartphone receives alerts command from the Smart Safety Unit, triggers multimodal alerts to the driver, and provides a graphical interface of the ADAS. In the case of both compelling and severe alerts, the smartphone plays an audio message to avoid further distraction. Conversely, in the case of moderate alerts, a message is displayed on driver’s smartphones.

As shown in Fig. 11.2, data will flow (through both wired and wireless connections) from the sensing elements of the SOs to the Smart Safety Unit; the latter in turns communicates using Bluetooth with the driver’s smartphone.

11.4 IoT Domain and Opportunistic Service Metamodeling

Although missing a formal definition, there is a wide consensus on describing IoT Services as accessible interfaces to IoT devices’ functionality [3]. Therefore, in the direction of the maximum interoperability, shareability, and usability, it makes sense providing a functional and non-functional IoT Service description through a metadata-based approach, thus exploiting metamodels that are completely application context-, implementation technology-, and communication protocol-agnostic. These considerations motivated us in designing a domain model purposely targeted at the IoT scenario and its services opportunistic features [8]. Indeed, the proposed metamodeling approach allows:

- providing a high-level description of the different entities involved in the service provision;
- presenting essential data for the service provision into a uniform data model to foster their jointly exploitation;
- considering by design the key Opportunistic properties of emergent IoT services, especially context-awareness, co-location, and dynamicity.

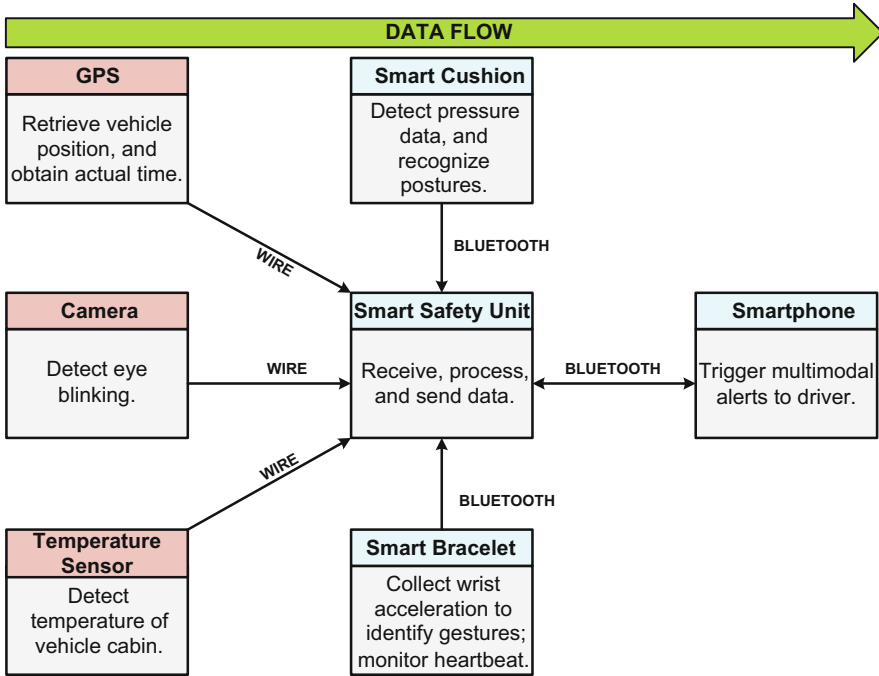


Fig. 11.2 Data Flow of the proposed driver assistance system. Data from several devices connected through different communication technologies are elaborated by the Smart Safety Unit for interacting with the driver’s smartphone

IoT Domain Model is presented in section “IoT Domain Model,” while Opportunistic IoT Service model in section “Opportunistic IoT Service Model.” Due to their generality, they have been already exploited in the context of a Smart City [3] and a Smart Workshop [9].

IoT Domain Model

IoT domain model of Fig. 11.3a relies on four building blocks, namely *IoT Entities*, *IoT Services*, *IoT Environment*, and *Context*. An *IoT Entity* represents any human, SO, or computing system which provides/consumes *IoT Services* according to both its *features* (namely static and dynamic attributes) and *functionalities* (namely cyberphysical capabilities subject to specific conditions or constraints). *IoT Entities* are co-located within and synergistically interacting with the *IoT Environment*, namely the physical and non-augmented space (a room, a beach, a wood) where the *IoT Service* takes place. Dependencies among *IoT Services* and both *IoT Entities* and *IoT Environment* constitute the *Context*, which contemplates any implicit or explicit information that may be of some benefit for the *IoT Service* provision. Indeed, any *IoT Service* is featured by a *Service Profile* specifying what it does and a *Service Model* detailing how it works, detailed in the following.

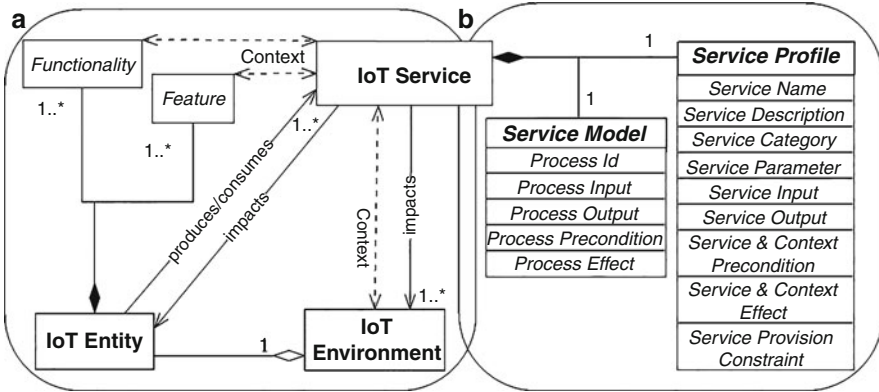


Fig. 11.3 (a) IoT domain model, describing main system’s building blocks; (b) IoT service model, describing main features of an IoT service and its operations

Opportunistic IoT Service Model

To foster its accurate description, automatic discovery, provision, and composing, an IoT Service is featured by a Service Profile, containing information about the IoT Service itself and its Context, and by a Service Model, which describes each operation concretely implementing the service itself. Opportunistic IoT Service model is depicted in Fig. 11.3b. A Service Profile is constituted by the set of attributes reported hereinafter:

- Service Name: the identifier of the IoT Service;
- Service Description: a description of the IoT Service;
- Service Category: an entry in some IoT Service ontology or taxonomy (e.g., monitoring and payment);
- Service Parameter: quality parameters featuring the provided IoT Service (e.g., accuracy and precision);
- Service Input: information required for the IoT Service execution;
- Service Output: information generated as output of the IoT Service execution;
- Service Precondition and Service Context Precondition: functional and IoT Entity-related conditions required for a valid IoT Service execution;
- Service Effect and Service Context Effect: events involving IoT Entities, which result from the IoT Service execution;
- Service Provision Constraint: IoT Entity’s constraints that are relevant to the IoT Service execution (e.g., the maximum allowed SO working temperature).

A Service Model, instead, details the operations realizing the IoT Service through the following IOPE (Input, Output, Precondition, Effect¹) attributes:

- Process Id: process identifier;

¹OWL-S: Semantic Markup for Web Services—W3C.

- Process Input: information required for the Process execution;
- Process Output: information generated from the Process execution;
- Process Precondition: condition(s) under which the Process can take place;
- Process Effect: event(s) or change(s) to the state of IoT Entities, which result(s) from the Process execution.

11.5 Case study: Driving Assistance Service

The outlined Driving Assistance Service is an Opportunistic IoT Service since it is enabled by highly contextualized interactions of cyberphysical SOs deployed and co-located within a physical environment (a vehicle cabin) with the final goal of dynamically alerting the driver if risky driving conditions are detected.

Models Instantiations

Figure 11.4 shows the Driving Assistance Domain Model. In particular, it reports the IoT Entities and the IoT Environment involved in the Driving Assistance Service and their contextual relationships, accordingly to the system architecture of Sect. 11.3. Please note that (1) car cabin is modeled as IoT Environment since it is considered without any augmentation; conversely, if we consider the whole car with its augmentation embedded devices, e.g., sensors, computer, it should be considered

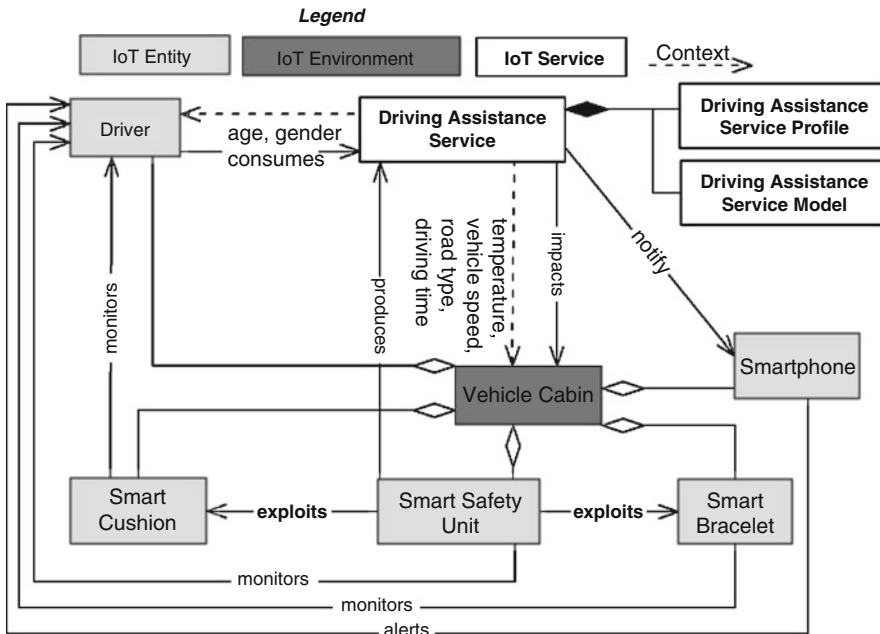


Fig. 11.4 Driving assistance domain model, reporting the IoT Entities and the IoT Environment involved in the driving assistance service and their contextual relationships

as an IoT Entity; (2) Context consists in information about Driver's age and gender (which are needed to set specific parameters for evaluating pulse), about cabin temperature, vehicle speed, driving time, type of taken road, weather information, time of day, which are purposely used for the provision of the opportunistic Driving Assistance Service; (3) at a higher degree of granularity, it could be possible to represent aggregated SOs such as the Smart Cushion in terms of its sub-features (pressure sensors, Arduino board, battery, etc.) and sub-functionalities (pressure data retrieving, data filtering and elaboration, etc.); however, since in this paper we focus on the final Driving Assistance Service, we will consider aggregates SO and their functionalities instead of their single sub-features and sub-functionalities.

Driving Assistance Service Model consists in ten operations, which all together concretely constitute the Driving Assistance Service and are listed hereinafter:

1. Road Type Acquisition: exploits Smart Safety Unit GPS information of current car location to acquire the type of road (highway, urban street, etc.) on which Driver is traveling;
2. Pulse Acquisition: driver pulse is retrieved from the Smart Bracelet;
3. Speed Acquisition: exploits Smart Safety Unit GPS information to determine the current car speed;
4. Temperature Acquisition: exploits Smart Safety Unit temperature sensor to determine the current car's cabin temperature;
5. Blink Acquisition: exploits Smart Safety Unit camera to estimate the Driver's blink rate;
6. Posture Recognition: exploits pressure data provided by the Smart Cushion to determine Driver posture;
7. Gesture Recognition: exploits Smart Bracelet's accelerometer and gyroscope to determine Driver gesture;
8. Emotion Inference: exploits information about Driver's posture, gesture, blink rate, and pulse that, correlated with cabins' temperature, allow estimating Driver's current psycho-physical status (boredom, tiredness, stress, agitation);
9. Risk Index Estimation: exploits information about road type, car speed, and Driver's psycho-physical status to estimate (moderate-severe-compelling) risk index;
10. Notification: exploits Smartphone to notify the Driver through a text or vocal message, according to the calculated risk index, suggesting action to be performed (open car windows, take a break, etc.).

The information flow outlined by the execution of these operations is the same already reported in Sect. 11.3. The first seven operations can be roughly classified as "retrieving operation," the eighth and ninth as "processing operation," and the last one as "actuation operation" accordingly to the kind of task they perform. For the sake of space, the Driving Assistance Service Model shown in Fig. 11.5 extensively reports (in terms of IOPE features) only one operation per class, i.e., Posture Recognition as "retrieving operation," Emotion Inference as "processing operation," and Notification as "actuation operation." As previously specified for the IoT Entities modeling, also Operations could be further detailed in terms of

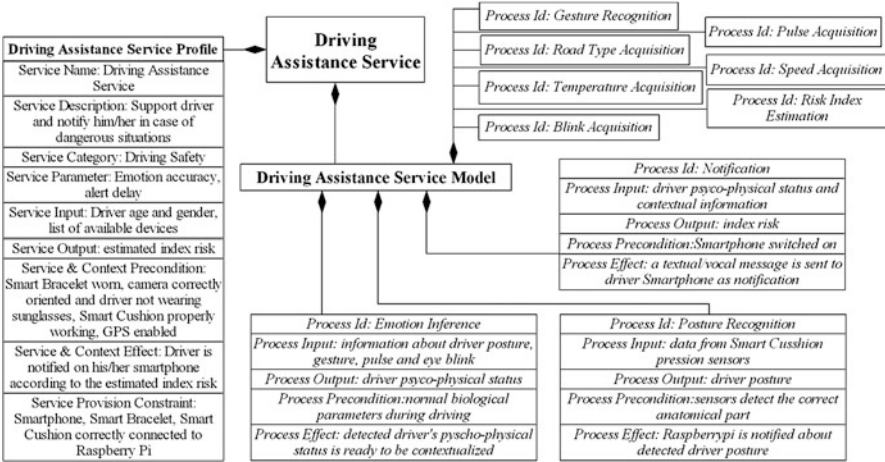


Fig. 11.5 Driving assistance service and profile models

Table 11.1 Already developed ADAS building blocks

Devices	Tested	On-going
GPS	X	
Temperature sensor	X	
Smart cushion with smart bracelet (motion)	X	
Camera with smart bracelet (physiology)		X

micro-operations (e.g., Emotion Inference operation could be further specified in terms of several atomic micro-operations such as Driver’s posture/gesture/blink rate/pulse information retrieving, inference rules retrieving, inference rules matching and evaluation).

Status of Development

While we have provided a comprehensive, modular architecture of the system, in its current status of development, the following building blocks have been already realized and successfully tested, as also summarized in Table 11.1:

- *GPS*—we are able to obtain the vehicle position, to track the route, and to pick the actual time (for recording driving duration);
- *Temperature Sensor*—we can measure the temperature of vehicle cabin;
- *Smart Cushion with Smart Bracelet (Motion)*—we exploit six pressure sensors on a seat and, differently from our previous research [18] in which two Shimmer2R motion sensors² were attached to the wrists, in this work we use a Xiaomi Mi Band 2 Smart Bracelet to obtain wrist inertial data.

²Shimmer, <http://shimmersensing.com>, last accessed June 2018.

- *Camera with Smart Bracelet (Physiology)*—we can monitor driver’s stress level [2] using the Smart Bracelet’ heart rate sensor. In addition, we are able to collect images of the driver’s face from the inward camera of the Smart Safety Unit; however, eye blinking/movement recognition and facial expression analysis algorithms have not been integrated yet.

11.6 Conclusion

It is well known that distraction, drowsiness, high stress level, and aggressive behaviors can reduce concentration to the driving, endanger safety, and therefore increase the risk of accidents. Therefore, ADASs are gaining consensus, although they typically rely on monolithic systems comprising embedded devices (e.g., infrared camera above the steering wheel), thus resulting costly and closed. Conversely, in this paper we presented a novel and open ADAS, called “Driving Assistance Service,” based on the jointly exploitation of both specific-purpose (Smart Cushion, Smart Safety Unit) and commercial devices (Smartphone, Xiaomi Mi Band 2). These SOs, adopting different communication protocols and standards and thus representing heterogeneous data sources, have been located within the vehicle to retrieve information about driver’s psycho-physical status, contextualize it with respect to environmental factors such as time of day and road type, and alert the driver if risky conditions are detected. The integrated “Driving Assistance Service” had been designed based on the Opportunistic IoT Service Metamodel, which captures the opportunistic characteristics of IoT services (context-awareness, dynamicity, co-location, transience) and focuses on those important information fundamental for the accurate IoT service analysis, automatic discovery, provision, and composition. Indeed, aiming at interoperability, shareability, and usability, the metamodel-based approach provided a functional and non-functional Opportunistic IoT Service description, resulting completely neutral with respect to the application context, implementation technology, communication protocol, and data standard. Differently from other literature works, we proposed an integrated, composite ADAS that takes into account heterogeneous data sources, spanning from psycho-physical driver’s indicators, to vehicle-related parameters and environmental/contextual factors.

As already reported in this paper, some building blocks of the system have been already and successfully tested, while it is an ongoing work to complete the development of the system with the integration of the necessary algorithms to recognize driver’s drowsiness from eyes blinking and to detect distraction from eyes gaze. Upon completing its development, we plan to perform an accurate field-trial of the system to obtain performance evaluation data in terms of effectiveness and precision in assessing imminent risks mining driving safety.

Acknowledgements This work has been carried out under the framework of INTER-IoT, Research and Innovation action—Horizon 2020 European Project, Grant Agreement #687283, financed by the EU.

References

1. Aloï, G., Caliciuri, G., Fortino, G., Gravina, R., Pace, P., Russo, W., Savaglio, C.: Enabling IoT interoperability through opportunistic smartphone-based mobile gateways. *J. Netw. Comput. Appl.* **81**, 74–84 (2017)
2. Andreoli, A., Gravina, R., Giannantonio, R., Pierleoni, P., Fortino, G.: SPINE-HRV: a BSN-based toolkit for heart rate variability analysis in the time-domain. In: *Wearable and Autonomous Biomedical Devices and Systems for Smart Environment*, pp. 369–389. Springer, Berlin (2010)
3. Casadei, R., Fortino, G., Pianini, D., Russo, W., Savaglio, C.V.M.: Modelling and simulation of opportunistic IoT services with aggregate computing. *Futur. Gener. Comput. Syst.* **91**, 252–262 (2019)
4. Castignani, G., Derrmann, T., Frank, R., Engel, T.: Driver behavior profiling using smartphones: a low-cost platform for driver monitoring. *IEEE Intell. Transp. Syst. Mag.* **7**(1), 91–102 (2015)
5. Darshana, K., Fernando, M., Jayawadena, S., Wickramanayake, S.: Riyadisi—intelligent driver monitoring system. In: *2013 International Conference on Advances in ICT for Emerging Regions (ICTer)*, pp. 286–286. IEEE, Piscataway (2013)
6. Daza, I.G., Bergasa, L.M., Bronte, S., Yebes, J.J., Almazán, J., Arroyo, R.: Fusion of optimized indicators from advanced driver assistance systems (ADAS) for driver drowsiness detection. *Sensors* **14**(1), 1106–1131 (2014)
7. Dong, Y., Hu, Z., Uchimura, K., Murayama, N.: Driver inattention monitoring system for intelligent vehicles: a review. *IEEE Trans. Intell. Transp. Syst.* **12**(2), 596–614 (2011)
8. Fortino, G., Russo, W., Savaglio, C., Viroli, M., Zhou, M.: Modeling opportunistic IoT services in open IoT ecosystems. In: *Proceedings of 18th Workshop From Objects to Agents*, pp. 90–95 (2017)
9. Fortino, G., Russo, W., Savaglio, C., Viroli, M., Zhou, M.: Opportunistic cyberphysical services: a novel paradigm for the future internet of things. In: *2018 IEEE 4th World Forum on Internet of Things (WF-IoT)*, pp. 488–492. IEEE, Piscataway (2018)
10. Fu, R., Wang, H., Zhao, W.: Dynamic driver fatigue detection using hidden Markov model in real driving condition. *Expert Syst. Appl.* **63**, 397–411 (2016)
11. Galarza, E.E., Egas, F.D., Silva, F.M., Velasco, P.M., Galarza, E.D.: Real time driver drowsiness detection based on drivers face image behavior using a system of human computer interaction implemented in a smartphone. In: *International Conference on Information Theoretic Security*, pp. 563–572. Springer, Berlin (2018)
12. Gao, H., Yüce, A., Thiran, J.P.: Detecting emotional stress from facial expressions for driving safety. In: *2014 IEEE International Conference on Image Processing (ICIP)*, pp. 5961–5965. IEEE, Piscataway (2014)
13. Gravina, R., Li, Q.: Emotion-relevant activity recognition based on smart cushion using multi-sensor fusion. *Inform. Fusion* **48**, 1–10 (2019). <https://doi.org/10.1016/j.inffus.2018.08.001>
14. Healey, J.A., Picard, R.W.: Detecting stress during real-world driving tasks using physiological sensors. *IEEE Trans. Intell. Transp. Syst.* **6**(2), 156–166 (2005)
15. Jung, S.J., Shin, H.S., Chung, W.Y.: Driver fatigue and drowsiness monitoring system with embedded electrocardiogram sensor on steering wheel. *IET Intell. Transp. Syst.* **8**(1), 43–50 (2014)
16. Li, G., Lee, B.L., Chung, W.Y.: Smartwatch-based wearable eeg system for driver drowsiness detection. *IEEE Sensors J.* **15**(12), 7169–7180 (2015)

17. Lisetti, C.L., Nasoz, F.: Affective intelligent car interfaces with emotion recognition. In: Proceedings of 11th International Conference on Human Computer Interaction, Las Vegas. Citeseer (2005)
18. Ma, C., Li, Q., Li, W., Gravina, R., Zhang, Y., Fortino, G.: Activity recognition of wheelchair users based on sequence feature in time-series. In: 2017 IEEE International Conference on Systems, Man, and Cybernetics (SMC), pp. 3659–3664. IEEE, Piscataway (2017)
19. Masala, G., Grosso, E.: Real time detection of driver attention: Emerging solutions based on robust iconic classifiers and dictionary of poses. *Transp. Res. C: Emerg. Technol.* **49**, 32–42 (2014)
20. Nass, C., Jonsson, I.M., Harris, H., Reaves, B., Endo, J., Brave, S., Takayama, L.: Improving automotive safety by pairing driver emotion and car voice emotion. In: CHI'05 Extended Abstracts on Human Factors in Computing Systems, pp. 1973–1976. ACM, New York (2005)
21. Rezaei, M., Klette, R.: Driver drowsiness detection. In: Computer Vision for Driver Assistance, pp. 95–126. Springer, Berlin (2017)
22. Streiffer, C., Raghavendra, R., Benson, T., Srivatsa, M.: DarNet: a deep learning solution for distracted driving detection. In: 18th ACM/IFIP/USENIX Middleware Conference (2017)
23. Wang, X., Xu, C.: Driver drowsiness detection based on non-intrusive metrics considering individual specifics. *Accid. Anal. Prev.* **95**, 350–357 (2016)
24. Wang, H., Zhang, C., Shi, T., Wang, F., Ma, S.: Real-time eeg-based detection of fatigue driving danger for accident prediction. *Int. J. Neural Syst.* **25**(2), 1550002 (2015)

Part IV
Communications and Networking

Chapter 12

Performance Evaluation of Bluetooth Low Energy Technology Under Interference



Heikki Karvonen, Konstantin Mikhaylov, Dinesh Acharya,
and Md. Moklesur Rahman

12.1 Introduction

The use of wireless sensor devices has been continuously increasing during recent years thanks to rising success of Internet of Things (IoT) applications. Sensor devices can be used in various scenarios, e.g., smart factories and homes, environmental monitoring, autonomous traffic, medical and healthcare applications. Wireless body area networks (WBANs) are designed for the smart healthcare applications, operating in hospitals or homes, as well as for versatile sport and fitness activities. WBAN sensors can be also connected to Internet, being a one specific IoT use case which is gaining an increasing business interest [1, 2].

IoT applications require low-power wireless communication solutions since most of the use cases imply long lifetime for the sensor nodes without battery replacement, or even using only the energy scavenged from the operation environment. There are various low-power communication technologies that have been proposed for wireless sensor nodes. The most well-known ones are Bluetooth Low Energy (BLE) [3] and IEEE Std. 802.15.4 [4] (ZigBee [5]). Specifically for WBAN purposes has been defined IEEE Std. 802.15.6 [6] and ETSI SmartBAN [7]. In [8] it was found that BLE is the most popular in commercially available products in healthcare and medical applications. Above mentioned technologies operate in the industrial, scientific, and medical (ISM) 2.4 GHz band, which is defined to be available worldwide for unlicensed usage. IEEE Std. 802.15.6 defines solutions also to sub-GigaHertz bands as well as for ultra wideband (UWB) up to 10.6 GHz. Today, the 2.4 GHz band is becoming congested since several wireless technologies, e.g., IEEE Std. 802.11 (Wi-Fi) and the unlicensed Long-Term Evolution (LTE-U)

H. Karvonen (✉) · K. Mikhaylov · D. Acharya · Md. M. Rahman
Centre for Wireless Communications, University of Oulu, Oulu, Finland
e-mail: heikki.karvonen@oulu.fi

solutions [9] operate in that frequency band. Therefore, coexistence issues may arise as the number of devices operating at that band increases rapidly.

It is important to evaluate the wireless communication performance in the congested scenario at 2.4 GHz ISM band especially for applications which require reliable communication as is the case in many healthcare and medical scenarios. In [10] authors studied analytically, the packet error rate (PER) of BLE under interference of ZigBee, Wi-Fi, and BLE 5 in hospital scenario. Here will be used experimental measurements to verify the analytical model findings in case of BLE under ZigBee interference. We have conducted our measurements for BLE 4, as well as for recently published BLE 5 coded ($S = 8$) mode.

The structure of the rest of the chapter is following. Section 12.2 briefly introduces the features of the BLE technology. Analytical model for PER calculation is introduced in Sect. 12.3. Measurement devices and setup are described in Sect. 12.4. Section 12.5 introduces the analytical and experimental results. Conclusions are given in Sect. 12.6.

12.2 Features of the BLE Technology

The low energy consuming version of Bluetooth, BLE 4, can nowadays be found in almost every smartphone, tablet, and laptop as well as in a large set of other wireless devices. The specification of most recent version, Bluetooth 5, was published in December 2016 [11] and the first development kits came to the market in early 2017. The long-range and mesh features have made the recent version of BLE very suitable for versatile IoT scenarios. The ambiguous target of BLE 5 specification was to increase the range up to four times, and data rate up to two times, when compared with BLE 4.2 [12]. Next we will introduce the most important updates of BLE 5 in comparison to BLE 4.2.

The communications range and the maximum throughput improvement has been enabled by specifying three new physical layer (PHY) options for BLE 5. The 1 Mbit/s Gaussian frequency shift keying (GFSK) PHY option of BLE 4 is named in Bluetooth v 5.0 core specification to be LE 1M. The new PHY layer options specified for Bluetooth 5 are: (1) GFSK PHY with 2 Mbit/s, named LE 2M; (2) Coded PHY option (LE Coded, $S = 2$) with payload coded at 500 kbit/s; (3) Coded PHY option (LE Coded, $S = 8$) with payload coded at 125 kbit/s. LE 2M is targeted for short range high-speed transmission by doubling the data rate in comparison to BLE 4.2. The LE coded versions target to improve the communication range. The LE Coded PHYs are using GFSK at 1 Msym/s rate and the payload data is coded in two stages as follows: (1) forward error correction (FEC) convolutional encoder and (2) spread by the pattern mapper. That procedure enables to improve the theoretical link budget of a coded transmission in comparison to LE 1M by 5 dB in case of LE Coded at 500 kbit/s, and by 12 dB in case of LE Coded at 125 kbit/s. However, note that only the LE 1M PHY support is mandatory.

The communication range improvement is supported in Bluetooth 5 specification also by increasing the maximum transmit power of a BLE from 10 mW (10 dBm) to 100 mW (20 dBm). However, higher transmit power cannot be used in some regions (namely, EU, Japan, and Korea) due to frequency regulations and since it does not provide any benefit in those areas. In order to improve the coexistence with other devices operating in the 2.4 GHz band, BLE 5 specification introduced a special interface for signaling and messaging mechanisms between collocated Bluetooth and other wireless devices.

The functionality of the broadcasting channels in BLE 5 has also been substantially enriched by introducing an optional extended advertising feature. At first, the specification introduces a concept of the secondary advertising channels which are co-allocated with the BLE data channels. The advertising packets' format used in the secondary channels has been adjusted by enabling them to carry up to 255 octets of PDU (instead of 37 octets in case of BLE 4) and also fragmentation is supported. BLE 5 specification supports also periodic advertisements. A periodic advertiser broadcasts the packets by hopping between the secondary channels in a predefined pseudo-random sequence at regular time intervals ranging from 7.5 ms to almost 82 s. Important improvement is that a scanner device may synchronize with one or even several non-overlapping (in time) periodic advertisers and receives the data from all of them. Therefore, BLE 5 version is more efficient and reliable solution for data broadcast in comparison to BLE 4.

The BLE 5 is backward-compatible with the earlier versions of BLE since all the discussed features are optional and does not need to be supported. However, it can be easily seen that the new features can enable substantially to increase the communications range or throughput or enable new modes of operation. Based on that fact, in the marketing materials of Bluetooth SIG [12], the BLE 5 is claimed to provide double data rate, up to four times higher range and up to eight times broadcasting capacity compared to BLE 4.2. However, it is important to notice that the improved data rate and communication range cannot be achieved at the same time because they are enabled by different PHY options.

12.3 Analytical Model

Here will be introduced an analytical model that can be used to compute the PER of BLE uncoded mode under interference. The developed model takes into account interference of multiple nodes by aggregating the signal power coming from them.

Several path loss models (2.4 GHz) have been proposed for indoor environments. For line-of-sight (LOS) scenarios the path loss equation is typically defined, as a function of distance d , as

$$PL(d) = PL_0 + 10n \log_{10} \left(\frac{d}{d_{h0}} \right), \quad (12.1)$$

where n is the path loss exponent and d_{h0} is the reference distance at which the reference path loss PL_0 is measured. In [13], measurements were conducted and a path loss model was specifically developed for a hospital indoor environment. Authors found in [13] that for a LOS hospital room case $n = 1.2$, which we are using in our calculations in the rest of the chapter.

The signal to interference ratio (SIR) at the affected receiver under multiple radios interference can be computed as [10].

$$SIR [dB] = \left(P_S - PL(L) - \sum_{i=1}^N (W_{D,I} P_i - PL(d_i)) \right), \quad (12.2)$$

where the desired signal's power is P_S and P_i is the power of the i :th interferer (in dB). The distance to the desired signal's transmitter is L , and d_i is the distance to the i :th interferer. $W_{D,I}$ is a coefficient that limits the interfering power to the bandwidth occupied by the technology being interfered with. It is defined in [14] as follows:

$$W_{D,I} = \begin{cases} 1, & \text{if } B_I \leq B_{DS} \\ B_{DS}/B_I, & \text{if } B_I > B_{DS} \end{cases}, \quad (12.3)$$

where B_I is the bandwidth of the interferer signal and B_{DS} is the bandwidth of the target node receiver filter. For this study the BLE is assumed to use GFSK modulation with bandwidth 1 MHz, bit rate $R_b = 1$ Mbit/s, $BT = 0.5$ and modulation index $h = 0.5$. For non-coherent demodulation, the symbol error rate (SER) is calculated as [10, 14].

$$SER = \frac{1}{2} e^{-E_s/2N_0} = \frac{1}{2} e^{-SIR/2}, \quad (12.4)$$

where E_s is the energy per symbol, N_0 is the noise power spectral density per Hz. In Eq. 12.4, $E_s/N_0 = E_b/N_0 = B_{DS}/R_b * SNR$, where E_b is the energy per bit and SNR is the signal-to-noise ratio. When replacing the noise power with the interference power after the receiver filter, SNR is equivalent to SIR [14], which has been inserted to Eq. (12.4).

Here we assume a worst-case scenario where full collision of interfering packets and the useful packet occurs, therefore SER can be assumed to be same for each transmitted symbol of the BLE packet. The PER for the affected BLE link can be calculated as

$$PER = 1 - (1 - \varepsilon)^K, \quad (12.5)$$

where K is the length of the packet of the desired signal and ε is the SER that can be calculated using Eq. 12.4.

12.4 Measurement Devices

In our measurements, a commercial chipset, nRF52840 [15] from Nordic Semiconductor, was used. The nRF52840 was one of the first commercial chipsets to support BLE 5.0. It is a system on chip (SoC) which integrates a multiprotocol 2.4 GHz transceiver with an ARM Cortex-M4F based microcontroller unit. A precompiled and linked binary software, S140 SoftDevice v6.0.0, implementing BLE protocol developed by Nordic Semiconductor was used in chipset.

Figure 12.1 illustrates the nRF52840 Preview DK development kit which was used in our experimental measurements. The firmware of the development kits was developed in this work based on the ATT_MTU Throughput Example of the nRF5 software development kit (SDK) v15.0.0. One of the boards was programmed to act as an advertiser, and the other one as scanner. The BLE physical layer to be used by the boards (i.e., LE 1M, LE 2M, or LE Coded) can be selected during the startup using the control buttons.

The methodology of our experiments was as follows. After placing the BLE boards in the specified locations, the scanner board was connected to a computer via serial over USB interface, configured to operate using the required PHY layer option, and forced to continuously scan a single advertisement channel. Approximately every second the scanner reported via serial interface the number of the received advertisements from the advertiser board, as well as the received signal strength indicator (RSSI) and the sequence identifier of the last advertisement it has received. Once the scanner board was activated, the advertiser was powered up and its PHY layer was configured. The advertiser started periodically sending the advertisements, each of which contained a unique sequence number. At the end of the experiment the PER was calculated from the total number of the packets received by the scanner and the sequence number of the last received packet.

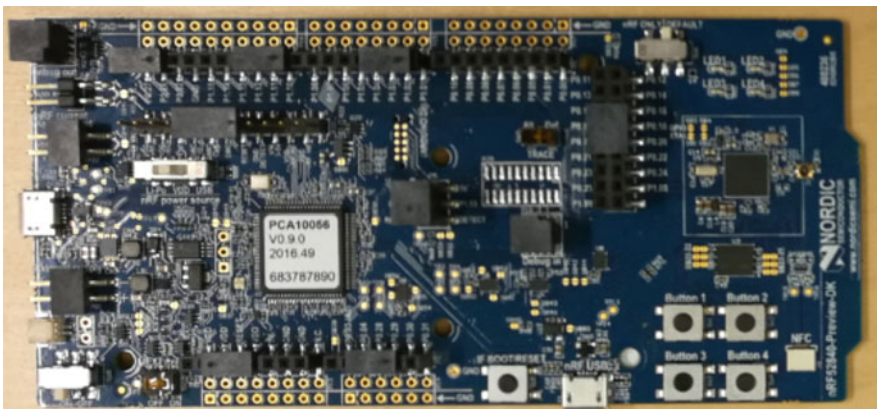


Fig. 12.1 nRF52840 Preview DK device used for measurements

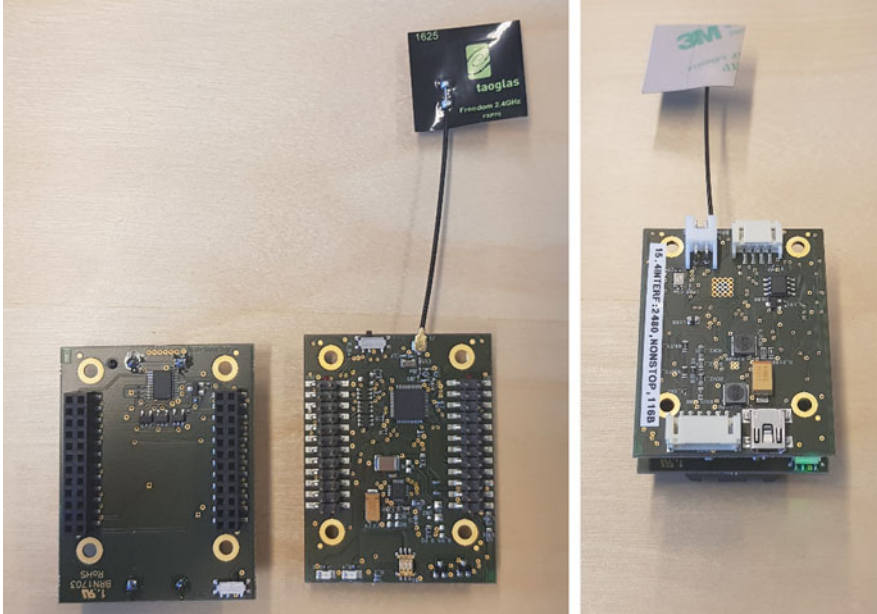


Fig. 12.2 CWC-MOD-POW platforms

In order to introduce the ZigBee interference to BLE communication, we used in our measurements the CWC-MOD-POW platforms (version two) [16, 17] illustrated in Fig. 12.2. These boards are built around Texas Instruments' CC2650 multi-standard system-on-chip [18]. The core middleware is based on CWC CC2650 IEEE Std. 802.15.4 proprietary driver and firmware, developed in TI CCS 7.4.0.00015 IDE. ZigBee nodes are equipped with an external antenna, Taoglas FXP70 [19]. The nodes were configured to start spamming the ZigBee packets with maximum possible payload without using any form of listen before talk at the same channel where BLE devices operate immediately after power up. The time between two sequential packets (due to radio re-configuration and uploading of the new packet) was well below 1 ms. In order to ensure continuity of the interferences multiple ZigBee interferers were used in our experiments.

In our measurement the BLE boards were set at the same height (1 m) so that antennas were pointing each other creating a LOS link. Three interfering ZigBee nodes were set around the BLE receiver, all at the same distance (Case1 = 4 m and Case2 = 6 m) to BLE receiver antenna. Different BLE link lengths were used (4–11 m) and number of transmitted and received packets was recorded for 10 min period (resulting in at least 10,000 BLE packets being sent).

Measurement environment was a restaurant at the University of Oulu during a time when there were not customers. This environment appeared to provide similar path loss as the hospital room LOS model introduced in [14] with path loss exponent $n = 1.2$. Therefore, this was a good environment to obtain results that can be applied

also to hospital case. Spectrum sniffers were used to find out that there was not interference from Wi-Fi or Bluetooth at the same band where our measurements were conducted.

12.5 Results

The developed analytical model was implemented to Matlab and measurements were conducted to evaluate BLE PER under ZigBee interference. Table 12.1 shows the parameters used in analytical and experimental performance evaluation of BLE 4. In addition, measurement were done for BLE 5 coded ($S = 8$) mode with the same parameter settings to find out the gain provided by forward error correction.

Figure 12.3 shows PER results for the scenario where three ZigBee nodes are interfering LOS BLE link which length was varied. ZigBee nodes were set at 4 meters distance from BLE receiver to create LOS interference. From Fig. 12.3, it can be observed that the effect of interference becomes visible in PER results when the BLE 4 link distance is longer than 5 m. PER increases very rapidly when the BLE link distance is increased and reaches its maximum value when BLE link length is 10 meters. After that point, almost all packets are lost since interference is too strong in comparison to BLE 4 signal strength. As a reference result, in cases without interference, the PER of BLE link remained below 15% for a link distance of 80 m. Further it can be seen that the measurement results are well aligned with the analytical results of BLE 4. It must be noted that in analytical calculations we used

Table 12.1 Parameters for analytical and experimental performance evaluation

Parameter	Value
Number of interfering nodes	3
Distance to interferers	Case1 = 4 m; Case2 = 6 m
Desired BLE link length	4–11 m
Frequency	2.480 GHz (BLE CH#39, ZigBee CH#26)
BLE bandwidth, B_{DS}	1 MHz
ZigBee bandwidth, B_I	2 MHz
Transmit power, BLE	0 dBm
Transmit power, ZigBee	0 dBm
Path loss exponent, n	1.2
RSSI at 1 m, BLE	-15 dBm
ZigBee Tx to BLE Rx loss	-9 dBm
Payload length, BLE	12 octets
Payload length, ZigBee	116 octets
Packet rate BLE node	One packet every 50 ms
Packet rate ZigBee node	One packet every 5 ms
Data rate (BLE)	1 mbps
Data rate (ZigBee)	250 kbps

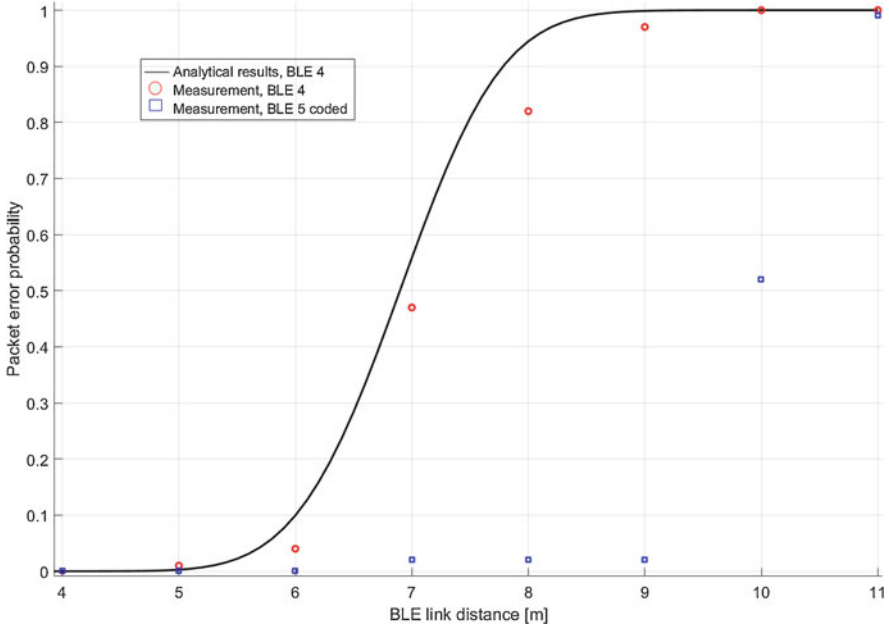


Fig. 12.3 BLE PER under interference of three ZigBee nodes at 4 m distance

–9 dBm loss for ZigBee to BLE receiver. The rationale for this negative gain is different antenna types and their orientations used in the ZigBee and BLE nodes, which are assumed to decrease the strength of experienced interference at BLE receiver. BLE 5 coded case measurement results of Fig. 12.3 show that the error correction enables to maintain low PER until the link distance increases to longer than 9 m, enabling 3 m (50%) higher communication range. After that point the PER increases rapidly also in the coded mode, i.e., the coding cannot correct the errors created by interference.

Figure 12.4 shows the PER for the case where ZigBee nodes were set at 6 m distance from BLE receiver. As expected, it can be observed that BLE 4 link can be longer in this case before the PER starts to increase due to interference. Also in this case it can be observed that the PER starts to increase rapidly when the BLE link length is increased beyond 6 meters. This result verifies that the analytical results are matching well with the measurement results even though there is a bit more variation in the results in comparison to Fig. 12.3 case. BLE 5 coded mode measurement results show similar behavior to that in Fig. 12.3, the coding gain being (2–3 m) in terms of increased BLE link length.

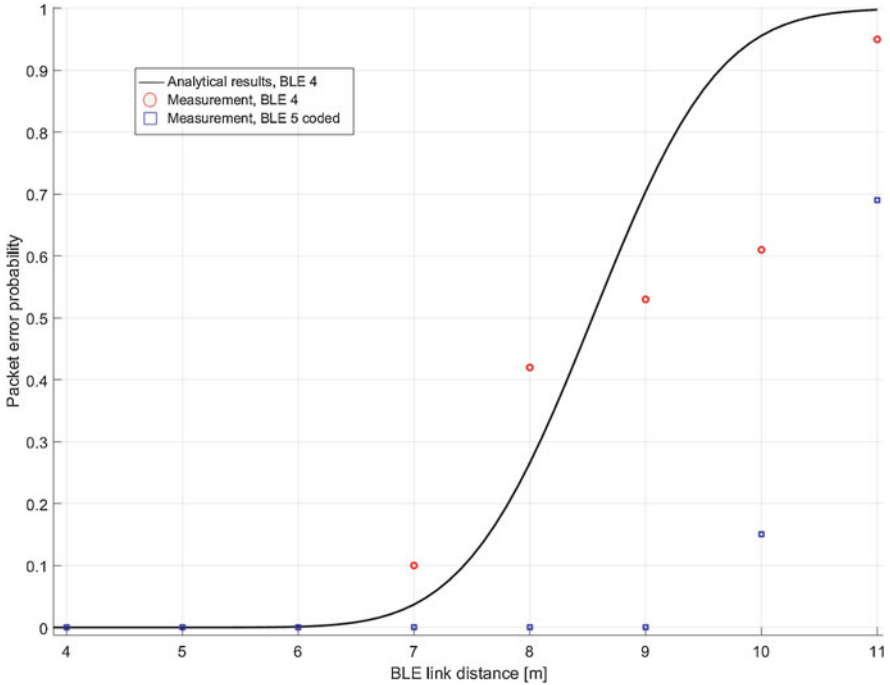


Fig. 12.4 BLE PER under interference of three ZigBee nodes at 6 m distance

12.6 Conclusions

This chapter reports the results of an experimental and analytical packet error rate evaluation of BLE under ZigBee interference. Analytical results were derived for the BLE 4 mode while measurements were conducted not only for BLE 4 but also for BLE 5 coded mode. Measurement results verified the analytical model results. Analytical model can be used to derive results also for other scenarios and as well as for other type of interferers.

Our results show that the worst-case interference is very harmful for BLE communication even when using the BLE 5 coded mode. Here the worst-case interference means that the interferers are at the same channel with the useful signal and full packet collisions occur. In terms of BLE link distance, the error correction coding gain was found to be only 2–3 m, i.e., approximately one-third of the used communication ranges. Results highlight that it is very important to pay attention to different technologies coexistence since the amount of IoT devices is increasing rapidly creating interference to each other.

Resilience toward interference is especially important in applications which require high reliability communications. Erroneous packet receptions will also decrease the energy efficiency which is highly important in IoT applications. Results of this chapter show that the BLE communication performance will decrease

drastically if there are interfering ZigBee nodes in a close vicinity (<6 m) at the same frequency channel. In future studies, we are going to evaluate different coexistence scenarios using analytical modeling and experimental measurements.

Acknowledgments This research has been financially supported in part by Academy of Finland 6Genesis Flagship (grant 318927).

References

1. Lamkin P.: Wearable Tech Market To Be Worth \$34 Billion By 2020. <https://www.forbes.com/sites/paullamkin/2016/02/17/wearable-tech-market-to-be-worth-34-billion-by-2020/#4cbe76e83cb5> (2016)
2. Tractica: Healthcare Wearable Device Shipments to Reach 98 Million Units Annually by 2021. <https://www.tractica.com/newsroom/press-releases/healthcare-wearable-device-shipments-to-reach-98-million-units-annually-by-2021/> (2016)
3. Haydon, R.: Bluetooth Low Energy: the Developer's Handbook. Pearson Education, Brooklyn (2013)
4. IEEE Standard for Low-Rate Wireless Networks, "IEEE Std 802.15.4–2015 (Revision of IEEE Std 802.15.4–2011)" (2016)
5. ZigBee Alliance, <http://www.zigbee.org/>
6. IEEE Std. 802.15.6: IEEE Standard for Local and metropolitan area networks—Part 15.6: Wireless Body Area Networks. Standard, The Institute of Electrical and Electronics Engineers, Inc. (2012)
7. Hämäläinen M., et al.: ETSI TC SmartBAN: Overview of the wireless body area network standard. International Symposium on Medical Information and Communication Technology (ISMICT) (2015)
8. Karvonen, H., Hämäläinen, M., Iinatti, J., Pomalaza-Ráez, C.: Coexistence of Wireless Technologies in Medical Scenarios. European Conference on Networks and Communications (EUCNC), Oulu, Finland (2017)
9. Nokia white paper, "LTE evolution for IoT connectivity," (2017)
10. Karvonen, H., Pomalaza-Ráez, C., Mikhaylov, K., Hämäläinen, M., Iinatti, J.: Interference of Wireless Technologies on BLE Based WBANs in Hospital Scenarios. IEEE International Symposium on Personal, Indoor and Mobile Radio Communications (PIMRC), Montreal, Canada (2017)
11. Bluetooth SIG: Bluetooth Core Specification v 5.0. <https://www.bluetooth.com/specifications/bluetooth-core-specification> (2016)
12. Bluetooth SIG: Bluetooth Core Specification 5.0 FAQ. <https://www.bluetooth.com/~media/files/specification/bluetooth-5-faq.ashx?la=en> (2016)
13. de Francisco, R.: Indoor Channel Measurements and Models at 2.4 GHz in a Hospital, IEEE Global Telecommunications Conference (GLOBECOM), Miami, FL, USA, 2010
14. Natarajan, R., Zand, P., Nabi, M.: Analysis of Coexistence between IEEE 802.15.4, BLE and IEEE 802.11 in the 2.4 GHz ISM band. 42th Conference of the IEEE Industrial Electronics Society (IECON 2016), Florence, Italy, 2016, pp. 6025–6032
15. Nordic nRF52840, <https://www.nordicsemi.com/eng/Products/nRF52840>
16. Mikhaylov, K.: Plug and play reconfigurable solutions for heterogeneous IoT. Ph.D. thesis, University of Oulu, 2018, online <http://jultika.oulu.fi/Record/isbn978-952-62-1841-0>
17. Mikhaylov, K., Petäjäjärvi, J.: Design and implementation of the Plug&Play enabled flexible modular wireless sensor and actuator network platform. Asian J Control. **19**(5), 1–21 (2017)
18. Texas Instruments, CC2650, online <http://www.ti.com/product/cc2650>
19. Taoglas, FXP70 data sheet, online <https://eu.mouser.com/datasheet/2/398/FXP70.07.0053A-1219667.pdf>

Chapter 13

A Hybrid Optical-Radio Wireless Network Concept for the Hospital of the Future



Iqrar Ahmed, Timo Kumpuniemi, and Marcos Katz

13.1 Introduction

There is currently a growing interest in developing concepts for the hospital of the future [1–3]. This is a multi-disciplinary development, including not only technology aspects but also medical and nursing sciences, architecture, management, etc. The role of technology in this concept is essential, as it makes possible and actively supports advanced healthcare methods, efficient use of hospital resources, exploitation of data, efficient management, automation, etc. In turn, most of these desired characteristics for tomorrow’s hospital rely on the concept of *connected hospital*, a notion allowing connectivity between all key stakeholders of the hospital, e.g., patients, healthcare personnel, equipment, data centers, other hospitals, and IoT nodes. In most of the cases, wireless connections are preferred, for the several well-known advantages of wireless networks. The key to the future hospital is to provide quality healthcare to all, regardless of the limited resources and increasing healthcare requirements and costs. The future hospital paradigms may include self and remote monitoring, mobility, hazard-free monitoring, data protection, and anonymity. In the future, different types of wireless networks will be deeply integrated in hospitals and healthcare centers.

Radio-technology has been the dominant approach to provide wireless connectivity in virtually any possible scenario. However, spectrum congestion, interference, security, privacy and safety issues, energy efficiency, and others are still challenges of radio-based systems. In recent years, optical wireless communication technology has emerged as a viable way to transmit information wirelessly. Visible light communications exploit the lighting infrastructure of solid-state light sources (e.g.,

I. Ahmed (✉) · T. Kumpuniemi · M. Katz
Centre for Wireless Communications, University of Oulu, Oulu, Finland
e-mail: iqrar.ahmed@oulu.fi; marcos.katz@oulu.fi

white light-emitting diodes) to provide light-based wireless connectivity. Light-based wireless systems complement effectively radio technologies, as the key advantages of the former can counteract the most important drawbacks of the latter, particularly the aforementioned spectrum shortage, security, safety, security, and interference. Recently, hybrid optical-radio networks have been proposed aiming at exploiting the flexibility and performance of both network approaches [4, 5]. This hybrid network is particularly attractive for sensitive environments such as hospitals, as the combined radio-optical network can be flexibly configured to adapt to particular scenarios and fulfill their associated requirements. A hospital equipped with hybrid optical-radio wireless networks will fulfill the most demanding requirements for performance, security, and safety. In this chapter, we discuss this concept in more detail.

This chapter is organized as follows. In Sect. 13.2, we discuss the possible wireless communication networks for future hospital. Section 13.3 introduces the proposed hybrid optical-radio network, operating scenarios, and applications within the hospital. Finally, in Sect. 13.4 we discussed the challenges associated with the proposed system and in Sect. 13.5 we concluded our study.

13.2 Wireless Networks for Tomorrow's Hospitals

In this section, we briefly describe the most important types of wireless networks exploited by hospitals and health centers, namely Wireless Body Area Network (WBAN), Wireless Local Area Networks (WLAN), and Wireless Wide Area Networks (WWAN). Figure 13.1 illustrates these networks from the hospital standpoint. In this chapter, particular attention will be paid to the short-range networks (i.e., local coverage) and their relationship to hospitals.

Wireless Wide Area Networks (WWAN)

Wireless wide area networks refer to wide coverage cellular networks. From a hospital perspective, large cells, e.g., macro- and micro-cells, cover large areas

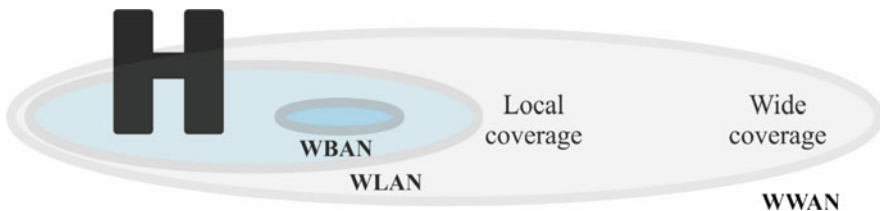


Fig. 13.1 Key wireless networks supporting the operation of a modern hospital: wireless body area networks (WBAN), wireless local area networks (WLAN), and wireless wide area network (WWAN)

(well outside the hospital itself), supporting also mobility. This is needed to support remote healthcare and healthcare on the move. Pico- and femto-cells can be also deployed inside hospitals to increase capacity and enhance service.

Wireless Local Area Networks (WLAN)

Wireless local area networks can provide cost-efficient high-performance local access to most of the typical hospital scenarios. These standardized general-purpose wireless networks have and will have an important role in hospitals, as they provide reliable, low-cost and locally controllable access to a variety of hospital scenarios, bridging healthcare equipment, people, computers, mobile devices, IoT nodes, and others.

Wireless Body Area Networks (WBAN)

During the past years, we have witnessed a rapid increase in the adoption of internet of things (IoT) technology. IoT sensors can be installed on a variety of objects and devices, such as body-worn devices, home appliances, environmental stations, buildings, and vehicles, to wirelessly monitor and control these elements through the internet infrastructure. Currently, huge global efforts are being made in the development and implementation of the fifth generation (5G) technologies, which will expand the number of IoT sensors into a totally new level, also allowing interoperation across different wireless networks. A WBAN is a close-range wireless network of nodes deployed on and in the human body. Nodes can include sensing and processing units, transceivers, and other functionalities. In a WBAN, one or more nodes can serve as access points or gateways, allowing exchange of data between the WBAN nodes and external devices. WBANs can be classified in *on-body* networks where the nodes are installed on the surface of the human bodies. In *off-body* cases, nodes are located in close vicinity of the humans (e.g., pockets, bags) while in an *in-body* cases nodes are placed inside the human bodies (e.g., implants). In *body-to-body* WBANs, nodes can exchange data between two or several individuals [6]. As population is ageing, the adoption of WBANs can provide a cost-effective solution to ease up the problem of monitoring health conditions, reducing costs and increasing the work efficiency of medical staff.

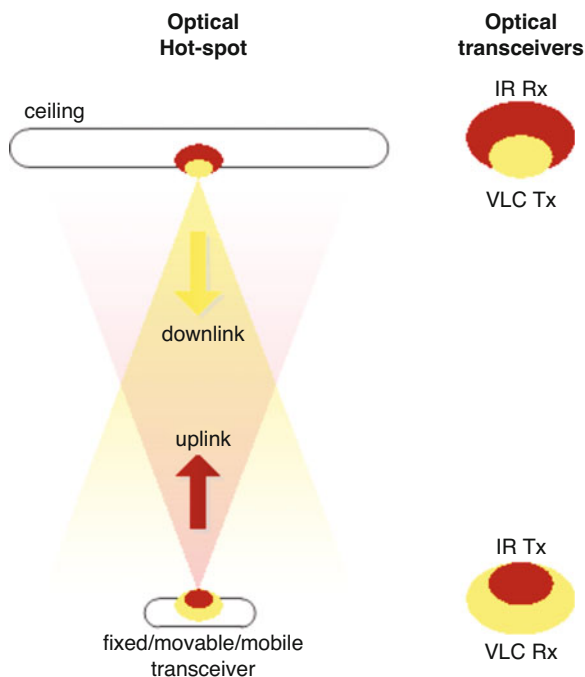
In fact, local networks enable to monitor the health of the patients in hospital wards, waiting rooms, and other premises of the hospitals and health centers without the constant presence of the medical staff. Cellular networks extend these capabilities when patients are outside the hospital, so remote monitoring can take place on the move, at home, etc. WBANs can also find applications in sports and training field, providing readily information on the effectiveness of training, for example. Moreover, WBANs can be used to monitor wellbeing, for instance

gathering information on sleep and day activity. Today, a number of different wireless technologies exist to be applied in medical scenarios, as discussed in [7]. They can be used to transmit body functions and parameters constantly through numerous sensors already commercially available [7]. However, these systems are based on radio frequency (RF) communications. Several systems operating at the same location might create interference as well as the body movement can increase the propagation channel interference that can eventually disrupt the data transmission [8].

Visible Light Communications (VLC)

Visible light communications is a relatively new wireless communication technology that exploits solid-state lighting infrastructure to create light-based wireless links. In recent years, a great deal of research and development on VLC was carried out, and VLC was shown to be an attractive wireless communication approach for indoor, outdoor, vehicular, and underwater scenarios. The principal advantages of VLC are the large and unregulated available bandwidth, the inherent security and privacy of optical systems, and due to the zero-radio emission, the suitability of VLC to both interference-sensitive environments and no radio exposure use cases. Figure 13.2 illustrates the basic structure of VLC transceivers using visible light for downlink and infrared light for uplink.

Fig. 13.2 Basic realization of uplink and downlink VLC transceivers



The use of VLC systems in medical environments has been proposed by several authors. Cahyadi et al. [9] demonstrated a system where the clinical data from three biosensors can be transmitted via VLC uplink. Predefined headers were added to each sensor to differentiate their signals at the receiver end. Authors reported minor interference in received signal caused by the flux of ceiling. The clinically interesting frequency range of mostly biosignals starts from DC and can be up to tens of Hertz; the biosignals might see several artifacts such as interference due to multiple sensors working at the same time when transmitted on RF. VLC presents an alternative solution for transmitting biosignals where these are less susceptible to artifacts. Dhatchayeny et al. [10] presented a study in which an EEG signal can be transmitted efficiently on VLC without any loss, as might be the case in radio transmissions. EEG signal comprises of multiple frequencies describing the ongoing activities in different parts of brain, thus transmitting each frequency separately is critical for proper diagnosis. Authors proposed a solution of duplicate parallel optical stream of EEG signal on RGB spectrum, and the received biosignals are identical when compared. Using three separate light wavelengths ensures zero interference in transmission. In [11], a concept of combining VLC and power line communications (PLC) in hospital for numerous purposes has been presented. PLC exploits the power lines to modulate the existing light resources for communications. Authors addressed the benefits VLC and PLC as a backbone of hospitals for transmitting the medical data. Following the evolution of e-health, the use of electronic patient records has been in common practice around the globe, where patients' clinical data is stored in a cloud. This is hugely advantageous to patients and hospitals, as patient data can be accessed from anywhere. However, due to the huge amount of data, high link capacity is crucial for efficient operation. Moreover, privacy and security are required for this type of communications. VLC can be used as an optimal solution in these applications. Authors demonstrated a 48 Mbit/s data link supporting data transmission, and connecting both patients and clinicians, as in the connected healthcare paradigm. Other proposed application scenarios could be operating smart devices and e-conferencing, and it could also help clinicians to give light therapy to patients suffering depression disorders. Similar studies, i.e., on VLC for transmitting biosignals, can also be found in [12].

Hybrid Networks

For more than a century, radio-technology has been the dominant approach to provide wireless connectivity in virtually any possible scenario. However, spectrum congestion, interference, security, privacy and safety issues, energy efficiency, and others are still challenges of radio-based systems. In recent years, optical wireless communication technology has emerged as a viable way to transmit information wirelessly. Light-based wireless systems, such as VLC, complement effectively radio technologies, as the key advantages of the former can counteract the most important drawbacks of the latter, particularly the aforementioned spectrum short-

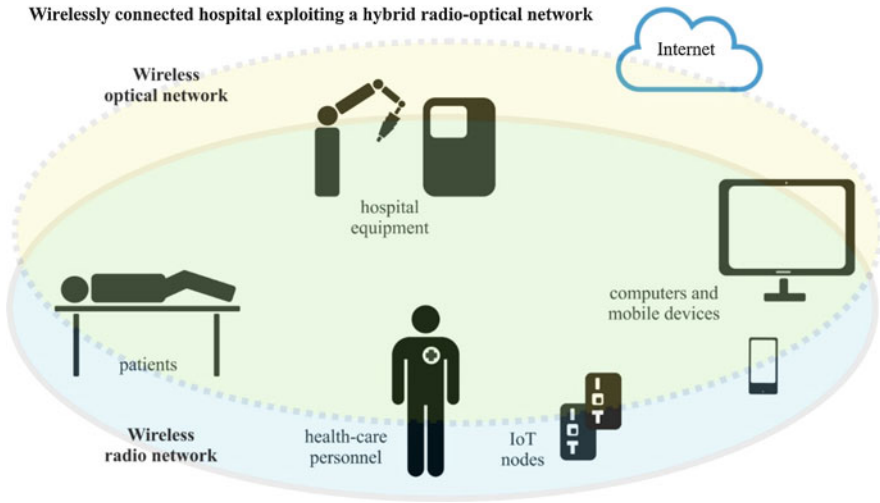


Fig. 13.3 Connected hospital of the future: exploiting radio and optical wireless networks

age, security, safety, security, and interference. In recent years, hybrid optical-radio networks have been proposed aiming at exploiting the flexibility and performance of both network approaches [4, 5]. Hybrid networks are particularly attractive for sensitive environments such as hospitals, as the combined radio-optical network can be flexibly configured to adapt to particular operation scenarios and their associated requirements. Figure 13.3 illustrates the key stakeholders of tomorrow's hospital, connected by both local radio and optical wireless networks. Patients, medical staff, equipment, computers, mobile devices, distributed sensors, and actuators will all be wirelessly networked in the hospital of the future. The highly complementary component networks bring redundancy to the system, which can be exploited in different manners. Indeed, an optical-radio network will guarantee flexibility, reliability, high performance, and efficient utilization of resources.

13.3 A Reconfigurable Optical-Radio Wireless Network for the Hospital of the Future

In this section, we present an optical-radio wireless network for future hospitals. Although the concept of the future hospitals has been discussed in many studies, the use of optical and radio links for medical data transmission has not been considered from this forward-looking perspective. Based on the hybrid optical-radio wireless network principle discussed in the previous section, we define a reconfigurable hybrid wireless network aimed for the hospital of the future. The network consists of (a) one or more *reconfigurable hybrid access points* and (b) one

or more *reconfigurable wireless body area networks*. The term reconfigurable refers here to the capability of the network to dynamically change the transmit and receive modes. More particularly, reconfiguration allows to select optical and radio modes for sending information between transmitting and receiving ends. Different mode selections will be defined later in this chapter.

Reconfigurable Optical-Radio Access Points

A reconfigurable optical-radio access point consists of hybrid transceiver with different operating modes. Downlink (DL) and uplink (UL) can be independently selected to transmit and receive using in each case either optical or radio links. This gives rise to four operating modes, namely (a) DL optical, UL optical; (b) DL optical, UL radio; (c) DL radio, UL optical; and (d) DL radio, UL radio. In addition, the system can be configured to exploit diversity, that is both transceivers are simultaneously used. A reconfiguration algorithm selects the most appropriate operating mode based on a number of inputs, such as optical/radio channel conditions, type of scenarios, service requirements, service provider/user decisions, and local policies. Note that reconfiguration is dynamic, and changes could occur over short-term periods (e.g., in response to sudden channel blockage) and also controlled over long-term periods, as such dictated by the operating scenarios and local policies, for instance. Figure 13.4 illustrates the concept of reconfigurable optical-radio wireless networks, particularly devised for tomorrow’s hospitals.

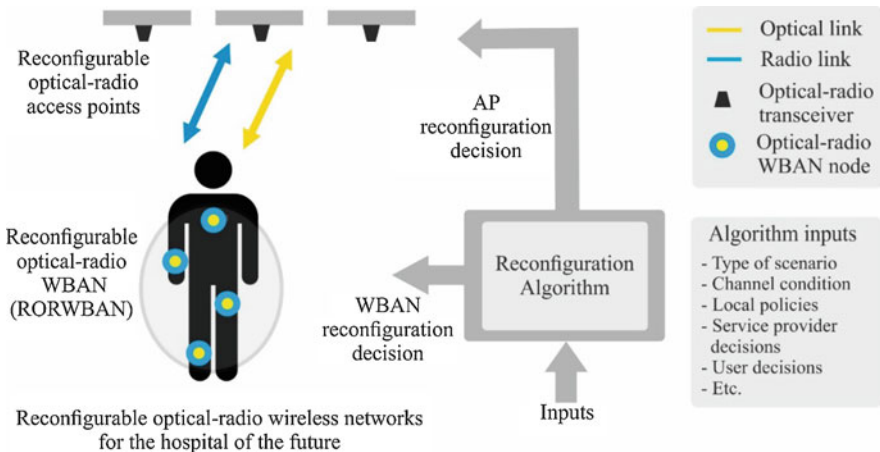


Fig. 13.4 Wireless communication networks for the hospital of the future: Reconfigurable Optical-Radio Access Points and Reconfigurable Optical-Radio WBANs

Reconfigurable Optical-Radio Wireless Body Area Network (RORWBAN)

We extend the conventional WBAN concept to consider a more generic network where some or all network nodes can be independently reconfigured in the same fashion as discussed for access points. That is, a generic node of the WBAN can be controlled to operate in different possible modes, exploiting optical and radio links. This defines a reconfigurable optical-radio wireless body area network, RORWBAN. In general, a RORWBAN has N nodes, out of which M are hybrid (optical/radio) and the remaining $(N-M)$ nodes are single-technology (either radio or optical). Eventually, all the nodes can be hybrid $N = M$ (fully hybrid WBAN). Figure 13.4 depicts a RORWBAN where $N = M = 4$. Note that if $N = 1$, the RORWBAN is reduced to a simple single-node case, as analyzed in our previous work [4, 5].

The RORWBAN can be configured dynamically (on the fly) according to the prevailing instantaneous conditions as well as some general environmental/context/policy situation (typically but not necessarily fixed), in the same way as discussed for the hybrid access points. Note that power consumption could also be used as a mode selection criterion. The reconfiguration algorithm selects the appropriate operating mode for the WBAN, action done jointly with the access point mode selection. Implementation of a hybrid node could be optimized to support simplicity and cost reduction. In such a case the node should use as much as possible common communicational blocks, only transmitting/receiving ends could be changed according to the selected optical/radio mode. Nodes could also be implemented as different parallel optical and radio branches, and the selection will then focus on the complete branch.

Operating Scenarios/Applications

Unique VLC features, such as high data rate support, inherent security, less interference to biosignals and to sensitive equipment, hazard-free transmission, and cost-effective implementation (existing PLC and light resources infrastructure can be reused), make VLC an attractive solution for hospital wireless connectivity. Added to this is the flexibility, simplicity, and performance of radio networks. Combining both technologies as suggested here will help to fulfill the communication requirements of the hospital of the future. Key objectives of future hospitals include enhancing the healthcare quality, management, i.e., self and remote, data security, and anonymity. We consider next two attractive operating scenarios for future hospitals.

Reconfigurable Optical-Radio Wireless Networks Within the Hospital We consider first the use of the hybrid wireless networks in different hospital scenarios,

and for a variety of requirements. By maximizing the use of optical links, the proposed architecture provides an efficient mean of reducing (a) radio exposure and (b) generated interference. In other words, whenever possible the traffic is sent through optical wireless communications. Some potential applications of proposed RORWBAN within a future hospital are discussed.

RF-restricted areas/coexistence The use of RF devices is prohibited in specific hospital areas, e.g., radiology and CT labs, since radio can interfere with other devices. This is also the case in heavily guarded facilities such as in oncology and catheterization labs, where radio interference is also an issue. In such situations, the wireless network can be configured a fully optical, so sensors data can be safely transmitted despite radio restrictions. In highly sensitive environments, e.g., operation rooms or premises with high fidelity medical measuring and treatment equipment, radio communications may be an unwanted technology as such. Optical links offer a simple solution, as well as protection against data leakage through eavesdropping. At homes, this is a convenient way to create a controllable, data transmission safe environment.

Off-loading While performing tests in the aforementioned labs, a large number of sensors is used to monitor the physiological state of the subject which is essential for proper diagnosis. Transferring this information using conventional radio could easily consume prohibitive amounts of bandwidth. Data could be here partitioned and transmitted in optical and radio links, and eventually only optical links could be utilized.

Support of mobility and localization Another potential advantage is indoor positioning, exploiting both optical and radio infrastructure for more accurate results. The ubiquity of optical and radio networks allows the data transmission while the subject is displaced from ward or moving. This could also help clinical robots to be remotely positioned and controlled when performing different tasks in highly hazardous areas. In other words, a hazard-free environment can be possible in future hospitals.

Data security Optical communications provide inherently secure communications as the signal is spatially confined in the area of operation. This feature could help to secure the data since the light waves cannot breach the walls or windows, so it secures the data to be hacked from outside. However, a hybrid network allows protection to a higher degree. We proposed a novel way of data encryption. Using the proposed hybrid network, we can divide and transmit the data in two domains, radio and optical. In order to decode the received data, both parts need to be present. Clearly the optical component is very local, whereas the radio part could be transmitted either by local or wire area (cellular) networks.

Energy efficiency/saving The hybrid network can be configured in a low-power mode, where the selection will depend on the power consumption profile of the optical and radio implementations, among others.

High reliability, high data throughput The multiplicity of nodes (RORWBAN) and possible links (optical/radio) creates a number of diversity branches that can be readily exploited to enhance reliability of the communications. The same principle can be applied to achieve high data rates, by using a number of parallel data pipes to transfer information.

Reconfigurable Optical-Radio Wireless Networks outside Hospital (Remote Hospital) An important scenario of the future hospital is that healthcare services are not confined exclusively to hospital territory. Remote and self-care in healthcare sector have strengthened this scenario; our proposed system allows homes to be turned into hospitals. This could help to reduce pressure on healthcare personnel, reduce costs, and improve wellbeing of patients, without compromising the healthcare quality. The considered hybrid network can be used for monitoring the subjects from home. WBAN sensors using both optical and radio links can accommodate the data loss in case either link fails, as a vertical handover mechanism (VHO) switches the links whenever a fail occurs. Since a remote location working as a hospital extension is not regulated (e.g., a hospital is a controlled environment), a conventional radio-based WBAN is more likely to be interfered (or create interference to near-by equipment). Again, optical systems or a combination of radio and optical approaches can eliminate or drastically reduce possible interference problems with surrounding equipment.

Operating Modes

In past recent years, hybrid optical-radio networks have been demonstrated aiming at exploiting the flexibility and performance of both network approaches [4, 5]. These hybrid networks utilize potential vertical handover (VHO) techniques for allocating network at predefined rules. Based on those studies our proposed hybrid network can also switch between five different operating modes. These modes are:

- Mode 1, *fully optical*. Both uplink and downlink are visible light channels in this case; the data is transmitted through LED driven by modulated signals.
- Mode 2, *fully radio*. In this case, RF uplink and downlink are utilized to transmit the data between the source and the sink.
- Mode 3, *hybrid 1*. In Hybrid 1 mode the uplink is established using optical channel, whereas all the downlink data can be transmitted through RF link.
- Mode 4, *hybrid 2*. Hybrid 2 mode is the opposite of Hybrid 1 where the uplink is established using RF channel and all the downlink data can be transmitted through optical link.
- Mode 5, *co-operative*. In co-operative mode, both RF and optical channels can be used as complementary to each other, and also simultaneously. VHO techniques allow networks to switch between both modes in case of failure of either link.

Hybrid modes 1 or 2 can be used when there is a large traffic imbalance between uplink and downlink, in off-loading situations, and due to uneven resources availability.

The considered system can select any mode based on the local policies defined by operator or user according to the ground situations as well as some predefined rules such as VHO strategies could also make selections among different operating modes discussed above.

13.4 Challenges

Since VLC is relatively new compared to well-established radio communications, numerous challenges need to be addressed, and current research in WBAN using radio could help to design and enhance the capabilities of RORWBAN.

Sensor The sensor package should match or fit the human body and each sensor should be kept small. Since our proposed system uses both radio and optical transmitter and the overall size also determines the weight carried, novel IC packaging is crucial for RORWBAN.

Throughput Though very high data rate of up to 1 Gbit/s has been achieved with OWC [13], the SNR could deteriorate progressively in non-LOS communications or when obstructed partially.

Reconfiguring mechanism/Complexity Devising a fast and flexible, yet robust control algorithm to reconfigure both access points and RORWBAN could be challenging task, as the number of input parameters could be significantly large, and their interrelationship complex. The use of machine learning and AI could help to design an effective decision-making mechanism.

Energy harvesting To be practically attractive, the expected power consumption of nodes is expected to be less than 1 mW [14]. In practice, however, the battery-powered WBAN sensor consumption should be as minimum as possible, and the overall size of sensor and circuitry play an important role in battery life. For our proposed system, energy harvesting could be a solution to enable sensor to work for longer durations. Note that light could not only power up the sensor but also convey data information as in VLC.

Security Data security is another key challenge; we proposed partial parallel radio-optical transmission of data. In that case, the data from either links is not meaningful unless the receiver obtains the other part of data. Coding for parallel radio-optical transmission is a challenging task.

Integrity and Intelligence The integrity of received signal is of utmost importance; any missed or falsely transmitted signal could risk a human life. Thus, the readout and sensing errors need to be addressed briefly. The intelligence for a complex system as RORWBAN is critical not only to handle network links and to pre-process

the biosignals before transmission. The proposed system could work in different operating modes as mentioned above; it requires an embedded intelligence to switch the links in case of failure. Also, the pre-processing intelligence of biosignal before transmitting is to remove artifacts embedded into them which could result in background noise or low SNR.

13.5 Conclusions

In this chapter, we proposed a novel architecture for wireless communication networks particularly focused for operating scenarios of future hospitals. Our proposed system exploits the relatively new VLC and conventional radio communicational techniques to build a flexible, secure and radiation/interference safe network which can satisfy the communication requirement of the hospital of the future. One of the most attractive features of VLC is its inherent interference-free operation with respect to radio, which means that both RF and VLC can coexist without any problem. This is because the VLC does not produce any electromagnetic interference to radio systems, so a coexisting optical-radio network could act as information backbone for future hospitals. We discussed the architecture and possible applications of coexisting radio-optical hybrid communication network. To build an efficient hybrid network apparently huge infrastructure changes might be required, but there are some studies that have demonstrated that VLC can be implemented with existing resources. Studies have shown that power line communication (PLC) can be used for VLC. The data signal modulating the light of the white LEDs in the ceiling and creating the downlink optical channel is sent to that optical source through the existing power lines, exploiting PLC technology. This is a simple, proven and inexpensive technology. Conversely, in the uplink direction, PLC is used to transmit the signal received by the photodetectors installed in the ceiling to the corresponding processing units. The presence of already existing power and light resources makes VLC favorable to implement as a low-cost communication backbone for future hospitals.

The proposed VLC network fulfills the architecture defined by IEEE 802.15.7, where the data can be transmitted either using peer-to-peer P2P or star topologies. The data transmission could be challenging when dealing with multiple users; IEEE 802.15.7 provides solution for handling multiple users in a VLC network. The channel contention terminology is introduced and the users contend for the channel, whoever get the free channel sends data on that. Using PLC for VLC will be very useful when broadcasting the information within the hospital premises and could save the new layout for communications.

Due to the fact that systems do not interfere each other, the coexistence of radio and optical communications could reduce the outage probability. Network adaptation in future hospitals is key for secure, private and high-performance operation. IEEE 802.15.7 describes the link adaptation process when receiving a dimming request from a given user, in such case the data communication is kept

at lower data rate instead of breaking the network link. Similarly the network adaptation in a coexisting optical-radio network can be made by the network controller, i.e., switching the optical to radio or vice versa or by some predefined rules, i.e., fuzzy logic can be used to decide the link adaptation by computing the probabilities of link failure and link restoration.

The reconfigurable nature of the system could provide a platform to implement and test novel resource allocation strategies for further enhancement of system intelligence. Operating scenarios and modes are discussed in detail and could help in self and remote healthcare diagnostics. The proposed system utilizes the existing solid-state-lighting-based structure for VLC and thus it can be adopted and could act as a backbone for data traffic connecting the hospital on a single highway. Several challenges are to be overcome to build and embed the proposed system into the hospital environment, but the flexibility, security, and user safety features make the proposed system an integral part of the future hospitals.

Acknowledgement “This research has been funded by HERONET project and partially funded by Academy of Finland 6Genesis Flagship (grant 318927).”

References

1. Future Hospital OYS 2030. <http://www.oys2030.fi/english.php>
2. Bardram, J.E.: Hospitals of the future—ubiquitous computing support for medical work in hospitals. In: UbiHealth 2003: The 2nd International Workshop on Ubiquitous Computing for Pervasive Healthcare Applications
3. White paper: the hospitals of the future, Advanced Wireless Technology Group, UK. <http://awtg.co.uk>
4. Saud, M.S., Chowdhury, H., Katz, M.: Heterogeneous software-defined networks: implementation of a hybrid radio-optical wireless network. In: Wireless Communications and Networking Conference (WCNC), 2017 IEEE, pp. 1–6. IEEE (2017)
5. Saud, M.S., Katz, M.: Implementation of a hybrid optical-RF wireless network with fast network handover. In: European Wireless 2017; Proceedings of 23th European Wireless Conference, pp. 1–6. VDE (2017)
6. Karvonen, H., Hämäläinen, M., Iinatti, J., Pomalaza-Ráez, C.: Coexistence of wireless technologies in medical scenarios. In: Proceedings of the 2017 European Conference on Networks and Communications (EuCNC), pp. 1-5, IEEE, Oulu, Finland (2017)
7. Karvonen, H., Mikhaylov, K., Hämäläinen, M., Iinatti, J., Pomalaza-Ráez, C.: Interference of wireless technologies on BLE based WBANs in hospital scenarios. In: Proceedings of the 2017 IEEE 28th Annual International Symposium on Personal, Indoor, and Mobile Radio Communications (PIMRC), pp. 1-6, IEEE, Montreal, Canada (2017)
8. Hall, P.S., Hao, Y.: Antennas and Propagation for Body-Centric Wireless Communications, 2nd edn. Artech House, Norwood (2012)
9. Cahyadi, W.A., Jeong, T.I., Kim, Y.H., Chung, Y.H., Adiono, T.: Patient monitoring using visible light uplink data transmission. In: 2015 International Symposium on Intelligent Signal Processing and Communication Systems (ISPACS), pp. 431–434. IEEE (2015)
10. Dhatchayeny, D.R., Sewaiwar, A., Tiwari, S.V., Chung, Y.H.: EEG biomedical signal transmission using visible light communication. In: 2015 International Conference on Industrial Instrumentation and Control (ICIC), pp. 243–246. IEEE (2015)

11. Ding, W., Yang, F., Yang, H., Wang, J., Wang, X., Zhang, X., Song, J.: A hybrid power line and visible light communication system for indoor hospital applications. *Comput. Ind.* **68**, 170–178 (2015)
12. Tan, Y.Y., Jung, S.J., Chung, W.Y.: Real time biomedical signal transmission of mixed ECG signal and patient information using visible light communication. In: *Engineering in Medicine and Biology Society (EMBC), 2013 35th Annual International Conference of the IEEE*, pp. 4791–4794. IEEE (2013)
13. Cossu, G., Ali, W., Corsini, R., Ciaramella, E.: Gigabit-class optical wireless communication system at indoor distances (1.5–4 m). *Opt. Express.* **23**(12), 15 700–15 705 (2015)
14. Mitcheson, P.D., Yeatman, E.M., Rao, G.K., Holmes, A.S., Green, T.C.: Energy harvesting from human and machine motion for wireless electronic devices. *Proc. IEEE.* **96**, 1457–1486 (2008)

Chapter 14

Signal Transmission with Intra-Body and Inter-Body Communications: Simulation-Based Models



Doaa Ahmed , Jens Kirchner, and Georg Fischer 

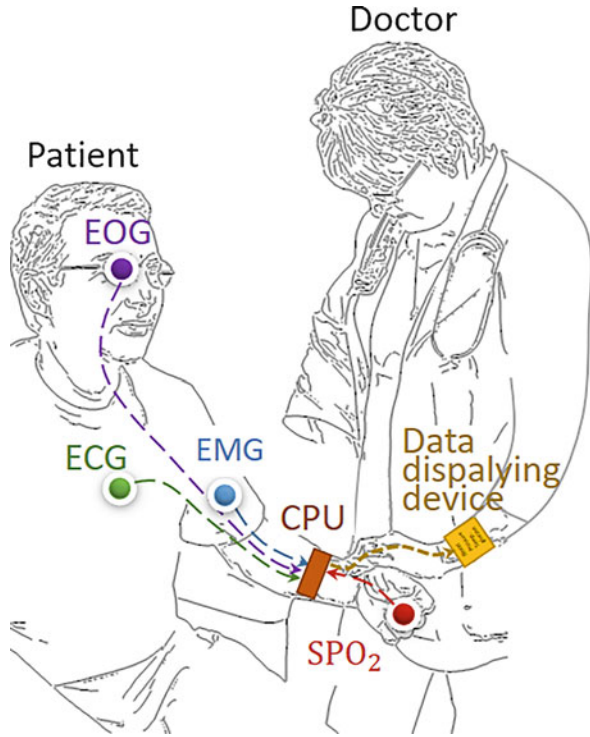
14.1 Introduction

Nowadays, many wireless electronic devices could be used to exchange data between different points on, inside, or at the proximity of the human body. Data could be medical related, e.g., electrocardiogram (ECG), electroencephalogram (EEG), electromyogram (EMG), etc., or consumer lifestyle related, e.g., photos, videos, messages, etc. Nevertheless, airborne transmission using antennas typically is a very energy intensive process implying large batteries. Therefore, low power consumption with high quality transmission techniques are highly needed. Human body communication (HBC) is one transmission technique defined for low power consumption in wireless body area networks (WBANs). Different ways can be used to establish BAN communication networks [1]. In this paper, we focus on HBC based on galvanic coupling approach. Here, the human body is considered as the transmission medium for data signals. Therefore, the signals are confined to the body, which ensures high security and less interference with neighboring transceivers during signal transmission. Moreover, HBC is a promising technique for low power consumption transmission, which helps the batteries of wearable or implantable devices to be reliable and longer lasting. In addition, harvesting energy from the human body could be used to continuously recharge HBC-enabled devices without the need for external power supplies [2].

HBC transmitter (TX) and receiver (RX) are each connected to a coupler that is composed of two electrodes, i.e., signal electrode and ground. In the galvanic coupling, digital information is exchanged by inducing weak AC currents

D. Ahmed (✉) · J. Kirchner · G. Fischer
Institute for Electronics Engineering, Friedrich-Alexander-Universität
Erlangen-Nürnberg (FAU), Erlangen, Germany
e-mail: doaa.ahmed@fau.de; jens.kirchner@fau.de; georg.fischer@fau.de

Fig. 14.1 Potential application scenario for human body communication: vital data from several sensors are transmitted to a central hub and processing unit (intra-body communication); relevant data is then sent to the treating physician (inter-body communication)



galvanically into the human body. Both TX and RX electrodes are hence attached directly to the body.

For applications of HBC, two possible communication connections can be established. In intra-body communication, data is transferred between sensors distributed across the same human body, which enables data fusion, e.g., for monitoring of health condition. In contrast, in inter-body communication, data is transferred between sensors distributed across different bodies that are in touch. This will allow users to be able to exchange data among several wearable devices just by touching each other [3]. One application is shown in Fig. 14.1: Different sensors are distributed across the human body of a patient, which collect his vital signs, e.g., EMG, ECG, (electrooculogram) EOG, etc., then send this data to a central processing unit (CPU) to be combined, encoded and further resent to an HBC-enabled device worn by a doctor for data decoding and displaying.

Several studies have been previously done to investigate transmission characteristics of intra-body communication either with experimental studies or with simulations [4–12]. In [4], an experimental study was done to send data through the tissues from an implanted telemetry device to be detected by surface electrodes. In vivo experiments were conducted in [5] to analyze the human data channel. The authors in [6] have developed a wearable ECG for vital signals transmission based on impulse radio type HBC. In addition, numerical simulations and experiments

were conducted in [7] to understand the influences from the electrode size, joints between TX and RX, and electrode positions on signal attenuation. In [8], the authors proposed a transfer function to represent the galvanic coupling in intra-body communication, moreover, some in vivo measurements were conducted. Also, a simulated-based model of the whole human body was introduced to measure the signal attenuation at different positions on the body. In [9], several types of electrodes are compared and signal attenuation between different positions on the human body was investigated via in vivo measurements. In [10], the authors proposed a 3D FEM multilayered cylindrical model of a human arm to simulate the current density and electric field through different tissues as a function of frequency for different channel lengths and inter-electrode distances. In [11, 12], we have tried to understand the transmission mechanism in intra-body communication based on a simulated model of the arm, the electric potential difference at TX and RX at different applied frequencies, the current density, inter-electrode distances, and the signal attenuation on the surface of the body, and inside tissues were investigated.

In this paper, the data transmission mechanism in the human tissues for both intra-body and inter-body communication is investigated, which to the best of the authors' knowledge, has not been enough covered in the HBC literature. Two different simulation-based models are implemented using COMSOL Multiphysics 5.3a software. In a model of a human arm consisting of different types of tissues, the transmission mechanism in intra-body communication in a straight simulated-based arm model is studied, in addition, some bending is introduced to the model to investigate its effect on signal attenuation. On the other hand, with the model of two contiguous human arms, signal transmission in inter-body communication while changing the area of contact between the arms is investigated.

This paper is organized as follows. In Sect. 14.2, we derived dielectric properties of the human tissues used in our simulation; in addition, some theoretical framework and approximations are given. In Sect. 14.3, the simulation setup and results are given. Finally, Sect. 14.4 concludes our work.

14.2 Dielectric Properties of Human Tissues and Approximations

The dielectric properties of body tissues at various frequencies are represented in graphical plots using a model based on the summation of 4-Cole–Cole expressions, which describes the complex relative permittivity as follows [13]:

$$\epsilon_r(\omega) = \epsilon_\infty + \sum_{m=1}^4 \frac{\Delta\epsilon_m}{1 + (j\omega\tau_m)^{1-\alpha_m}} + \frac{\sigma_i}{j\omega\epsilon_0} \quad (14.1)$$

where $\epsilon_r(\omega)$ represents the frequency-dependent complex relative permittivity, ϵ_∞ is the material permittivity at very high frequencies, $\Delta\epsilon_m$, τ_m , and α_m are material

Table 14.1 Parameters for the derivation of dielectric properties of different human tissues (adapted from [14])

Tissue	Skin (dry)	Fat	Muscle	Cortical	Cancellous
ϵ_∞	4.00	2.50	4.00	2.50	2.50
$\Delta\epsilon_1$	32	9	50	10	18
τ_1 (ps)	7.234	7.958	7.234	13.263	13.263
α_1	0.000	0.200	0.100	0.200	0.220
$\Delta\epsilon_2$	1100	35	7000	180	300
τ_2 (ns)	32.481	15.915	353.678	79.577	79.577
α_2	0.200	0.100	0.100	0.200	0.250
σ_i	0.000	0.035	0.200	0.020	0.070
$\Delta\epsilon_3$	0.00E+0	3.30E+4	1.20E+6	5.00E+3	2.00E+4
τ_3 (μ s)	159.155	159.155	318.310	159.155	159.155
α_3	0.200	0.050	0.100	0.200	0.200
$\Delta\epsilon_4$	0.00E+0	1.00E+7	2.50E+7	1.00E+5	2.00E+7
τ_4 (ms)	15.915	15.915	2.274	15.915	15.915
α_4	0.200	0.010	0.000	0.000	0.000

parameters, σ_i is the ionic conductivity, j denotes the imaginary unit $\sqrt{-1}$, ω is the angular frequency, and ϵ_0 the permittivity of free space. Table 14.1 shows the parameters needed to find the complex relative permittivity of the human tissues used in our models [14]. From Eq. (14.1) with Table 14.1, we derived the required dielectric properties for our simulation.

Due to [15], quasi-static approximation can be applied if the dimensions of the system are small compared to the wavelength of the applied signal. In our study, we used electrical signals with frequencies up to 1 MHz, which means that the operating wavelength is large enough compared to the dimension of the human body. Therefore, the electro-quasi-static approximation can be applied and Maxwell's equation can be simplified to the Laplace equation

$$-\nabla \cdot \left(\left(\epsilon + \frac{\sigma}{j\omega} \right) \nabla V \right) = 0 \quad (14.2)$$

where σ is the conductivity and V represents the scalar electric potential.

14.3 Simulation-Based Human Arm Models

Simulation Setup

Two finite element method (FEM) models were implemented using COMSOL Multiphysics 5.3a. In order to investigate intra-body communication, the complex structure of the human arm was approximated by a five-layers concentric cylinder of

radius 3.5 cm and length 60 cm. The layers are skin, fat, muscle, cortical bone, and cancellous bone of thicknesses 0.126, 0.58, 1.55, 0.6, and 0.644 cm, respectively. These values were chosen to be within the anatomical range [16–19]. For inter-body communication, on the other hand, a second contiguous similar cylinder was added, where the cylinders represent two human arms that touch each other. For simplicity, the single arm model connected to the TX was termed “Arm₁” and the second contiguous arm was called “Arm₂.” The dielectric properties of the human tissues used in our models at different frequencies were derived as described in Sect. 14.2 and applied in COMSOL using interpolation functions. The tissues were defined as homogeneous frequency dependent materials. Extra-fine mesh size was applied to the geometry. The domain around the geometry was chosen to be air that extends to infinity. The two TX and two RX electrodes are in direct contact to the human body. In our work, the electrodes were assumed to be circular and made of copper with radius 1 cm and thickness 0.2 cm. The electrical parameters of the copper material are already defined in COMSOL. An inner-distance of $l_i = 4.5$ cm was taken between TX or RX electrodes. A current controlled waveform with different amplitudes, i.e., 1 and 4 mA, was applied that meet the safety standardization according to [20]. The current amplitudes are galvanically coupled into the arm model through the TX signal electrode with a frequency sweep from 10 kHz up to 1 MHz. This frequency range was chosen to be above the frequencies of the biological signals and still fulfills the quasi-static approximation. The main parameters used in the simulation are summarized in Table 14.2.

Model for Intra-Body Communication

Model Geometry and Setup In the intra-body communication model, two studies have been conducted. In one study, a straight arm model, i.e., Arm₁, has been used.

Table 14.2 Parameters for the simulation-based model

Parameters	Value
Frequency range “ f ” [Hz]	$10^4 - 10^6$
Length of the Arm [cm]	60
Skin layer thickness [cm]	0.126
Fat layer thickness [cm]	0.58
Muscle layer thickness [cm]	1.55
Cortical bone thickness [cm]	0.6
Cancellous bone thickness [cm]	0.644
Current amplitude “ I ” [mA]	1, 4
Radius of copper electrodes [cm]	1
Thickness of copper electrodes [cm]	0.2
Distance between TX and RX “ l_{lr} ” [cm]	20, 30, 40, 50
Inner-distance between TX or RX electrodes “ l_i ” [cm]	4.5

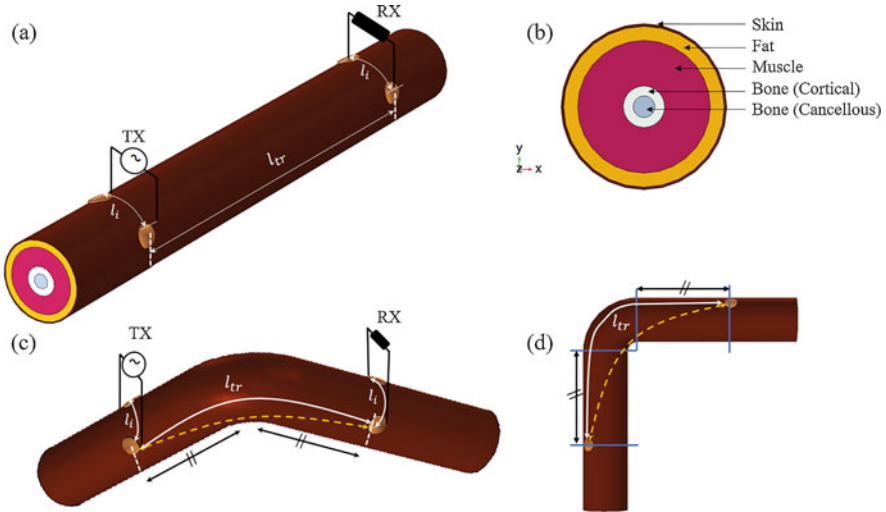


Fig. 14.2 Simulation-based model of a single human arm: (a) 3D straight model, (b) cross-sectional view, (c) 3D model with 90° bending, (d) side view of the bended model

In a second study, a 90° bending has been introduced to the model to imitate the elbow bending and investigate its effect on the received signal. Transmitting and receiving electrodes were placed symmetrically around the curvature of the bended arm as seen in Fig. 14.2.

Results and Discussion Figure 14.3a shows the electrical potential distribution for a cross sectional area of the arm model at TX at an induced current of 1 mA, and applied frequency 10 kHz. The same setup but at applied frequency of 1 MHz is shown in Fig. 14.3b. In Fig. 14.3c, we changed the induced current to 4 mA with 10 kHz applied frequency. In Fig. 14.3d, 4 mA induced current with frequency of 1 MHz was applied. Regardless of the induced current, the electric potential decreases with the increase of the applied frequency. At the lower frequency, i.e., 10 kHz, the relative permittivity of the human tissues is high and conductivity is low. Therefore, penetration of the signal into the tissue is high. As seen, the electric potential is mainly confined to the skin and fat layers, while less potential exists in the muscle and bones layers. At the higher frequency, i.e., 1 MHz, in contrast, when the relative permittivity is low and conductivity is high, signal transmission is limited to the surface of the body. However, increasing the amplitude of the induced current at a fixed applied frequency has a significant effect on the generated signal. Nevertheless, we should follow the human safety standardization for not harming the biological tissues.

In Fig. 14.4a, we studied the effect of increasing the surface distance between TX and RX, i.e., l_{tr} , when keeping constant current of 1 mA, while in Fig. 14.4b,

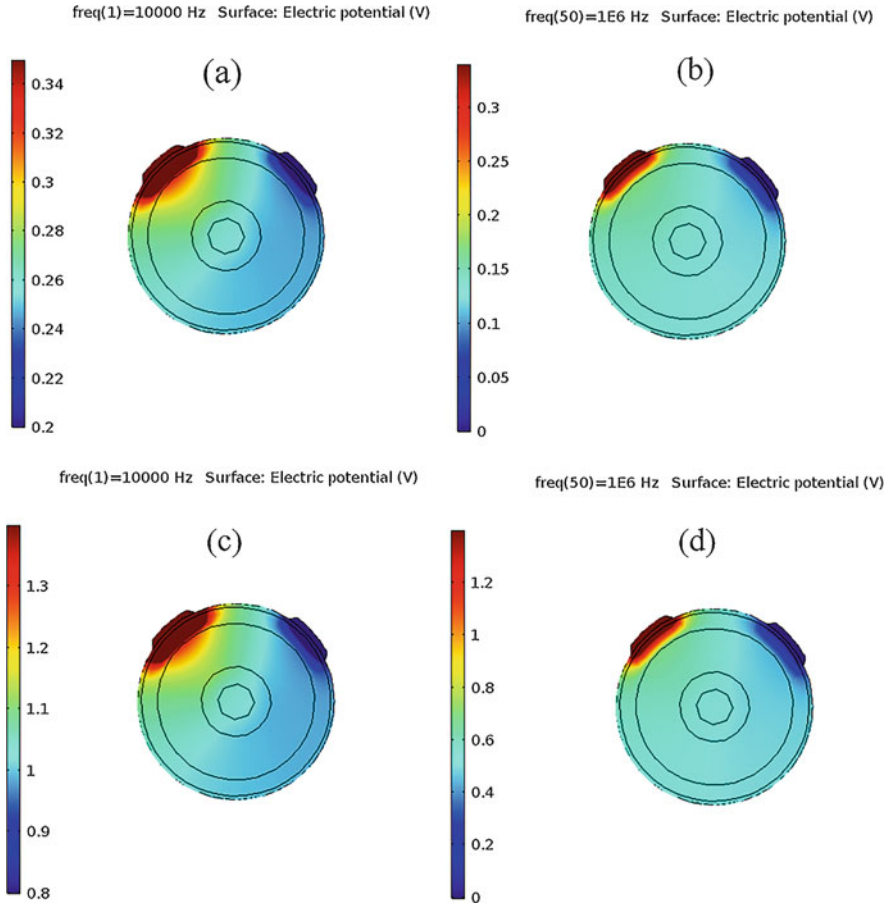


Fig. 14.3 Electric potential distribution for cross sectional area of the straight arm model at TX when: (a) $I = 1 \text{ mA}$, $f = 10 \text{ kHz}$, (b) $I = 1 \text{ mA}$, $f = 1 \text{ MHz}$, (c) $I = 4 \text{ mA}$, $f = 10 \text{ kHz}$, and (d) $I = 4 \text{ mA}$, $f = 1 \text{ MHz}$

the signal attenuation is shown. The attenuation factor between TX and RX was calculated according to [7]

$$\text{Attenuation [dB]} = 20 \cdot \log_{10} \frac{\Delta V_{\text{RX}}}{\Delta V_{\text{TX}}} \quad (14.3)$$

where ΔV_{RX} and ΔV_{TX} denote the potential difference at the receiver and transmitter electrodes, respectively. At low frequencies, the increase of I_{tr} has a weak effect on the received signal. This gives a good opportunity to use intra-body communication at low frequencies, e.g., up to 50 kHz, for sending data between distant locations on the body. However, frequencies above the biological signals frequencies should be used to avoid interference. On the other hand, a significant

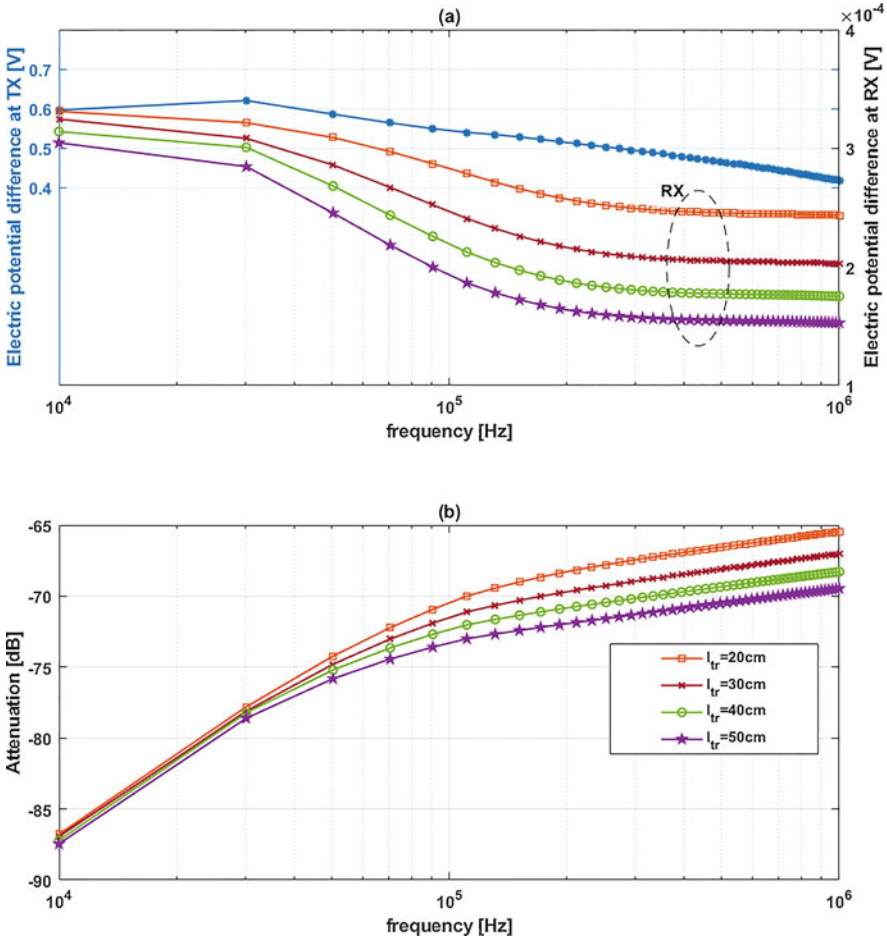


Fig. 14.4 (a) Electrical potential difference at TX and RX at $I = 1$ mA, when $l_{tr} = 20$ cm, $l_{tr} = 30$ cm, $l_{tr} = 40$ cm, and $l_{tr} = 50$ cm. (b) Signal attenuation [dB] at RX for different channel lengths

effect can be seen at higher frequencies, where the signal loss inside the tissues is high. Therefore, the attenuation increases, which agrees with the results in [7]. In another study, to investigate the effect of 90° bending of the arm model and compare it to the straight model, we calculated the electric potential difference at RX for both cases when the induced current is 1 mA for different l_{tr} . As seen in Fig. 14.5, the electric potential difference at RX of the bended model is higher than that of the straight model. The reason is the actual channel length or the shortest distance between TX and RX. In the straight model, the channel length equals the direct horizontal distance from TX to RX. In the bended model, the actual channel length, shown as dashed yellow line in Fig. 14.2, is shorter than the surface length we considered. At short distances between TX and RX, the relative discrepancy

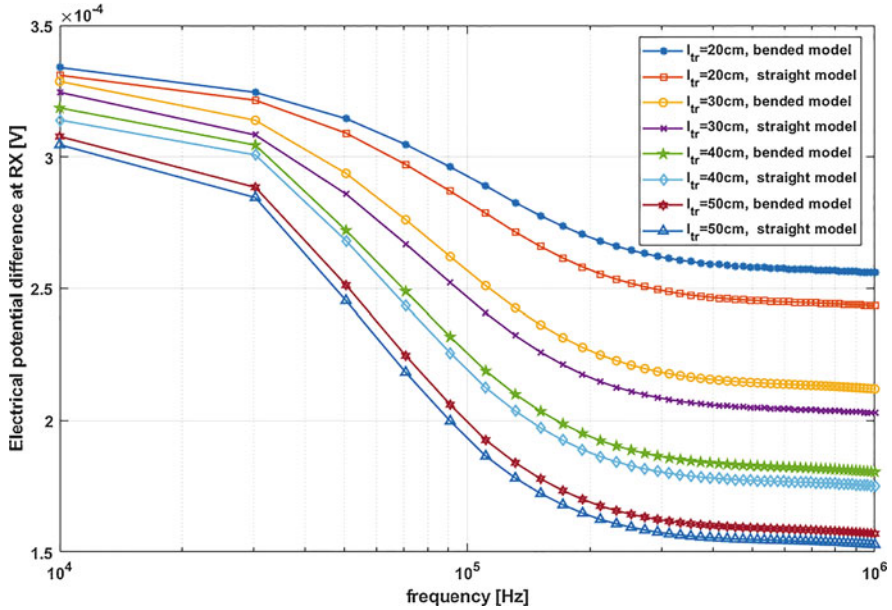


Fig. 14.5 Electrical potential difference at RX for both bended and straight models at $I = 1$ mA

between the actual channel length in the straight model and the bended model is large. On the other hand, for longer models and distant transceivers around the arm curvature, the relative discrepancy becomes small and both models tend to behave in a close manner, see Fig. 14.5 when $l_{tr} = 40$ and 50 cm.

Model for Inter-Body Communication

Model Geometry and Setup In the inter-body communication model, the second contiguous similar cylinder “Arm₂” was added, as shown in Fig. 14.6. Different common lengths $l_c = 5, 10,$ and 20 cm between Arm₁ and Arm₂ were assumed. A contact plate of width 2 cm and length l_c was added between the two arms to increase their contact area and defined in COMSOL as skin material, shown in Fig. 14.6 inside dotted blue ellipsoids.

Results and Discussion Figure 14.7 shows the electric potential difference at RX for a horizontal distance $l_{tr} = 20$ cm between TX and RX and common length $l_c = 20$ cm at two different induced current amplitudes, i.e., 1 and 4 mA. As expected, the electric potential is directly proportional to the amplitude of the induced current. Maximum value is achieved at 10 kHz, then the signal decreases rapidly with frequency.

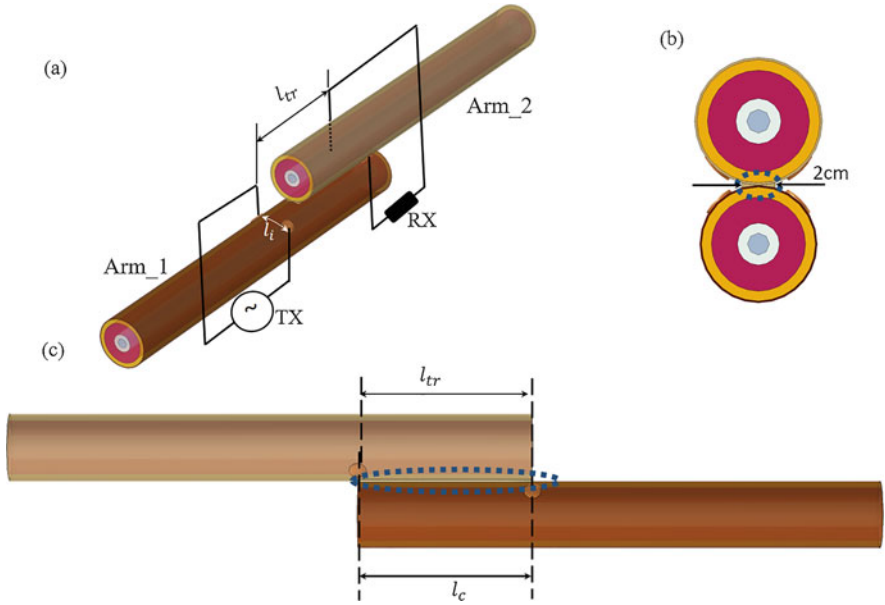


Fig. 14.6 Simulation-based model of two contiguous human arms. (a) 3D model, (b) cross sectional view, (c) side view

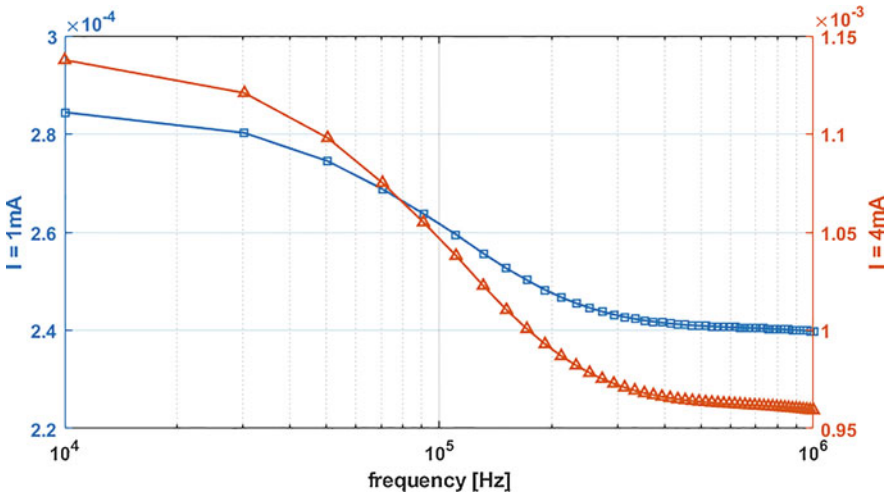


Fig. 14.7 Electric potential difference at RX for $l_c = 20\text{ cm}$ and $l_{tr} = 20\text{ cm}$ with two different induced current amplitudes

For a comparison between inter-body and intra-body communication transmission mechanisms, we have created Fig. 14.8a at three different common lengths, i.e., $l_c = 5, 10,$ and 20 cm , between Arm₁ and Arm₂ when the current amplitude is 1 mA

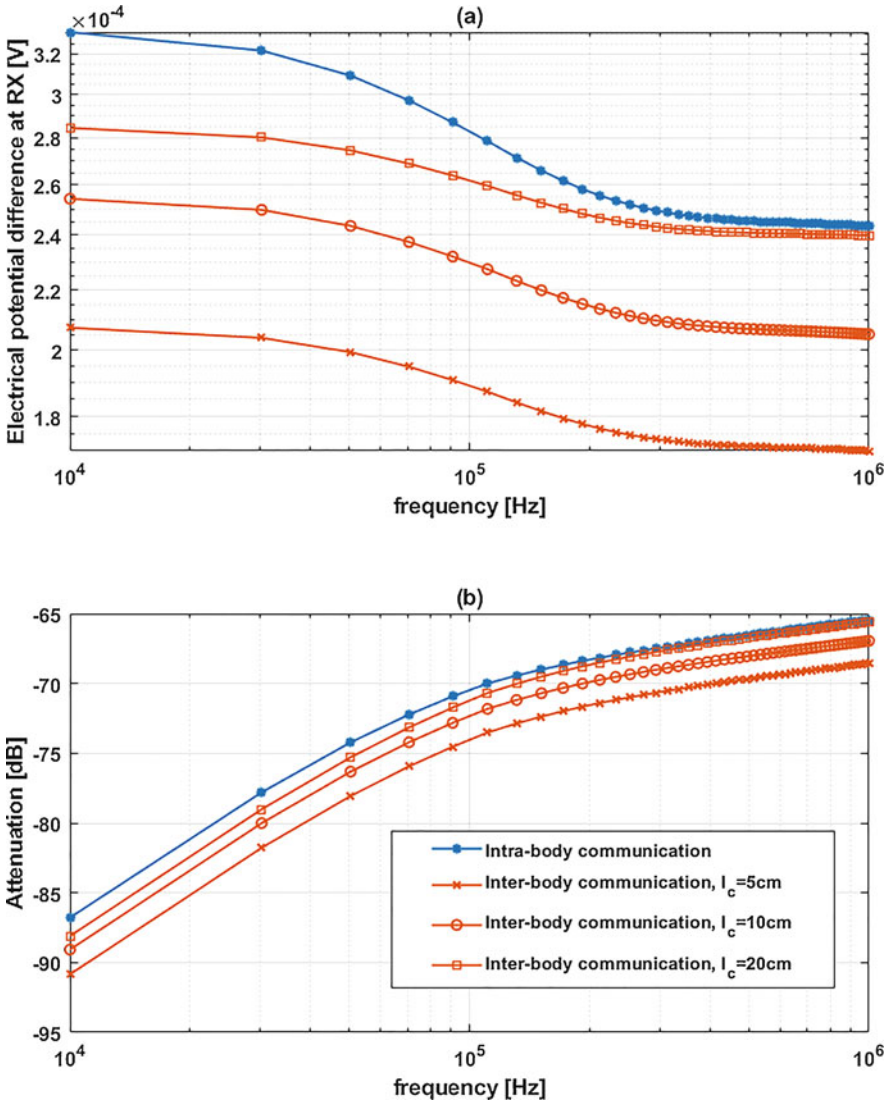


Fig. 14.8 (a) Electric potential difference at RX for both intra-body and inter-body communications with three different l_c values at an induced current of 1 mA and $t_{tr} = 20$ cm. (b) Signal attenuation [dB] at RX

and $l_{tr} = 20$ cm, while the signal attenuation from (14.3) is depicted in Fig. 14.8b. We can see the same behavior with frequency as in intra-body communication, the potential difference decreases with the frequency increment. In addition, increasing the length of contact, i.e., l_c , and hence the contact area between the two arms has a significant effect on the detected signal. By increasing the contact area

between the two arms, the detected signal increases. As seen at frequencies above 200 kHz when $l_c = l_{lr} = 20$ cm, intra-body and inter-body communication give close values. Such that the two arms together can be considered as one geometry that uses intra-body communication. For shorter l_c , high signal degradation is detected at the RX at Arm₂. Hence, one factor to improve the received signal in inter-body communication is to avoid gaps and increase the contact area between the two bodies. However, inter-body communication might be power consuming communication technique and hence adaptive HBC-enabled devices are needed.

14.4 Conclusion

Galvanic coupling is one of the approaches used for coupling in human body communication (HBC), which enables electronic devices in or on the human body to interconnect with each other and exchange information at very low power consumption. In this paper, we have studied the transmission mechanism on the human body for intra-body and inter-body communication based on galvanic coupling. Two FEM simulations representing a single human arm and two human arms in contact to each other have been proposed. Both models took into account the different types of tissue that the arm consists of. The influence of different HBC key parameters including applied frequency, distance between TX and RX (i. e., transmission length), bending, contact area between two bodies, and induced current was investigated. The results show that the transmission loss increases with the increase of the transmission length and operating frequency. The electric potential is mainly confined to the skin and fat layers at lower frequencies, as the relative permittivity of the human tissues is high and conductivity is low. At high frequencies, when the relative permittivity is low and conductivity is high, the transmitted signal is limited to the surface of the body. Furthermore, increasing the transmission length has a significant effect on the signal degradation at high frequencies, hence it is more appropriate to use low frequencies, i. e., up to 50 kHz, for transmission over long distances on the body. Bended models improve the received signal in the cases of short distance between TX and RX around the bending. For distant transceivers, both straight and bended models tend to behave in a close manner.

Concerning inter-body communication, we found that the received signal is directly proportional to the induced current and inversely proportional to the applied frequency. Due to the dielectric properties of the human tissues and the increase of the actual transmission distance between TX and RX (in order for the signal to leave one arm and enters the other), the signal degradation is considerably higher compared to intra-body communication at the same horizontal distance between TX and RX. At higher frequencies, i. e., >200 kHz, both inter-body and intra-body communication give close values when the contact area between the arms covers the distance between TX and RX electrodes. Increasing the contact area between the models helps to improve the detected signal.

In conclusion, the results demonstrate the feasibility of HBC for establishing wireless communication between distributed sensor nodes in or on the human body as well as the exchange of information between different individuals. The approach hence promises diverse ways application, e.g., in healthcare and telecommunications.

References

1. Nikita, K.S.: Numerical and experimental techniques for body area electromagnetics. In: Handbook of Biomedical Telemetry, 1st edn. Wiley, Hoboken (2014). <https://doi.org/10.1002/9781118893715.ch6>
2. Johnny, B., Anpalagan, A.: Body area sensor networks: requirements, operations, and challenges. *IEEE Potentials* **33**, 21–25 (2014). <https://doi.org/10.1109/MPOT.2013.2286692>
3. Ruiz, J.A., Shimamoto, S.: A study on the transmission characteristics of the human body towards broadband intra-body communications. In: Proceedings of the Ninth International Symposium on Consumer Electronics, pp. 99–104 (2005). <https://doi.org/10.1109/ISCE.2005.1502350>
4. Lindsey, D.P., McKee, E.L., Hull, M.L., Howell, S.M.: A new technique for transmission of signals from implantable transducers. *IEEE Trans. Biomed. Eng.* **45**, 614–619 (1998). <https://doi.org/10.1109/10.668752>
5. Gao, Y., Ma, R., Pun, S., Mak, P., Vai, M.: Measurement system with experiments for galvanic coupling type intra-body communication. In: 5th International Conference on Biomedical Engineering and Informatics, pp. 761–764 (2012). <https://doi.org/10.1109/BMEI.2012.6513147>
6. Wang, J., Fujiwara, T., Kato, T., Anzai, D.: Wearable ECG based on impulse radio type human body communication. *IEEE Trans. Biomed. Eng.* **63**, 1887–1894 (2016). <https://doi.org/10.1109/TBME.2015.2504998>
7. Wegmueller, M.S., Kuhn, A., Froehlich, J., Oberle, M., Felber, N., Kuster, N., Fichtner, W.: An attempt to model the human body as a communication channel. *IEEE Trans. Biomed. Eng.* **54**(10), 1851–1857 (2007). <https://doi.org/10.1109/TBME.2007.893498>
8. Song, Y., Hao, Q., Zhang, K.: Review of the modeling, simulation and implement of intra-body communication. *Def. Technol.* **9**, 10–17 (2013). <https://doi.org/10.1016/j.dt.2013.10.001>
9. Wegmueller, M.S., Oberle, M., Felber, N., Kuster, N., Fichtner, W.: Signal Transmission by galvanic coupling through the human body. *IEEE Trans. Instrum. Meas.* **59**(4), 963–969 (2010). <https://doi.org/10.1109/TIM.2009.2031449>
10. Callejón, M.A., et al.: Galvanic coupling transmission in intrabody communication: a finite element approach. *IEEE Trans. Biomed. Eng.* **61**, 775–782 (2014). <https://doi.org/10.1109/TBME.2013.2289946>
11. Ahmed, D., Kirchner, J., Fischer, G.: Wave propagation with human body communications in BANs. In: IEEE MTT-S International Conference on Numerical Electromagnetic and Multiphysics Modeling and Optimization for RF, Microwave, and Terahertz Applications, pp. 16–18 (2017). <https://doi.org/10.1109/NEMO.2017.7964172>
12. Ahmed, D., Kirchner, J., Fischer, G.: Wave propagation with HBC in a human arm model. In: IEEE International Symposium on Medical Measurements and Applications (MeMeA) (2017). <https://doi.org/10.1109/MeMeA.2017.7985918>
13. Gabriel, S., Lau, R.W., Gabriel, C.: The dielectric properties of biological tissues: II. Measurements in the frequency range 10 Hz to 20 GHz. *Phys. Med. Biol.* **41**, 2251–2269 (1996). <https://doi.org/10.1088/0031-9155/41/11/002>

14. Hall, P.S., Hao, Y.: Electromagnetic properties and modeling of the human body. In: *Antennas and Propagation for Body-Centric Wireless Communications*, 2nd edn., chap. 2. Artech House, London (2012)
15. larsson, J.: Electromagnetics from a quasistatic perspective. *Am. J. Phys.* **75**(3), 230–239 (2007). <https://doi.org/10.1119/1.2397095>
16. Wilkinson, P.F., Millington, R.: *Skin* (Digitally printed version edn.). Cambridge University Press, Cambridge (2009)
17. Hwang, I.D., Shin, K.: Fat thickness measurement using optical technique with miniaturized chip LEDs: a preliminary human study. In: *Proceedings of the 29th Annual International Conference of the IEEE EMBS*, pp. 4548–4551 (2007). <https://doi.org/10.1109/IEMBS.2007.4353351>
18. Dupont, A., et al.: Real-time sonography to estimate muscle thickness: comparison with MRI and CT. *J. Clin. Ultrasound* **29**, 230–236 (2000). <https://doi.org/10.1002/jcu.1025>
19. Horsman, A., Leach, A.E.: The estimation of the cross-sectional area of the ulna and radius. *Am. J. Phys. Anthropol.* **40**, 173–186 (1974). <https://doi.org/10.1002/ajpa.1330400204>
20. International Commission on Non-Ionizing Radiation Protection: Guidelines for limiting exposure to time-varying electric, magnetic, and electromagnetic fields (up to 300 GHz). *Health Phys.* **74**(4), 494–522 (1998)

Chapter 15

Indoor Energy Harvesting for WE-Safe Wearable IoT Sensor Nodes



Fan Wu, Jean-Michel Redouté, and Mehmet Rasit Yuce

15.1 Introduction

With the emergence of Internet of Things (IoT), many wearable devices are required and deployed in both personal and commercial applications. However, the power supply still remains a challenge for them because many devices are still battery-powered and required regularly battery replacement or recharging which is inconvenient [1].

Wearable sensor nodes are traditionally attached to human body forming wireless body area networks (WBAN) to monitor the physiological signals of the human body [2–4]. In addition to physiological signals, wearable sensors are also used to monitor the environmental data around the subject's body, for example, in environmental applications [5, 6] or safety applications [7].

A wearable wireless sensor network system for urban environmental monitoring application is proposed in [5]. The wearable sensor node consists of 7 different environmental sensors with a rechargeable battery that can last for 7 days. A wearable sensor network system for safety monitoring application is proposed in work [7]. The system can detect some hazardous environmental conditions for exposed workers, such as temperature, relative humidity, and carbon dioxide (CO₂). A 800 mAh rechargeable lithium battery supplies the power for the wearable sensor node. A wearable sensor network for environmental monitoring is reported in work [6]. A rechargeable lithium battery also supplies the power to the sensor node. However, all of these sensor nodes require regular battery recharging, which is inconvenient.

F. Wu · J.-M. Redouté · M. R. Yuce (✉)

Electrical and Computer Systems Engineering, Monash University, Clayton, VIC, Australia
e-mail: Jean-Michel.Redoute@monash.edu; mehmet.yuce@monash.edu

It is necessary to design a powerful and reliable energy harvesting system that can improve the above drawbacks. Thermoelectric energy, solar energy, electromagnetic, and piezoelectric can be possible energy sources for energy harvesting system [8, 9]. Among all those sources, solar cell has the highest power density (15 mW/cm^3) outdoors. However, it provides only $100 \mu\text{W/cm}^3$ indoors. Thermoelectric provides $40 \mu\text{W/cm}^3$ at 5°C gradient. Vibrations such as piezoelectric can provide up to $330 \mu\text{W/cm}^3$ power density.

Some works already utilize these energy sources, for example, solar energy, thermoelectric, and piezoelectric are utilized in works [2, 10] and [11], respectively. The work [2] presents a solar-powered WBAN system to measure body temperature, heartbeat, and detect falls. Providing that the subject is staying outdoors for 30–60 min under sunlight per day, the sensor node is able to operate 24 h autonomously. Reference [11] presents a hybrid wearable energy harvester using piezoelectric and electromagnetic. The work [10] presents a wearable thermoelectric generators that can harvest body heat and can output sufficient power for an accelerometer, ozone sensor, and electrocardiogram (EKG) sensor.

In this paper, an indoor energy harvesting module for a wearable IoT sensor network is presented. This is a part of WE-Safe project conducted at Monash University targeting IoT sensors for safety related applications. The energy harvesting module is able to harvest light energy from ambient light at low illumination and its maximum power point, and store the energy into a 12.5 F super-capacitor. The module can provide sufficient power for sensing and data transmission via a LoRa IoT network as shown in Fig. 15.1 [12] and enable autonomous wearable sensing. In addition, the wearable node can automatically change the sleep time based on the present light intensity and voltage level. The remainder of this paper is organized as follows: Sect. 15.2 outlines the system implementation; Sect. 15.3 discusses the experimental results, and a brief conclusion is given in Sect. 15.4.

Fig. 15.1 WE-Safe project system architecture

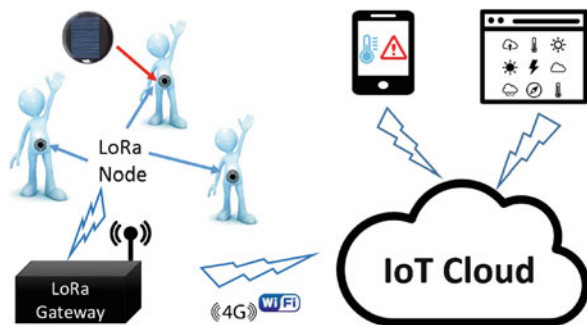




Fig. 15.2 Energy harvesting module

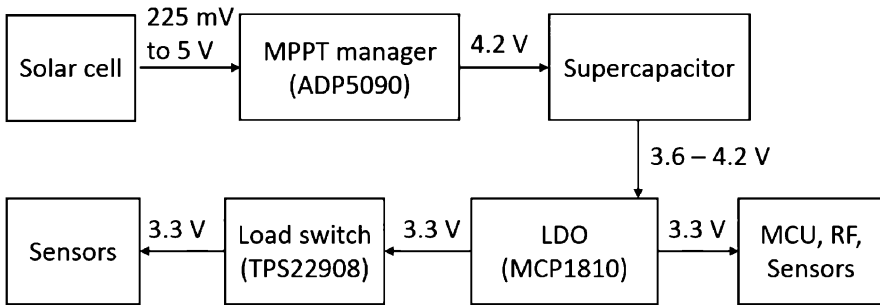


Fig. 15.3 The block diagram of the WE-Safe node

15.2 Energy Harvesting for WE-Safe

Energy Harvesting Module Hardware Implementation

The energy harvesting module consists of a solar panel ($55.0 \times 67.5 \times 3.2$ mm from Shenzhen Chuanningsheng Electronics), an ultra-low power maximum power point tracking (MPPT) boost regulator, and a super-capacitor. The printed circuit board (PCB) of the energy harvesting module is shown in Fig. 15.2. The block diagram for the sensor node is shown in Fig. 15.3.

ADP5090 from analog devices can convert DC power from solar cells to a constant voltage [13]. The device has an MPPT function that can harvest power at the solar cell's maximum power point. The MPPT controller first senses the solar panel's open circuit voltage (OCV) every 19 s and then operates at a programmable MPPT ratio for approximately 19 s. The IC consumes minimum 260 nA quiescent current and can start to operate from 80 mV input voltage. All of these features make it a suitable boost regulator for wearable design.

The super-capacitor is selected as the energy storage unit because it does not involve chemical reactions while charging or discharging, has high charge–discharge efficiency and almost unlimited life-cycles, and does not degrade over time. It has higher power density but lower energy density compared to batteries. Because super-capacitors are normally restricted to low voltages for a higher capacity, two 25 F super-capacitors (2.7 V each) are connected in series to provide 12.5 F (5.4 V) and act as the energy storage unit.

WE-Safe IoT Sensor Node

The sensor node utilized in this work consists of a microcontroller (MCU) (ATmega-328p from Atmel), a LoRa module (RFM95 from HOPE Microelectronics), an ultra-low quiescent current voltage regulator (MCP1810 from Microchip), a low power load switch with quick output discharge function (QOD) and low on resistance (TPS22908 from Texas Instruments), and two sensors (BME680 from Bosch and ADXL345 from Analog Devices). It can be configured to achieve minimal power operation.

Power Requirements The sensor node has four different modes in each duty cycle: (1) sense mode, (2) transmit mode, (3) idle mode, and (4) sleep mode.

In sense mode, the sensor node is active and measures environmental parameters. It consumes 4.2 mA while lasting 0.2 s. After gathering the environmental data, the sensor node will enter transmit mode and transmit the data to the gateway. It consumes 48 mA and lasts 0.05 s. The sensor node will enter idle mode when the data is transmitted. In idle mode, all the sensors enter sleep mode. The MCU is still active to measure the remaining voltage level and adjust the sleep time for the next duty cycle. In idle mode, the sensor node consumes 14 mA for 0.05 s. Here, the average current consumption can be calculated using $(4.2 \text{ mA} * 0.2 \text{ s} + 48 \text{ mA} * 0.05 \text{ s} + 14 \text{ mA} * 0.05 \text{ s}) / 0.3 \text{ s} = 3.94 / 0.3 \approx 13.13 \text{ mA}$.

The sensor node is programmed to sleep most of the time in order to reduce the power consumption. The MCU itself consumes 4.4 μA current, the LoRa module consumes 0.2 μA , the voltage regulator consumes 20 nA, and the load switch consumes 1 μA . In total, approximately 5.6 μA is consumed in the sleep mode.

Duty-Cycle Adjustment A current waveform of the sensor node is shown in Fig. 15.5. The power consumption based on different sleep time is presented in Eq. (15.1). In the equation, the sleep time can be adjusted by the MCU based on the voltage level and light intensity. The power consumption vs sleep time using Eq. (15.1) is shown in Fig. 15.4. Equation (15.2) presents the sleep time required in order to achieve energy neutral and is derived from Eq. (15.1).

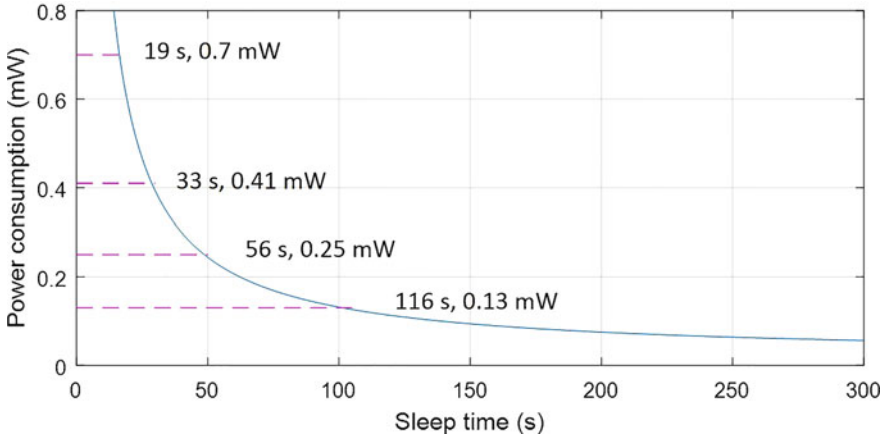
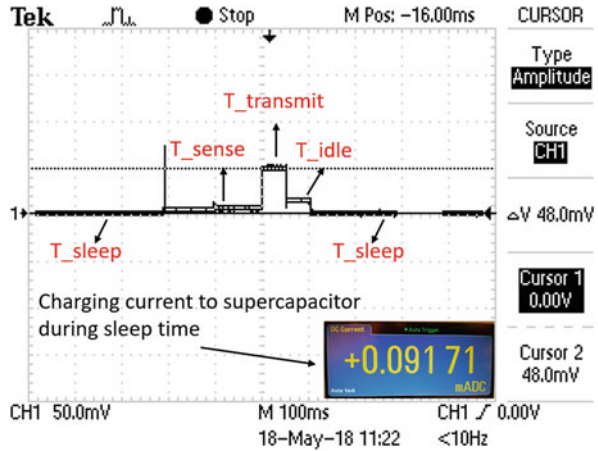


Fig. 15.4 Power consumption of the WE-Safe IoT sensor node vs sleep time (s)

Fig. 15.5 WE-Safe wearable IoT sensor node’s current waveform with energy harvesting module



$$P = V * I = 3.3 \text{ V} * (3.94 + 0.0056 * T) / (T + 0.3) \text{ mA} \text{ (mW)} \tag{15.1}$$

$$T = (13 - 0.3 * P) / (P - 0.0185) \tag{15.2}$$

The MCU measures the solar cell’s voltage every duty cycle using an analog-to-digital converter (ADC). When the voltage is measured at 1.2 V, according to Fig. 15.6, it indicates that the solar panel is working under 600 lux light intensity with 0.7 mW power. By substituting 0.7 mW into Eq. (15.2), the sleep time can be calculated as 19 s. Therefore, the MCU will change the sleep time for the coming duty cycle to be greater than 19 s so that the harvested energy is greater than the power consumed.

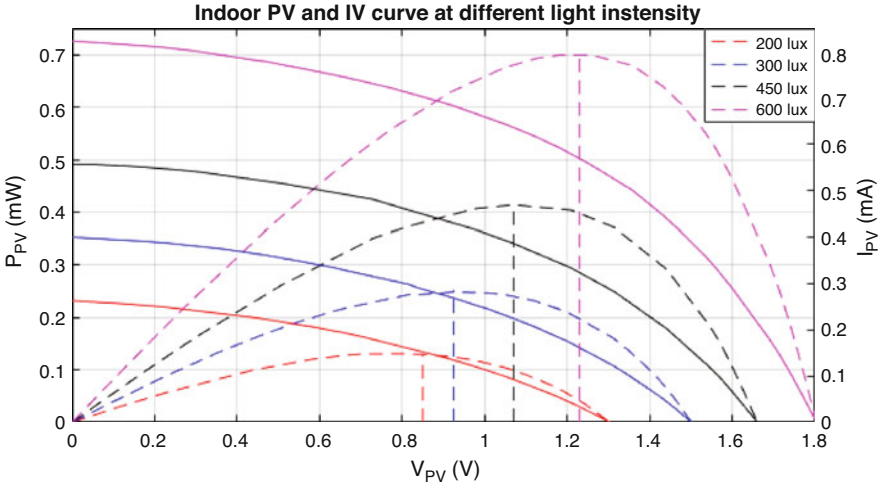


Fig. 15.6 Solar panel’s characteristic on indoor ambient light conditions (IV: solid lines; PV: dashed lines)

15.3 Experimental Results

Solar Panels’ Characteristic

The solar panel’s PV curve and IV curve under different light intensity are presented in Fig. 15.6. As you can see from the figure, the solar cell’s maximum power is 0.13 mW at 0.85 V with OCV equal to 1.3 V under 200 lux. The MPPT ratio under 200 lux can be calculated as $0.85 \text{ V} / 1.3 \text{ V} \approx 66\%$. Similarly, the MPPT ratio under 600 lux is equal to $1.24 \text{ V} / 1.8 \text{ V} \approx 70\%$. The outdoor illuminance can be up to 120,000 lux under direct sunlight. Therefore, 200–600 lux can be considered as low light intensity compared to the outdoor condition.

Current Waveforms

The current waveform of the sensor node is shown in Fig. 15.5. As can be seen in the figure, the charging current to the super-capacitor in sleep mode is 91.71 μA when the light intensity is 400 lux. The sleep current of the sensor node is 5.6 μA . This means the energy harvesting unit is able to charge the super-capacitor.

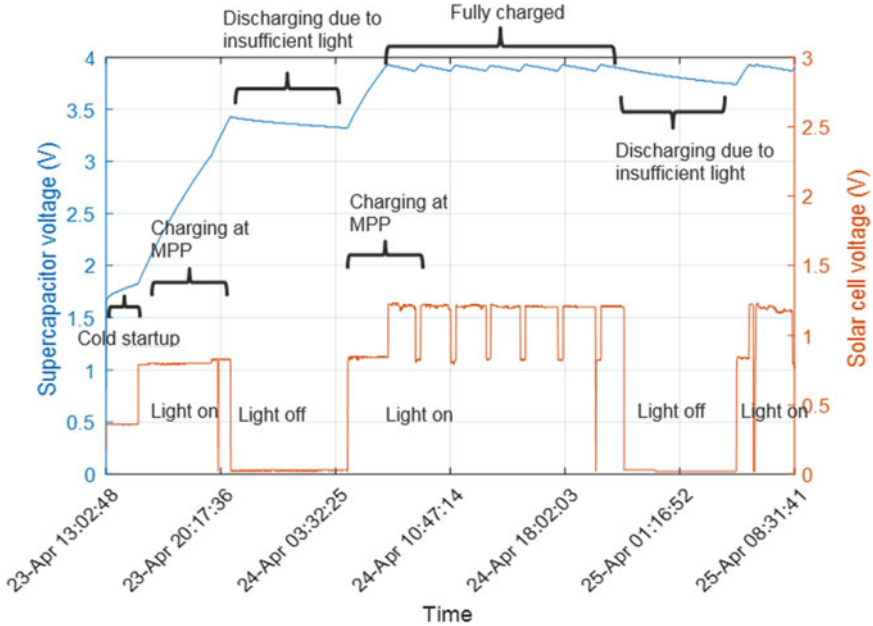


Fig. 15.7 Energy harvesting module charging a 0.33 F super-capacitor

Energy Harvester Module Test

The charging characteristics when the energy harvesting is charging a 0.33 F super-capacitor are shown in Fig. 15.7. As can be seen in the figure, the blue line indicates the continuous monitoring of the super-capacitor voltage. The red line indicates the continuous monitoring of the solar cells voltage. The initial voltage for the super-capacitor is approximately 1.6 V. The light is turned on at first. The charging rate is very low (0.0631 V/h) because the super-capacitor voltage is under 1.93 V that is the cold-startup voltage threshold. The solar panel is working at cold-start mode at approximately 0.5 V. After the super-capacitor's voltage increased to 1.93 V, the solar panels' voltage increases and it starts to work at its MPPT point which is around 0.8 V. During this period, the charging rate is relatively fast at 0.2382 V/h. When the light is off, the super-capacitor's voltage decreases slightly due to insufficient light. After the super-capacitor is fully charged, there are some small dips and small increases showing on the graph from the blue line. At the same time, the red line is oscillating between its open circuit voltage and maximum power point. This is due to the self-leakage current of the super-capacitor. Once the super-capacitor's voltage decreases to a certain level, the energy harvesting module starts to work again at its maximum power point.

15.4 Conclusion

This paper presents an indoor energy harvesting unit for the WE-Safe project to establish a wearable IoT sensor platform for indoor applications. The energy harvesting unit is able to harvest light energy from low light intensity and convert the solar energy into an energy storage unit. The module can then provide adequate power for sensing and data transmission via a LoRa network. In addition, the wearable node can automatically modify the sleep time based on the current energy level and light intensity in order to reach an energy neutral state.

Acknowledgements The work is supported, in part, by Monash University's Faculty of Engineering Seed Funding, and by Australian Research Council Future Fellowships Grant FT130100430.

References

1. Wu, F., Rüdiger, C., Yuce, M.R.: Real-time performance of a self-powered environmental IoT sensor network system. *Sensors* **17**(2), 282 (2017). <https://doi.org/10.3390/s17020282>
2. Wu, T., Wu, F., Redouté, J.M., Yuce, M.R.: An autonomous wireless body area network implementation towards IoT connected healthcare applications. *IEEE Access* **5**, 11413–11422 (2017). <https://doi.org/10.1109/ACCESS.2017.2716344>
3. Yuce, M.R., Khan, J.Y.: *Wireless body area networks: technology, implementation and applications* (2011). <https://doi.org/10.4032/9789814241571>, <http://www.scopus.com/inward/record.url?eid=2-s2.0-84881815399&partnerID=tZOtx3y1>
4. Latré, B., Braem, B., Moerman, I., Blondia, C., Demeester, P.: A survey on wireless body area networks. *Wirel. Netw.* **17**(1), 1–18 (2011). <https://doi.org/10.1007/s11276-010-0252-4>
5. Wilhelm, E., Siby, S., Zhou, Y., Ashok, X.J.S., Jayasuriya, M., Foong, S., Kee, J., Wood, K.L., Tippenhauer, N.O.: Wearable environmental sensors and infrastructure for mobile large-scale urban deployment. *IEEE Sensors J.* **16**(22), 8111–8123 (2016). <https://doi.org/10.1109/JSEN.2016.2603158>
6. Serbanescu, M., Placinta, V.M., Hutanu, O.E., Ravariu, C.: Smart, low power, wearable multi-sensor data acquisition system for environmental monitoring. In: 2017 10th International Symposium on Advanced Topics in Electrical Engineering (ATEE 2017), pp. 118–123 (2017). <https://doi.org/10.1109/ATEE.2017.7905059>
7. Antolín, D., Medrano, N., Calvo, B., Pérez, F.: A wearable wireless sensor network for indoor smart environment monitoring in safety applications. *Sensors* **17**(2), 365 (2017). <https://doi.org/10.3390/s17020365>, <http://www.mdpi.com/1424-8220/17/2/365>
8. Compber, E.M., Gupta, M.C., Wilson, W.C., Madaras, E.I.: Solar powered micrometeorite sensors using indoor ambient light for the International Space Station. *Solar Energy* **85**(9), 1899–1905 (2011). <https://doi.org/10.1016/j.solener.2011.04.029>, <http://linkinghub.elsevier.com/retrieve/pii/S0038092X11001496>
9. Zhou, G., Huang, L., Li, W., Zhu, Z.: Harvesting ambient environmental energy for wireless sensor networks: a survey. *J. Sens.* **2014**, 815467 (2014). <https://doi.org/10.1155/2014/815467>
10. Hyland, M., Hunter, H., Liu, J., Veety, E., Vashaee, D.: Wearable thermoelectric generators for human body heat harvesting. *Appl. Energy* **182**, 518–524 (2016). <https://doi.org/10.1016/j.apenergy.2016.08.150>

11. Hamid, R., Yuce, M.R.: A wearable energy harvester unit using piezoelectric electromagnetic hybrid technique. *Sens. Actuators A* **257**, 198–207 (2017). <https://doi.org/10.1016/j.sna.2017.02.026>
12. Wu, F., Redout, J., Yuce, M.R.: We-safe: a self-powered wearable IoT sensor network for safety applications based on LoRa. *IEEE Access* **6**, 40846–40853 (2018). <https://doi.org/10.1109/ACCESS.2018.2859383>
13. Analog Devices: Ultralow power boost regulator with MPPT and charge management [Datasheet] (2015). <http://www.analog.com/media/en/technical-documentation/data-sheets/ADP5090.pdf>

Chapter 16

Learning and Recognition with Neural Network of Heart Beats Sensed by WBAN for Patient Stress Estimate for Rehabilitation



Yukihiro Kinjo, Yoshitomo Sakuma, and Ryuji Kohno

16.1 Introduction

In rehabilitation, not only the categorical approach based on patient's disability but also the individual approach that takes patient's personality into account is important in order to apply high quality rehabilitation to patients and aim for early recovery[1]. However, unlike the categorical approach, the individual approach does not have clear criteria to determine it, and in many cases it is based on experiences of experienced physiotherapists. In recent years, with the declining birth rate and ageing population, the proportion of elderly people has increased; the number of physiotherapists is insufficient for the number of patients, and it is becoming difficult for inexperienced physiotherapists to devise individual approaches for each patient[2].

Therefore, it is necessary to set criteria of individual approaches, so that all physiotherapists perform appropriate individual approaches and can apply equal quality rehabilitation to all patients. In order to determine this criteria, we estimate stress of the patient by applying machine learning analysis by neural network(NN) to R-R interval (RRI) of the patient's heart beat obtained by Wireless Body Area Network (WBAN)[3, 4].

However, machine learning processing needs big data and a large amount of computational complexity and sending heart rate data via cloud network to AI server computer like Watson for machine learning processing which costs much and causes network delay. So we propose how to reduce computational complexity to enable to calculate by limited processing power in embedded processor of BAN coordinator.

Y. Kinjo (✉) · Y. Sakuma · R. Kohno

Graduate School of Engineering Science, Yokohama National University, Yokohama, Kanagawa, Japan

e-mail: kinjo-yukihiro-vm@ynu.jp; sakuma-yoshitomo-cm@ynu.jp; kohno-ryuji-ns@ynu.ac.jp

© Springer Nature Switzerland AG 2020

C. Sugimoto et al. (eds.), *13th EAI International Conference on Body Area Networks*, EAI/Springer Innovations in Communication and Computing, https://doi.org/10.1007/978-3-030-29897-5_16

195

Specifically, we aim to reduce it to use NN with preprocessing by wavelet transform and extraction of coefficient of variance of RRI, i.e. CVRR. We evaluated the learning speed, the discrimination rate of the presence or absence of stress, and the computational complexity of proposal system by computer simulation and indicated that the learning efficiency of the NN was increased by preprocessing.

16.2 Proposal System

System Model

In this research, we estimate two classes whether or not the patient feels stress. Figure 16.1 shows the system model of stress estimate by NN with preprocessing. This system is composed of two preprocessing based on medical knowledge, Pre-Learning and Main Learning. Details of each process are described in the following section.

Preprocessing

It is known that RRI in heartbeat correlates with stress, and it is known that when the patient feels stress, the value of RRI and the magnitude of the variation are smaller than usual. Therefore, CVRR which is the variation coefficient of RRI is derived from the formula[5] as Preprocessing 1. If this value is small, it can be estimated that the patient feels stress.

$$CVRR = \frac{SDRR * 100}{mRR} \tag{16.1}$$

mRR and SDRR denote mean RRI and standard deviation of RRI respectively.

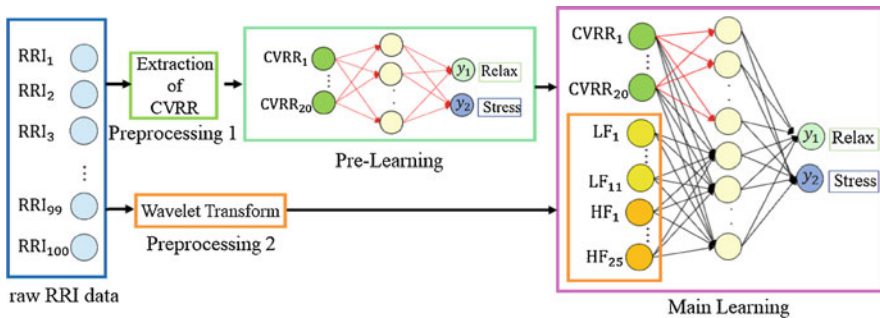


Fig. 16.1 System model of stress estimate

In Preprocessing 2, we extract frequency components that can be divided into High Frequency(HF) from 0.15 to 0.40 Hz and Low Frequency(LF) from 0.04 to 0.15 Hz. The effects of parasympathetic and sympathetic nerves are reflected in HF and LF, respectively. Furthermore, it is known that respiration is related to HF and blood pressure fluctuation is correlated with LF. In this research, we extract frequency component by performing wavelet transform using Morlet wavelet[6].

Pre-Learning

Pre-Learning is performed with three-layer NN that inputs CVRR to the input layer and performs two class estimation of “relax” or “stress” in the output layer. After learning of this NN, stress features of CVRR can be extracted in the hidden layer and we use the obtained weight and bias parameters in the Main Learning.

Main Learning

In Main Learning, we use three-layer NN that inputs CVRR and frequency components of RRI and performs two class estimation in the output layer. Stress features from only CVRR are extracted in the first group, and stress features from both of CVRR and frequency components are extracted in the other group. Features from only CVRR are extracted in Pre-Learning, so weight of nodes between neurons to which CVRR is input and neurons with features from only CVRR (red nodes of Main Learning NN in Fig. 16.1) are not updated. In Main Learning, NN learns to extract features from both of CVRR between input layers and hidden layer and frequency components and estimate stress from these features between hidden layer and output layer.

16.3 Performance Evaluation

In this research, we performed following two computer simulations and evaluated performance of accuracy, learning speed, and computational complexity of proposal system. The computational complexity was evaluated by the number of multiplications.

- Comparison of performance of NN of stress estimate by type of preprocessing
- Comparison of performance of NN with or without Pre-Learning on CVRR

Table 16.1 Simulation parameters

Number of input neurons	56
Number of hidden neurons	30
Number of output neurons	2
Batch size	20
Number of epoch	1200
η : learning rate	0.01
RRI signal size	100
Number of training data	200
Number of test data	10,000
Activation function (hidden layer)	ReLU
Activation function (output layer)	Softmax
Loss function	Crossentropy
Optimizer	SGD

Simulation Model and Parameters

Table 16.1 shows parameters of NN of Main Learning used in simulation. Artificial data of RRI generated using normal distribution was used to guarantee reproducibility.

In first simulation, we compared performance of NN by type of preprocessing. The types of preprocessing compared are without preprocessing (input RRI data), with only Preprocessing 1, with only Preprocessing 2, and both of Preprocessing 1 and 2 (Proposal). Pre-Learning is not performed in this simulation.

In second simulation, we compared performance of NN with or without Pre-Learning on CVRR. In the case without Pre-Learning, the NN same to first simulation with preprocessing both of extraction of CVRR and frequency components is used. In the case with Pre-Learning, the NN of Pre-Learning has 20 input neurons for CVRR, 10 hidden neurons, and other parameters same to the NN of Main Learning without Pre-Learning. The NN of Main Learning with Pre-Learning has same parameters without Pre-Learning. Preprocessing same to the case without Pre-Learning is performed. However, ten of the hidden layer neurons are connected only with neurons of the input layer to which CVRR is input. Also, the bias of these neurons and weights between these hidden neurons and input neurons are not updated.

Results

Figure 16.2 shows learning curves for comparison of learning speed. Table 16.2 shows accuracy by type of preprocessing in first simulation. From these results, preprocessing of extraction of CVRR and frequency components improve learning efficiency. However, in the case with preprocessing of only extraction of frequency

Fig. 16.2 Comparison of learning speed by type of preprocessing

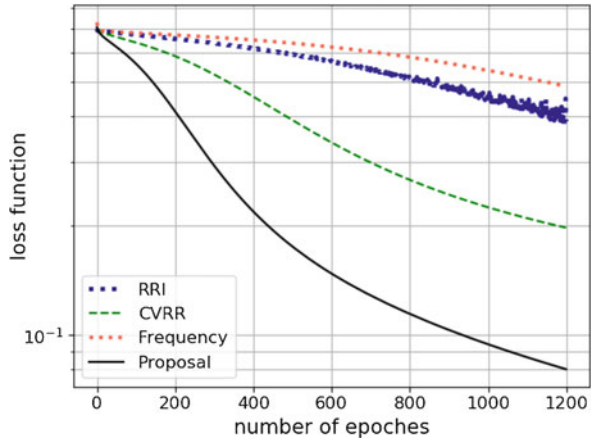


Table 16.2 Comparison of accuracy by type of preprocessing

	RRI	CVRR	Frequency	Proposal
Accuracy [%]	81.131	89.664	68.5805	93.41

Table 16.3 Comparison of number of multiplication by type of preprocessing

Number of multiplication	RRI	CVRR	Frequency	Proposal
Preprocessing	0	36,000	180,007,200	180,043,200
Learning	2,595,360,000	232,320,000	197,280,000	892,320,000
Total	2,595,360,000	232,356,000	377,287,200	1,072,363,200

components, the performance is worse than in the case without preprocessing. This indicates that both of CVRR and frequency components can be used as a feature of stress but CVRR is more important feature than frequency component. Table 16.3 shows number of multiplication for comparison of computational complexity. From this table, preprocessing, especially wavelet transform requires a lot of calculation. However, calculation complexity of learning reduces because the dimension of the data input to the NN becomes smaller and the number of parameters to be updated decreases by preprocessing. Therefore, the calculation complexity of this system with preprocessing is less complex than that of this system without processing.

Figure 16.3, Tables 16.4, and 16.5 shows learning curve, accuracy, amount of multiplication in second simulation, respectively. From Fig. 16.3, it turns out that the initial value of cross entropy is reduced and learning speed improved by Pre-Learning from Table 16.5. Although the amount of calculation by preliminary learning is required, since the parameters to be updated in the Main Learning are reduced, the amount of calculation in this learning has been reduced. However, Table 16.4 shows accuracy with Pre-Learning is lower than the other. It is considered that overfitting on learning data declined accuracy.

From these two simulations, the effectiveness of preprocessing and Pre-Learning was shown for calculation complexity.

Fig. 16.3 Comparison of learning speed with or without Pre-Learning

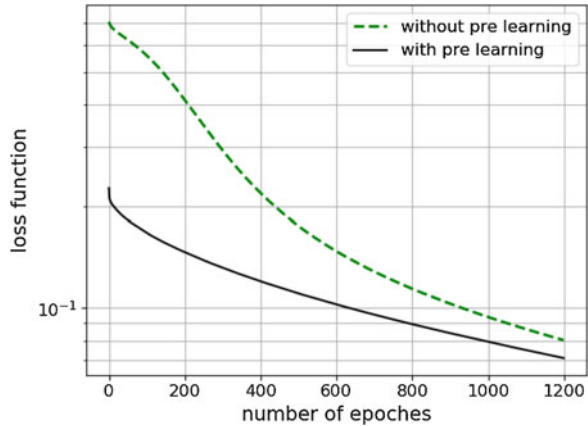


Table 16.4 Comparison of accuracy with or without Pre-Learning

	Without Pre-Learning	With Pre-Learning
Accuracy [%]	93.41	90.77

Table 16.5 Comparison of number of multiplication with or without Pre-Learning

Number of multiplication	Without Pre-Learning	With Pre-Learning
Pre-learning	–	232,320,000
Main learning	892,320,000	538,080,000
Total	892,320,000	770,400,000

16.4 Conclusion

In this research, we proposed the method reduced calculation complexity of stress estimate and enable to calculate by embedded processor of WBAN coordinator. We confirmed preprocessing based on medical knowledge and Pre-Learning can improve performance of NN of stress estimate at the point of calculation complexity and learning speed. However, the accuracy with Pre-Learning declined compared to the accuracy without Pre-Learning. So we will try to improve accuracy while maintaining low calculation complexity. Moreover, we will consider multi-class stress classification model in the future.

References

1. Maclean, N., Pound, P.: A critical review of the concept of patient motivation in the literature on physical rehabilitation. *Soc. Sci. Med.* **50**, 495–506 (2000)
2. Lunenfeld, B.: An aging world-demographics and challenges. *Gynecol. Endocrinol.* **24**, 1–3 (2008)

3. Ali, M., et al.: Emotion recognition involving physiological and speech signals: a comprehensive review. In: *Recent Advances in Nonlinear Dynamics and Synchronization*. Springer, Cham, pp. 287–302 (2018)
4. Barakah, D.M., Ammad-uddin, M.: A survey of challenges and applications of wireless body area network (WBAN) and role of a virtual doctor server in existing architecture. In: *2012 Third International Conference on Intelligent Systems, Modelling and Simulation (ISMS)*, IEEE, Piscataway (2012)
5. Cernat, R.A., et al.: Stress influence on drivers identified by monitoring galvanic skin resistance and heart rate variability. In: *E-Health and Bioengineering Conference (EHB)*, IEEE, Piscataway (2017)
6. Ivanov, P.C., et al.: Scaling behaviour of heartbeat intervals obtained by wavelet-based time-series analysis. *Nature* **383**, 323–327 (1996)

Chapter 17

A Machine Learning Based Method for Coexistence State Prediction in Multiple Wireless Body Area Networks



Yongmei Sun, Tingshuo Chen, Jingxian Wang, and Yuefeng Ji

17.1 Introduction

A wireless body area network (WBAN) is a human-centered wearable wireless network with sensor nodes deployed in/on/around a human body which have features of low power, small size, and intelligence [1]. With the development of sensor workmanship, WBAN is more and more widely applied in people's daily life.

Due to limitation of available bandwidth, interference appears when more than one WBAN in a limited space occupy the same channel simultaneously. This is called coexistence problem of WBAN. It is expected to know the multi-WBAN environment in the next period of time by predicting coexistence state of WBAN. Then, interference management method, e.g., power control in [2], can be executed in time to improve the performance.

The coexistence issue in other wireless technologies has been researched actively, but it is still insufficient in the field of WBAN. In [3], a pilot-assisted scheme was proposed to align interference and schedule radio resource in multicell wireless interference networks. A method to detect interference prior to transmission at the physical (PHY) layer based on wireless local area network (WLAN) technologies was proposed in [4], but it is not good for WBAN which requires low power consumption. A method using signal to interference plus noise ratio (SINR) to detect interference was proposed in [5]. However, the instantaneous SINR estimation is inaccurate because the wireless environment changes frequently with users' physical and postural movements. In some studies, received signal strength indicator

Y. Sun (✉) · T. Chen · J. Wang · Y. Ji
The State Key Laboratory of Information Photonics and Optical Communications, Beijing
University of Posts and Telecommunications, Beijing, China
e-mail: ymsun@bupt.edu.cn

(RSSI) is used as criterion for detecting interference at PHY layer [6] while packet error rate (PER) at medium access control (MAC) layer [7]. However, it is not reliable to predict the coexistence state based on a single parameter. There are other studies on measuring the performance degradation of WBAN [8, 9] and relationship between interference and distances [10] in the multi-WBAN environment, but they didn't provide efficient detection or prediction schemes. On the other hand, machine learning is getting more and more attention in WBAN, e.g., the radio signal strength of WBAN is input into neural network to identify human movement [11], reinforcement learning is used for dynamic power control in WBAN [12, 13], decision tree and genetic algorithm are used for optimizing predictive classification and scheduling E-Health traffic [14], and support vector machine (SVM) is used for posture detection [15]. Therefore, it is useful to introduce machine learning in the study of the coexistence state of WBANs, e.g., a novel algorithm was proposed to predict the coexistence state using SINR, packet reception ratio (PRR) and previous-state via naive Bayes classifier in [16], but it consumes too much time.

To overcome limitations in above methods, this chapter proposes a machine learning based method to improve the accuracy and timeliness of coexistence state prediction in the multi-WBAN environment. The main contributions are summarized as follows:

- By adopting decision tree (DT) and naive Bayes classifier (NBC), and utilizing PER and 11 features extracted from SINR, which reflect human relative movement and interference strength, the coexistence states are predicted and classified into four types: None, Static, Semi-dynamic, and Dynamic. Based on this method, the coexistence problem can be detected and handled in time.
- Based on the above prediction method and data collected by CC2530 2.4-GHz low-power transceivers for training and testing, a set of models are compared and the best one is selected for state prediction. Experimental results show that the decision tree at the head node, which uses 100 of continuous SINRs and the combination of PER, SINR Square Integral (SSI) and Level Change (LC), can reach up the highest accuracy of 96.67%. In addition, this chapter quantitatively defines the multi-WBAN coexistence states by experimental results.
- Compared with the existing machine learning based method that uses SINR, PRR, and NBC [16], simulation results show that the proposed method achieves better performance in terms of accuracy and timeliness.

The rest of the chapter is organized as follows. Section 17.2 briefly introduces decision tree and naive Bayes classifier. Section 17.3 illustrates system model in detail, including problem description, feature extraction, and prediction algorithm. Section 17.4 discusses the performance evaluation by experimental results and simulation results. Finally, Sect. 17.5 concludes the chapter.

17.2 Decision Tree (DT) and Naive Bayes Classifier (NBC)

DT and NBC are supervised learning methods considered in this chapter, because they have lower computational complexity and higher interpretability than other supervised learning methods, and can be easily applied in sensor devices.

Decision Tree

DT is a popular classification and prediction method with top-down construction process [17]. The key to create a decision tree is to choose a feature to divide samples on each node to achieve the optimal performance. The most popular algorithms for creating decision tree are ID3, classification and regression tree (CART) and C4.5, which is adopted in this chapter. This C4.5 algorithm is based on information gain ratio to choose the best division feature. The information entropy of sample set D is defined as follows:

$$\text{Ent}(D) = - \sum_{k=1}^{|Y|} p_k \log_2 p_k, \quad (17.1)$$

where $p_k (k = 1, 2, \dots, |Y|)$ indicates the percentage of the k_{th} class occupying in D , and Y indicates the class space. The value of $\text{Ent}(D)$ is smaller, the purity of is higher.

Supposed that feature a has V possible values $\{\alpha^1, \alpha^2, \dots, \alpha^V\}$, and if a is used to divide sample set D , there will be V branch nodes. The v_{th} node contains all samples of D whose value is α^v on feature, and the set is denoted by D^v . The algorithm puts weight $|D^v|/|D|$ to each node to ensure that the node with more samples can have more obvious influence. Then, the information gain ratio of D divided by feature a is calculated as follows:

$$\text{Gain_ratio}(D, a) = \frac{\text{Ent}(D) - \sum_{v=1}^V \frac{|D^v|}{D} \text{Ent}(D^v)}{IV(a)}, \quad (17.2)$$

$$IV(a) = - \sum_{v=1}^V \frac{|D^v|}{D} \log_2 \frac{|D^v|}{D}, \quad (17.3)$$

where $IV(a)$ indicates intrinsic value (IV) of feature a . The C4.5 algorithm uses a heuristic method. In detail, it chooses a feature with the highest information gain ratio from those features whose information entropy is higher than the average value. Therefore, the information gain ratio becomes an evidence for choosing feature as follows:

$$a_* = \arg \max_{a \in A} \text{Gain_ratio}(D, a). \quad (17.4)$$

Creating decision tree is a recursive process. There are three conditions that make recursion return: (1) if the samples on the current node belong to the same class, there is no need to divide them; (2) if the current feature set is empty or all samples have same values on all features, mark the current node as leaf node and set the class as the one containing most samples; (3) if the sample set is empty on the current node, mark the node as leaf node and set the class as the one containing most samples on the father node.

Naive Bayes Classifier

NBC is based on Bayes' theorem and conditional independence assumption [18]. Given all related probabilities are known, Bayesian decision theory considers how to use these probabilities and misclassification loss to choose the best class. For every sample \mathbf{X} , the classifier chooses the class with the biggest posterior probability $P(c|\mathbf{x})$:

$$h^*(\mathbf{x}) = \arg \max_{c \in Y} P(c|\mathbf{x}), \quad (17.5)$$

where $h^*(\mathbf{x})$ represents the optimal Bayes classifier, and c is one of N possible classes in the class space $Y = \{c_1, c_2, \dots, c_N\}$.

Based on the Bayes' theorem, $P(c|\mathbf{x})$ is written as follows:

$$P(c|\mathbf{x}) = \frac{P(\mathbf{x}, c)}{P(\mathbf{x})} = \frac{P(c)P(\mathbf{x}|c)}{P(\mathbf{x})}. \quad (17.6)$$

Because $P(c|\mathbf{x})$ is the joint probability for all features of sample \mathbf{X} , it is difficult to be evaluated directly by occurrence frequency of samples. Alternatively, NBC adopts conditional independence assumption: for a known class, assume all features of it are independent of each other. Thus Eq. (17.6) can be rewritten as follows:

$$P(c|\mathbf{x}) = \frac{P(c)P(\mathbf{x}|c)}{P(\mathbf{x})} = \frac{P(c)}{P(\mathbf{x})} \prod_{i=1}^d P(x_i|c), \quad (17.7)$$

where d indicates the number of features and x_i represents the value of the i_{th} feature of \mathbf{X} . $P(x)$ is same for all classes, the Bayes decision rule based on Eq. (17.5) is:

$$h_{nb}(\mathbf{x}) = \arg \max_{c \in Y} P(c) \prod_{i=1}^d P(x_i|c). \quad (17.8)$$

This is the expression of NBC.

17.3 System Model

Problem Description

IEEE Std. 802.15.6 defines three mobility levels: static, semi-dynamic, and dynamic just in a qualitative way [19]. Based on this, [16] used the time duration of interference T_{SINR} , PRR and previous-state to quantitatively define four coexistence states which are None, Static, Semi-dynamic, and Dynamic as shown in Fig. 17.1. Here, T_{SINR} indicates the duration of time when SINR value is lower than or equal to a threshold value SINR_{th} . Although the prediction algorithm proposed in [16] achieved high accuracy, the two threshold values of T_{SINR} , i.e., α and β , are 3 s and 19 s respectively, which are too long for WBANs for medical applications which require strictly real-time and reliable performance because a long prediction time will cause interference not to be processed. Therefore, this chapter redefines more appropriate multi-WBAN coexistence states as follows:

- None (N) state indicates that there is no interference.
- Static (S) state indicates that there is a constant interference which causes high PER and low SINR.
- Semi-dynamic (SD) state indicates that there is an intermittent interference which causes PER and SINR waving.

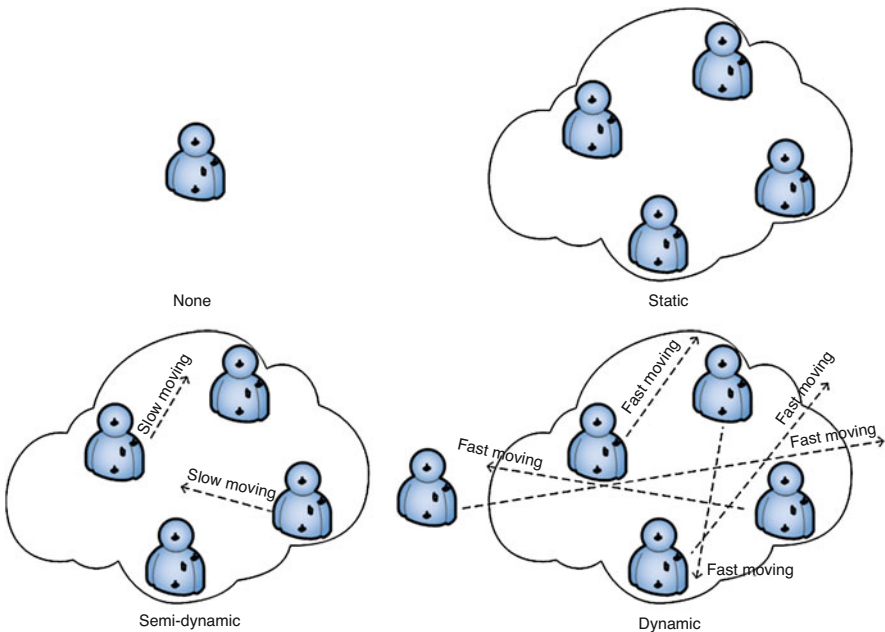


Fig. 17.1 Multi-WBAN coexistence states

- Dynamic (D) state indicates that there is a temporary interference which causes high PER and low SINR instantaneously.

The exact values used for classifying the states are given by experimental results in Sect. 17.4.2. The purpose of this chapter is to find the model with the highest accuracy for state prediction.

Feature Extraction

The multi-WBAN coexistence states change with human relative movement. This chapter chooses and improves 11 time-domain features which have less computational cost [11, 20]. They are integrated SINR Level (ISL), mean value (MV), modified mean value 1 (MMV1), modified mean value 2 (MMV2), SINR square integral (SSI), variance (VAR), root mean square (RMS), level change (LC), level crossing (LCR), slope change (SC), and Willison amplitude (WAMP) as follows:

$$\text{ISL} = \sum_{n=1}^N |x_n|, \quad (17.9)$$

$$\text{MV} = \frac{1}{N} \sum_{n=1}^N |x_n|, \quad (17.10)$$

$$\begin{aligned} \text{MMV1} &= \frac{1}{N} \sum_{n=1}^N w_n |x_n| \\ w_n &= \begin{cases} 1 & \text{if } 0.25N \leq x \leq 0.75N \\ 0.5 & \text{otherwise} \end{cases}, \end{aligned} \quad (17.11)$$

$$\begin{aligned} \text{MMV2} &= \frac{1}{N} \sum_{n=1}^N w_n |x_n| \\ w_n &= \begin{cases} 1 & \text{if } 0.25N \leq x \leq 0.75N, \\ 4n/N & \text{if } 0.25N > n \\ 4(N-n)/N & \text{if } 0.75N < n \end{cases}, \end{aligned} \quad (17.12)$$

$$\text{SSI} = \sum_{n=1}^N |x_n|^2, \quad (17.13)$$

$$\text{VAR} = \frac{1}{N} \sum_{n=1}^N (x_n - \mu)^2, \quad (17.14)$$

$$\text{RMS} = \sqrt{\frac{1}{N} \sum_{n=1}^N (x_n - \mu)^2}, \quad (17.15)$$

$$\text{LC} = \sum_{n=1}^{N-1} |x_{n+1} - x_n|, \quad (17.16)$$

$$\text{LCR} = \sum_{n=2}^N [f(x_n \times x_{n-1}) \cap f(|x_n - x_{n-1}|)], \quad (17.17)$$

$$\text{SC} = \sum_{n=3}^N [f(|x_{n-1} - x_{n-2}| \times |x_n - x_{n-1}|)], \quad (17.18)$$

$$\text{WAMP} = \sum_{n=2}^N f(|x_n - x_{n-1}|), \quad (17.19)$$

where N is the number of continuous SINRs for calculating features, $f(x)$ is the threshold function that returns 1 when x is greater or equal to the defined threshold value, otherwise it returns 0. At this moment, threshold values of $x_n \times x_{n-1}$, $|x_n - x_{n-1}|$ and $|x_{n-1} - x_{n-2}| \times |x_n - x_{n-1}|$ of all data have been calculated. The median value of the last round of calculation is selected as the threshold in this round of calculation. Note that, the PER is added to the feature set as a common criterion for detecting interference. Thus, there are totally 12 features in the candidate feature set for training models.

Prediction Algorithm

Figure 17.2 shows pseudocode of the proposed prediction algorithm. Firstly, 12 candidate features are extracted from a sequence of received SINRs and PERs over

Fig. 17.2 Pseudocode for overall flow of the proposed prediction algorithm

```

input: Continuous SINRs and PERs
output: State
1. Extract ISL, MV, MMV1, MMV2, SSI, VAR, RMS, LC, LCR, SC and WAMP
   from  $N$  continuous SINRs, and PER is the average of  $N$  continuous PERs.
2. Create TSSL.
3. for each node  $j$  in all nodes:
4.   features = FeatureSelection (ISL, MV, MMV1, MMV2, SSI, VAR, RMS, LC,
                               LCR, SC, WAMP, PER),
5.   state  $j$  = DT or NBC (features),
6.   Add state  $j$  to TSSL.
7. State = DecisionFunction(TSSL).
8. return State.

```

one time period. The parameter N needs to be determined by the best DT model or the best NBC model obtained by experiment. Then, a temporarily storing state list (TSSL) is created to temporarily store state set. For each sensor node, feature selection is to select the most suitable feature subset for the current node and the value of N , the results are different for different machine learning methods. After that, these features are input into the model to predict a state and store it. Finally, the coordinator node uses the decision function defined in Sect. 17.4.2 to determine the state.

This chapter adopts stability selection as feature selection method, which is based on sub-sampling and selection algorithm that can be random logistic regression (LRC), SVM, or other similar algorithms [21], here LRC is adopted. The main idea is to repeat running the algorithm on different data subsets and feature subsets to collect the results at last.

In the learning procedure of DT and NBC, the performance is evaluated by the accuracy defined as follows:

$$\text{Accuracy} = \frac{\text{number of correct prediction}}{\text{total number of prediction}} \times 100\% \quad (17.20)$$

17.4 Performance Evaluation

Experimental Setup

A multi-WBAN experiment was carried out in an 8 m × 6 m indoor office environment, and CC2530 2.4 GHz Chipcon low-power transceivers, which is based on narrowband PHY of IEEE Std. 802.15.4, were used to collect data (Note: Here we used Chipcon CC2530 because no IEEE 802.15.6 chip is available until now.). In the experiment, a WBAN consisting of three sensor nodes and one coordinator node was interfered by sensor nodes belonging to the other WBANs. The sensor nodes used a fixed transmitting power of 0 dBm, and each sensor node sent a 16-byte packet to its coordinator node every 10 ms. Referring to [22], chest was chosen for placing the coordinator node on, and head, left arm, and waist were chosen for placing the sensor nodes on.

The experiment collected data of four coexistence states in four cases of interference environment. In the first case for evaluating N state, there is no interference. In the second case for evaluating S state, there are multiple fixed interfering nodes, which are 0.5 to 1.5 m away from the measured WBAN, that affect the measured WBAN's communication. In the third case for evaluating SD state, the interfering nodes move around the WBAN with a speed of 0.5 m/s (slow). In the fourth case for evaluating D state, the interfering nodes pass the WBAN with a speed of 1.5 m/s (fast). Each case was performed for 30 s. The coordinator node calculates SINR based on measurements taken from the sensor nodes using the equation below.

$$\text{SINR} = 10 \log_{10} \frac{10^{\text{RSS}/10} \cdot 10^{n/10}}{10^{\text{RIS}/10}} \quad (17.21)$$

where RSS is the received signal strength from the sensor nodes, RIS is the received interference signal strength from the other WBANs, and n is the noise level measured at the coordinator node.

The labeled data is divided into training data and testing data at a proportion of 7:3. The training data are used to train prediction models while the testing data are used to evaluate the accuracy of these models.

Experimental Results

Choosing different number of continuous SINRs or features can influence the performance of the models significantly. For example, Fig. 17.3 illustrates that the accuracy of DT changes sharply with the different number of continuous SINRs, when the model uses all 12 features. The highest accuracy is 96.30% when the model uses 110 continuous SINRs. Figure 17.4 illustrates that the highest accuracy of DT at the head node is 96.67%, when the model uses three features and 100 continuous SINRs. The combination of the different number of features is chosen by the scores calculated by feature selection method. The scores from high to low are PER (0.97), SSI (0.51), LC (0.50), ISL (0.49), MMV2 (0.43), MV (0.41), VAR (0.39), MMV1 (0.35), and RMS (0.28), respectively. The best combination is composed of PER, SSI, and LC.

Due to the uncertain trend, the experiment tried all suitable combinations of the different number of continuous SINRs and features. The line chart of the best prediction models is shown in Fig. 17.5, in which each line belongs to a certain node using DT or NBC, and each point represents the model with the highest prediction accuracy using the best combination of features and the current number of continuous SINRs.

Fig. 17.3 The accuracy of DT using different number of continuous SINRs and all 12 features (head node)

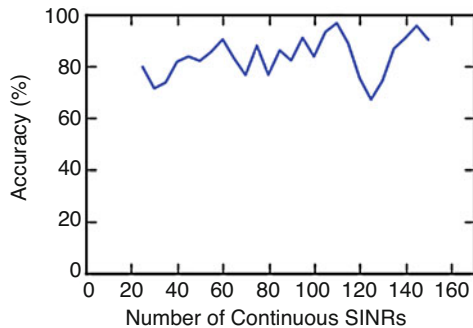


Fig. 17.4 The accuracy of DT using different number of features and 100 continuous SINRs (head node)

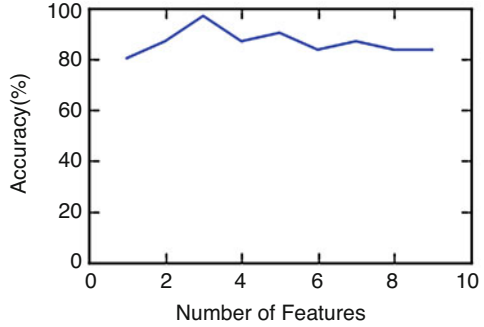


Fig. 17.5 The accuracy of the best prediction model using the best combination of features and different number of continuous SINRs (all nodes)

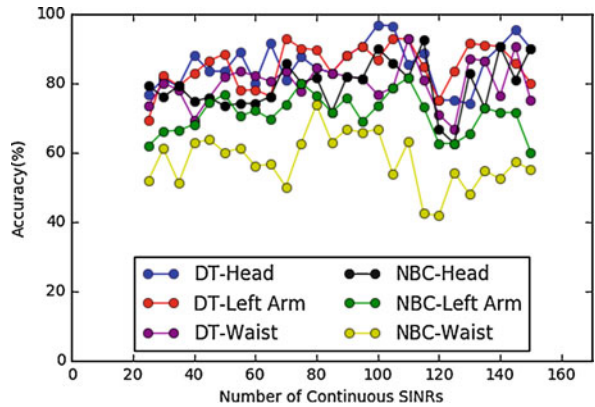


Table 17.1 The best prediction models

Model	Location	Continuous SINRs	Combination of features	Accuracy (%)
DT	Head	100	PER, SSI, LC	96.67
	Left arm	70	PER, SSI, LC, MV, ISL, MMV1	92.86
	Waist	110	MMV1, PER, LC, SSI, ISL, MMV2, MV, RMS	92.59
NBC	Head	115	PER, SSI, VAR, LC	92.31
	Left arm	110	PER, SSI, LC, MMV2, ISL	81.48
	Waist	80	SSI, LC	73.68

The best prediction models in Table 17.1 are acquired from Fig. 17.5. The accuracy of the DT on each location is higher than that of NBC. They are all above 90%, and the highest one is 96.67% at the head node. Therefore, this chapter chooses DT for machine learning. The decision function has two implementation ways, only using the prediction result of DT at the head node or making the decision by voting decision function shown in Fig. 17.6.

Because the states input into the decision function need to be synchronized, 100 is chosen as the number of continuous SINRs on considering the performance of DT. The computing time is 1 s. In comparison, Table 17.2 compares the accuracy

Fig. 17.6 Pseudocode of the voting decision function

```

input: The temporarily stored states from the head node, the left arm node and the
waist node using DT
output: State
1. if some state appears more than twice then
2.     State = this state,
3. else
4.     State = the state predicted from the head node model,
5. return State.
    
```

Table 17.2 Performance results of different methods

	Proposed method (%)	SINR (%)	PER (%)
Head	96.67	77.17	76.20
Left arm	90.00	92.33	53.63
Waist	73.33	71.93	45.83
Voting decision	93.33	86.87	62.93

using feature extraction and the methods using only SINR or PER. The proposed method is better than the others, and decision only by the head node is better than that by the voting decision function.

Therefore, the four coexistence states can be quantitatively defined by the classification information of DT at the head node. Among them, PER illustrates the stability of the communication, SSI illustrates the overall absolute level of continuous SINRs and LC illustrates the fluctuation velocity of continuous SINRs. Note that, because of the bifurcation operation in DT and considering the fitting degree, they have some overlaps.

- N state: Average PER is less than 0.05%, SSI of 100 continuous SINRs is bigger than 122,528, and LC is less than 330.
- S state: Average PER is bigger than 36.38%, SSI of 100 continuous SINRs is bigger than 16,638, and LC is less than 459.
- SD state: Average PER is between 10.37% and 38.27%, SSI of 100 continuous SINRs is between 825 and 32,512, and LC is between 272 and 519.
- D state: Average PER is between 0.05% and 28.54%, SSI of 100 continuous SINRs is less than 11,391, and LC is bigger than 325.

Simulation Results

Furthermore, the performance of the proposed method is compared with NBC model generated in [16] by simulation. Figure 17.7 shows a simulation area of 15 m × 15 m with 16 WBANs. There are four indoor regions of 5 m × 5 m, except region R5. Regions R1 and R3 are low interference area, and regions R2 and R4 are high interference area. The biggest region R5 has only 1 passing by WBAN which may suffer from no interference or low interference. All interference sources move at random speeds of at most 1 m/s in random directions. The measured subject WBAN, i.e., M-WBAN, starts from the position of the red person and moves along the path

Fig. 17.7 Simulation area

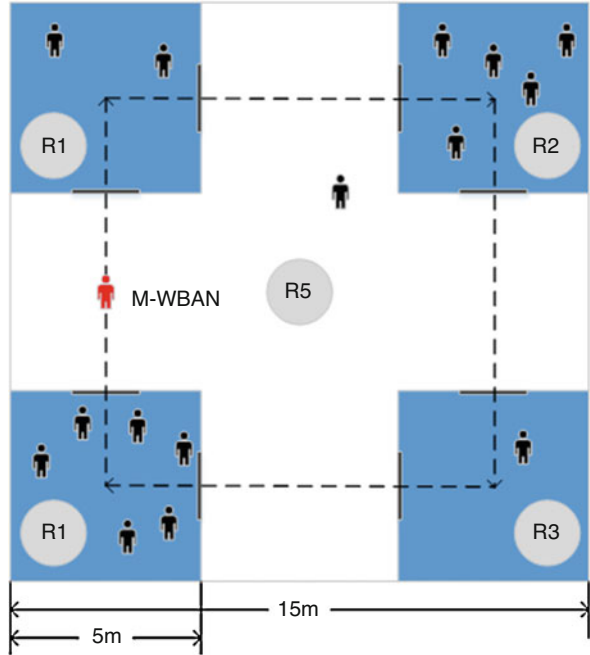
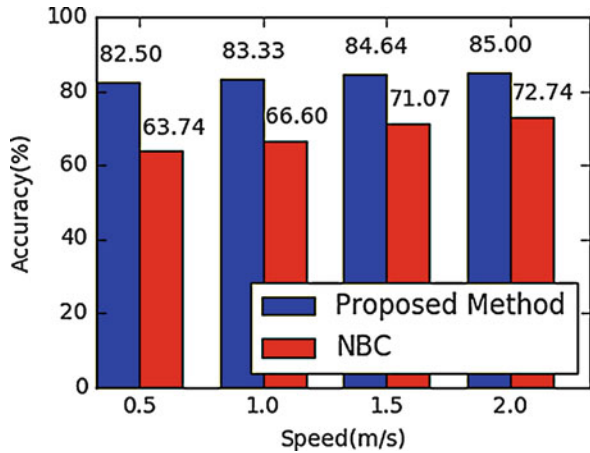


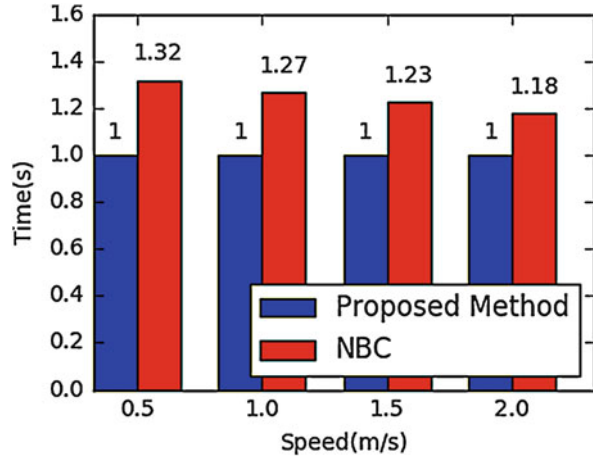
Fig. 17.8 The accuracy of two methods at different moving speeds



at speeds of 0.5 m/s, 1.0 m/s, 1.5 m/s, and 2.0 m/s for 5 minutes, respectively. The setup of every WBAN’s sensor nodes and coordinator node is the same as the experimental setup. When the subject M-WBAN moves, the coordinator node collects data of PER and SINR, and predicts current coexistence state.

Figure 17.8 shows the accuracy of two methods at different moving speeds. Because the simulation environment is different from the experimental environment, the accuracy of the proposed method is lower than that in the experimental

Fig. 17.9 The computing time of two methods at different moving speeds



environment. But it is still higher than 80% and above 10% higher than that of the NBC method in [16]. The simulation environment has more random factors and comes closer to reality, that is why the NBC method of [16] did not perform well. The accuracy of two methods increases with speed, which indicates that low interference states are easier to be detected than high interference states.

Figure 17.9 shows the computing time of two methods at different moving speeds. The computing time of the NBC method of [16] is higher than the constant value of 1 s of the proposed method because of the big threshold values as mentioned in Sect. 17.3.1.

17.5 Conclusion

This chapter proposed a machine learning method for predicting coexistence state in the multi-WBAN environment. Decision tree and naive Bayes classifier methods are adopted for learning, and PER and 11 features extracted from SINR are utilized as features. The coexistence states are quantitatively classified into four types: None, Static, Semi-dynamic, and Dynamic. Experimental results showed that, DT at the head node that uses 100 of continuous SINRs and the combination of PER, SSI, and LC can reach the highest accuracy of 96.67%. Compared with NBC based method, the simulation results show that the proposed method has better performance in terms of accuracy and timeliness. The major reason is attributed to the selected feature set and position of sensor node.

References

1. Cavallari, R., Martelli, F., Rosini, R., Buratti, C., Verdone, R.: A survey on wireless body area networks: technologies and design challenges. *IEEE Communications Surveys & Tutorials*. **16**(3), 1635–1657 (2014)
2. Wang, J.X., Sun, Y.M., Ji, Y.F.: QoS-based adaptive power control scheme for co-located WBANs: a cooperative bargaining game theoretic perspective. *Wirel. Netw.* **2017**(3), 1–11 (2017)
3. Farhadi, H.: Coordinated Transmission for Wireless Interference Networks. Ph.D. thesis, KTH, 2014
4. Pang, Q., Leung, V.C.M.: Channel clustering and probabilistic channel visiting techniques for WLAN interference mitigation in Bluetooth devices. *IEEE Trans. Electromagn. Compat.* **49**(4), 914–923 (2007)
5. Villegas, E. G., Lopez-Aguilera, E., Vidal, R., Paradells, J.: Effect of adjacent-channel interference in IEEE 802.11 WLANs. In: *International Conference on Cognitive Radio Oriented Wireless Networks and Communications 2007, Crowncom*, pp. 118–125. IEEE, Orlando, (2007)
6. Won, C., Youn, J. H., Ali, H., Sharif, H., Deogun, J.: Adaptive radio channel allocation for supporting coexistence of 802.15.4 and 802.11b. In: *Vehicular Technology Conference, 2005, VTC-2005-Fall*, vol. 4, pp. 2522–2526. IEEE, Dallas (2005)
7. Yoon, D. G., Shin, S. Y., Kwon, W. H., Hong, S. P.: Packet error rate analysis of IEEE 802.11b under IEEE 802.15.4 interference. In: *Vehicular Technology Conference, 2006, VTC-2006-Spring*, vol. 90, pp. 1186–1190. IEEE, Melbourne (2006)
8. Deylami, M., Jovanov, E.: Performance analysis of coexisting IEEE 802.15.4-based health monitoring WBANs. In: *International Conference of IEEE Engineering in Medicine and Biology Society 2012, EMBC*, vol. 2012, pp. 2464. IEEE, San Diego (2012)
9. Kazemi, R., Vesilo, R., Dutkiewicz, E.: A novel genetic-fuzzy power controller with feedback for interference mitigation in wireless body area networks. In: *Vehicular Technology Conference, 2011, VTC-2011-Spring*, pp. 1–5. IEEE, Yokohama (2011)
10. Hanlen, L.W., Miniutti, D., Smith, D., Rodda, D., Gilbert, B.: Co-channel interference in body area networks with indoor measurements at 2.4GHz: distance-to-interferer is a poor estimate of received interference power. *Int. J. Wireless Inf. Networks*. **17**(3–4), 113–125 (2010)
11. Archasantisuk, S., Aoyagi, T.: The human movement identification using the radio signal strength in WBAN. In: *International Symposium on Medical Information and Communication Technology, ISMICT*, vol. 40, pp. 59–63. IEEE, Kamakura (2015)
12. Kazemi, R., Vesilo, R., Dutkiewicz, E., Liu, R.: Dynamic power control in Wireless Body Area Networks using reinforcement learning with approximation. In: *International Symposium on Personal Indoor and Mobile Radio Communications, PIMRC*, vol. 6613, pp. 2203–2208. IEEE, Toronto (2012)
13. Kazemi, R., Vesilo, R., Dutkiewicz, E., Liu, R. P.: Design considerations of reinforcement learning power controllers in Wireless Body Area Networks. In: *International Symposium on Personal Indoor and Mobile Radio Communications, PIMRC*, pp. 2030–2036. IEEE, Toronto (2012)
14. Kathuria, M., Gambhir, S.: Leveraging machine learning for optimize predictive classification and scheduling E-health traffic. *Recent Advances and Innovations in Engineering*. **2014**, 1–7 (2014)
15. Paschalidis, I. C., Dai, W. Y., Guo, D., Lin, Y. W., Li, K. Y., Li, B. B.: Posture detection with body area networks. In: *Proceedings of the 6th International Conference on Body Area Networks 2011, BodyNets*, pp. 27–33. ACM, Palmerston (2011)
16. Han, Y., Jin, Z., Cho, J., Kim, T. S.: A prediction algorithm for coexistence problem in multiple WBANs environment. In: *International Conference on Ubiquitous Information Management and Communication, ICUIMC*, vol. 2015, pp. 68. ACM, Siem Reap (2014)
17. Quinlan, J.R.: Induction on decision tree. *Mach. Learn.* **1**(1), 81–106 (1986)

18. Rish, I.: An empirical study of the naive Bayes classifier. *J. Univ. Comput. Sci.* **1**(2), 127 (2001)
19. IEEE Standard for Local and metropolitan area networks - Part 15.6: Wireless Body Area Networks, 1–271 (2012)
20. Veer, K., Sharma, T.: A novel feature extraction for robust EMG pattern recognition. *J. Med. Eng. Technol.* **40**(4), 149–154 (2016)
21. Meinshausen, N., Bühlmann, P.: Stability selection. *J. R. Stat. Soc.* **72**(4), 417–473 (2010)
22. Roy, S.V., Quitin, F., Liu, L.F., Oestges, C., Horlin, F., Dricot, J.M., Doncker, P.D.: Dynamic channel modeling for multi-sensor body area networks. *IEEE Trans. Antennas Propag.* **61**(4), 2200–2208 (2013)

Part V
Systems and Applications

Chapter 18

Private Audio-Based Cough Sensing for In-Home Pulmonary Assessment Using Mobile Devices



Ebrahim Nemati, Md. Mahbubur Rahman, Viswam Nathan,
and Jilong Kuang

18.1 Introduction

Pulmonary illnesses are among the most common chronic diseases affecting the general population. Chronic obstructive pulmonary disease (COPD) is the third leading cause of death in the United States [1]. Asthma is another prevalent chronic condition which affects approximately 24.6 million Americans, including 8.3% of all children [2]. Both of these conditions are characterized by breathing difficulties which affect the quality of life and can lead to severe complications if left unchecked. Thus, it is of high importance to effectively track and manage these illnesses. Specifically, continuous sensing and monitoring of these patients, using mobile devices, offers a number of advantages. Measurements can be made in the natural context of the user's activities of daily living, long-term monitoring is feasible, and the sensors can be unobtrusive and convenient for the user [3, 4]. More importantly, continuous collection of a large amount of data can better inform any clinical decisions, and in conjunction with machine learning techniques can lead to accurate tracking and prediction of disease trajectories. This can be critical for anticipating extreme adverse events and taking the necessary steps to prevent them.

Diagnosis and tracking of these pulmonary illnesses begins with the detection of symptoms, which can include shortness of breath, tightness of chest, and coughing [5]. Of the many symptoms, cough is particularly important as studies have established that it is predictive of exacerbation events in COPD patients [6, 7], which can very often result in expensive hospitalizations for acute cases. Cough is also an important diagnostic symptom for asthma as it is a possible predictor of future asthmatic episodes and in some variants of asthma, cough is the

E. Nemati (✉) · Md. M. Rahman · V. Nathan · J. Kuang
Digital Health Lab, Samsung Research America, Mountain View, CA, USA
e-mail: e.nemati@samsung.com; m.rahman2@samsung.com

predominant or sole symptom [8]. When it comes to mobile monitoring, leveraging the existing microphones on smartphones and smartwatches to acoustically detect coughs represents a feasible and efficient solution. Some acoustic features have already been associated with coughs [9] include: cough frequency, cough intensity and cough pattern. In this work, we propose a hierarchical cough detection algorithm with three stages to accurately segment the cough incidents. This ultimately enables deriving of the aforementioned cough features. The contributions of this work are the design of the algorithm framework to be time and energy-efficient, while also preserving the privacy of the user, so that it can be applicable to daily monitoring in the field with existing mobile devices. In the next Section, we go over some of the relevant audio-based cough detection systems. Section 18.4 provides the details of the sensing algorithm together with the results. Eventually highlights and limitation of the work will be given in the conclusion and future work Section.

18.2 Related Works

Due to the importance of cough as a diagnostic feature of pulmonary diseases, and the widespread prevalence of mobile devices with audio recording capabilities, cough detection using audio features has attracted interest from several other researchers.

One of the key challenges for a system trained to detect coughs is variations in the environment of the user, and the associated changes in the soundscape. For instance, a system solely trained to detect coughs in a quiet home environment may suffer from several false negatives in detection of coughs when the user is walking through streets with a high amount of traffic. Conversely, the risk of false positives can also be high due to the occurrence of other confounding sounds associated with throat clearing, speech, sneezing, laughing as well as other environmental sources [10]. It is not a feasible solution to solely rely on training a machine learning system for all the various scenarios for these false positives and negatives, since it is practically impossible and computationally inefficient to account for all the different possible environments as well as confounding sources of sound in a training dataset. The personal aspects of the individual user must also be taken into consideration. A system trained for one user may not work for another due to differences in cough profiles among individuals. Moreover, it is also important throughout this process to keep in mind the individual's right to privacy; the audio recordings must be processed in a way to preserve privacy.

Cough detection has been done using different algorithms and sensor placements. Vitalojak et al. employed a contact-based microphone on the throat and achieved 91% sensitivity and 94% specificity for in-lab collected data [11]. Amoh et al. and Matos et al. used chest contact microphones and showed similarly promising results using different algorithms [10, 12]. While contact microphones can provide better detection of internally generated body sounds and a more powerful rejection of surrounding noise, they are not the most effective and convenient solutions,

especially for long-term monitoring. Birring et al. collected cough data using a free-field necklace microphone from 15 patients with different chronic lung diseases, for 6 h each [13]. The algorithm had two stages: Hidden Markov Model (HMM) was used as the first stage. After rejecting some of the sound events detected by the first stage using, a keyword-spotting algorithm was used to generate a statistical model. Although the dataset includes a variety of different lung disease patients, the final dataset is limited to only 2 h per subject, from which a big portion of sound events have already been rejected by the previous stage. While the work claims 91% and 99% for sensitivity and specificity, the dataset itself is not as diverse as claimed in terms of sound events.

With recent prominence of deep learning, it is no surprise to see cough detection algorithms based on neural networks. One of the very early deep-learning-based cough detection efforts was the work by Barry et al. in which spectral and temporal features were fed to a probabilistic neural net achieving a sensitivity and specificity of 80% and 96% [14]. However, validation is done only through comparing the number of detected coughs in the period of data collection and the ground truth. Swarnkar et al. took a similar neural-net-based approach but performed a more fine-grained algorithm verification, reporting 93% and 94% for sensitivity and specificity [15]. However, the number of subjects in this study were limited to just three.

With the dominance of smartphones and smartwatches in the past decade, many researchers have tried to investigate the feasibility of cough detection using these platforms. SymDetector, assessed the capability of the smartphone in detecting sound-related respiratory symptoms including cough, sneeze, snuffle, and throat clearing by using a hierarchical structure and a mix of decision tree and SVM classifiers [16]. They were able to detect more than 82% of the symptoms. Lane et al. similarly used smartphone data but engaged a deep neural net algorithm to generally detect audio events [17]. While the focus was not on pulmonary symptoms, they achieved 82.5% accuracy in detection of audio events in a noisy environment by incorporating different environment profiles into the data using a mixed condition approach. Although these works enable convenient sensing using the microphone of the smartphone, the detection accuracy still seems too low for a robust cough sensing module. In addition, a big concern in continuous audio recording is privacy preservation, and this is not addressed in these works, making them less suitable for secure, private long-term monitoring of patients.

The main focus of this work is to provide an accurate, ambulatory, and private solution for cough detection based on a mobile platform. For that reason, smartwatch and smartphone devices are used for data collection. In order to achieve high sensitivity and specificity in the field, and to tackle the audio sensing challenges (mentioned in the beginning of this section), we propose a 3-layer cough detection algorithm to minimize the false positive and negative rates.

18.3 Proposed Cough Detection Algorithm

In order to be able to detect cough patterns and model them, we need to first observe the cough waveform and visualize its frequency components. A great way to observe cough manifestation from an audio stream is using a spectrogram. Spectrogram is the visual representation of the spectrum of frequencies of a sound as they vary with time. Figure 18.1 depicts the waveforms of audio and the spectrogram of both speech and cough samples. The speech sample has a 10-s duration and the cough sample consists of 2 cough events and is chosen to have a 1-s duration for better visualization of cough phases. Although there can be variations across different individuals and disease phases, the cough reflex consists of four main phases in general [18]:

1. An initial large inhalation and glottis closure.
2. Diaphragm and external intercostal muscles contract against the closed glottis.
3. The vocal cords reflex and an explosive burst of air exits the lungs.
4. A voiced sound as the exhalation continues.

Figure 18.1 clearly shows that the burst and the voiced part of the cough can be identified in the audio signal and therefore can be automatically detected. The accumulated duration of these two parts is different across individuals and varies between 300 and 500 ms [18]. In addition to the duration, coughs have other unique characteristics such as loud intensity and a specific frequency range. This can be observed in the spectrogram of the cough as well. It is evident that the loudness and the frequency components of the cough are very different than those of normal speech. In order to be able to detect these unique features, we are proposing a hierarchical structure. Figure 18.2 shows the architecture of the cough detection algorithm we propose. Both raw audio and the obfuscated version of the audio can be fed to the algorithm for cough detection. After pre-processing and segmentation of the input audio, segments with significant audio events will be found using the first stage. Then classification of “Cough” vs. “Speech” vs. “None” will be

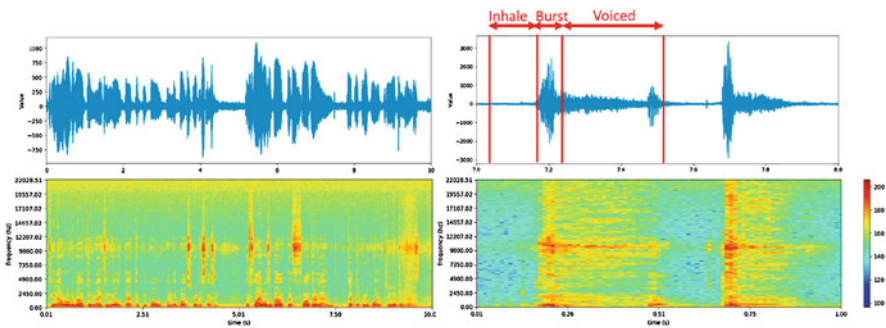


Fig. 18.1 Speech waveform and spectrogram (left) vs. Cough waveform and spectrogram (right)



Fig. 18.2 General architecture of the proposed cough detection algorithm

performed, and eventually a majority voting algorithm will choose the final label based on the results of the classification of each frame in the processed time window.

The benefit of the three-stage structure is that a large portion of the audio will be discarded after passing the first stage. This leaves only a small portion to be further processed in the second and third stages (which consume more processing power and energy). Overall, this helps the whole cough detection algorithm be less power-hungry and time consuming, making it suitable for implementing on mobile devices. This will be further discussed as we describe the different stages of the cough detector.

Sound Event Detector

A large portion of the collected audio on a daily-basis can carry information that is not of interest. This can include environmental outdoor noise, TV sounds, and the sounds of people having conversations around the device. The objective of the “sound event detector” is to filter out these parts of the audio to be able to reduce the burden on the following stages. On the other hand, no sound events of interest should be rejected in the process. Coughs, speech, and similar events of interest usually carry higher energy and sudden change of amplitude. Whereas, for instance, a fan running in the background carries lower energy and a flatter signal amplitude. While some of the previous works used only energy or standard deviation (STD) within a time frame to filter out these parts [10, 13, 14], it is important to realize that the energy of the frame by itself is not sufficient to detect a sound event. A fan can be running very close to the recording device, making the amplitude of the signal and its energy high. Although this should not be considered an event, Figure 18.3 shows the STD and energy of the audio from a cough session in a noisy environment vs. a quite environment.

Evidently, the same energy threshold cannot be used to filter out the noninteresting parts of the audio file. Instead we propose using the relative energy and STD (Eq. 18.1).

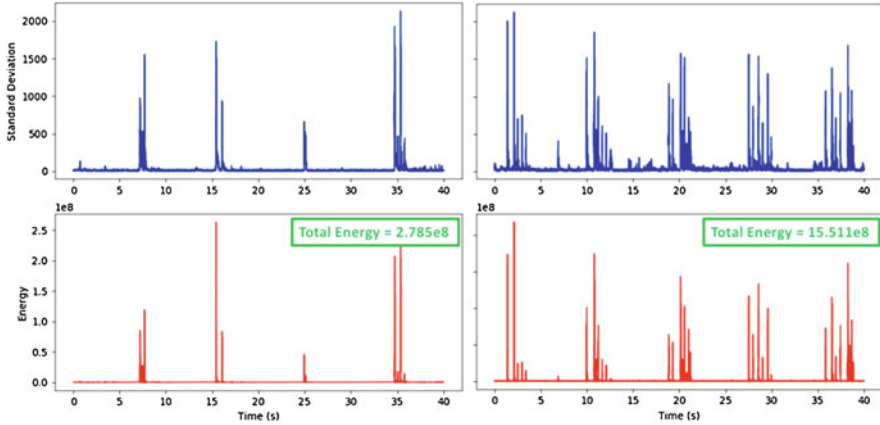


Fig. 18.3 Standard deviation and energy of cough: In quiet (left) and noisy environment (right)

$$\text{Relative Energy} : \frac{\sum_0^N a_i^2}{\sum_0^M a_j^2} \tag{18.1}$$

$$\text{Relative STD} : \sqrt{\frac{\sum_0^N (a_i - \bar{a})}{N}} / \sqrt{\frac{\sum_0^M (a_j - \bar{a})}{M}}$$

where a_i represents a sample in the wave vector and \bar{a} is the mean of the vector for the selected time window. N and M are two parameters incorporated to fulfil this relative notion (N being the number samples in a time window and M being the number of samples in the surrounding of the time window with size of multiple time windows). N is selected to be the number of samples in 1 s, which represents the maximum duration of a sound event. M is selected to be 10 s; wide enough to represent the general energy level and STD of the environment that the user is in, while not so wide as to be irrelevant to the corresponding sound event. If a time window is tagged with an event, 1 window (500 ms) before and 1 window after that are also considered to be events to make sure not to miss any important piece of information. Using this method, the quiet part of the audio will be removed in the first stage, along with the parts with low-enough energy (environmental noise) to be considered “nonevents.” Table 18.1 shows the results of the proposed event detector algorithm applied to an audio sample containing speech in a quiet environment and a noisy environment. For comparison, we reported the results from nonrelative STD

Table 18.1 Sound event detection based on thresholding on standard deviation and energy level for 2-min recording (mixture of cough, speech, and noise) in quiet and noisy environments

Environment type	Thresholding			Relative thresholding	
	STD (% error)	Energy (% error)	STD + Energy (% error)	STD + Energy (% error)	Actual number of eventful seconds
Quiet environment	71 (9%)	65 (16.6%)	73 (6.4%)	77 (1.3%)	78
Noisy environment	91 (9.6%)	88 (6%)	87 (4.8%)	85 (2.4%)	83

and energy thresholding as well. It is apparent that relative thresholding provides a much more robust and sensitive filtering of the nonevents.

Cough Classifier

Once events are recognized by the sound event detector, they need to be analyzed as potential cough events. Supervised machine learning can be used for this. As the target of this work is mainly indoor cough detection, we assume the main sources of sound, other than the environmental noninteresting part, is cough (or similar to cough symptoms such as sneeze) and speech. Therefore, we propose a classification task between cough, speech, and none (neither of the two) classes.

Study Design and Data Collection. We have conducted an in-lab data collection from 21 subjects (including 4 females) performing multiple tasks including speech and simulated voluntary coughs. The age range of the subjects was 20–40 years. Demographics included Caucasian, Pacific Islander, Middle Eastern, and Asian. The subject cohort consisted of healthy individuals with no reported breathing disorders for this initial proof-of-concept study.

Audio was recorded from both a smartphone and smartwatch, and the audio sampling rate was 44.1 kHz for both devices. Participants wore a Zephyr chest band [19] under their clothing as one source of ground-truth signal, and wear a Samsung Gear S3 smartwatch on their left hand. They held the smartphone (Samsung Galaxy Note 5) on the left side of the chest and held the smartwatch on the abdomen. In this way, we capture breathing movement both from the chest and the abdomen using the two devices. The experiment protocol included the following sessions for 1 min each:

1. Sit-Silent: Stay seated while remaining silent.
2. Sup-Silent: Lie down in a supine position while remaining silent.
3. Sit-ReadLoud: Reading neutral sentences [20] while remaining seated. The sentences are carefully chosen to avoid provoking an emotional response.
4. Sup-SpontSpeech: Speaking spontaneously (monologue) while lying down in a supine position.

5. Sit-Dirrhythmic: First half (30s) in one simulated breathing pace (e.g., fast) and the second half in another simulated breathing pace (e.g., slow).
6. Sit-BreathHold: Within 1 min, the participant is requested to hold their breath for a number of times.
7. Sit-Cough: Simulate few coughs while seated.
8. Sit-Silent-Phone-Watch: Both phone and the watch are held on the chest while the participant is sitting silently.

Some of the choices of activity may seem esoteric in this context, but this data collection was part of a larger-scale study also including speech and respiratory rate monitoring for pulmonary disease assessment. The data collection is a mix of both in-room (quiet environment) and out-of-room (with environmental noise). However, all of the data collection is done in an enclosed environment. This means that the amount of environmental noise is not comparable to that of a noisy outdoor environment. Sessions 3 and 4 of the data collection were used as a source of speech after removing of the nonspeech parts using the algorithm proposed in 3.1, generating the class “Speech.” Similarly, coughs were segmented and used from session 7 recordings, generating class “Cough.” Further manual listening and adjusting of the start and stop times of each cough was done to make sure cough instances are purely coughs. The rest of the recordings, including quiet segments and environmental sound segments are used to generate the class “None.”

Pre-Processing and Feature Extraction. The cough, speech, and none wave sources are denoised using a high-pass filter with corner frequency of 200 Hz (to address frequency range of cough and speech). Then the data is segmented using a sliding window algorithm with 500 ms window size (the maximum duration of a cough event) and 50 ms jump size and Hamming window function. This is done using a very common toolbox for speech processing called OpenSmile [21]. The same toolbox is used for feature generation. A total of 61 features including 42 Mel-Frequency Cepstral Coefficients (MFCC) features, total energy, zero crossing, and some other spectral features such as spectral variance, kurtosis, and skewness are generated using OpenSmile. These features are then normalized and fed to machine learning algorithms.

Classification. Tenfold cross-validation is used to test the classification algorithm. For our classification purpose, we have tried four different algorithms including Logistic Regression, SVM, Random Forest, and MultiLayer Perceptron (chosen based on a survey of the literature of cough detection). The classification result is calculated using the mean and standard deviation over 50 iterations of Monte Carlo cross-validation. Table 18.2 shows the classification results for these different algorithms. It can be seen that the random forest classifier outperforms the other classifiers.

Table 18.2 Cough/speech/none classification results using different algorithms

Algorithm	Precision (%)	Recall (%)	F-Measure (%)	ROC Area (%)
Logistic regression	95.1	95.1	95	91.3
SVM	94.7	94.7	94.7	90.6
Multilayer perceptron	95.8	95.8	95.7	92.6
Random forest	96.1	96.1	96.1	93

Majority Voter

To recap the flow of the previous stages: In the first layer (sound event detector), the possibility of each 1-s window to contain sound events is assessed. The 1-s windows with sound events are fed to the classification algorithm in the second layer. After segmentation in the second layer, each 1-s window contains ten 500-ms frames. Each of the frames is labeled using the classification in the second layer. The purpose of the majority voting stage is to determine if the 1-s window is cough, speech, or none, based on the individual classes of the constituent phrase. This stage applies a smoothing function on the often-discrepant outcome sequence of classifier. As an example, the classification results (which have resolution of 50 ms) might have 6 cough labels in 1-s window time. This does not mean that there has been 6 coughs in that 1 s.

Privacy Preservation

The setup for the privacy preservation algorithm used here is fully discussed in our previous work [22]. Recorded data is filtered using the proposed algorithm and then uploaded to a remote server for storage and analysis. The filtering algorithm operates on 30 ms audio frames with a 10 ms step size. For each audio frame Linear Predictive Coding (LPC) coefficients, gain and whether or not the frame was voiced are calculated. For frames that are voiced, the LPC coefficients are replaced with a randomly chosen set of coefficients for prerecorded vowel sounds. Therefore, the speech is obfuscated and becomes unintelligible. In this work we investigated whether the speech obfuscation had an adverse effect on our cough/speech/none classification. Figure 18.4 represents the confusion matrix for both non-obfuscated and obfuscated audio data.

It can be observed that the obfuscation method does not significantly affect classification performance, and represents a feasible block of the proposed framework for privacy preserving cough detection. The average accuracy of classification declines from 91% to 80% which is an 11% reduction which indicates that the result is still promising, even after obfuscation. In terms of intra-class deterioration, it should be noted that “Speech” and “Cough” are not as affected as “None” class (only about 8%). This is encouraging due to the fact that eventually a lot of “None” class

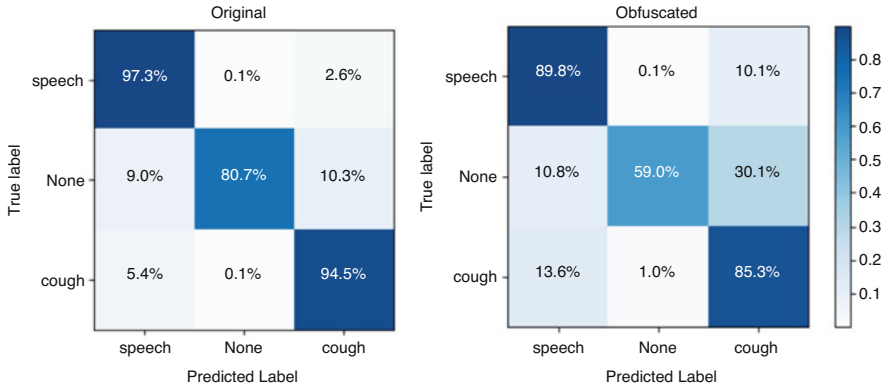


Fig. 18.4 Confusion matrix for cough/speech/none classification using random forest for both non-obfuscated (left) and obfuscated (right) audio data

segments will be filtered out by the “sound event detector” anyway, before getting to the obfuscation and classification modules.

18.4 Conclusion and Future Works

Cough frequency/pattern detection and cough/voice classification are two significant sources of information that can help determine pulmonary disease severity and predict exacerbation events for these patients. This work proposes an ambulatory system with the ultimate goal of unobtrusive recording of speech and cough from patients in a private manner. Since the ultimate goal is to shift a lot of the processing to the device (for mobility and privacy reasons), the proposed algorithm is designed to minimize the machine learning burden by implementing a three-staged cough detection algorithm. Sound event detection, as the first stage, correctly detected the events of interest and filtered out the noninteresting parts with a 2.4% error rate in an indoor environment with minimal noise. The classification result showed 96.1% accuracy for cough and speech detection using a random forest classifier. A privacy preserving algorithm, based on LPC coefficient manipulation, ensures the private collection of data while not deteriorating the classification significantly (only 11% reduction of classification accuracy).

The promising results achieved in this initial study encourage testing on real patients in the field as a next step. Data collected in the field contains a variety of sound events that can mislead the classification. Investigating the effect of obfuscation on speech pattern recognition and cough type and intensity detection are other future effort potentials. Since location of the device (such as smartphone or smartwatch) with respect to the user may affect the signal quality, considering those practicalities in the natural settings will further enrich the model in future [23,

24]. Finally, robust detection of all the different pulmonary symptoms privately and accurately in an ambulatory, noninvasive manner is the ultimate goal for which this work tries to build the foundation for.

References

1. American Lung Association. How serious is COPD. <http://www.lung.org/lung-health-and-diseases/lung-disease-lookup/copd/learn-about-copd/how-serious-is-copd.html>. Accessed 29 May 2018
2. Environmental Protection Agency. Asthma Facts. https://www.epa.gov/sites/production/files/2018-05/documents/asthma_fact_sheet_0.pdf. Accessed 29 May 2018
3. Nemati, E., Liaqat, D., Rahman, M.M., Kuang, J.: A novel algorithm for activity state recognition using smartwatch data. In Healthcare Innovations and Point of Care Technologies (HI-POCT), 2017 IEEE (pp. 18–21). IEEE, 2017
4. Nemati, E., Suh, Y.S., Motamed, B. and Sarrafzadeh, M.: Gait velocity estimation for a smartwatch platform using kalman filter peak recovery. In Wearable and Implantable Body Sensor Networks (BSN), 2016 IEEE 13th International Conference on (pp. 230–235). IEEE, 2016
5. Tehrani, R. M.: Speech breathing patterns in health and chronic respiratory disease. 2015
6. Miravitlles, M.: Cough and sputum production as risk factors for poor outcomes in patients with copd. *Respir. Med.* **105**(8), 1118–1128 (2011)
7. Burgel, P.-R., Nesme-Meyer, P., Chanez, P., Caillaud, D., Carre, P., Perez, T., Roche, N.: Cough and sputum production are associated with frequent exacerbations and hospitalizations in copd subjects. *Chest.* **135**(4), 975–982 (2009)
8. Dipinigaitis, P.V.: Chronic cough due to asthma: ACCP evidence-based clinical practice guidelines. *Chest.* **129**(1), 75S–79S (2006)
9. Shi, Y., Liu, H., Wang, Y., Cai, M., Xu, W.: Theory and application of audio-based assessment of cough. *Hindawi J Sensors*, 2018, 9845321, 10 pages, (2018)
10. Matos, S., Birring, S.S., Pavord, I.D., Evans, D.H.: An automated system for 24-h monitoring of cough frequency: the Leicester cough monitor. *IEEE Trans. on Biomed. Eng.* **54**, 1472–1479 (2007)
11. McGuinness, K., Kelsall, A., Lowe, J., Woodcock, A., Smith, J. A.: Automated cough detection: a novel approach. *J Resp Crit Care Med* (2007)
12. Amoh, J., Odame, K.: Deep neural networks for identifying cough sounds. *IEEE TCAS* (2016)
13. Birring, S., Fleming, T., Matos, S., et al.: The Leicester cough monitor: Preliminary validation of an automated cough detection system in chronic cough. *Eur. Respir.* (2008)
14. Barry, S., Dane, A., Morice, A., Walmsley, A.: The automatic recognition and counting of cough. *Cough J.* **2**, 8, (2006)
15. Swarnkar, V., Abeyratne, U.R., Amrulloh, Y., Hukins, C., Triasih, R., Setyati, A.: Neural network based algorithm for automatic identification of cough sounds. *IEEE EMBC.* **2013**, 1764–1767 (2013)
16. Sun, X., et al.: SymDetector: detecting sound-related respiratory symptoms using smartphones. In: Proceedings of ACM International Joint Conference on PerComp and UbiComp (2015)
17. Lane, N.D., Georgiev, P., Qendro, L.: DeepEar: robust smartphone audio sensing in unconstrained acoustic environments using deep learning. In Proceedings of the 2015 ACM International Joint Conference on Pervasive and Ubiquitous Computing (pp. 283–294). ACM (2015)
18. Korpas, J., Sadlonova, J., Vrabec, M.: Analysis of the cough sound: an overview. *Pulm. Pharmacol.* 261–268 (1996)
19. Zephyr HomePage. <http://www.zephyranywhere.com/>. Accessed 17 May 2018

20. Sheikh, Naveed A., and Debra, A.: Titone. "Sensorimotor and linguistic information attenuate emotional word processing benefits: An eye-movement study." *Emotion* (2013)
21. Eyben, F., Wenginger, F., Gross, B.: Schuller Recent developments in openSMILE the munich open-source multimedia feature extractor ACM Press pp. 835–838 (2013)
22. Liaqat, D., Nemati, E., Rahman, M., Kuang, J.: A method for preserving privacy during audio recordings by filtering speech. In *Life Sciences Conference (LSC), 2017 IEEE* (pp. 79–82). IEEE, 2017
23. Rahman, M., Nemati, E., Nathan, V. and Kuang, J., Instant, R.R.: Instantaneous Respiratory Rate Estimation on Context-aware Mobile Devices. In *EAI BodyNets*, (2018)
24. Nemati, E., Sideris, K., Kalantarian, H., Sarrafzadeh, M.: A dynamic data source selection system for smartwatch platform. In *Engineering in Medicine and Biology Society (EMBC), 2016 IEEE 38th Annual International Conference of the* (pp. 5993–5996). IEEE, 2016

Chapter 19

Using an Indoor Localization System for Activity Recognition



Andrea Aliperti, José Corcuera, Chiara Fruzzetti, Gianluca Marchini, Francesco Miliani, Simone Musetti, Andrea Primaverili, Riccardo Rocchi, Davide Ruisi, and Alessio Vecchio 

19.1 Introduction and Related Work

Automatic recognition of user's activity is useful in numerous application domains. In e-health, activity recognition can be used to understand if the user is characterized by a sedentary lifestyle or to automatically assess his/her training sessions [13]. In home automation, services and applications can be customized according to what the user is doing [4]. In industrial environments, automatic recognition of activities can be useful to implement smart control systems or to put advanced safety policies in place [22]. From a more general perspective, activity recognition is considered a key element of context-aware computing, as it provides relevant information about the user and the surrounding environment [11].

Given its relevance, research on activity recognition has been rather prolific during the last years, both from the point of view of adopted technologies and inference methods. In particular, a wide range of sensing mechanisms has been explored to collect information about the user, from 3D cameras to smart textile [2, 7]. However, the vast majority of proposed approaches rely on wearable devices equipped with inertial sensors like accelerometers and gyroscopes [6]. Sensors attached to users' limbs are used to collect information about their raw movements and then, at a higher level, to determine which activity is currently performed [18].

In a seminal paper, Bao and Intille used five biaxial accelerometers to recognize physical activities [3]. Devices were worn at the right wrist, right hip, left arm, left thigh, and right ankle, whereas classification was carried out using the following methods: decision table, k -Nearest Neighbors, C4.5 decision tree, and Naive Bayes.

A. Aliperti · J. Corcuera · C. Fruzzetti · G. Marchini · F. Miliani · S. Musetti · A. Primaverili · R. Rocchi · D. Ruisi · A. Vecchio (✉)
University of Pisa, Pisa, Italy
e-mail: alessio.vecchio@unipi.it

The methods that provided the best results were decision trees and k -Nearest Neighbors.

In [15], a single triaxial accelerometer positioned on the belt was used to recognize some activities of daily living. Classification was carried out using two methods: Naive Bayes and k -Nearest Neighbors. A leave-one-person-out strategy was adopted for validation: two users were involved in the training phase, and five other users were recruited for the evaluation. The set of considered activities included: jumping, running, walking, sitting, and the transitions from sitting to standing and from standing to kneeling (and vice versa).

A comparison of different architectural solutions in activity recognition and the effects of some parameters of operation are presented in [14]. Solutions based on both a single sensor and multiple sensors were evaluated. As far as classification methods are concerned, Neural Network achieved the best accuracy results. However, if also the training costs are considered, decision trees were identified as one of the best methods for the reference scenario. Additional experiments showed that solutions based on multiple sensors are able to achieve better recognition accuracy, even when using light-weight algorithms. Also the effects of sampling rate on recognition accuracy were analyzed. Results showed that sampling rates greater than 20 Hz may provide limited benefits.

Fusion of data originating from multiple accelerometers is discussed in [8]. Using data from two accelerometers significantly improves the accuracy of activity recognition with respect to the use of a single device. Using three or more sensors, on the contrary, seems to bring only limited benefits. When two accelerometers are used, ankle and wrist were identified as particularly favorable positions.

Given their popularity, smartphones and smartwatches have been frequently considered as suitable sensing devices for recognizing human activities. In addition, smartphones and smartwatches are characterized by reduced invasiveness and thus they provide the opportunity to make recognition systems more acceptable for the end users [5, 17]. Smartphones, for instance, proved to be effective to distinguish falls from other activities of daily living [1]. A wrist-worn accelerometer can be extremely useful in detecting gait segments, especially when used in combination with a model tailored to the user [10]. Also the strength of the Wi-Fi signal received by a smartphone can be used as a means for activity recognition [21].

This paper contributes to existing literature by showing that an indoor localization system characterized by high resolution can be used for activity recognition. Differently from the vast majority of known methods, the proposed approach does not rely on inertial sensors. The accurate position of a set of devices worn by the user is first estimated and then used to extract some characterizing features. Experimental results show that, for the considered set of users and activities, average accuracy values as high as $\sim 95\%$ can be obtained. For some users the method is able to obtain perfect, or close to perfect, results. A prototypical implementation of the method based on IEEE 802.15.4-2011 ultra-wideband (UWB) is also described.

19.2 Method

The proposed activity recognition method is based on the idea of observing the user's movements by means of a fine-grained indoor localization system. A number of UWB-enabled devices with known position, called *anchors*, are placed in the environment. Anchors are able to determine the distances between themselves and *tags*, devices that are free to move in the considered space. Distances between tags and anchors are used to determine the tags' position, e.g., using a multi-lateration algorithm. We suppose that the user carries (wears) a number of tags, which could represent smart devices like fitness tracking wristbands, smartshoes, smartwatches, smartglasses, or a simple smartphone carried in a pocket. The basic idea is that the position of these devices (tags) in the environment can be used to infer the activity currently performed by the user. In particular this is achieved by means of three steps: first, the position of tags in the environment¹ is used to compute a set of metrics that do not depend on the absolute position of the user; second, a set of features is extracted from these metrics; third, a previously trained machine learning algorithm is fed with feature values to determine which activity is currently performed. The three steps are detailed in the following.

From Global Positions to Local Metrics

Let us call A_1, A_2, \dots, A_n the n anchors, and T_1, T_2, \dots, T_m the m active tags worn by the user. Anchors periodically estimate the distances between themselves and all the tags via UWB. The n distances between A_1, \dots, A_n and the i th tag are used to derive the position of the latter in the global reference system. The position of the i th tag in the global reference system at time t and its components are indicated as $g_i(t) = \{g_i^X(t), g_i^Y(t), g_i^Z(t)\}$. Global positions are not directly used to infer the activity of the user, as they would make the activity recognition process dependent on the specific environment. To make the recognition process as general as possible, the position of tags in the global space is converted in a set of metrics that do not depend on the absolute coordinates of the devices. First, a set of differences between position vectors are calculated: $d_{ij}(t) = g_j(t) - g_i(t) = \{g_j^X(t) - g_i^X(t), g_j^Y(t) - g_i^Y(t), g_j^Z(t) - g_i^Z(t)\}$ with $i, j \in 1 \dots m, j \neq i$. Then the following Position Independent Metrics (PIMs) are calculated:

$$L_{ij}(t) = |d_{ij}(t)| \quad \text{with } i, j \in 1 \dots m, j > i$$

¹We will also use the term *global* to indicate the environment-based reference system, as it is common to all users.

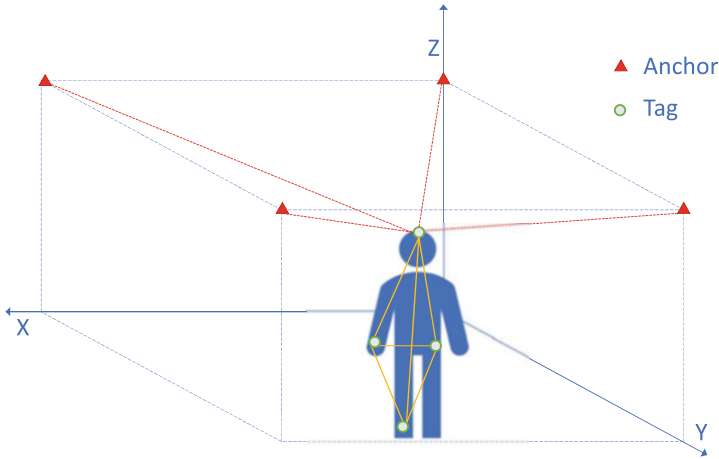


Fig. 19.1 The global reference system and the set of computed distances

and

$$\Theta_{ijk} = \arccos \left(\frac{d_{ji}(t) \cdot d_{jk}(t)}{|d_{ji}(t)| |d_{jk}(t)|} \right) \quad \text{with } i, j, k \in 1 \dots m, i \neq j, k \neq j, k > i.$$

Hereafter, the two sets of PIMs will be indicated as L -PIMs and Θ -PIMs respectively. Figure 19.1 shows an exemplificative scenario with four anchors and four tags. The dashed lines represent the distances between one of the tags and the anchors placed in the environment (for the sake of image clarity only the distances between the head-mounted device and the anchors are shown). These distances are used by the indoor localization system to estimate the position of the tags in the global reference system. The four tags define a general tetrahedron, with the tags placed at the vertices. L -PIMs correspond to the length of the edges of the tetrahedron (the six continuous lines in the example), whereas Θ -PIMs are equal to the angles on the faces of the tetrahedron. The total number of angles is equal to twelve, but the space of all shapes, for tetrahedra, is five-dimensional [19]. Thus, the set of Θ -PIMs is not completely independent. Similar considerations may be made when the number of tags is smaller/greater than four.

Feature Extraction

The set of PIMs is first preprocessed using a low-pass Butterworth filter. Processed signals are then segmented using a window with fixed duration R . Let us indicate the k th window concerning L_{ij} as $W_{ij}(k)$ (i.e., $L_{ij}(t)$ with $t \in ((k-1)R, kR)$). A set of functions is used to extract F characteristic indicators from $W_{ij}(k)$, for

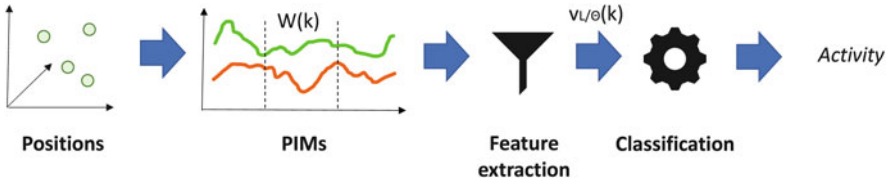


Fig. 19.2 Overview of the method

every k . In summary, a vector $v_L(k)$, the feature vector, is produced with period R . The same is done with Θ -PIMs, thus generating an analogous $v_\Theta(k)$ feature vector.

Inferring Activities

The vector of feature values ($v_L(k)$, $v_\Theta(k)$, or both) is given as input to a previously trained machine learning classifier. For the training phase we explored two possible solutions, one based on a single model for all users and the other based on a personalized model. Both solutions have advantages and drawbacks: the first is characterized by a simpler training phase, as it does not require user-dependent customization; the second relies on a training phase that is user specific, but it is expected to provide better results.

An overview of the method is provided in Fig. 19.2.

19.3 Prototype and Data Collection

A prototype of the system has been implemented using a Decawave MDEK1001 kit [12]. The kit is composed by a set of Decawave DWM1001-DEV boards, and a real-time localization application. Each DWM1001-DEV board is equipped with a DW1000 IEEE 802.15.4-2011 UWB transceiver and a Nordic nRF52832 BLE microcontroller (based on ARM Cortex M4). The Bluetooth connection was used only to define a network and to set the parameters of operation. Four boards were used as anchors and attached to the walls at the corners of a square area of 3.60×3.60 m (corresponding to a $\sim 13\text{m}^2$ room). Anchors were placed 2 m above the ground. Four other boards were used as tags and attached at the head, right wrist, left pocket, and right ankle of the user. Figure 19.3 shows a volunteer wearing the prototype. Another board operating as a listener was attached to a common PC, where the position of tags was logged. The position of tags was estimated with 10 Hz frequency, the maximum allowed by the current version of the kit.

Ten volunteers participated in the data collection phase. Their main characteristics are listed in Table 19.1. Each volunteer was asked to perform the following activities: standing, sitting, walking in circle, lying on the floor, and crouching.

Fig. 19.3 Volunteer wearing four tags (head, right wrist, left pocket, right ankle)

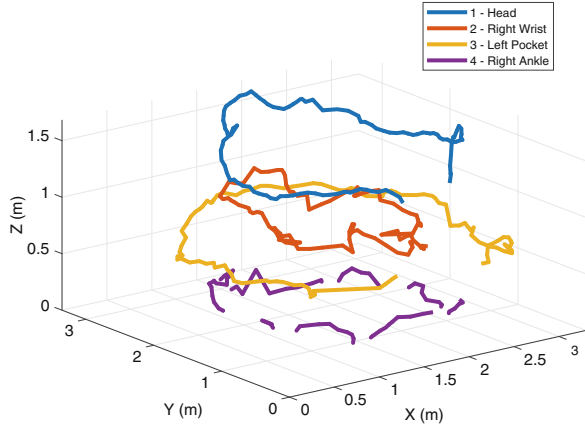


Table 19.1 Ten users participated in the data collection phase

User ID	Age (yr)	Weight (kg)	Height (m)	Gender (M/F)
1	24	79	1.72	M
2	24	55	1.66	F
3	25	76	1.87	M
4	33	74	1.72	M
5	24	80	1.80	M
6	25	80	1.80	M
7	25	77	1.82	M
8	26	45	1.43	F
9	24	80	1.82	M
10	23	66	1.75	M

Each activity was performed for 60 s. The activities of all volunteers were video recorded. This was done to simplify the subsequent manual labeling of acquired traces and to document the whole process in case of unexpected results. Figure 19.4 shows a 3D representation of the walking activity of one of the users (approximately

Fig. 19.4 3D trajectories of the four worn devices when the volunteer is walking in circle



12 s, corresponding to an almost-complete circle). The trajectory of the ankle-worn device is not always visible because of positioning errors producing negative values on the Z axis.

All traces were segmented using 3 s windows ($R = 3$ s). Traces were then manually annotated assigning one of the following labels to each window: *standing*, *sitting*, *walking*, *lying*, *crouching*, *transition*, and *invalid*. The first five labels were used as ground truth during the training and evaluation phases. The *transition* label was used to identify the time windows containing multiple activities (e.g., when the user stops walking and starts lying on the floor). The last label was used to mark a limited number of segments containing data to be discarded (in few occasions, one of the tags suffered from short disconnections).

Labeled traces are publicly available at the following address: <http://vecchio.iet.unipi.it/vecchio/other/data/>

19.4 Results

The following set of statistical and signal processing functions was considered for the feature extraction phase: mean, max-min, min, Average Absolute Variation (AAV), Standard Deviation (SD), Root Mean Square (RMS), Mean Crossing Rate (MCR), max, Mean Absolute Deviation (MAD). AAV is a function successfully used in similar contexts [9], and it is defined as follows:

$$AAV = \frac{1}{N-1} \sum_{i=1}^{N-1} |a_{i+1} - a_i|$$

where a_i is the i th observed value and N is the number of values in the considered window.

Table 19.2 Selected features

	Mean	Max-min	Min	AAV	SD	RMS	MCR	Max	MAD
L_{12}	✓		✓			✓			
L_{13}	✓	✓	✓	✓		✓		✓	
L_{14}	✓		✓	✓		✓		✓	
L_{23}	✓		✓			✓			
L_{24}	✓		✓	✓		✓		✓	✓
L_{34}	✓	✓	✓	✓	✓	✓			✓

Table 19.3 Results obtained by some well-known classifiers

Classification method	Accuracy (%)
ENS	93.0
SVM	92.6
KNN	92.0

First, we evaluated the performance of the method using only the set of L -PIMs. With $m = 4$, a vector v_L with 54 features was produced every R seconds (the size of v_L is equal to the number of functions multiplied by the number of different L -PIMs). The number of features was then reduced to 30 using the RELIEFF method [16]. The final set of features is shown in Table 19.2.

Transitions between different activities are not considered in this study, as we are interested in understanding which is the performance of the method in steady conditions. However, an approach like the one proposed in [20] can be possibly incorporated.

The reduced set of features was given as input to a number of machine learning methods (those available in the MATLAB classification learner toolbox). Evaluation was carried out according to tenfold cross validation. The dataset was divided into ten disjoint subsets. Nine subsets were used to train the machine learning method, and the left out subset was used to evaluate the method on previously unseen data. The process was repeated ten times using all the different subsets for the evaluation phase and then averaging the results. Table 19.3 shows the obtained accuracy values for the top three performing methods: Ensemble Subspace KNN (ENS), Support Vector Machine (SVM), k -Nearest Neighbors (KNN). The three classifiers provided very close results with 92–93% accuracy. The confusion matrix for the set of considered activities is shown in Fig. 19.5.

Such results were obtained using the data of all users for training the system. This approach corresponds to building a global model of users' activities. We then evaluated the possible benefits introduced by a personalized model. To this aim we performed the feature selection, training, and evaluation phases again, using the data of a single user at a time. Also in this case tenfold cross validation was used to avoid overfitting. Results are reported in Table 19.4. When using a personalized model, accuracy values are generally better than the ones obtained by the global model. On average, the personalized approach is able to obtain accuracy values that

Fig. 19.5 Confusion matrix

		Predicted class				
		Crouching	Lying	Sitting	Standing	Walking
True class	Crouching	146	4	4		
	Lying	8	153	1	4	5
	Sitting	5	1	153	6	10
	Standing		2	2	193	3
	Walking	1	6	2	1	180

Table 19.4 Accuracy for the different users when using a personalized model

User ID	Accuracy (%)		
	ENS	SVM	KNN
1	98.8	97.7	98.8
2	96.7	97.8	97.8
3	86.2	87.5	83.7
4	96.7	94.4	95.6
5	97.9	97.9	97.9
6	93.7	95.0	95.0
7	85.6	87.8	84.4
8	95.7	96.8	96.8
9	96.8	95.7	95.7
10	100.0	97.7	98.9
Mean	94.8	94.8	94.4

are close to ~95%. For some users, accuracy values are equal, or very close, to 100%. In summary, the use of a personalized model has a positive impact on the proposed method.

We then repeated the same analysis using the set of Θ -PIMS. In particular, six different Θ values were computed and given as input to the same classification algorithms (the number of degrees of freedom, as mentioned, is equal to five, but we decided to include one more value to mitigate the effects of measurement errors). The number of features was again limited to 30 using RELIEFF. The set of selected features is similar to the one produced for L -PIMS, with mean, min, RMS, max, and AAV the most popular functions (selected 6, 6, 6, 5, and 3 times respectively). Also in this case we considered both the approach based on the definition of a global model and the one based on a personalized model. With the global model, the following accuracy values were obtained by ENS, SVM, and KNN

respectively: 91.3, 91.2, and 91.9%. With the personalized model, the obtained accuracy values were equal to 94.4, 93.9, and 94.0%. Results obtained with Θ -PIMs are thus approximately equal to the ones obtained with L -PIMs. Finally, the same analysis was carried out using both L - and Θ -PIMs (but still limiting the set of features to the best 30). With the global model, the following accuracy values were obtained by ENS, SVM, and KNN respectively: 92.4, 93.4, and 93.8%. With the personalized model, the obtained accuracy values were equal to 94.6, 95.5, and 94.9%, thus achieving slightly better final results.

19.5 Conclusion

Recent advancements in communication technologies, e.g., IEEE 802.15.4-2011 UWB, not only make fine-grained localization of devices and people possible, but also provide the opportunity to devise new applications or to improve existing ones. This paper shows that an indoor localization system can be successfully used for automatic activity recognition. To be as general as possible, the proposed approach relies on a set of metrics and features that are not dependent on the position of the user in the environment. Experimental results show that excellent accuracy values can be achieved, especially when using a model tailored to the user. Obviously, it is also possible to combine PIMs with the user's position in the environment (already provided by the indoor localization system), to further improve the recognition process. For instance, if the user is in the kitchen the set of possible activities could be expanded/reduced with respect to the one used in this paper (e.g., adding cooking and removing lying).

Acknowledgements This work was funded in part by University of Pisa, grant PRA_2017_37 “IoT and Big Data: metodologie e tecnologie per la raccolta e l'elaborazione di grosse moli di dati.”

References

1. Abbate, S., Avvenuti, M., Bonatesta, F., Cola, G., Corsini, P., Vecchio, A.: A smartphone-based fall detection system. *Pervasive Mob. Comput.* **8**(6), 883–899 (2012). <https://doi.org/10.1016/j.pmcj.2012.08.003>
2. Aggarwal, J., Xia, L.: Human activity recognition from 3D data: a review. *Pattern Recogn. Lett.* **48**, 70–80 (2014). <https://doi.org/10.1016/j.patrec.2014.04.011>
3. Bao, L., Intille, S.S.: Activity recognition from user-annotated acceleration data. In: Ferscha, A., Mattern, F. (eds.) *Pervasive Computing*, pp. 1–17. Springer, Berlin (2004)
4. Benmansour, A., Bouchachia, A., Feham, M.: Multioccupant activity recognition in pervasive smart home environments. *ACM Comput. Surv.* **48**(3), 34:1–34:36 (2015). <https://doi.org/10.1145/2835372>
5. Brezmes, T., Gorricho, J.L., Cotrina, J.: Activity recognition from accelerometer data on a mobile phone. In: *International Work-Conference on Artificial Neural Networks*, pp. 796–799. Springer, Berlin (2009)

6. Bulling, A., Blanke, U., Schiele, B.: A tutorial on human activity recognition using body-worn inertial sensors. *ACM Comput. Surv.* **46**(3), 33:1–33:33 (2014). <https://doi.org/10.1145/2499621>
7. Cheng, J., Amft, O., Bahle, G., Lukowicz, P.: Designing sensitive wearable capacitive sensors for activity recognition. *IEEE Sens. J.* **13**(10), 3935–3947 (2013). <https://doi.org/10.1109/JSEN.2013.2259693>
8. Chowdhury, A.K., Tjondronegoro, D., Chandran, V., Trost, S.G.: Physical activity recognition using posterior-adapted class-based fusion of multiaccelerometer data. *IEEE J. Biomed. Health Inform.* **22**(3), 678–685 (2018). <https://doi.org/10.1109/JBHI.2017.2705036>
9. Cola, G., Avvenuti, M., Vecchio, A., Yang, G.Z., Lo, B.: An unsupervised approach for gait-based authentication. In: 2015 IEEE 12th International Conference on Wearable and Implantable Body Sensor Networks (BSN). pp. 1–6 (2015). <https://doi.org/10.1109/BSN.2015.7299423>
10. Cola, G., Avvenuti, M., Musso, F., Vecchio, A.: Personalized gait detection using a wrist-worn accelerometer. In: 2017 IEEE 14th International Conference on Wearable and Implantable Body Sensor Networks (BSN). pp. 173–177 (2017). <https://doi.org/10.1109/BSN.2017.7936035>
11. Davies, N., Siewiorek, D.P., Sukthankar, R.: Activity-based computing. *IEEE Pervasive Comput.* **7**(2), 20–21 (2008). <https://doi.org/10.1109/MPRV.2008.26>
12. Decawave. <http://www.decawave.com>. Accessed 15 May 2018
13. Ermes, M., Prkk, J., Mntyjrvi, J., Korhonen, I.: Detection of daily activities and sports with wearable sensors in controlled and uncontrolled conditions. *IEEE Trans. Inf. Technol. Biomed.* **12**(1), 20–26 (2008). <https://doi.org/10.1109/TITB.2007.899496>
14. Gao, L., Bourke, A., Nelson, J.: Evaluation of accelerometer based multi-sensor versus single-sensor activity recognition systems. *Med. Eng. Phys.* **36**(6), 779–785 (2014). <https://doi.org/https://doi.org/10.1016/j.medengphy.2014.02.012>
15. Gupta, P., Dallas, T.: Feature selection and activity recognition system using a single triaxial accelerometer. *IEEE Trans. Biomed. Eng.* **61**(6), 1780–1786 (2014). <https://doi.org/10.1109/TBME.2014.2307069>
16. Kononenko, I., Šimec, E., Robnik-Šikonja, M.: Overcoming the myopia of inductive learning algorithms with RELIEFF. *Appl. Intell.* **7**(1), 39–55 (1997)
17. Kwapisz, J.R., Weiss, G.M., Moore, S.A.: Activity recognition using cell phone accelerometers. *SIGKDD Explor. Newsl.* **12**(2), 74–82 (2011). <https://doi.org/10.1145/1964897.1964918>
18. Lara, O.D., Labrador, M.A.: A survey on human activity recognition using wearable sensors. *IEEE Commun. Surv. Tutorials* **15**(3), 1192–1209 (2013)
19. Rassat, A., Fowler, P.W.: Is there a most chiral tetrahedron? *Chem. Eur. J.* **10**(24), 6575–6580. <https://doi.org/10.1002/chem.200400869>
20. Reyes-Ortiz, J.L., Oneto, L., Sam, A., Parra, X., Anguita, D.: Transition-aware human activity recognition using smartphones. *Neurocomputing* **171**, 754–767 (2016). <https://doi.org/https://doi.org/10.1016/j.neucom.2015.07.085>
21. Sigg, S., Blanke, U., Tröster, G.: The telepathic phone: frictionless activity recognition from WiFi-RSSI. In: 2014 IEEE International Conference on Pervasive Computing and Communications (PerCom). pp. 148–155 (2014). <https://doi.org/10.1109/PerCom.2014.6813955>
22. Ward, J.A., Lukowicz, P., Troster, G., Starner, T.E.: Activity recognition of assembly tasks using body-worn microphones and accelerometers. *IEEE Trans. Pattern Anal. Mach. Intell.* **28**(10), 1553–1567 (2006). <https://doi.org/10.1109/TPAMI.2006.197>

Chapter 20

Indoor-Outdoor Detection Using Head-Mounted Lightweight Sensors



Tommaso Martire, Payam Nazemzadeh, Alberto Sanna, and Diana Trojaniello

20.1 Introduction

The growth of technology has led to radical changes in everyday life [1]. An increasing number of people spend their workdays indoors under fluorescent lights or in front of computers and digital screens, while less time is devoted to outdoor activities. However, several factors such as the increased production of vitamin D [2], the improvement of mood and self-esteem [3, 4] as well as the reduction of the risk of developing myopia in children [5] and the increased level of physical activities associated to outdoor time [6] lead to the importance of spending more time outdoors. Therefore, monitoring the amount of time spent indoors and outdoors could inform about the health status of people. With the development of wearable technologies, the information of time spent indoors and outdoors may be easy to extract. In recent years, several mobile apps for indoor-outdoor (IO) detection have been developed using smartphones sensors data, i.e., ambient light, GPS, magnetometer, and accelerometer [7, 8]. Mobile apps utilize the recognized IO condition to automatically adjust volume and screen brightness, or trigger other services like GPS or Wi-Fi, and help the navigation system technology [7]. One of the major applications for the IO detection regards the seamless IO navigation and localization area [9]. However, the use of common lightweight smartphone sensors (e.g., ambient light, GPS, magnetometer) for the IO detection showed some limitations [10]: the ambient light intensity usually employed for IO detection [7–10] may not be always available (e.g., sensor is covered by pocket, clothes, etc.); the GPS signal power changes according to the environment, wall material, and

T. Martire · P. Nazemzadeh · A. Sanna · D. Trojaniello (✉)
Center for Advanced Technology in Health and Wellbeing, San Raffaele Hospital, Milan, Italy
e-mail: martire.tommaso@hsr.it; trojaniello.diana@hsr.it

weather condition; the magnetometer noise can be similar in indoor places and outdoor places near to the buildings.

The use of head-mounted smart wearable devices, such as glasses, virtual reality, and augmented reality devices and headphones, as well as the availability of new generation of light sensors (able to analyze separate components of light, i.e., RGB and XYZ light components) can overcome such limitations. Recently, a new head-mounted color light sensor (i.e., able to discriminate among the X, Y, and blue light components) has been proposed for IO detection [11]. In that study, the authors compared the performances of five different supervised machine learning algorithms (decision tree, logistic regression, k-NN, naïve Bayes, and random forest) in detecting IO condition using only the color light sensor. Although a good accuracy in IO detection (86.2%) has been found with one of the tested algorithms (i.e., random forest), the small sample number (five subjects) employed as test set as well as the low accuracy in presence of critical environments, i.e., semi-indoor and semi-outdoor, represent limitations.

Therefore, the aims of the present study are (a) to enlarge the test set by including the data acquired on 28 subjects; (b) to include the data acquired with additional lightweight sensors such as ultraviolet (UV) light, pressure, accelerometer, and gyroscope to increase both the overall and the critical environment-related accuracy; and (c) to compare the performances of the previously tested algorithms in IO detection. Two additional supervised machine learning algorithms (i.e., bagged trees and linear regression) have been included in the comparison.

20.2 Materials and Methods

Discriminating IO environments is essentially a classification problem in machine learning. In the present study, relevant features to discriminate between indoor and outdoor contexts derive from a combination of color light channels according to [12], features from UV sensor, pressure sensor, accelerometer, and gyroscope. In the following, the data acquisition system (see section “System Overview”) along with the data acquisition protocol (see section “Data Acquisition”) and the data analysis procedure (see section “Data Analysis”) has been reported.

System Overview

Data have been acquired using four lightweight sensors mounted on the forehead: color light “CL” sensor (AMS AS7264A), “UV” sensor (ALPS HSUDDD003A), an inertial measurement unit “IMU” featuring a triaxial accelerometer, and a triaxial gyroscope (ST LSM6DSL) and a pressure “P” sensor (TE MS5837). The CL sensor is a tristimulus sensor, which provides measurements of colors that closely match the human eye’s response to the visible light spectrum. The sensor also accurately

measures blue light wavelengths, which has been linked to important health effects such as disruption or management of the circadian rhythm, accelerated eye aging, and eye strain [13, 14]. The UV sensor is able to distinguish the UVA and UVB wavelengths of ultraviolet portion of the electromagnetic spectrum. The data have been acquired with different sampling frequency (sf) and acquisition settings (e.g., gain), according to the manufacturer specifications: CL sensor data have been acquired with $sf = 2$ Hz, integration time = 500 ms, and gain = 3.6; UV sensor data have been acquired with $sf = 5$ Hz and gain = 1; IMU and P sensors data have been acquired with $sf = 50$ Hz and $sf = 10$ Hz, respectively.

A tagging system (Sensor Log App), synchronized with the sensors data acquisition, has been used to provide the true classes (I/O).

Data Acquisition

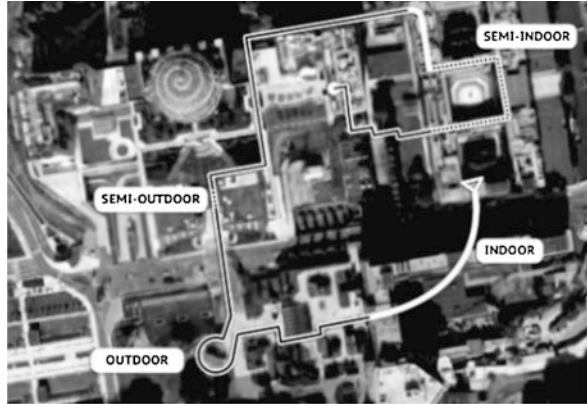
Training Dataset The training dataset (train-set) consisted of 3 h and 30 min of data acquired by the researchers in different places, weather conditions, and daytime hours around the city of Milan (Italy). Data acquired in different environments, e.g., metro, supermarket, outdoor market, garden, playground, offices, city center etc., have been included. Each sample of each sensor has been labeled as indoor or outdoor with the tagging system.

Testing Dataset Data from 28 different subjects have been acquired and used as test dataset (Test Set). Subjects (19 males and 9 females, 24 ± 3 years old) have been asked to follow a predesigned flow of activities in various environments (i.e., defined route) while wearing the sensors on the head. Acquisitions have been performed in different hours (from 09:00 to 16:30) and different weather conditions (sunny, cloudy, and variable). Researchers followed the subjects during the data acquisition and ensured the correct I/O tagging. The route traveled by the subjects (Fig. 20.1) was designed in order to cover different kinds of environments, i.e., indoor, outdoor, semi-indoor (i.e., environment with huge windows and massive exposed to outdoors sources of light), and semi-outdoor (i.e., environment close to or semi-opened building). The last two environments were defined according to [10]. Semi-indoor and semi-outdoor environments represent, respectively, indoor and outdoor “border” conditions (i.e., interesting for the classifiers performances evaluation). The total acquisition time of test set was more than 11 h.

Data Analysis

Six different classifiers (decision tree *DecTr*, bagged trees *BagTr*, logistic regression *LogRg*, linear regression *LinRg*, naïve Bayes *NaiBa*, and random forest *RanFo*) have

Fig. 20.1 Route traveled by the 28 subjects around the San Raffaele Hospital



been implemented. In the following, the feature extraction process and the classifier performances evaluation have been explained.

Feature Extraction In order to train and test the six chosen classifiers, train-set data were arranged in windows of 5 s, for a total of 2575 windows. The feature extraction procedure was based on [12] for the CL sensor and consisted in extracting virtual channels combining CL channel raw data, i.e., a total of nine virtual channels were then available. For the other sensors involved, only raw data were windowed. For each window, seven statistical parameters (i.e., mean, standard deviation, variance, root mean square, min, max, and range) have been computed. Therefore, the total number of features extracted was equal to 63 for the CL sensor, 14 for the UV sensor, 42 for the IMU (i.e., 21 for Acc, 21 for Gyr), and 7 for the P sensor. Then the features have been ranked according to the employed classifier and available sensor data using sorting methods (filter or ensemble [15]).

Classifier Performance After selecting the related number of features, each classifier has been trained with the entire train-set (2575 windows, 1372 indoor, and 1203 outdoor) and tested with the test set (8451 windows, 3162 indoor, and 5289 outdoor).

For each classifier, the number of features (*optimal features set*) allowing to reach the 99% of the maximum accuracy on test set has been computed considering only the data from CL sensor (CL_{test}). Then, using the optimal features set, each classifier has been trained and tested first involving data of CL sensor and UV ($CL|UV_{test}$) and then including the data from IMU and P sensors ($CL|UV|IMU|P_{test}$), considering only the first ranked number of features.

The confusion matrices of the best performing classifiers (containing all the raw information about the predictions done by a classification model on a given dataset [16]) have been computed.

20.3 Results

The *optimal feature set* size using only the CL sensor data was obtained considering the lowest amount of features that return 99% of maximum accuracy reached on test set. The number of features changed according to the classifier: 8 for *DecTr*, 15 for *BagTr*, 21 for *LogRg*, 50 for *LinRg*, 10 for *NaiBa*, and 14 for *RanFo*.

Table 20.1 shows the accuracy obtained on the overall test set (*ALL*: indoor, outdoor, semi-indoor, and semi-outdoor) and accuracies obtained in the critical environments (semi-indoor, S-I; and semi-outdoor, S-O) in the three tested configurations: (1) CL_test, (2) CL|UV_test, and (3) CL|UV|IMU|P_test. Results showed an increased accuracy in IO detection for all the classifiers, with the only exception of *LinRg*, by adding UV sensor data (CL|UV_test). Regarding the S-I and S-O environments, the inclusion of additional sensors (i.e., UV) decreases the accuracy in S-I and S-O detection. In particular, accuracy in detecting S-I environment decreases for four classifiers (*BagTr*, *LogRg*, *LinRg*, *NaiBa*) while accuracy in detecting S-O environment decreases for three classifiers (*DecTr*, *BagTr*, *RanFo*).

On the contrary, the inclusion of IMU and P sensors data seems to have no influence on the accuracy of none of the tested classifiers, as shown in Fig. 20.2.

The best classifiers in terms of overall accuracy are the *NaiBa* and *BagTr* that reached, respectively, 88.9% and 87.3% in CL|UV_test and CL|UV|IMU|P configurations. Confusion matrices for the CL|UV_test (i.e., the configuration including the less number of sensors) of the two classifiers are reported in Tables 20.2 and 20.3.

Table 20.1 Overall (ALL), semi-indoor (S-I), and semi-outdoor (S-O) accuracies characterizing different classifiers (class) in different test conditions (test): CL (including only CL sensor data), CL|UV (including CL and UV sensors data), and CL|UV|IMU|P (including CL, UV, IMU, P sensors data)

Class	Test								
	CL			CL UV			CL UV IMU P		
	ALL [%]	S-I [%]	S-O [%]	ALL [%]	S-I [%]	S-O [%]	ALL [%]	S-I [%]	S-O [%]
<i>DecTr</i>	85.6	84.4	6.8	86.0	88.4	4.9	86.0	88.4	4.9
<i>BagTr</i>	82.1	83.7	5.5	87.3	83.4	3.6	87.3	83.4	3.6
<i>LogRg</i>	67.2	66.5	8.3	78.2	27.7	99.2	78.2	27.7	99.2
<i>LinRg</i>	82.6	78.4	7.0	74.8	5.8	16.1	74.8	5.8	16.1
<i>NaiBa</i>	82.7	65.2	41.4	88.9	42.6	87.8	88.9	42.6	87.8
<i>RanFo</i>	84.4	83.2	7.0	86.1	83.6	4.7	86.1	83.6	4.7

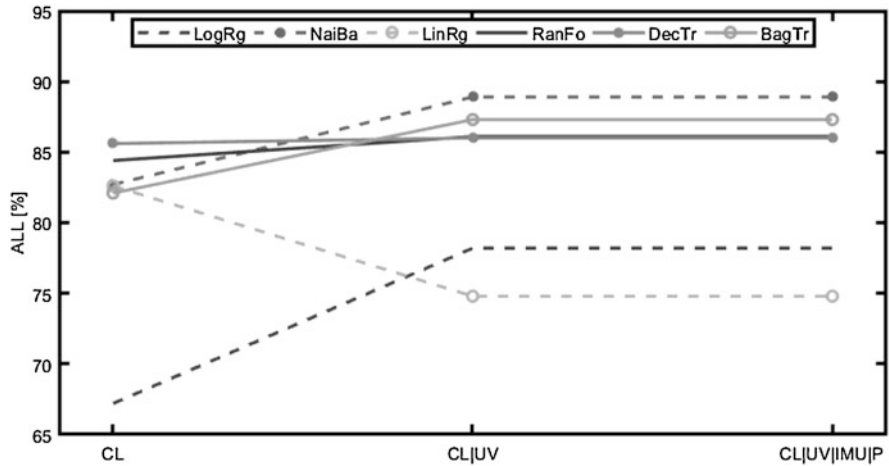


Fig. 20.2 Accuracy trend characterizing different classifiers in different test conditions

Table 20.2 Naïve Bayes confusion matrix applied on CL|UV test set

<i>NaiBa</i> (CL UV)	Predicted indoor	Predicted outdoor
True indoor	3039	123
True outdoor	813	4476

Table 20.3 Bagged trees confusion matrix applied on CL|UV test set

<i>BagTr</i> (CL UV)	Predicted indoor	Predicted outdoor
True indoor	2958	204
True outdoor	725	4564

20.4 Discussion

In this study, the performances of six different classifiers in detecting IO environments using lightweight sensors mounted on the head have been evaluated.

The importance of detecting IO condition relies on a number of factors including the possibility to monitor the health status of people (e.g., the amount of vitamin D absorbed during the day, when the subject is outdoor) and the possibility to trigger other important functions in smart devices (i.e., IO navigation in GPS-inhibited areas, when the subject is indoor). In this study, various environmental conditions have been included, i.e., indoor, outdoor, S-I, and S-O environments. In fact, similar environmental conditions characterize S-I/O and S-O/I environments. However, the erroneous detection of S-I (S-O) environment as O (I) environment affects the overall estimation of O (I) time spent during the day. Depending on the specific application, a greater accuracy in detecting S-I and S-O environments is requested, e.g., a greater accuracy in S-I detection for those applications requiring a most accurate O detection (e.g., preventing health conditions) and a greater accuracy in S-O detection for those ones requiring a most accurate I detection (e.g., IO navigation).

Overall, the results obtained in this study confirm those obtained in [11]: in fact, the random forest classifier showed an acceptable accuracy (84.4%) in the overall conditions with respect to other classifiers using only the CL sensors data (CL_test). However, the accuracy in S-O environments detection has been found not acceptable (7%). The main reason is that the visible light and, therefore, the CL measurements, characterizing S-O and indoor environments, are quite similar.

The UV sensor data added valuable information to the I/O detection, thus improving the accuracy of all the algorithms (with the exception of the linear regression one). This result is expected since the presence of UV light, especially during the day, strongly characterizes outdoor environments while is quite absent in indoor environments (i.e., windows shield the UV light) and S-O environments (i.e., the UV light is shielded from the roof), thus allowing a more reliable estimation of the IO condition. On the contrary, both IMU and P sensors did not increase the IO detection accuracy in none of the tested classifiers. This result is quite unexpected since the amount of dynamic activity (and thus the related signals as registered by IMU and P sensors) is expected to be greater outdoor (i.e., where the people generally walk, run, etc.) with respect to indoor (i.e., where the people generally sit, work, etc.). However, this result could be explained with the fact that the training dataset included a similar amount of activities (static and dynamic) performed both indoors and outdoors, and, therefore, the ranking of features didn't take into account data coming from IMU and P sensor (i.e., similar for both I/O).

In particular, by adding UV sensor data, as reported in Table 20.1, the bagged trees and the naïve Bayes showed very good performances in terms of IO detection accuracy, 87.3% and 88.9%, respectively (CL|UV_test). The accuracies obtained are in line with those obtained in other studies (71–92%) for similar applications [7–10]. However, in those studies, a higher number of sensors (i.e., all the smartphone sensors and GPS) have been employed.

Considering only the S-I and S-O environments, naïve Bayes outperformed other classifiers showing an acceptable level of accuracy for both S-I and S-O environments. On the contrary, bagged trees showed a very low accuracy (3.6%) in detecting S-O environments. Although a slight increase in the IO accuracy overall is shown by adding the UV sensors data (still less than the naïve Bayes accuracy), the random forest is still characterized by an unacceptable accuracy in S-O environments detection.

Therefore, considering also the low computational cost (i.e., required in wearable applications) characterizing the naïve Bayes, according to this study, the naïve Bayes could be considered as the best performing one in detecting IO environments (and critical environments) for wearable applications including both CL and UV sensors data.

20.5 Conclusion and Future Works

Understanding and monitoring the user's daily life context provide useful information about the user health status. The development of wearable technologies has led to the possibility to understand the context of the user. The present study consisted of a preliminary evaluation of the feasibility of using a single sensor (CL sensor) or a combination of sensors (CL, UV, IMU, and P sensors) for discriminating IO environments by applying an appropriate classifier.

The performances of six different supervised machine learning algorithms have been compared.

The highest accuracy (88.9%) was obtained with the naïve Bayes classifier trained with ten features considering both CL and UV sensors and thus identified as the most suitable solution for wearable applications.

Moreover, the problem concerning S-I and S-O spaces has been deepened. In fact, the accurate detection and monitoring of time spent in outdoor environments (including S-O spaces) is of great importance since it informs about aspects (i.e., reducing myopia risk, producing the correct amount of vitamin D, increase the level of physical activities) influencing the subject's health status.

In the future, more data in different seasons, times, and weather conditions are needed in order to ensure the reliability and robustness of the classifier.

Acknowledgments The research leading to these results has received funding from the European Union's Horizon 2020 research and innovation program under grant agreement No. 720571—I-SEE project.

References

1. Green, N.: On the move: technology, mobility and the meditation of social time and space. *Inf. Soc.* **18**(28), 281–292 (2002)
2. Webb, A.R., et al.: The role of sunlight exposure in determining the vitamin D status of the U.K. white adult population. *Br. J. Dermatol.* **163**(5), 1050–1055 (2010)
3. Barton, J.O., Pretty, J.: What is the best dose of nature and green exercise for improving mental health? A multi-study analysis. *Environ. Sci. Technol.* **44**(10), 3947–3955 (2010)
4. Mejia, R.: Green exercise may be good for your head. *Environ. Sci. Technol.* **44**(10), 3649–3649 (2010)
5. Rose, K.A., et al.: Outdoor activity reduces the prevalence of myopia in children. *Ophthalmology.* **115**(8), 1279–1285 (2008)
6. Cleland, V., et al.: A prospective examination of children's time spent outdoors, objectively measured physical activity and overweight. *Int. J. Obes.* **32**(11), 1685–1693 (2008)
7. Li, M.O., Zhou, P., Zheng, Y., Li, Z.: IODetector: a generic service for indoor/outdoor detection. *ACM Trans Sens. Netw.* **11**(2), 28 (2014)
8. Jia, H., Su, S., Kong, W.: MobilO: push the limit of indoor/outdoor detection through human's mobility traces. In: *International Conference on Indoor Positioning and Indoor Navigation*, pp. 197–202 (2014)
9. Urcola, P., Lorente, M.T., Villarroel, J.L., Montano, L.: Robust navigation and seamless localization for carlike robots in indoor-outdoor environments. *J. Field Rob.* **34**(4), 704–735 (2017)

10. Radu, V., Katsikouli, P., Sarkar, R., Marina, M.K.: A semi-supervised learning approach for robust indoor-outdoor detection with smartphones. In: 12th ACM Conference on Embedded Network Sensor Systems (2014)
11. Martire, T., Nazemzadeh, P., Cristiano, A., Sanna, A., Trojaniello, D.: Indoor-outdoor detection using head mounted color light sensors. In: National Congress on Bioengineering (2018)
12. Wahl, F., Kasbauer, J., Amft, O.: Computer screen use detection using smart eyeglasses. *Front. ICT*. **4**, 1–12 (2017)
13. Loperfido, F., Alessandro, M.: Exploring clinical evidence and the benefits off filtering out harmful light. In: *Points de Vue International Review of Ophthalmic Optic* (2016)
14. Lucas, R.J., et al.: Measuring and using light in the melanopsin age. *Trends Neurosci*. **37**(1), 1–9 (2014)
15. Hira, Z., Gillies, D.F.: A review of feature selection and feature extraction methods applied on microarray data. *Adv. Bioinforma*. **2015**, 1 (2015)
16. Caelen, O.: A Bayesian interpretation of the confusion matrix. *Ann. Math. Artif. Intell*. **81**(3–4), 429–450 (2017)

Chapter 21

Analysis of Walking Body Using Kinect2 and Application of Integer Code to WBAN



Hirohisa Kitahara , Hiroyoshi Morita , and Akiko Manada 

21.1 Introduction

A wireless body area network (WBAN), standardized by IEEE 802.15.16 or SmartBAN [3, 5], is a short-range human body communication technology proposed mainly for health-care or exercise. A WBAN is a kind of Wireless Sensor Networks (WSNs) in which the devices are placed in or on human bodies [11].

In typical WBAN applications, sensors in or on a human body transmit biological information (e.g., pulse, blood pressure, heart rate) to near medical equipment so that patients' conditions are constantly monitored. However, since the devices must be light and portable, they need to be driven by small batteries.

For designing WBANs, it is strongly demanded to consider communication schemes and devices suitable for power-saving and communication paths in the vicinity of human bodies. Moreover, the effects of human motions should be counted for practical analysis. Indeed, in the study of WBANs, there are many perspectives approaching these issues [11].

In this paper, we will clarify the influence of the temporal change of the body under the communication condition. To do so, we use Kinect2, which is a motion capture device, to measure walking motions. To design a WBAN system, we need to know changes in propagation characteristics caused by motions in daily life. However, the use of markers by a user for motion capture is not suitable for

H. Kitahara (✉) · H. Morita
Graduate School of Information Systems, The University of Electro-Communications,
Chofu, Tokyo, Japan
e-mail: k1462002@edu.cc.uec.ac.jp; morita@uec.ac.jp

A. Manada
Shonan Institute of Technology, Fujisawa, Kanagawa, Japan
e-mail: amanada@info.shonan-it.ac.jp

measuring such a motion. On the other hand, Kinect 2 does not require markers, which can be a great advantage compared with other existing studies. Furthermore, although we deal only with walking motions in this work, it is easy to extend the idea for other body motions because we only have to install the Kinect2 camera. Indeed, even though there are some examples of the construction of several posture models [4], such examples are not fully utilized despite of advantages of Kinect2. Thus, it will be a new approach of applications of Kinect2.

Based on the results derived from Kinect2, we also propose a use of integer codes as an appropriate error correcting code for WBANs. Integer codes are defined over the ring of integers modulo A , where A is a positive integer. Comparing with other linear codes including BCH codes, integer codes possess a remarkable advantage such that integer codes are suitable to correct nearest neighbor errors on various constellations, such as 8-PSK or m-QAM [8, 13]. In IEEE 802.15.6, BCH codes are adopted as error correcting codes for Differential Phase-Shift Keying (DPSK) such as D8PSK, but there is no sufficient discussion regarding why BCH codes are adopted. However, as for integer codes, a look-up table can be used for decoding due to their simplicity, and it is also possible to improve error correction performance by soft decoding. We therefore compare the Bit Error Rate (BER) of an integer code with that of an adopted BCH code to see an effectiveness of the integer code for WBANs.

The rest of the paper is organized as follows: In Sect. 21.2, we recall basic background regarding coding theory, especially integer codes. In Sect. 21.3, we extract a cycle of walking motions by Kinect2, and an electromagnetic field simulation model with time variation is created using the coordinates of each joint based on the measurement results. We then analyze this time-sequentially changing model to capture the temporal change of those transmission coefficients in a cycle of walking motions. After the review of encoding and simulation schemes in Sect. 21.4, we execute BER simulations in Sect. 21.5 in order to propose adoption of integer codes with WBANs, where BER simulations are performed based on the derived transmission coefficients. We terminate this paper with conclusions and future works in Sect. 21.6.

21.2 Basic Background on Coding Theory

Linear Codes

Let Σ be a finite alphabet. Suppose that $\Sigma = \mathbb{F}_q$; that is, a finite field of q elements. An (n, k, d) linear code C over \mathbb{F}_q is a linear subspace of \mathbb{F}_q^n with dimension k and minimum distance $d = \min_{\mathbf{c}, \mathbf{c}' \in C} d(\mathbf{c}, \mathbf{c}')$, where $d(\mathbf{c}, \mathbf{c}')$ is the distance between \mathbf{c} and \mathbf{c}' . Each (n, k, d) linear code C can be characterized by an $(n - k) \times n$ parity-check matrix H (of full-rank) in the form that

$$C = \{\mathbf{c} \in \mathbb{F}_q^n : \mathbf{c}H^T = \mathbf{0}\},$$

where H^T is the transpose of H and $\mathbf{0}$ is the all-0 vector.

Suppose that a codeword $\mathbf{c} \in C$ is transmitted and $\mathbf{r} = \mathbf{c} + \mathbf{e}$ (with some additive error \mathbf{e}) is received. One way to decode \mathbf{r} is to compute the *syndrome*

$$\mathbf{s} = \mathbf{r}H^T = (\mathbf{c} + \mathbf{e})H^T = \mathbf{e}H^T,$$

and find the simplest error \mathbf{e}' (a *coset leader*) satisfying $\mathbf{s} = \mathbf{e}'H^T$. Then

$$\hat{\mathbf{c}} = \mathbf{r} - \mathbf{e}'$$

is obtained as an estimated codeword.

A typical example of linear codes is *BCH codes* that can be defined by *generator polynomials* $G(X)$ (see, for example, [9]). Given a primitive element α of \mathbb{F}_{q^m} , consider the minimal polynomials $M_i(X)$ of α^i . Then the generator polynomial of an (n, k, d) BCH code (where $n \leq p^m - 1$) is given by

$$G(X) = \text{l.c.m.}(M_1(X), M_2(X), \dots, M_{d-1}(X)).$$

Integer Codes

An integer code is a code defined over the ring of integer modulo A , denoted by \mathbb{Z}_A [13]. More precisely, an integer code $C(H, \mathbf{d}) \subset \mathbb{Z}_A^n$ of length n , characterized by a parity-check matrix $H \in \mathbb{Z}_A^{m \times n}$ and $\mathbf{d} \in \mathbb{Z}_A^m$, is defined as

$$C(H, \mathbf{d}) = \{\mathbf{c} \in \mathbb{Z}_A^n \mid \mathbf{c}H^T = \mathbf{d} \pmod{A}\}. \quad (21.1)$$

When \mathbf{r} is received, integer codes can decode by searching the syndrome $\mathbf{r}H^T$ and corresponding coset leader from a look-up table, so integer codes can reduce computational complexity. Because of the simple decoding of integer codes, integer codes have been applied in such as 8-PSK, 16-QAM, 64-QAM, or 256-QAM constellation. In addition, receiver devices are able to use soft decoding to improve performance. In this paper, we focus on the 8-PSK constellation which will be discussed in the later sections.

21.3 Electromagnetic Simulation of Walking Motion

Measuring of Walking Motion Using Kinect2

Two Kinect2s are connected to two PCs, where a pair of a Kinect2 and a PC is called “Master” and the other pair is called “Slave,” and the results measured by the “Slave” node is transmitted via LAN and integrated in the “Master” node. The positional relation of Kinect2s is shown in Fig. 21.1.

Fig. 21.1 Positional relation of two Kinect2s

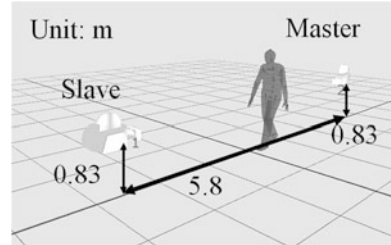
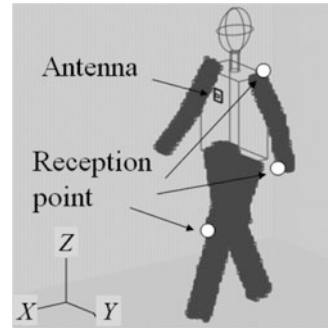


Fig. 21.2 Example of simulation model



Integrated data from Kinect2s is recorded using “iPi Recorder” by iPi Soft [7]. Recorded video data is then transformed into the coordinates of joints using “iPi MOCSP STUDIO” by iPi Soft [7].

Electromagnetic Simulation

The performance simulation is conducted using OpenFDTD, the Finite Difference Time-Domain (FDTD) method simulator released by EEM [2]. Simulated frequency is set to be 2.4 GHz of ISM band which is used for medical equipment. As for antenna analysis, given the wavelength λ , then it is recommended to set the side of one cell to be less than $(1/10)\lambda$ mm [10]. We therefore define 8 mm cubic cells since $\lambda = 125$ mm at 2.4 GHz.

An example of simulation model is depicted in Fig. 21.2 in which sensor nodes are installed on the left wrist, the left knee, and the left shoulder, and the coordinator node is installed on the chest. To simulate the motions of the model that are decomposed in time series, we use a time series of the 25 joint coordinates captured by Kinect2. Since the frame rate of the Kinect2 is 30 fps, we thin the obtained coordinate by a quarter of the time, so that our simulation model can be captured every $4/30$ s. In this model, the relative permittivity ϵ and the permeability μ of human body are set to be 35.194 and 1.13667 S/m, respectively, and these values are $2/3$ of human muscles at 2.4 GHz [6].

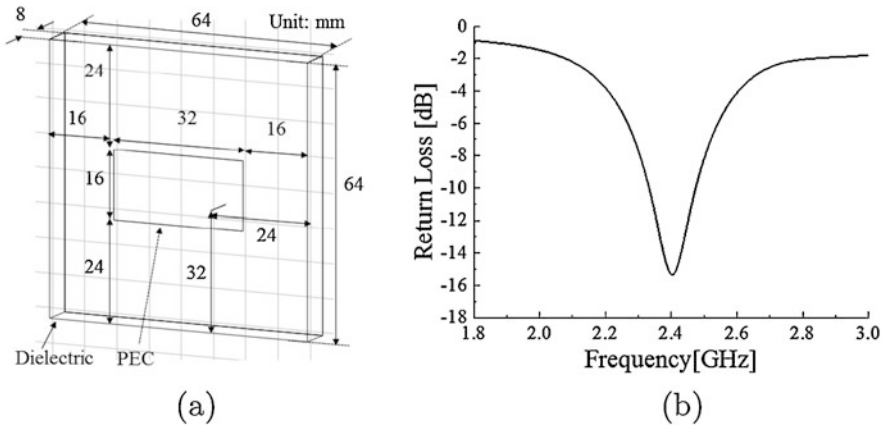


Fig. 21.3 Properties of patch antenna. (a) Antenna dimension. (b) Return loss characteristics

The size of the patch antenna is shown in Fig. 21.3a. The relative permittivity of the dielectric is 1.92 and Perfect Electric Conductor (PEC) is used for the patch antenna. Using this antenna model, we calculate the return loss R_L of this patch antenna, which is defined to be

$$R_L = 20 \log(V_1/V_0). \tag{21.2}$$

Thus, the return loss R_L represents the ratio of reflected voltage V_1 to incident voltage V_0 .

The return loss characteristics are shown in Fig. 21.3b. Since the return loss has the lowest value at 2.4 GHz, it is confirmed that this antenna can be used at 2.4 GHz.

Based on the electric field intensity E at each reception point in Fig. 21.2, the transmission coefficient S_{21} is derived. Here, we assume that half wavelength dipole antennae are placed at reception points. The electric field intensity E is transformed into the power flux-density [1], and then we can obtain the available power P_r [12, 14]. Since the feeding voltage V_t is an input to the transmission antenna, we transform P_r into the received voltage V_r as

$$V_r = \sqrt{50P_r} , \tag{21.3}$$

where characteristic impedance is 50 Ω . Therefore, S_{21} is given by

$$S_{21} = 20 \log(V_r/V_t). \tag{21.4}$$

21.4 Encoding Scheme and Simulation of Communication

In IEEE 802.15.6, double error correcting (63, 51) BCH code is proposed as an error correcting code. The generator polynomial $G(X)$ of the BCH code defined in IEEE 802.15.6 is given by

$$G(X) = 1 + X^3 + X^4 + X^5 + X^8 + X^{10} + X^{12}. \tag{21.5}$$

Recall from Sect. 21.2 that integer codes are codes defined over finite rings of integers, and look-up tables can be used for decoding. Therefore, we aim to consider integer codes as an appropriate coding scheme for power-saving WBAN systems, and compare the results of integer codes with the results of BCH codes. In our simulations, a (± 1) single error correcting integer code [8] of length $n = 3$ over \mathbb{Z}_8 whose parity-check matrix is $H = (1, 2, 3)$ is used for comparison. The code is originally used for 8PSK but we use it for D8PSK in this paper. Moreover, we used soft decoding to increase the error correction capability.

Figure 21.4 shows the block diagram for the BER simulation. First, an input random binary sequence is encoded by the BCH code or the integer code, and modulated into a complex signal. The complex signal is affected by the S_{21} calculated in previous section and noise. The resulting (noisy) complex signal is demodulated and decoded to a received sequence. Finally, the received sequence is compared with the input random sequence, and the number of positions at which errors occur is counted. The BER is calculated as

$$BER = \frac{\sum_{i=1}^{\ell} N_i}{\ell \times k}, \tag{21.6}$$

where ℓ is the number of simulations, N_i is the number of error positions in a received sequence at the i -th simulation, and k is the message bits size. In our simulation, $\ell = \lceil \frac{10^8}{51} \rceil$ for the BCH code and $\ell = \lceil \frac{10^8}{6} \rceil$ for the integer code, so that the number of transmission bits is greater than or equal to 10^8 .

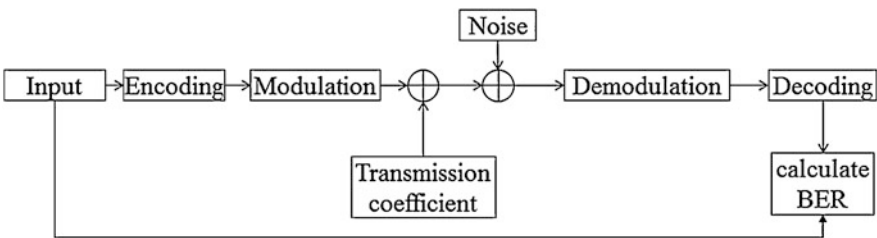


Fig. 21.4 Block diagram of BER simulation

21.5 Simulation Results

Figure 21.5a shows the electric field distribution (x - z plane) of the center of the body at $t = 1.2$ s. As is in the figure, the electric field is strongly radiated in front of the body and very weak in the back of the body. Figure 21.5b shows the S_{21} characteristics of three reception points during the walking motion. In the case of the left wrist, S_{21} takes the maximum value at 1.2 and 2.7 s. Then, the left arm is positioned in front of the body. That is, the left wrist is in the strong electric field as in the Fig. 21.5a. On the other hand, S_{21} takes the minimum value at around 2.0 s. Then, the left arm is positioned in the back of the body, where the electric field behind the body is very weak. In IEEE 802.15.6, a transmitter shall be capable of transmitting at most -10 dBm Effective Isotropic Radiated Power (EIRP) at 2.4 GHz. Furthermore, a receiver shall achieve receiver sensitivities from -92 to -83 dBm depending on the information data rate [5]. Therefore, in the case of the left wrist, the received signal level becomes lower than the reference value, momentarily.

Table 21.1 shows the maximum values, the minimum values, and the average values of each position. From Fig. 21.5b and Table 21.1, the value of the left shoulder is more stable than the others. There is the largest change in the S_{21} of the left wrist. The average of S_{21} of the left knee is same as the one of the left wrist. However, the change of the left knee is smaller than the left wrist due to the condition of the farthest and no interruption.

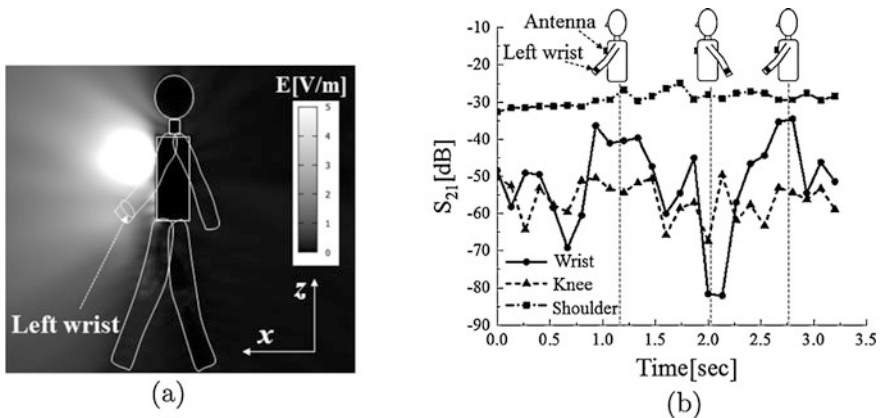


Fig. 21.5 The electromagnetic simulation result. (a) The electric field distribution (the center of the body, $t = 1.2$ s). (b) The transmission coefficient characteristics during walking

Table 21.1 Maximum, minimum and average value of S_{21} (unit: dB)

Position	Minimum	Maximum	Average
Left wrist	-82.1	-34.5	-42.7
Left knee	-67.5	-49.6	-54.1
Left shoulder	-32.6	-24.9	-28.7

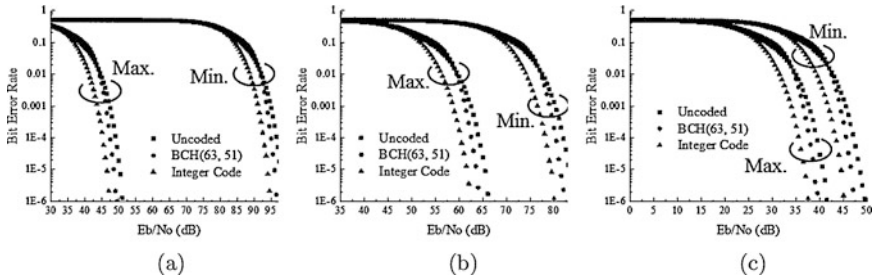


Fig. 21.6 The BER characteristics using D8PSK. (a) The left wrist. (b) The left knee. (c) The left shoulder

Next, we execute the BER simulation based on the attenuation in the Table 21.1 using D8PSK. The results of the BER simulation are depicted in Fig. 21.6a, b, and c. From these figures, we can observe that when the BER is 10^{-4} , the integer code produces about 2.2 dB of gain in SNR compared to the BCH code. In addition, it can also be confirmed that the integer code influences the BER performance at the smaller value of E_B/N_o compared to BCH code. For example, for Max. in the left wrist, the BCH code starts to influence the BER performance from around 45 dB, whereas the integer code does from around 37 dB.

21.6 Conclusion

In this paper, we analyzed the walking motion using two Kinect2s capturing the motion from the front and the back. We then obtained the transmission coefficients S_{21} for the walking model by the electromagnetic simulation using FDTD method. Using the obtained S_{21} as an attenuation, we next executed simulations on BERs for the (63, 51) BCH code and the integer code ($n = 3, H = (1, 2, 3), \mathbb{Z}_8$) for comparison. We confirmed that the integer code produces gains in SNR compared to the BCH code, which supports the efficiency of the index code.

As a future work, we will evaluate the cost difference of the index code by calculating the power consumption from the computational complexity, such as encoding methods and codeword lengths. We also aim to further evaluate the performance of the index code for a practical perspective by comparing with other effective error correcting codes, such as LDPC codes.

References

1. 525-1, C.R.: Calculation of free-space attenuation. Recommendations and Reports of the CCIR (V) (1991)

2. EEM: OPEN FDTD (in Japanese) (2018). <http://www.e-em.co.jp/OpenFDTD/index.html>
3. ETSI: Smart body area networks (2018). <http://www.etsi.org/technologies-clusters/technologies/smart-body-area-networks>
4. Fujie, A., Naganawa, J.-I., Kim, M., Aoyagi, T., Takada, J.-I.: Voxel model construction by kinect for propagation channel simulation. In: Proceedings of the 7th International Symposium on Medical Information and Communication Technology, pp. 164–168 (2013)
5. IEEE: IEEE 802.15.6 (2018). <http://www.ieee802.org/>
6. IFAC-CNR: Institute for applied physics, an internet resource for the calculation of the dielectric properties of the body tissues in the frequency range 10Hz-100GHz (2017). <http://niremf.ifac.cnr.it/tissprop/>
7. iPi Soft: ipi soft llc. (2018). <http://ipisoft.com/>
8. Kostadinov, H., Morita, H., Iijima, N., Vinck, A.J.H., Manev, N.: Soft decoding of integer codes and their application to coded modulation. *IEICE Trans. Fundam.* **E93-A**(7), 1363–1370 (2010)
9. Lin, S., Costello, D.J.: Error Control Coding: Fundamentals and Applications. Prentice Hall, Upper Saddle River (1983)
10. Qian, Y., Itoh, T.: FDTD Analysis and Design of Microwave Circuits and Antennas (Software and Applications). Realize, Noblesville (1999)
11. Shah, S.N., Jhaveri, R.H.: Recent research on wireless body area networks: a survey. *Int. J. Comput. Appl.* **142**(11), 42–48 (2016)
12. Stutzman, W.L., Thiele, G.A.: Antenna Theory and Design, 2nd edn. Wiley, Hoboken (1997)
13. Vinck, A.J.H., Morita, H.: Codes over the ring of integers modulo m . *IEICE Trans. Fundam.* **E81-A**, 2013–2018 (1998)
14. Yadava, R.L.: Antenna and Wave Propagation. Phi Learning, New Delhi (2011)

Part VI
Medical Applications

Chapter 22

InstantRR: Instantaneous Respiratory Rate Estimation on Context-Aware Mobile Devices



Md. Mahbubur Rahman, Ebrahim Nemati, Viswam Nathan,
and Jilong Kuang

22.1 Introduction

Chronic obstructive pulmonary disease (COPD) refers to a class of lung ailments that cause difficulty in breathing which progressively leads to serious complications, and it is the third leading cause of death in the USA [1]. According to the American Lung Association, more than 35 million people are living with chronic pulmonary diseases. The cost of pulmonary diseases in the USA is as high as \$154 billion per year with a 6% increase every year [2]. Early detection of lung worsening for chronic pulmonary patients would greatly reduce hospital readmissions, improve patient outcomes and their quality of life. Acute exacerbation is a severe pulmonary attack for a COPD patient which can lead to hospital readmission and elongated hospital stays up to 30 consecutive days [3]. This acute event can be predicted as early as 5 days before the attack [3], and taking the necessary medications and precautions could prevent it altogether.

The current mode of treating acute COPD exacerbation is predominantly reactive, with remedial steps being taken only after a serious adverse event. Sensing and monitoring using mobile devices such as smartphones and smartwatches in users' natural environment and applying machine learning techniques to predict exacerbation can transform the current paradigm from being reactive to proactive.

This work is motivated by the fact that respiratory rate is an important predictor for acute COPD exacerbation [3] and can reliably be measured in-home using ubiquitous consumer devices such as smartphones and smartwatches. By analyzing respiratory rate trends over several days, along with the blood oxygen saturation (SpO₂, which is also available on Samsung Galaxy smartphones [4]) can help

Md. M. Rahman (✉) · E. Nemati · V. Nathan · J. Kuang
Digital Health Lab, Samsung Research America, Mountain View, CA, USA
e-mail: m.rahman2@samsung.com; e.nemati@samsung.com

predict and prevent acute exacerbation. Previous research has shown the feasibility of estimating respiratory rate using low-cost accelerometers embedded in mobile devices [5, 6]. However, those approaches are not focused to handle chronic pulmonary patient conditions and are less resilient to varying contexts in a patient's natural environment such as conversation, coughing, and stressful conditions.

Currently chestbands are used for reliable respiratory measurements. However, the chestbands are uncomfortable and cumbersome [7], particularly for the COPD patients who are more likely to be among the elderly population [8], and are not as accessible as smartphones. Recent works have shown the promise of utilizing sensors such as accelerometer, gyroscope, photoplethysmograph (PPG) embedded in smartphones and smartwatches to extract physiological parameters such as heart rate [4]. Such examples include BioWatch [6], BioPhone [9], HeartSense [10], and SleepMonitor [11]. HeartSense [10] instantly measures heart rate using a smartphone held against the user's chest. Inspired by them, we present here a context-aware framework to instantly check respiratory rate, which is another important vital parameter for COPD patients, on the spot using commodity mobile devices. Our work enhances the patient's ability to measure respiratory rate using their smartphones or smartwatches anytime, anywhere.

In this paper, we present an approach which takes various patient conditions into account and finds the optimal trade-offs across sensing, analytical algorithms, and user contexts to estimate respiratory rate. We designed a study protocol focusing on pulmonary patient conditions in-home settings and collected carefully labeled inertial sensor data from 23 subjects using smartphones and smartwatches. We developed an automated device placement detection algorithm which can detect whether the device is placed on the chest or the abdomen with 97% accuracy using tenfold cross validation with a bagged decision tree model. Utilizing the device placement context and the other available context information, our approach represents a novel method for the optimal fusion among sensors and related algorithms to reliably estimate respiratory rate. We show that mean estimation error can be as low as 0.85 breaths per minute by applying a simple zero-crossing algorithm in the time domain on the Gyroscope X-axis data stream when the system automatically determines that the user placed the device against their abdomen in a supine position. Therefore, we can avoid using computationally intensive frequency domain algorithms for the same estimation. We further show that additional, more sophisticated processing steps such as using a Kalman filter can improve the average estimation accuracy by 21.31%.

22.2 Related Works

In this section we summarize some of the related works that have attempted to estimate respiratory parameters using mobile or wearable devices. One of the earliest notable works to use accelerometer data to estimate respiration rate did so by attaching the motion sensor to the chest [12]. This work provided valuable

results in terms of the feasibility of this approach, but was validated only for the sole scenario of a patient at rest in a supine position. BioWatch [6] and BioPhone [9] built on these efforts by estimating respiratory rate using a smartwatch worn on the wrist, and a smartphone placed in a pocket/bag respectively. These represent more convenient and feasible form factors for continuous sensing in daily life scenarios. While the algorithms from those works were tested for three different postures, there was no formal definition of a framework for context-aware sensing to handle any of the many possible variations such as speech activity and breathing pattern changes. Another work called SleepMonitor [11] also used a smartwatch worn on the wrist to calculate respiration rate using the motion sensors, but again this was optimized and validated exclusively for the scenario where the user is sleeping. Previous research has shown the potential of including context-awareness to improve activity recognition. For example, Nemati et al. utilized knowledge of the location of the device inside a house and knowledge of the user's current posture to improve accuracy of detection and reduce battery consumption [13, 14]. However, the contexts related to breathing measurement are different; these can include the placement of the device on the user's body, signal dampening due to heavy clothing or fat mass, motion artifacts, and the user's existing pulmonary conditions such as asthma or COPD to name a few.

The contribution of this work is a presentation of a framework that is purpose-built to handle the myriad of variations in device placement, user posture, user activity, user health condition, and so on in daily life scenarios in the real world to measure breathing rate using mobile devices. Previous works have shown the feasibility of using low-cost motion sensors already present in mobile devices to estimate respiratory rate, and in this work we formulate a framework to improve the robustness of these estimates by detecting and optimizing for variations in context.

22.3 Study Design and Data Collection

Study Description

To collect carefully labeled training data, we designed and conducted a pilot study with 23 healthy subjects. Participants were instructed to wear a Zephyr chestband [15] under their clothing (Fig. 22.1b) as a source of ground-truth signal, and wear a Samsung Gear S3 smartwatch on their left hand. They held a smartphone (Samsung Galaxy Note 5) on the left side of the chest and held the smartwatch on the abdomen as shown in the Fig. 22.1a. In that way, we capture breathing movement both from the chest and the abdomen. Moreover, each sample from the phone, watch, and the zephyr device were associated with Unix timestamp to aid subsequent synchronization.

Sensor Data

Raw sensor data includes 3-axis accelerometer (200 Hz), 3-axis gyroscope (200 Hz), 3-axis magnetometer (200 Hz), PPG (100 Hz), and audio (44.1 KHz). Derived sensor data includes oxygen saturation (SpO₂), 3-axis rotation, 3-axis orientation, and heart rate. In this paper, we focus on accelerometer and gyroscope data, with the incorporation of other sensing modalities for other applications left for future work.

Study Protocol

Our study protocol includes eight 1 min tasks, with the study coordinator marking the start and end of each activity session (Fig. 22.1c) using another smartphone. It must be noted that all the devices including the smartwatch and the chestband are synchronized before collecting data from each subject. The study coordinator explained the task to the participants before each task. Including instructions, the whole data collection duration ranges from 15 to 20 min.

1. Sit-Silent: breathing at a normal, regular pace while seated.
2. Supine-Silent: lying on the back, breathing at regular pace.
3. Sit-Read Out Loud: reading neutral sentences [16] for 1 min. These sentences are carefully chosen to avoid emotional stimuli inherent in the texts for this task.
4. Supine-Deliver Speech: perform free, undirected speech for 1 min on any non-private topic. The participants were given around 1 min for preparation and 1 min for the delivery. This session creates more cognitive load than the reading task,

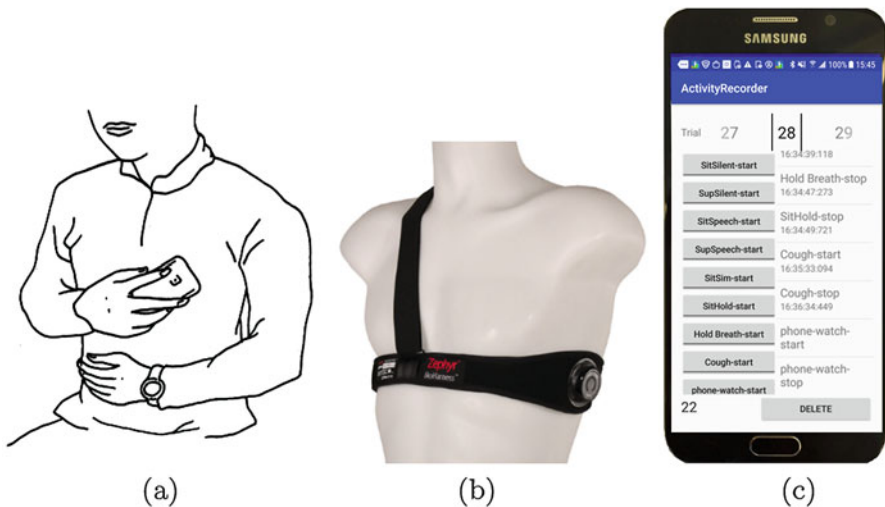


Fig. 22.1 Data collection setup. (a) Device placement. (b) Zephyr Bioharness3. (c) Data annotation

since it engages the memory and requires speech planning. Moreover, public speaking is a known stressor [17].

5. **Sit-Dirhythmic Breath:** Dirhythmic breathing is one of the important breathing characteristics of COPD patients. In our dataset, our subjects are instructed to simulate the first half (30 s) in one breathing pace (e.g., fast) and the second half in another breathing pace (e.g., slow).
6. **Sit-Breath Hold:** Within 1 min, the participant is requested to hold their breath for a few times.
7. **Sit-Cough:** Simulate at least three coughing episodes within a 1 min session.
8. **Sit-Silent-Phone-Watch:** Both phone and the watch are held on the chest, and data is collected while the participant is sitting in silence.

We included the sitting and supine postures since these are the most likely postures for COPD patients. The study coordinator annotated each session on a time synchronized smartphone. Task 6 and Task 8 are not collected for respiratory rate analysis, and will be reported in separate manuscript. Therefore, in this paper, we report the results on the remaining six tasks.

Data Collected

We have collected data from 23 healthy subjects including four females. The age range of the subjects is 20–40 years. Demographics include Caucasian, Pacific Islander, Middle Eastern, and Asian. The subject cohort did not include any individuals with reported breathing disorders for this initial pilot study.

22.4 Methods

System Overview

The overview of the context-aware respiratory rate estimation framework (Fig. 22.2) shows how the patient is taking the measurement and our approach finds the optimal fusion among contexts, sensors, and algorithms. Contexts can include user contexts such as health condition, posture and motion; device contexts such as placement whether it is on the chest, abdomen or somewhere else, and its orientation; social context such as conversation, and data context such as signal quality. Algorithms can include a set of data analytic steps with varying computation processing requirements. For example, frequency domain analysis can be more computationally intensive than time domain analysis. In this approach, if the current context indicates that applying simple time domain analysis on a single axis of accelerometer data is sufficient for reliable estimation, our approach will select that combination

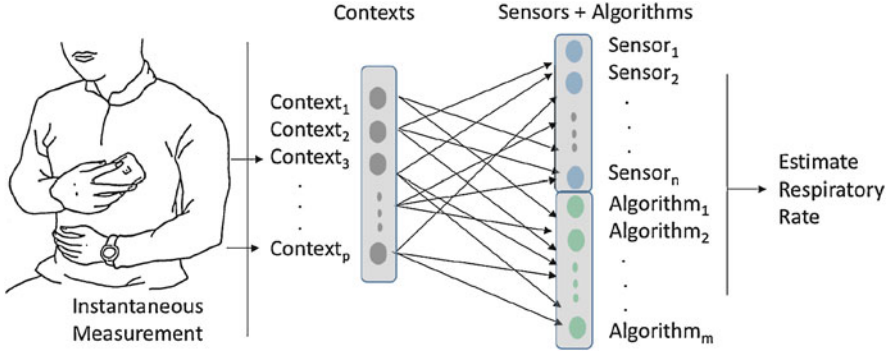


Fig. 22.2 Overview of the context-aware estimation framework for respiratory rate

and reduce the power consumption and processing cycles, while maintaining high estimation accuracy.

Given a set of algorithms $\mathbf{A} = \{A_1, A_2, \dots, A_m\}$, sensors $\mathbf{S} = \{S_1, S_2, \dots, S_n\}$ and contexts $\mathbf{C} = \{C_1, C_2, \dots, C_p\}$, we optimize the following equation based on training data:

$$(A_f, S_f) = \underset{A_i \in \mathbf{A}, S_i \in \mathbf{S}}{\operatorname{argmin}} \varepsilon(A_i, S_i) \mid C_d$$

Where, (A_f, S_f) is the final selection of algorithm and sensor pair, $\varepsilon(A_i, S_i)$ is the expected error w.r.t the ground truth estimate for algorithm and sensor pair (A_i, S_i) which is obtained from the training data, and C_d is the detected context among the set of contexts \mathbf{C} .

Data Analysis Pipeline

Data Preprocessing

In order to extract respiratory rate from a specific stream of sensor data (e.g., 20 s of accelerometer, or gyroscope, or their combinations), we perform several preprocessing steps. First, all the data streams are down-sampled to 100 Hz (to make it comparable with BioWatch [6]). We then compute the magnitude as $\sqrt{a_x^2 + a_y^2 + a_z^2}$. Since the magnitude data is independent of device orientation [7], we consider the magnitude as another source of data stream for analysis. We then detect the segments of the signal affected by the motion artifacts. Although our data collection setup includes only sitting and supine activities where movement is expected to be minimal, some spurious movement of the body parts (e.g., moving hands, or upper body) could create motion artifacts and affect data quality.

Therefore, we remove the motion artifacts for each session by discarding the samples outside of the range $[Q1 - 1.5 \times IQR, Q3 + 1.5 \times IQR]$, where IQR is the inter-quartile range, $Q1$ is the first quartile, and $Q3$ is the third quartile [18]. Removing the motion artifacts creates gaps in the data. If the gap is more than 50% of the time window, we discard the window. Otherwise, we use an auto-regressive time-series model to interpolate and fill the gaps while following the underlying pattern in the time-series signal.

Context Identification

Context information can include device placement (e.g., ribcage vs abdomen), user health condition (e.g., coughing), user posture (e.g., sitting), user social interaction (e.g., speech) among others. In this subsection, we describe how we can automatically detect device placement on user's body using machine learning algorithms. Here, we detect and distinguish device placements on the ribcage (chest) and the abdomen as a novel context for respiratory rate estimation. Other contexts such as speech detection, cough, posture can either be identified by other models (e.g., social interaction from [19] and cough from [20] or be derived from a smartphone's default health applications (e.g., posture information from Samsung Health app [4]).

- **On-body device placement:** To detect the device placement on the user's body, we used supervised classification techniques. We collected additional accelerometer and gyroscope data when the device is off-body (e.g., smartphone on-table which is the most likely placement of the device at home and at office [21, 22]). To measure reliable respiratory rate, the most suitable device placement is to place the device against the ribcage or the abdomen. Therefore, we develop a three-class classifier for ribcage, abdomen, and on-table (off-body) placement. Carefully labeled training data for ribcage and abdominal placement is used from the study described in Sect. 22.3. For this classification task, we use 3-axis accelerometer and 3-axis gyroscope data.

First, the sensor signals are filtered using a band-pass filter of the range from 0.13 to 2.5 Hz to include both the breathing motion and the heart motion as an indicator of on-body placement. This is because, when the device is placed on the ribcage, both the heart motion and breathing motion will be present. On the other hand, when the device is placed against the abdominal wall, breathing motion is more likely to be dominant because of heart motion dampening as the signal moves towards the abdomen. After signal normalization using z-score, we extract features from each session of the labeled data as described in 22.3.

To extract features, sensor data from each session is segmented into 5 s window with 50% overlap. We extracted features that are found to be discriminative for device placement detection on the user's body. For example, Incel [22] found that mean, variance, zero-crossing-rate, absolute difference in time domain, and the first 5-FFT coefficients and spectral energy in frequency domain, were the

most discriminative features for device position detection. Fujunami [23] found that the distribution of the frequency components, and correlations among axes are very useful to detect phone on-body. Moreover, since we are mostly interested in detecting ribcage and abdominal positions where the heart motion and lung motion are particularly important, we extracted bin features from the frequency component, by finding the sum of the frequency component in lower [0.1–0.66 Hz] and higher frequency bins [0.66–2.5 Hz]. In total, we extracted 75 features from both accelerometer and gyroscope data. One example scatter-plot for two of those features is shown in Fig. 22.3a.

We performed 3-class classification of the dataset using the MATLAB Machine Learning Toolbox [24]. Bagged Decision Tree model gives the best performance (97.2%) accuracy followed by Boosted Tree (94%), Linear Support Vector Machine (89.3%), and Weighted k-Nearest Neighbors (KNN) (88.4%) with tenfold cross validation. The confusion matrix for Bagged Decision Tree is shown in Fig. 22.3b.

- **Other Contexts:** Similarly, other contexts such as speech, cough, posture, patient condition can also be determined from the same set of sensors in use here. For example, we are identifying breathing motion from the motion artifacts Fig. 22.4a and detecting peaks and troughs of the breathing motion. Breathing motion can be used to detect speech and conversation [19]. The ratio between inhalation (temporal distance from trough to peak) and exhalation (temporal distance from peak to trough) is found to be one of the most discriminative features for speech cycle identification. Once the cycle is identified as speech, the current context can be determined as a social interaction. Cough can be detected using the microphone samples collected on the mobile device (e.g., smartphone) [20]. Posture and activity contexts are commonly available on a smartphone’s wellness monitoring ecosystems (e.g., Samsung Health [4]).

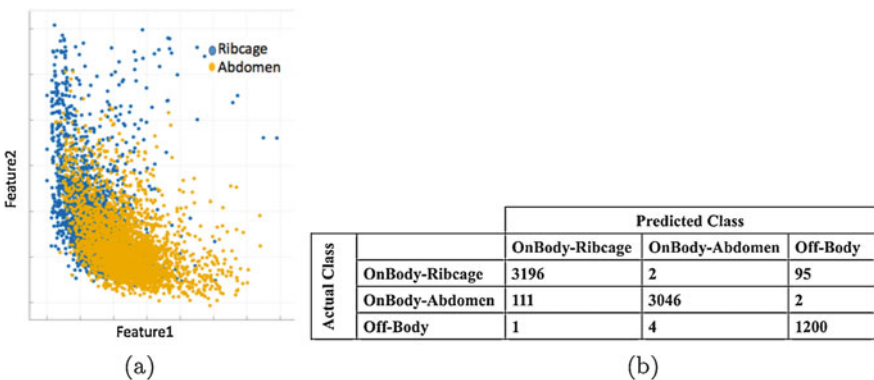


Fig. 22.3 Device placement detection. (a) Scatterplot for abdominal and ribcage placement. (b) Confusion matrix for Bagged Decision Tree

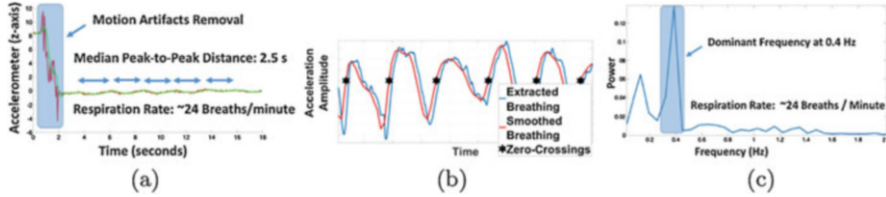


Fig. 22.4 Set of algorithms. (a) Peak detection method. (b) Zero-crossing method. (c) FFT-based method

Set of Respiratory Rate Estimation Algorithms

There can be several algorithms with varying computational requirements. For example, a zero-crossing based time domain algorithm can be much lighter than a Fast Fourier transform (FFT) based frequency domain approach. Moreover, if the sensor stream is unreliable, we may need more expensive filters (e.g., Total Variation Filter [11]) to extract the underlying signal from noisy sensor data. Therefore, for the purposes of this paper, we refer to an algorithm as a set of computation steps that can estimate the respiratory rate from sensor data. In the following, we describe three such algorithms to show that our approach can perform satisfactorily even with relatively basic algorithms. More sophisticated customization of the processing steps (e.g., adding Kalman filter as a post-processing step) inside those algorithms can further improve the performance of our approach. For instance, all of the tested algorithms show relatively higher mean absolute error (MAE) in the presence of Dirhythmic breathing and breath-holds; this can be improved by developing more sophisticated algorithms customized for those breathing patterns, and utilizing them when the corresponding context is detected.

Algorithm#1—Peak Detection Based Estimation in Time Domain One example of a time domain algorithm is shown in Fig. 22.4a. First the signal affected by movement artifacts (highlighted first 2 s) is removed, then the signal is normalized using z-score, segmented into 20 s windows with 50% overlap, and filtered using a band-pass filter of range 0.133 to 0.66 Hz corresponding to a respiratory rate ranging from 8 to 40 breaths per minute. Since breathing is a semi-voluntary physiological phenomena, the subject can hold breath at any time inside a breathing cycle, and there can be several candidate peaks that are not removed by the band-pass filter. Therefore, the signal is further smoothed using a 0.5 s time window to avoid spurious peaks in the breathing waveform. Finally, we use the rConverse [19] algorithm to detect respiratory peaks and compute the respiratory rate from the median peak-to-peak distances within each time window.

Algorithm#2—Zero-Crossing Based Estimation in Time Domain In a breathing cycle, inhalation is shorter in duration and a sharply upward-going signal compared to that of exhalation. Therefore, identifying the zero-crossing points of inhalation signal within a breathing cycle can be a robust way to estimate respiratory rate in

the time domain. Similar to Algorithm#1, we filter and smooth the signal. Then, we subtract the mean and identified zero-crossing points of the inhalation signal that crosses the zero line (Fig. 22.4b). Finally, we compute the respiratory rate from the median of temporal distances between zero-crossing points.

Algorithm#3—FFT-Based Estimation in Frequency Domain We first applied an averaging filter to each of the data streams (e.g., x -axis from accelerometer) independently. The size of the window was set to be the duration of a respiration cycle at a predefined maximum breathing rate of 40 breaths per minute, which enables removing the higher frequency cardiac motions. We then selected the component with the most periodic signal to become the final respiratory wave. In this case, the periodicity level was defined as the maximum amplitude observed within 0.13 and 0.66 Hz in the frequency domain (corresponding to 8 and 40 breaths per minute, respectively). Figure 22.4c shows one example of a maximum amplitude component under the highlighted box that determines the respiration rate for that period.

Respiratory Rate Estimation from Context-Aware Fusion

Our approach will first automatically detect current device context (e.g., device placement on the chest or the abdomen), then compute the optimal combination of the algorithms and sensor data streams to measure respiratory rate. In the training phase, our approach will apply all the available algorithms on all the relevant sensor data streams. Then, using the equation described in Sect. 22.4, it determines the best combination of sensor data and the algorithm that gives the least estimation error in the given context. Our current framework creates a mapping table (see Table 22.1) of algorithms and sensors data streams for each context. In the testing phase, our approach will first determine the context, and then perform a look-up of the mapping table to process a particular data stream and use the associated algorithm and sensor to estimate respiratory rate, rather than exhaustively computing all algorithms on all sensor data streams. For example, if the current context is that the device is on the chest and the user is sitting and having intermittent coughs, then, our approach will process only the accelerometer magnitude data stream and apply only the zero-crossing algorithm to estimate respiratory rate since this combination is expected to have the lowest estimation error according to the training data.

Kalman Filter for Enhanced Robustness

The availability of computational resources, the required latency for an estimate, and the required accuracy level of an estimate can all vary depending on the application scenario. In the event that there is room for offline analysis using more computational resources, the proposed framework can still accommodate more sophisticated algorithms to improve the robustness of the estimates. For instance,

Table 22.1 Fusion mapping table for algorithm and sensor fusion in various contexts

Placement	Posture	User contexts	Sensor data	Algorithm	MAE
Chest	Sitting	Silent	Accelerometer Y-axis	FFT-based	0.93
Chest	Supine	Silent	Gyroscope magnitude	FFT-based	1.53
Chest	Sitting	Speech	Gyroscope magnitude	FFT-based	2.47
Chest	Supine	Speech	Accelerometer magnitude	FFT-based	2.91
Chest	Sitting	Dirhythmic breaths	Accelerometer magnitude	FFT-based	4.82
Chest	Sitting	Coughing	Accelerometer magnitude	Zero-crossing	2.50
Abdomen	Sitting	Silent	Gyroscope X-axis	Zero-crossing	0.85
Abdomen	Supine	Silent	Accelerometer magnitude	Zero-crossing	1.59
Abdomen	Sitting	Speech	Gyroscope magnitude	FFT-based	3.98
Abdomen	Supine	Speech	Gyroscope X-axis	FFT-based	2.90
Abdomen	Sitting	Dirhythmic breaths	Gyroscope Z-axis	FFT-based	3.99
Abdomen	Sitting	Coughing	Gyroscope magnitude	FFT-based	1.67

This table shows what sensors and which algorithms are optimal for the given contexts. Here, FFT-based algorithm refers to Algorithm#3, and Zero-crossing algorithm indicates Algorithm#2 described in Sect. 22.4. Accelerometer and Gyroscope magnitude data is calculated from the combination of their three axes respectively. MAE refers to the mean absolute error with respect to the Zephyr ground-truth signal

we demonstrated that the use of a Kalman filter on top of the direct estimates of respiration rate from the accelerometer data can further reduce the estimation error. The prediction and update equations for the Kalman filter were defined as follows:

Prediction:

$$R'_t = R_{t-1}$$

$$P'_t = P_{t-1} + Q$$

Update:

$$k = \frac{P'_t}{P'_t + M}$$

$$R_t = R'_t + k(Z_t - R'_t)$$

$$P_t = (1 - k)P'_t$$

Where, R_t is the estimate of respiration rate at time t , P_t is the estimation error variance at time t , Q is the model error variance (set to be 4 BPM in this work), M is the measurement error variance (set to be 5 BPM in this work), k is the Kalman gain and Z_t is the measured respiration rate according to the sensor at time t . The fixed error variance values were chosen somewhat empirically based on observations of the dataset; however, there is room to increase sophistication here as well by learning

these values from training data and making them context-aware by modifying the expected error variance based on the current conditions; this is left for future work as it is not the focus of this initial presentation of the context-aware framework.

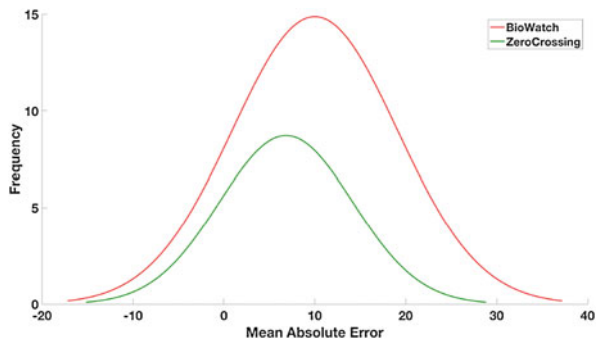
We found that the Kalman filter always improves the respiration rate estimation performance, with an average improvement of 21.31% across all tasks and subjects. A one-sided t-test showed this is a statistically significant improvement with p -value < 0.005 across all activities. This demonstrates another avenue for modularity, wherein the sophistication of the algorithm can be chosen based on the detected resources and requirements.

22.5 Results

We compare our approach with respect to the Zephyr ground-truth and an existing approach called BioWatch [6] as a baseline model. It must be noted that the BioWatch is a frequency domain analysis of sensor streams from 3-axis accelerometer and 3-axis gyroscope. Therefore, it involves processing all of the data streams to find the best accuracy. Whereas our approach will select only a few of them to estimate the respiratory rate and will use a less intensive time domain approach whenever appropriate. For example, Fig. 22.5 shows that the zero-crossing based time domain algorithm can outperform the more complex state-of-the-art BioWatch algorithm in more than 41% of the possible combinations in our dataset. It implies that deploying the zero-crossing algorithm in those cases will give more reliable estimates while it is more likely to reduce the CPU usage and battery consumption. This shows how context-awareness can help recognize situations wherein more efficient algorithms can be applied while still maintaining or even improving the accuracy of the estimates.

We observe that ‘Sit-silent’ has the best reliability for respiratory rate estimation across frequency and time domain algorithms for both the chest and abdominal placement (Fig. 22.6). ZCR algorithm (MAE = 0.85) performs better than the FFT algorithm (MAE = 0.93) on the Gyroscope X-axis sensor stream, illustrating the

Fig. 22.5 Error distribution comparison with BioWatch and with respect to the ground truth



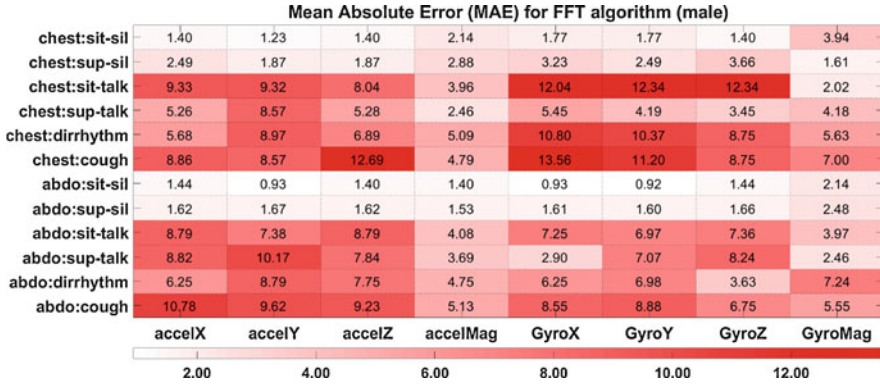


Fig. 22.6 Error variation across contexts for FFT algorithm with a male participant’s data. Each column indicates one sensor data stream and each row indicates one context. A deeper red hue indicates higher error

need for different algorithm and sensor combinations for different contexts. The presence of speech, cough, and Dirhythmic breathing in the other activities lead to increased error rates and warrant more sophisticated and customized algorithms than the ones explored in this initial study. However, the context-aware framework presented here can accommodate these additional algorithms or processing steps and utilize them when those challenging contexts are detected.

22.6 Discussion and Limitations

Although we presented a limited number of algorithms and a limited number of contexts in this paper, our framework can accommodate a myriad of other contexts and algorithms. Several of the contexts can be automatically determined. For example, we presented on-body device placement context detection using accelerometer and gyroscope. Self-reporting via user-prompt on a smartphone can be leveraged to determine unknown, undetermined contexts. For example, male and female users can have different sets of optimal algorithm and sensor combinations because of differences in body-shape. We can incorporate the information from self-reports and find the optimal fusion for each gender.

There are several advantages for context-aware estimation. First, the system becomes more reliable and can handle varying situations in real-life. Second, by smartly switching among the algorithms or computational steps, it can save processing power (CPU) and battery consumption for hand-held mobile devices where power and CPU cycles are in constant demand for other apps and communication. The system can deploy light-weight computational processing steps (e.g., time domain) on less power hungry sensors (e.g., accelerometer) when the contexts are

relatively easier and conducive for high quality estimation. Third, the user burden is alleviated by reducing the need for readjustment and re-measurement.

One limitation of the current study is the limited amount of data with a limited number of contexts. However, using post-processing steps such as Kalman filter can add enhanced robustness and give more reliable estimates in other unknown and more challenging situations. Moreover, in this paper, we tested the framework using three algorithms. More algorithms and their customizations could improve overall estimation accuracy further.

Another limitation of the current study is that we collected data from a limited number of healthy subjects who simulated the pulmonary symptoms such as cough, Dirhythmic breathing in a controlled experiment setting. In the future, we will recruit COPD patients with varying levels of severity and collect data in more natural settings to validate our approach.

22.7 Conclusion and Future Works

We present a novel approach of estimating respiratory rate using inertial sensor data from consumer mobile devices by finding the optimal combination of sensors and algorithms for each underlying context which can also be automatically detected by the same sensor data. For automatic context identification, we used a Bagged Decision Tree on accelerometer and gyroscope data to determine whether the device is placed on the chest or the abdomen with 97% accuracy using tenfold cross validation. We show that mean estimation error can be as low as 0.85 breaths per minute by applying a simple zero-crossing algorithm in time domain on Gyroscope X-axis data when the system determines that the user has placed the device against the abdomen in the supine posture. Therefore, we can avoid computationally intensive frequency domain algorithms and unnecessary analysis of other sensor data. We further show that additional sophisticated processing steps such as using a Kalman filter can improve average estimation accuracy by 21.31% on average. Although we developed our context-aware approach focusing on respiratory rate estimation, it can further be extended for other physiological parameter estimation in future, such as heart rate, which also varies across contexts.

References

1. American Lung Association. How Serious is COPD. <http://www.lung.org/lung-health-and-diseases/lung-disease-lookup/copd/learn-about-copd/how-serious-is-copd.html>. Accessed 21 May 2018
2. <https://lunginstitute.com/blog/the-cost-of-lung-disease/>. Accessed 6 June 2018
3. Burge, S., Wedzicha, J.A.: COPD exacerbations: definitions and classifications. *Eur. Respir. J.* **41**, 46s–53s (2003)
4. <https://www.samsung.com/us/support/answer/ANS00062448/>. Accessed 6 June 2018

5. Bates, A., Ling, M.J., Mann, J., Arvind, D.K.: Respiratory rate and flow waveform estimation from tri-axial accelerometer data. In: IEEE Body Sensor Networks (BSN) (2010)
6. Hernandez, J., McDuff, D., Picard, R.W.: Biowatch: estimation of heart and breathing rates from wrist motions. In: Pervasive Computing Technologies for Healthcare (2015)
7. Rahman, M.M., Bari, R., Ali, A.A., et al.: Are we there yet?: Feasibility of continuous stress assessment via wireless physiological sensors. In: ACM Conference on Bioinformatics, Computational Biology, and Health Informatics (2014)
8. <https://www.healthline.com/health/copd/age-of-onset#onset>. Accessed 6 June 2018
9. Hernandez, J., McDuff, D.J., Picard, R.W.: Biophone: physiology monitoring from peripheral smartphone motions. In: IEEE Engineering in Medicine and Biology Society (EMBC) (2015)
10. Mohamed, R., Youssef, M.: HeartSense: ubiquitous accurate multi-modal fusion-based heart rate estimation using smartphones. In: ACM Interactive, Mobile, Wearable and Ubiquitous Technologies (IMWUT) (2017)
11. Sun, X., Qiu, L., Wu, Y., Tang, Y., Cao, G.: SleepMonitor: monitoring respiratory rate and body position during sleep using smartwatch. In: ACM Interactive, Mobile, Wearable and Ubiquitous Technologies (IMWUT) (2017)
12. Bates, A., Ling, M.J., Mann, J., Arvind, D.K.: Respiratory rate and flow waveform estimation from tri-axial accelerometer data. In: IEEE Body Sensor Networks (BSN) (2010)
13. Nemat, E., Sideris, K., Kalantarian, H., Sarrafzadeh, M.: A dynamic data source selection system for smartwatch platform. In: IEEE Engineering in Medicine and Biology Society (EMBC) (2016)
14. Pourhomayoun, M., Nemat, E., Mortazavi, B. and Sarrafzadeh, M.: Context-aware data analytics for activity recognition. In: Data Analytics (2015)
15. Zephyr HomePage. <http://www.zephyranywhere.com/>. Accessed 17 May 2018
16. Sheikh, N., Titone, D.: Sensorimotor and linguistic information attenuate emotional word processing benefits: an eye-movement study. *Emotion* **13**(6), 1107 (2013)
17. Feldman, P., Cohen, S., Hamrick, N. and Lepore, S.: Psychological stress, appraisal, emotion and cardiovascular response in a public speaking task. *Psychol. Health* **19**(3), 353–368 (2004)
18. Rahman, M., Ali, A., Plarre, K., Al’Absi, M., Ertin, E., Kumar, S.: mconverse: inferring conversation episodes from respiratory measurements collected in the field. In: ACM Wireless Health (2011)
19. Bari, R., Adams, R.J., Rahman, M.M., Parsons, M.B., Buder, E.H., Kumar, S.: rConverse: moment by moment conversation detection using a mobile respiration sensor. In: ACM Interactive, Mobile, Wearable and Ubiquitous Technologies (IMWUT) (2018)
20. Sun, X., Lu, Z., Hu, W., Cao, G.: SymDetector: detecting sound-related respiratory symptoms using smartphones. In: ACM Ubiquitous Computing (2015)
21. Wiese, J., Saponas, T.S., Brush, A.J.: Phoneprioception: enabling mobile phones to infer where they are kept. In: ACM SIGCHI (2013)
22. Incel, O.D.: Analysis of movement, orientation and rotation-based sensing for phone placement recognition. *Sensors* **15**(10), 25474–25506 (2015)
23. Fujinami, K.: On-body smartphone localization with an accelerometer. *Information* **7**(2), 21 (2016)
24. <https://www.mathworks.com/products/statistics.html>. Accessed 6 June 2018

Chapter 23

Pre-Ejection Period (PEP) Estimation Based on R-Wave in ECG and On-Body Continuous Wave Radar Signal During Daily Activities



Malikah Pour Ebrahim, Fatemeh Heydari, Jean-Michel Redouté, and Mehmet Rasit Yuce

23.1 Introduction

The pre-ejection period (PEP) (a systolic time interval) is one of the important parameters to monitor cardiac activities noninvasively. The PEP is the time interval between the Q-wave of electrocardiogram (ECG) (ventricular depolarization onset) and the initial point of ejection of blood from the left ventricle (the opening of the aortic valve). The PEP illustrates an electrical-mechanical delay from the commencement of depolarization and the beginning of ventricular contraction. The PEP represents the duration of electrical and mechanical activities duration prior to ejection [1].

A common way to obtain the PEP is measuring the latency between the B-point of the impedance cardiogram (ICG) (reflects the opening of the aortic valve) and the Q-wave onset of the ECG. An accurate calculation for the PEP can also be done by measuring the time interval between the R-wave peak of the ECG signal and the minimum point of dZ/dt of the ICG signal. This time interval which is the initial systolic time interval (ISTI), is a remarkable predictor for the real PEP. As a result, the PEP is calculated as a fixed QR interval added to the estimated ISTI [2, 3]. [2, 3] demonstrated that the QR interval is fixed for both laboratory and ambulatory conditions. A new detection method was also discussed in [4] to improve the dZ/dt B-point measurement. A major limitation of the existing techniques is the high sensitivity to noise and artifacts.

M. Pour Ebrahim · F. Heydari · J.-M. Redouté · M. R. Yuce (✉)
Department of Electrical and Computer Systems Engineering, Monash University, Melbourne, VIC, Australia
e-mail: Fatemeh.heydari@monash.edu; Jean-Michel.Redoute@monash.edu; mehmet.yuce@monash.edu

A comparison between measurements of the PEP obtained from pulsed Doppler echocardiography and ICG is presented in [5]. A comparison was done between beat-to-beat ICG-based calculation of PEP and monitoring the ascending aorta using echocardiography for two different positions, supine and tilting. The PEP from echocardiography was noticeably lower than the ICG-based PEP for both positions. The variance of ICG-based PEP for the supine position was higher than the one from echocardiography [5].

The work [6] presents a method to record the electrical and mechanical activity of the human heart simultaneously using ECG and ultra-wideband (UWB) radar technology. The study demonstrates that the sharp edge of the UWB signal, which represents the starting of ventricular ejection phase, happens after complete ventricles electrical excitation.

A radiofrequency (RF) continuous wave radar (CWR) using body-contact antennas has been used to monitor the diastolic and systolic activities of heart. In our previous work [7], the combination of the antenna location on body and phase recovery methods have been investigated to indicate the most reproducible CWR signal. It was detected that best placement for antennas is at the sternum. In [8], by placing radar antennas at the sternum, it was discovered that the features in CWR signals, i.e., the foot of signal will be the closest to the ICG B-point.

Postural effects on the PEP have been examined in few studies. In [9] a combination of postural changes (supine, sitting, and standing) with paced breathing at three different frequencies, is presented to validate ICG as a means to measure the PEP. In [3], the validity of the PEP computed for different laboratory and ambulatory experiments were evaluated. The experiments included a variety of posture and physical activities.

In the current study, we evaluate our CWR sensors to measure the PEP in various experiments, including different postures and exercise activities. Normal daily activities have been considered, and the study validates that CWR sensors can track the PEP changes in ambulatory situations.

23.2 Methods and Materials

Monitoring Setup

The used CWR system (see Fig. 23.1) includes two transmitter and receiver parts to record the mechanical activities of the heart. The transmitter part sends a radio frequency signal $T_{cw}(t)$ described by (23.1) through the body using a transmitter antenna as on-body sensor. The received signal $R_{cw}(t)$ as described by (23.2) which passes the receiver antenna, contains the distance d and organ movement $m(t)$ information in its phase. A mixer is used to derive the information from the received signal and a demodulator is adopted to convert them to in-phase (I) and quadrature (Q) components as Eqs. (23.3) and (23.4).

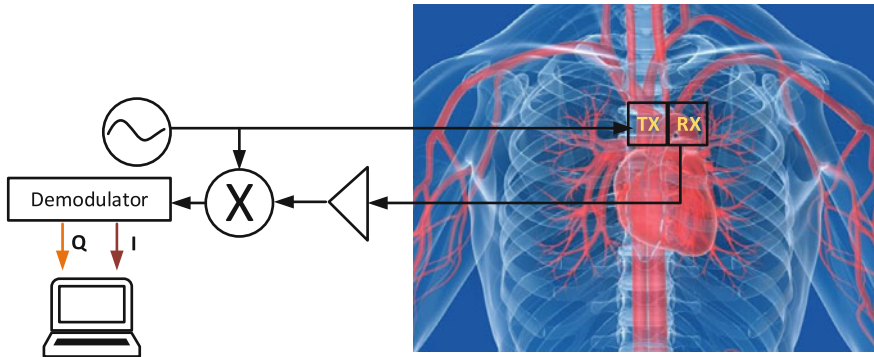


Fig. 23.1 The CWR system and the location of the sensor. (Source: taringa.net)

$$T_{cw}(t) = E_T \cos (\omega t + \varphi) \tag{23.1}$$

$$R_{cw}(t) = E_R \cos (\omega t - \omega_0 (d + m(t)) + \theta) \tag{23.2}$$

$$I(t) \approx \sin (\omega_0 m(t) + \theta_0) \tag{23.3}$$

$$Q(t) \approx \cos (\omega_0 m(t) + \theta_0) \tag{23.4}$$

In the equations, φ is the phase noise of the system, θ is mix of system, and environment noise and θ_0 is a combination of all the noises.

Our previous study [7] shows that the radar signal is most reproducible at the sternum; therefore, the aortic arch was selected as the approximate location for the antennas (see Fig. 23.1). The foot of CWR signal, comparing to the ICG B-point, is validated to correspond to the opening of the aortic valve [8].

Experimental Protocol

Forty-three healthy volunteers aged 40 ± 15 years old, 168 ± 10 cm height, and 60 ± 16 kg weight, 52% male and 48% female, participated in the experiments. None of them reported any cardiovascular problems. The data collection was done at the Cabrini Hospital, Melbourne, Australia, and an emergency physician accompanied the subjects during the tests. ECG and CWR signals were measured simultaneously, and the data from 40 participants was considered.¹ The experiments

¹The CWR data from three subjects was corrupted during signal recording and was omitted for this work.

were done in two sessions. For session one, all volunteers participated, and 23 subjects among them were selected randomly to take part in session two. All subjects were asked to breathe normally during tests.

Session one contained measuring all signals for three different postures, 6 min of sitting, 6 min of standing, and 6 min in the supine position. Session two was as follows:

1. Holding handgrip for 2 min following by 1 min rest
2. Cycling with fixed speed in three different bike-resistant settings as light, moderate, and heavy, each one for 2 min followed by 1 min rest
3. Two recovery stages after the cycling tasks, which the subjects sit on the bike without any activity, signals were recorded for 3 min for each one

Signal Processing and Data Analyzing

The ECG and CWR signals of all participants were recorded. At first, high-pass and low-pass filters (Chebyshev type II) were applied to eliminate the 50 Hz components and other unknown noise and artifacts. The cut-off frequencies of the filters were selected to remove respiration components as well. The cut-off frequencies of the filters were chosen subject to derive their accurate heart rate; therefore, each subject's cut-off frequency is different.

After filtering, the location of the ECG R-peak was recognized, and the boundaries of each heartbeat were measured. As mentioned previously, the foot of CWR signal, comparing to the ICG B-point, is validated to correspond to the opening of the aortic valve, which can be used to measure the PEP. Therefore, the location of the CWR signal's foot was detected as PEP using the minimum of the second derivation for each corresponding beat.

Since there were two signals (I and Q) as the outputs of the radar sensor, the polarity of these signals was detected, and then their feet were calculated. The foot of arctangent of Q/I as Eq. (23.5) was also calculated. At last, a comparison was done between the detected radar signals to select the best result. Figure 23.2 illustrates the block diagram of the signal processing protocol.

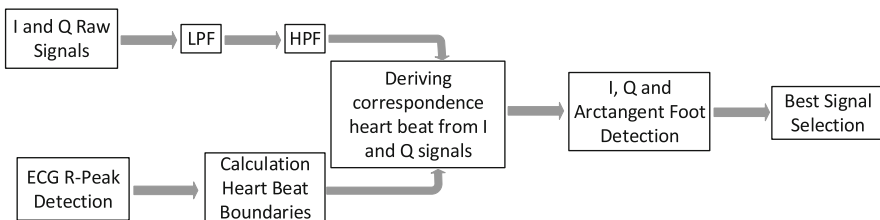


Fig. 23.2 Signal processing block diagram

$$\varphi(t) = \tan^{-1} Q(t)/I(t) = \omega_0 m(t) + \theta_0 \tag{23.5}$$

In [2, 3], it was shown that a fixed value for the QR intervals can be assumed. This fixed interval was 39 ms in their stationary conditions and 42 ms in the ambulatory study.

Figure 23.3a shows a sample beat of the ECG and CWR signals and also the QR interval for ECG. Since the QRs are assumed fixed, we initially calculate PEP just as the interval between ECG R-Peak and CWR foot. Then, we add the fixed value of QR interval. An example of ECG, I , and Q signals is shown in Fig. 23.3b. The foot of the CWR signal is indicated as point t .

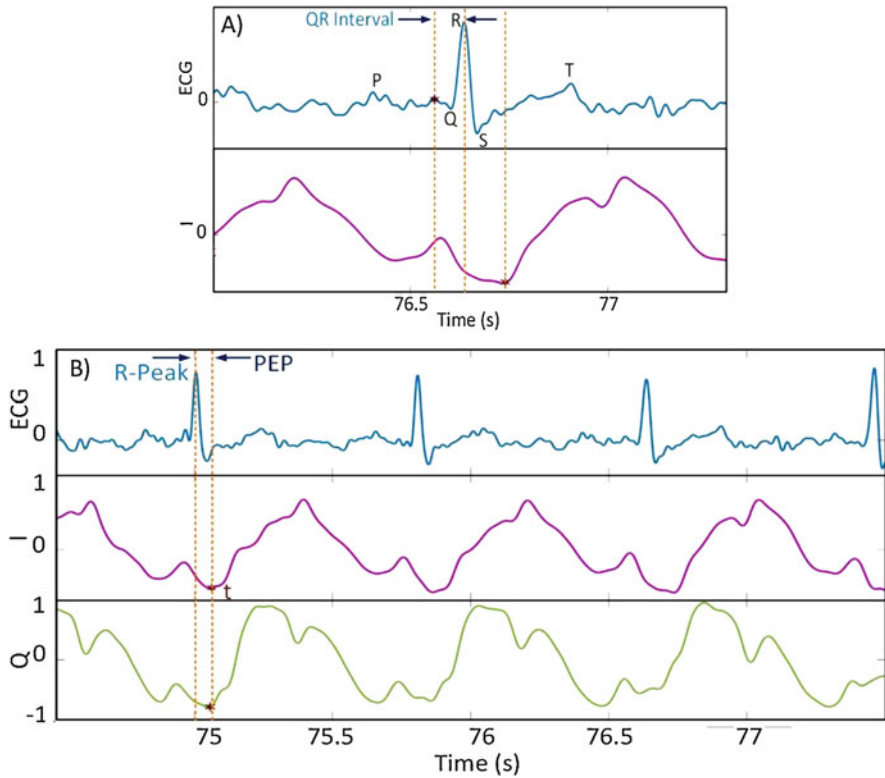


Fig. 23.3 An example of collected signals, (a) one sample heartbeat and related QR interval, (b) sample of ECG, I , and Q signals. The R-peak and t points (foot) of CWR signals were shown for one beat

23.3 Results

Two box plots are illustrated in Fig. 23.4 showing the median values of the PEP in our study for two different sessions of tests based on the measurements of each session's related population.

The bar charts of mean values and standard deviations (SD) for three different positions are shown in Fig. 23.5. The results show that the lowest PEP value (mean 47.24 ms) is obtained in supine posture and the highest PEP (mean 66.22 ms) is obtained in the standing situation. The PEP for sitting position (mean 64.8 ms) is between these two measurements; however, it is closer to standing.

Figure 23.6 indicates the bar charts of mean values and SDs for six different exercise tasks. The mean values of exercise tasks are as follows: handgrip 60.94, light exercise 55.56, moderate exercise 52.37, heavy exercise 47.96, recovery 1 59.42, and recovery 2 53.8. Comparing the results of three different stages of cycling

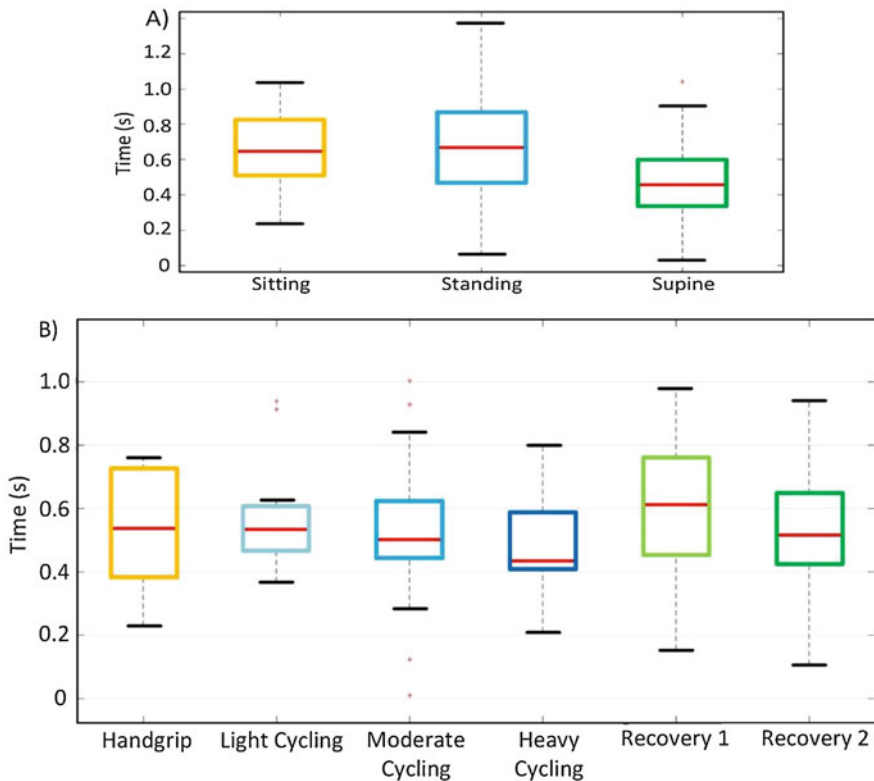


Fig. 23.4 Box plots of PEP median values for all participants, (a) three different positions: sitting, standing, and supine, (b) six different tasks of exercise session included handgrip, light cycling, moderate cycling, heavy cycling, and two recoveries

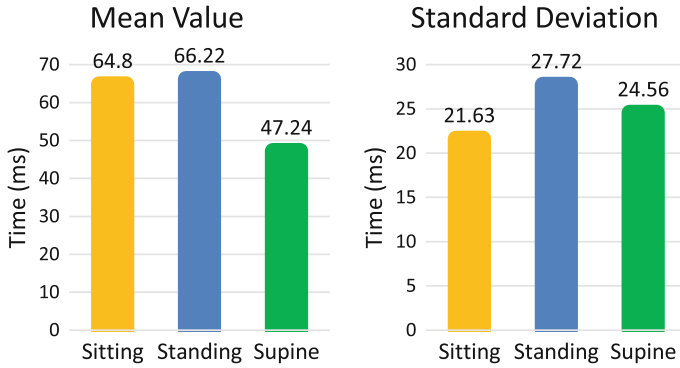


Fig. 23.5 The mean values and SDs measured for all population for three different positions: sitting, standing, and supine

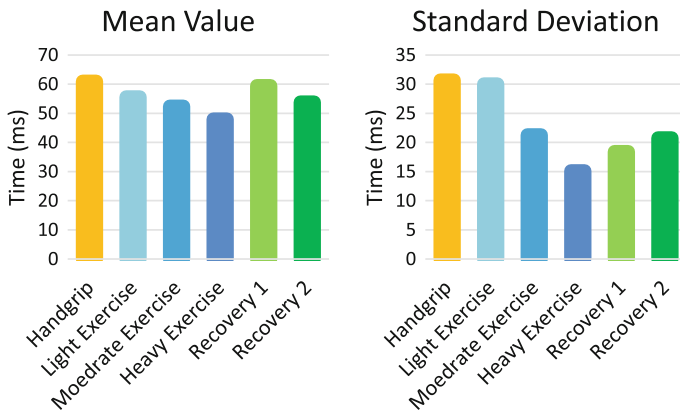


Fig. 23.6 The mean values and SDs measured for 23 subjects for six different exercise tasks: handgrip, light, medium and heavy cycling, and recovery 1 and 2

exercise shows a negative trend between the strength of activities and measured PEPs.

The means and SDs for the PEP for different postures and exercise conditions are presented in Table 23.1. The table also gives a comparison between the measured PEP from CWR signals and the results of using ICG B-point based on [3]. It should be considered that the experiments' conditions are not exactly the same as [3]. Accordingly, the measured PEPs are different; similar trends are expected related to postures and exercise tasks.

Table 23.1 The means and SDs for PEP measured for different experimental conditions

Experimental conditions	PEP (ICG_R-peak—CWR_foot) Mean (SD) (ms)	PEP [3], included QR mean (SD) (ms)
Sitting	64.80 (21.63)	108 (18)
Standing	66.22 (27.72)	117 (16)
Supine	47.24 (24.56)	95 (19)
Handgrip	60.94 (30.67)	112 (17)
Light cycling	55.56 (30.00)	115 (17)
Moderate cycling	52.37 (21.27)	77 (20)
Heavy cycling	47.96 (15.10)	66 (17)
Recovery 1	59.42 (18.40)	90 (25)
Recovery 2	53.80 (20.75)	NA

23.4 Discussion and Conclusions

A comparison between PEP measurements obtained for different daily activities has been studied in this work. The results show that not only changes in position but also different body activities influence the PEP measurement. The calculated means and SDs follow the trends which ICG results show in previous studies. The measured PEPs based on R-peak to CWR foot intervals which do not include the QR intervals demonstrate reasonable values when compared with the derived PEPs from Q onset to B-point of ICG signals.

The values of PEPs in recovery sessions show that although the body position and subject activity are the same for both, there is a change in the measured PEP. This leads to the fact that the PEP is not related just to the body position or activities but, there are other factors such as heart rate affecting this time interval.

Since there is a difference between measured PEP from CWR signals and the ones obtained with ICG, a future validation of CWR signals with echocardiography with the gold standard is required to have an accurate and reliable measurement for CWR-based PEP to be utilized in medical applications.

Acknowledgments The authors would like to thank Dr. D. Buxi, as well as previous members of the Biomedical Integrated Circuits and Sensors (BICS) Laboratory, Monash University, for preparing the prototype for data collections. The authors would like to thank Keith Joe and Katie Walker from Cabrini Health for the data collection obtained for a medical monitoring project and all participants for their collaboration as human subjects.

This work is supported in part by an ARC Linkage Project (LP160101823). M. R. Yuce's work is supported by Australian Research Council Future Fellowships Grant FT130100430. The authors gratefully acknowledge the support of the Monash Institute of Medical Engineering for this project.

References

1. Newlin, D.B., Levenson, R.W.: Pre-ejection period: measuring Beta-adrenergic influences upon the heart. *Psychophysiology*. **16**(6), 546–552 (1979)
2. Lien, R.V., Schutte, N.M., Meijer, J.H., Geus, E.J.C.D.: Estimated preejection period (PEP) based on the detection of the R-wave and dZ/dt -min peaks in ECG and ICG. *J. Phys. Conf. Ser.* **434**(1), 012–046 (2013)
3. Lien, R.V., Schutte, N.M., Meijer, J.H., Geus, E.J.C.D.: Estimated preejection period (PEP) based on the detection of the R-wave and dZ/dt -min peaks does not adequately reflect the actual PEP across a wide range of laboratory and ambulatory conditions. *Int. J. Psychophysiol.* **87**(1), 60–69 (2013)
4. Forouzanfar, M., Baker, F.C., Zambotti, M.D., McCall, C., Giovangrandi, L., Kovacs, G.T.A.: Toward a better noninvasive assessment of pre-ejection period: a novel automatic algorithm for B-point detection and correction on thoracic impedance cardiogram. *Psychophysiology*. **0**(0), e13072 (2018)
5. Cybulski, G., Michalak, E., Kozluk, E., Piatkowska, A., Niewiadomski, W.: Stroke volume and systolic time intervals: beat-to-beat comparison between echocardiography and ambulatory impedance cardiography in supine and tilted positions. *Med. Biol. Eng. Comput.* **42**(5), 707–711 (2004)
6. Helbig, M., Zender, J., Ley, S., Sachs, J.: Simultaneous electrical and mechanical heart activity registration by means of synchronized ECG and M-sequence UWB sensor. In: 10th European CONFERENCE on Antennas and Propagation (EuCAP) (2016)
7. Buxi, D., Hermeling, E., Mercuri, M., Beutel, F., Westen, R.G.V.D., Torfs, T., Redoute, J.M., Yuce, M.R.: Systolic time interval estimation using continuous wave radar with on-body antennas. *IEEE J. Biomed. Health Inform.* **22**(1), 129–139 (2018)
8. Buxi, D., Dugar, R., Redoute, J.M., Yuce, M.R.: Comparison of the impedance cardiogram with continuous wave radar using body-contact antennas. In: 39th Annual International CONFERENCE of the IEEE Engineering in Medicine and Biology Society (EMBC) 2017
9. Houtveen, J.H., Groot, P.F.C., Geus, E.J.C.D.: Effects of variation in posture and respiration on RSA and pre-ejection period. *Psychophysiology*. **42**(6), 713–719 (2005)

Chapter 24

Wearable Continuous Blood Pressure Estimation with Photoplethysmography Sensors Array on the Arm



Chunkai Qiu, Taiyang Wu, Jean-Michel Redouté, and Mehmet Rasit Yuce

24.1 Introduction

High-normal blood pressure (BP), or hypertension, has been a global public health issue leading to cardiovascular diseases (CVD), such as heart attacks, strokes, and heart failure [1–3]. About one billion people are affected by hypertension globally and the complications of hypertension account for 16.7% of all deaths worldwide every year [2]. The early detection of hypertension relies on monitoring BP continuously. The traditional cuff-based BP monitoring method is unsuitable for a long-term BP monitoring, due to its occlusiveness and limited frequency of measurement [4]. Pulse transit time (PTT) is defined as the transit time of the arterial pulse wave (PW) at two consecutive sites along an arterial within the same cardiac cycle. Therefore, pulse wave velocity (PWV) can be calculated using PTT [5, 6]. The correlation between PWV and BP has been proved in previous literature [7–9].

In [10], it shows there is a strong correlation between BP and the mean value of the 1 min peripheral pulse transit time (PPTT) based on a dual-channel photoplethysmography (PPG) sensor placed on the forearm and wrist. In this paper, a 4-channel PPG array for continuous beat-to-beat BP monitoring is presented, BP changes can be captured more effectively with the proposed setup. Through the 4-channel PPG array, PW can be obtained from four positions along the arm simultaneously, and local PWV segments along the arm can be calculated. Therefore, more details about how the PW transits along the arm can be examined, which has a potential to achieve a better model for cuff-less BP monitoring in the future.

C. Qiu · T. Wu · J.-M. Redouté · M. R. Yuce (✉)
Electrical and Computer Systems Engineering, Monash University, Clayton, VIC, Australia
e-mail: Chunkai.Qiu@monash.edu; Taiyang.Wu@monash.edu;
Jean-Michel.Redoute@monash.edu; mehmet.yuce@monash.edu

24.2 Method

System Overview

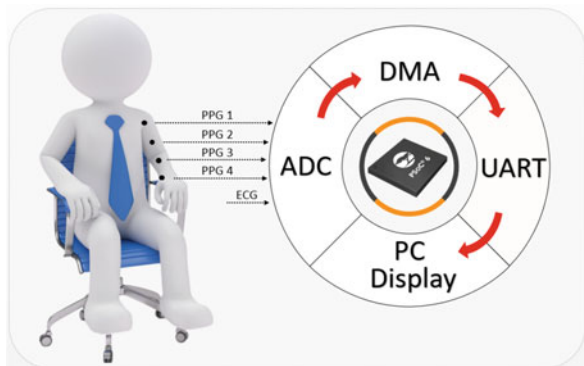
The proposed system is illustrated in Fig. 24.1. Four reflectance-mode PPG sensors are employed in the system. Each PPG sensor utilizes a green LED (Kingbright®, AM2520ZGC09, 525 nm) to illuminate blood vessel as the green LED is found to be more suitable for detecting the PW than a red or a blue LED [11, 12]. The light reflected from the blood vessel is then collected by a photosensor (Broadcom Limited®, APDS-9008-020).

In order to align the 4-channel PPG signals in the same cardiac cycle, electrocardiogram (ECG) signal is recorded as a reference of the cardiac cycle. The signal collected by the ECG sensor and the 4-channel PPG array are sampled at 2 kHz by a 5-channel sequential Analog-to-Digital Converter (ADC). The sampled data is transmitted to the output buffer of a universal asynchronous receiver-transmitter (UART) module by a Direct-Memory-Access (DMA) module, then the UART module transmits data to MATLAB® through a USB cable in real time. MATLAB® receives and stores the data in memory, and also displays the signal waveforms on the computer screen in real time. After the experiment, beat-to-beat PTT values are calculated from various combinations of the signals obtained from the 4-channel PPG array.

PTT Determination

In [4, 6, 13], pulse delay derived from the ECG ‘R-peak’ and PPG is the pulse arrival time (PAT), because it includes a pre-ejection period, which can affect the PTT significantly. In [4, 6, 13], PTT is defined as the time between two pulse signals within the same cardiac cycle. The proposed method has the advantage of

Fig. 24.1 System overview



excluding the pre-ejection period naturally. In this work, as illustrated in Fig. 24.2, three PTT values (PTT2-4, PTT1-3, and PTT1-4) derived from PPG-to-PPG sensors in the array along the left arm have been considered, and the PTT values derived from the ECG ‘R-peak’ to the maximum inclination point of PPG signal (PTT_{ref1}, PTT_{ref2}, PTT_{ref3}, and PTT_{ref4}) have been used as a reference for result comparison purpose. The maximum inclination point of a PPG signal is found by computing the first derivative on the PPG signal, the peak of the first derivative plot indicates the maximum inclination point in the PPG signal.

After getting PTT values, PWV can be calculated as [10, 14]

$$PWV = \frac{\Delta L}{PTT}, \tag{24.1}$$

where ΔL is the pulse propagation distance, which is the distance between two sensors.

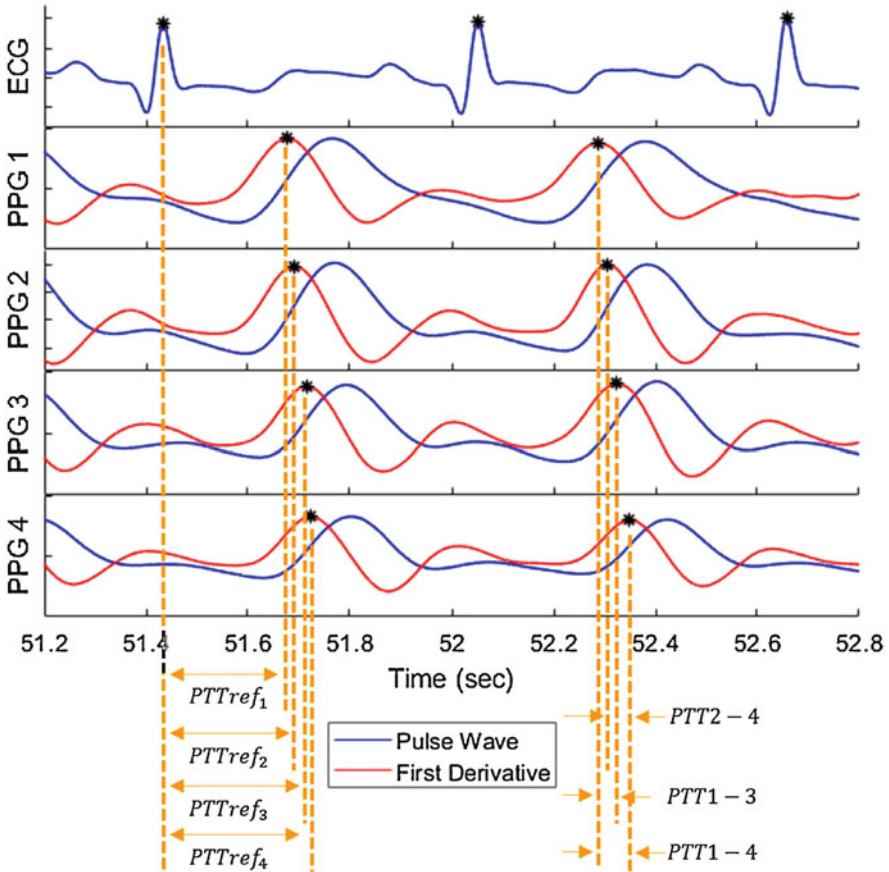


Fig. 24.2 PTT derived from different combinations of PPG sensors

Experimental Setup

To evaluate the feasibility of the system, the experiment has been conducted on 5 healthy male subjects, with age 26 ± 2 years. The subject is required to sit in a comfortable ergonomic chair, with both arms placed on the desk. A 4-channel PPG array is placed on the left arm, targeting axillary artery, brachial artery, radial artery (elbow), and radial artery (wrist) respectively to obtain PW. The position of each PPG sensors is illustrated in Fig. 24.1. An ECG sensor is located at the chest to record ECG signal as a reference of cardiac cycle.

The Finapres[®] NOVA is employed to measure BP continuously as a reference. The non-invasive beat-to-beat finger arterial BP pulse is measured on the middle finger of the subject's right hand through a finger-cuff. Using this unit, the BP pulse waveform is shown as a yellow line plot in Fig. 24.3. At the beginning of the measurement, an arm-cuff calibration module on the subject's right arm is used to calibrate the BP value measured by the finger-cuff. After the calibration, a reliable beat-to-beat continuous BP waveform can be measured by the finger-cuff, the reconstructed systolic BP waveform is shown as a red line plot in Fig. 24.3, while the reconstructed diastolic BP waveform is shown in green in the figure.

In order to obtain the changes in BP, the subject is required to perform a squat posture 3 times during the experiment. The time duration for each experiment trial is 12 min. For the first 3 min, the subject is sitting comfortably, as shown in Fig. 24.4a. After that, the subject stands up slowly and performs squat posture for 1 min as shown in Fig. 24.4b, and then sit down to rest for 2 min. The same process is repeated 3 times for each trial.

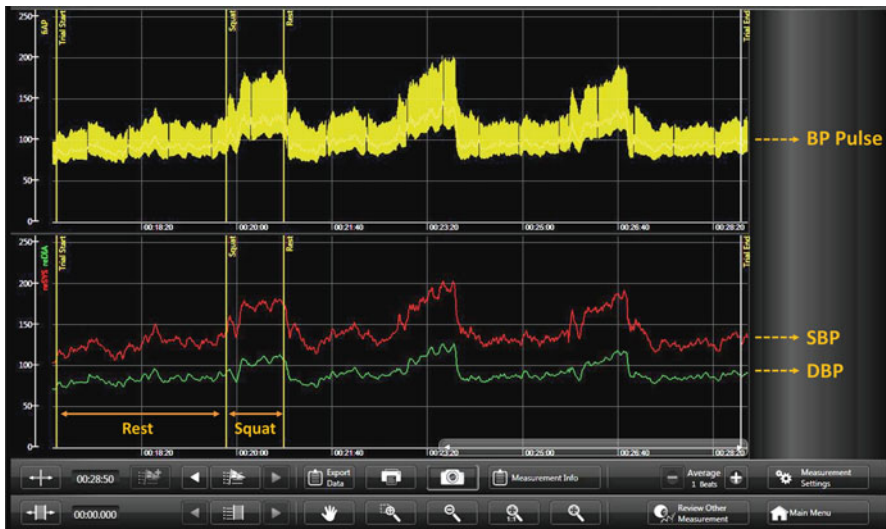


Fig. 24.3 Screenshot of Finapres[®] NOVA system

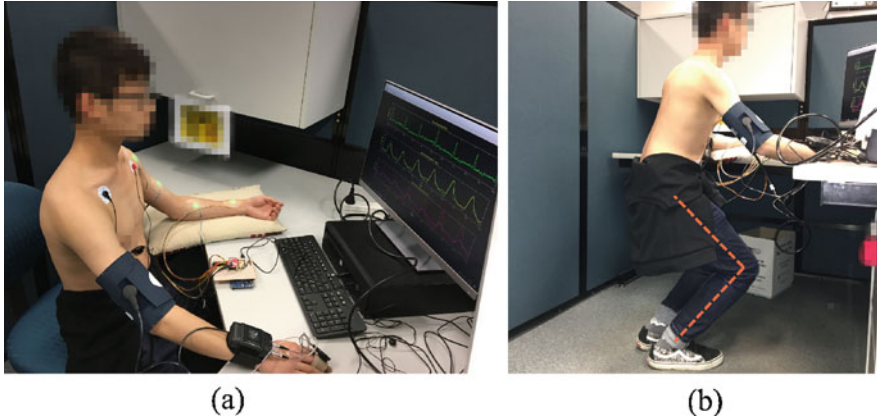


Fig. 24.4 Two postures during experiment to intervene BP. (a) Sit down and rest; (b) perform squat posture for 1 min to increase BP

24.3 Results

The collected data is processed and analyzed by MATLAB[®]. To examine the feasibility of the PWV derived from PPG-to-PPG sensor, the PWV derived from the ECG ‘R-peak’ and PPG sensor is also calculated. Figure 24.5a, b show the comparison between the PWV calculated from PTT_{ref1} and PTT_{ref4} and systolic blood pressure (SBP) respectively for subject_1. As shown in the plot, when the subject starts to perform squat posture, BP and PWV are increasing and then decreasing when the subject starts to rest. Figure 24.5c shows the comparison between the PWV calculated from PTT1-4 and SBP of subject_1, and Fig. 24.5d shows the correlation between PWV calculated from PTT1-4 of subject_1 and measure SBP, the correlation is 0.81 with a p -value (p) < 0.01.

The correlations (r) between PWV derived from PTT1-3, PTT2-4, and PTT1-4 and measured SBP for each of the 5 subjects are calculated and summarized in Table 24.1. The correlations for PWV and measured diastolic blood pressure (DBP) are shown in Table 24.2.

A correlation is an effect size, and using a guide provided in [15], the absolute value of r :

- $0 \leq r \leq 0.19$: very weak
- $0.20 \leq r \leq 0.39$: weak
- $0.40 \leq r \leq 0.59$: moderate
- $0.60 \leq r \leq 0.79$: strong
- $0.80 \leq r \leq 1.00$: very strong

From Tables 24.1 and 24.2, it can be observed that there is a strong or very strong positive correlation between the beat-to-beat PWV derived from PPG-to-PPG and the measured SBP and DBP respectively, except the PWV calculated from PTT1-

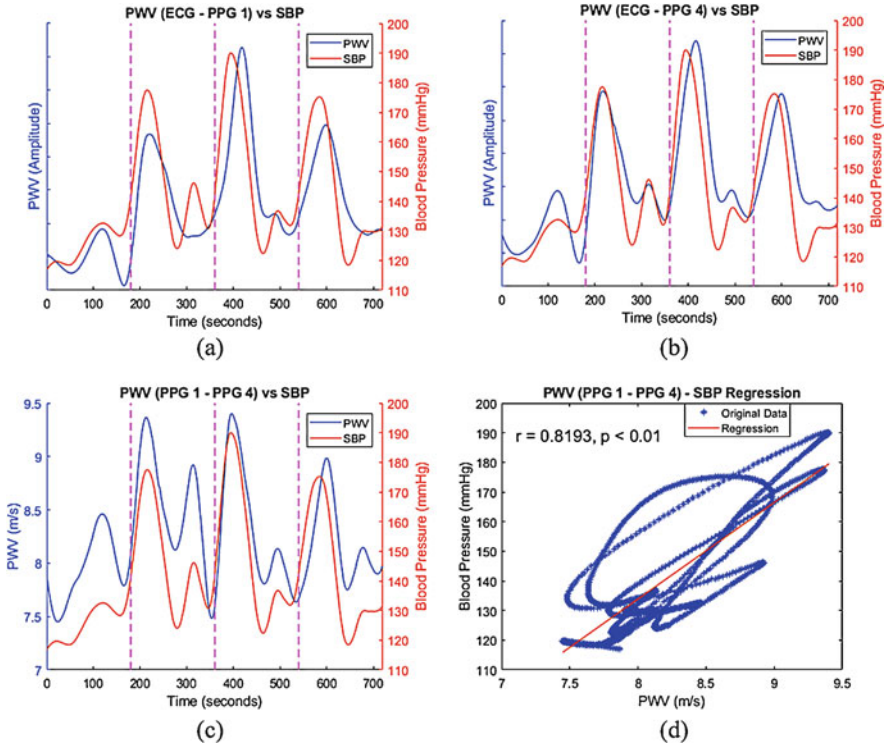


Fig. 24.5 Comparison between PWV and blood pressure for subject_1. (a) Comparison between the PWV derived from PTT_{ref1} and SBP; (b) comparison between the PWV derived from PTT_{ref4} and SBP; (c) comparison between the PWV derived from PTT1-4 and SBP; (d) the correlation between the PWV derived from PTT1-4 and SBP

Table 24.1 Correlations between PWV and SBP

Sensors combination	Subject 1	Subject 2	Subject 3	Subject 4	Subject 5
PPG1–PPG3	0.7079	0.9163	<i>0.4989</i>	0.6070	0.7735
PPG2–PPG4	0.7766	0.7181	0.6215	0.7943	0.6260
PPG1–PPG4	0.8193	0.8764	0.8797	0.7353	0.9080

Bold values represents strong to very strong correlation. Italic value represents moderate correlation

Table 24.2 Correlations between PWV and DBP

Sensors combination	Subject 1	Subject 2	Subject 3	Subject 4	Subject 5
PPG1–PPG3	0.6635	0.8873	<i>0.5539</i>	0.7172	0.7204
PPG2–PPG4	0.7599	0.7645	0.7284	0.8472	0.6819
PPG1–PPG4	0.7936	0.8096	0.9378	0.8027	0.8981

Bold values represents strong to very strong correlation. Italic value represents moderate correlation

3 for subject_3 shows a moderate correlation to both SBP and DBP. The result confirms that when BP increases, PWV will increase and vice versa. It also shows PWV derived from PPG-to-PPG sensors can be used to estimate beat-to-beat BP values.

24.4 Conclusion

In this paper, a wearable continuous BP monitoring system based on PPG sensors array is presented. The system places four PPG sensors along the left arm, and an ECG sensor located at the chest is used as a reference of the cardiac cycle for signal aligning. The PWV values derived from the combinations of these sensors (e.g., PTT1-3, PTT2-4, and PTT1-4) have been examined on 5 healthy male subjects. The result shows that there is a strong correlation between PWVs and BP. More detailed PWV along the arm can be derived from such PPG sensors array with multiple combinations of the PPG sensors. A more accurate BP estimation model can be achieved based on these PWV values. An algorithm will be developed in future work for a wearable continuous beat-to-beat BP estimation model.

Acknowledgements M. R. Yuce's work is supported by Australian Research Council Future Fellowships Grant FT130100430.

References

1. Vasan, R.S., Larson, M.G., Leip, E.P., Evans, J.C., O'Donnell, C.J., Kannel, W.B., Levy, D.: Impact of high-normal blood pressure on the risk of cardiovascular disease. *N. Engl. J. Med.* **345**(18), 1291–1297 (2001)
2. World Health Organization: A global brief on hypertension: silent killer, global public health crisis: World health day 2013 (2013)
3. Kannel, W.B.: Blood pressure as a cardiovascular risk factor: prevention and treatment. *JAMA* **275**(20), 1571–1576 (1996)
4. Buxi, D., Redouté, J.M., Yuce, M.R.: A survey on signals and systems in ambulatory blood pressure monitoring using pulse transit time. *Physiol. Meas.* **36**(3), R1 (2015)
5. Fiala, J., Bingger, P., Foerster, K., Heilmann, C., Beyersdorf, F., Zappe, H., Seifert, A.: Implantable sensor for blood pressure determination via pulse transit time. In: *Sensors, 2010 IEEE*. pp. 1226–1229. IEEE, Piscataway (2010)
6. Hennig, A., Patzak, A.: Continuous blood pressure measurement using pulse transit time. *Somnologie-Schlafforschung und Schlafmedizin* **17**(2), 104–110 (2013)
7. Tang, Z., Tamura, T., Sekine, M., Huang, M., Chen, W., Yoshida, M., Sakatani, K., Kobayashi, H., Kanaya, S.: A chair-based unobtrusive cuffless blood pressure monitoring system based on pulse arrival time. *IEEE J. Biomed. Health Inform.* **21**(5), 1194–1205 (2017)
8. Heravi, M.Y., Khalilzadeh, M., Joharina, S.: Continuous and cuffless blood pressure monitoring based on ECG and SpO2 signals by using Microsoft visual C sharp. *J. Biomed. Phys. Eng.* **4**(1), 27 (2014)

9. Wong, M.Y.M., Poon, C.C.Y., Zhang, Y.T.: An evaluation of the cuffless blood pressure estimation based on pulse transit time technique: a half year study on normotensive subjects. *Cardiovasc. Eng.* **9**(1), 32–38 (2009)
10. Wang, Y., Liu, Z., Ma, S.: Cuff-less blood pressure measurement from dual-channel photoplethysmographic signals via peripheral pulse transit time with singular spectrum analysis. *Physiol. Meas.* **39**(2), 025010 (2018)
11. Lee, J., Matsumura, K., Yamakoshi, K.i., Rolfe, P., Tanaka, S., Yamakoshi, T.: Comparison between red, green and blue light reflection photoplethysmography for heart rate monitoring during motion. In: 2013 35th Annual International Conference of the IEEE Engineering in Medicine and Biology Society (EMBC), pp. 1724–1727. IEEE, Piscataway (2013)
12. Tamura, T., Maeda, Y., Sekine, M., Yoshida, M.: Wearable photoplethysmographic sensors—past and present. *Electronics* **3**(2), 282–302 (2014)
13. Sola, J., Proença, M., Ferrario, D., Porchet, J.A., Falhi, A., Grossenbacher, O., Allemann, Y., Rimoldi, S.F., Sartori, C.: Noninvasive and nonocclusive blood pressure estimation via a chest sensor. *IEEE Trans. Biomed. Eng.* **60**(12), 3505–3513 (2013)
14. Thomas, S.S., Nathan, V., Zong, C., Akinbola, E., Aroul, A.L.P., Philipose, L., Soundarapandian, K., Shi, X., Jafari, R.: Biowatch—a wrist watch based signal acquisition system for physiological signals including blood pressure. In: 2014 36th Annual International Conference of the IEEE Engineering in Medicine and Biology Society (EMBC), pp. 2286–2289. IEEE, Piscataway (2014)
15. Evans, J.D.: *Straightforward statistics for the behavioral sciences*. Brooks/Cole, Pacific Grove (1996)

Chapter 25

Cuffless Blood Pressure Estimation Based on Pulse Arrival Time Using Bio-impedance During Different Postures and Physical Exercises



Fatemeh Heydari, Malikeh Pour Ebrahim, Taiyang Wu, Katie Walker, Keith Joe, Jean-Michel Redouté, and Mehmet Rasit Yuce

25.1 Introduction

Non-invasive cuffless BP monitoring is based on measuring the time delay occurring when a given blood volume travels from heart to other organs. The propagation characteristic is normally obtained as pulse arrival time (PAT) or pulse transition time (PTT) [1–4], which requires at least two vitals signs such as an electrocardiograph (ECG) and pulse wave. PAT refers to a time delay between ECG's R-peak and characteristic points on the rising slope of the pulse wave such as the maximum, the foot, the maximum of its first derivative, maximum of its second derivative, maximum of its second derivative, and foot of pulse as determined by the intersecting tangent method [5]. There are significant numbers of methods and studies that have been used to obtain the relation between PAT and BP using photoplethysmography (PPG) signal [6].

In [7], BP pulse wave is obtained with bio-impedance (BImp) across the shoulder in order to calculate PAT from carotid and subclavian arteries.

This method is more beneficial since it measures the PAT over the central elastic arteries instead of the peripheral arteries. Electrical impedance or BImp is a response of a human body (generally any tissue) to an external electrical current, which changes relatively by blood flow and is often used for measuring cardiac output

F. Heydari (✉) · M. Pour Ebrahim · T. Wu · J.-M. Redouté · M. R. Yuce
Department of Electrical and Computer Systems Engineering, Monash University, Melbourne,
VIC, Australia
e-mail: Fatemeh.heydari@monash.edu; Jean-Michel.Redoute@monash.edu;
mehmet.yuce@monash.edu

K. Walker · K. Joe
Emergency Department, Cabrini Health, Melbourne, VIC, Australia

(or especially diagnostics of the cardiovascular system) and blood flow (without Doppler sonography).

In this study, the relation between systolic blood pressure (SBP) and PATs extracted from BImp is investigated under different experimental conditions including physical exercise or different postures (sitting, standing, and supine) in order to provide different BP trends. Furthermore, for each point, a mathematical model is used in order to estimate SBP and the accuracy of the SBP is compared to using a cuff device.

25.2 Methodology

Subjects

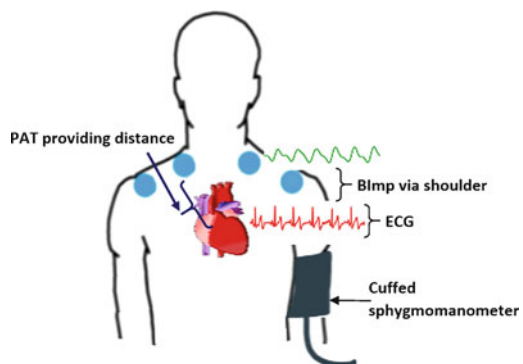
Healthy adult volunteers attended Cabrini Hospital, Melbourne, Australia for data collection (Oct. to Nov. 2017) and emergency physicians monitored their health during the data recording. The data was obtained from 43 healthy adults aged 40 ± 15 years old, being 168 ± 10 cm tall and with weight of 60 ± 16 kg (52% male). All the volunteers were chosen randomly and recordings were started during subjects' normal state.

Procedure

In order to verify different trends of BP, the following steps were administrated during data collection.

Firstly, all 43 subjects undertook one task, lasting 3 min, six consecutive times, while simultaneously wearing a calibrated cuffed sphygmomanometer, the ECG and BImp electrode dots. The placement of sensors and the sphygmomanometer cuff is

Fig. 25.1 Placement of sensors and cuffed sphygmomanometer on the body



shown in Fig. 25.1. The sphygmomanometer cuff was used to extract mathematical model parameters required for BP estimation with PATs. Each one of 43 participants was asked to stay two times in the following 3-min posture tasks respectively, sitting, standing, and supine. The first 2 min of each task allowed the subject to settle. At 120 s, the control cuffed oscillating sphygmomanometer commenced measurement and returned a reading value after 60 s.

Secondly, among all participants (43 participants), 26 of them (57% male) were seated on an exercise bike and cycled for intervals of 2 min followed by a 1 min rest. They cycled at a target of 20–25 km/h with light, moderate, and heavy resistance bike settings, undertaking the 2 min cycling for each resistance level. Cuff BP readings were commenced at the start of each rest period.

For both posture and exercise testing protocols, ECG and BImp signals were recorded 30 s before and after the cuff measurement commencement.

Signal Processing

The block diagram of the signal processing part is shown in Fig. 25.2. Recorded signals are filtered by a bandpass filter (BPF) which sets the pass and stop frequencies for each signal based on the heart rate frequency (HRF) range. The frequency range is calculated by applying fast Fourier transform (FFT) on the ECG signal to extract HRF and putting the maximum and minimum frequency limitations around HRF.

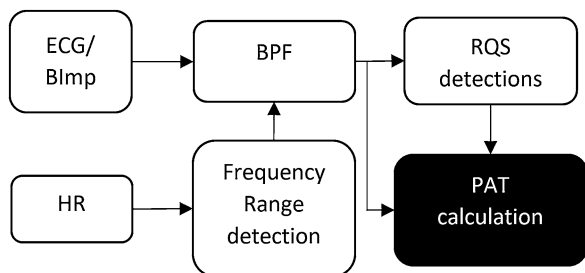
Then, a Chebyshev type II BPF designed using Matlab was generated based on the frequency range and applied to all signals. In Fig. 25.3, two samples (sitting and heavy exercise) of system processing outputs (ECG and BImp) are shown.

There are various PAT extraction methods that measure the required time delay between the ECG's R-peak and different landmarks on the pulse wave [2, 6, 8].

In this chapter, PAT is calculated as the time interval between the R-Peak of ECG signal and four "landmarks" in the BImp wave using the following methods:

1. *Foot value* (PAT_{ft}), the maximum value in second derivative of pulse wave.
2. *Intersecting tangents value* ($PAT_{Int. Tan.}$), the intersection point of the tangent to maximum gradient and tangent of the foot.

Fig. 25.2 Signal processing block diagram



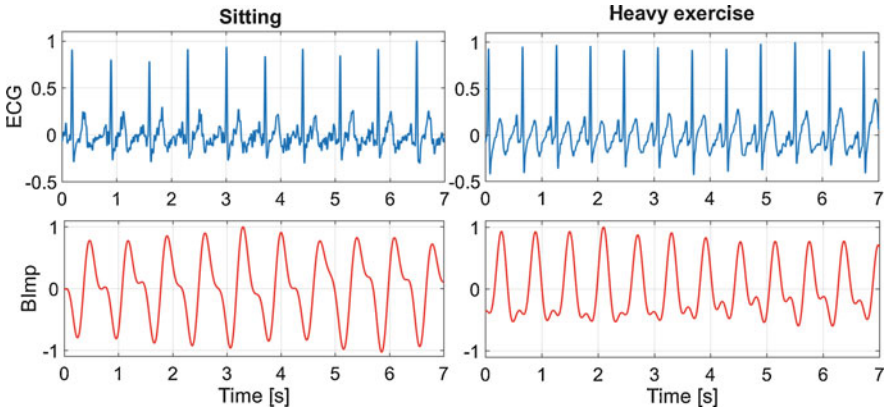


Fig. 25.3 Filtered ECG and BImp signals samples captured during first sitting posture and heavy exercise

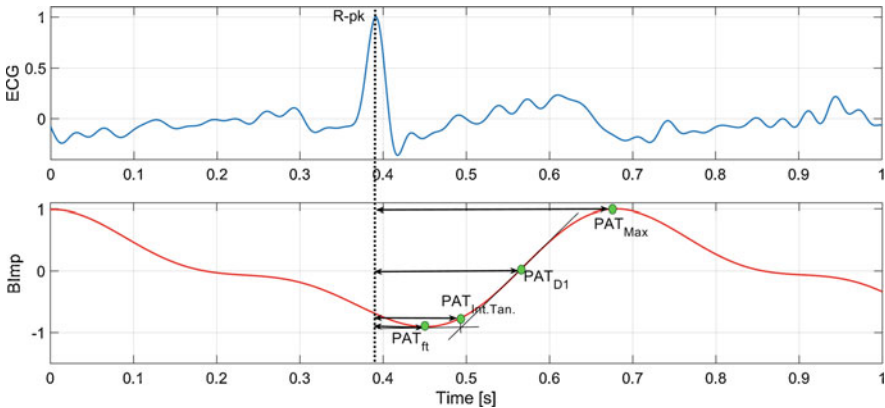


Fig. 25.4 PAT feature selection

3. *First derivative maximum value* (PAT_{D1}), the maximum value in first derivative of pulse wave.
4. *Maximum value* (PAT_{Max}), the maximum value in pulse wave.

PAT selection characteristics are shown in Fig. 25.4.

25.3 Results and Discussion

The PAT values are extracted by zero-crossing detection of BImp signal with first and second derivatives. Then, the results are analyzed to omit any out of range values by putting minimum and maximum thresholds. The final PAT values are

Table 25.1 BP estimation accuracy percentage for ≥ 8 mmHg and ≥ 10 mmHg

	Cumulative accuracy percentage	
	Postures (%)	Exercises (%)
≥ 8 mmHg		
PAT _{Max}	91.21	90.77
PAT _{ft}	78.21	87.50
PAT _{D1}	93.31	90.77
PAT _{Int. Tan.}	92.89	87.69
≥ 10 mmHg		
PAT _{Max}	95.40	90.77
PAT _{ft}	80.34	91.67
PAT _{D1}	95.82	93.85
PAT _{Int. Tan.}	94.98	92.31

averaged after passing through a moving average filter with a length of five samples for posture and ten samples for exercise.

Under normal circumstances, the SBP should not vary more than ± 10 mmHg in two consecutive measurements: a greater than ± 15 mmHg variation in BP may indicate anatomical abnormalities [9]. The accuracy of cuffed sphygmomanometer in this study was ± 3 mmHg [10]. So, the cuff values with higher than 20 mmHg ($>15 + 3$ mmHg) between both previous and next measurements with their respected recorded signals have been removed from the data as this was an indication of measurement errors. In practice, 24 out of 258 records have been removed (0.09%).

In Table 25.1, the accuracy percentage of PAT-based SBP estimation using $\frac{a}{\overline{PAT}} + b$ equation, compared to that of measured with cuff, for two different categories (≥ 8 mmHg and ≥ 10 mmHg), is presented, in both postures and exercises data. The a and b coefficients are calculated using the Matlab curve fitting techniques. It is clear that the SBP estimation using PAT_{D1}) (or the maximum value in first derivative of BImp pulse array) overall has the highest accuracy rate compared to other PATs with 95.82% accuracy in postures data and 93.85% in exercises data. The difference of calculated SBP using $\frac{a}{\overline{PAT}} + b$ equation with corresponding cuff values is presented in Figs. 25.5 and 25.6 for postures and exercises, respectively. Based on these results, our future work will include testing a larger number of subjects and beat-to-beat BP calculations.

25.4 Conclusion

In this chapter, we investigated cuffless systolic blood pressure estimation based on different PAT extraction methods using the bio-impedance signal, calculated from the maximum value, foot value, first derivative maximum value, and intersecting tangents value of the bio-impedance pulse signal. Two experiments (43 healthy participants alternated between sitting, standing, and supine positions, and 26 were

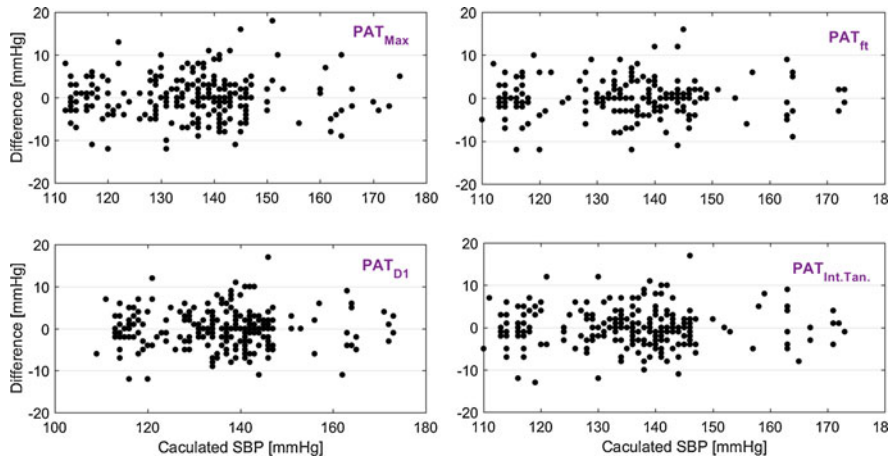


Fig. 25.5 Scatter plot of difference between estimated SBP and measured SBP with cuff device for four PAT reading methods in posture experiment

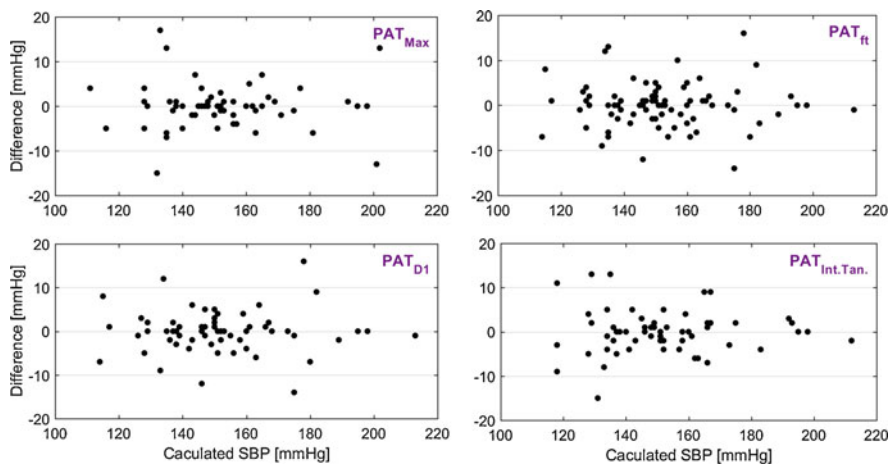


Fig. 25.6 Scatter plot of difference between estimated SBP and measured SBP with cuff device for four PAT reading methods in exercise experiment

cycling) were performed. We assessed systolic blood pressure estimation by using $\frac{a}{\text{PAT}} + b$ mathematical model for each experiment and compared all the results for each PAT. Overall, the results of systolic blood pressure estimation using the maximum value of first derivative which represents the inflection point are considerably more accurate compared to other PAT's reading points. As can be seen from this study, bio-impedance signal recording is easier and more comfortable than other pulse wave representative signals. Clearly, there is a considerable merit in using bio-impedance signal for BP estimation systems. For our future work, we

will study larger samples and continuous (beat to beat) BP estimation using bio-impedance-based pulse wave.

Acknowledgments The authors would like to thank Dr. D. Buxi, previously working at the Biomedical Integrated Circuits and Sensors (BICS) Laboratory, Monash University, for preparing the prototype for the data collections. The authors would like to thank P. Howley and M. Hebblewhite from Planet Innovation for their help in organizing the data collection at Cabrini Health, and all participants for their collaboration and patience.

The work is supported by the Victorian Government through the Future Industry Fund Sector Growth Program Stream 1. M. R. Yuce's work is supported by Australian Research Council Future Fellowships Grant FT130100430. The authors gratefully acknowledge the support of the Monash Institute of Medical Engineering for this project.



References

1. Steptoe, A., Smulyan, H., Gribbin, B.: Pulse wave velocity and blood pressure change: calibration and applications. *Psychophysiology*. **13**(5), 488–493 (1976)
2. Phillips, J.P., Kyriacou, P.A.: Comparison of methods for determining pulse arrival time from Doppler and photoplethysmography signals. *Conf. Proc. IEEE Eng. Med. Biol. Soc.* **2014**, 3809–3812 (2014)
3. Mukkamala, R., Hahn, J.O.: Toward ubiquitous blood pressure monitoring via pulse transit time: predictions on maximum calibration period and acceptable error limits. *IEEE Trans. Biomed. Eng.* **65**(6), 1410–1420 (2018)
4. Buxi, D., Redout, J.-M., Yuce, M.R.: A survey on signals and systems in ambulatory blood pressure monitoring using pulse transit time. *Physiol. Meas.* **36**(3), R1 (2015)
5. Sol, J., Vetter, R., Renevey, P., Chtelat, O., Sartori, C., Rimoldi, S.F.: Parametric estimation of pulse arrival time: a robust approach to pulse wave velocity. *Physiol. Meas.* **30**(7), 603 (2009)
6. Sharma, M., Barbosa, K., Ho, V., Griggs, D., Ghirmai, T., Krishnan, S.K., Hsiai, T.K., Chiao, J.-C., Cao, H.: Cuff-less and continuous blood pressure monitoring: a methodological review. *Technologies*. **5**(2), 21 (2017)
7. Buxi, D., Redout, J.M., Yuce, M.R.: Blood pressure estimation using pulse transit time from bioimpedance and continuous wave radar. *IEEE Trans. Biomed. Eng.* **64**(4), 917–927 (2017)
8. Hemon, M.C., Phillips, J.P.: Comparison of foot finding methods for deriving instantaneous pulse rates from photoplethysmographic signals. *J. Clin. Monit. Comput.* **30**(2), 157–168 (2016)
9. Brzezinski, W.A.: Chapter 16: Blood pressure. In: Walker, H.K., Hall, W.D., Hurst, J.W. (eds.) *Clinical Methods: The History, Physical, and Laboratory Examinations*, 3rd edn. Butterworths, Boston (1990)
10. Norav medical, blood pressure monitor, nbp-24ng datasheet. [online]. <http://www.norav.com>

Chapter 26

Estimation Method of Abdominal Fat Thickness by Microwave



Nobuaki Tanaka  and Takahiro Aoyagi 

26.1 Introduction

In aging society, workload of medical workers is a big problem. Preventive medicine to reduce their workload is very important. This study focuses on metabolic syndrome that causes lifestyle diseases. To prevent this, the Ministry of Health, Labor and Welfare of Japan has been conducting abdominal girth measurements at annual health examinations since 2008. The diagnostic criteria are that the abdominal circumference is less than 85 cm for men and less than 90 cm for women [1]. However, the visceral fat mass is not accurately reflected even when only measuring the abdominal girth. Some instruments, such as CT scan and MRI, accurately measure the amount of visceral fat, but expensive costs are necessary for patients.

To overcome this issue, a measurement method for estimating abdominal fat amount at low cost by electrical impedance tomography (EIT method) was proposed [2]. There is also a study to measure lung density in the measurement example using the EIT method [2]. However, in the EIT method, it is necessary to attach the electrode to the skin, and the state of the electrode largely affects measurement results. In order to improve the disadvantages of these measurement methods, a non-contact and inexpensive measurement method is required.

Meanwhile, electromagnetic waves are frequently used as a non-contact measurement method. A dielectric constant estimation method using a waveguide, waveguide penetration method, has been proposed [3]. Muscle and fat and other body tissues have been shown to have different dielectric constants [4]. From the above, the author's group supposed that the dielectric constant of human tissue can

N. Tanaka · T. Aoyagi (✉)
Tokyo Institute of Technology, Tokyo, Japan
e-mail: aoyagi.t.aa@m.titech.ac.jp

be estimated by microwave measurement and have proposed a measurement method of abdominal fat [5].

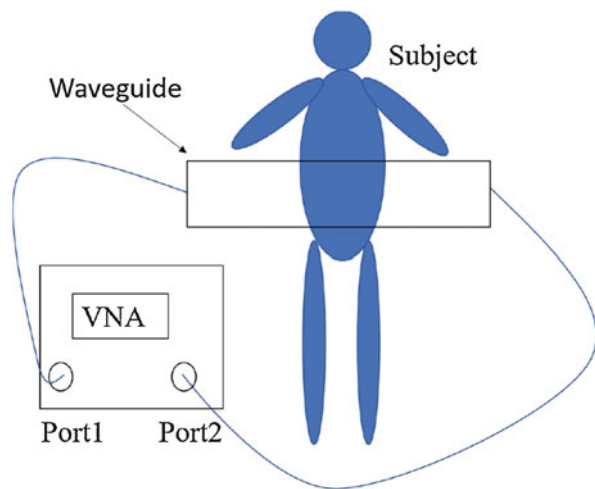
In the ref. [5], overview of novel measurement to estimate abdominal fat amount method and possibility of estimation was shown. However, specific fat amount estimation algorithm is not shown. Therefore, in this study, as an early challenge to measure fat mass using microwaves, a method of estimating subcutaneous fat was examined. In this paper, a novel method to estimate fat thickness from the relationship between fat thickness and resonance position at each frequency is proposed. Since the shape of the abdomen of the human body is not a clean cylinder, it is difficult to estimate by the method of finding the amount of fat from analytical solutions such as waveguide penetration method. So as an initial study of the nonparametric estimation method, a fat thickness estimation model using a neural network was created.

This paper is organized as follows: Section 26.2 briefly describes the outline of the measurement assumed in this research and the idea of the estimation method. Section 26.3 shows the conditions and results of the analysis conducted to show the effectiveness of proposed method. Also, since the estimation model uses a neural network, its estimation accuracy is also shown. Section 26.4 gives the summary of this paper and future possibilities are discussed.

26.2 Outline of the Measurement Method

Figure 26.1 shows the outline of the measurement method. Both ends of the waveguide covering the abdomen of the human body are connected to a vector network analyzer (VNA) having two ports using a coaxial cable. The S parameters,

Fig. 26.1 Concept of the proposed subcutaneous fat estimation method



reflection and transmission coefficient, in the waveguide into which the abdomen of the human body is inserted are measured by VNA.

Since the electrical constants of fat and muscle of the human body constituting the abdomen are different, it is considered that the S parameter obtained depending on the fat thickness varies from frequency to frequency. In this method, a cavity resonator having a circle of a size through which the abdomen of the human body passes is configured, and ports are provided at both ends of the cavity. The next section shows analysis models, considerations, and analysis results.

26.3 Conditions and Results of Numerical Simulation

Estimation of Fat Thickness by Proposed Method

Figure 26.2 shows a simulation model of the measurement method proposed in this research. Figure 26.2a is the side view and Fig. 26.2b is the top view. In this paper, XFDTD is used for calculation of the simulation model [6]. In order to simplify

Fig. 26.2 Analysis model of the measurement. (a) Side view. (b) Top view

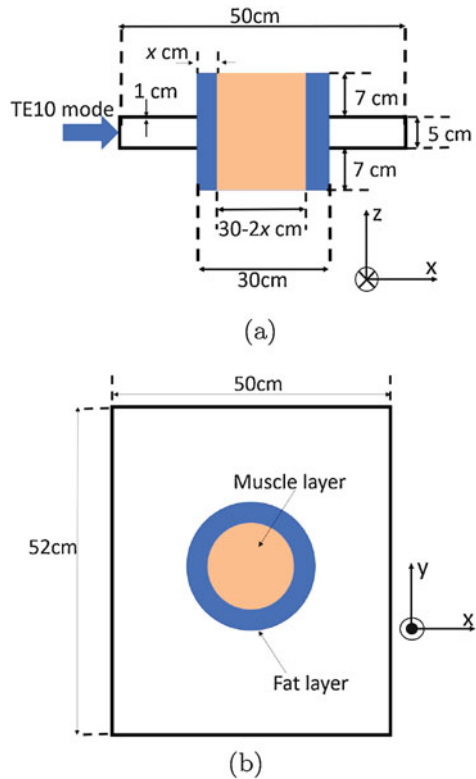
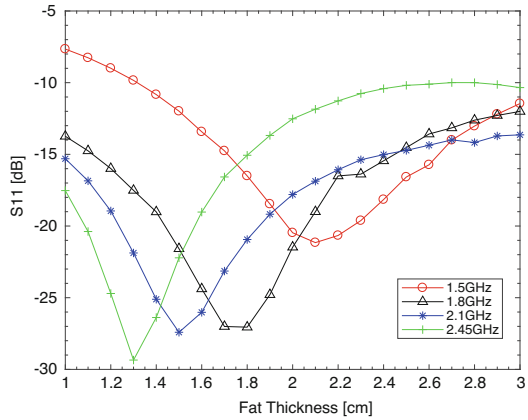


Table 26.1 Electric constant of human tissue and waveguide at 2.45 GHz

Material	Relative permittivity	(S/m) Conductivity (S/m)
Waveguide of constant	1	5.98×10^7
Relatively of muscle	53.96	1.19
Relatively of fat	5.38	0.068

Fig. 26.3 S_{11} -fat thickness



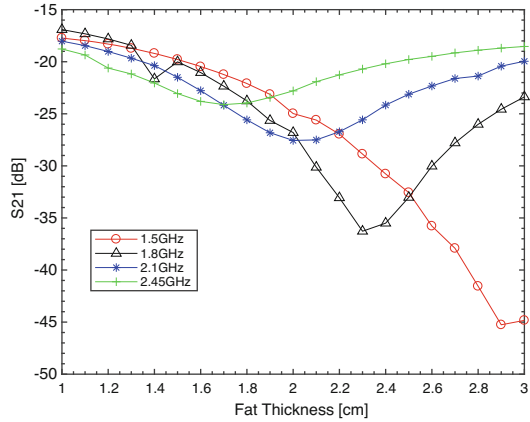
numerical calculation, a TE_{10} propagation mode of the rectangular waveguide is used. The size of the cavity of the waveguide is $0.52 \times 0.07 \times 0.5$ m and the thickness of the waveguide wall is 1 cm. At the center of the waveguide, a hole with a radius of 0.15 m is provided so that a model of the abdomen can be inserted.

To reduce reflections, PML is employed as a boundary condition. The frequencies (1.5, 1.8, 2.1, and 2.45 GHz) are used, the fat thickness x cm varies from 1 cm to 3 cm, and the S parameters (S_{11} and S_{21}) are measured every 1 mm. As a consideration of the fat thickness estimation algorithm, the model of the abdomen of the human body is a cylindrical dielectric composed of two layers with fat and muscle electrical constants. A muscle layer is placed inside the cylindrical dielectric and a fat layer is placed on the outside.

Table 26.1 shows the electrical constants of the waveguide and human body composition [7] used for analysis at 2.45 GHz. As shown in Table 26.1, the dielectric constant of muscle is about 10 times fat and the conductivity of muscle is about 17 times fat. In this study, the electric constant of pure copper is given to the electric constant of the waveguide in consideration of the fabrication of the waveguide. Since the electric constant of the human body composition varies with the frequency, as the frequency used for analysis changes, the electric constant also changes.

Figure 26.3 shows the relationship between S_{11} and fat thickness. From the results, it was found that the resonance position varies depending on the fat thickness. In other words, it is considered that there is a possibility of estimating the fat thickness from the resonance position by using a plurality of frequencies.

Figure 26.4 shows the relationship between S_{21} and fat thickness. From the result of S_{21} at each frequency is -25 dB or more at the desired minimum resonance

Fig. 26.4 S_{21} -fat thickness

position, it can be considered that it can actually be measured. In the next section we will describe the fat thickness estimation model designed using the analysis data of S_{11} and S_{21} .

The Fat Thickness Estimation Model by a Neural Network

Possibility of estimating the dielectric constant of the abdomen of the human body analytically from S_{11} and S_{21} obtained by measurement was shown in [5]. The shape of the abdomen of the human body is complicated, it is difficult to estimate the visceral fat mass analytically. Accordingly, it is considered that an estimation model from data is necessary in the future. In this paper, as an initial consideration, the fat thickness estimation model created using neural network is shown. The S_{11} and S_{21} obtained by numerical simulation results are used as learning data, and each data amount is 4 elements \times 21 samples. The four elements mean frequencies (1.5, 1.8, 2.1 and 2.45 GHz) and the 21 samples mean the result of S_{11} or S_{21} having a fat thickness of 1 cm to 3 cm (1 mm interval). After letting the neural network learn the data, the estimation accuracy when data was read again was confirmed. There are three types of input data: S_{11} only, S_{21} only, both S_{11} and S_{21} . As a result of learning of 3 patterns, the highest estimation accuracy was shown when only S_{21} was input. This result is shown in Fig. 26.5.

Figure 26.5 shows four results of the modeling process. 12 of 21 samples are used for the training. The upper-left figure shows the training result. The horizontal axis shows actual abdominal fat thicknesses and the vertical axis shows estimated thicknesses. The six samples are used for the test and the three samples are used for the validation. The upper-right figure and the lower-left figure show the validation and the test results respectively. The lower-right figure shows overall result that three phase of the modeling is superimposed together. As shown in the test result,

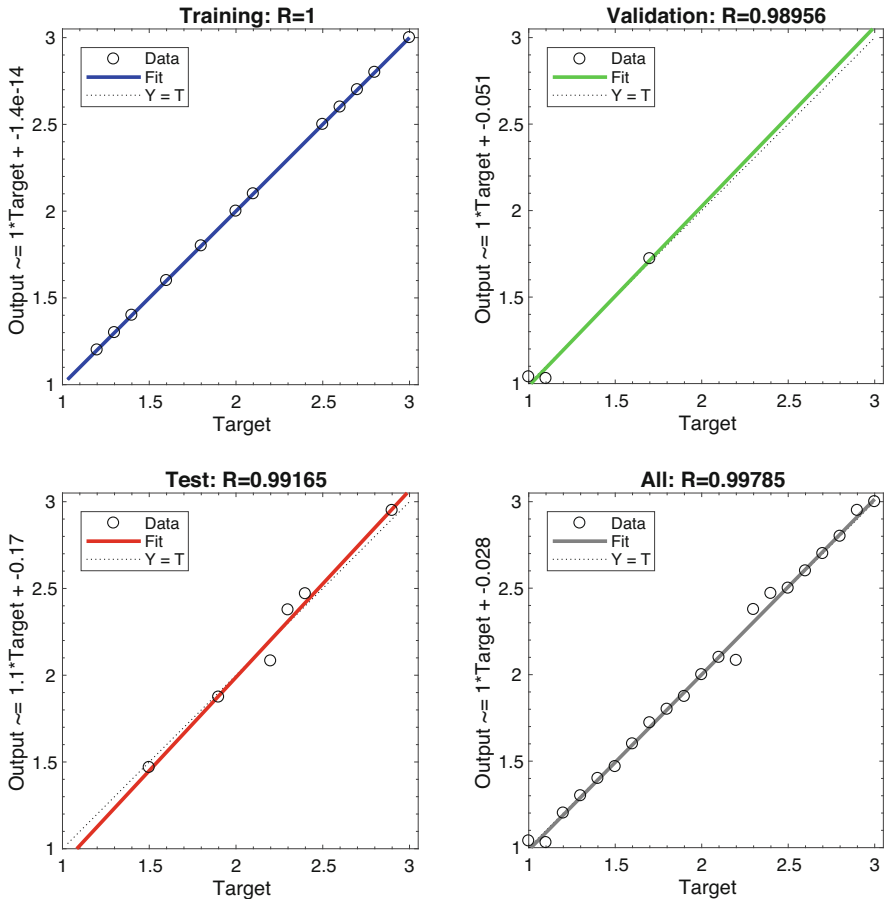


Fig. 26.5 The fat mass estimation model in which the input data is only S_{21}

the regression coefficient R is 0.99 which is very high value to estimate the fat thickness. Despite the small number of samples in current study, this result indicates the possibility that estimation of fat thickness can be performed when the number of specimens in S_{21} increases.

26.4 Conclusion

In this paper, novel fat thickness estimation method using microwaves is proposed. The principle and outline used for the measuring method are explained. From the results of numerical calculation, it is considered that a method for actual human

body measurement was established. The fat thickness estimation model using analysis data is shown, indicating that the estimation accuracy is high. In the future, in order to estimate the fat thickness more accurately by actual measurement, the following investigation is carried out.

- Change the cylindrical analysis model of the two layers to the shape of the actual human abdomen (ellipse, others).
- Change analysis model to numeric human body model.
- Increase the number of data to improve the accuracy of the estimation model.
- Design an equivalent circuit model.

Acknowledgement This work was supported by JSPS KAKENHI Grant Number 15K06054.

References

1. Ministry of Health, Labor and Welfare. <https://www.e-healthnet.mhlw.go.jp/information/metabolic/m--01--004.html>. Accessed 13 June 2017
2. Nebuya, S., Mills, G.H., Miles, P., Brown, B.H.: In-direct measurement of lung density and air volume from electrical impedance tomography (EIT) data. *Physiol. Meas.* **32**, 1953–1967 (2011)
3. Hamaji, T., Kik, A., Aoyagi, T., Nishikata, A., Watanabe, S.: In-vivo measurement of equivalent complex permittivity of fingers using the waveguide-penetration method. *IEICE Trans. B* **EJ94-B(11)**, 1503–1507 (2011) (in Japanese)
4. Gabriel, S., Lau, R.W., Gabriel, C.: The dielectric properties of biological tissues: III. Parametric models for the dielectric spectrum of tissues. *Phys. Med. Biol.* **41**, 2271–2293 (1996)
5. Aoyagi, T.: Fundamental study on measurement of dielectric constant of human abdomen by waveguide-penetration method. In: *Proceedings 10th International Conference on Communications, Electromagnetics and Medical Applications (CEMA'15)*, pp. 95–98 (2015)
6. Remcom: XFDTD 3D Electromagnetic Simulation Software. Website at <https://www.remcom.com/xfddt-3d-em-simulation-software/>. Accessed 20 April 2018
7. Andreuccetti, D., Fossi, R., Petrucci, C.: Internet resource for the calculation of the Dielectric Properties of Body Tissues in the frequency range 10 Hz – 100 GHz. IFAC–CNR, Florence (Italy) (1997). Based on data published by C. Gabriel et al. in 1996. <http://niremf.ifac.cnr.it/tissprop/>. Accessed 08 Mar 2018

Chapter 27

Exposure to RF EMF from 5G Handheld Devices



Kamya Yekeh Yazdandoost and Ilkka Laakso

27.1 Introduction

Wireless connectivity is providing substantial functionalities in daily life. Henceforth, demands to have higher data rates at very high speed are increasing day by day. The fifth generation (5G) of wireless communication is promising to meet the requirements of future wireless communications with many possibilities and potentials that have not yet provided with any previous generations [1].

The 5G will operate at millimeter wave frequency bands, and as a result, there will be a number of technical challenges, because this new generation of wireless communication comes with a new concept that will have an effect on antenna and electromagnetic field radiation. The Federal Communication Commission (FCC) adopted a new rule for wireless broadband operations in frequencies above 24 GHz. The new frequency bands are 27.5–28.35 GHz, 37–38.6 GHz, 38.6–40 GHz, and 64–71 GHz [2]. This new rule opens up 10.85 GHz of high-frequency spectrum. Therefore, with this new frequency spectrum, mobile communications is shifting from microwave frequency band to the millimeter wave frequency band. The use of millimeter wave frequencies will affect current mobile antenna configurations, along with a number of other antenna-associated challenges [3].

The quality of communications and link coverage of mobile devices are related to the maximum output power of handheld devices. However, maximum available output power has direct impact on the radiofrequency (RF) electromagnetic field (EMF) exposure, absorbed by human body tissues. Hence, for safety reason of human body to the RF radiation, the EMF radiation is restricted to certain level.

K. Yekeh Yazdandoost (✉) · I. Laakso
Department of Electrical Engineering and Automation, School of Electrical Engineering,
Aalto University, Espoo, Finland
e-mail: kamya.yekehyazdandoost@aalto.fi

The limits imposed by the international organizations, i.e., International Commission on Non-Ionizing Radiation Protection (ICNIRP) [4], Federal Communication Commission (FCC) [5], and the IEEE [6] for the current generation of mobile and wireless devices, are based on Specific Absorption Rate (SAR). The SAR shows the amount of the RF energy absorbed in biological tissues and is expressed in W/kg. However, at frequencies higher than 3–10 GHz, with respect to different standards, restrictions on RF EMF exposure are shifting from SAR to the incident power density (PD) and are expressed in W/m².

This paper presents the EMF exposure study to the head tissue model from a single printed antenna on the allocated frequency bands for 5G by FCC, i.e., 27.5–28.35 GHz, 37–38.6 GHz, 38.6–40 GHz, and 64–71 GHz.

The structure of this paper is as follows. In Sect. 27.2, antenna is discussed. Section 27.3 explains the tissue model. In Sect. 27.4, results and analysis are presented. Finally, conclusion is given in Sect. 27.5.

27.2 Antenna

Frequency allocation for 5G devices makes it very sensitive to the environment, as signal attenuation and path loss are higher at millimeter wave frequency band. One of the design keys could be to maximize radiated power while keeping the antenna size enough small to fit in the limited space allocated for the antenna in the handheld devices. Therefore, refined antenna designs are required for millimeter wave communication systems with satisfactory gain and low losses to overcome the severe attenuation and path loss between the transmitters and receivers. Due to the importance and impact of antenna in the mobile networks, there are a number of antenna designs for sub-6 GHz frequency band and some of them are found in [7–10]. However, for millimeter wave 5G mobile handsets, it is remained short, and further works are needed.

The planar monopole antenna has a capability to provide a wide impedance bandwidth. Moreover, printed monopole antennas have simple design and easy integration with the RF circuit. Figure 27.1 shows the configuration of the antenna that is used in this study. The antenna was made on FR4 Epoxy substrate with 0.5 mm thickness that has electrical properties of $\epsilon_r = 4.4$ and $\tan\delta = 0.02$. The

Fig. 27.1 Antenna configuration and size (mm)

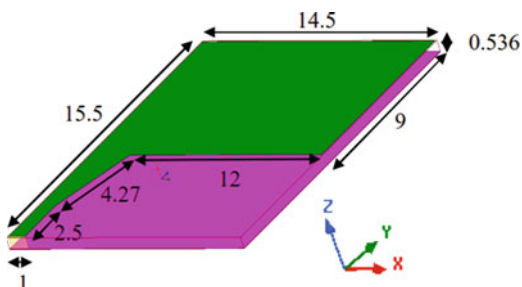


Fig. 27.2 Tissue model for the RF EMF exposure setup



copper cladding on both sides has 0.018 mm thickness. The antenna has 50Ω port impedance with 1 V of input voltage to the antenna port. The overall size of antenna is $15.5 \times 14.5 \times 0.536 \text{ mm}^3$.

27.3 Head Modeling

Devices emitting RF EMF need to comply with relevant regulatory requirements and limits on the human exposure to the electromagnetic field. These guidelines represented by the SAR for the frequencies are used by second- to fourth-generation mobile communications and can be used to minimize local tissue heating and related thermal hazards for sub-6 GHz band mobile devices [4–6]. The exposure limits change from SAR to PD, at frequencies above 3 GHz (IEEE), 6 GHz (FCC), and 10 GHz (ICNIRP).

To investigate the effect of millimeter wave 5G antenna handheld devices, a tissue model with electrical properties, i.e., conductivity S/m, relative permittivity, and loss tangent, of muscle is used (Fig. 27.2). The investigation on the tissue model is based on the tissue electrical properties from [11]. To evaluate the effect of head tissue on the antenna characteristics and effect of RF EMF distribution in the human head at 5G frequency bands, an antenna is placed in close proximity to the tissue at a distance of 10 mm.

27.4 Results and Analysis

Numerical analysis and optimization of the antenna have been performed using ANSYS High Frequency Structure Simulator (HFSS) software [12]. Figure 27.3 shows the simulated antenna S_{11} function of frequency, in the free space and close to the tissue. The 10 dB impedance bandwidth of the antenna is achieved for all the frequency bands, i.e., 27.5–28.35 GHz, 37–38.6 GHz, 38.6–40 GHz, and 64–71 GHz. It is verified that the antenna input impedance is well matched to the reference impedance, and it is confirmed that there is no frequency shift on the antenna characteristics due to the effect of tissue electrical properties.

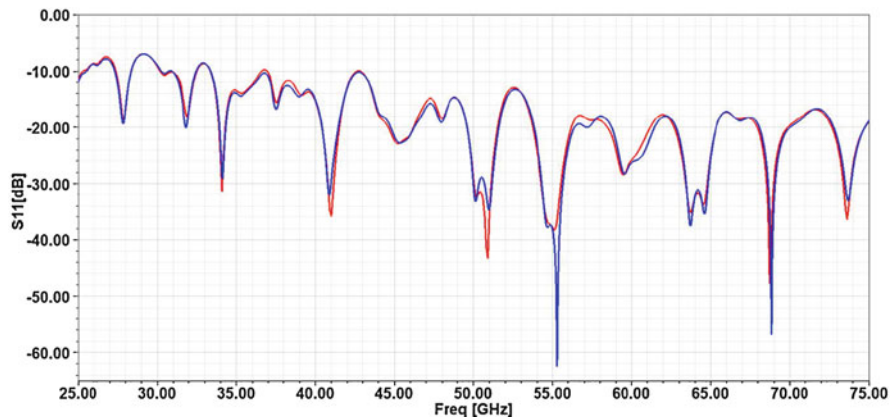


Fig. 27.3 Antenna return loss in free space (blue) and at distance of 10 mm from tissue (red)

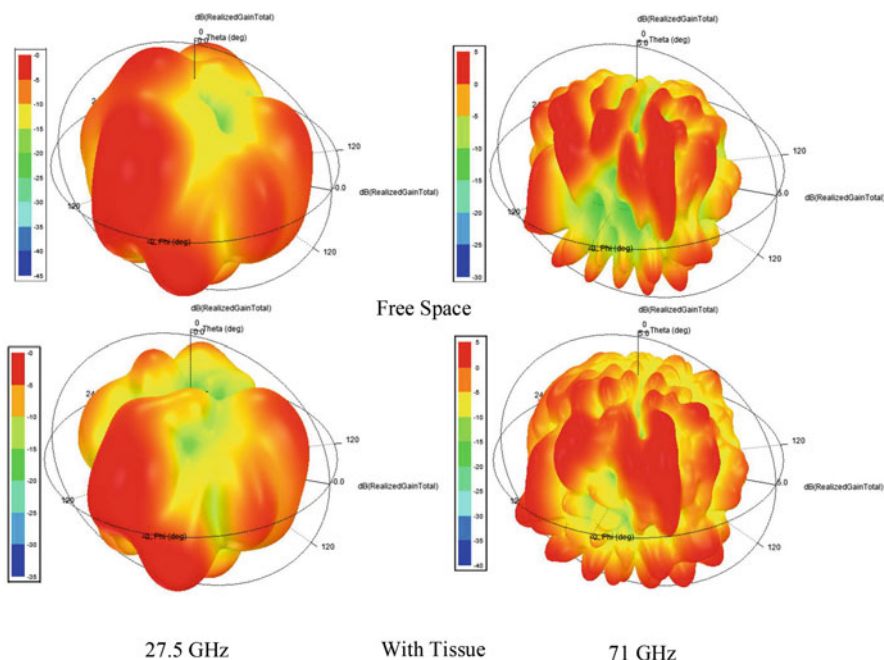
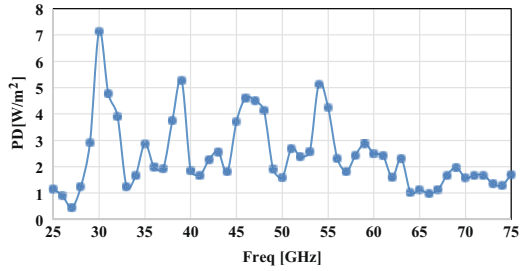


Fig. 27.4 Antenna 3D total realized gain pattern at 27.5 GHz and 71 GHz, in free space and with 10 mm distance to the tissue

Antenna 3D total realized gain pattern at the low-frequency band, i.e., 27.5 GHz, and high-frequency band, i.e., 71 GHz, in the free space and at distance of 10 mm to the tissue is shown in Fig. 27.4. It can be seen that the realized gain pattern is several dB higher at higher frequency for the both free space and with tissue environments,

Fig. 27.5 Maximum value of power density on the tissue surface at distance of 1 cm from radiation source



because the antenna is more directive at the higher frequency. It also shows that gain is not uniform in all the directions.

Figure 27.5 shows the maximum value of power density on the tissue surface at distance of 1 cm from antenna with input voltage of 1 V to the antenna port. It shows that it is much below the limit, imposed by international regulations, i.e., ICNIRP, 10 W/m^2 for the average area (A_v) of 20 cm^2 and 200 mW/m^2 for the A_v of 1 cm^2 in frequency range of 10–300 GHz; FCC, 10 W/m^2 for the A_v of 1 cm^2 in frequency range of 6–100 GHz; and IEEE, 10 W/m^2 for the A_v of $100 \lambda^2$ in the frequency range of 3–30 GHz and 10 W/m^2 for the A_v of 100 cm^2 in the frequency range of 30–100 GHz.

27.5 Conclusion

In this paper, radiofrequency electromagnetic field exposure assessment of 5G antenna for handheld devices is presented. The study is based on the numerical simulation, and results are found to be in the range limit of safety for the RF radiation, with 1 V of input voltage to the antenna port.

The RF EMF exposure will vary at each frequency band; hence, the maximum input power of devices intended to be used in the close vicinity of the body should be selected based on the frequency band of use.

As mentioned earlier, three different regulatory approaches are used worldwide, and they have different restrictions on the level of power density and surface area; hence, it will cause further technical challenges.

References

1. Daniels, R.C., Heath, R.W.: 60 GHz wireless communications: emerging requirements and design recommendations. *IEEE Veh. Technol. Mag.* **2**(3), 41–50 (2008)
2. FCC Homepage. https://apps.fcc.gov/edocs_public/attachmatch/DOC-340301A1.pdf
3. Hong, W.: Solving the 5G Mobile antenna puzzle: assessing future directions for the 5G mobile antenna paradigm shift. *IEEE Micro. Mag.* **18**(7), 86–102 (2017)



4. International Commission on Non-Ionizing Radiation Protection: Health physics: guidelines for limiting exposure to time-varying electric, magnetic, and electromagnetic fields (up to 300 GHz). *Health Phys.* **74**(4), 494–522 (1998)
5. FCC: Code of Federal Regulations CFR title 47, part 1.1310 (2010)
6. Standard for safety levels with respect to human exposure to radio frequency electromagnetic fields, 3 kHz to 300 GHz. IEEE C95.1 (2005)
7. Trinh, L.H., Ferrero, F., Staraj, R., Ribero, J.-M.: Mobile phone antenna for 2G, 3G and 4G standards. In: *International Conference on Advanced Technologies for Communications* (2013)
8. Chu, F.H., Wong, K.L.: On-board small-size printed LTE/WWAN mobile handset antenna closely integrated with system ground plane. *Microwave Opt. Technol. Lett.* **53**, 1336–1343 (2011)
9. Wong, K.-L., Lee, G.-Y., Chiou, T.-W.: A low-profile planar monopole antenna for multiband operation of mobile handsets. *IEEE Trans. Antennas Propag.* **51**, 121–125 (2003)
10. Chu, F.H., Wong, K.L.: Planar printed strip monopole with a closely-coupled parasitic shorted strip for eight-band LTE/GSM/UMTS mobile phone. *IEEE Trans. Antennas Propag.* **58**, 3462–3431 (2010)
11. Andreuccetti, D., Fossi, R., Petrucci, C.: An internet resource for the calculation of the dielectric properties of body tissues in the frequency range 10 Hz–100 GHz. IFAC-CNR, Florence, Italy (1997). <http://niremf.ifac.cnr.it/tissprop/htmlclie/htmlclie.php>
12. ANSYS Homepage. <https://www.ansys.com/products/electronics/ansys-hfss>

Part VII
Case Studies and Wearable Devices

Chapter 28

Driving Operation Recognition Using Smart Cushion Based on Deep Neural Network



Xiong Li, Meng Yu, Wenfeng Li, Congcong Ma, Raffaele Gravina ,
and Giancarlo Fortino 

28.1 Introduction

With the increasing numbers of car, our life has become more and more convenient but several issues raised at the same time. The traffic safety problems attract many researches, and intelligent transportation could better support their solution along with the increasing number of vehicles and drivers.

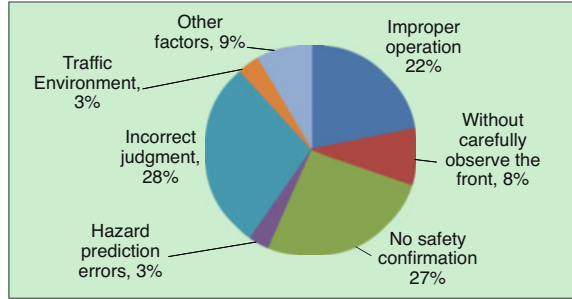
According to the statistical analysis data shown in Fig. 28.1, most accidents are caused by driver's behavior and personal factors [1, 2]. Therefore, it is of great significance to study and analyze the driver's driving operation to improve the level of traffic safety management.

Various literature studies have introduced driving operations recognition methods based on computer vision, multi-sensor fusion, etc. Škrjanc et al. presented an evolving cloud-based algorithm for the recognition of drivers' actions [3]. The general idea is to detect different maneuvers by processing the standard signals that are usually measured in a car, such as the speed, the angle of the steering wheel, and the position of the pedals without additional intelligent sensors. Deng et al. presented a driving style recognition method using braking characteristics based on hidden Markov model [4]. Chen et al. proposed a driving behavior analysis method based on the vehicle on board diagnostic (OBD) information and

X. Li · M. Yu · W. Li (✉) · C. Ma
School of Logistics Engineering, Wuhan University of Technology, Wuhan, China
e-mail: jlixiong@whut.edu.cn; liwf@whut.edu.cn; macc@whut.edu.cn

R. Gravina · G. Fortino
Department of Informatics, Modeling, Electronics and Systems, University of Calabria, Rende,
Italy
e-mail: r.gravina@dimes.unical.it; g.fortino@unical.it

Fig. 28.1 Distribution of traffic accidents statistics [1, 2]



AdaBoost algorithms [5]. Tran et al. proposed a vision-based framework where Hidden Markov Model (HMM) was used to analyze the driver's foot behavior [6].

Smart cushion was also used for activity and sitting posture recognition. Huang et al. proposed the sensor array-based smart-chair to recognize sitting postures [7]; artificial neural network (ANN) was applied to classify eight different postures. Ma et al. proposed a cushion-based posture recognition system [8, 9]; they developed several applications such as wheelchair user's posture recognition, fatigue detection [10], also by combining cloud platforms to develop a wheelchair assist system to help the caregivers monitor the wheelchair user's status [11].

According to the above literature, current major research directions of driving operations recognition include driving data collection and modeling algorithms. Driving data collection includes automotive video capture, car-mounted sensors, and the on board diagnostic (OBD). In terms of driving operations modeling algorithms, there are HMM, support vector machine (SVM), and decision trees, among other methods. This chapter proposes a novel driving operations recognition method based on smart cushion and deep neural network (DNN) algorithms. The proposed method collected pressure data when the driver is seated on the car seat equipped with four pressure sensors. After preprocessing and reducing the dimensions using principal component analysis (PCA) for the data, this chapter constructs a driving operations classification model to finally recognize driving operations with a DNN algorithm including normal driving, stepping on the brakes, stepping on the accelerator, stepping on the clutch, and rotating the steering wheel. The experimental result shows that the proposed driving operations recognition method can achieve an average recognition accuracy rate of about 97%.

The remaining sections of this chapter are organized as follows. The detail of the proposed driving operations recognition method is presented in Sect. 28.2. The experiments and results are detailed in Sect. 28.3. Finally, Sect. 28.4 concludes the chapter.

28.2 Methods

The proposed driving operations identification consists of hardware design, data processing and constructing classification model. The hardware design is used to collect driving operations data. The driving operations data will be divided into a training set and a test set by 8 to 2 ratio. The data processing module includes signal filtering, sliding time window extracted signal, and PCA dimension reduction. The data processing applies to both the training set and the test set. The trained classifier passes the test sample to the driving operations recognition model based on the DNN algorithm to classify the test sample class. The number of correct or misclassified samples divided by the number of total samples in the test set is the classification accuracy or error rate, respectively.

The proposed method first collects pressure data for five different driving operations. Then, such data is divided into training set and test set. Data is filtered, extracted features by sliding time window and processed by PCA dimension reduction. Each processed sample slice can be considered as a representation of the driving operations. This chapter uses the training set to establish a driving operations classification model based on DNN algorithm, and then uses the test set to judge the accuracy of the model. Finally, the feasibility of this method is analyzed and the advantages and disadvantages of using this method to classify driving operations are illustrated. Figure 28.2 shows a workflow of the entire proposed method.

Hardware Design

Cushion and Pressure Sensors

The smart cushion used in this experiment consists of a cushion, four pressure sensors, a Bluetooth module, a micro control unit, and a battery.

The cushion is a common 3 cm thick sponge cushion, which is neither thick enough to degrade the accuracy of the sensor nor affect the normal operation of the driver.

The pressure sensor is the FSR406 produced by Interlink Electronics. Its sensing value changes according to the weight exerted onto the pressure sensor. Table 28.1 reports the main parameters of the FSR406 sensor.

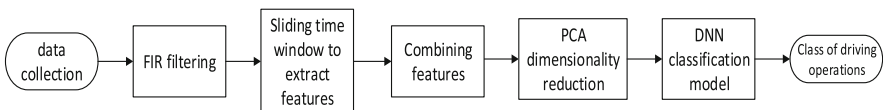


Fig. 28.2 The overall workflow of the proposed method

Table 28.1 The main parameters of FSR406 pressure sensor

Parameter name	Value
Sensor size	4.5 × 4.5 [cm]
Pressure sensing range	<100 [g] to >10 [kg]
Number of sensors	4 (2 × 2)
Sensing area	4.45 × 3.8 cm

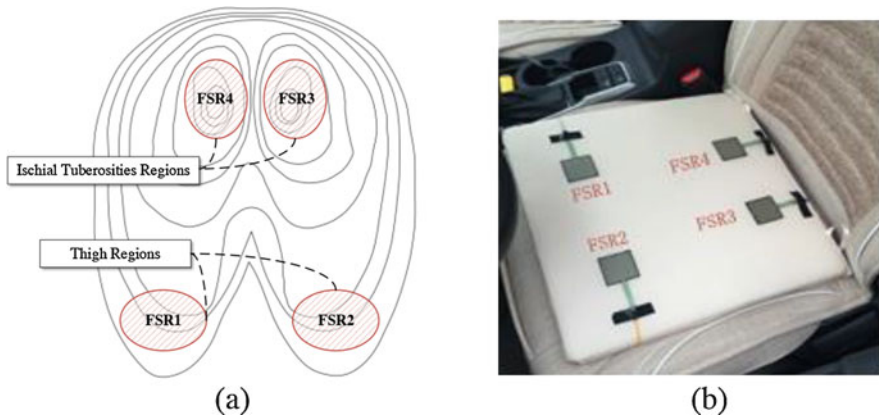


Fig. 28.3 (a) Body–seat interface of human body; (b) pressure sensor deployment

Distribution of the Sensors

In order to collect pressure sensor data more accurately, efficiently, and reduce the cost of the cushion, this chapter provides a sensor distribution method considering the human anatomy. The pressure distribution of the body–seat interface could be converted to image data [12]. Some researches found that the body–seat interface could divide into two ischial tuberosity (IT) [13–15] regions and two thigh regions as shown in Fig. 28.3a. When sitting posture changes, the movement of the trunk or leg will cause the ischial tuberosity area or thigh area pressure values to change. These four areas are highly sensitive to the body movement. On the basis of these observations, we developed a smart cushion with the sensor distribution as shown in Fig. 28.3b.

Data Processing Method

Finite Impulse Response Filter Method

The raw data are typically affected by noise, e.g., caused by the driver’s body movement or electrical signal noise from the smart cushion itself. In order to reduce the impact of noise on the experimental results, the original signal needs to be

preprocessed before analysis. This chapter selects the Finite Impulse Response (FIR) [16, 17] filter to reduce the noise of the original signal.

The FIR filter is defined as Eq. (28.1).

$$y(n) = \sum_{m=0}^{N-1} h(m)x(n-m) = h(n) \otimes x(n) \quad (28.1)$$

where N is the length of the filter, $h(m)$ is the specific pulse of filter system, and $x(n)$ and $y(n)$ are the input and output. The filtering system is shown in Eq. (28.2).

$$h(n) = w_n(n)h_d(n) \quad (28.2)$$

where $h_d(n)$ is ideal filter and $w_N(n)$ is form function. We use Hamming window function as shown in Eq. (28.3).

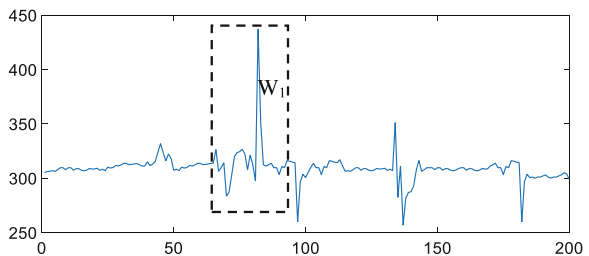
$$w_N(n) = \begin{cases} 0.5 - 0.5 \cos \frac{2\pi n}{N-1} & 0 \leq n \leq N-1 \\ 0 & \end{cases} \quad (28.3)$$

Sliding Time Window

The driving operation is a time series signal. In addition, in order to remove the interference caused by abrupt motion, bumpy signals, and other invalid actions, and to ensure that the extracted signal can reflect real-time and near-term behavior before establishing the recognition model, in this chapter we select the sliding time window to extract the real-time effectiveness of the driver information. The sample taken by the sliding window is then used as a training sample set.

As shown in Fig. 28.4, W_1 is the sliding time window, the time window length is T_1 , and the sampling frequency of the information is F_1 . The length of the time window should not be too long nor too short. If it is too long, the real-time performance will be affected. If it is too short, it will affect the recognition accuracy. After many experiments, we selected a rectangular window with a time window length $T_1 = 25$, and the data sampling frequency $F_1 = 10$ Hz.

Fig. 28.4 Sliding time window schematic



In order to improve the efficiency of model construction and programming, we merge the pressure signals of four pressure sensors that are processed by filtering and sliding time windows, that is, time window signals on four pressure sensors in series.

Principal Component Analysis Dimensionality Reduction

The merged data set is with a very high dimension and has high similarity between samples. If it is directly introduced into the training of the DNN network model, the final accuracy of the model will be affected. In addition, training in ultra-high-dimensional data will require increasing neural network model depth, reducing model training speed and wasting computer memory.

Therefore, this chapter uses PCA dimension reduction after merging data and reduces the dimension so that fewer dimensions can represent more data information, which can increase the efficiency of model construction and improve the final accuracy of the model. We found that the relationship between the accuracy of the model and the retention dimension was parabolic through multiple experiments, and the information retained after PCA dimensionality reduction accounted as shown in Table 28.2.

Considering the model accuracy and the ratio of retention information comprehensively, this chapter finally chooses to reduce the high-dimensional sample data to 5 dimensions, which can retain more original data information and ensure the accuracy of the final model identification.

Classification Model Construction

The data processed by the PCA will be directly input into the DNN model for training and testing. Since the current DNN still belongs to the black box model, the selection of some hyperparameters in the DNN model is still in an empirical stage. This chapter experimentally compares the model accuracy and training time to select a better DNN model structure and its hyperparameters. The final hyperparameters in the model are shown in Table 28.3.

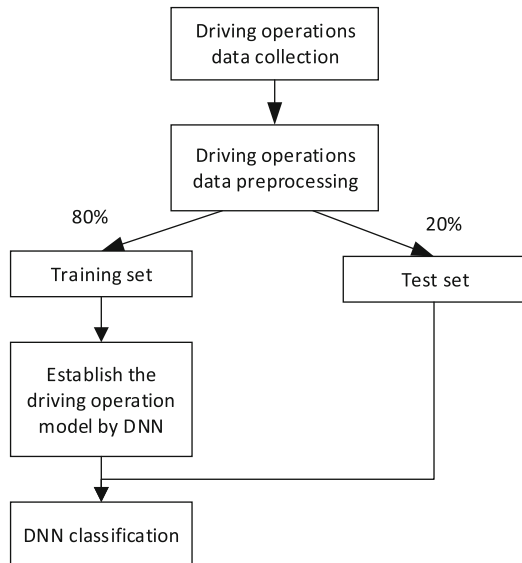
Table 28.2 Information retention ratio after PCA dimension reduction

Reserved dimensions	Reserved information retention ratio
3	0.9057
5	0.9567
10	0.9857

Table 28.3 DNN model structure hyperparameters

Hyperparameters	Value
The number of input layer nodes	5
The number of nodes in hidden layers 1, 2, and 3	5, 5, 5
Output layer node number	5
Batch size	32
Activation function	Relu
Optimization method	Adam
Loss function	Cross entropy
Number of iterations	300

Fig. 28.5 The flowchart of driving operations recognition experiment



28.3 Experiment and Result

The specific process of the experiment is shown in Fig. 28.5. First, the pressure data of the smart cushion is collected; then the data is preprocessed. Data is further divided into a training set and a test set, and the classification model is constructed and trained through the training set. Finally, the trained classification model is verified through the test set.

Data Collection

In our experiments, we used a vehicle driving simulator instead of a real vehicle to collect pressure data. Vehicle driving simulator, shown in Fig. 28.6, contains the



Fig. 28.6 Vehicle driving simulator

same operating components as the real vehicle: steering wheel, clutch, throttle, and brake.

The purpose of the experiment is to verify that the previous model can effectively identify the driver's single driving operations. Therefore, in this chapter we selected five basic single driving operations for recognition classification. The description of these driving operations is as follows:

- Rotating the steering wheel: rotating the steering wheel to the left or the right.
- Step on Brakes: Contact brake pedal—brake pedal pressed to the end.
- Step on the accelerator: Contact accelerator pedal—accelerator pedal pressed to the end.
- Step on clutch: Contact clutch pedal—clutch pedal pressed to the end.
- Normal: Keep normal driving behavior.

Considering that individual differences of the test subjects (e.g., height, weight, gender) may affect the seat pressure distribution, to obtain more general experimental results, when determining the experimental subjects, we recruited 5 healthy workers (4 males (A, B, C, D) and 1 female (E)) with driving experience with a weight of 50–75 kg and a height of 150–180 cm. The personal characteristics of the participants to the experiments are shown in Table 28.4.

We correctly installed the cushion on the seat of the vehicle driving simulator. The subjects sat in a comfortable position on the seat and operated the steering wheel, accelerator, brake, and other operating components to become familiar with the simulated driving operations platform.

Table 28.4 Personal characteristics of the participants

Personnel number	Sex	Age	Height	Body weight (kg)
A	Male	25	171	65
B	Male	24	180	75
C	Male	25	172	68
D	Male	26	176	55
E	Female	29	155	50

After the participants are ready, we request to start the driving operations through the computer in front of the driving simulator. The five types of driving operations are performed separately. After one type of operation is completed, the following one is performed. Each type of driving operation is carried out 20 times (each execution is separated from the previous one by 10 s); before starting a new type of driving operation, the subject rests for 30 s. The five participants completed the described protocol once. In order to prevent increasing the identification error due to the imbalance of the samples in each type of operations, the number of valid samples of the various types of operations finally acquired must be basically the same. Each participant performs 20 operations of each type, each execution takes 0.5 s, and the sampling frequency of the four pressure sensors is 10 Hz. So the size of the original sample data set is 500×4 .

Data Preprocessing

Due to individual differences of the driver's body, noise signals generated by small movements not related to driving operations, and disturbing electrical signals caused by voltage instability or other factors, in order to ensure the accuracy of the processed data, filter preprocessing must be applied to the original signal before analyzing it. In this chapter, FIR filter is used to smooth the original signal. During the filtering process, the sampling frequency of the pressure sensor is 10 Hz. The detection period is determined according to the specific content of the experiment. Each set of data has 500 points and the filter form length is $N = 100$.

In order to transfer the pressure signal to the classification model and identify the signal over a period of time, this experiment uses the sliding time window with a sliding step of 1 to extract the first 25 sample data points each time as part of the new sample data, and merge the features of the new sample data of 4 sensors as a complete sample data point.

The data preprocessing workflow for one type of driving operations is shown in Fig. 28.7. Among them, $S1$, $S2$, $S3$, and $S4$ are the data of four pressure sensors in sequence, and each data has 500 sampling points. The data size of each sensor is 500×1 . First, it is filtered with FIR and its data size is unchanged. Then, by sliding the time window to extract features, the size relation between the data before and after the feature is extracted from the sliding time window is as follows:

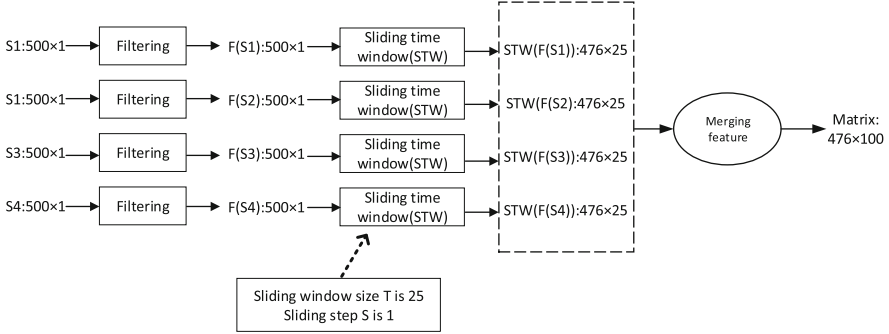


Fig. 28.7 Data processing workflow for a type of driving operations

$$r_2 = r_1 - (T \times S) + 1 \quad (28.4)$$

$$c_2 = T \quad (28.5)$$

where r_1 , r_2 are the number of rows before and after the sliding time window is extracted, and T is the window size of the sliding time window. T is set to 25 in this chapter. S is the step size of the sliding time window. In this chapter, we select S equal to 1. C_2 is the number of columns of data after the sliding time window is extracted. Therefore, the size of each sensor's data after extracting features through the sliding time window is 476×25 . The data features of the four sensors are then combined into a matrix of size 476×100 . Finally, this experiment combines the data of the five types of driving operations into a feature matrix of size 2380×100 for subsequent analysis.

In order to verify whether the collected data can identify five types of single driving operations after preprocessing, this chapter visualizes the data after preprocessing. In this chapter, the high-dimensional feature matrix is firstly reduced to a 3-dimensional data matrix by PCA, as shown with scatter plots in Fig. 28.8.

In particular, Fig. 28.8b is an enlarged side view of the data on the brakes and the accelerator in Fig. 28.8a. After reducing the high-dimensional feature matrix to 3 dimensions and visualization, it can be found that normal driving, operating steering wheel, and pressing clutch are clearly separable. Although there are confusion points between brake and throttle, the classification boundary still exists.

Model Construction

As mentioned in the method, this article uses experiments to synthesize the accuracy and efficiency, selects the DNN model that is used to reduce the 100-dimensional

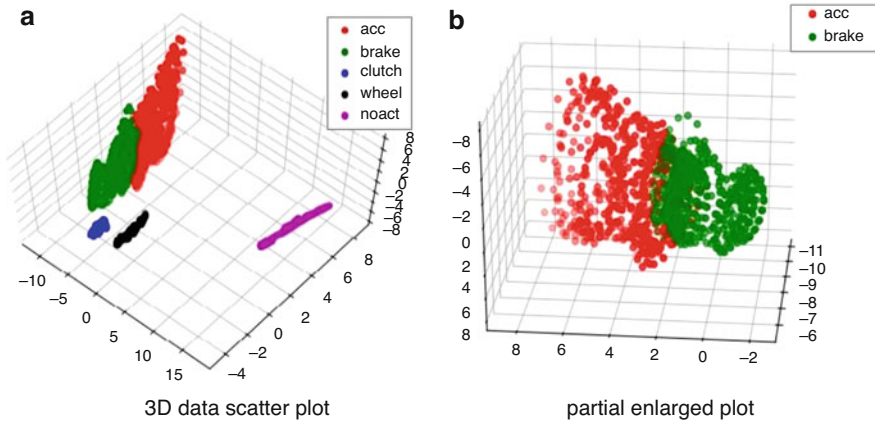


Fig. 28.8 3D data visualization of five driving operations. (a) 3D data scatter plot; (b) Partial enlarged plot

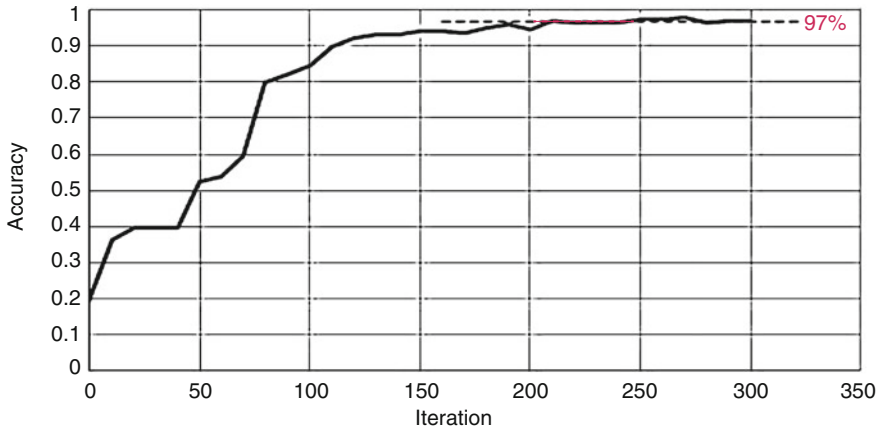


Fig. 28.9 Accuracy of training set

feature data to 5 dimensions, and uses the DNN model parameters determined in Table 28.3 to train a high precision classifier.

We firstly train the DNN model with the prepared training set and then we obtain the appropriate parameters through back propagation and gradient descent, which increases the model accuracy for the data set (including the training set and the test set). The accuracy of the training set is shown in Fig. 28.9.

As shown in Fig. 28.9, the average accuracy of the training set increases with the number of iterations, and after 210 rounds of iterations, the accuracy rate rises slowly reaching 97%. Therefore, this chapter chooses the iteration number as 300, and then apply the trained DNN model to the test set.

Table 28.5 Confusion matrix of classification results

Actual operation	Recognized operation				
	Step on accelerator	Step on clutch	Brake	Rotating the steering wheel	Normal
Step on accelerator	79	0	26	0	0
Step on clutch	0	96	0	0	0
Brake	1	0	91	0	0
Rotating the steering wheel	0	0	0	90	0
Normal	0	0	0	0	95

Table 28.6 Performance of the classification model

Driving operations	Accuracy	Precision	Recall
Step on accelerator	0.9435	0.9875	0.7524
Step on clutch	1	1	1
Brake	0.9435	0.7778	0.9891
Rotating the steering wheel	1	1	1
Normal	1	1	1
Average	0.9774	0.953	0.9483

Recognition Results

Table 28.5 shows the confusion matrix for the classification results, and Table 28.6 shows the performance of the classifier for different driving operations. The results in Tables 28.5 and 28.6 show that the accuracy of the classification model for brake and stepping on the accelerator were 94.35%. The rest of the driving operations was almost 100%, and the average accuracy was 94.5%. The results show that stepping on clutch, rotating the steering wheel, and normal driving all have their own distinct behavioral characteristics, so the recognition accuracy is very high. However, the results show that the recall rate of stepping on the accelerator and the precision of the brakes are low, and the stepping on the accelerator is particularly easy to be mistakenly recognized as brake. Through the review of the details of the experiment, it was found that since both the step on the brake and the step on the accelerator are right-footed, the actions are very similar, and it is easy to misclassify. Therefore, the next step will be to identify the driving operations in combination with multiple sensors to enrich the identified driving operations and improve the recognition accuracy.

28.4 Conclusions

For the purpose of recognizing driving operations, a DNN-based classification algorithm and model are proposed. In this system, our aim is to recognize five kinds of driving operations like stepping on the accelerator, stepping on the brake,

stepping on the clutch, rotating the steering wheel, and normal driving. The sensors deployed according to the physiological characteristics of the human anatomy. In order to reduce noise, the data collected from the sensors was preprocessed by FIR filtering. Then, in order to identify the time segment signal, the signal is subjected to a sliding time window and feature fusion processing [18]. Finally, the merged data is passed to the model training classifier, and five kinds of single driving operations can be recognized.

Recognition of driving operations remains an open research challenge, and in our vision, the use of smart cushion can provide a new perspective for solving this problem. As a smart object in a car, the driver's convenience and alarm function are of great significance in the field of traffic safety. Although our results are still preliminary, this smart, convenient and non-invasive method can provide a reference for future research. In particular, we will focus on enriching operations; for this purpose, more experiments are needed. Finally, in the light of the fact that the pressure cushion alone is not able to provide reliable data for the detection of complex activities, in the future we will add more kinds of sensors to enrich the functions of the proposed system.

Acknowledgements The research is financially supported by National Natural Science Foundation of China (Grant Nos: 61571336 and 71672137). This work has been also carried out under the framework of "INTER-IoT" Project financed by the European Union's Horizon 2020 Research & Innovation Programme under Grant 687283.

References






1. Miyaji, M., Danno, M., Oguri, K.: Analysis of driver behavior based on traffic incidents for driver monitor systems. In: Intelligent Vehicles Symposium, IEEE, pp. 930–935 (2008)
2. Liang, J., Cheng, X., Chen, X.: The research of car rear-ends warning model based on mas and adaboost algorithms. Lect. Notes Eng. Comput. Sci. **2215**(1), 102–106 (2015)
3. Škrjanc, I., Andonovski, G., Ledezma, A., et al.: Evolving cloud-based system for the recognition of drivers' actions. *Exp. Syst. Appl.* **99**, 231–238 (2018)
4. Deng, C., Wu, C., Lyu, N., et al.: Driving style recognition method using braking characteristics based on hidden Markov model. *PLoS One.* **12**(8), e0182419 (2017)
5. Chen, S.H., Pan, J.S., Lu, K.: Driving behavior analysis based on vehicle OBD information and adaboost algorithms. *Lect. Notes Eng. Comput. Sci.* **2215**(1), 102–106 (2015)
6. Tran, C., Doshi, A., Trivedi, M.M.: Modeling and prediction of driver behavior by foot gesture analysis. *Comput. Vis. Image Understanding.* **116**(3), 435–445 (2012)
7. Huang, M., Gibson, I., Yang, R.: Smart chair for monitoring of sitting behavior. *KnE Eng.* **2**(2), 274–280 (2017)
8. Ma, C., Li, W., Gravina, R., et al.: Posture detection based on smart cushion for wheelchair users. *Sensors.* **17**(4), 719 (2017)
9. Ma, C., Li, W., Gravina, R., et al.: Activity recognition and monitoring for smart wheelchair users. In: IEEE, International Conference on Computer Supported Cooperative Work in Design. IEEE, pp. 664–669 (2016)
10. Ma, C., Li, W., Cao, J., et al.: A fatigue detect system based on activity recognition. In: International Conference of Internet and Distributed Computing Systems, vol. 8, pp. 195–202 (2014)

11. Ma, C., Li, W., Cao, J., et al.: Cloud-based wheelchair assist system for mobility impaired individuals. In: *Internet and Distributed Computing Systems*. Springer International, Cham (2016)
12. Aissaoui, R., Kauffmann, C., Dansereau, J., et al.: Analysis of pressure distribution at the body–seat interface in able-bodied and paraplegic subjects using a deformable active contour algorithm. *Med. Eng. Phys.* **23**(6), 359–367 (2001)
13. Fisher, S.V., Patterson, P.: Long term pressure recordings under the ischial tuberosities of tetraplegics. *Spinal Cord*. **21**(2), 99–106 (1983)
14. Bush, C.A.: Study of pressures on skin under ischial tuberosities and thighs during sitting. *Arch. Phys. Med. Rehabil.* **50**(4), 207–213 (1969)
15. Liu, C., Qiu, Y., Griffin, M.J.: Dynamic forces over the interface between a seated human body and a rigid seat during vertical whole-body vibration. *J. Biomech.* **61**, 176–182 (2017)
16. Chen, K.H., Chiueh, T.D.: A low-power digit-based reconfigurable FIR filter. *IEEE Trans. Circuits Syst. II Exp. Briefs.* **53**(8), 617–621 (2006)
17. Mohanty, B.K., Meher, P.K.: A high-performance FIR filter architecture for fixed and reconfigurable applications. *IEEE Trans. Very Large Scale Integr. (VLSI) Syst.* **24**(2), 444–452 (2016)
18. Gravina, R., Alinia, P., Ghasemzadeh, H., Fortino, G.: Multi-sensor fusion in body sensor networks: state-of-the-art and research challenges. *Inform. Fusion.* **35**, 68–80 (2017)

Chapter 29

A Wearable Device for Brain–Machine Interaction with Augmented Reality Head-Mounted Display



Mattia Salvaro , Simone Benatti , Victor Kartsch ,
Marco Guermandi , and Luca Benini 

29.1 Introduction

Global market analyses forecast that wearable device business will break the five billion dollars barrier by 2020 [1], with recent advancements in microelectronics and wireless communication pushing devices more and more towards low-power, miniaturized, lightweight implementations, with wireless communication capabilities. A plethora of new devices belonging to the so-called Wireless Body Area Networks (WBANs) [2] is emerging, whose potential can be exploited in several domains, including healthcare, industry, fitness, and infotainment. More specifically, WBANs are widely used for biosignal and activity monitoring [3–6], ambient assistance as well as for human– machine interactions (HMI).

Among the available methods and devices to allow effective interactions between humans and machines, the possibility to build interfaces directly exploiting brain signals (EEG) represents a fascinating challenge. This type of interaction, called brain–computer interfaces (BCIs), was initially developed at the end of the 1980s to enable external world communication for people with severe disabilities, such as locked-in syndrome or amyotrophic lateral sclerosis [7]. Once relegated to medical-

M. Salvaro (✉)
DEI, University of Bologna, Bologna, Italy
e-mail: mattia.salvaro@unibo.it

S. Benatti · V. Kartsch · M. Guermandi
Energy Efficient Embedded Systems Lab (EEES), DEI, University of Bologna, Bologna, Italy
e-mail: simone.benatti@unibo.it; victorjavier.kartsch@unibo.it; marco.guermandi@unibo.it

L. Benini
Energy Efficient Embedded Systems Lab (EEES), DEI, University of Bologna, Bologna, Italy
Integrated System Laboratory (IIS), ETH Zurich, Zürich, Switzerland
e-mail: luca.benini@unibo.it; lbenini@ee.iis.ethz.ch

oriented application targeting small groups of users with very specific needs, they have recently spread to non-medical application fields by virtue of their promising and fascinating features.

Wireless BCI systems have been proposed in recent years to overcome traditional HMI paradigms based on touch-screen or gesture and voice recognition [8]. Several non-medical BCI applications are already commercially available, mostly in the field of gaming and entertainment: MindMaze Mask [9], Neurosky MindWave [10], and Emotiv Insight and EPOC+ [11], just to name a few. All these systems feature a head-mounted device for biosignals acquisition, but they differ in the number and position of sensors, and the types of biosignal they process (EEG, EMG, or EOG). Other commercial BCI systems include OpenBCI [12], a general purpose wearable acquisition and processing platform, and g.tec Intendix [13], a desktop based BCI speller.

One of the major hindrances to the diffusion of non-medical BCIs among able-bodied users is the so-called BCI deficiency, i.e., the inability of BCIs to detect the intentions of a vast portion of users accurately enough to allow them to control applications. BCI deficiency is lessened in BCI systems based on external stimulation such as event-related potential (ERP) or steady state visual evoked potential (SSVEP) [8]. ERP consists in cerebral responses to specific events or sensory stimuli that can be detected in the acquired EEG signal [14]. In ERP-based BCIs, several trials are averaged to reduce background noise and derive the ERP response, typically searched around 300 ms after the stimulus onset (P300). SSVEP potential is elicited in the primary visual cortex, as well, but this time by a periodic external visual stimulus, and results in a response which is locked in frequency and phase with the stimulus. SSVEP-based BCIs process the EEG signal to identify which stimulus (i.e., at which frequency and, possibly, phase) evoked it. Recent works [15] have shown that SSVEP-based BCIs can outperform those based on P300 in terms of information transfer rate (ITR). In addition, if we disregard the phase information, SSVEP-based BCIs do not need synchronization with the stimulus onset. For these reasons, SSVEP is a promising paradigm for designing wearable, low-power and high-speed BCI.

Despite BCIs moving towards being embedded in wearable devices, visual stimuli are still mostly presented on large LCD monitors, limiting their application to fixed locations of the environment (e. g., [16]). By combining BCIs with AR tools such as smart glasses, microprojectors, or head-mounted displays (HMD), the system flexibility can be dramatically increased. As an example, visual stimuli can be triggered adaptively according to the user's position or action. So, if the user approaches a specific object, a BCI starts to interact with that object through the HMD.

An example of the integration of a P300 based BCI system used to enable HMI is reported in [17], where an EEG acquisition system is coupled with an AR system to enable the control of a smart home. The system is tested on three subjects for tasks of domotic control (i.e., TV channel switching, opening and closing doors.). The subjects were firstly trained in numbers and characters spelling based on their P300 response. The final needed time for recognition task is typically around 30s

with accuracy ranging from 83 to 100%. This system reaches high accuracy but it is intended for users with severe disabilities, based on a full coverage EEG cap and not suitable for a wearable consumer application.

The work of [18] presents a wearable interface which combines an eye-tracker with a BCI trigger to detect the response to visual stimulation using a binary classifier. Basically, the eye-tracker detects where the user is looking, and enables the SSVEP stimuli mapped on the intended object, enabling the user to choose how to interact with the object. The system is based on a modified version of the Emotiv NeuroHeadset, using wet saline electrodes which acquire the EEG signal at 128 Hz. Samples are sent wirelessly to an Odroid board, powered by a high-end processor (i.e., Samsung Exynos4412 Prime chip operating with 1.7 GHz ARM Cortex-A9 Quad Cores). The average classification accuracy is 73.5% while the time needed to perform a recognition task is higher than 4 s.

Another solution, presented in [19], relies on a simpler approach, since it uses a QR code recognition to enable the interaction with the selected object and a commercial smart glasses system [20] to present the SSVEP stimuli. The embedded camera of the eyeglasses executes a QR-code recognition when the user is looking in the direction of the intended object, and enables the SSVEP stimulation accordingly. The EEG data are acquired with an Emotiv EEG neuroheadset and processed by a bench top host PC. This system was tested on 7 subjects reaching an average accuracy of 85.7% with a recognition latency that ranges from 3 to 6 s. The aforementioned solutions are inspiring attempts to enable a natural, hand and voice free control strategy, but they are based on bulky setups, where the EEG interface requires skin preparation and the digital computing platforms are power-hungry and cumbersome, hence not suitable to be integrated into an unobtrusive wearable form factor.

In this paper, we propose an embedded fully-wearable BCI composed of a low-power EEG acquisition system connected with commercial smart glasses (Moverio BT-200), which provides the visual stimuli exploiting AR techniques. The stimuli presentation is performed on the see-through display of the eyeglasses and it is synchronized via Bluetooth to the embedded processing node, which executes the canonical correlation analysis (CCA) based algorithm to recognize the user command. The system has been tested on five subjects, reaching an average accuracy of 80% with a recognition latency of 3 s, suitable for a fast and reliable BCI. EEG is acquired on a minimum number of electrodes (three) with active dry sensors which do not require skin preparation, granting a high level of users' acceptability. Power consumption of the device is less than 32.12 mW, guaranteeing more than 100 h of operation on a standard 1000 mAh battery.

This paper is organized as follows. In Sect. 29.2 we describe the different components of the complete BCI; in Sect. 29.3 we validate the system by illustrating experiments carried out on five subjects and analyze the results. Finally, in Sect. 29.4 we draw conclusions and compare our system to the state-of-the-art.

29.2 System Description

The proposed system is the body sensor network (BSN) depicted in Fig. 29.1. An active EEG sensor array is interfaced with a custom node which mounts a dedicated AFE and a low-power microcontroller with a DSP extended instruction set. The node is connected via Bluetooth to a commercial smart glasses platform [20], equipped with an optical see-through head-mounted display (HMD) that provides visual stimuli presentation.

Acquisition and Processing Platform

To maximize ease-of-use, the system adopts three zero-preparation dry electrodes for interfacing with the subject. To cope with the high contact impedance typical of non-prepared skin-electrode interfaces, we used active sensors, which leverage an amplification stage placed right on the electrodes. The operational amplifier is connected in an unity-gain voltage follower configuration, and it buffers the EEG signals to the acquisition and processing platform, which is based on a low-power ARM Cortex M4 microcontroller (MCU, STM32F407) coupled with a multichannel commercial analog front end (AFE, T.I. ADS1298). In view of future developments, we adopted an 8-channel AFE, although we could have adopted a 4-channel IC of the same family (ADS1294). The positive inputs of the analog channels are connected to the active EEG sensors. Ground potential from the subject is on

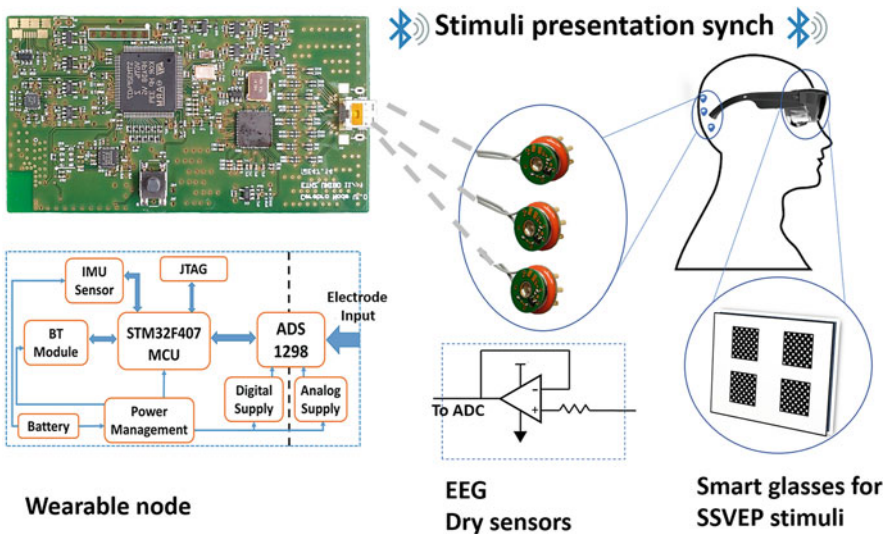


Fig. 29.1 Architectural diagram of the proposed system

linked mastoid electrodes (i.e., a widely used re-referencing technique [21]), and is connected to the negative inputs of the AFE. The MCU can operate up to 168 MHz and features 192 kB of RAM and 1 MB of Flash memory. Particular attention was dedicated to the design of the 6-layers PCB for the system. The solid ground plane minimizes the current return paths, while the power planes are kept separated, minimizing the high-frequency noise on the analog components. The power supplies are provided by separate LDO regulators for analog and digital blocks, as shown in Fig. 29.1. The communication interface is provided by an integrated Bluetooth module, connected via USART to the MCU.

AR Stimuli Presentation

EPSON Moverio BT-200 is a commercial smart glasses running Android 4.0.4 on a dual-core ARM Cortex A9. The device allows for WiFi and Bluetooth connectivity. The display is a TFT active matrix with LCD size of 0.42 inches, 16:9 aspect ratio, and 60 Hz refresh rate. The viewer, a binocular see-through that renders a screen of 80 inch virtual size at a virtual distance of 5 m, makes Moverio BT-200 particularly suitable for 3D AR applications. The processor and battery are enclosed in a handheld trackpad for standard interaction. Once the BCI app is launched, there is no need to control it via trackpad, enabling a complete hand-free interaction.

In normal condition, the display is set to maximum transparency and nothing is shown. Using the integrated camera and Vuforia SDK for digital eyewear [22], we developed a BCI App which detects whenever the user is staring at tags which can be freely applied to objects in the environment, and informs the BCI wearable node that the user wants to interact with a certain object. Different tags can trigger different numbers of stimuli but, remarkably, different tags can trigger stimuli using the same set of frequencies, overcoming the bottleneck problem of pushing as many target frequencies as possible in a small bandwidth between 5 and 10 Hz, where the SSVEP response is maximized. Each stimulus consists of a PNG image representing an 8×8 black and white square checkerboard, with a gray diagonal cross to guide user's gaze. The frequency of the stimulus is rendered by modulating the image opacity from 0 to 1 with a sine waveform. The app can dynamically arrange up to six different checkerboards at the same time, however in this work we focus on a four checkerboard setup. Each checkerboard is controlled by its own ValueAnimator object, initialized for linearly animating float values from 0 to 2, representing the coefficient of π in the sine wave equation. The duration of the animation reflects the stimulus frequency, and it is computed from the frequency attribute, which can be set directly in the XML layout file. An AnimatorUpdateListener object is used to intercept the updates of the ValueAnimator animation, and set the opacity of the image accordingly. The animation is then repeated for a number of times calculated on the predefined stimulation length, and then the checkerboard disappears. Figure 29.2 shows an example of the application usage from the user's perspective: when the user looks at a tag, four flickering checkerboards appear on

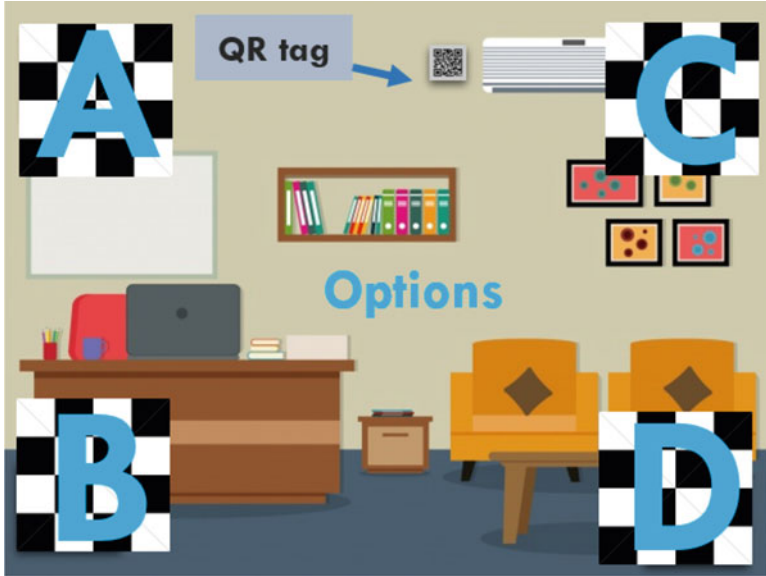


Fig. 29.2 Example of the application usage from the user's perspective

the HMD, representing four possible actuations on the corresponding item. The app notifies via Bluetooth the BCI wearable node when stimulation begins and ends, allowing the MCU to execute the classification algorithm only when SSVEP can be detected, significantly reducing power consumption.

Processing Algorithm: CCA

CCA is a well-known, state-of-the-art signal processing algorithm for SSVEP-based BCIs [23]. This method quantifies the linear dependency between two multidimensional variables by finding a couple of linear combinations, one for each multidimensional variable, that maximizes their correlation. CCA retrieves a set of maximized correlations, called canonical coefficients, each one resulting from a couple of linear combination belonging to subspaces that are orthogonal to each other. A single execution of the CCA algorithm returns a set of size $d = \min(n, m)$ of canonical correlation coefficients that quantifies the correlation between the EEG signal window and one specific stimulus. To calculate an output, the application executes CCA with different reference signals for each possible stimulus. We acquire EEG signals from the three dry electrodes ($n = 3$), and we keep reference signals up to the first harmonic ($m = 4$), therefore the CCA will output $d = 3$ canonical coefficients, on which we apply the Euclidean norm to have one final correlation value. The classification of the BCI output is done by thresholding the four correlation values computed for each frequency.

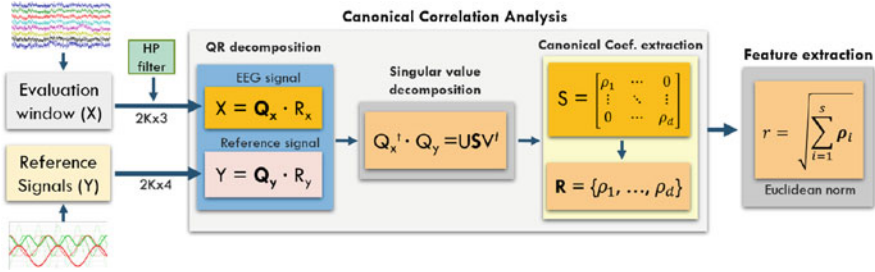


Fig. 29.3 Signal processing scheme for SSVEP Signal classification using CCA. Raw data is buffered into the matrix X (2000 samples \times 3 channels). Reference signals are stored in the Y matrix. Subsequently, QR decomposition is applied on both matrices allowing the extraction of the diagonal S matrix from Q_x and Q_y after singular value decomposition. The diagonal elements of this matrix (called canonical coefficients) are finally used to calculate the feature of the signal (Euclidean norm). This process is repeated for each target frequency

Our implementation of the CCA is based on the Golub algorithm [24], which relies on the computation of two QR decompositions of the input and the reference signals, followed by a SVD factorization of the product between the two orthogonal matrices. The block scheme of the Golub algorithm is depicted in Fig. 29.3. We applied three levels of optimization: (1) usage of CMSIS DSP optimization functions whenever possible [25], (2) precomputation and storage in Flash memory of the orthogonal matrices resulting from the QR decomposition of all the reference signals, and (3) input filtering and downsampling. This approaches allow us to compute a stimulus classification on an input window of 2 s in 5 ms. To maximize accuracy, input preprocessing is necessary, especially when signals are acquired with dry electrodes, to remove power line interference (PLI) and out-of-band noise. Since we are using stimulus frequencies in the 5–10 Hz band and we are interested in the first two harmonics of the signal, we apply a decimation filter to downsample the signal by a factor 10. The filter is based on a 120-tap low-pass FIR filter with 25 Hz cutoff frequency. After decimation, a fourth order IIR high pass filter removes frequency content below 4 Hz. The Golub algorithm computes at each iteration the QR decomposition of the reference signal, which is a constant matrix. Therefore, we can store the orthogonal matrix of the decomposition for each set of reference signals in the MCU Flash memory, skipping this operation and computing directly the $Q_x^T Q_y$ product. Total speedup is in excess of 13X, as will be shown in Sect. 29.3.

29.3 Experimental Results

Our BCI system was validated on five healthy subjects (aged 25–43), with normal or corrected-to-normal vision. All participants reported no history of neurological or psychiatric disorders and provided written consent to participate in the experiments.

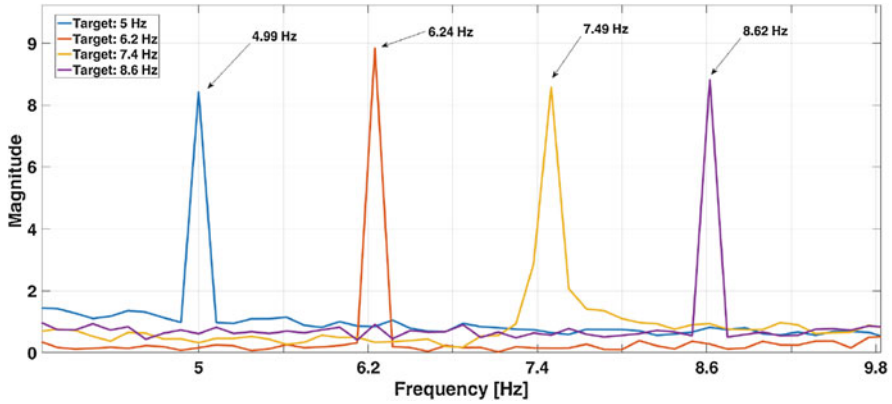


Fig. 29.4 Frequency response of stimuli generated on the AR glasses and captured by a photo-resistor. The deviation from the target frequency is < 0.1 Hz

The tests have been carried out in an lab environment, which is particularly harsh in terms of electrical and electromagnetic noise.

The first test is intended to validate the stimulus presentation described in Sect. 29.2. To this end, we connected a photo-resistor to one input of the system, to capture light variations generated by the projection of the flickering checkerboards on the glasses. Figure 29.4 shows the power spectral density (PSD) of the resulting signal, indicating that the maximum deviation from the original target frequency is confined below 0.1 Hz. Such variations do not affect the final accuracy of the system for time windows up to a few seconds.

SSVEP-Based BCI Performance

SSVEP signals are elicited employing four black and white checkerboards as described in Sect. 29.2, arranged in a 2×2 pattern, located at the corners of the visual field of the smart glasses display. Four equally spaced frequency-coded stimuli (5.0, 6.2, 7.4, and 8.6 Hz) are used as targets. During the tests, the subjects will fix the eyesight at a target indicated with a red cue before the onset of the stimulation. Later, all the stimuli will remain active for 10 s, followed by 5 s of pause to reduce visual fatigue. This process is repeated four times to cover all checkerboards, and the trial is repeated three times for each subject (Fig. 29.5).

Concurrently, EEG data is acquired using the hardware presented in Sect. 29.2 from three electrodes placed at the occipital lobe (P5, POZ, and P6), with reference and ground located at A1 and A2, respectively. An example of the complete setup is presented at Fig. 29.6.

Before each test with the smart glasses, we performed a control test using a regular 24-inch LED (60fps) display. The results obtained are later used to evaluate

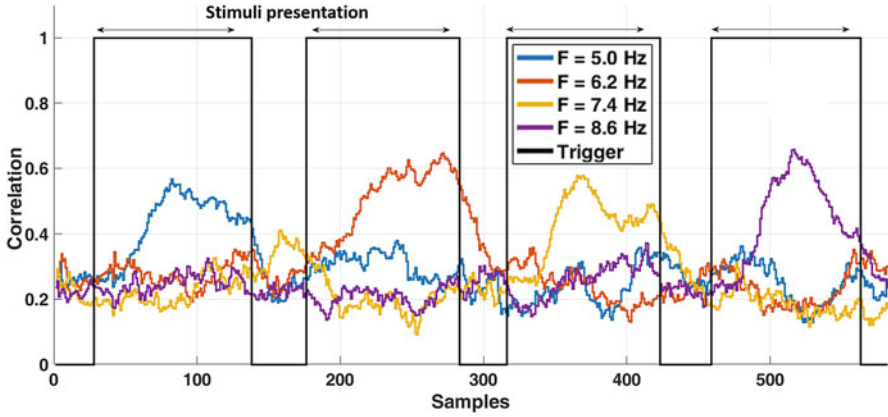


Fig. 29.5 CCA correlation

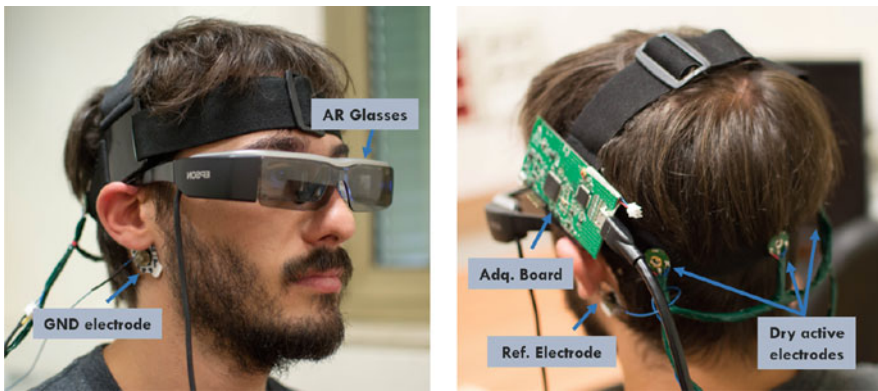


Fig. 29.6 Front and back view of the complete setup during a test. The HDMI cable attached to the board is used only for testing purpose, and it is not required during normal operation of the system. Similarly, the current size and weight of the PCB allow an easy debugging. Nevertheless, the entire hardware dimensions can be reduced to a half

the performance of the AR projections with respect to the classical technique for SSVEP stimulation [26]. Table 29.1 reports detailed results for all subjects. To account for some occasional variabilities regarding the acquisition setup each subject has repeated the test three times. Of the five subjects, only S5 has performed poorly, possibly due to attention issues. Nevertheless, the average results show that the system is reliable (average accuracy 80%) and responsive (average latency of about 3 s), with an average ITR with four targets of 0.42 b/s.

The results demonstrate that our embedded implementation outperforms systems based on AR eyeglasses while being also aligned with the SoA traditional SSVEP systems. Moreover, we show that online and real-time processing is achievable

Table 29.1 Experimental results

Subject	Latency (s)	Accuracy	ITR (b/s)
S1	2.57	1.00	0.78
	4.50	1.00	0.44
	3.08	1.00	0.65
S2	2.95	0.67	0.19
	3.85	0.91	0.37
	2.25	1.00	0.89
S3	3.03	0.63	0.15
	3.78	0.68	0.16
	2.00	0.87	0.62
S4	1.70	0.91	0.83
	3.13	0.85	0.37
	1.58	0.82	0.65
S5	5.63	0.69	0.11
	3.00	0.50	0.07
	2.50	0.50	0.08
Average	3.04	0.80	0.42

For each subject results of three trials are reported

through a low-intrusivity setup, which is a significant step forward with respect to the current offline and bulky systems.

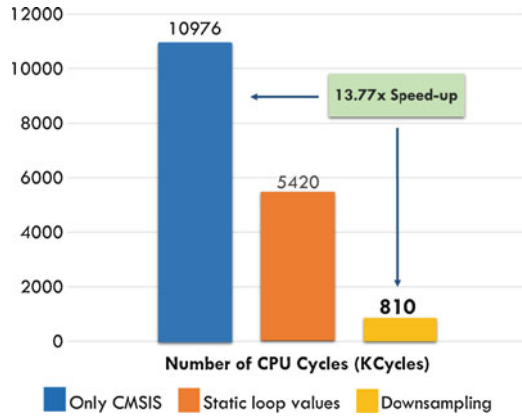
Power Consumption

Execution of advanced signal processing on a microcontroller requires particular attention due to the limitations on MCU resources and power availability. Executing the CCA in real time is computationally intensive, hence we applied code optimizations to reduce the computational cost of the application. Specifically, we noticed that downsampling the current evaluation window (2K samples) by a factor of 10 would provide lighter processing without accuracy degradation.

We have also exploited the static nature of some parameters of the CCA. The orthogonal matrix Q_y , resulting from the QR decomposition of the reference signals, does not have to be recalculated unless new frequency targets are added to the system. Since set of stimulation frequencies is fixed, the Q_y matrices have been precalculated and stored as static values on the final firmware, reducing the computational load of the MCU. All these changes finally led to a 13.77X speed up of the system from a non-optimized code using only CMSIS DSP libraries.

The results of each optimization step are presented in Fig. 29.7. As a result, the CCA execution time is less than 5 ms, allowing to trade-off the percentage of window overlap to compute successive feature points. While a substantial overlap would provide better granularity and reduction of the classification delay (i.e.,

Fig. 29.7 Reduction of the CPU cycles after the optimization steps



increasing the ITR) it comes at a higher power cost. Empirical results suggest that 100 ms (95% overlap) can reduce the power consumption of the system to 32.12 mW while guaranteeing an average ITR of 0.42 b/s.

Therefore, this demonstrates the ability of our system to provide a real-time user experience, aligned with SoA performance. We go a step further combining a deeply embedded platform with dry electrodes, which enhanced the contribution of this work with regards of current system based on cumbersome processing platforms and wet electrodes. Coupling this with the use of an AR environment delivers a realistic BCI, promising a more intuitive and accessible approach for brain communication in consumer applications.

29.4 Conclusions

In this paper, we proposed a fully-wearable BCI composed of a low-power EEG acquisition system for SSVEP detection connected to a pair of commercial smart glasses for stimuli presentation. We go a step further combining a deeply embedded platform with dry electrodes, which highlights the contribution of this work with regards of current system based on cumbersome processing platforms and wet electrodes. Coupling this with the use of an AR environment delivers a realistic BCI, promising a more intuitive way of brain communication. Our wearable BCI offers the performance of the current SoA systems while also providing a real-time EEG signal classification through a non-intrusive, embedded processing platform featuring dry electrodes. The system has been validated on five subjects, achieving an average ITR of 0.42 b/s and an average output latency of 3.0 s. This performance substantially improves those of SoA wearable systems employing AR and smart glasses in terms of both accuracy and delay [18, 19]. Firmware optimization of the algorithm has been shown helpful in keeping power consumption as low as 32.12 mW, essential for providing extended hours of operation. The usage

bottleneck of the system is therefore constituted by the battery duration of the commercial HMD device.

This work aims at spreading the usage of BCI systems by devising a wearable easy-to-use online system ready to be deployed in fields where reliability constraints are stronger, such as smart environments like industry 4.0. The ability of our system to provide a real-time user experience highlights the contribution of this work towards a more realistic and useful BCI.

Future work includes efforts for increasing the robustness of the system and the ITR by incorporating more advanced signal processing methods (PCA, ICA) and classification techniques (such as neural networks and support vector machine) that will allow us to recognize a more significant number of targets while reducing the classification delay.

Acknowledgements This work was supported by the EU H2020 project “OPRECOMP.OPEN TRANSPRECISION COMPUTING” (grant no. 732631)

References

1. Market Research Engine, Inc., <https://www.marketresearchengine.com/wearable-devices-market> (2018)
2. Latré, B., et al.: A survey on wireless body area networks. *Wirel. Netw.* **17**(1), 1–18 (2011)
3. Nick, T.A., Berman, L.M., Barnehama, A.Z.: Personalized neuroscience: user modeling of cognitive function and brain activity in the cloud. In: Proceedings of the 10th EAI International Conference on Body Area Networks, ICST (Institute for Computer Sciences, Social-Informatics and Telecommunications Engineering), pp. 78–84 (2015)
4. Benatti, S., Milosevic, B., Tomasini, M., Farella, E., Schoenle, P., Bunjaku, P., Rovere, G., Fateh, S., Huang, Q., Benini, L.: Multiple biopotentials acquisition system for wearable applications. In: SmartMedDev BIODEVICES, pp. 260–268 (2015)
5. Kartsch, V., Benatti, S., Rossi, D., Benini, L.: A wearable EEG-based drowsiness detection system with blink duration and alpha waves analysis. In: 2017 8th International IEEE/EMBS Conference on, IEEE, Neural Engineering (NER), pp. 251–254 (2017)
6. Kartsch, V.J., Benatti, S., Schiavone, P.D., Rossi, D., Benini, L.: A sensor fusion approach for drowsiness detection in wearable ultra-low-power systems. *Inform. Fusion* **43**, 66–76 (2018)
7. Farwell, L.A., Donchin, E.: Talking off the top of your head: toward a mental prosthesis utilizing event-related brain potentials. *Electroencephalogr. Clin. Neurophysiol.* **70**(6), 510–523 (1988)
8. Blankertz, B., Tangermann, M., Vidaurre, C., Fazli, S., Sannelli, C., Haufe, S., Maeder, C., Ramsey, L.E., Sturm, I., Curio, G., et al.: The Berlin brain–computer interface: non-medical uses of BCI technology. *Front. Neurosci.* **4**, 198 (2010)
9. Mindmaze, Mindmaze Mask, <https://www.mindmaze.com/mask/> (2018)
10. Neurosky, Neurosky MindWave, <http://neurosky.com/biosensors/eeg-sensor/biosensors/> (2018)
11. Emotiv, <https://www.emotiv.com/> (2018)
12. OpenBCI, <http://openbci.com/> (2018)
13. g.tec GmbH, g.tec Intendix, <http://www.gtec.at/Products/Complete-Solutions/intendiX-Specs-Features> (2018)
14. Sur, S., Sinha, V.: Event-related potential: an overview. *Ind. Psychiatry J.* **18**(1), 70 (2009)

15. Nicolas-Alonso, L.F., Gomez-Gil, J.: Brain computer interfaces, a review. *Sensors* **12**(2), 1211–1279 (2012)
16. Salvaro, M., Kartsch, V., Benatti, S., Milano, M., Benini, L.: Towards a novel HMI paradigm based on mixed EEG and indoor localization platforms, in: 2017 New Generation of CAS (NGCAS), pp. 217–220. IEEE, Piscataway (2017)
17. Guger, C., Holzner, C., Grönegress, C., Edlinger, G., Slater, M.: Control of a smart home with a brain-computer interface, Citeseer (2008)
18. Kim, Y., Kaongoen, N., Jo, S.: Hybrid-BCI smart glasses for controlling electrical devices. In: 2015 54th Annual Conference of the Society of Instrument and Control Engineers of Japan (SICE), pp. 1162–1166. IEEE, Piscataway (2015)
19. Saboor, A., Rezeika, A., Stawicki, P., Gemblar, F., Benda, M., Grunenberg, T., Volosyak, I.: SSVEP-based BCI in a smart home scenario. In: International Work-Conference on Artificial Neural Networks, pp. 474–485. Springer, Berlin (2017)
20. EPSON, Moverio BT-200, <https://www.epson.it/products/see-through-mobile-viewer/moverio-bt-200> (2018)
21. Yang, P., Fan, C., Wang, M., Li, L.: A comparative study of average, linked mastoid, and REST references for ERP components acquired during fMRI. *Front. Neurosci.* **11**, 247 (2017)
22. Vuforia, Vuforia SDK for digital eyewear, <https://library.vuforia.com/articles/Training/Vuforia-for-Digital-Eyewear> (2018)
23. Lin, Z., Zhang, C., Wu, W., Gao, X.: Frequency recognition based on canonical correlation analysis for SSVEP-based BCIs. *IEEE Trans. Biomed. Eng.* **53**(12), 2610–2614 (2006)
24. Golub, G.H.: Matrix decompositions and statistical calculations. In: *Statistical Computation*, pp. 365–397. Elsevier, Amsterdam (1969)
25. ARM, CMSIS Library, <https://www.arm.com/products/processors/cortex-m/cortex-microcontroller-software-interface-standard.php> (2016)
26. Zhu, D., Bieger, J., Molina, G.G., Aarts, R.M.: A survey of stimulation methods used in SSVEP-based BCIs. *Comput. Intell. Neurosci.* **2010**, 1 (2010)

Chapter 30

A Cost-Effective Embedded Platform for Scalable Multichannel Biopotential Acquisition



Simone Benatti , Marco Guermandi , and Luca Benini 

30.1 Introduction

Recent years have witnessed an explosive growth in the diffusion of systems for decoding neural signals. They allow to monitor physiological events from the human body and use them to enable direct interaction between a subject and machines, allowing the design of HMI suitable for healthcare and rehabilitation applications, especially based on electroencephalography (EEG) and electromyography (EMG) by virtue of their cost-effectiveness and unobtrusiveness.

Although most commercially available devices and many research works in the field rely on platforms with a limited number of channels (ranging from 2 to 8) [1], recent studies demonstrate that medium to high density sensor arrays and more advanced processing techniques have the potential to significantly improve performance both for EEG and EMG applications. For instance, in EEG applications, it has been shown that increasing sensor density can provide higher-resolution neural information in several domains, such as steady state evoked potentials (SSVEP) decoding [2], epilepsy detection [3], or sleep analysis [4]. As for EMG, most of the applications are in the field of advanced HMI for prosthetic controls or rehabilitation, and recent results demonstrate that a fine-grain coverage of the muscle surface increases control performance both in terms of accuracy [5] and robustness [6].

S. Benatti (✉) · M. Guermandi

Energy Efficient Embedded Systems Lab (EEES), DEI, University of Bologna, Bologna, Italy
e-mail: simone.benatti@unibo.it; marco.guermandi@unibo.it

L. Benini

Energy Efficient Embedded Systems Lab (EEES), DEI, University of Bologna, Bologna, Italy

Integrated System Laboratory (IIS), ETH Zurich, Zürich, Switzerland

e-mail: luca.benini@unibo.it; lbenini@ee.iis.ethz.ch

© Springer Nature Switzerland AG 2020

C. Sugimoto et al. (eds.), *13th EAI International Conference on Body Area Networks*, EAI/Springer Innovations in Communication and Computing,
https://doi.org/10.1007/978-3-030-29897-5_30

353

Several studies present dedicated integrated solution based on research ASICs [7–9] which benefit from a large number of channels in a reduced form factor. Unfortunately, most of them are prototypes not directly accessible to those who were not involved in their design. Moreover, such solutions are not clinically validated and compliant to CE/FDA regulation and most of the research projects cannot sustain the huge validation costs in terms of time and resources.

Commercially available Analog Front-Ends (AFE) for biomedical applications traditionally feature a limited number of channels (up to 8) [1]. Recently, a few integrated solutions with higher channel count in a single chip solution have been presented [10, 11]. Such systems are modular, providing the possibility to reach hundreds of channels in the form factor of cm^2 and they are commercially available. Unfortunately, solutions based on such ICs are quite expensive, since the single chip is available at several hundreds of dollars with a cost per channel of approximately 10 USD. Moreover, being developed mostly for implantable applications, their input-referred noise performance can hardly satisfy requirements for several applications (e.g., EEG, ERPs, VEPs, etc.).

This work proposes a cost-effective modular multichannel system for EMG acquisition with 32/64 channels, entirely based on Commercial Off-The-Shelf (COTS) components. The system is based on a 24-bit COTS AFE [1], connected to a network of analog multiplexers (MUXs) which scales up the channel count. Our solution is suitable for embedded implementation in a reduced form factor, with bandwidth and noise figures of merit suitable for medical-grade biopotential acquisition and processing [12]. To evaluate the cost per channel of our solution we consider the commercial ADC, whose cost is 7.15 USD and the 8 analog MUXs, which are available for 1.31 USD in a 4×1 or 8×1 configuration. Furthermore, since our platform is digitally controlled we can also add the cost of the Cortex M4 microcontroller which is 7.3 USD. Using eight 4×1 MUX for a 32 channels configuration leads to a 0.77 USD per channel, while if we consider a 64 channels configuration (with the 8×1 MUXs) the cost per channel decreases to 0.38 USD.

A key challenge also addressed in this work is that the Sigma-Delta architecture of the ADC in the AFE would lead to a reduction of the sample rate, caused by the need to wait for the internal decimation sinc filter to settle after each multiplexer switching to avoid crosstalk between channels. To overcome this limitation, we devised a method to process the digital output stream from the AFE through a custom digital FIR filter, which compensates the decimation filter behavior. We prove that this method reduces crosstalk by a factor of more than 25, allowing the system to both satisfy specifications for high-quality EEG signal acquisition and be effectively used in a common EMG application without degrading performance. For a sampling frequency of 1 ksp/s, this approach allows to reduce input-referred noise by a factor 1.6, leading to $0.75 \mu\text{V}_{\text{RMS}}$ integrated noise in the [0.5–100] Hz band and $1.15 \mu\text{V}_{\text{RMS}}$ in the [20–250] Hz with 24-bit resolution, which favorably compares to the multichannel systems presented in [10, 13] ($2.4\text{--}3.1 \mu\text{V}_{\text{RMS}}$ with 16-bit accuracy) and with specifications for EEG and EMG signal acquisition [14].

To experimentally validate our solution within and end-to-end application context, we tested the system in a typical EMG-based pattern recognition application,

using 32 electrodes to acquire 4 hand gestures and classify them with a SVM algorithm [8]. Recognition accuracy ranges from 93.5 to 95.2% showing results aligned with current SoA wearable systems [6, 15].

30.2 System Overview

The high-level block diagram of the proposed system is shown in Fig. 30.1. It includes a custom flex PCB strip with 16 passive electrodes, a rigid PCB for signal acquisition and processing, and two wireless modules for Wi-Fi and Bluetooth connectivity. On the rigid board, the 24-bits $\Sigma \Delta$ ADC [1] is interfaced with a Cortex M4 microcontroller, responsible for controlling the overall functionality of the board and managing acquisition and communication. The PCB layout has been carefully designed to minimize electrical noise, by separating digital and analog sections in order to reduce the digital high-frequency noise injected in the analog signals. The board has been fabricated on a 4-layer PCB with a split-plane that distributes the power supplies and a solid ground plane, to minimize current return paths.

To enable the communication with an external gateway, the board is connected to both a Wi-Fi module and to a Bluetooth transceiver. The Wi-Fi interface is used to stream out the data at full-bandwidth, while the Bluetooth interface can be used for configuration or debug purposes where the data stream is less demanding. For instance, streaming 32 channels at 24-bit with a bandwidth of 1 kHz requires 6 Mb/s, which is by far out of range for a Bluetooth transmission, while 700 kHz bandwidth of the WT12 Bluetooth module is suitable for debug purposes. The Wi-Fi module

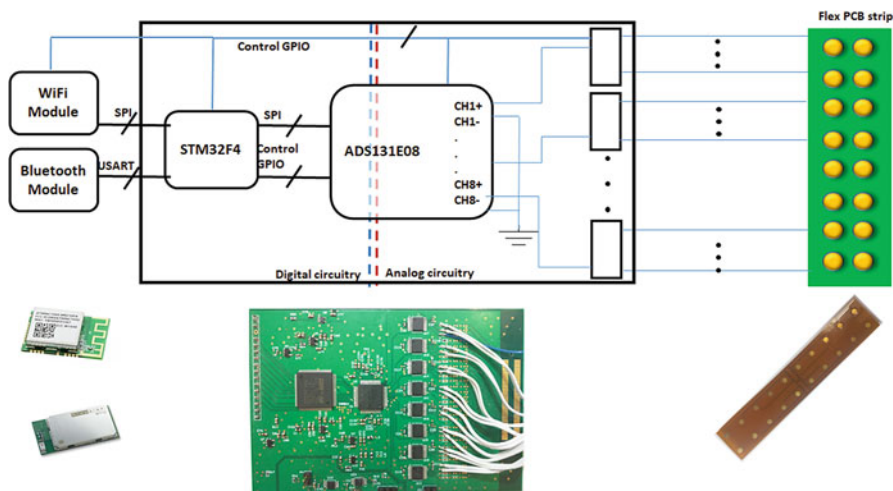


Fig. 30.1 High level diagram of the proposed system highlighting the hardware architecture and photo of the proposed PCB board and strip

is the ATWINC1500 by Microchip [16], a single-band 2.4 GHz b/g/n, connected to the microcontroller via 40 MHz SPI interface, while the Bluetooth connection is enabled by the Bluegiga WT12 module [17].

Finally, a Driving Right Leg (DgRL) circuit is implemented [18], which increases the system CMRR of up to 70 dB, mitigating the effect of common mode interferences which can pose major problems in devices designed to operate outside clinical environments, as they can easily present less-than-perfect contact quality and operate in noisy environment.

The power budget of the system is dominated by the digital platform, since the Cortex M4 microcontroller consumes 100 mW, while the ADS1299 consumes 40 mW. Leveraging power optimization techniques and accurate component selection it is possible to dramatically reduce the current consumption of the whole system even though power optimization is out of the purpose of this work.

Signal Acquisition

Traditional passive electrodes, like [19], are not adequate for placing a high number of sensors in a reduced area, hence we designed a custom polyimide 2-layers flex PCB strip with 5 mm gold-plated round electrodes. To enable a better contact, the skin-to-electrode interface is provided by semi-rigid adhesive hydrogel patches which add mechanical stability as well electrical connection. The electrodes are connected to a network of analog MUXs, which scale up the channel count of the ADC from 8 to 32 or 64, depending on the MUX configuration. In this first prototype, the board is designed to support 32 channels by using ADG709 4-to-1 MUXs. The MUX switching is managed by the microcontroller, according to the acquisition frequency. In normal operating condition, as the decimation filter of the ADC has a settling time of 3 samples, it is necessary to wait at least 3 sampling periods for a stable ADC read after every switching of the MUX. Hence, to calculate the effective sampling rate of the ADC (ESR_{kspss}) we can use the following formula:

$$ESR_{kspss} = \frac{N_{\text{settling_samples}} \cdot \text{MUX}_{\text{positions}}}{DSR_{kspss}} \quad (30.1)$$

where DSR_{kspss} is the desired sampling rate, $N_{\text{settling_samples}}$ is the number of samples to settle the internal oversampling of the ADC (typically $3 + 1$ to allow some extra time for the MUX transient), and $\text{MUX}_{\text{positions}}$ is the number of possible configuration of the MUX. For instance, if we want a sampling rate of 1 kspss (DSR_{kspss}) by switching the MUX 4 times and considering the standard setting time of 4 samples, we need to set ADC sampling frequency at 16 kspss.

Inverse Filter Signal Reconstruction

As the limitation set by Eq. (30.1) is due to the settling time of the digital decimation filter and we know its exact characteristics from the ADS131E08 datasheet (sinc^3 filter with decimation factor $1.024 \cdot 10^3 / DSR_{kspss}$), we can remove this limitation by processing the output of the AFE through a suitably designed filter. Assuming that the signal at the input of the decimation filter will present fast transitions when the

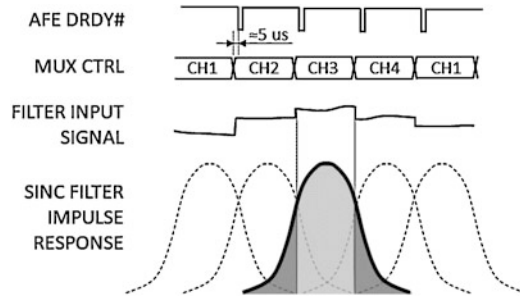


Fig. 30.2 The input signal of the filter can be approximated as piecewise constant (top) and is convolved with a sinc^3 filter (bottom). The decimation filter can be represented as a 3-tap FIR filter (h_{-1} , h_0 and h_1) operating at the output frequency. The area of dark gray regions is equal to h_{-1} and h_1 (1/6), light gray to h_0 (2/3)

MUX switches and then be slowly varying in a sample interval, we can approximate the signal as piecewise constant (see Fig. 30.2). As a result, the decimation filter can be represented as a 3-tap FIR filter operating at the output frequency. The taps value can be easily computed as the areas of the 3 gray regions in Fig. 30.2 (2/3 for the central light gray region and 1/6 for the lateral ones). We can then numerically compute the inverse of such a filter. As the inverse filter will present an infinite impulse response, we decided to truncate the tap number at 32, as the sum of the absolute values of the neglected taps is less than 10^9 times the central tap. The AFE shows a fixed delay between the time instant when an acquisition ends (and the following one starts) and the edge of the DRDY (data-ready) signal which we estimated to be approximately $5 \mu\text{s}$. We therefore aligned the instant at which the multiplexer switches to the correct time at which the new acquisition starts by anticipating it with respect to the DRDY signal by $5 \mu\text{s}$. Additional non-ideal behaviors (e.g., finite transition times in MUXs and analog conditioning circuits, high-frequency content in the input signal, limited synchronization between ADC and MUX) will reduce the accuracy of the reconstruction. However, we will prove in the next section that the approximation does not significantly affect performance both with respect to common electrical specifications for EEG/EMG acquisition systems and in real case scenarios such as gesture recognition while allowing to increase signal bandwidth for a given AFE sampling frequency (Fig. 30.3).

30.3 Experimental Results

Evaluation of the acquisition performance is a key element for a biopotential recording system, both from the electrical and functional standpoints. As the main drawbacks of our architectures can be considered to be increased noise and crosstalk between channels due to input signal multiplexing, we mostly focus on these

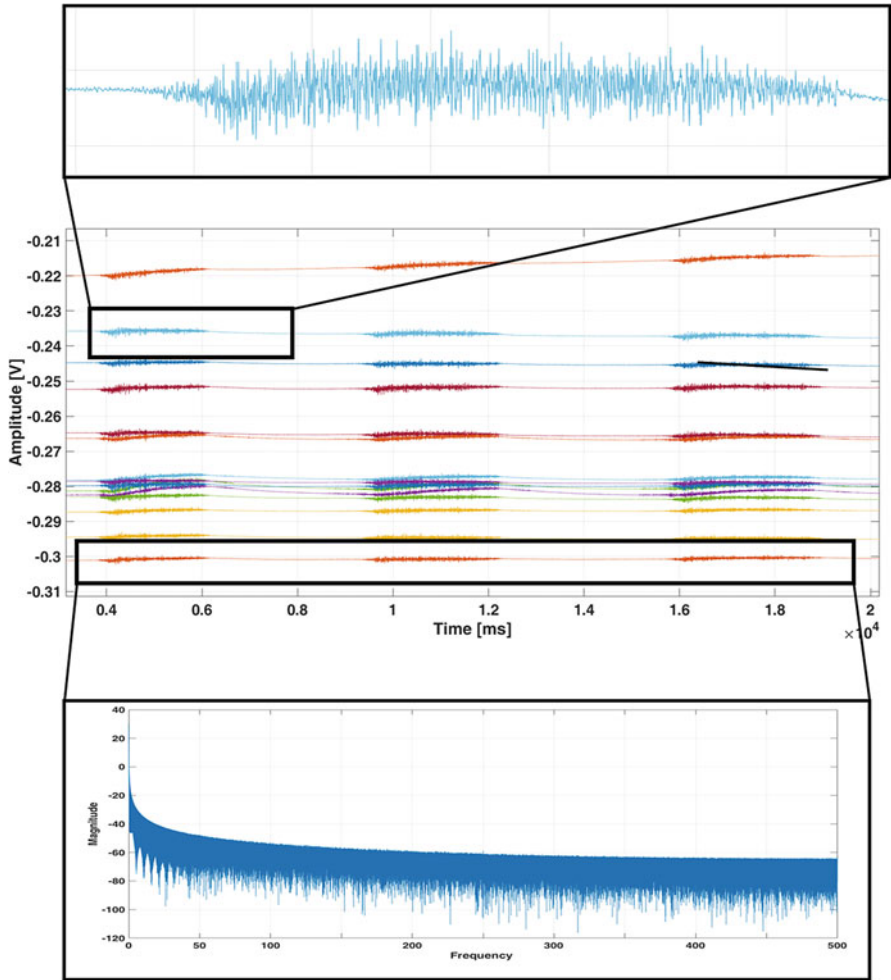


Fig. 30.3 EMG acquired signal. In the bold boxes: a single contraction (above) and the FFT calculated on one channel (below)

two figures of merit. Secondly, we evaluate the performance of a typical pattern recognition application, based on the “*de facto*” standard algorithm and compare it with literature golden standard. We show how, even though multiplexing results in a partial superposition of adjacent channels which can be reduced but not canceled by our approach, it does not significantly affect the performance of the classifier algorithm, demonstrating how it is possible to optimize system parameters depending on the specific application.

Table 30.1 Input-referred noise integrated in the typical EEG and EMG bands for different configurations and sample rates

Integrated noise [μV_{RMS}]	1 ksps waiting $4 T_{\text{sample}}$	1 ksps	2 ksps	4 ksps
EEG band [0.5–100] Hz	1.19	0.75	0.86	1.08
EMG band [20–250] Hz	1.79	1.15	1.2	1.67

Electrical Characterization

One of the most critical parameter to evaluate the performance of a signal acquisition system is the input-referred noise, measured by shorting inputs to a fixed potential.

Table 30.1 shows input-referred noise integrated in typical EEG and EMG bands ([0.5–100] Hz and [20–250] Hz, respectively). Using the same sampling frequency, noise is reduced by a factor 1.6 in the implementation with the AFE running at 4 ksps and using the inverted sinc filter to reconstruct the signal, with respect to the standard implementation which waits $4 T_{\text{sample}}$ for the filter to settle. This is due to the reduction of noise performance of the AFE at increased sample rates. The value of $0.75 \mu\text{V}_{\text{RMS}}$ is slightly higher than what prescribed by IFCN ($0.5 \mu\text{V}_{\text{RMS}}$) [14] but is still considered widely acceptable for high-quality EEG acquisition [20]. Moreover, the requirement can be easily satisfied by replacing the AFE with an ADS1299, specifically designed for EEG signal acquisition, at the cost of increase in price and power consumption. As a comparison, the datasheet of Intan chip RHD2132 [10] declares an input-referred noise of $2.4 \mu\text{V}_{\text{RMS}}$, while the system presented in [13] shows a noise performance of $3.1 \mu\text{V}_{\text{RMS}}$.

As described in section “Inverse Filter Signal Reconstruction,” non-idealities will affect the capability of the inverse sinc filter to reduce crosstalk between channels due to the multiplexing of signals on the same AFE channel. Figure 30.4 shows performance for different sampling rates at varying frequency, as compared to specification set by IFCN recommendations for high-quality EEG signal acquisition (1% of 40 dB) [14]. Measurement is performed by connecting one input to a variable frequency signal, 100 mV peak-to-peak amplitude. All other inputs are shorted and crosstalk is measured as the ratio between the amplitude of the signal leaking on adjacent channels at the output of the system and the input signal amplitude. To simulate the effect of the interface between skin and electrode, we inserted a standard model of contact impedance (series between a $1 \text{ K}\Omega$ resistor and the parallel between a $51 \text{ K}\Omega$ resistor and a 47 nF capacitor). We observe how the specification is satisfied for all sampling rates in the EEG band (up to 100 Hz). As a proof of the effectiveness of our approach, crosstalk before post-processing is 25% on adjacent channels.

The flexibility of the system allows to tailor the trade-off between bandwidth, noise, and crosstalk to satisfyingly address different applications. If we consider EEG applications, our approach allows to acquire up to 32 channels sampled at 1 ksps with a good noise level. At the same time, we could extend the channel

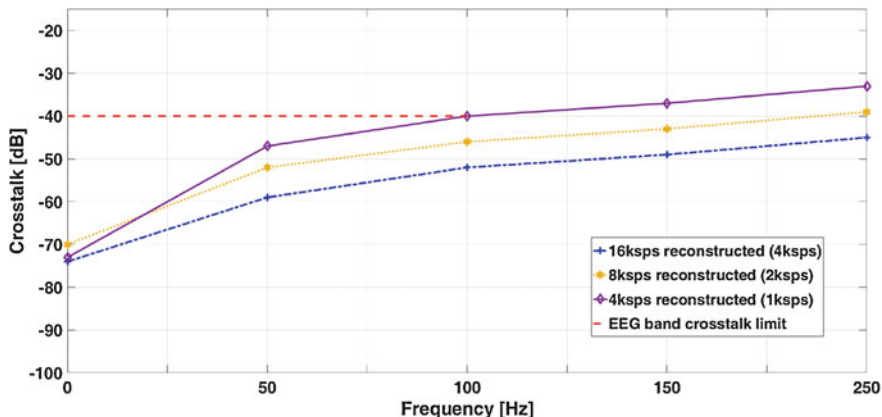


Fig. 30.4 Crosstalk between adjacent channels. For all sampling rates, we satisfy specifications prescribed by IFCN recommendations for high quality acquisition of EEG signals

number to 64 (using 8:1 MUXs), with a noise degradation of approximately 25%. If the application allows for additional increase in noise level (such as for most EMG signals), we could even consider 16:1 multiplexing, extending channel number up to 128 with a single AFE. This would not be possible if we had to wait for the decimation filter to settle. Moreover, for 32-channel solutions, our approach allows to increase sampling rate by a factor 4, up to 4 kps. As crosstalk decreases for increased sample rate, we observe that higher sampling rates can be beneficial for signals with higher bandwidth but relaxed requirements on input-referred noise, such as EMG.

Application to EMG Gesture Recognition

In this experiment, we tested the system by applying the EMG flexible strip on the forearm of one able-bodied subject without previous history of neuromuscular diseases. The first test is performed using the acquisition system without the digital reconstruction (i.e., waiting for the $3 + 1$ sampling periods, as explained in section “Signal Acquisition”). The system acquired the 32 EMG channels at 1 kps (DSR_{kps}) on a set of 4 gestures: power grip, precision grasp, open hand, and rest position. The subject executed each gesture 4 times, holding contractions for 3 s and separating the repetitions with 3 s of hand relaxation (rest position). Figure 30.3 showcases a trace of the EMG signal acquired with the multiplexed ADC. It is noticeable that the FFT does not present peaks caused by the MUX switching and, thanks to the DgRL circuit [18], which increases the CMRR of 70 dB, the Power Line Interference (PLI) on the traces is negligible.

We evaluate the performance of our approach on a typical gesture recognition application, using the processing scheme depicted in Fig. 30.5, based on the Discrete Wavelet Transform (DWT) and on SVM algorithm to classify the acquired samples. The DWT based preprocessing is a well-accepted feature extraction technique which gives time–frequency domain information on the acquired sample. In this

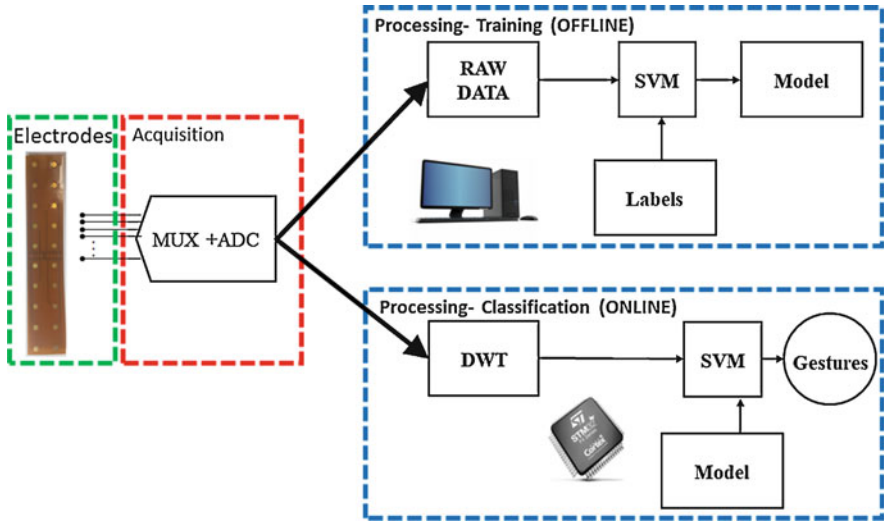


Fig. 30.5 Computational scheme

experiment we used as feature vectors, the Detail Coefficients (decomposition level 4), calculated on the HAAR Mother Wavelet.

During the training phase, performed offline on a PC platform, we acquire the EMG data to train the SVM model (i.e., an array of Support Vectors), using 10% of the data acquired in one single session. During the classification, performed online, we calculate the output of the SVM over the continuous stream of acquired gestures. The accuracy, measured as the difference between the gesture labels annotated by hand and the SVM output values, reaches 95.56% with a model of 710 Support Vectors, resulting aligned with values presented in literature and suitable for the implementation of a real-time gesture recognition system [15, 21].

In the last experiment we tested the aforementioned pattern recognition application, leveraging the developed method to suppress crosstalk. We acquire EMG data by setting the ADC at 8 ksp/s and switching the MUX input at every new sample (i.e., without waiting for the 4 settling samples, as described in section “Inverse Filter Signal Reconstruction”). The resulting sampling rate of the EMG channels is $8 \text{ ksp/s} / 4_{\text{MUX position}}$, i.e., 2 ksp/s.

Figure 30.6 shows the difference between a single muscular contraction acquired in normal operating conditions (AFE sampling rate set to 16 ksp/s and waiting $4 T_{\text{sample}}$ for the filter to settle, Fig. 30.6-top) and the signal obtained running the AFE at 4 ksp/s and post-processing data to remove crosstalk (Fig. 30.6-bottom). The muscular contraction is clearly detectable in both configurations.

Testing the SVM hand gesture recognition application with the reconstructed signal, we obtain that the SVM algorithm calculates 819 vectors, and reaches an average accuracy of 93.54% over the 4 hand position, again aligned with SoA literature [15].

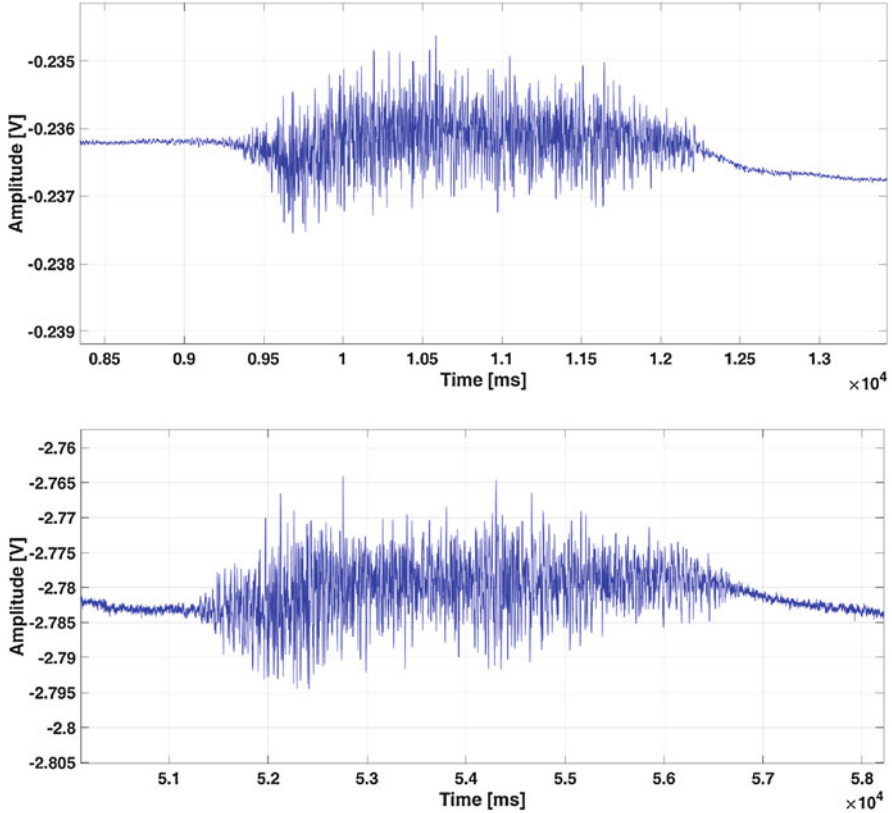


Fig. 30.6 Difference between EMG signal acquired with standard 4-samples settling (above) and digital reconstruction (below)

This experiment shows how, thanks to our approach, we can safely increase sample rate without degrading performance of the system. On the other hand, although this was not possible in this work as the interface has a limited number of electrodes, we can exploit the trade-off between channel number and bandwidth to use our system in configurations requiring extended number of channels. This is of the uttermost importance as recent results have demonstrated that a fine-grain coverage of the muscle surface increases control performance both in terms of accuracy [5] and robustness [6].

30.4 Conclusions and Future Work

This paper presents a cost-effective scalable multichannel system for acquiring medium-density arrays of biopotentials. The presented framework allows to acquire up to 64 channels maintaining the cost below 1 USD per channel with electrical

performance aligned with those of SoA systems. To overcome physical limitations of the Sigma-Delta ADCs and increase the sampling rate of the multiplexed signal (or the number of channels for a given sample rate), we presented a method to process the digital output stream from the AFE through a custom digital FIR filter, which compensates the decimation filter behavior. We proved this method to be able to reduce crosstalk by a factor of more than 25, allowing the system to both satisfy specifications for high-quality EEG and EMG signal acquisition. For a sampling frequency of 1 ksp/s, this approach allows to reduce input-referred noise to $0.75 \mu V_{RMS}$ integrated noise in the [0.5–100] Hz band and $1.15 \mu V_{RMS}$ in the [20–250] Hz with 24-bit resolution, which favorably compares to the multichannel systems presented in [10, 13] ($2.4\text{--}3.1 \mu V_{RMS}$ with 16-bit accuracy) and with specifications for EEG and EMG signal acquisition. Moreover, we tested the system on a typical pattern recognition application and we verified that it achieves accuracy value above 95% in line with the literature.

Thanks to the modular design and to the simple backend interface of the ADC, this solution is particularly suitable for designing embedded interfaces based on low-power microcontrollers. Future work targets the system optimization, minimizing the PCB layout with more aggressive place&routing, Vias-in-Pads, and smaller component packages. Furthermore, we will explore techniques to maximize performance of the system in terms of number of channels, bandwidth, noise as well as we will test the system on a wider range of signals and applications.

Acknowledgement This work was supported by the European H2020 FET project OPRECOMP (g.a. 732631).

References

1. Texas Instruments (2016). <http://www.ti.com/product/ADS131E08>. Date Last Accessed 28 May 2018
2. Robinson, A.K., Venkatesh, P., Boring, M. J., Tarr, M. J., Grover, P., Behrmann, M.: Very high density EEG elucidates spatiotemporal aspects of early visual processing. *Sci. Rep.* **7**(1), 16248 (2017)
3. Chu, C.J.: High density EEG—what do we have to lose? *Clin. Neurophysiol.* **126**(3), 433 (2015)
4. Murphy, M., Bruno, M.-A., Riedner, B.A., Boveroux, P., Noirhomme, Q., Landsness, E.C., Brichant, J.-F., Phillips, C., Massimini, M., Laureys, S., et al.: Propofol anesthesia and sleep: a high-density EEG study. *Sleep* **34**(3), 283–291 (2011)
5. Merletti, R., Holobar, A., Farina, D.: Analysis of motor units with high-density surface electromyography. *J. Electromyogr. Kinesiol.* **18**(6), 879–890 (2008)
6. Moin, A., et al.: An EMG gesture recognition system with flexible high-density sensors and brain-inspired high-dimensional classifier. In: 2018 IEEE International Symposium on Circuits and Systems (ISCAS), pp. 1–5. IEEE, Piscataway (2018)
7. Carboni, C., et al.: Earnest: a 64 channel device for neural recording and sensory touch restoration in neural prosthetics. In: 2017 IEEE Biomedical Circuits and Systems Conference (BioCAS), pp. 1–4 (2017). <http://doi.org/10.1109/BIOCAS.2017.8325549>

8. Benatti, S., et al.: A sub-10 mW real-time implementation for EMG hand gesture recognition based on a multi-core biomedical Soc. In: 2017 7th IEEE International Workshop on Advances in Sensors and Interfaces (IWASI), pp. 139–144. IEEE, Piscataway (2017)
9. Farnsworth, B.D., et al.: Wireless implantable EMG sensing microsystem, in: 2008 IEEE Sensors, pp. 1245–1248 (2008)
10. **INTAN Technologies Inc** (2014). <http://www.intantech.com/>. Date Last Accessed 28 May 2018
11. Lopez, C.M., et al.: A neural probe with up to 966 electrodes and up to 384 configurable channels in 0.13 μm SOI CMOS. *IEEE Trans. Biomed. Circuits Syst.* **11**(3), 510–522 (2017)
12. Song, H., et al.: Fully integrated biopotential acquisition analog front-end IC. *Sensors* **15**(10), 25139–25156 (2015)
13. Erickson, J.C., et al.: Intsy: a low-cost, open-source, wireless multi-channel bioamplifier system. *Physiol. Meas.* **39**(3), 035008 (2018)
14. Nuwer, M.R., Comi, G., Emerson, R., Fuglsang-Frederiksen, A., Guérit, J.-M., Hinrichs, H., Ikeda, A., Luccas, F.J.C., Rappelsburger, P.: IFCN standards for digital recording of clinical EEG. *Clin. Neurophysiol.* **106**(3), 259–261 (1998)
15. Oskoei, M.A., Hu, H.: Support vector machine-based classification scheme for myoelectric control applied to upper limb. *IEEE Trans. Biomed. Eng.* **55**(8), 1956–1965 (2008)
16. **ATMEL ATWIN1500** (2015). <https://www.microchip.com/wwwproducts/en/ATWINC1500>. Date Last Accessed 20 Nov 2017
17. **Bluegiga WT12** (2012). <https://www.silabs.com/products/wireless/bluetooth/bluetooth-classic-modules/wt12-bluetooth-class-2-module>. Date Last Accessed 20 Nov 2017
18. Guermandi, M., et al.: A driving right leg circuit (DgRL) for improved common mode rejection in bio-potential acquisition systems. *IEEE Trans. Biomed. Circuits Syst.* **10**(2), 507–517 (2016)
19. **COVIDIEN Electrodes** (2014). <http://products.covidien.com>. Date Last Accessed 28 May 2018
20. Yazicioglu, R.F., et al.: A 200 μW eight-channel EEG acquisition ASIC for ambulatory EEG systems. *IEEE J. Solid-State Circuits* **43**(12), 3025–3038 (2008)
21. Benatti, S., et al.: A prosthetic hand body area controller based on efficient pattern recognition control strategies. *Sensors* **17**(4), 869 (2017)

Chapter 31

A Pilot Study on Electrode–Skin Impedance Analysis of Embroidered EMG Electrodes



Bilge Guvenc Tuna , Gozde Goncu Berk , Nese Topcuoglu, and Umit Ozorhan

31.1 Introduction

Surface electromyography is a method of retrieving the changes in the physiological state of muscle fiber membranes as voltage noninvasively from the skin. Electromyography (EMG) analysis is widely used to track sports performance in addition to diagnosis of neural and muscular diseases in medical sciences. While some surface EMG equipment could be a large size system composed of a PC, printer, keyboard, screen, and electrodes, wireless EMG devices also exist. In surface EMG applications for sports performance analysis, it is vital to conduct wireless EMG to not to interfere with the movement of the athlete. Measuring EMG data wirelessly in a wearable form, through electronic textile (e-textile) based electrodes integrated within the clothing could provide several advantages compared with the conventional silver/silver chloride (Ag/AgCl) electrodes. E-textile electrodes are unobtrusive since they are flexible and do not contain the hydrogel pads that require skin preparation and that can cause skin irritation in the long-term use. Unlike the conventional, hydrogel Ag/AgCl electrodes whose performance degrades over time as the gel dries, e-textile electrodes are reusable and washable and can come in different compositions, sizes, and shapes.

B. G. Tuna · U. Ozorhan
Yeditepe University, Istanbul, Turkey
e-mail: bilge.tuna@yeditepe.edu.tr

G. Goncu Berk (✉)
University of California, Davis, CA, USA
e-mail: ggoncuberk@ucdavis.edu

N. Topcuoglu
Istanbul Technical University, Istanbul, Turkey

One of the most important problems of surface EMG is masking of EMG signals by unwanted electrical activity or noise. The masking of signal by noise is caused by the relatively low signal-to-noise ratios (SNRdB). Especially in EMG diagnosis where muscle activity is low, SNRdB should also be very low. A significant potential noise source with respect to surface EMG is the electrode–skin interaction. This source of noise is composed of voltage and current noise, and the current noise is higher when the electrode–skin impedance is high [1]. The electrode–skin impedance is an important feature since it affects the captured EMG signal quality. Since e-textile electrodes are dry unlike self-adhesive hydrogel Ag/AgCl electrodes, they are subject to higher levels of noise caused by motion and loosening of the contact between skin and the electrode [2]. In this study, we aim to develop dry, e-textile EMG electrodes using computer-aided embroidery method and test the effect of embroidery parameters using two different silver conductive threads on electrode–skin impedance and SNRdB values in comparison with conventional Ag/AgCl electrodes.

Based on the literature review, there exists research on clothing with integrated e-textile electroencephalography (EEG), electrocardiography (EKG), and EMG electrodes. E-textile electrodes have typically been produced by one of the several methods. Knitting or weaving of conductive threads and screen printing of conductive ink into electrodes have been used commonly as manufacturing methods. Catarino et al. [3] used the weft knitting method to develop EMG electrodes using knit, tuck, and float structure variations with steel and silver conductive threads. Results showed that the float and knit loop structures in producing the EMG electrodes provided high-quality EMG signals comparable to Ag/AgCl electrodes. Paul et al. [4] developed screen-printed electrodes using conductive rubber and conductive tracks using silver paste insulated with a top layer of polyurethane paste. The screen-printed electrodes were evaluated for bio-potential monitoring applications of EKG and EMG. The study concluded that the screen-printed electrodes are useful in EMG diagnosis, however represent baseline drift in EKG applications. Oliveira et al. [2] studied the electrode–skin impedance and the signal-to-noise ratio of EMG signals from embroidered textile electrodes with no hydrogel over time. The study concluded that the pressure provided by garment plays an important role in decreasing the noise caused by movement and assuring a good electrical and mechanical contact between the electrodes.

CAD embroidery has been an important manufacturing technique for e-textiles since it provides repeatable results, rapid integration of electrodes, sensors, and conductive tracks together with electrical components in a single step as an embedded system [5]. However, current literature does not provide knowledge on embroidery parameters and their effect on electrical characteristics of embroidered EMG electrodes. This research represents a preliminary study on the effect of embroidery stitch type using conductive thread on electrode–skin impedance and SNRdB values of embroidered EMG electrodes.

31.2 Materials and Methods

Polyamide silver-plated Madeira HC12 (<math><300 \Omega/m</math>) and HC40 (<math><100 \Omega/m</math>) threads are used to manufacture EMG electrodes with a ZSK Sprint XL CAD embroidery machine. Hundred percent polyester knit fabric is used to prototype arm bands with embroidered EMG electrodes. A total of eight samples, each having five sets of embroidered electrodes for muscle stimulation and EMG analysis, were prototyped (Fig. 31.1).

Five different embroidery stitch types of satin, fill, star, zigzag, and chain, which all provide different surface textures, were employed in designing the EMG electrodes using the Tajima DG 15 by Pulse embroidery software (Table 31.1). Different stitch types were used to create different surface textures and determine the best stitch type for high-quality EMG signal. Embroidered electrodes were covered with an additional fabric layer for insulation purpose on the outer surface. Metal snaps were installed on the electrodes to connect them with the EMG sensors.

Two volunteers participated in the experiments at this stage and two sets of data were retrieved from each participant using eight different e-textile electrode

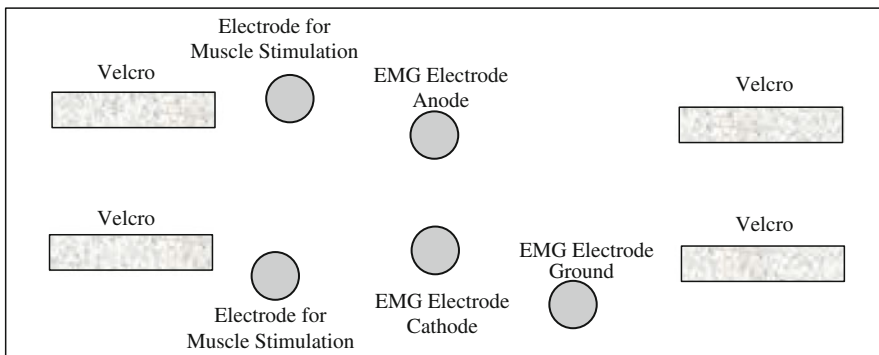






Fig. 31.1 A visual illustration of sleeve band prototype with embroidered electrodes

Table 31.1 Embroidered e-textile electrode samples

Sample	Embroidery stitch type
	Fill stitch
	Satin stitch
	Star stitch
	Zigzag stitch

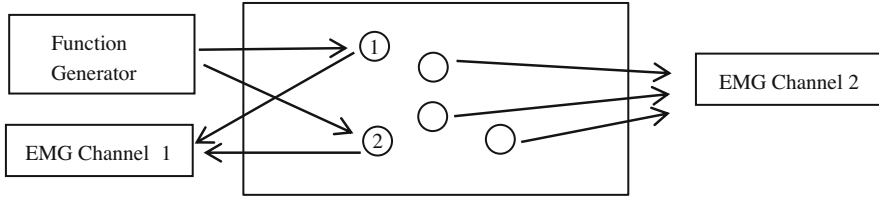


Fig. 31.2 Experimental setup

types. A four-channel wireless eMotion EMG device was used for the retrieval of signals from the participants via the embroidered electrodes and conventional electrodes. Sampling frequency of eMotion EMG device was 1000 Hz. The electrode–skin impedance was first measured using four-electrode configuration (Fig. 31.2). Sinusoid signal at frequencies of 1, 2, 3, 4, 5, 10, 20, 30, 40, 50, 100, 200, 300, 400, and 500 Hz was applied by a function generator. The function generator was used to stimulate the biceps muscle of the participants. One EMG channel was connected to the embroidered electrode function generator probe connection to retrieve the stimulating signal input. A second EMG channel was connected to the three embroidered EMG electrodes to retrieve the EMG output data from the biceps muscle. DC component of the signal was removed by subtracting its mean value. Magnitude and phase angle between signals due to range of frequencies between 1 and 500 Hz were calculated by fast Fourier transform (FFT) in MATLAB R2018.

In addition, two sets of electrode–skin impedance data were retrieved from three volunteers at higher frequencies compared to the first set of experiments. Each participant used eight different e-textiles electrode types. The electrode–skin impedance of embroidered electrodes and conventional electrodes was measured using a spectrum analyzer (HP 4396B). The measurements were performed using two-electrode configuration (Fig. 31.2 (connected 1 and 2)) at frequencies of 1000, 5000, and 10,000 kHz.

Signal-to-noise ratio (SNRdB) was calculated to compare sensing performance of all e-textile electrode alternatives versus the conventional Ag–AgCl electrodes. SNRdB was calculated using Eq. (31.1) where S_{rms} represents the RMS of the signal amplitude during 10 Hz stimulation with function generator and N_{rms} represents the RMS of the noise during rest.

$$SNRdB = 20 \log_{10} \left(\frac{S_{rms}}{N_{rms}} \right) \quad (31.1)$$

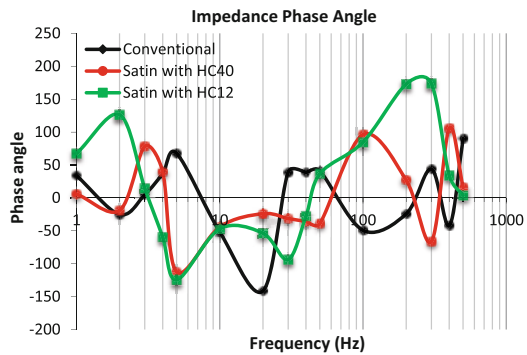
31.3 Results and Discussion

Results showed that all types of embroidered e-textile electrodes showed comparable or better results than the conventional Ag/AgCl electrodes in surface EMG applications. SNRdB values of embroidered e-textiles electrodes (Table 31.2) all

Table 31.2 Signal-to-noise ratios of conventional and textile electrodes

Electrodes	SNRdB
Conventional	60.63
Fill with HC40	61.19
Fill with HC12	61.22
Satin with HC40	70.83
Satin with HC12	70.74
Star with HC40	61.45
Star with HC12	62.43
Zigzag with HC40	60.84
Zigzag with HC12	70.52

Fig. 31.3 A comparative display of impedance phase angle of conventional and embroidered electrodes with satin stitch



showed better results compared to the conventional Ag/AgCl electrodes. Among embroidery stitch types, satin stitch showed the highest SNRdB value, followed by zigzag stitch and chain stitch types. The conductive thread types HC12 (<300 Ω/m) and HC40 (<100 Ω/m) did not show significant difference for SNRdB values except for zigzag stitch pattern. Electrodes manufactured using the zigzag embroidery stitch displayed higher SNRdB values with HC40 (<100 Ω/m) conductive thread. Although, conductive thread types with higher resistance were expected to have higher SNRdB, it can be suggested that other parameters such as contact area or fiber properties has more influence on SNRdB.

The analysis of electrode–skin impedance showed that conventional electrodes and embroidered e-textile electrodes do not show significant difference in terms of phase angle (Fig. 31.3). E-textile electrodes with satin stitch show higher impedance magnitude in comparison with the conventional electrode between frequencies 1 and 100 Hz (Fig. 31.4). Although the SNRdB was higher in satin stitch, measured high magnitude compared to conventional electrodes might be due to varieties among the volunteers at low frequency range. Values of impedance (phase and magnitude) were variable among the volunteers. Contact pressure is reported to be one of the main reasons for this variability, and it is an additional parameter to consider [6].

However, two-electrode configuration impedance measurements at higher frequencies (1000, 5000, and 10,000 kHz) showed less variance between volunteers. In these experiments, e-textile electrodes with satin stitch with HC40 showed

Fig. 31.4 A comparative display of impedance magnitude of conventional and embroidered electrodes with satin stitch at low frequencies

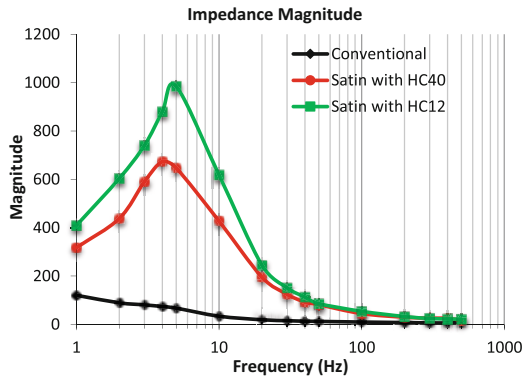
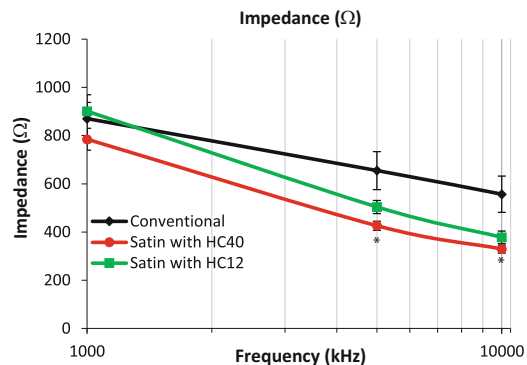


Fig. 31.5 A comparative display of impedance of conventional and embroidered electrodes with satin stitch at high frequencies



significantly lower impedance at 5000 and 10,000 kHz in comparison with the conventional electrode (Fig. 31.5). The impedance of satin stitch with HC12 was significantly lower than the conventional electrode at 10,000 kHz. In future measurements, these experiments will be carried on with higher number of volunteers and under optimum pressure conditions.

This pilot study is aimed to characterize embroidered e-textile electrodes and compare them to conventional Ag/AgCl electrodes. This characterization can be used to determine the properties of e-textile electrodes, which can detect high-quality EMG signal comparable to Ag/AgCl electrodes. Impedance of e-textile materials is highly influenced by contact area formed with the skin. Contact area is reported to be variable due to fiber properties, thickness of the fibers, fiber density, the number of fibers per cross-section, and hairiness [7]. There might be an influence between better SNRdB and impedance of electrode–skin interface; however, the number of the volunteers was not enough to determine this relation. The relation between performance of ECG electrodes and impedance was reported for textile electrodes such as cotton, Lycra, or cotton-polyester [8]. As a future work, optimization of the pressure and increase in the number of volunteers are necessary.

31.4 Conclusion

E-textile, embroidered electrodes demonstrate superior results and advantages compared to conventional Ag/AgCl electrodes. E-textile electrodes for surface EMG applications could be embedded in clothing offering reusability and wearability advantages. The results of this showed that e-textile EMG electrodes could provide higher signal quality compared to conventional electrodes. E-textile electrodes demonstrate comparable results to conventional electrodes in term of electrode–skin impedance performance. This research analyzed electrode–skin impedance by externally stimulating the muscles via a function generator when the body limb is at rest. Future research could further analyze electrode–skin impedance for e-textile electrodes during physical muscle activity when the body limbs are in motion. It is expected that the friction between skin and the e-textile electrode during movement, the pressure applied by the clothing with embedded e-textile electrode to the skin, and sweating will affect the electrical characteristics of e-textile electrodes.

Acknowledgment This research is funded by The Scientific and Technological Council of Turkey (TUBITAK), under grant number 117M275, Career Development Program 3501.

References

1. Hermens, H.J., Freriks, B., Merletti, R., Stegeman, D., Blok, J., Rau, G., Hägg, G.: European recommendations for surface electromyography. *Roessingh Res. Dev.* **8**(2), 13–54 (1999)
2. Oliveira, C.C., Machado da Silva, J., Trindade, I.G., Martins, F.: Characterization of the electrode-skin impedance of textile electrodes. In: *Design of Circuits and Integrated Circuits (DCIS) Proceedings*, pp. 1–6. Madrid (2014)
3. Catarino, A.P., Carvalho, H., Barros, L., Dias, M.J.: Surface electromyography using textile-based electrodes. In: *The Fiber Society 2012 Fall Meeting and Technical Conference Proceedings*, Boston (2012)
4. Paul, G., Torah, R., Beeby, S., Tudor, J.: The development of screen printed conductive networks on textiles for biopotential monitoring applications. *Sens. Actuators A Phys.* **206**, 35–41 (2014)
5. Goncu Berk, G.: Design of a wearable pain management system with embroidered TENS electrodes. *Int. J. Clothing Sci. Technol.* **30**(1), 38–48 (2018)
6. Scalisi, R.G., Paleari, M., Favetto, A., Stoppa, M., Ariano, P., Pandolfi, P., Chiolerio, A.: Inkjet printed flexible electrodes for surface electromyography. *Org. Electron.* **18**, 89–94 (2015)
7. Priniotakis, G., Westbroek, P., Van Langenhove, L., Hertleer, C.: Electrochemical impedance spectroscopy as an objective method for characterization of textile electrodes. *Trans. Inst. Meas. Control.* **29**(3–4), 271–281 (2007)
8. Castrillón, R., Pérez, J.J., Andrade-Caicedo, H.: Electrical performance of PEDOT: PSS-based textile electrodes for wearable ECG monitoring: a comparative study. *Biomed. Eng. Online.* **17**(1), 38 (2018)

Chapter 32

Toward a Wearable Epileptic Seizure Monitoring: A Case Study



Javad Birjandtalab, Diana Cogan, Mehrdad Nourani, and Jay Harvey

32.1 Introduction

Motivation and Prior Works

With the advances in information technology, health-care monitoring and alert systems have become attractive topics of research and development [24]. Seizure prediction is very important since it gives a patient the chance to at least find a safe position and environment and thus minimize the impact of an imminent seizure. Realistically, using the available technology, accurate prediction is an elusive objective. Seizure detection is also a challenging problem but more achievable goal and offers two advantages. First, an alert can be sent to caregivers which can prevent serious harms to patients such as SUDEP (sudden unexpected death in epilepsy). Second, an annotated diary of seizure episodes can be generated, which would be considered very beneficial for clinicians [17] in making treatment decisions. Although electroencephalography (EEG) is considered as the gold standard for seizure detection, it is not practical for daily life monitoring since it needs the use of full (e.g., 23-channel) EEG setup or implantable sensors in the brain.

J. Birjandtalab · D. Cogan · M. Nourani (✉)

Department of Engineering and Computer Science, The University of Texas at Dallas,
Richardson, TX, USA

e-mail: birjandtalab@utdallas.edu; diana.cogan@utdallas.edu; nourani@utdallas.edu

J. Harvey

Department of Neurology and Neurotherapeutics, UT Southwestern Medical Center, Dallas,
TX, USA

e-mail: jay.harvey@utsouthwestern.edu

© Springer Nature Switzerland AG 2020

C. Sugimoto et al. (eds.), *13th EAI International Conference on Body*

Area Networks, EAI/Springer Innovations in Communication and Computing,

https://doi.org/10.1007/978-3-030-29897-5_32

The first serious effort for predicting seizures was made in 1970 [15]. The authors used scalp electrodes for this purpose. Although the proposed system provided high sensitivity, it suffered from a large number of false positives. The series of public forums such as International Workshop on Seizure Prediction (IWSP) played an important role on developing new techniques for seizure prediction [13].

Researchers have used various biosignals that can be recorded using wrist worn devices, which have potential to predict the seizure. These biosignals include heart rate (HR), arterial oxygenation (SpO₂), accelerometry (ACC), electrodermal activity (EDA), and temperature (Temp). High HR changes at the beginning of some types of seizures are reported in the literature [14]. In [22], ECG and PPG, obtained from wrist worn devices, were used in a clinical setting to automatically detect epileptic seizures. Researchers have also found patterns that seizures may change the level of SpO₂ [12]. They validated their findings by showing that seizures can disrupt the patient respiration [19]. Movement measured by ACC and changes in EDA have been found to effectively find the beginning of convulsive seizures [18]. Although Temp is considered as an indicator of febrile seizures, it has the potential to be used in detecting other type of seizures [23].

Contribution

We have previously investigated patterns in HR, SpO₂, and EDA biosignals during seizures in patients suffered from epilepsy. These patterns are not commonly observed during non-seizure events. In [10], we implemented a new method which finds features of biosignals in time domain and used these features to distinguish seizure from non-seizure events. In another work, we reported that a limited-channel EEG (1 to 3 scalp electrodes carefully chosen for each patient) will be sufficient to detect seizures with high accuracy [5]. We used a public-domain (MIT) database [6] to show the feasibility of designing a wearable seizure monitoring system and achieving high accuracy for automatic seizure detection.

To validate the basic concept and feasibility, we conducted a clinical study and applied the previous techniques for analysis of seizures captured from ten patients. The main purpose is investigating the efficacy of a multi-modal system for automatic seizure detection. This hybrid system utilizes both a wrist worn non-EEG device as well as 1–3 EEG nodes. This clinical study shows that such hybrid platform will be capable of providing accurate seizure diary/detection in daily life of patients. Non-EEG monitoring was sufficient for six out of ten patients. For the remaining four cases, limited EEG monitoring was needed to avoid false positives. Once integrated within an alert platform, the proposed hybrid platform will help patients and care givers to manage the uncontrolled seizures.

32.2 Background

Non-EEG-Based Seizure Detection

We selected two wrist worn devices capable of capturing five biosignals—HR, SpO₂, EDA, skin temperature (Temp—needed to properly interpret the EDA signal), and motion by use of three-dimensional accelerometry (Acc). The two devices are the Nonin WristOx2, which captures HR and SpO₂ [21] and the Affectiva Q Curve, which captures EDA, Temp, and Acc [2]. Because a seizure is a severe neurological stress on the affected person, we designed an experiment to determine the effectiveness of our selected biosignals for distinguishing among four stress states people encounter in normal life experiences (Fig. 32.1).

We executed the experiment in our laboratory under UT Dallas IRB Protocol No. 12–29. Use of neural networks and the nearest neighbor algorithm on the resulting data produced accuracy of over 90% in distinguishing among the four stress states. Figure 32.2 shows the raw data collected from one of our volunteers. We used these biosignals and machine learning techniques to distinguish the seizure episodes. Our experimental procedure and results were presented in detail in [9].

EEG-Based Seizure Detection

Several researchers used EEG data to monitor seizures among epileptic patients. A neural network model is trained for seizure detection using features extracted from wavelet transform [11]. A hybrid EEG-based classifier for seizure detection is presented in [1]. Authors in [20] extracted a combination of temporal and spectral features and used principal component analysis (PCA) as visualization technique by reducing the original dimensions of data.



Fig. 32.1 (a) The wrist worn Affectiva records EDA, Acc, and Temp; (b) the Nonin 3150 Wireless WristOx2 records HR and SpO₂

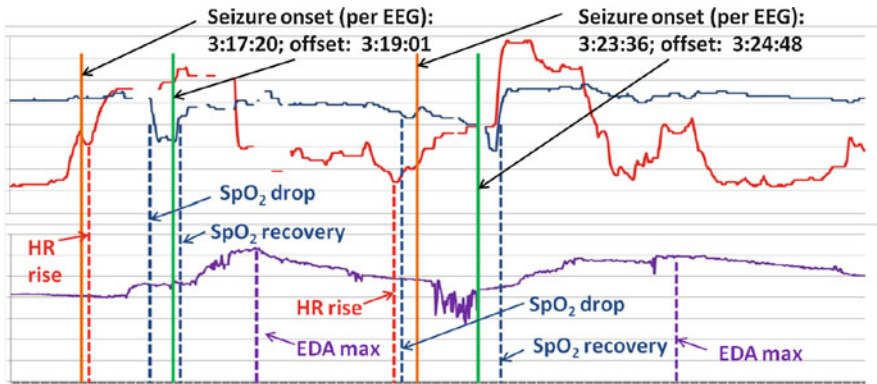


Fig. 32.2 The HR \uparrow \Rightarrow SpO₂ \downarrow \Rightarrow EDA \uparrow pattern produced by two seizures suffered by one patient [7]

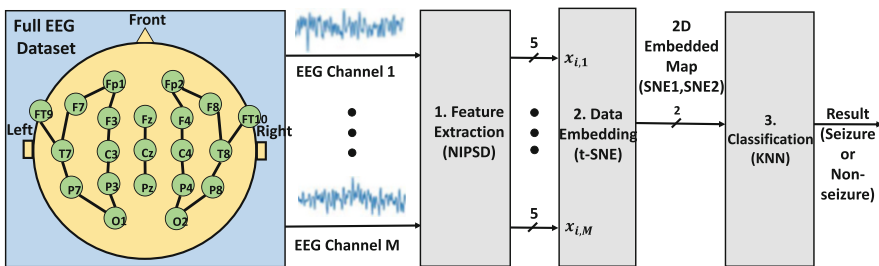


Fig. 32.3 The overall view of EEG-based seizure detection [4]

Our research group has explored several aspects of EEG signal analysis. We reported a 21-channel EEG-based seizure detector which uses a nonlinear dimension reduction technique in [4]. The data flow for this method is illustrated in Fig. 32.3. Figure 32.4 illustrates a window of seizure and non-seizure EEG signals analyzed by our detector. Our proposed nonlinear technique provides higher accuracy than conventional dimension reduction approaches. We used spectral domain features for unsupervised clustering of seizure and non-seizure events. We have also demonstrated that spectral domain features can be used to identify among the EEG patterns of different subjects in MIT database [6].

32.3 Case Study and Experimental Results

Setup and Data Collection

We recorded biosignals from patients, after IRB approval, at an Epilepsy Monitoring Unit in Dallas, Texas. Our medical collaborators have annotated the seizure events using EEG data [16]. Two commercial devices are used to collect data from patients

Fig. 32.4 A sample window of EEG signal in time domain showing the seizure and non-seizure

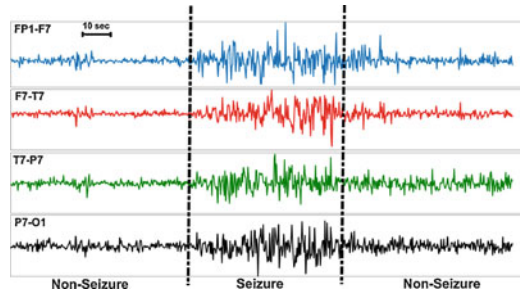


Table 32.1 Non-EEG seizure detection effectiveness per patient [8]

Patient ID	Duration	Seizure type and numbers	Seizure focus	Seizures detected	False alarms
4	11 h, 50 min	1—CPS	Left temporal	1	0
5	43 h, 15 min	2—Secondary GTCS	Left temporal	2	0
9	31 h, 13 min	3—CPS	Left temporal	0	1
10	54 h, 3 min	4—CPS	Right temporal	4	0
11	25 h, 21 min	1—CPS	Right temporal	1	0
12	35 h, 24 min	2—CPS	Frontal	0	1
16	28 h, 27 min	1—CPS	Right temporal	1	0
18	30 h, 20 min	1—CPS	Right temporal	0	1
19	39 h, 52 min	11—CPS	rt and lt temporal	0	0
20	40 h, 2 min	1—Primary GTCS	Non-focal	1	1

CPS Complex Partial Seizure, *GTCS* Generalized Tonic Clonic Seizure

at the same time that EEG data was collected: (1) collecting HR and SpO₂ using a Nonin WristOx 3150 device [21] and (2) monitoring EDA, Temp, and ACC using Affectiva Q Curve wrist worn device [2]. We synced the wrist worn devices to the EEG recording platform. This setting and protocol were used to accurately identify the same seizure onset and offset timing for all biosignals.

Our dataset includes biosignals from ten patients who experienced total of 27 seizure episodes. As Table 32.1 shows, the six patients who experienced pattern of the HR↑ ⇒ SpO₂ ↓ ⇒ EDA↑ (patients 4, 5, 10, 11, 16, 20) had 2 secondarily generalized, 1 primary generalized, and 7 complex partial seizure events. We used MATLAB to perform the biosignal data analysis of 108 h of data.

Limitations of Non-EEG Seizure Detection

Non-EEG seizure detection is limited by the fact that different people have different physiological responses to seizures. For example, HR changes commonly occur in close temporal proximity to seizure onset as determined by EEG. Typically, the change is a large, abrupt increase (tachycardia) [17]. Cyberonics has developed a

closed-loop system for its aspire vagus nerve stimulator (VNS) that uses tachycardia to detect seizure onset. When a seizure is detected, the vagus nerve is stimulated to try to prevent or shorten the seizure.

Respiratory changes (and resulting SpO₂ changes) are associated with seizures that affect the temporal lobes, but not all seizures affect this part of the brain. EDA increases, caused by changes in the sympathetic nervous system, are typically caused by seizures, but our prior work indicates that this response may be attenuated by some antiepileptic drugs (AED) [7]. Surface electromyography (sEMG) has been used to detect the tonic (stiffening) phase of convulsive seizures, and monitoring of motion has been widely used to detect the convulsive motion associated with these seizures; but neither sEMG nor motion sensors have been shown to be effective in detecting nonconvulsive seizures [23].

Seizure detection by non-EEG metrics requires a personalized system and will likely not be useful for all patients; however, for those patients whose non-EEG physiological response to seizure follows a specific pattern that can be captured by wearable devices, there is a very real promise of accurate detection using a noninvasive and nonstigmatizing system. Table 32.1 shows the results of non-EEG seizure detection by patient. Notice that our algorithm detects all seizures experienced by six of the patients and none of the seizures suffered by the other four. This result underscores the consistency (in most cases) of an individual's physiological response to seizure, as well as the limitation of non-EEG detection.

Effectiveness of Limited-Channel EEG

Selecting limited number of EEG channels is reported in the literature for various applications including automatic sleep analysis [3] and brain–computer interface. Here, the goal is to achieve high accuracy while making the devices practically wearable in daily living. We do this by developing a seizure detection platform that relies on a limited number of EEG channels instead of having the full channel EEG setup. We investigated this possibility on four patients from our preliminary study whose seizures were not detected (patients 9, 12, 18, and 19) using non-EEG signals. The results are tabulated in Table 32.2 showing that the accuracy of limited-channel EEG is very close to that of the full-channel EEG. These patients all experienced CPSs, without having any particular sign of automatism. Expectedly, ACC signals do not reveal any pattern for these patients. We selected possible seizure times based on non-EEG signal activity, then further analyzed the selected times using the three channels of EEG that our filtering and classification process had chosen.

Table 32.2 Full channel vs. limited-channel EEG comparison for four patients for whom our non-EEG analysis did not work [8]

Patient ID	Seizure Focus	EEG Channels	Specificity	Sensitivity	Accuracy
9	Left temporal lobe	All 21	1.00	0.97	0.97
		T5, C4, P3	1.00	0.98	0.98
12	Frontal lobe	All 21	0.99	0.97	0.97
		Pz, O2, Cz	0.99	0.98	0.98
18	Right temporal lobe	All 21	1.00	0.96	0.96
		F8, F7, A2	1.00	0.97	0.97
19	Right and left temporal lobe	All 21	0.99	0.98	0.98
		A1, F7, Fz	0.98	0.96	0.96

32.4 Conclusions

Based on a clinical study and the corresponding data analysis, we propose the integration of (1) non-EEG monitoring by means of a wrist worn device with (2) limited-channel EEG monitoring by means of 1–3 single-channel EEG sensors to create a wearable multi-modal seizure monitoring system. We believe such hybrid system will be capable of providing accurate seizure detection in daily life for most patients. Such assistive wearable technologies for monitoring patients with uncontrolled seizures hold the possibility of impacting hundreds of thousands of people’s quality of life. Accurate detection will allow for feedback to the patient and an alert to his/her caregiver. The system will also record patient biosignals on a long term basis, thereby allowing physicians to monitor disease progression and SUDEP risk.

References

1. Aarabi, A., Wallois, F., Grebe, R.: Automated neonatal seizure detection: a multistage classification system through feature selection based on relevance and redundancy analysis. *Clin. Neurophysiol.* **117**(2), 328–340 (2006)
2. Affectiva Inc. <http://www.affectiva.com/q-sensor/>. Accessed 21 March 2013
3. Berthomier, C., Drouot, X., Herman-Stoica, M., Berthomier, P., Prado, J., Bokar-Thire, D., Benoit, O., Mattout, J., d’Ortho, M.P.: Automatic analysis of single-channel sleep EEG: validation in healthy individuals. *Sleep* **30**(11), 1587 (2007)
4. Birjandtalab, J., Pouyan, M.B., Nourani, M.: Nonlinear dimension reduction for EEG-based epileptic seizure detection. In: 2016 IEEE-EMBS International Conference on Biomedical and Health Informatics (BHI), pp. 595–598. IEEE, Piscataway (2016)
5. Birjandtalab, J., Baran Pouyan, M., Cogan, D., Nourani, M., Harvey, J.: Automated seizure detection using limited-channel EEG and non-linear dimension reduction. *Elsevier Comput. Biol. Med.* **82**(C), 49–58 (2017)
6. Blanke, O., Lantz, G., Seeck, M., Spinelli, L., de Peralta, R.G., Thut, G.: Temporal and spatial determination of EEG-seizure onset in the frequency domain. *Clin. Neurophysiol.* **111**(5), 763–772 (2000)

7. Cogan, D.: Multi extracerebral biosignal analysis for epileptic seizure monitoring. Ph.D. Thesis, University of Texas at Dallas (2016)
8. Cogan, D., Birjandtalab, J., Nourani, M., Harvey, J.H., Nagaraddi, V.: Multi-biosignal analysis for epileptic seizure monitoring. *Int. J. Neural Syst.* **27**(1), 1650031 (2017)
9. Cogan, D., Pouyan, M.B., Nourani, M., Harvey, J.: A wrist-worn biosensor system for assessment of neurological status. In: Engineering in Medicine and Biology Society (EMBC), 2014 36th Annual International Conference of the IEEE, pp. 5748–5751. IEEE, Piscataway (2014)
10. Cogan, D., Nourani, M., Harvey, J., Nagaraddi, V.: Epileptic seizure detection using wristworn biosensors. In: Engineering in Medicine and Biology Society (EMBC), 2015 37th Annual International Conference of the IEEE, pp. 5086–5089. IEEE, Piscataway (2015)
11. Ghosh-Dastidar, S., Adeli, H., Dadmehr, N.: Mixed-band wavelet-chaos-neural network methodology for epilepsy and epileptic seizure detection. *Biomedical Engineering. IEEE Trans. Biomed. Eng.* **54**(9), 1545–1551 (2007)
12. Ives, J., Al-Aweel, I., Blum, A., Krishnamurthy, K., Goldberger, A., Schomer, D.: Spo2 changes precede EEG changes during seizures. *J. Clin. Neurophysiol.* **14**(2), 162 (1997)
13. Lehnertz, K., Litt, B.: The first international collaborative workshop on seizure prediction: summary and data description. *Clin. Neurophysiol.* **116**(3), 493–505 (2005)
14. Leutmezer, F., Scherthaner, C., Lurger, S., Potzelberger, K.: Electrocardiographic changes at the onset of epileptic seizures. *Epilepsia* **44**(3), 384–354 (2003)
15. Litt, B., Echauz, J.: Prediction of epileptic seizures. *Lancet Neurol.* **1**, 22–30 (2002)
16. NeuroWork. <http://www.neurowork.net/en/products/>. Accessed 11 May 2014
17. Osorio, I.: Automated seizure detection using EKG. *Int. J. Neural Syst.* **24**(02), 1450001 (2014)
18. Poh, M.Z.: Continuous assessment of epileptic seizures with wrist-worn biosensors. Ph.D. Thesis, Massachusetts Institute of Technology (2011)
19. Regan, M.E., Brown, J.K.: Abnormalities in cardiac and respiratory function observed during seizures in childhood. *Dev. Med. Child Neurol.* **47**, 4–9 (2005)
20. Smart, O., Chen, M.: Semi-automated patient-specific scalp EEG seizure detection with unsupervised machine learning. In: 2015 IEEE Conference on Computational Intelligence in Bioinformatics and Computational Biology (CIBCB), pp. 1–7. IEEE, Piscataway (2015)
21. Turner Medical Inc. <http://www.turnermedical.com/>. Accessed 21 March 2013
22. Vandecasteele, K., Cooman, T.D., Gu, Y., Cleeren, E., Claes, K., Paesschen, W.V., Huffel, S.V., Hunyadi, B.: Automated epileptic seizure detection based on wearable ECG and PPG in a hospital environment. *Sensors* **17**, 2338 (2017)
23. Van de Vel, A., Cuppens, K., Bonroy, B., Milosevic, M., Jansen, K., Van Huffel, S., Vanrumste, B., Lagae, L., Ceulemans, B.: Non-EEG seizure-detection systems and potential SUDEP prevention: state of the art. *Seizure* **22**(5), 345–355 (2013)
24. Zhang, Y., Qiu, M., Tsai, C.W., Hassan, M.M., Alamri, A.: Health-cps: healthcare cyber-physical system assisted by cloud and big data. *IEEE Syst. J.* **11**(1), 88–95 (2017)

Chapter 33

Virtual Machine Execution for Wearables Based on WebAssembly



Martin Jacobsson  and Jonas Willén 

33.1 Introduction

A complete wearable system consists of the wearable device, but also gateway nodes, back-end servers, and client applications. Consequently, there will be many different programming languages involved in creating an end-to-end system for IoT applications. On the wearable sensor node itself, it is embedded programming in C. On the gateway, it may be a high-level language, such as Python. In the cloud, it may be Java, and finally on the web client, it is HTML and JavaScript. On smartphones and tablets, yet other languages may be used. Needless to say, this diversity of programming languages is a challenge even for experienced programmers. Instead, we want to create a system where domain experts, rather than the very best embedded programmers, should be able to create the application logic and, at the same time, allow for easy tailoring of the systems to the application and user needs. The idea is to use standardized hardware and be able to tailor it to the need at hand. For instance, an inertial measurement unit (IMU) can both be used for activity tracking throughout a day, but also in detecting dangerous working positions in ergonomics depending only on the software it runs.

To enable reconfigurable wearables and one single language everywhere, we propose to use a simple virtual machine (VM). We propose to use WebAssembly for this, which is a new VM designed for fast execution of code on the web [13]. Despite its design target, WebAssembly is also suitable for resource-constrained devices, including wearables, as it requires much less code size and other resources compared to other alternatives, such as Java VM or a JavaScript interpreter. Currently, WebAssembly is gaining significant attention, for example, there is already

M. Jacobsson (✉) · J. Willén
KTH Royal Institute of Technology, Huddinge, Sweden
e-mail: martin.jacobsson@sth.kth.se; jwi@kth.se

support in all major web browsers today, and this promises wide adoption in the future. Several compilers, linkers, and other tools already exist. Since WebAssembly is based on compilation, you can use existing code to generate WebAssembly byte code. Nevertheless, to the best of our knowledge, no one has actually run WebAssembly on embedded devices.

In this paper, we implement a WebAssembly interpreter on embedded systems, such as wearables, with support for over-the-air programming based on Bluetooth low energy (BLE) Generic Attribute (GATT) services. Using WebAssembly is the first step in allowing the same code to run everywhere in a complete wearable system as WebAssembly already is supported in web browsers and on servers. Furthermore, since our system uses BLE, it can be used together with common smartphones and laptops without the need for special hardware.

33.2 Related Work

There are many alternatives to WebAssembly. First, it is possible to do over-the-air programming with native code and dynamic linking. For instance, Dunkels et al. [5] demonstrated this on Contiki-OS. Similar support is available for other sensor node operating systems. However, every platform requires their own native binary code. While you can support over-the-air reprogramming, you cannot run the same code everywhere with these techniques.

Other alternatives are JavaScript engines and Java Virtual Machines (JVMs) for embedded devices. Some attempts have been made to port JVMs to embedded devices, such as TakaTuka [1] and Darjeeling [3]. Neither of these is active today. One reason is that it is difficult to fit a complete JVM with full library support on resource-constrained devices, and this means that these solutions have to make sacrifices, which means that standard Java programs may not run on these JVMs. The same problem also holds for JavaScript engines. Nevertheless, several options exist for running JavaScript code on embedded devices. One popular example is Espruino [9], which also comes with web-based tools for development and testing. However, there are many more, such as Duktape, MuJS, Tiny-JS, JerryScript, and Mongoose OS. Recently, Baccelli et al. [2] implemented a JavaScript engine for embedded wireless sensor nodes based on CoAP [11]. However, complete implementations of JavaScript engines are usually still very large. For instance, Duktape [4] is one of the smallest and still requires 160 kB flash and 64 kB RAM, and even then, it only supports the JavaScript versions ECMAScript E5.1 and not the entire ECMAScript E6 or E7.

Even though WebAssembly has already been around for some time, the amount of research is limited and mainly concerns programming language design and semantics (e.g., [6, 12]). We have not been able to identify any research work about running WebAssembly on embedded systems.

33.3 Implementation

We have developed a prototype system that is able to program wearable sensor nodes over-the-air using WebAssembly modules. The focus has been on Bluetooth Low Energy (BLE), since this allows direct communication with standard devices, such as smartphones and laptops without special hardware. We implemented a WebAssembly interpreter that runs on resource-constrained embedded devices. In this section, we highlight how we did this. Our implementation uses the Texas Instruments development platform CC26x2R LaunchPad and their BLE stack SimpleLink. The code is based on the Simple Peripheral example script provided by TI. However, our WebAssembly implementation is platform agnostic and we also have it working on Contiki-OS as well.

WebAssembly, WAC, and libwabt.js

WebAssembly is a structured stack machine with strict typing [13]. Hence, both compilers and interpreters are easy to implement. WebAssembly uses byte code for efficient representation of compiled code, which is known as a WebAssembly module (wasm) and contains functions for modularization of code and linking. There is also a textual representation. The small size of wasm modules enables redeployment of the code between sensor nodes, gateways, cloud servers, and web clients efficiently, automatically, and over-the-air. Despite being designed for high-performance code execution for web applications, it is a simple and efficient VM that is also suitable for embedded systems.

Currently, there are two C/C++ compilers that can generate WebAssembly byte code, where one is based on the extendable compiler infrastructure project LLVM. Both compilers have support for more programming languages, such as Rust. It is not hard to imagine and implement simpler to use compiler front-ends based on low-code concepts [10], such as Google Blockly or MIT Scratch.

In addition to compilers, many tools have been developed for WebAssembly. One set of tools is the WebAssembly Binary Toolkit (WABT), which implements several useful tools for the handling of WebAssembly binaries, including converting between the binary representation (wasm) and the textual representation. WABT also includes a WebAssembly interpreter in C++. Furthermore, this project has also been compiled to a JavaScript library called libwabt.js that can be used to do what WABT does in web browsers. This library allows for online writing of WebAssembly code and the creation of binary wasm modules.

WebAssembly in C (WAC) [7] is a WebAssembly VM engine written in C. This code is small, but still a complete implementation of a WebAssembly interpreter. As we need to write code in C for our embedded system, we base our implementation on WAC.

WebAssembly on Embedded Systems

Our implementation of WebAssembly on embedded systems can be divided into three parts: the WebAssembly module loader, the interpreter, and the BLE application with the API to the rest of the embedded operating system (OS).

The module loader accepts the binary wasm module from the BLE application. It allocates heap space for the execution of the module and places the wasm binary in the first part of the heap space as shown in the left part of Fig. 33.1. Our implementation has a fixed-sized struct for the management of the module, which is placed right after the wasm module on the heap space. A handle to this struct shown with the blue hollow arrow is passed around by the application. The struct points out where everything else is located on the heap. The struct also includes run-time data, such as the program pointer (PC), operand stack pointer, and the call stack pointer, all three shown as bold arrows in the figure.

Then, the module loader places additional data on the heap in the order shown in Fig. 33.1. In the first parts, we place data that has a fixed length or will never

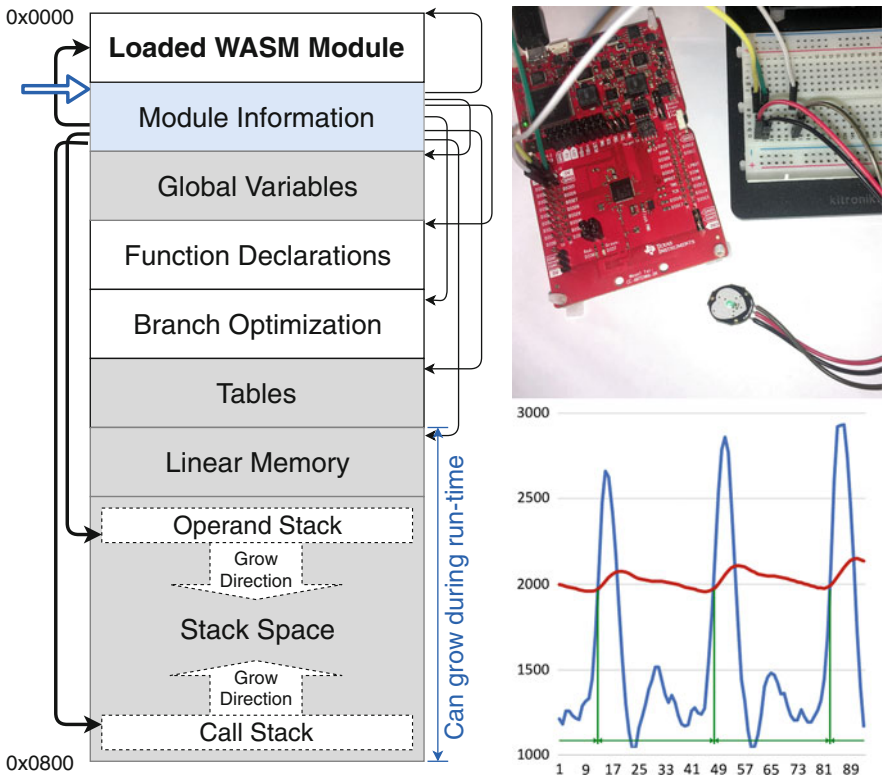


Fig. 33.1 The proof-of-concept implementation. The wasm module heap space (left), hardware setup (top right), and an example input signal from the pulse sensor (bottom right)

grow after load time. In the end, we place data that may need to grow, i.e., the linear memory and the stacks. First, we place the global variables on the heap. The global variables may change, but the number of variables will never change. Then we place the function declarations, followed by the branch optimization, which is used to speed up the execution of branching in the code. For instance, when executing an if-opcode, we can look up the start location of the else-branch when we should branch there, instead of searching for it in the function code.

Tables and linear memory are constructs specified by the WebAssembly specification. Tables can be used by indirect function calling and will have a fixed length determined by the module at load time. The linear memory acts as heap storage for the module itself. A module can reserve zero or more memory pages at load time, but can also grow the allocated memory at run-time by reserving additional memory pages. This means that this part of the space may need to grow. Finally, we have space for the stacks. Our implementation, being based on WAC, uses two stacks, one for operands and one for function calls and blocks, such as if-then-else-end-blocks or loop blocks. They grow in opposite directions to make the maximum use of the available space. When they meet, we will have a stack overflow, which will terminate the WebAssembly execution. Future versions may instead extend the allocated memory if possible.

Gray areas in Fig. 33.1 indicate the run-time state that needs to be migrated if a running wasm module needs to move from one node to another. White areas can always be reloaded from the binary wasm module.

The interpreter part is a classic while-loop with a large switch statement implementing all the 192 opcodes defined by WebAssembly. Some of the opcodes implement functions using 64-bits integers and floating-point data types (both single and double precision). Since the ARM Cortex M4F microcontroller in CC2652R, used by our LaunchPad sensor node, does not have native support for all these data types, some are implemented in software by the compiler.

Bluetooth Low Energy Implementation

The WebAssembly module is executed by a dedicated task in the BLE stack. In our current implementation, the operating system and the BLE stack have most of the control and only the application logic is done by the wasm module. In future implementations, we imagine that wasm modules will have much more control of the stack and the operating system, such as creating own GATT services or implementing standardized BLE profiles.

Our current BLE application implements three functions that can be used by the wasm module, namely `millis()`, `analogRead()`, and `notify()`. The first one returns the number of milliseconds since the device started, the second function reads one of the analog-to-digital converter (ADC) pins, and the last one emits a 32-bit integer over a BLE characteristic, which will be sent over-the-air to subscribed clients, such as a smartphone app.

The wasm module must export two functions: `interval()` and `periodic()`. The first function is called only once after the module is loaded and must return a time interval in milliseconds. Then, `periodic()` is called regularly by an OS timer according to the interval. A single low priority OS task executes all this and this means that concurrent calls to `periodic()` are impossible, even if the interval is very short or the execution of `periodic()` is prolonged.

To program and interact with the wasm module application, our BLE implementation implements a custom-made GATT service with three characteristics (attributes that can be read or written). The first is `ModuleValue` and allows for notifications, which means that BLE clients can subscribe to it and receive values when the attribute changes. The characteristic `ModuleStatus` is for management and tells whether the module is loaded, running, resetted, or terminated with an error. The third characteristic is `ModuleUpload` and this one is for uploading the wasm module binary over-the-air to the device. The binary is divided into 20-bytes segments and sequentially written to this characteristic to upload the module. When finished, the module is loaded and initialized with a special command.

33.4 A Proof-of-Concept Evaluation

To demonstrate the usage of our WebAssembly system in a BLE device, we developed software for extracting the heart rate from a photoplethysmogram (PPG) sensor connected to a BLE node. We use the TI Launchpad CC26x2 as sensor node and connects a PPG sensor (Pulse sensor [14]) to one of the analog pins on the node. The top right part of Fig. 33.1 shows the hardware setup. By sampling the pin with an analog-to-digital converter (ADC) when the pulse sensor is attached to a fingertip, we can obtain the pulse curve shown in the bottom right part of the figure.

Our proof-of-concept wasm module implements a simple signal processing application of the raw sensor data (blue curve in Fig. 33.1) into the heart rate. The heart rate will be sent via the `ModuleValue` characteristic to all BLE subscribers. It is based on finding the average value of the curve with a simple exponentially weighted moving average and an offset (red curve). The program calculates the time between the events when the blue curve crosses the red curve from below (the green time intervals) and calculates the beats per minutes (BPM) from this.

In order to test the BLE over-the-air programming of the sensor node, we developed a simple HTML/JavaScript web application. The Google Chrome web browser supports the Web Bluetooth API and can be used to interact with BLE devices. Figure 33.2 shows our web application running in Chrome from a standard laptop. From it, we can connect to and control the sensor node and upload compiled wasm modules. Through the same web application, we can receive the output from the wasm module once it starts running. In Fig. 33.2, we show a use-case where we first connect to the sensor node, load a saved wasm module, upload it to the sensor node, and then start to receive the heart rate in BPM. The received values are indicated with the red boxes in the figure. Since a lot happens in the background, we show the JavaScript log console from Chrome to the right, where we log the actions

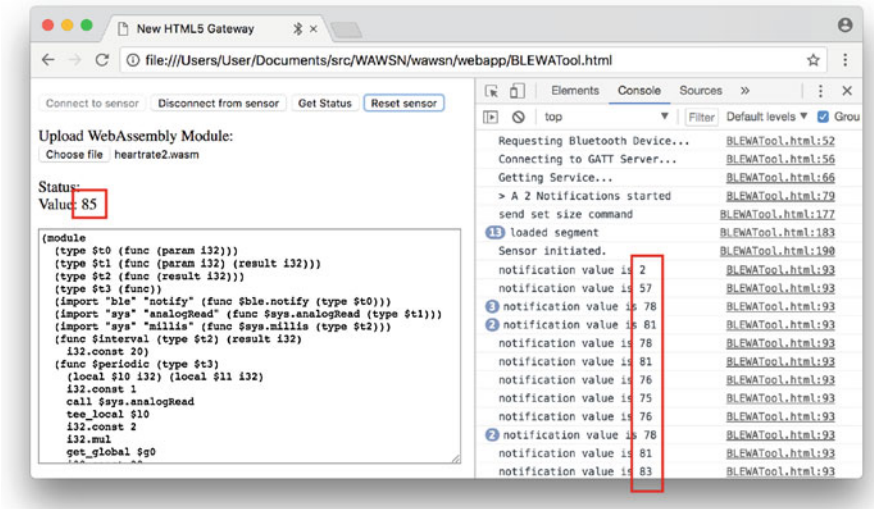


Fig. 33.2 Screenshot of the BLE Gateway tool running in Chrome on a laptop and connected with the device over BLE. The red boxes are the reported BPM values from the wasm module running on the device. To the right is the JavaScript console log

performed by the web application. Using the libwabt.js library, the web application also disassembles the wasm module and displays what is being uploaded in the text box to the left. A simpler version of the web application was developed and tested on Android tablet PC as well as on an iPhone. For the iPhone, you have to use the experimental web browser WebBLE as Safari does not yet have Web Bluetooth API support.

Size Overhead

Our small proof-of-concept evaluation script compiles to a mere 209 bytes binary wasm module. This size can be compared to a native binary code (ELF) of around 900 bytes or 185 bytes for a minimal equivalent JavaScript, and 1263 bytes for Java (.jar). Our WebAssembly interpreter and module loader implementation only require 13 kB flash memory (including support for 64-bit integer and floating-point arithmetic) and 1.1 kB SRAM (both heap and stack). On top of this, the example script requires 526 bytes for the run-time states and optimization. This can be compared to Baccelli et al. [2], which reports a 12 kB RAM usage and 160 kB flash memory usage for their JavaScript Engine alone. Hence, WebAssembly is significantly more space efficient compared to JavaScript. There are smaller JavaScript implementations, but they tend to support even less features from the JavaScript standard. The Mongoose [8] JavaScript engine, mJS, which claims only

50 kB flash memory, is a good example. When it comes to Java VM, TakaTuka [1] reports around 55 kB flash for a near complete implementation of the Java VM on Atmel's 8-bit AVR microcontroller.

Discussions

For most parts, there are very few problems with running WebAssembly on embedded systems. However, one feature is a problem on today's embedded microcontroller platforms and that is the linear memory feature. It is designed for more capable devices and therefore works with memory pages of 64 KiB. Many of the latest embedded systems cannot reserve even a full single page. Hence, another mechanism is needed to reduce the use of real memory for a WebAssembly module that uses the linear memory feature. A solution is perhaps a mechanism that allocates real memory only on demand, i.e., when a certain part of the memory page is being used.

33.5 Conclusions and Future Work

In this paper, we have demonstrated how a WebAssembly interpreter can be implemented on resource-constrained wearable sensor nodes. Due to the effectiveness of WebAssembly, we thereby have enabled the possibility to run exactly the same code anywhere in a complete wearable sensor system. This will finally allow us to use one single programming language and environment to program all parts of a complete wearable sensor system, from sensor nodes, to back-end servers, to client applications if we want to. We will now continue this work by designing a suitable distributed run-time environment for such systems and design suitable front-ends for the WebAssembly compilers based on low-code concepts. We believe that this will lead to faster and less demanding development of wearable sensor systems in the future.

References

1. Aslam, F., Fennell, L., Schindelbauer, C., Thiemann, P., Ernst, G., Haussmann, E., Rührup, S., Uzmi, Z.A.: Optimized Java binary and virtual machine for tiny motes. In: The 6th IEEE International Conference on Distributed Computing in Sensor Systems, DCOSS '10. IEEE, Piscataway (2008) https://doi.org/10.1007/978-3-642-13651-1_2
2. Baccelli, E., Doerr, J., Kikuchi, S., Padilla, F., Schleiser, K., Thomas, I.: Scripting over-the-air: towards containers on low-end devices in the Internet of things. In: The IEEE International Conference on Pervasive Computing and Communications, PerCom '18, Athens (2018)

3. Brouwers, N., Langendoen, K., Corke, P.: Darjeeling, a feature-rich VM for the resource poor. In: The 7th ACM Conference on Embedded Networked Sensor Systems, SenSys '09, Berkeley (2009). <https://doi.org/10.1145/1644038.1644056>
4. Duktape: <http://duktape.org/>
5. Dunkels, A., Finne, N., Eriksson, J., Voigt, T.: Run-time dynamic linking for reprogramming wireless sensor networks. In: The 4th International Conference on Embedded Networked Sensor Systems, SenSys '06. ACM, Boulder (2006). <https://doi.org/10.1145/1182807.1182810>
6. Haas, A., Rossberg, A., Schuff, D., Titzer, B., Gohman, D., Wagner, L., Zakai, A., Bastien, J., Holman, M.: Bringing the web up to speed with WebAssembly. In: The 38th ACM SIGPLAN Conference on Programming Language Design and Implementation, PLDI '17. Barcelona, Spain (2017). <https://doi.org/10.1145/3140587.3062363>
7. Martin, J.: GitHub – Kanaka/wac: WebAssembly interpreter in C. <https://github.com/kanaka/wac>
8. Mongoose OS: Reduce IoT firmware development time up to 90%. <https://mongoose-os.com/>
9. Pur3 Ltd: Espruino – JavaScript for microcontrollers. <https://www.espruino.com/>
10. Richardson, C., Rymer, J.R.: Vendor landscape: the fractured, fertile terrain of low-code application platforms. Forrester Research Report, 15 Jan 2016
11. Shelby, Z., Hartke, K., Bormann, C.: Constrained application protocol (CoAP). IETF RFC 7252 (2014). <https://tools.ietf.org/html/rfc7252>
12. Watt, C.: Mechanising and verifying the WebAssembly specification. In: The ACM SIGPLAN International Conference on Certified Programs and Proofs, CPP '18, Los Angeles (2018). <https://doi.org/10.1145/3167082>
13. WebAssembly: <http://webassembly.org/>
14. World Famous Electronics Ilc.: PulseSensor, <https://pulsesensor.com/>

Part VIII
Antenna/Propagation and WiBEC Project

Chapter 34

Biometallic Orthopedic Implant with Printed Antenna



Ildiko Peter and Ladislau Matekovits

34.1 Introduction

Mechanical behavior, biocompatibility in body environment, and chemical stability are the most important requirements for the effective use of any implant materials in the human body and in particular for internal support and biological tissue replacement [1, 2]. Metallic materials are continuously employed in the fields of orthopedics and dentistry [3, 4]. One of the most important engineering approaches when using metallic alloys is to guarantee as much as possible minor biological stress to the human system. Simultaneously, to maintain as much as possible the whole integrity and functionality of the human being, where the elastic modulus is very important; it should be as close as possible to that of cortical bones [5] in order to avoid essentially the “stress shielding.” β -type Ti alloys can be considered appropriate candidates for such purpose; additionally, their elastic modulus can be reduced following cold working [6]. Biometals, like Ti-based alloys, are widely employed thanks to their structural functions that show better mechanical resistance than some polymeric or ceramic ones, and due to their particular behavior, they can be considered in a significant position among other biometals and alloys [7]. Over the years the extension of metal made implants has been enlarged and recently there is a higher tendency to their use in non-conventional treatments too, replacing different human organs and tissues. Even if Ti6Al4V alloy shows exceptional mechanical resistance, high biocompatibility leading to a good implant-bone integration, during

I. Peter

University of Medicine, Pharmacy, Science and Technology, „George Emil Palade”, Faculty of Engineering and Information Technology, Târgu Mures, Romania
e-mail: ildiko.peter@umfst.ro

L. Matekovits (✉)

Department of Electronics and Telecommunications, Politecnico di Torino, Torino, Italy

© Springer Nature Switzerland AG 2020

C. Sugimoto et al. (eds.), *13th EAI International Conference on Body Area Networks*, EAI/Springer Innovations in Communication and Computing,
https://doi.org/10.1007/978-3-030-29897-5_34

393

the time some faults have been observed. In the years, efforts have been made to overcome these weaknesses, and for example a special class of β -type Ti alloys, developed in Japan, show remarkable possibilities in medical applications because they combine a particularly low elastic modulus (closer to the elastic modulus of cortical bones) with good mechanical strength [8]. Accordingly, in this chapter a complex medical device, based on TiNb biometallic alloy, exhibiting properties close to the bone ones, avoiding for example stress shielding, and characterized by the added-value of being also appropriate for communication purposes, is proposed.

Real-time monitoring or transmitting data from inside the body towards an external receiver requires the presence of an appropriate implanted system. Every such system includes an antenna, the shapes and dimensions of which are strongly influenced by different parameters, as for example the position inside the body. Managing space constraint is a challenging issue in the design. The shape of the antenna, in turn, determines its electric performances and operational bandwidth. Due to the presence of high water content, a body is a dispersive, lossy medium and the power density decays vary rapidly. Because of the different tissues present in the body, an accurate modelling of them is mandatory to avoid loss of communication and to increase the power supply operational time.

The extended shape of hip implants can be used as ground plane for an implanted, conformal, printed antenna, representing an intrinsically reduced space solution. Printed antennas have classical space saving configurations, but they require a relatively large (in terms of wavelength) ground plane, and here the large extension of the hip is used for such purpose.

The configuration proposed in this paper is placed inside an accurate body-like environment and it is numerically characterized by electromagnetic perspective. The results confirm that the proposed solution can be efficiently used for data transmission, for example monitoring some human vital functions, from inside the body to the external environment, where the signal can be captured.

In fact, in literature, the main attention is oriented to the necessary impedance matching realization in the body environment and considers only some features related to the communication channel between the inside-outside body environments [9]. At the best of the author knowledge, the biocompatibility of the material used for the manufacturing of the antenna or of the shielding screen to fulfill electromagnetic interference reduction is only marginally considered with no clear definition of the materials used and of their properties.

34.2 Materials' Characteristics

Numerical electromagnetic simulations have been carried out using a commercial available software package, namely Microwave Studio (MS) from CST [10], to investigate the performances of the structure when implanted in a multilayer body-like model.

Table 34.1 Electric parameters of the different tissues and materials at the central frequency of the considered 2.4–2.5 GHz ISM band

Tissue	Relative dielectric constant	Electrical conductivity [S/m]	Thickness [mm]
TiNb	–	$1e7$	$30 (2 \cdot R_{TiNb})$
Muscle	57.1	0.79	70
Fat	5.6	0.04	4
Skin	46.7	0.69	2
PDMS	2.667	0.037	$2 + 2 = 4$

The patch antenna and the feeding line are made of the same TiNb material of 0.5 mm thickness. They are bended around the metallic cylinder and supported by the biocompatible polydimethylsiloxane (PDMS) layer of total thickness of 4 mm. The antenna is embedded in the polymer that totally covers the cylinder's perimeter to ease the manufacturing.

The radius of the central TiNb is $R_{TiNb} = 15$ mm. The different tissues have been modeled according to dielectric data available in the literature, and available in MS. The considered values and their radial dimensions are reported in Table 34.1.

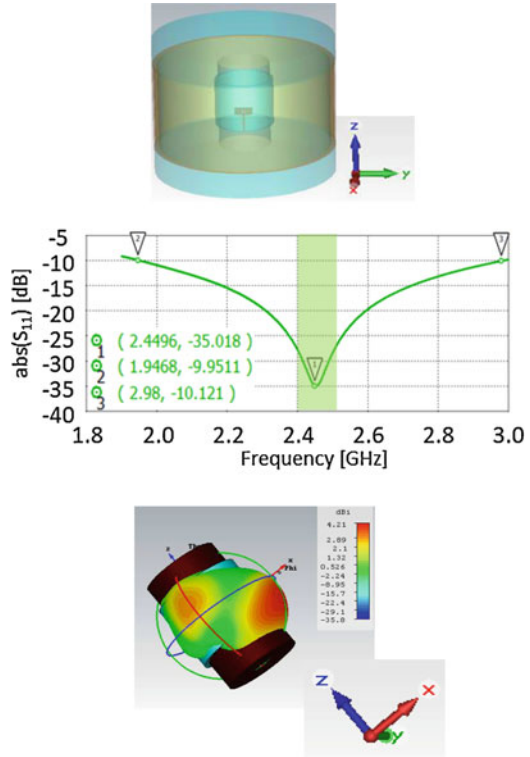
34.3 Results and Discussion: Electromagnetic Characterization of the Implanted Antenna

Figure 34.1 (top left) reports the CAD model used for the numerical analysis.

The 1.5 mm width of the feeding line has been obtained by genetic algorithm optimization (available in CST MS) enforcing the standard 50Ω line characteristic impedance in the operating conditions, i.e., considering the curvature and multilayer substrate-superstrate scenario. The radiating element is a rectangular patch of dimensions 9.86×20 mm², that guarantees a matching of $S_{11} = -35$ dB, see Fig. 34.1 (center), at the central frequency $f_c = 2.45$ GHz of the 2.4–2.5 GHz Industrial Scientific and Medical (ISM) frequency band [11] available worldwide. The two identical slots, each of 4.35×1 mm² dimension, on the two sides of the feeding line have the role of increasing the impedance matching. The 20 mm length of the antenna is well below the length of the hip of an adult. The feeding line is longer than in the case of an actual system when the antenna could be directly connected to the sensor node. Because of the high loss in the tissues, the boundaries of the cylindrical geometries do not influence the considered performances—matching and radiation pattern—since the reflected field from the open end is very low. However, in the simulations an Ecosorb type material has been used at the two ends of the truncated structure to reduce the reflection.

The 3D radiation pattern at the central frequency, reported in Fig. 34.1 (bottom), of the considered configuration exhibits a wide-angle $\pm 120^\circ$ coverage with a ripple of less than 3 dB. Unavoidably, the main radiation is in the direction almost orthogonal to the antenna (xz -plane). The small tilt is due to the radiation

Fig. 34.1 The proposed antenna inside the multilayer model and its electromagnetic performances: (top) CAD model—antenna with the surrounding tissues. The top and bottom layers are electromagnetic absorbers, used in the numerical simulations; (center) the scattering parameter S_{11} : the ISM band and the -10 dB bandwidth limits are clearly indicated; (bottom) Directivity at the central frequency of the ISM band



from the surface waves propagating parallel to the cylinder and from the feeding line. As already mentioned above, in the actual scenario, the length of this line which in turn will also reduce the losses and the tilt angle can be strongly reduced. Furthermore, the radiation pattern presents two other lobes in the backward direction, symmetrically positioned with respect to the antenna. They are due to the surface waves propagating along the metal–PDMS interface around the metallic cylinder. While usually the presence of different lobes is not desired, because for example of the reduced gain or reduced bit rate, in some applications their presence allows free movement of the incorporating body; the continuous link between the body and the external receiver is guaranteed by the more omnidirectional-like pattern.

34.4 Conclusions

Electromagnetic performances of an implanted conformal printed antenna have been described. The numerically investigated biometallic cylindrical model, corresponding to an implant, equipped with a printed antenna exhibits good matching and radiation properties for body centered communication applications.

References

1. Park, J., Lakes, R.S.: *Biomaterials an Introduction*, 3rd edn, pp. 99–137. Springer, Berlin (2007)
2. Ashby, M.F., Jones, D.R.: *Handbook of Biomaterials Evaluation: Scientific, Technical and Clinical Testing of Implant Materials-An Introduction to Microstructures, Processing and Design*, pp. 33–40. Pergamon Press, London (1980)
3. Liu, X., Chu, P.K., Ding, C.: Surface modification of titanium, titanium alloys and related materials for biomedical applications. *Mat. Sci. Eng.* **47**, 49–121 (2004)
4. Peter, I., Rosso, M.: Study of Ti-enriched CoCrMo alloy for dental application. *IEEE Access.* **3**, 73–80 (2015)
5. Niinomi, M.: Recent research and development in titanium alloys for biomedical applications and healthcare goods. *Sci. Technol. Adv. Mater.* **4**, 445–454 (2003)
6. Besse, M., Castany, P., Gloriant, T.: Mechanisms of deformation in gum metal TNTZ-O and TNTZ titanium alloys: a comparative study on the oxygen influence. *Acta Mater.* **59**, 5982–5988 (2011)
7. Geetha, M., Singh, A.K., Asokamani, R., Gogia, A.K.: Ti based biomaterials, the ultimate choice for orthopaedic implants—a review. *Prog. Mater. Sci.* **54**, 397–425 (2009)
8. Saito, T., Furuta, T., Hwang, J., Kuramoto, S., Nishino, K., Suzuki, N., Chen, R., et al.: Multifunctional alloys obtained via a dislocation-free plastic deformation mechanism. *Science.* **300**, 464 (2003)
9. Merli, F., Fuchs, B., Mosig, J.R., Skrivervik, A.K.: The effect of insulating layers on the performance of implanted antennas. *IEEE Trans. Antennas Propag.* **59**, 21–31 (2011)
10. Microwave Studio, Computer Simulation Technology, vol. 2018
11. Radio Regulations, Edition of 2012. ITU-R. Retrieved 2014-11-10

Chapter 35

EM Imaging-Based Capsule Endoscope Localization with Peak-Formed Incident Electric Fields



Hisato Kobayashi, Daisuke Anzai , and Jainqing Wang

35.1 Introduction

Recent years, along with rapid development of wireless body area networks (BANs), medical treatments have been greatly advanced [1]. One of the most important medical devices using implant BANs is wireless capsule endoscopy (WCE). A typical wired endoscope has a critical disadvantage that patients should suffer from a serious pain due to its too long cable. Furthermore, the wired endoscope is not applied to diagnosis in small intestine. On the other hand, WCE gives patients fewer stress and pain since only swallowing the small-sized capsule makes it possible to diagnose all digestive organs including small intestine, so that WCE has so far attracted a lot of attention as an advanced medical device. The technical problems on WCE include the battery life time and accurate motion control from outside the human body. To solve these problems, it is important to obtain the location information of the capsule endoscope inside the body [2]. For the reasons, various kinds of localization methods have been discussed such as received signal strength indicator (RSSI)-based method and time of arrival (TOA)-based methods [3], both of which utilize radio frequency (RF) signals transmitted by WCE. However, we need the wireless channel model inside the human body, and hence large-scale measurement phase (such as CT or MRI) is beforehand needed in order to obtain the internal structure of human body.

Compared with the RF methods, an electromagnetic (EM) imaging method can avoid such a preliminary measurement. Several conventional EM imaging methods assume a plane wave as an incident source; however, it is pointed out that the conventional methods are more difficult to accomplish precise localization accuracy

H. Kobayashi · D. Anzai (✉) · J. Wang
Nagoya Institute of Technology, Nagoya, Japan
e-mail: 29413088@stn.nitech.ac.jp; anzai@nitech.ac.jp

when the frequency band is getting higher as in 2.4 GHz. In order to improve the estimation accuracy at high frequency, we pay attention to peak-formed incident electric fields by overlaying the plane waves. By sweeping the position of the peak, we can obtain more information on scattered electric fields than the conventional methods, which result in accurate location estimation at high frequency band. In this chapter, we evaluate the estimation accuracy of the proposed method through computer simulations to demonstrate the superiority of the proposed method over the conventional EM imaging methods.

35.2 Mathematical Formulation of Scattered Electromagnetic Fields

A human body is composed of various kinds of tissues, and each tissue has its own electrical constants such as permittivity and conductivity [4, 5]. When the electromagnetic wave irradiates the human body, we observe scatter electric fields represented by following equations under 2-dimensional transversal magnetic (TM) condition [6]:

$$E^s(x, y) = -\frac{jk^2}{4} \iint_S \tilde{\epsilon}_r(x', y') \mu(x', y') E^{\text{total}}(x', y') H_0^{(2)}(k\rho) dx' dy' \quad (35.1)$$

where (x, y) and (x', y') are the coordinates of the observation point outside the body and the source point inside the body, respectively. $H_0^{(2)}$ is the second kind Hankel's function with the order of zero, k is the wave number, and ρ is the distance between the observation point and the source point. Figure 35.1 shows the definitions of the variables in Eq. (35.1). The total electric fields can be expressed as the sum of the incident electric field and the scattered fields. Taking the method of method (MoM) into consideration, we obtain the matrix equations as [6]:

$$\mathbf{E}^{\text{total}} = (\mathbf{A}\epsilon\mu + \mathbf{I})^{-1} \mathbf{E}^i \quad (35.2)$$

$$\mathbf{E}^s = \mathbf{B}\mathbf{E}^{\text{total}}\epsilon\mu \quad (35.3)$$

where \mathbf{I} is the unit matrix, \mathbf{A} and \mathbf{B} are the matrices whose elements are determined by the geometric arrangement of the human body model. In order to perform the implant device localization, we can directly measure the scattered electric fields outside the human body.

Fig. 35.1 Electromagnetic scattering environment by heterogeneous object

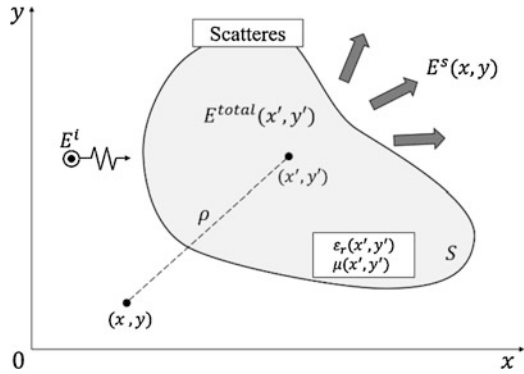
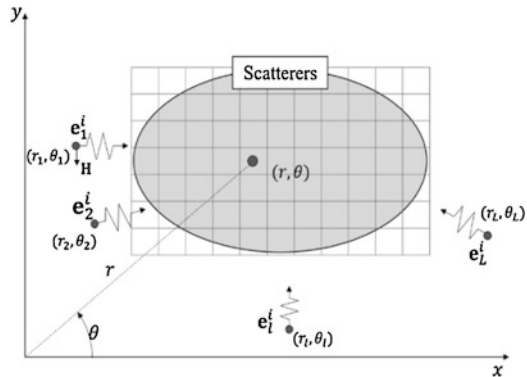


Fig. 35.2 Model of irradiation with multiple incident electric fields



35.3 Estimation Algorithm Using Peak-Formed Electric Fields

Peak-Formed Electromagnetic Fields

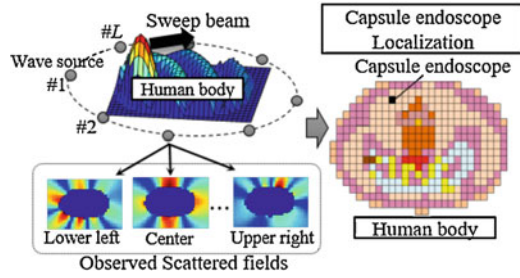
The position of the peak can be adjusted by changing the phase of each incident electric fields irradiated from each wave source. We show the model of irradiation with multiple wave sources in Fig. 35.2.

In this chapter, a peak-forming of incident electric field intensity at a specific location is realized by using L overlaid multiple plane waves as

$$E^i(r, \theta) = \sum_{l=1}^L E_0 \exp[-jk_0 \{r \cos(\theta_l - \theta) - r_l\}] \tag{35.4}$$

where E_0 is the incident electric field intensity, and (r_l, θ_l) is the polar coordinate of the l th wave source position. In the proposed localization system, the implant

Fig. 35.3 System model of EM-imaging using peak-formed incident electric fields



device location can be estimated based on the measured scattered electrical fields $E_{\text{measured}}^s(r, \theta)$ as

$$(\hat{r}, \hat{\theta}) = \operatorname{argmax}_{r, \theta} |E_{\text{measured}}^s(r, \theta) - E_{\text{init}}^s(r, \theta)| \quad (35.5)$$

where $(\hat{r}, \hat{\theta})$ is the estimated location of the implant device, and $E_{\text{init}}^s(r, \theta)$ denotes the scattered electric fields observed before the implantable device is implanted into the body. In (35.5), note that the coordinates indicate the peak location of the peak-formed electromagnetic fields. Figure 35.3 shows the system model and overview of the proposed peak-forming EM imaging method.

35.4 Performance Evaluation

Simulation Environment

Figure 35.4 shows the human body model employed in the computer simulation, where the electric constants of the tissues at 2.4 GHz were assumed. Among the cells shown in Fig. 35.4, we randomly selected one cell and replaced it with the capsule endoscope that was assumed as a perfect conductor. For generating peak-formed incident electric field distribution, we used 100 wave sources placed around the human body, and 102 points of measuring points were set at the points 1 cm away from the human body surface. The simulation parameters are shown in Table 35.1. In addition, additive Gaussian noise caused by thermal noise at the receivers was superposed on the observed scattering electric fields. Here the SNR can be calculated by

$$\text{SNR} = \frac{|V_{\text{measured}}|^2}{P_N} \quad (35.6)$$

where V_{measured} is the received voltage measured at the each receiver, and P_N represents the noise power.

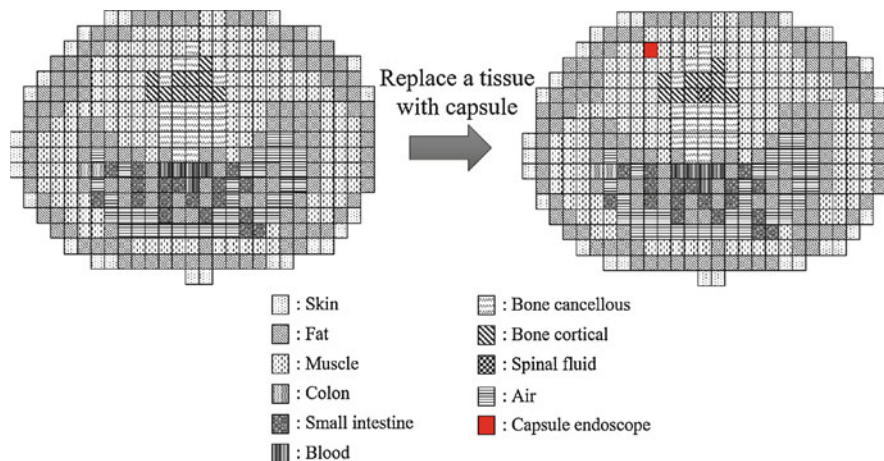


Fig. 35.4 Simulation model of heterogeneous human body

Table 35.1 Simulation parameters

Parameters	Values
Number of cells	391
Number of measuring points	102
Number of wave sources	100
Number of trials	391
Cell length	1 cm
Relative permittivity around the body ϵ_{rm}	24.9
Conductivity around the body σ	0.99 S/m
Frequency of incident electric field	2.4 GHz

Estimation Accuracy

Figure 35.5 shows an example result of an evaluation function in each cell of the human body model when a capsule endoscope is located at (10, 7). Here, we define the evaluation function as

$$f(x, y) = |E_{\text{measured}}^S(x, y) - E_{\text{init}}^S(x, y)| \tag{35.7}$$

where x and y denote the peak location of the incident fields. It is found that the evaluation value is maximized at which the capsule endoscope locates, which means that the proposed method is able to estimate the capsule endoscope correctly in this example.

For comparison purpose, we also evaluated the performance of the conventional method which uses only one plane wave [7]. From Fig. 35.6 proposed method, when noise is not superimposed, achieved to estimate the location of capsule endoscope with a probability of 90% with a tolerance of 1 cm. From these results, the proposed

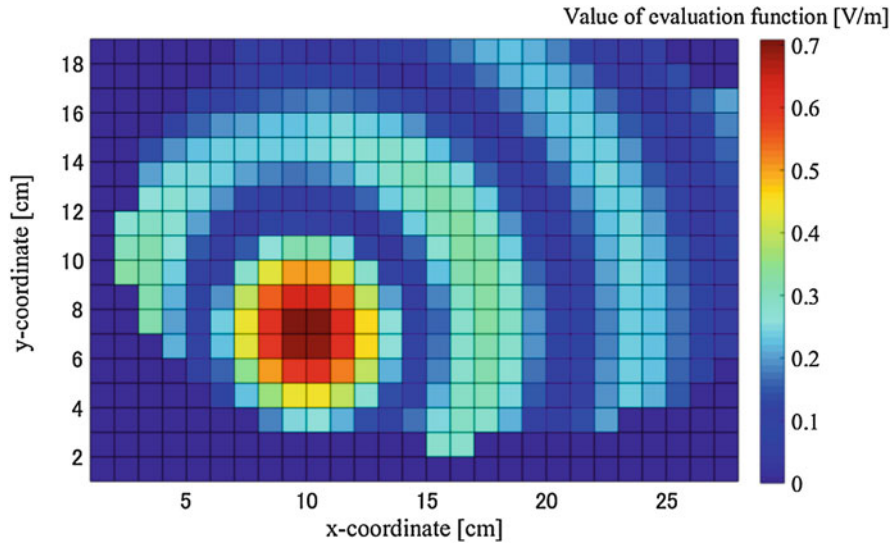


Fig. 35.5 Distribution of the evaluation function

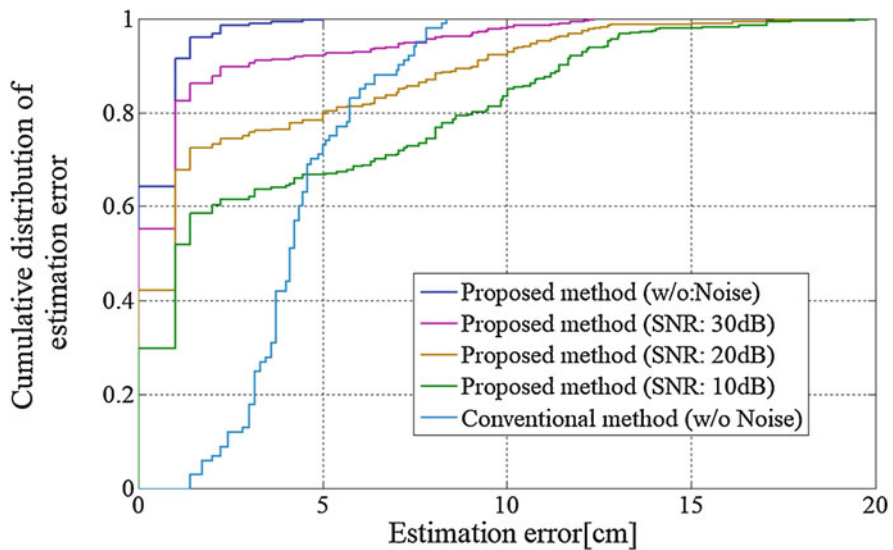


Fig. 35.6 Cumulative distribution of location estimation error

method can achieve a remarkable improvement in accuracy compared with the conventional method, and even in the environment where noise is superimposed, we achieved the improvement of the estimation accuracy.

35.5 Conclusion

We have proposed a peak-forming-enhanced EM imaging method and demonstrated that the proposed method achieves much better estimation accuracy than the conventional method, so that it can contribute high-quality medical treatment offered by implantable devices with highly accurate estimated positions. According to the evaluation results, the estimation accuracy is achieved to 1 cm ensuring the cumulative probability of 80% even if additive Gaussian noise is assumed at the observed scatter electric fields.

Acknowledgement This research was supported by the MIC/SCOPE #185106002.

References

1. Yuce, M.R., Dissanayake, T.: Easy-to-swallow wireless telemetry. *IEEE Microw. Mag.* **13**(6), 90–101 (2012)
2. Kawasaki, M., Kohno, R.: Position estimation method of medical implanted devices using estimation of propagation velocity inside human body. *IEICE Trans. Commun.* **92**(2), 403–409 (2009)
3. Hara, S., Anzai, D., Yabu, T., Lee, K., Derham, T., Zemek, R.: A perturbation analysis on the performance of TOA and TDOA localization in mixed LOS/NLOS environments. *IEEE Trans. Commun.* **61**(2), 679–689 (2013)
4. Wang, J., Takagi, T.: A noninvasive method for dielectric property measurement of biological tissue. *IEICE Trans. Commun.* **E77-B**(6), 738–742 (1994)
5. Chew, W.C., Wang, Y.M.: Reconstruction of two-dimensional permittivity distribution using the distorted born iterative method. *IEEE Trans. Medical Imaging.* **9**(2), 218–225 (1990)
6. Richmond, J.H.: Scattering by a dielectric cylinder of arbitrary cross section shape. *IEEE Trans. Antennas Propagat.* **13**(3), 334–341 (1965)
7. Iida, T., Anzai, D., Wang, J.: Performance evaluation on WCE localization using GA-based three dimensional electromagnetic imaging. In: 10th International Symposium on Medical Information and Communication Technology (ISMICT), Massachusetts, USA, 20–23 March 2016

Chapter 36

Information Theoretic Analysis for Securing Next Generation Leadless Cardiac Pacemaker



Muhammad Faheem Awan, Kimmo Kansanen, and Deepak Palaksha

36.1 Introduction

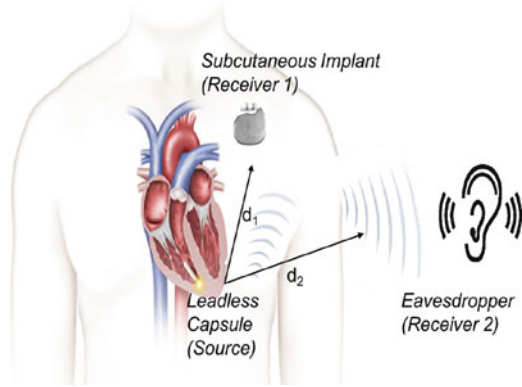
The technological advancements in personal health systems result in number of wearable and implantable medical devices. These devices help in the automatic diagnosis and treatment of several medical ailments, thus improving the life quality.

Implantable medical devices (IMDs) are designed to monitor and treat regularly several physiological conditions of the body. The most significant among them are cardiac pacemakers and implantable cardioverter defibrillators (ICDs). Pacemakers and ICDs are used to treat cardiac arrhythmia. These devices are equipped with sensors that sense the pathological conditions and deliver proper actuation, e.g., by retaining the cardiac rhythm.

Cardiac pacemakers are designed to maintain the regular heart rhythms. The current generation of these pacemakers consist of a subcutaneous implant, implanted in the pectoral pocket under the shoulder which is connected to the wired electrodes in the heart chambers through the subclavian vein. The traditional cardiac pacemakers are anticipated to be wireless in near future. These implanted devices transmit patient data (offline and real-time) along with other critical device information and indicators. In addition, the transmitted indicators may contain information about diagnosed ailments along with performed therapies. In order to maintain the proper configuration of a pacemaker along with regular patient monitoring, the data transmissions play a critical role. The physician is also continuously updated regarding the current status of a patient and alarms if the critical condition is detected. The frequency of data transmissions varies depending upon different configurations. The most common configuration follows the retrieval of data while

M. F. Awan (✉) · K. Kansanen · D. Palaksha
Norwegian University of Science and Technology, NTNU, Trondheim, Norway
e-mail: faheem.awan@ntnu.no; deepak.palaksha@ntnu.no

Fig. 36.1 Pacemaker scenario with an eavesdropper



visiting a physician. In some cases, a bed side external device is also provided, in which the data is logged automatically on everyday basis. However, the future leadless cardiac pacemaker is shown in Fig. 36.1, with a capsule inside the heart chamber and a subcutaneous implant will transmit the data on each heartbeat.

The wireless communication in next generation IMDs could be a substantial source of security risks. It increases the visibility of IMD and can help eavesdropper to overhear the communication [1]. Thus, in case of an insecure communication channel, the eavesdropper can easily execute attacks on implants, as like they are performed in other communication networks and devices. If the eavesdropper succeeds in gaining access to the implanted device, she can fetch the patient data (medical or non-medical) or can forge or alter the information. Furthermore, the eavesdropper can modify the device configuration without knowledge of physician or a patient.

The security analysis of IMDs was first provided by Halperin et al. [2], in which it has been shown that the insecure link between IMDs can be compromised. This work was succeeded by various research activities that mainly emphasize on various encryption mechanisms for confidentiality between authentic nodes [3–6].

In traditional wireless networks, the security of a communication network is viewed as an independent task with no or limited association with other features of a network. This leads to the development of state-of-the-art algorithms for privacy and security of these networks. But IMDs majorly focus on device application rather than features like security, due to which wireless IMDs have weak security algorithms and are more prone to privacy and security threats.

Security and privacy in conventional wireless networks is studied and implemented via various traditional cryptographic algorithms that include AES, RSA, DES, etc. Cryptographic algorithms ensure confidentiality by encrypting data using secret keys. These keys help, encrypt, and decrypt the information at sender and receiver, which can be achieved by keys distribution among them. They work on an assumption that eavesdropper has limited computational resources. But sometimes it is difficult to implement these techniques in low power devices because of keys management issues and computational complexity. Another approach to secure data

is using physical layer security, which relies on concepts of information theory. Security with information theoretic measures can be cryptanalytically unbreakable regardless of eavesdropper unlimited computational resources. Physical layer security is based on information theoretic measures which ensures that third party or eavesdropper is not able to eavesdrop communication. It can be additionally provided together with cryptographic methods.

The key idea of information theoretic security (ITS) is to utilize properties of the eavesdropper and legitimate receiver channels. The idea of ITS was pioneered by Shannon in [7]. Wyner in [8] further extended the concept by introducing a wiretap channel. It was shown in [8] that secrecy can be provided by wireless channel itself without depending on secret keys and can degrade the ability of eavesdropper to collect information. Notable mechanisms among them exploit channel attenuation, interference, and fading in a communication channel. He added that perfect secrecy can be achieved, if the channel capacity of a link between source and legitimate receiver is greater than the channel capacity of link between source and eavesdropper. In Wyner model, eavesdropper is considered to have unlimited computational resources. Using the assumption, that an eavesdropper channel is a degraded version of the main channel, Wyner proved the existence of positive secrecy capacity. This work was extended by [9] for broadcast channels where nondegraded version of eavesdropper channel was considered. These studies provide an important performance metric of secrecy capacity. Secrecy capacity is the maximum communication rate with which the legitimate nodes can communicate securely without leakage of information to the eavesdropper.

This work explores the potential of physical layer security methods for securing future leadless cardiac pacemaker (LCP). We utilize the strategy of sending information over the Gaussian broadcast channel in order to ensure secrecy. This can be achieved by manipulating transmission rates for different broadcast receivers. As the name suggests, broadcast scenario involves simultaneously transmission of information to multiple receivers, thus securing information involving Gaussian broadcast channel requires sending of information to two distant receivers in a way that one message X_1 is intended for receiver one and second message X_2 is intended for receiver two. Receiver one which can be regarded as legitimate receiver can decode both messages, if his signal-to-noise ratio is greater than receiver two, whereas receiver two can only decode second message X_2 with an inferior signal-to-noise ratio. Signal-to-noise ratio of both receivers varies due to channel attenuation ($|h|^2$). Receiver one's higher signal-to-noise ratio is achieved because it is close to leadless capsule, thus resulting in lower channel attenuation or path loss than that of receiver two, which is physically away from the body of implanted capsule. In this work, path loss model from [10] is utilized to formulate attenuation between nodes.

The rest of this paper is organized as follows: System model is provided in Sect. 36.2, whereas Sect. 36.3 contains numerical results. Section 36.4 provide conclusions and followed by acknowledgments.

36.2 System Model

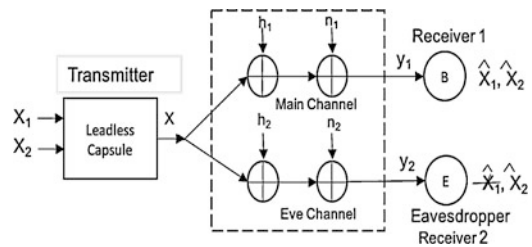
This section focuses on providing system model used in the analysis. For our scenario, the system model consists of an LCP implanted in the right ventricle of human heart. The LCP wants to communicate with a subcutaneous implant, whereas an eavesdropper tries to overhear the communication as shown in Fig. 36.1. The subcutaneous implant is considered to be placed at a distance of 150 mm below the collarbone under the skin, thus having lower channel attenuation than eavesdropper. The eavesdropper is assumed to be physically away from a body in which leadless capsule is implanted. As mentioned earlier, in order to ensure secrecy we utilized strategy of Degraded Gaussian Broadcast Channel (DGBC) with confidential messages, which can be presented schematically in Fig. 36.2. This method is utilized because of its resemblance to our scenario, where eavesdropper channel is always degraded version of legitimate channel. In context of DGBC, subcutaneous implant is considered as the receiver one, whereas the eavesdropper is considered as receiver two. Leadless capsule will transmit two different messages intended for two receivers. Message 1 (X_1) will be confidential information intended for receiver one and message 2 (X_2) will be dummy message or jamming signal intended for receiver two.

Encoding

In order to encode messages, the encoder of leadless capsule will encode message X_1 with rate R_1 and power (αP) for receiver one and X_2 with rate R_2 and power $(1 - \alpha)P$ for receiver two, where α is the power allocation factor that distributes total power between confidential message X_1 and jamming signal X_2 . Transmitter then calculates sum of useful information and jamming signal and transmits sum X over a channel as shown in Fig. 36.2. The transmitted signal along with signals received by the two receivers is expressed, respectively, as

$$X = X_1 + X_2 \tag{36.1}$$

Fig. 36.2 Gaussian broadcast channel with confidential information



$$\begin{aligned} Y_1 &= \sqrt{P}h_1X + n_1 \\ Y_2 &= \sqrt{P}h_2X + n_2 \end{aligned} \quad (36.2)$$

X is subject to average power constraint $\frac{1}{n} \sum_{i=1}^n E[X_i]^2 \leq P$, h_1, h_2 are channel gains, and $n_1 \sim \mathcal{N}(0, N_1)$, $n_2 \sim \mathcal{N}(0, N_2)$ is additive white Gaussian noise (AWGN). Multipath small scale fading is assumed to be negligible and channel gain only constitutes path loss which can be expressed in logarithmic scale as

$$\begin{aligned} PL(d)_i &= PL(d_o) + 10\gamma \log_{10}(d_i/d_o), \\ d &\geq d_o, i \in (1, 2) \end{aligned} \quad (36.3)$$

$$|h_i|^2 = 10^{-\frac{PL(d)_i}{10}}, i \in (1, 2) \quad (36.4)$$

In (36.3), $PL(d)_2$ is path loss at distance d_2 between implant and receiver two (eavesdropper) and $PL(d)_1$ is path loss between implant and receiver one at distance d_1 . d_o is the reference distance, where $PL(d_o)$ is path loss at reference distance and γ is path loss exponent.

Decoding

The respective receivers then decode messages. Our aim is to maximize mutual information $I(X; Y_1)$ between capsule and receiver, keeping mutual information between eavesdropper and capsule to zero s.t. $I(X; Y_2) = 0$. First, consider receiver two, which is the eavesdropper. She will try to map a received sequence to a message pair (X_1, X_2) . Her effective signal-to-noise ratio of X is $\frac{(1-\alpha)P|h_2|^2}{(\alpha P|h_2|^2 + N_2)}$, where $\alpha P|h_2|^2$ acts as noise. Thus, she will be able to decode only X_2 . Receiver one which is subcutaneous implant first decodes X_2 , which he can accomplish because of his higher SNR, i.e., $\frac{\alpha P|h_1|^2}{N_1}$. Then he will decode the confidential message X_1 intended for himself. Thus, in order to have confidential messages, information rates R_1 and R_2 must satisfy secrecy condition.

Secrecy Capacity

Secrecy capacity region is the set of information rates that can be achieved by keeping confidentiality of secret information to maximum from eavesdropper. The secrecy capacity region for one confidential message and one dummy message or jamming signal can be expressed as

$$C_s = \bigcup_{0 \leq \alpha \leq 1} \left\{ \begin{array}{l} R_1, R_2 : \\ R_1 \leq \left[\frac{1}{2} \log \left(1 + \frac{\alpha P |h_1|^2}{N_1} \right) - \frac{1}{2} \log \left(1 + \frac{\alpha P |h_2|^2}{N_2} \right) \right]^+ \\ R_2 \leq \min \left\{ \frac{1}{2} \log \left(1 + \frac{(1 - \alpha) P |h_1|^2}{N_1 + \alpha P |h_1|^2} \right), \frac{1}{2} \log \left(1 + \frac{(1 - \alpha) P |h_2|^2}{N_2 + \alpha P |h_2|^2} \right) \right\} \end{array} \right\} \quad (36.5)$$

Equation (36.5)¹ provides secrecy rate pairs (R_1, R_2) depending upon different values of α and channel attenuation $(|h_i|^2), i \in (1, 2)$. Noise variance for receiver one is N_1 and N_2 for receiver two. For simplicity, $N_1 = N_2 = N_0$ is considered, suggesting same noise for both receivers. The only thing that varies SNR for both receivers is channel attenuation and power allocation factor α . As α increases, information rate R_1 will increase, whereas R_2 will reduce. In Eq. (36.5), R_1 is a positive confidential information rate when inequality holds.

Analysis of the Strategies

The strategy above provides the secrecy operating regions for leadless cardiac capsule where our motive is to keep confidential information secret from receiver two. In our analysis, we focus on fixing certain information rate R_1 for legitimate receiver and find the value of α where eavesdropper distance is maximum which can then be related to maximum threat distance. Consider, fixed secrecy information rate $R_1 = R_1^*$, which is chosen to be decodable at channel attenuation $(|h_1^*|^2)$ (corresponds to distance d_1). Eavesdropper threshold attenuation $(|h_2|^2)$ can be expressed from (36.5) as

$$\log(2^{R_1^*}) + \frac{1}{2} \log \left(1 + \frac{\alpha P |h_2|^2}{N_0} \right) \leq \frac{1}{2} \log \left(1 + \frac{\alpha P |h_1^*|^2}{N_0} \right) \quad (36.6)$$

Using properties of log, (36.6) transforms into

¹All bases are log₂, else specified.

$$\log \left(2^{R_1^*} \left(1 + \frac{\alpha P |h_2|^2}{N_0} \right)^{\frac{1}{2}} \right) \leq \log \left(1 + \frac{\alpha P |h_1^*|^2}{N_0} \right)^{\frac{1}{2}} \quad (36.7)$$

For simplicity, we put inequalities to equality. After simplification,

$$\begin{aligned} |h_2|^2 &= \frac{N_0}{\alpha P} \left(\left(1 + \frac{\alpha P |h_1^*|^2}{N_0} \right) \frac{1}{2^{2R_1^*}} - 1 \right) \\ |h_2|^2 &= \frac{N_0}{\alpha P} \left(\frac{1}{2^{2R_1^*}} - 1 \right) + \frac{|h_1^*|^2}{2^{2R_1^*}} \end{aligned} \quad (36.8)$$

Equation (36.8) provides maximum eavesdropper threshold attenuation for fixed R_1^* and $|h_1^*|^2$, which can be transformed to maximum eavesdropper distance by using (36.3) and can be expressed as

$$10 \log_{10} |h_2|^2 = 10 \log_{10} K \quad (36.9)$$

where $K = \frac{N_0}{\alpha P} \left(\frac{1}{2^{2R_1^*}} - 1 \right) + \frac{|h_1^*|^2}{2^{2R_1^*}}$. From (36.3), (36.9) can be expressed as

$$\begin{aligned} 10 \log_{10}(K) &= PL(d_o) + 10\gamma \log_{10}(d_2/d_o) \\ d_2 &= d_o \times 10^{\left(\frac{1}{10\gamma} (10 \log_{10}(K) - PL(d_o)) \right)} \\ d_2 &= d_o \times 10^{\left(\log_{10}(K)^{\frac{1}{\gamma}} - \frac{0.1}{\gamma} PL(d_o) \right)} \\ d_2 &= d_o \times \frac{K^{\frac{1}{\gamma}}}{10^{\frac{1}{10\gamma} PL(d_o)}} \\ d_2 &= d_o \times \frac{\left(\frac{N_0}{\alpha P} \left(\frac{1}{2^{2R_1^*}} - 1 \right) + \frac{|h_1^*|^2}{2^{2R_1^*}} \right)^{\frac{1}{\gamma}}}{10^{\frac{1}{10\gamma} PL(d_o)}} \end{aligned} \quad (36.10)$$

Equation (36.10) provides eavesdropper threshold distance, for a fixed secrecy rate R_1^* . Thus, at this distance, eavesdropper will be able to decode only R_2^* . When eavesdropper is closer, she will be able to partially decode R_1^* as well. Eventually a point will reach when eavesdropper attenuation becomes equal to receiver one, where she will be able to decode both R_1^* and R_2^* . Thus d_2 from (36.10) is the distance from which eavesdropper can eavesdrop the confidential message for a given fixed information rate R_1 . So, eavesdropper should be outside this threat distance d_2 for data confidentiality. Beyond d_2 , entire region will be in secure zone.

36.3 Numerical Results

The system model of Fig. 36.1 is considered, with a leadless capsule and subcutaneous implant at a distance $d_1 = 150$ mm, where an eavesdropper attempts to eavesdrop communication at a distance $d_2 \geq 150$ mm. The main interest is to find secrecy capacity region (C_s) for different values of α and eavesdropper distance. In addition, a threat zone around implanted body will also be found for fixed information rate R_1 .

For numerical results, we consider that legitimate nodes are communicating in medical implant communication (MICS) band. MICS band ranges between 402 and 405 MHz with authorized channel bandwidth of 300 kHz. Implanted medical devices operate on low operational power usually between -16 and -25 dBm due to which transmitted power of $P = -16$ dBm is considered[11]. In addition, noise power spectral density (PSD) of -100 dBm/channel is considered for both receivers. Channel attenuation is obtained from (36.3) in which path loss $PL(d_o)$ at reference distance of 50 mm is 47.14 dB and path loss exponent (γ) is 4.26 [10]. This is the case for communication between leadless capsule and subcutaneous implant, whereas for an eavesdropper link, a reference distance of 150 mm is considered, and beyond its free space path loss is applied with path loss exponent $\gamma = 2$.

Figure 36.3 shows capacity and secrecy capacity region (R_1, R_2) for a particular distance pair (150 mm, 300 mm). In this case, receiver two is considered at a

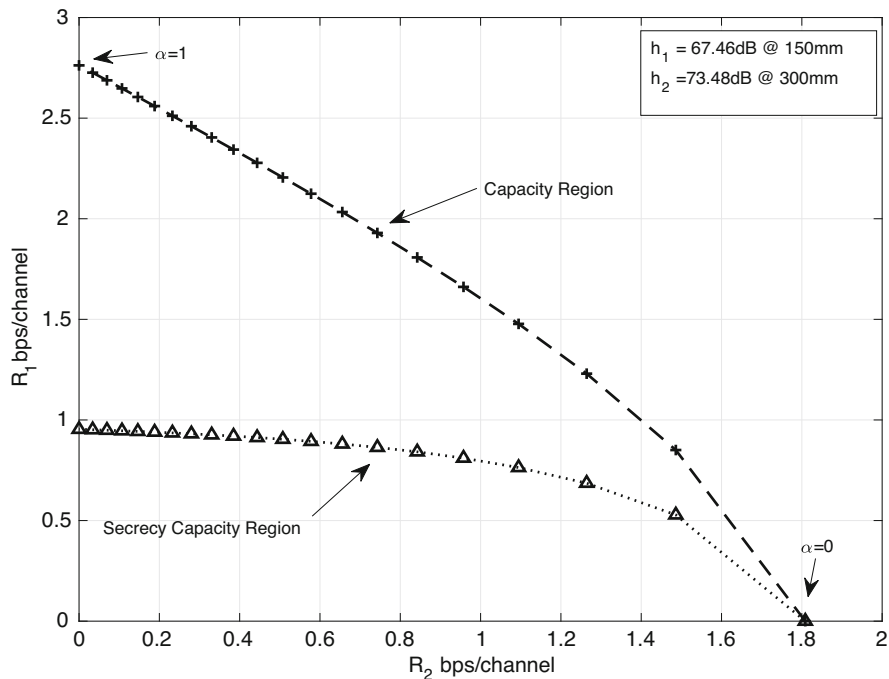


Fig. 36.3 Secrecy capacity region C_s

distance of 300 mm, resulting in channel attenuation of 73.48 dB. It can be seen that when power allocation factor α increases, information rate R_1 to legitimate receiver increases, while information rate R_2 to receiver two reduces. In addition, cost for making communication secure can also be seen by observing a difference between capacity region and secrecy capacity region. Now consider a case, when $\alpha = 0.9$, receiver two (eavesdropper) is at a distance of 300 mm, and receiver one is at mentioned fixed distance of 150 mm. The secrecy rate pair (R_1, R_2) is approx. (1,0.4) bps/channel. Now, if eavesdropper move closer towards receiver one, its channel SNR improves, this results in decoding a part of confidential message as well. Thus, 300 mm is threshold distance for an eavesdropper to support that secrecy capacity region. If eavesdropper moves closer than 300 mm, rate R_1 should be reduced by reducing alpha (α) and feeding more power to jamming signal; otherwise, eavesdropper will be able to eavesdrop communication partially and will be able to decode completely when she reaches the same distance as legitimate receiver.

Similarly, in Fig. 36.4 it is shown that if eavesdropper distance (d_2) increases, attenuation increases due to which information rate R_2 reduces, whereas R_1

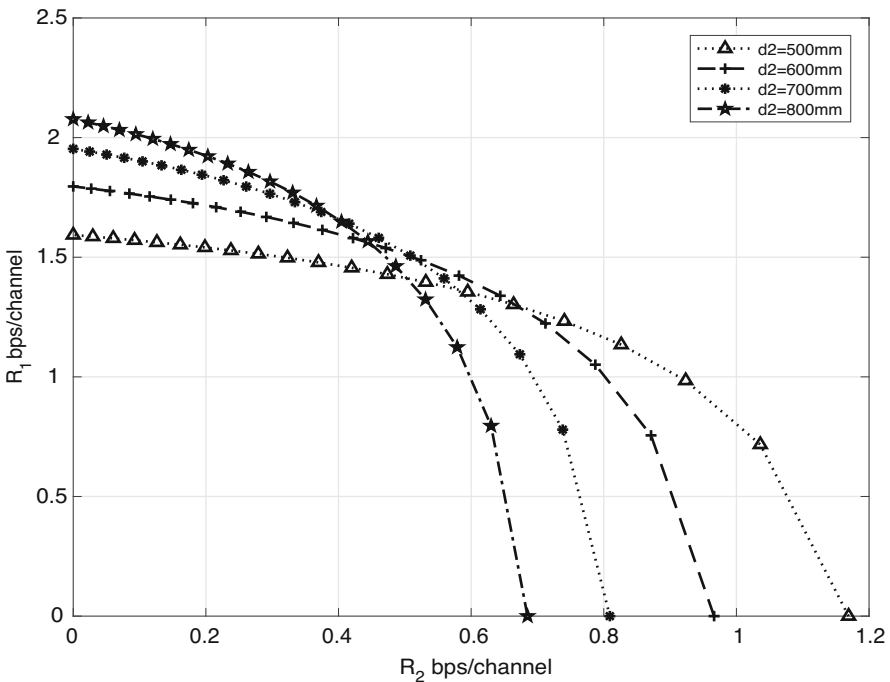


Fig. 36.4 Secrecy capacity region C_s for varying eve distance

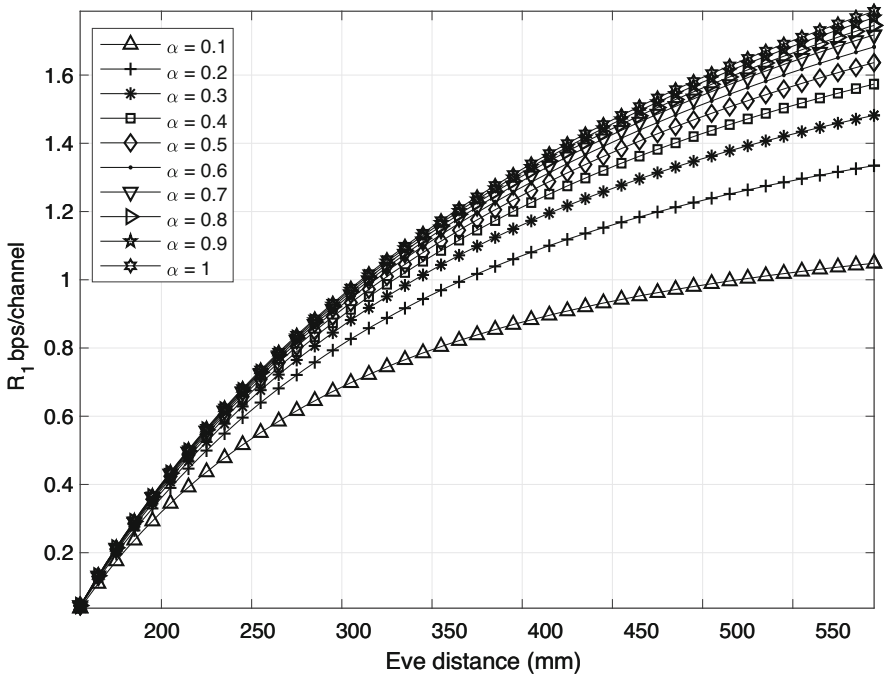


Fig. 36.5 Information rate R_1 versus eve distance

increases. Thus, making information rate adaptable by estimating eavesdropper distance can help increasing the secrecy capacity. Figure 36.5 shows change in information rate R_1 with changing Eve distance for different values of α . It is evident that if eavesdropper distance increases, rate R_1 can be increased.

Furthermore, by using (36.10) maximum eavesdropping distance is depicted for different values of total power (P), information rate (R_1), and α in Fig. 36.6, mirroring the threat zone around the implanted node. The region beyond threat zone is considered to be in secure zone. Secure zone can be increased by reducing the total power which has twofold advantages, one by conserving energy for low power implanted devices such as cardiac pacemaker that help increasing the longevity of a device and also results in increased secure zone. The eavesdropper then needs to move closer to eavesdrop the legitimate transmission. As shown in Fig. 36.6, with $\alpha = 0.2$, $P = -16$ dBm, and $R_1 = 3.5$, the threat zone can be reduced to about 400 mm.

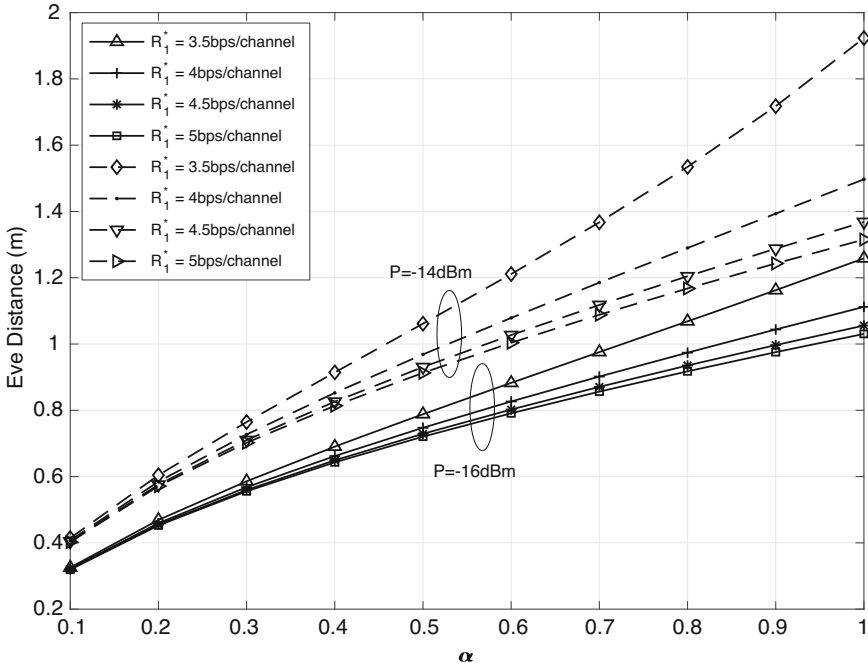


Fig. 36.6 Eavesdropping distance with changing information rate (R_1), α and total power (P)

36.4 Conclusions

This work includes information theoretic security analysis of leadless cardiac pacemaker, transmitting data over a wireless channel to a subcutaneous implant, with an eavesdropper in the near premises to overhear the communication. For securing leadless cardiac pacemaker (LCP), we intend to use degraded Gaussian broadcast channel approach in which a node broadcasts the information to different receivers in a way that legitimate node can decode all the information, whereas other receivers can only decode the information intended for them.

The secure information rates region is depicted where LCP can communicate securely with legitimate receiver in the presence of eavesdropper. A fixed distance between legitimate nodes is considered, whereas eavesdropper distance is varied. LCP sends confidential message to legitimate receiver, whereas noise signal or common signal is used to jam the eavesdropper. Legitimate receiver with lower attenuation and higher SNR will be able to decode both the messages, whereas eavesdropper with inferior SNR will be able to decode only the common signal. In order to find channel attenuation between nodes, a path loss model from [10] is used. Total power is distributed between both messages by power distribution factor (α). By increasing α information rate to legitimate receiver is increased whereas information rate to eavesdropper decreases. We also fixed certain information rate

between legitimate nodes and find the maximum eavesdropping distance in order to decode confidential information by eavesdropper. If eavesdropper is at maximum eavesdropper distance for certain fixed value of α , it will not be able to decode any information, but when it starts getting close to legitimate receiver it will be able to partially decode the confidential information, until it reaches to a point where she will decode entire information. It has been seen that if distance between eavesdropper and legitimate node is increased, information rate between legitimate nodes is increased, whereas information rate for noise signal can be reduced. Similarly, by increasing information rate and total power between the legitimate nodes, the threat zone increases. In this work, maximum eavesdropping distance reflects the threat zone around the pacemaker, beyond which the region can be considered secure.

Acknowledgement This work was funded by the European Union's H2020:MSCA:ITN program for the Wireless In-body Environment Communication-WiBEC project under the grant agreement no. 675353.

References

1. Awan, M.F., Kansanen, K.: Estimating eavesdropping risk for next generation implants. In: *Advances in Body Area Networks I*, pp. 387–398. Springer, Berlin (2019)
2. Halperin, D., Heydt-Benjamin, T.S., Ransford, B., Clark, S.S., Defend, B., Morgan, W., Fu, K., Kohno, T., Maisel, W.H.: Pacemakers and implantable cardiac defibrillators: software radio attacks and zero-power defenses. In: 2008 IEEE Symposium on Security and Privacy, SP 2008, pp. 129–142. IEEE, Piscataway (2008)
3. Zhang, M., Raghunathan, A., Jha, N.K.: MedMon: securing medical devices through wireless monitoring and anomaly detection. *IEEE Trans. Biomed. Circuits Syst.* **7**(6), 871–881 (2013)
4. Son, S., Lee, K., Won, D., Kim, S.: U-healthcare system protecting privacy based on cloaker. In: 2010 IEEE International Conference on Bioinformatics and Biomedicine Workshops (BIBMW), pp. 417–423. IEEE, Piscataway (2010)
5. Gollakota, S., Hassanieh, H., Ransford, B., Katabi, D., Fu, K.: They can hear your heartbeats: non-invasive security for implantable medical devices. In: *ACM SIGCOMM Computer Communication Review*, vol. 41, no. 4, pp. 2–13. ACM, New York (2011)
6. Awan, M.F., Perez-Simbor, S., Garcia-Pardo, C., Kansanen, K., Bose, P., Castelló-Palacios, S., Cardona, N.: Experimental phantom-based evaluation of physical layer security for future leadless cardiac pacemaker. In: 2018 IEEE 29th Annual International Symposium on Personal, Indoor and Mobile Radio Communications (PIMRC), pp. 333–339. IEEE, Piscataway (2018)
7. Shannon, C.E.: Communication theory of secrecy systems. *Bell Labs Tech. J.* **28**(4), 656–715 (1949)
8. Wyner, A.D.: The wire-tap channel. *Bell Labs Tech. J.* **54**(8), 1355–1387 (1975)
9. Csiszár, I., Körner, J.: Broadcast channels with confidential messages. *IEEE Trans. Inf. Theory* **24**(3), 339–348 (1978)
10. Sayrafian-Pour, K., Yang, W.-B., Hagedorn, J., Terrill, J., Yazdandoost, K.Y.: A statistical path loss model for medical implant communication channels. In: 2009 IEEE 20th International Symposium on Personal, Indoor and Mobile Radio Communications, pp. 2995–2999. IEEE, Piscataway (2009)
11. Islam, M.N., Yuce, M.R.: Review of medical implant communication system (MICS) band and network. *ICT Express* **2**(4), 188–194 (2016)

Chapter 37

Feasibility Analysis for Pulse-Based Synchronization in a Dual Chamber Leadless Pacemaker System



Deepak Palaksha, Kimmo Kansanen, and Muhammad Faheem Awan

37.1 Introduction

Pacemakers are implanted for patients with bradyarrhythmias. Innovation in pacemakers has led to many different configurations of pacing like single-, double-, and multichamber transvenous systems. In the last years, pacemaker therapy has considerably expanded, exceeding 700,000 implantations annually worldwide [1, 2].

Despite the progress, pacemaker therapy may still be associated with significant post-procedural complications, with transvenous lead remaining the weakest link at the chain of pacing [3]. In some cases, implantation also leads to complications like infection in valves. This issue has given way to develop a new system of pacing by eliminating leads, such devices are called leadless pacemakers.

Currently available versions of leadless pacemaker system in market are the Nanostim Leadless Pacemaker System (LCP) (St. Jude Medical, St Paul, MN, USA), introduced in 2012, and the Micra Transcatheter Pacing System (TPS) (Medtronic, Minneapolis, MN, USA), introduced in 2013 [4, 5]. The capsule has embedded electronics for pacing and sensing, with battery source powering the electronics, which is encapsulated in a biocompatible material.

Traditionally single chamber pacemakers, both atrial and ventricular devices, make up <10% of pacemaker implants, whereas dual chamber pacemakers make up to 49% of pacemaker implants. Dual chamber pacing allows for atrioventricular synchrony, which has been shown to minimize pacemaker syndrome [6]. The most significant limitation of the existing leadless pacemaker devices is the restriction to single chamber ventricular pacing. Extending the system from single chamber system to dual chamber system can be achieved by establishing synchronization

D. Palaksha (✉) · K. Kansanen · M. F. Awan
Norwegian University of Science and Technology, NTNU, Trondheim, Norway
e-mail: deepak.palaksha@ntnu.no; faheem.awan@ntnu.no

between leadless pacemakers to maintain atrial-ventricular synchrony, in other terms to maintain atrial-ventricular delay in the desirable range.

In this chapter, a novel strategy is discussed, a radio frequency (RF) pulse-based technique is used to establish the synchronization between the leadless pacemakers where the RF pulse is transmitted from transmitter leadless pacemaker (atrial unit) to receiver leadless pacemaker (ventricular unit) on every beat. The energy consumed for the synchronization operation is directly reflected on the longevity of leadless pacemaker, hence, in the chapter, the energy consumed for synchronization operation is evaluated and this information is used to analyze the feasibility of the system.

Currently, in this chapter, the system is studied in MICS band. For analysis, channel attenuation in an in-body environment and noise behavior at receiver are considered in MICS band [7]. The channel bandwidth available for the RF pulse is 300 kHz, in other terms pulse width (T_s) and symbol rate (R_s) of the pulse is $6.7 \mu\text{s}$ and 150 kbps.

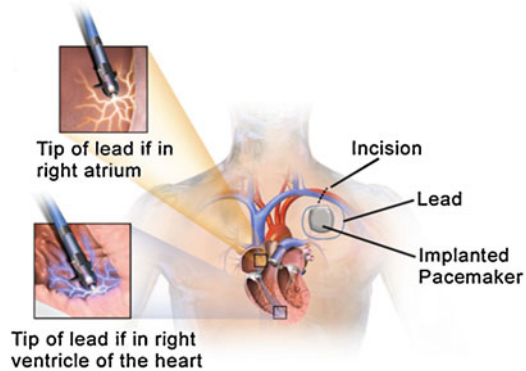
The chapter is structured to give background in Sect. 37.2 on dual chamber pacing and DDD pacing mode. In Sect. 37.3, a wireless dual chamber leadless pacemaker system is proposed and a system description for maintaining the atrioventricular synchrony is provided. Section 37.4 consists of numerical results and feasibility analysis of the system. Section 37.5 contains conclusion and outline of our future work.

37.2 Background

Conventional Dual Chamber Pacemaker

In dual chamber configuration, as the name suggests, pacing and sensing are performed in two chambers of the heart, namely, atrium and ventricle. A dual chamber pacemaker system is illustrated in Fig. 37.1. The pacemaker unit is surgically placed under the skin, beneath collarbone, and is connected to heart by one or more wires, or leads. A dual chamber pacemaker has one lead in the upper chamber, or atrium of the heart and one in a lower chamber, or ventricle of the heart [6]. The leads sense the electrical activity (EGM signal) at their respective placement sites and the pacemaker unit detects the depolarization activity from the sensed signals. The depolarization of heart can physiologically be understood as the contraction of the heart chambers. A dual chamber pacemaker can be operated in several pacing modes. In this chapter, DDD pacing mode is considered as it provides atrial-ventricular coordination. DDD pacers pace both the chambers (D stands for “dual”), they sense both chambers, and each of the two leads inhibits pacing by sensing an intrinsic beat.

Fig. 37.1 Conventional dual chamber pacing system



DDD Pacing Mode

At the start of the cardiac cycle, the heart relaxes and expands while receiving blood into both ventricles through both atria; The Sino-Atrial (SA) node releases electrical stimuli, this creates a wave of contraction in both atria, and each atrium pumps blood into the ventricle below it. To ensure that the atria have ejected their blood into the ventricles before the ventricles contract, the atrioventricular node delays electrical impulses for a brief time (AV-delay) before reaching ventricle; consequently, the ventricles contract vigorously ejecting two separated blood supplies from the heart—one to the lungs and one to all other body organs and systems. This precise coordination between atrial and ventricular contraction is established by AV-delay [6]. The DDD mode of operation is the most common dual chamber pacing mode, and it maintains the AV-delay time (T_{avd}) in desirable range to provide atrial-ventricular coordination which otherwise is lost with single chamber ventricular pacing [8]. Physicians pre-program the atrioventricular delay value (T_{avd}) based on the condition of the heart. In our analysis, the system performance is limited to constant heart rate condition. In systems responsive to adaptive heart rate (rate response systems), the atrial and the ventricular window ranges are changed with increase or decrease in heart rate. This can be handled by including adaptive observation window sizes and rate response algorithms, but it is beyond the scope of this chapter [9]. The DDD pacemaker operation is detailed below.

The implanted pacemaker unit (see Fig. 37.1) senses the EGM signal from the atrial and ventricular lead. The depolarization of atrium is detected by pacemaker unit from the sensed EGM signal (P wave) (see Fig. 37.2) [10]. The depolarization at atrium is either because of natural contraction or by pacing. The atrium is paced if the pacemaker unit does not detect the P wave within a certain time interval (T_{asmax}). The time instant when the P wave is sensed or paced is denoted as T_{as} . In case of atrial pacing, the cardiac electrical conduction path requires a longer time than the natural conduction as electrical stimuli do not start from SA node. Therefore, the pacemaker unit adds an offset time (T_{offset}) to compensate for the delay. Consequently, the pacemaker unit expects ventricular depolarization

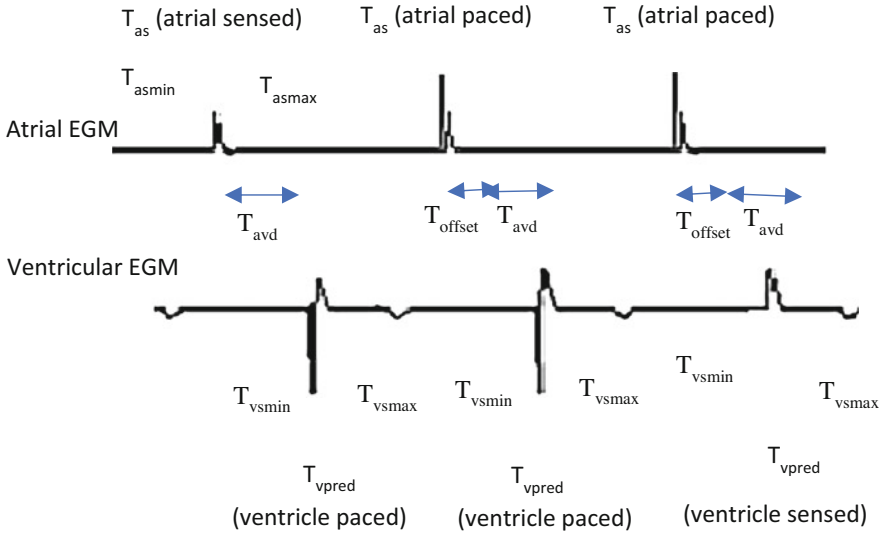


Fig. 37.2 Timing intervals at atrial and ventricular EGM sensor leads

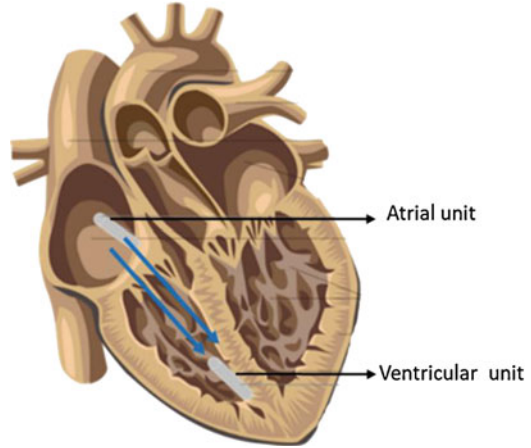
(QRS complex) as soon after the pre-programmed AV-delay (T_{vpred}). If it detects ventricular depolarization as soon after T_{vpred} , then it will inhibit pacing else performs ventricular pacing. T_{vpred} is given by $T_{as} + T_{avd}$ for atrial sensed and is $T_{as} + T_{avd} + T_{offset}$ for atrial paced case (see Fig. 37.2). In case the pacemaker unit fails to provide atrial-ventricular coordination because of switching of pacing modes, and there is no ventricular contraction in the ventricular sensing window then the ventricle is paced at T_{vsmax} . The sensing window at atrium and ventricle is in the range $[T_{asmin}, T_{asmax}]$ and $[T_{vsmin}, T_{vsmax}]$, respectively; the typical value for atrial and ventricular sensing window is ≈ 100 ms or 150 ms (see Fig. 37.2).

It is clear that in conventional dual chamber DDD pacing mode the micro-controller in the pacemaker unit handles the functionality of maintaining the atrial-ventricular coordination. On the other hand, leadless pacemakers are independent pacing units measuring local activity at respective placement sites, and therefore the conventional approach is not possible. In the next section, a model is proposed where an RF pulse-based synchronization technique is used between leadless pacemakers to implement the DDD pacing mode.

37.3 System Description

In this section, dual chamber leadless pacemaker system working in DDD pacing mode (wireless-DDD) is detailed. In addition, synchronization methodology

Fig. 37.3 Dual chamber leadless pacemaker system



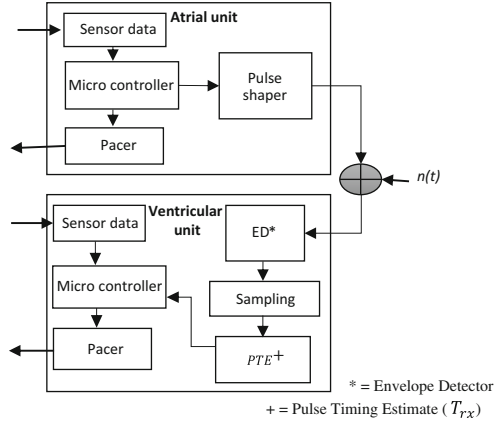
employed to overcome the shortcomings of traditional single chamber leadless pacemaker is described.

Dual Chamber Leadless Pacemaker System

The proposed system has two leadless pacemakers, at the apex in the right ventricle (RV) and next to tricuspid valve in the right atrium (RA). Both the units locally sense the electrical activity and pace at the implanted location. For implementing a wireless DDD pacing mode, the ventricle unit needs to know the expected time of ventricular depolarization (T_{vpred}). RF pulse is transmitted from atrial unit to ventricular unit on every heartbeat notifying the expected time of ventricular depolarization. The pictorial representation of dual chamber leadless pacemaker system is shown in Fig. 37.3.

The simplified functional block diagram for leadless pacemakers is as shown in Fig. 37.4. The block diagram shows major functional components involved in right atrium leadless pacemaker (RA LP) or atrial unit, and in right ventricle leadless pacemaker (RV LP) or ventricle unit. At the atrial unit, the transmitter electronics consume 2 nJ/symbol [11]. The RF pulse detection at the receiver is performed by the energy detector and the power consumed by electronics at MICS band is ≈ 90 pJ/symbol. For an observation window of 100 ms and longevity of 10 years, the energy consumed by transmitter and receiver electronics is around 0.14 mAh and 40 mAh [12]. Clearly, the energy consumed by electronics is below the energy limits (220 mAh); however, future research focuses on implementing an algorithm to optimize the energy consumed by electronics.

Fig. 37.4 Functional block diagram of leadless pacemaker units



System Operation

The functionality of wireless-DDD pacing mode majorly differs from conventional DDD mode by its technique of maintaining atrioventricular delay (AV-delay, T_{avd}) and offset time (T_{offset}). At atrium, the depolarization is possible either by natural contraction of the atrium or by pacing at the atrium. If depolarization is because of pacing at atrium, the RF pulse is sent from the atrial unit after an offset time (T_{offset}). On the contrary, if depolarization is sensed, the pulse is sent with no delay. A typical value of T_{offset} is around 32 ms. Let transmit time of RF pulse from atrial unit be T_{tx} as shown in Fig. 37.5, T_{tx} can be either T_{as} or $T_{as} + T_{offset}$ based on atrial sensed or paced condition. At the ventricle unit, the received pulse location in time after successful pulse detection is T_{rx} (see Fig. 37.5). The received pulse timing (T_{rx}) with pre-programmed AV-delay (T_{avd}) provides a reference in time to expect ventricular depolarization. The expected ventricular depolarization time is given by $T_{vpred} = T_{rx} + T_{avd}$. If ventricle unit does not detect ventricular depolarization as soon after T_{vpred} , ventricle unit paces the ventricle or inhibits pacing if it detects the ventricular depolarization. The operation repeats on every beat, achieving atrial-ventricular coordination. RF pulse transmission and reception is described in next subsection.

We calculate the pulse propagation time from a basic distance and speed equation. In practice, the propagation time is in the order of nanoseconds for distance range in cm. As the order of timing windows is in millisecond range for our application, we consider $T_{rx} \approx T_{tx}$. At ventricular unit, the communication reception starts at T_{rxmin} and the observation window allows reception until T_{rxmax} . The observation window range is around 100 ms. The size of the observation window is obtained from atrial window size (T_{asmin} , T_{asmax}), and this ensures that the atrial activity is not missed in the observation window. The analysis of estimating the pulse timing (T_{rx}) is performed over observation window.

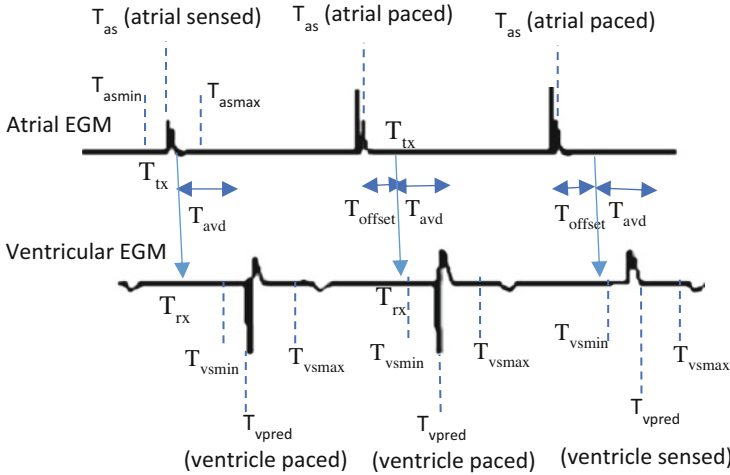


Fig. 37.5 Timing diagram of synchronization mechanism

Synchronization Methodology

In this subsection, technical details on transmission and reception of RF pulse are discussed. A non-coherent pulse detection technique is used at the ventricle unit.

Both the units have their own internal clocks that are not synchronized, and these clocks are used for internal synchronization of operations performed. The typical value of a clock drift for a crystal oscillator is 20 ppm at room temperature [13]; this implies that the leadless pacemaker clocks might drift from each other with 20 ppm, and one focus of future research is to overcome this issue. In this chapter, it is assumed that the atrial and ventricular units have their clocks synchronized, as the RF pulse transmission and reception is performed only at clock intervals. At the atrial unit, the time vector is pulse shaped to get the transmitted signal. The transmitted pulse is expressed as (Eq. 37.1),

$$x_i = g(t - iT_s) \tag{37.1}$$

where T_s is the RF pulse width and $g(t)$ is the impulse response of raised cosine pulse shaper.

The signal x_i propagates through a lossy medium with channel attenuation h , in the presence of white Gaussian noise with power spectral density N_o . The signal at the receiver is given by

$$y(t) = h x_i(t) + w(t) \tag{37.2}$$

where $i = 0, 1, 2, \dots, M-1$.

There are M pulse symbol location, where “ i ” represents i th symbol location.

The maximum likelihood non-coherent detector does not use the random phase in the decision process and chooses the message vector that maximizes the joint conditional pdf $p(y|x_i)$ [14]. After solving the expression for observations with equal prior probability, the equation is simplified to the maximum likelihood (ML) rule as shown in Eq. 37.3 [14].

$$l_i = \operatorname{argmax}_{i \in \{0, 1, \dots, M-1\}} \left(\left| \int_0^T y(t) * x_i(t) dt \right| \right) \quad (37.3)$$

The estimated pulse location provides the timing location of the pulse in the observation window, which is an estimate of pulse receive time (T_{rx}); this in combination with pre-programmed AV-delay (T_{avd}) gives the time instant at which right ventricular depolarization time (T_{vpred}) can be expected.

Since Nyquist pulse is used, the signals are orthogonal to each other. An error is committed if “ i ” is the true hypothesis, but l_i is not the maximum. Expression for probability of error for large M is given by [15]:

$$\Pr_M(e) \leq \frac{(M-1)}{2} \exp\left(-\frac{\text{SNR}}{2}\right) \quad (37.4)$$

where SNR = Signal to Noise Ratio.

In cases of erroneous detection of pulse location at the receiver unit, the synchronization between –leadless pacemakers is lost and the coordination of atrium and ventricle could be disturbed. Nevertheless, because the pacing is performed in the sensing window range [T_{vsmin} , T_{vsmax}], it is not fatal to the functioning of the heart.

Power Consideration

One of the major focus of the chapter is to study the relationship between transmit signal power and power needed at the receiver for reliable pulse detection. In this chapter, the probability of error is used as the metric for measuring the performance. From the clinical application, it is found that the system is reliable for a target probability of error in pulse detection = 10^{-3} . In addition, the power analysis also provides an insight into the longevity of leadless pacemaker, i.e., energy consumed for having successful pulse transmission and reception for a span of 10 years (standard life cycle of leadless pacemaker).

The transmitted RF pulse has a signal power P_t ; the signal propagates through the lossy medium inside the heart from the atrial unit (transmitter) to the ventricular unit (receiver). The signal undergoes attenuation P_L , which is a function of distance. Considering optimal placement sites of a leadless pacemaker in the right atrium and right ventricle, on an average, the distance between these is around 8–9 cm, which is generally patient specific [16]. In this chapter for analysis, the distance between leadless pacemakers is considered as 9 cm. From channel attenuation

model obtained by simulation, P_L was found to be -82 db [17]. Therefore, the received power at the right ventricular leadless pacemaker is given by P_r .

$$P_r(\text{dbm}) = P_t(\text{dbm}) - P_L(\text{db}) \quad (37.5)$$

For MICS band in an in-body implant, the receiver noise floor is given by -120 dbm [7]. The Signal to Noise Ratio (SNR) is calculated from the received signal power and noise power at the receiver. SNR is calculated as

$$\text{SNR}(\text{db}) = P_r(\text{dbm}) - N_o(\text{dbm}) \quad (37.6)$$

In numerical results, the analysis is performed on the required SNR for maintaining the target probability of error (10^{-3}). Transmit power (P_t) at atrium is evaluated for the target probability of error using Eq. 37.5 and Eq. 37.6. The symbol energy per pulse is calculated from transmit power and symbol rate (R_s) as

$$E_s = P_t/R_s \quad (37.7)$$

37.4 Numerical Results

In the current study, raised cosine pulse with roll-off factor 1 is used as the pulse shaper. The pulse bandwidth is adapted to MICS band and each narrowband channel has 300 kHz bandwidth [7]. The RF pulse width (T_s) is $6.7 \mu\text{s}$ and the symbol rate is (R_s) 150 kbps [15].

From channel model, P_L is -82db for a distance of 9 cm. Figure 37.6 indicates simulation results between target error probability vs number of symbol location = 4096, 8192, 16,384. The observation window considered is in the order of 100 ms, i.e., $16,384 \times T_s$, therefore the number of possible symbol location is 16,384. From Fig. 37.6, for number of symbol location = 16,384 and target probability of error $\approx 10^{-3}$, the scheme requires an SNR = 28.55 dB. Using Eqs. 37.5 and 37.6 transmit power needed at the atrial unit is evaluated; for SNR = 28.55 dB the required transmit power (P_t) is $75\mu\text{W}$. Using Eq. 37.7 symbol energy (E_s) per pulse is calculated to be 0.52 nWs. Considering the pulse is sent on every heartbeat, the energy consumed for synchronization of leadless pacemakers for 10-year longevity is 15.4 μAh . The battery energy rating in the existing leadless pacemaker system is 220 mAh for a longevity of 10 years. Therefore, it can be seen that the energy consumed for pulse transmission and reception operation is five orders less in magnitude than the available energy; hence, claiming feasibility of system is positive.

The above analysis is performed for the distance between the leadless pacemakers = 9 cm. In reality, the size of the heart is patient specific and the distance between leadless pacemakers change for the same implant sites. Since attenuation offered by the medium is a function of distance, Fig. 37.7 depicts for a longevity of 10 years, the

Fig. 37.6 Plot of SNR vs probability of error for different symbol locations

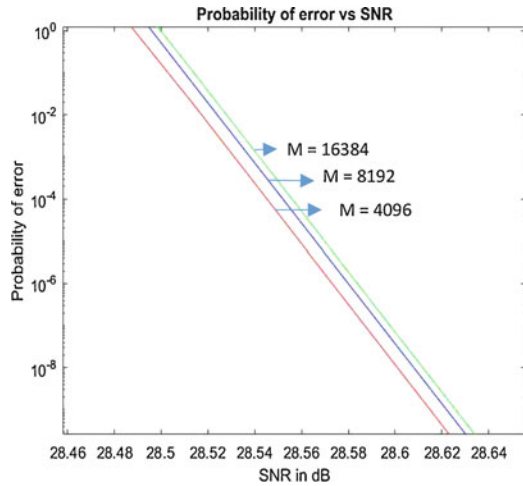
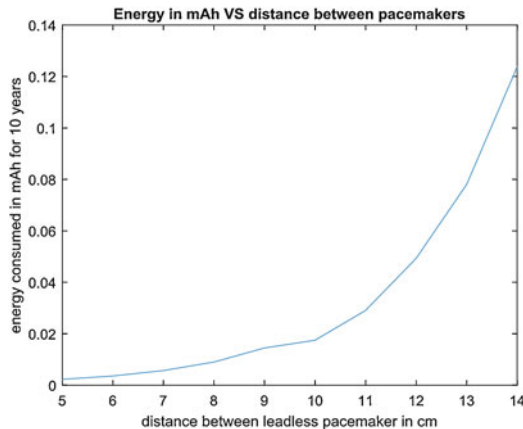


Fig. 37.7 Plot of energy consumed for synchronization for a lifecycle of 10 years vs the distance between the leadless pacemakers in cm



energy consumed for pulse transmission and reception operation for different inter-pacemaker distances. The energy consumed is obtained by varying path loss (P_L) in Eq. 37.5 in relation with the distance; furthermore Eq. 37.7 is used to calculate the absolute energy consumed for a life span of 10 years. It follows the intuition that there is an increase in energy consumption with an increase in distance between leadless pacemakers.

37.5 Conclusion

In the dual chamber leadless pacemaker system, wireless-DDD pacing mode is implemented by establishing synchronization between leadless pacemakers at right atrium and right ventricle.

Minimum SNR that the receiver unit requires to do pulse detection with target probability of error value is evaluated. SNR in turn provides information on transmit power needed to perform successful pulse detection. In our simulation studies, it is found that the transmit pulse power of $75 \mu\text{W}$ per pulse is needed to detect the pulse with target probability of error $\approx 10^{-3}$. The energy consumed for synchronization operation (pulse transmission and reception) by the dual chamber leadless pacemaker system operated in wireless DDD mode for a longevity of 10 years is $15.4 \mu\text{Ah}$. The battery energy rating in the existing leadless pacemaker system is 220mAh for a longevity of 10 years. Therefore, it can be seen that the energy consumed for pulse transmission and reception in an in-body environment of leadless pacemakers is five orders less in magnitude than the available energy, hence claiming that system feasibility is positive. It is also observed that energy consumption increased with increase in distance between leadless pacemakers.

In our future research, we try to address the problem considering an inhomogeneous medium for pulse propagation. It is also interesting to include clock drift in the model and evaluate the system performance.

Acknowledgments This work is funded by the European Union's H2020: MSCA: ITN program for the "Wireless In-body Environment Communication—WiBEC" project under the grant agreement no. 675353. I would also like to thank the people in the department of Electronic System for valuable discussions.

Appendix: Stepwise Algorithm for System Operation (Wireless-DDD)

1. Open the atrial sensing window, i.e., from T_{asmin} , this is decided from the basic rate set by the physician for the subject.
2. Observe for any activity in the atrium (atrial depolarization).
3. If depolarization is sensed (T_{as}), based on the prescribed rate, a new value for timers T_{asmin} and T_{asmax} is set.
4. If atrial depolarization is not sensed, we pace the atrium and reset timer T_{asmin} and T_{asmax} to new value considering paced time as T_{as} .
5. If sensed, then T_{tx} is equal to T_{as} but if it is paced T_{tx} is equal to $T_{\text{as}} + T_{\text{offset}}$, where T_{offset} is to compensate for the delay in conduction due to pacing.
6. At receiver, leadless pacemaker pulse is received at T_{rx} , which is the sum of T_{tx} and T_{pt} time.
7. The receiver starts T_{vpred} timer which is the sum of $T_{\text{rx}} + T_{\text{AVD}}$, this predicts when we can expect a ventricular depolarization.
8. In parallel, based on the prescribed rate the values for timers T_{vsmin} and T_{vsmax} are calculated, ventricular sensing window is opened at T_{vsmin} .
9. If ventricular natural depolarization is not sensed (T_{vs}) after predicted depolarization time (T_{vpred}), the ventricle is paced, hence maintaining the coordination between atrium and ventricle.

10. New timer values for T_{vsmin} and T_{vsmax} are calculated from paced time T_{vpred} or ventricular sensed time T_{vs} .
11. Repeat the operation for every beat.

References

1. Mond, H.G., Proclemer, A.: The 11th world survey of cardiac pacing and implantable cardioverter-defibrillators: calendar year 2009—a World Society of Arrhythmia's project. *Pacing Clin. Electrophysiol.* **34**(8), 1013–1027 (2011)
2. Clerk Maxwell, J.: *A Treatise on Electricity and Magnetism*, vol. 2, 3rd edn, pp. 68–73. Clarendon, Oxford (1892)
3. Kirkfeldt, R.E., Johansen, J.B., Nohr, E.A., et al.: Complications after cardiac implantable electronic device implantations: an analysis of a complete, nationwide cohort in Denmark. *Eur. Heart J.* **35**, 1186–1194 (2014)
4. Miller, M.A., Neuzil, P., Dukkupati, S.R., Reddy, V.Y.: Leadless cardiac pacemakers: back to the future. *J. Am. Coll. Cardiol.* **66**, 1179–1189 (2015)
5. Sperzel, J., Burri, H., Gras, D., et al.: State of the art of leadless pacing. State of the art of leadless pacing. *Europace.* **17**, 1508–1513 (2015)
6. Islama, M.N., Yuceb, M.R.: Review of medical implant communication system (MICS) band and network. *ICT Express.* **2**(4), 188–194 (2016). ISSN 2405-9595
7. Islam, M.N., Yuce, M.R.: Review of Medical Implant Communication System (MICS) band and network. *ICT Express.* **2**(4), 188–194 (2016). <https://doi.org/10.1016/j.ict.2016.08.010>, ISSN 2405-9595
8. Dretzke, J., Toff, W.D., Lip, G.Y.H., Raftery, J., Fry-Smith, A., Taylor, R.S.: Dual chamber versus single chamber ventricular pacemakers for sick sinus syndrome and atrioventricular block. *Cochrane Database Syst. Rev.* (2):CD003710 (2004). <https://doi.org/10.1002/14651858.CD003710.pub2>
9. Pilat, E., Mlynarski, R., Wlodyka, A., Kargul, W.: Influence of DDD rate response pacing with integrated double sensors on physical efficiency and quality of life. *Europace.* **10**(10), 1189–1194 (2008). <https://doi.org/10.1093/europace/eun212>. Epub 2008 Aug 18
10. Stubhan, M., Markert, M., Mayer, K., et al.: Evaluation of cardiovascular and ECG parameters in normal, freely moving Göttingen minipig. *J. Pharmacol. Toxicol. Methods.* **57**, 202–211 (2008)
11. Goodarzy, F., Skafidas, S.E.: Ultra-low-power wireless transmitter for neural prostheses with modified pulse position modulation. *Healthcare Technology Letters* **1**(1):37–39 (2014). PMC. Web. 5 May 2018
12. Lee, D., Mercier, P.P.: Introduction to ultra low power transceiver design
13. Best-microcontroller-projects, Clock accuracy in ppm. <http://www.best-microcontroller-projects.com/ppm.html>
14. Kay, S.M.: Fundamentals of statistical signal processing: detection theory. *IEEE Trans. Biomed. Eng.* **65**(12), 2798–2807 (2018)
15. Proakis, J.G., Salehi, M.: Chapter 7. Probability of error for noncoherent detection of FSK. In: *Communication Systems Engineering*, p. 430. Prentice Hall, Upper Saddle River
16. Kruse, J., Redmond, C.: Detecting and distinguishing cardiac pacing artifacts. *Analog Dialogue.* **46**, 11 (2012)
17. Bose, P., Khaleghi, A., Albatat, M., Bergsland, J., Balasingham, I.: RF channel modeling for implant to implant communication and implant to sub-cutaneous implant communication for future leadless cardiac pacemakers. In: *IEEE Transactions on Biomedical Engineering*, pp. 1–1 (2018). <https://doi.org/10.1109/TBME.2018.2817690>

Chapter 38

Low-UWB Directive Antenna for Wireless Capsule Endoscopy Localization



Chaïmaâ Kissi, Mariella Särestöniemi, Carlos Pomalaza-Raez, Marko Sonkki,
and Mohamed Nabil Srifi

38.1 Introduction

In recent years, UWB directive antennas have been in demand for applications in radar, sensing, and telemetry systems. UWB have also been of interest in the area of Wireless Capsule Endoscopy (WCE) in particular when investigating its use in clinical studies of the small intestine, a component of the gastrointestinal (GI) tract [1, 2].

In the context of WCE, using UWB band [3.1–10.6 GHz] has the advantage of providing high resolution, in the order of millimeters, and low power consumption in contrast with the use of narrow-band systems [3]. On the other hand, the use of higher frequencies in on-/in body communications incurs large path losses. Thus the goal is to use as low-UWB band as possible for WCE localization purposes [4, 5] to minimize path losses and obtain high image resolutions [5].

Several published papers emphasize the importance to comply with the low-UWB band IEEE 802.15.6 standard [6, 7]. Therefore a number of implantable antennas working in the 3.4–4.8 GHz range have been implemented [5, 8–10]. An UWB trapezoid monopole antenna [11], a broadband horn antenna [5], a planar unbalanced dipole antenna [12], and a helical receiving antenna [9] have been used

C. Kissi (✉) · M. N. Srifi

Electronics and Telecommunication Systems Research Group, National School of Applied Sciences (ENSA), Ibn Tofail University, Kenitra, Morocco

M. Särestöniemi · M. Sonkki

Center for Wireless Communications, Faculty of Information Technology and Electrical Engineering, University of Oulu, Oulu, Finland

C. Pomalaza-Raez

Department of Electrical and Computer Engineering, Purdue University, West Lafayette, IN, USA

© Springer Nature Switzerland AG 2020

431

C. Sugimoto et al. (eds.), *13th EAI International Conference on Body Area Networks*, EAI/Springer Innovations in Communication and Computing,
https://doi.org/10.1007/978-3-030-29897-5_38

as receiving antenna for tests and measurement in WCE localization scenarios using different frequency ranges.

In this chapter, an UWB antenna operating in the low-UWB band of the IEEE 802.15.6 standard is presented. The proposed antenna is directional and provides high gain. A comparative study of published UWB antennas is found in [13], confirming that the proposed antenna has a very good performance and that is a good candidate as a receiving antenna for WCE localization systems. The detailed antenna structure is described in Sect. 38.2. Antenna configuration, analysis, and discussion are provided in Sect. 38.3. Conclusions and future work are included in Sect. 38.4.

38.2 Antenna Structure

Antenna Design

The proposed antenna is a dipole type of antenna. The structure is printed on a FR-4 material with 1.6 mm thickness (h_s), 30 mm width (W_s), and 25 mm length (L_s). Let $\lambda (\frac{c}{f})$ be the wavelength at 4 GHz (center frequency of the IEEE 802.15.6 low-UWB band). The antenna size then corresponds to $0.41 \lambda \times 0.33 \lambda \times 0.021 \lambda$. The ground plane is a combination of a rectangle and an inverted-L form, while the radiator element has a close inverted-L shape. The antenna structure is fed by a microstrip line of 3 mm width. Front and back sides of the proposed UWB antenna geometry are depicted in Fig. 38.1. Optimized parameters of the proposed low-UWB antenna are summarized in Table 38.1.

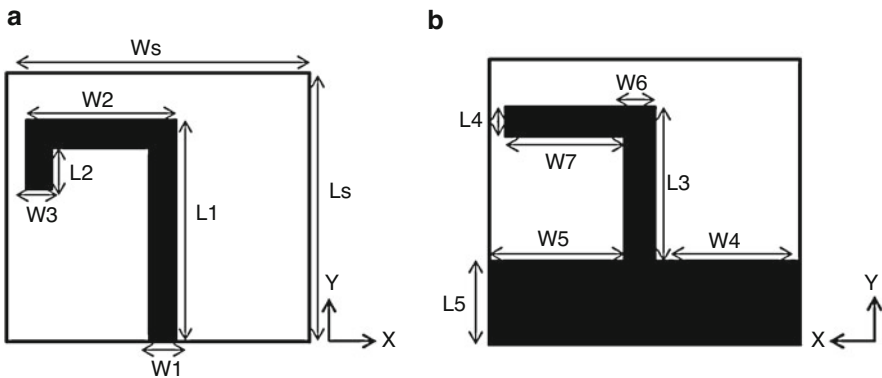


Fig. 38.1 Geometry of the proposed low-UWB band antenna. (a) Front side (b) Back side

Table 38.1 Optimized parameters of the proposed low-UWB antenna

Parameter	Ws	Ls	hs	W1	W2	W3	W4	W5
Value (mm)	30.3	25	1.6	3	16.4	3	13.15	13.15
Parameter	W6	W7	L1	L2	L3	L4	L5	
Value (mm)	4	9.5	20.14	2.9	12	2	7.14	

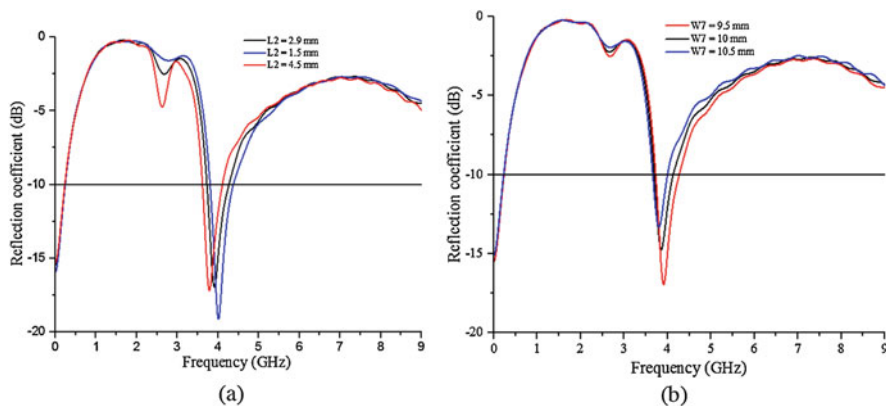


Fig. 38.2 Reflection coefficient of the proposed single UWB antenna (a) by varying L2 (b) by varying W7

38.3 Antenna Configuration and Analysis

Single Low-UWB Antenna

Every parameter affects the antenna’s impedance and resonant frequency. For the sake of brevity, the parametric study here is limited to L2 and W7 tune effects on the antenna frequency response.

The effect of L2’s length on the reflection coefficient of the proposed UWB antenna is illustrated in Fig. 38.2a. Varying L2 values from 1.5 to 4.5 mm resulted in a significant shift in the bandwidth and in the resonant frequency in the low-UWB band. The optimal L2 value that complies with the IEEE 802.15.6 standard is chosen to be 2.9 mm. By using this value, the covered bandwidth is 3.74–4.25 GHz and the achieved resonant frequency is 3.906 GHz with maximum reflection coefficient of about −17.16 dB. For the case when the length of L2 is increased to 4.5 mm, the bandwidth shifts to the left [3.63–4.12 GHz] and the achieved resonant frequency is at 3.789 GHz with the reflection coefficient of −17.39 dB. When L2 is set to 1.5 mm, the bandwidth shifts to the right [3.8–4.37 GHz] and the achieved resonant frequency is at 4.014 GHz with the reflection coefficient of −19.32 dB.

The effect of W7’s length on the reflection coefficient of the proposed antenna is illustrated in Fig. 38.2b. Varying W7 values from 9.5 to 10.5 mm with a step of 0.5 mm reveals that the lower frequency remains quite constant, while increasing

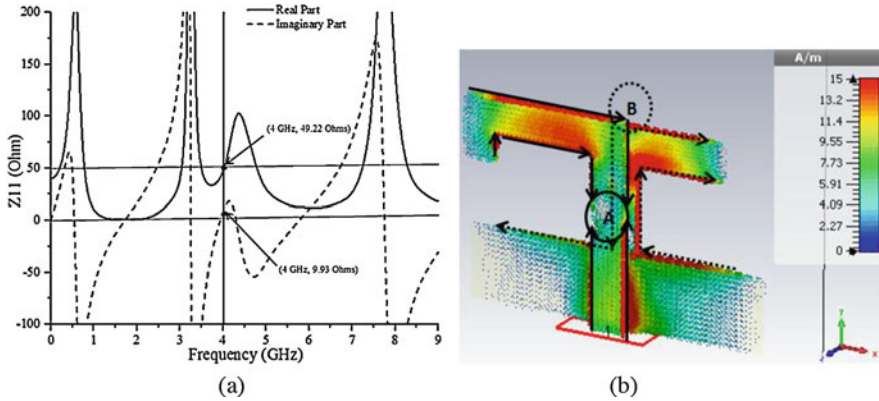


Fig. 38.3 (a) Input impedance and (b) Surface current distribution of the single low-UWB antenna at 4 GHz (Solid arrow: Front side, Dashed arrow: Back side)

W7 leads to a decrease of the upper frequency which degrades significantly the resonant frequency and the maximum reflection coefficient from 3.906 to 3.8 GHz and from -17.16 to -13.33 dB, respectively.

The input impedance of the proposed low-UWB single antenna is shown in Fig. 38.3a. At 4 GHz, the real part of the parameter Z_{11} is $49.22 \approx 50 \Omega$ and the imaginary part is about 9.93Ω . It can be then concluded that the proposed antenna has an inductive behavior at 4 GHz center frequency. Besides, these results show that the antenna has a good impedance matching of about 50Ω .

The surface current distribution of the low-UWB antenna at 4 GHz is illustrated in Fig. 38.3b. Current directions in the front and back sides are represented by solid and dashed arrows, respectively. It is clearly seen on this illustration that currents are cancelling each other at part A while at part B currents are moving in opposite directions.

Directivity results of the proposed single low-UWB antenna at the frequencies 3.74, 4, and 4.26 GHz are shown in Fig. 38.4. These results show that the single antenna is directive toward Y -axis. At the three frequencies, total and radiation efficiencies are less than 1 dB, which implies a good operation of the proposed antenna. Additionally, it is worth noting that directivity achieves high values up to 6.18, 6.04, and 5.52 dBi at the frequencies 3.74 GHz, 4 GHz, and 4.26 GHz, respectively.

Radiation patterns of the single low-UWB antenna at 3.74, 4, and 4.26 GHz are plotted in Fig. 38.5. Gain values, by cutting axis planes at $\Theta = 90^\circ$, $\Phi = 90^\circ$, and $\Phi = 0^\circ$, are summarized in Table 38.2. It is clearly shown that, with the frequency increase from 3.74 to 4.26 GHz, the directivity decreases slightly to reach 6.18 and 5.52 dBi, respectively. However, maximum directivity is always toward Y -axis ($\Theta = 90^\circ$).

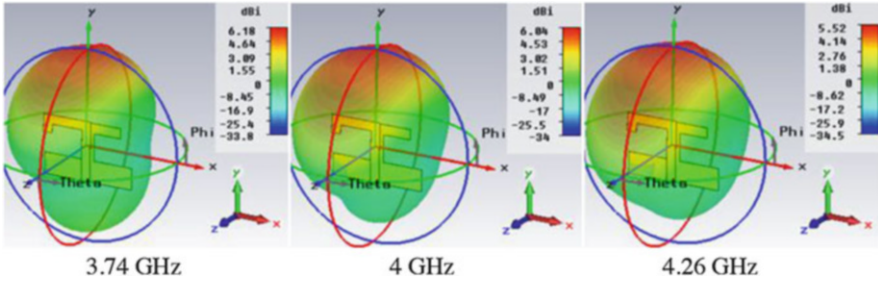


Fig. 38.4 Directivity of the single low-UWB antenna with the hidden substrate at 3.74, 4, and 4.26 GHz

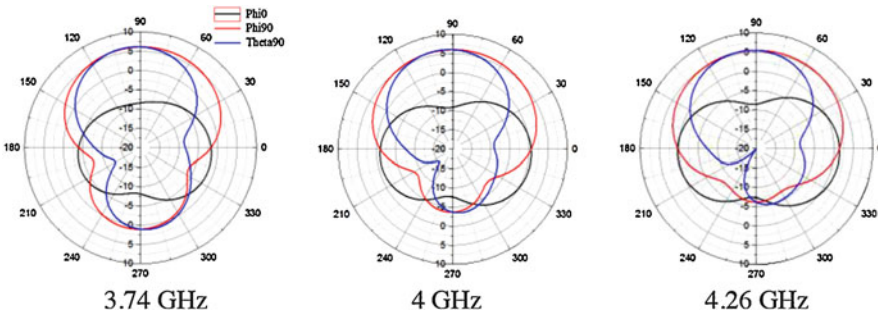


Fig. 38.5 Radiation patterns of the single low-UWB antenna at 3.74, 4, and 4.26 (Black \geq Phi = 0°, Red \geq Phi = 90°, and Blue \geq Theta = 90°)

Table 38.2 Gain values of the proposed single low-UWB antenna by cutting axis planes

Frequency [GHz]	Theta = 90° [dBi]	Phi = 90° [dBi]	Phi = 0° [dBi]
3.74	6.17	6.14	-1.46
4	6.04	5.99	0.674
4.26	5.52	5.46	1.51

Cavity Approach

In this second part, a metallic box serving as a cavity with a thickness of 0.5 mm is used. The cavity approach is used to act as a reflector ensuring good directivity and high gain improvement [14, 15]. The single antenna is positioned in the cavity center. The cavity size is $90.8 \times 85 \times 39.5 \text{ mm}^3$ which corresponds to $1.21 \lambda \times 1.13 \lambda \times 0.52 \lambda$ (λ is the wavelength at 4 GHz). The overall configuration of the proposed cavity-backed low-UWB antenna is illustrated in Fig. 38.6a.

Antenna parameter values are reviewed when introducing the cavity. The most influencing parameters are W2, L2, and L3; the antenna is more sensitive to these parameters. Figure 38.6b shows the reflection coefficient of the single

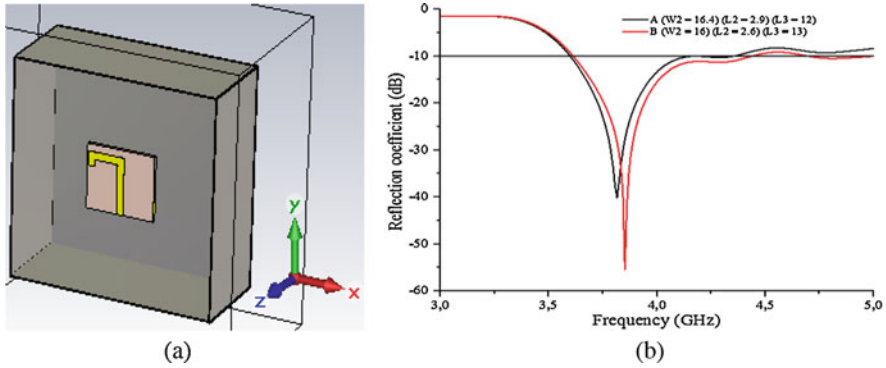


Fig. 38.6 (a) Overall view of the cavity-backed low-UWB antenna. (b) Reflection coefficient of the cavity-backed low-UWB antenna by tuning W2, L2, and L3 parameters

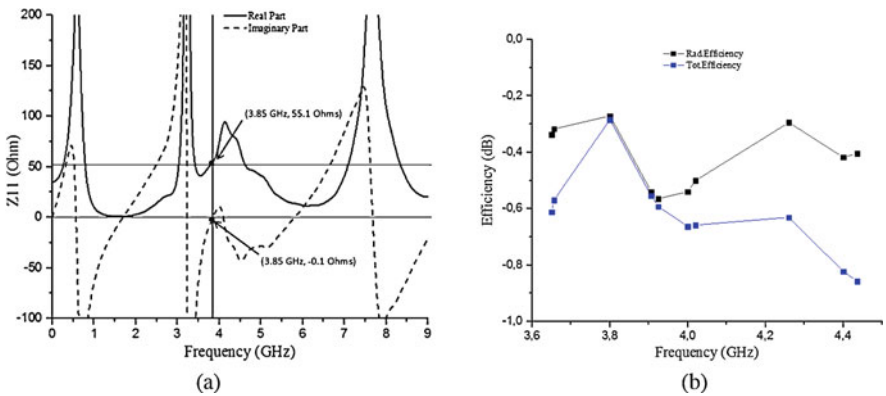


Fig. 38.7 (a) Input impedance of the cavity-backed low-UWB antenna at $F_r = 3.85$ GHz. (b) Radiation and total efficiency of the cavity-backed low-UWB antenna over the desired bandwidth

antenna inserted within the cavity (case A). However, tuning slightly the previously mentioned parameters adapts well the antenna to improve its performance (case B).

Input impedance matching of the proposed cavity-backed low-UWB antenna at the resonant frequency of 3.85 GHz is presented in Fig. 38.7a real part of the parameter Z_{11} is 55.1 Ω and the imaginary part is about $-0.1 \approx 0 \Omega$. It can be concluded from this input impedance study that the proposed antenna has a good impedance matching around 50 Ω .

Radiation and total efficiency of the cavity-backed low-UWB antenna over the covered bandwidth is between -1 and 0 dB as presented in Fig. 38.7b. Therefore, the antenna seems to operate well at low-UWB band which shows its conformity with IEEE 802.15.6 standard.

Directivity results of the cavity-backed low-UWB antenna at the frequencies 3.63, 4, and 4.43 GHz are given in Fig. 38.8. These results show that the single

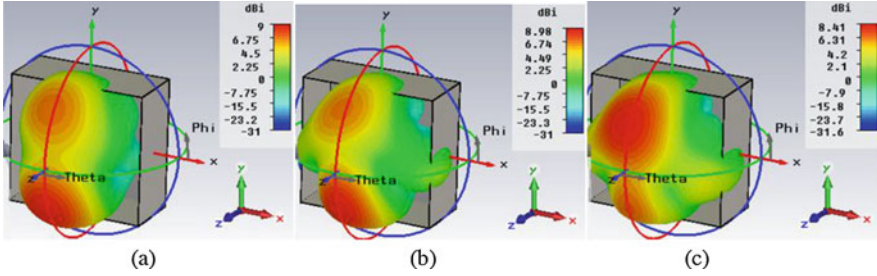


Fig. 38.8 Directivity of the cavity-backed low-UWB single antenna at (a) 3.63 GHz, (b) 4 GHz, and (c) 4.43 GHz

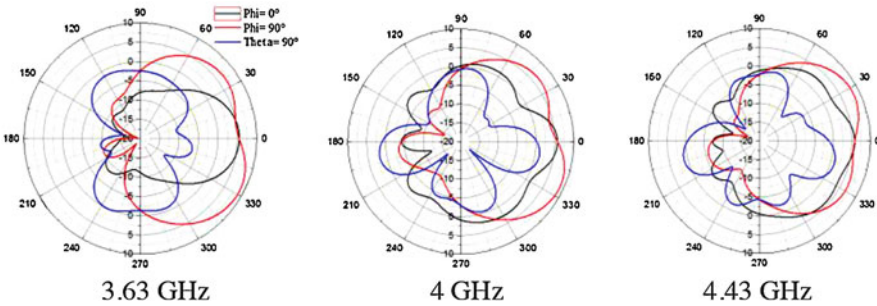


Fig. 38.9 Radiation patterns of the cavity-backed low-UWB antenna at (a) 3.63 GHz, (b) 4 GHz, and (c) 4.43 GHz. (Black $\geq \Phi = 0^\circ$, Red $\geq \Phi = 90^\circ$, and Blue $\geq \Theta = 90^\circ$)

Table 38.3 Gain values of the proposed cavity-backed low-UWB antenna by cutting axis planes

Frequency [GHz]	Theta = 90° [dBi]	Phi = 90° [dBi]	Phi = 0° [dBi]
3.6558	0.072	8.95	5.57
3.906	0.751	9.32	6.86
4	1.89	8.93	5.83
4.4361	1.12	8.39	5.7

antenna is directive toward Z-axis. At the three frequencies, total and radiation efficiencies are between -1 and 0 dB, which implies the good operation of the proposed cavity-backed antenna. Additionally, it is worth noting that directivity achieves high values up to 9 , 8.98 , and 8.41 dBi at the frequencies 3.63 GHz, 4 GHz, and 4.43 GHz, respectively.

Radiation patterns of the single low-UWB antenna at 3.63 , 4 , and 4.43 GHz are plotted in Fig. 38.9. Gain values, by cutting axis planes at $\Theta = 90^\circ$, $\Phi = 90^\circ$, and $\Phi = 0^\circ$, are summarized in Table 38.3. It is worth noting that the directivity decreases from 9 to 8.41 dBi with the increase of frequency from 3.63 to 4.43 GHz. However, maximum directivity is always toward Z-axis ($\Phi = 90^\circ$). It is concluded that the cavity approach comes as a solution to change antenna directivity from Y-axis to closely Z-axis. The cavity approach has proved a significant increase of the

maximum gain from 6.04 to 8.98 dBi at 4 GHz. Therefore, the aim of this approach for wireless capsule endoscopy localization is to reinforce the radiation to Z-axis and hence to direct the field to the body, so the penetration is better with lower power.

On-Body Simulation Results

The performance of a cavity-backed low-UWB antenna in the vicinity of a human body is investigated in this section as illustrated in Fig. 38.10a. Since WCE localization is important within the small intestine part of GI tract, for simplicity and as a preliminary realistic study, multi-layers in close proximity of the proposed antenna are placed and introduced to emulate dielectric properties of the skin, fat, muscle, and small intestine at 4 GHz. The layer arrangement with the associated thickness is as followed: Skin (2.3 mm), fat1 (11 mm for males and 18 mm for females), muscle (2.7 mm for males and 4.3 mm for females), fat2 (10 mm for males and 30 mm for females), and small intestine (2 mm) [16, 17]. The dielectric properties of the human tissues at 4 GHz are presented in Table 38.4 [18, 19].

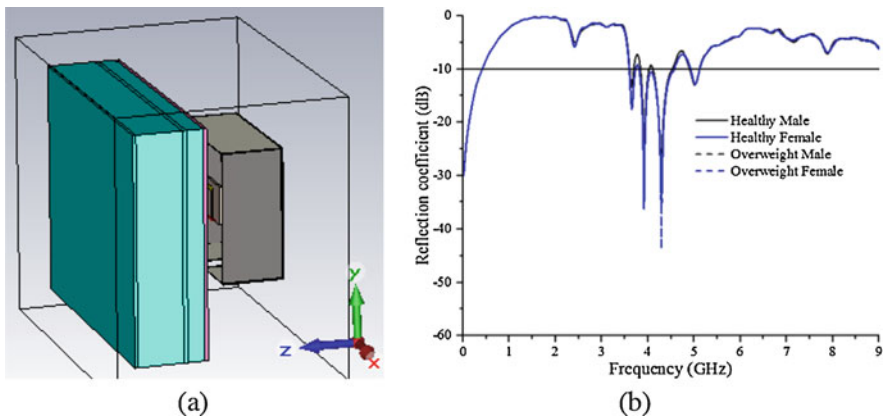


Fig. 38.10 (a) Cavity-backed low-UWB antenna in close proximity to the human model. (b) Comparison of reflection coefficient with different study cases

Table 38.4 Dielectric properties of human tissues at 4 GHz

Tissue layer	Permittivity	Conductivity (S/m)	Tang loss
Small intestine	51.7	4.62	0.402
Muscle	50.8	3.01	0.267
Fat	5.13	0.183	0.16
Skin	36.6	2.34	0.287

Table 38.5 Antenna performance per study case

Study case	Fr [GHz]	BW [GHz]	S11 Fr [dB]
Healthy male	4.28	[3.62–4.52]	−26.71
Healthy female	4.29	[3.62–4.55]	−36.97
Overweight female	4.29	[3.6–4.59]	−43.75
Overweight male	4.29	[3.6–4.55]	−27.54

In the literature, for example in [11], the distance between the receiving antenna and the human model is 5 cm. In this study case, the simplified layer is placed at 3 cm from the proposed cavity-backed low-UWB antenna.

A comparison study based on the reflection coefficient of the proposed cavity-backed antenna in proximity to human model is shown in Fig. 38.10b. The study cases distinguish between healthy and overweight persons by selecting the gender (male and female). The introduction of the multi-layer model in vicinity to the proposed cavity-backed antenna assures a bandwidth around 3.62–4.55 GHz, for all the study cases, which covers the required bandwidth [3.75–4.25 GHz] for low-UWB band of IEEE 802.15.6 standard for Body Area Network (BAN). However, it is clearly seen from the results presented in Table 38.5 that maximum reflection coefficient for overweight persons is higher than for healthy persons. Furthermore, the maximum reflection coefficient for female tissues is higher than for male tissues. The resonant frequency is around 4.27 GHz for different human tissues. From Table 38.5, it is concluded that the proposed cavity-backed low-UWB antenna is suitable to WCE purposes and conforms well with the IEEE 802.15.6 standard.

Radiation patterns of the single low-UWB antenna at 3.57, 4, and 4.43 GHz in vicinity to human tissues are plotted in Fig. 38.11. Gain values, by cutting axis planes at $\Theta = 90^\circ$, $\Phi = 90^\circ$, and $\Phi = 0^\circ$, are summarized in Table 38.6. Results show that high gain is still maintained even in close proximity to different human tissues (multi-layer model). However, maximum gain is slightly decreased for overweight person cases. It is clearly seen that different human tissues features (gender, thickness) do not affect too much the resulted radiation pattern.

38.4 Conclusion and Perspectives

A new low-UWB band directive antenna for WCE localization systems is presented in this chapter. Good directivity is achieved for both single antenna and cavity-backed antenna. Furthermore, they both comply with IEEE 802.15.6 standard requirements. For the single antenna, the gain reaches a value of 6.14 dBi at 4 GHz. For the proposed cavity-backed antenna, the gain is increased to 8.93 dBi at 4 GHz. The work was not restricted to free space investigations, but also an on-

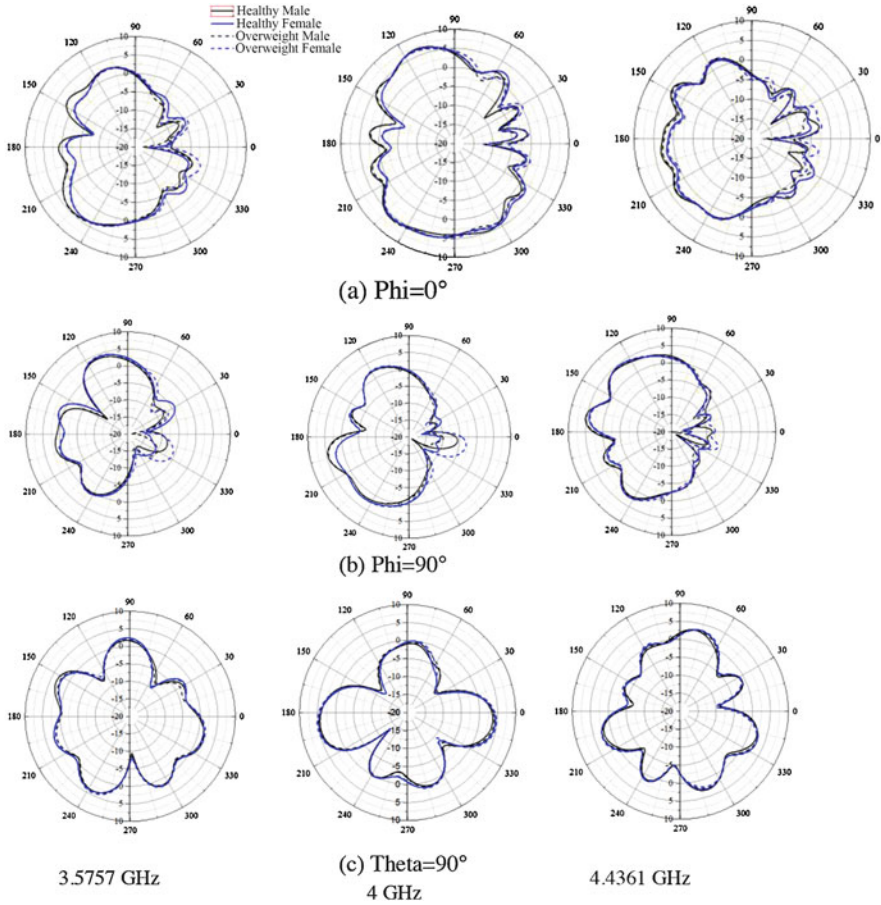


Fig. 38.11 Radiation patterns of the cavity-backed low-UWB antenna at 3.57, 4, and 4.43 GHz. (a) $\Phi = 0^\circ$, (b) $\Phi = 90^\circ$, and (c) $\Theta = 90^\circ$ (Black solid \geq Healthy Male, Blue solid \geq Healthy Female, Black dashed \geq Overweight Male, and Blue dashed \geq Overweight Female)

body preliminary realistic study was carried out. For this end, a multi-layer model emulating dielectric properties of the different human tissues at 4 GHz was used and satisfying results are concluded. According to the presented simulated results, it is concluded that both single antenna and cavity-backed antenna provide satisfying results for WCE localization purposes. Fabrication, measured results, and necessary tests using phantoms and realistic scenarios will be presented in the future work to validate these simulated results.

Table 38.6 Gain values of the proposed cavity-backed low-UWB antenna in vicinity to human model layers by cutting axis planes

Study case	Frequency [GHz]	Theta = 90° [dBi]	Phi = 90° [dBi]	Phi = 0° [dBi]
Healthy male	3.5757	3.82	3.78	4.51
	4	4.53	4.63	6.81
	4.4361	3.06	5.32	3.89
Healthy female	3.5757	3.92	4.24	3.9
	4	4.89	2.53	6.63
	4.4361	3.19	4.57	2.87
Overweight female	3.5757	4.33	4.43	3.99
	4	5.32	2.58	6.38
	4.4361	3.18	4.59	2.51
Overweight male	3.5757	3.84	3.88	4.67
	4	4.83	4.47	6.53
	4.4361	2.97	5.21	3.54

References

1. Neumann, H., Fry, L.C., Nagel, A., Neurath, M.F.: Wireless capsule endoscopy of the small intestine: a review with future directions. *Curr. Opin. Gastroenterol.* **30**, 463–471 (2014)
2. Chen, W., Yan, G., Wang, Z., Jiang, P., Liu, H.: A wireless capsule robot with spiral legs for human intestine. *Int. J. Med. Robot.* **10**, 147–161 (2013)
3. Yazdandoost, K.Y., Takizawa, K., Miura, R.: UWB antenna and propagation for wireless endoscopy. In: 2014 IEEE 25th Annual International Symposium on Personal, Indoor, and Mobile Radio Communication (PIMRC), pp. 2155–2159 (2014)
4. Shi, J., Wang, J.: Channel characterization and diversity feasibility for in-body to on-body communication using low-band UWB signals. In: 3rd International Symposium on Applied Sciences in Biomedical and Communication Technologies (ISABEL 2010), pp. 1–4 (2010)
5. Thotaheva, K.M.S., Redouté, J.M., Yuce, M.R.: Propagation, power absorption, and temperature analysis of UWB wireless capsule endoscopy devices operating in the human body. In: *IEEE Transactions on Microwave Theory and Techniques*, vol. 63, pp. 3823–3833 (2015)
6. Santiago, R.C., Pour, K.S., Khaleghi, A., Takizawa, K., Wang, J., Balasingham, I., Li, H.B.: Propagation models for IEEE 802.15.6 standardization of implant communication in body area networks. In: *IEEE Communications Magazine*, vol. 51, pp. 80–87 (2013)
7. IEEE Standard for Local and metropolitan area networks _Part 15.6: Wireless Body Area Networks, pp. IEEE Std 802.15.6–2012, pp. 1–271 (2012)
8. Thotaheva, K.M.S., Redouté, J.M., Yuce, M.R.: Electromagnetic power absorption of the human abdomen from IR-UWB based wireless capsule endoscopy devices. In: *IEEE International Conference on Ultra-Wideband (ICUWB)*, pp. 79–84 (2013)
9. Anzai, D., Katsu, K., Santiago, R.C., Wang, Q., Plettemeier, D., Wang, J., Balasingham, I.: Experimental evaluation of implant UWB-IR transmission with living animal for body area networks. In: *IEEE Transactions on Microwave Theory and Techniques*, vol. 62, pp. 183–192 (2014)
10. Arefin, M.S., Redoute, J.M., Yuce, M.R.: Meandered conformal antenna for ISM-band ingestible capsule communication systems. In: 2016 38th Annual International Conference of the IEEE Engineering in Medicine and Biology Society (EMBC), pp. 3031–3034 (2016)
11. Wang, Q., Wolf, K., Plettemeier, D.: An UWB capsule endoscope antenna design for biomedical communications. In: *Applied Sciences in Biomedical and Communication Technologies (ISABEL)*, 2010 3rd International Symposium on, pp. 1–6, IEEE (2010)

12. Morimoto, Y., Anzai, D., Wang, J.: Design of ultra wide-band low-band implant antennas for capsule endoscopy application. In: Proc. 7th Intl. Symp. On Medical Information and Commun. Technol. (ISMICT), pp. 61–65 (2013)
13. Arzate, E.L., Mendez, J.A.T., Franca, J.C., Leal, R.F., Aguilar, H.J., Solis, M.A.P.: Ultra-wideband directive antenna based on an inclined cone body. In: IET Microwaves, Antennas & Propagation, vol. 12, pp. 339–345 (2018)
14. Munir, A., Simorangkir, R.B.V.B.: Performance enhancement of cavity-backed UWB printed monopole antenna. In: IEEE Asia Pacific Microwave Conference (APMC), pp. 587–587 (2017)
15. Edalati, A., Shao, W., McCollough, T., McCollough, W.: A novel cavity backed monopole antenna with UWB unidirectional radiation. PIER C. **72**, 1–13 (2017)
16. Bunce, S.M., Moore, A.P., Hough, A.D.: M-mode ultrasound: a reliable measure of transversus abdominis thickness? Clin. Biomech. **17**, 315–317 (2002)
17. Akkus, O., Oguz, A., Uzunlulu, M., Kizilgul, M.: Evaluation of skin and subcutaneous adipose tissue thickness for optimal insulin injection. J Diabetes Metab. **3**, 8 (2012)
18. <http://www.fcc.gov/oet/rfsafety/dielectric.html>
19. <https://www.itis.ethz.ch/virtual-population/tissue-properties/database/dielectric-properties/>

Chapter 39

Experimental Path Loss Models Comparison and Localization of Wireless Endoscopic Capsule in the Ultra-Wideband Frequency Band



Sofia Perez-Simbor, Martina Barbi, Mehrab Ramzan, Xiao Fang,
Concepcion Garcia-Pardo, Narcis Cardona, Qiong Wang, Niels Neumann,
and Dirk Plettemeier

39.1 Introduction

The usage of wireless medical devices is growing in the biomedical sector due to the advantages compared with traditional procedures. Wireless Capsule Endoscopy (WCE) is an example of these medical devices. However, the current WCE transmits low quality images with low data rate [1], which leads to long and tedious time for the physician while watching the images and searching for polyps, tumors, and diseases. In addition, the position estimation of the WCE is currently very inaccurate that makes the localization of detected diseases very hard for the doctors [2]. Higher data rate would improve the transmitted and received signal enabling the transmission of high quality videos as well as the accuracy of the capsule localization.

The current frequency band defined in the standard for implant to surface body transmission (in-body to on-body, IB2OB), i.e., WCE case, is the narrowband Medical Implanted Communication Service (MICS) band. Although this band offers good penetration of the RF signal inside the human body, it provides low data rate (up to 500 kbps) [2]. As a result, Ultra-Wideband (UWB) [3, 4] frequency band is becoming more attractive for the scientific community due to its many advantages such as the small antenna size, the low power consumption, and the high data

S. Perez-Simbor (✉) · M. Barbi · C. Garcia-Pardo · N. Cardona
Institute of Telecommunications and Multimedia Applications (iTEAM), Universitat Politècnica
de València (UPV), València, Spain
e-mail: sopresim@iteam.upv.es

M. Ramzan · X. Fang · Q. Wang · N. Neumann · D. Plettemeier
Communication Laboratory, TU Dresden, Dresden, Germany
e-mail: qiong.wang@tu-dresden.com

rate. On the contrary, propagation losses caused by the human body are higher and frequency dependent [5].

In order to overcome this issue, a good characterization of the channel is required. There are plenty of works in literature that present path loss (PL) models for the IB2OB scenario [6, 7]. Nevertheless, the antenna effect is theoretically being considered part of the RF link, it is common that the path loss models consider this effect as antenna dependent. The way the antenna pattern affects the RF link is still unknown. Thus, a fair comparison of PL models for different antennas is required to explore this dependence.

In this chapter, a formal comparison between different antennas and their RF link budget (hereinafter path loss) is performed in the UWB frequency band for IB2OB scenario. Laboratory measurements are conducted, where the transmitting antenna is an omnidirectional in-body antenna and the receiving antennas are an omnidirectional and a directive antenna, respectively. Particularly, experimental measurements are performed using a customized phantom-based testbed. Moreover, in order to check whether the PL model is well characterized, a practical case of localization is performed. Concretely, an RSS-based localization [8] technique of the in-body antenna is investigated and compared when using different path loss models.

This chapter is organized as follows: in Sects. 39.2 and 39.3 an explanation of the setup, antennas, phantom, and methodology is given. Section 39.4 presents and compares the obtained results for the two different on-body antennas.

39.2 Setup

Measurement Setup

The measurement setup was developed for the purpose of IB2OB measurements in the UWB frequency band and it was exactly the same for the measurements performed for both antennas. It consists of a robotic arm that precisely moves along XYZ axis, a magnetic tracker, in-body antenna, on-body antennas, a laptop, and a vector network analyzer. All the necessary components of measurement setup are enclosed inside a large wooden box and each side of the box is internally covered by absorbers and aluminum to minimize the reflections from the boundaries and reduce the outside interference during the measurement process [6]. As a remark, the magnetic tracker by means of two wired nodes, one usually attached to the on-body antenna and the other one to the in-body antenna is used to track the relative position of the in-body antenna inside the phantom, being possible to know where both antennas are spatially located.

Antennas Used for the Path Loss Model

For channel modeling setup, a common in-body antenna and two different kinds of on-body antennas are used for the measurement. The first on-body antenna is a simple UWB planar patch antenna which is fabricated on a Rogers 4003 substrate with ϵ_r , length, width, and a thickness of 3.28, 40, 50, and 0.813 mm, respectively (Fig. 39.1a) [8]. The second on-body antenna is a UWB antipodal Vivaldi antenna fabricated on a bit flexible substrate of Rogers RO 3010 with ϵ_r , length, width, and a thickness of 10.2, 40, 50, and 0.25 mm, respectively (Fig. 39.1c) [9]. A small UWB in-body antenna which is based on CPW feeding structure, with length 23 mm and width 20 mm is used (Fig. 39.1b) [10].

Figure 39.2 shows the measured reflection coefficients for the three antennas. As seen all the antennas have a value lower than -10 dB in the UWB frequency regime.

Figure 39.3 shows the radiation pattern for both on-body antennas in free space for three different frequencies, at 3.1, 4, and 5 GHz. As noticed, the patch antenna is omnidirectional, while the Vivaldi antenna is a directional antenna.

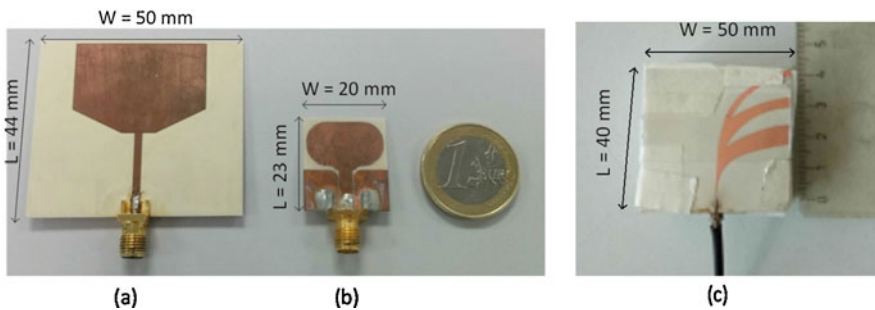
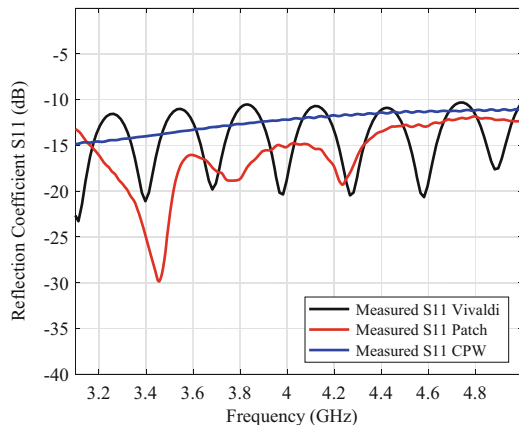


Fig. 39.1 (a) Monopole on-body antenna (b) In-body antenna (c) Antipodal on-body antenna

Fig. 39.2 S-parameters of the antennas



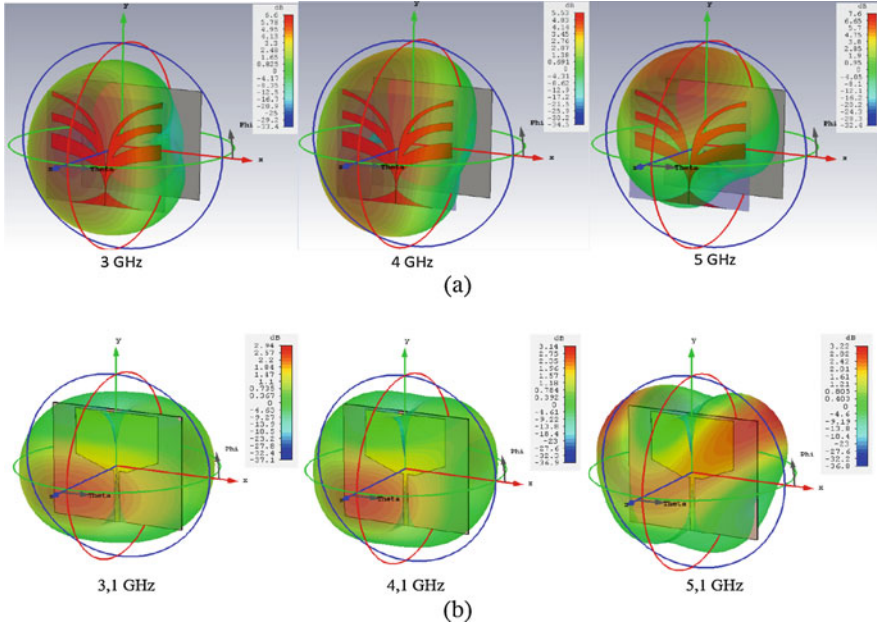


Fig. 39.3 Far field for (a) Vivaldi antenna and (b) Patch antenna

Phantom Properties

A simple UWB phantom was developed based on the proportion of sugar and water content recipe to approximately mimic the properties of muscle tissue in the frequency regime of 3–6 GHz [11]. The development of UWB phantom is done on a large scale on the basis of 1 L (1 mole/L = 342.297 g). Fourteen liters of UWB phantom were prepared on the basis of defined recipe and stored in a large container with capacity of 16 L of water in order to provide flexibility for the movement of the in-body antenna. The measurement of the tissue-based phantom is done by initially calibrating the probe in open air, short circuit, distilled water, and methanol [12] and then used for the measurement of the permittivity and conductivity of the UWB liquid phantom. Figure 39.4 shows the measured relative permittivity and conductivity of the UWB phantom from 3 to 6 GHz. Concretely, the relative permittivity varies from 1 to 9% and from 23 to 25% for the conductivity. Nevertheless, for the means of comparison between antennas in the UWB frequency band these discrepancies are the same for both antennas, maintaining the same conditions between antennas.

Fig. 39.4 Dielectric properties

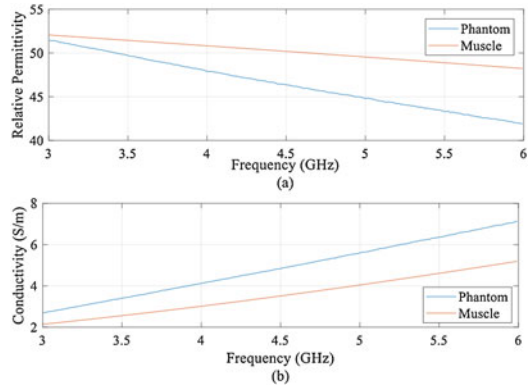


Fig. 39.5 Measurement setup and in-body and on-body positions for the channel modeling in lossy tissue

39.3 Methodology

The measurement setup described in the previous section is shown in Fig. 39.5. Before measurement, a two-port calibration was performed at the reference plane of two long 50Ω coaxial cables used to connect one to the on-body antenna and other to the in-body antenna. The on-body antenna is only moved manually in YZ plane on the external wall of the container, as seen on the right side of Fig. 39.5. The on-body antenna is placed in 13 different locations. From Fig. 39.5, the distance between receivers in the internal grid ($R \times 1 - R \times 9$) is $d_{in} = 3$ cm, while the distance between the external grid ($R \times 10 - R \times 13$) is $d_{out} = 5$ cm. At each location of the on-body antenna, the in-body antenna is placed at different sample points in $X, Y,$ and Z axis, achieving a 3D lattice. As seen on the left side of Fig. 39.5, the in-body antenna is moved with a spatial resolution of $(d_x, d_y, d_z) = (3, 1, 3)$ and a total number of sample points per axis of $(N_x, N_y, N_z) = (3, 11, 3)$. Moreover, five snapshots of the measurements are saved to minimize the fluctuation of results due to the movement of a robotic arm while moving from one in-body position to another. The system parameters were set as $f_{initial} = 3$ GHz, $f_{final} = 6$ GHz with $N = 3201$ resolution points, achieving a resolution frequency of $\Delta f = 937.21$ kHz.

Moreover, the intermediate frequency and the output power were set as $f_{IF} = 3$ kHz and $P = 8$ dBm. Finally, the noise threshold level measured for each antenna under these conditions was $NL_{O\text{mni}} = -90$ dB while the $NL_{V\text{ivaldi}} = -110$ dB.

39.4 Results

Comparison of the PL Models

From the measurements performed with the VNA, the forward transmission coefficient (S_{21}) per position is obtained. Then channel transfer function is calculated as:

$$H(f) = (|S_{21}| e^{-j\theta S_{21}}) \quad (39.1)$$

Graphically, the absolute value of the channel transfer function is depicted for both antennas in Fig. 39.6, where the channel transfer function, $|H(f, \text{dB})|$, as a function of the frequency in dB for different distances is shown.

In Fig. 39.6a, the response of the directional Vivaldi antenna is shown for different distances, while the omnidirectional antenna is plotted in Fig. 39.6b. Figure 39.6b shows that for distances greater than 6.5 cm the noise floor threshold level is reached for frequencies around 4.5 GHz. Whereas for the Vivaldi directional antenna, longer distances are achieved. For that, the behavior of the omnidirectional antenna is more restrictive than the directional antenna in terms of distance and frequency bandwidth as a function of frequency. Therefore, in order to have the maximum components above the noise level for both antennas, the maximum distance chosen for the calculation of the path loss is $d_{\text{max}} = 6.5$ cm and a maximum frequency of $f_{\text{max}} = 5.1$ GHz.

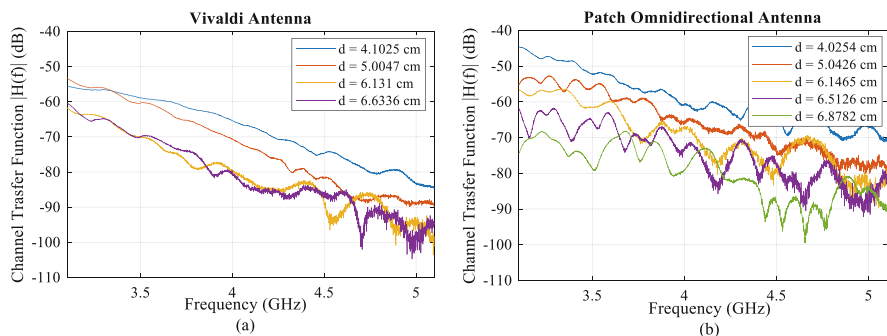


Fig. 39.6 Channel transfer function (a) Vivaldi antenna (b) Patch omnidirectional antenna

From the response of the $|H(f, dB)|$ is seen that the Vivaldi antenna has smoother response and greater slope, whereas the omnidirectional antenna is more irregular and has a lower slope. This behavior is reflected in the PL values, which are extracted from the channel transfer function by Eq. 39.2. In order to execute the calculation of the PL values, an averaging of the values of $H(f)$ is performed for the full bandwidth (3.1–5.1 GHz).

$$PL_{\text{meas}} (dB) = -10 \log \left(\sum_{i=N} \frac{|H(f_i)|^2}{N} \right) \tag{39.2}$$

In Fig. 39.7, the path loss values are depicted for both antennas and their different evident behavior. As expected from the results in Fig. 39.6, the directional Vivaldi antenna has a higher path loss values than the omnidirectional patch antenna (greater slope). A possible explanation might be due to the high path losses that the directional antenna experiences when the antennas are not located in the area of the directive beam. Besides, in Fig. 39.7, the aligned samples of the omnidirectional patch antenna are highlighted in brown. As seen, they have similar behavior to the PL values of the Vivaldi antenna.

From the path loss values, different path loss models are computed from Eq. 39.3 and summarized in Table 39.1.

$$PL (d, dB) = PL_0(dB) + 10n \log_{10} \left(\frac{d}{d_0} \right) + N (\mu, \sigma) \tag{39.3}$$

In Eq. 39.3, PL_0 is the reference path loss values for the given reference distance d_0 . In addition, $N(\mu, \sigma)$ is the scattering normal function being μ the mean and σ the variance in dB .

From the results, the Vivaldi antenna shows a higher path loss exponent (n), than the other two models, which was expectable from the results. Nevertheless, it may

Fig. 39.7 Path loss values for different antennas

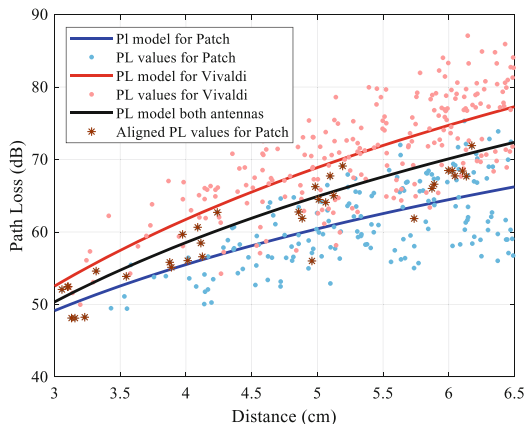


Table 39.1 Path loss models for different antennas

Path loss model Vivaldi	Path loss model patch	Path loss model both antennas
$d = [3, 6.5]$ cm $f = [3.1, 5.1]$ GHz $PL_0 = 17.35$ dB $d_0 = 1$ cm $n = 7.37$ $\mu \approx 0$ $\sigma = 5.72$ dB	$d = [3, 6.5]$ cm $f = [3.1, 5.1]$ GHz $PL_0 = 24.86$ dB $d_0 = 1$ cm $n = 5.09$ $\mu \approx 0$ $\sigma = 4.26$ dB	$d = [3, 6.5]$ cm $f = [3.1, 5.1]$ GHz $PL_0 = 19.05$ dB $d_0 = 1$ cm $n = 6.56$ $\mu \approx 0$ $\sigma = 6.79$ dB

come as a surprise that the variance (σ) of the omnidirectional antenna is smaller than directive one. As expected, the path loss model resulting from the combination of both antennas has a path loss exponent in between the other two models and a variance higher than the other models. This is due to the widespread and wide difference that appear between the measured path loss values.

RSS-Based Ranging and Localization

In this section performance of the two antennas, presented in the previous sections, are analyzed and compared when used for the localization of the in-body antenna. Because UWB signals are distorted in a frequency-dependent manner by the body tissues, accurate estimation of parameters such as ToA (time of arrival) or TDoA (time difference of arrival) is difficult [13]. Consequently, using the Received Signal Strength (RSS) metric for ranging purposes appears more feasible.

The real positions of the in-body antenna, as well as the estimated ones, are evaluated with respect to the magnetic tracker transmitter's reference system (Fig. 39.5). Ranging distance estimation is performed as in [14] by using the path loss models evaluated in section "Comparison of the PL Models". Considering the setup depicted in Fig. 39.5, only two coordinates of the in-body antenna (y and z) could be estimated as all receivers (on-body antenna locations) share the same x -coordinates. Trilateration is used for the estimation of the in-body antenna coordinates, i.e., the position of the in-body antenna corresponds to the point of intersection of at least three circles, whose centers are the locations of the selected receivers and whose radii are the estimated distances between in-body antenna and selected receivers (ranging distances). In this study, different combinations of three receivers were considered to locate the in-body antenna. In order to solve the system of three nonlinear equations, the linearized method described in [15] is adapted [14] and implemented for two-dimensional positioning. In this approach, one of the three selected receivers is taken as reference to find the unique solution (y and z coordinate of the in-body antenna) of the linearized system of two equations in two unknowns.

Performance is evaluated in terms of relative localization error as in [14]. Figure 39.8 shows a comparison of the Cumulative Distribution Function (CDF) of the

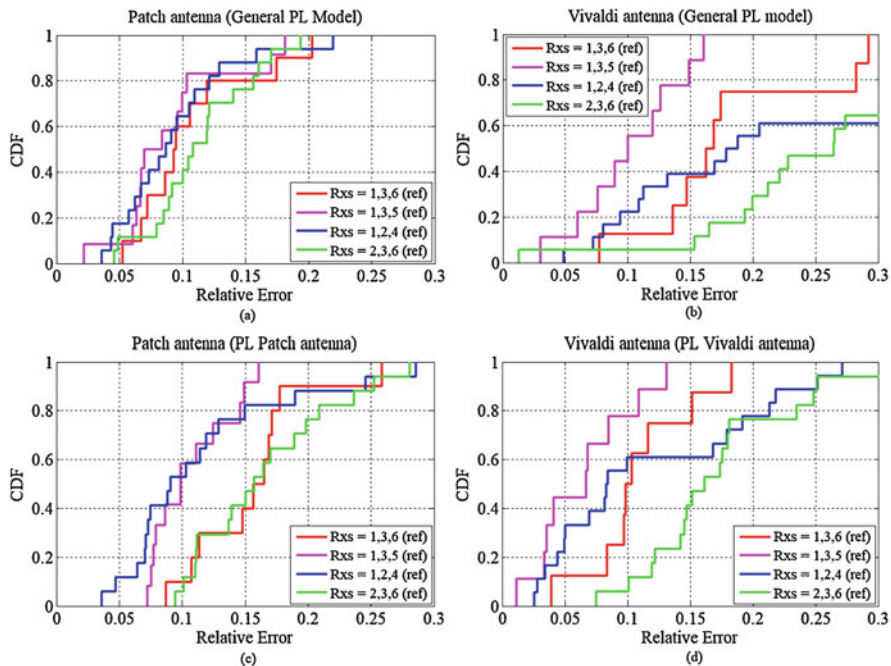


Fig. 39.8 CDF of relative localization error for (a) Patch antenna using the general PL model, (b) for the patch antenna using the related PL model, (c) for the Vivaldi antenna using the general PL model and (d) for the Vivaldi antenna using the related PL model

relative error calculated as in [14] for the patch and Vivaldi antenna, using different combinations of three receivers and two different path loss models. Particularly, results for each antenna are evaluated and compared when using the general path loss model and the antenna related path loss model (see Table 39.1).

For both antennas, performance obtained using the antenna-related path loss models (Fig. 39.8c, d) are slightly better than those obtained with the general path loss models (Fig. 39.8a, b). The best combination of receivers, leading to lowest error values, is receiver 1, 3, and 5 (taken as reference), i.e., the magenta curve in Fig. 39.7. In fact, for this combination of receivers the average ranging error (distance between the real antennas distance and the estimated one) has been assessed to be the lowest compared to the other receivers combinations. This, in turn, results in better accuracy in the estimation of the in-body antenna coordinates when solving the linearized system of eqs. [14].

Considering the best combination of receivers (i.e., 1, 3, and 5 as reference), error values obtained using the patch antenna and its antenna-related model are 2–3% higher than those obtained using the Vivaldi antenna and its corresponding model. In terms of localization error and considering the same combination of receivers, an average error of 1.6 cm is obtained with the patch antenna and of 0.98 cm with the Vivaldi antenna, using the antenna-related path loss models. The reason behind

this behavior can be explained by the fact that when using the Vivaldi antenna path loss values corresponding to receivers 1, 3, and 5 are closer to the antenna-related fitting model curve. This turns into a lower average ranging error and, consequently, a slightly lower localization error compared to the one obtained using the patch antenna.

39.5 Conclusions

In this chapter, in-body to on-body UWB transmission experiments are performed inside a lossy tissue based on liquid phantoms. A fair comparison was performed between two different receiver antennas to compare different channel characteristics. Three different path loss models are extracted from the measurements, one general PL model considering all the PL values and two of them related with each antenna (omnidirectional and directive antenna). From the results, it is observed that the directional antenna has higher path loss exponent and variance. Nevertheless, from the results obtained in the RSS-based localization algorithm, there is a slightly better performance for the path loss obtained with the directive antenna. This result might seem contrary as the expected ones, since, as said the path loss exponent is higher for the directive antenna. These results show the necessity of a good understanding of the effect of the antenna in the channel characterization to properly characterize the IB2OB channel in the UWB frequency band. As a further research, a deeper study in how the antenna affects the RF link should be performed.

Acknowledgments This research is supported by “WiBEC” (Wireless In-Body Environment) project funded by the European Union Horizon 2020 research and innovation program under grant agreement No 675353.

References

1. IEEE Standards Association: IEEE Standard for Local and Metropolitan Area Networks—Part 15.6: Wireless Body Area Networks (2012)
2. Ciuti, G., Menciassi, A., Dario, P.: Capsule endoscopy: from current achievements to open challenges. *I.E.E.E. Trans. Biomed. Eng.* **4**, 59–72 (2011)
3. Molisch, A.F.: Ultra-wide-band propagation channels. *Proc. IEEE.* **97**(2), 353–371 (2009)
4. Garcia-pardo, C., Andreu, C., Fomes-leal, A., Perez-simbor, S., Barbi, M., Vallés-lluch, A.: Ultrawideband technology for medical in-body sensor networks. *IEEE Antennas Propag. Mag.* **60**(3), 19–33 (2018)
5. Khaleghi, A., Chavez-Santiago, R., Balasingham, I.: An improved ultra wideband channel model including the frequency-dependent attenuation for in-body communications. In: Proceedings of the Annual International Conference of the IEEE Engineering in Medicine and Biology Society, EMBC, pp. 1631–1634, 2012
6. Perez-Simbor, S., Barbi, M., Garcia-Pardo, C., Castelló-Palacios, S., Cardona, N.: Initial UWB in-body channel characterization using a novel multilayer phantom measurement setup. In: IEEE Wireless Communications and Networking Conference, WCNC, p. 6, 2018

7. Andreu, C., Castello-Palacios, S., Garcia-Pardo, C., Fornes-Leal, A., Valles-Lluch, A., Cardona, N.: Spatial in-body channel characterization using an accurate UWB phantom. *IEEE Trans. Microwave Theory Tech.* **64**(11), 3995–4002 (2016)
8. Tarin, C., Marti, P., Traver, L., Cardona, N., Diaz, J.A., Antonino, E.: UWB channel measurements for hand-portable devices: a comparative study. In: *IEEE International Symposium Personal Indoor Mobile Radio Communication, PIMRC, 2007*
9. Fang, X., Ramzan, M., Wang, Q., Plettemeier, D.: Compact antipodal Vivaldi antennas for body area communication. In: *International Conference on Body Area Networks, BodyNets*, vol. 17, p. 7, 2017
10. Andreu, C., Garcia-Pardo, C., Fornes-Leal, A., Cabedo-Fabrés, M., Cardona, N.: UWB in-body channel performance by using a direct antenna designing procedure. In: *11th European Conference on Antennas and Propagation (EUCAP)*, p. 5, 2017
11. Gabriel, C.: Compilation of the dielectric properties of body tissues at RF and microwave frequencies. In: *Environmental Health, Report No.*, p. 21, 1996
12. Fornes-Leal, A., Garcia-Pardo, C., Cardona, N., Castello-Palacios, S., Valles-Lluch, A.: Accurate broadband measurement of electromagnetic tissue phantoms using open-ended coaxial systems. In: *International Symposium Medical Information and Communication Technology ISMICT*, pp. 32–36, 2017
13. Kawasaki, M., Kohno, R.: A TOA based positioning technique of medical implanted devices. In: *International Symposium Medical Information and Communication Technology ISMICT, 2009*
14. Barbi, M. et al.: Localization for capsule endoscopy at UWB frequencies using an experimental multilayer phantom. In: *IEEE Wireless Communications and Networking Conference, WCNC*, p. Submitted, 2018
15. Arshak, K., Adepoju, F.: Adaptive linearized methods for tracking a moving telemetry capsule. In: *IEEE International Symposium on Industrial Electronics*, pp. 2703–2708, 2007

Chapter 40

Planar Elliptical Ring Implanted Antennas for UWB Body Area Communication



Qiangbo Zhang, Xiao Fang, Qiong Wang, and Dirk Plettemeier

40.1 Introduction

One of the most popular research areas of body area network (BAN) is design of miniaturized and high efficiency electronic devices. Many kinds of BAN applications have been proposed. And especially, one of the most interesting fields is wireless capsule endoscope. To achieve high data rate and real-time imaging transform for communicating between implanted and wearable devices, the UWB is the feasible operating frequency band for the transmitter and receiver systems [1]. The co-authors have designed some wearable antennas working at lower part of UWB band, which can be used as on-body antennas. In this chapter, we propose a novel type of UWB implanted antenna which can be used as the in-body antenna to communicate with on-body devices.

The proposed antennas are planar double elliptical rings antenna operating at lower part of UWB inside human body. The double elliptical rings are used for radiation and provide a wideband characteristic for the antenna. In addition, the thick and large permittivity substrate also is utilized to extend the operating frequency band further. Based on the application of wireless endoscope capsule, the dimensions of antennas are shrunk and the shapes are cut into circular plate to fit in capsules. The application scenarios decide that the antennas perform inside the human body; therefore, in our simulation the parameters of antennas are optimized within the muscle tissue. The simulated and measured reflection coefficients show that the designed antennas can satisfy the requirement operating at the lower part of UWB. The radiation characteristic of implanted antenna is evaluated through

Q. Zhang (✉) · X. Fang · Q. Wang · D. Plettemeier
Communication Laboratory, TU Dresden, Dresden, Germany
e-mail: qiangbo.zhang@tu-dresden.de; qiong.wang@tu-dresden.com

measuring the transmission coefficient between two implanted antennas in phantom. As well, the receipt of phantom of muscle tissue is proposed to simulate the electric properties of muscle tissue.

40.2 Antenna Design

The proposed antenna is working at UWB and has small dimension so that it could be embedded in a capsule, which can be swallowed into the human body through esophagus. So a basic antenna type “Elliptical Ring” is chosen due to its simplicity and good performances for wideband communications [2]. Considering ease of fabrication, a planar double elliptical ring antenna is designed [3]. As shown in Fig. 40.1, the dimension of antenna is designed as a circular plate (radius = 5.9 mm) to take full advantage of the volume of cylinder capsule. The substrate is Rogers TMM10 (thickness = 75 mil, $\epsilon_r = 10.2$). The thickness and high permittivity of substrate are used to reduce the dimension of the antenna and extend the bandwidth. The top layer of substrate is double elliptical ring while bottom layer is the ground plane. The antenna is fed by the coaxial cable whose conducting shield is welded with the ground plane while inner conductor goes through the dielectric material and is connected with the radiation part, which is on top of the substrate.

The Top-View in Fig. 40.1a shows the concept of the antenna configuration for its radiation part. It consists of two elliptical rings and one elliptical branch. The two elliptical rings are the radiation parts of antenna, which have different current

Fig. 40.1 Structure of the proposed antenna (a) Top-View (b) Side-View (c) Bottom-View

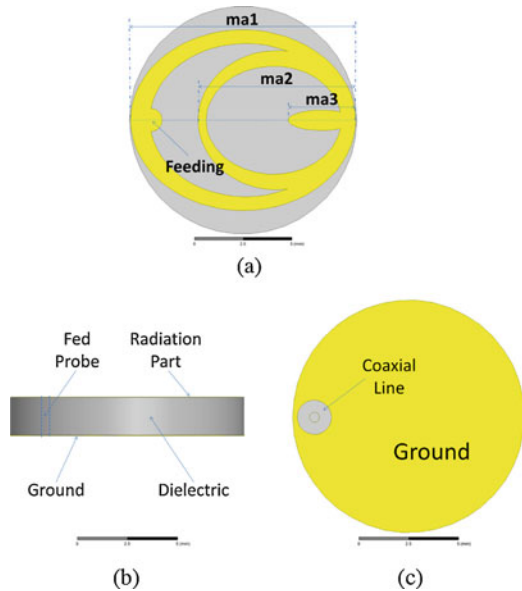


Fig. 40.2 Two actual antenna configurations (a) first type (b) second type

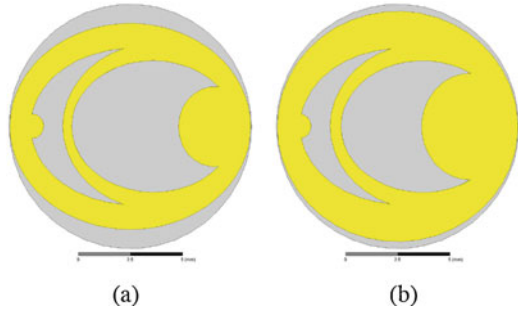


Table 40.1 Configuration specification of two proposed antennas

Type	First type	Second type
ma1 (mm)	5.85	5.85
ma2 (mm)	1.76	2.34
ma3 (mm)	4.56	4.56
ar1	0.85	0.95
ar2	1.1	1.1
ar3	0.88	0.88

lengths providing two relative narrow frequency bands that are somehow close with each other and merged into one wideband. Sequentially, the two rings have similar dimensions and as a result they have partly overlapped with each other. The elliptical branch is a wideband matching branch used to match the antenna with 50Ω coaxial cable in the whole demanded band. There is another small disc partly overlapping with the biggest elliptical ring at one side of it. It is used for connecting with the inner conductor of coaxial cable.

As shown in Fig. 40.1a, the major axis's lengths of three elliptical parts are *ma1*, *ma2*, and *ma3*, respectively. And the axis ratios are defined as *ar1*, *ar2*, and *ar3*, respectively. Based on the former design principle, two different configurations of antennas have been proposed in Fig. 40.2. The parameters of these two types are listed in Table 40.1. The radiuses and operating frequencies of both are 5.9 mm and lower part of UWB band, separately.

40.3 Simulation and Measurement

Body Area Environment

The designed antenna works inside the human body; therefore, the electric properties of human tissues are significant for antenna design. As we all know, human body has the high lossy and large permittivity characteristics for EM-Wave propagation, and its electric properties are frequency depended. According to Gabriel's work [4], the defined 4-Cole-Cole models can be utilized to describe the

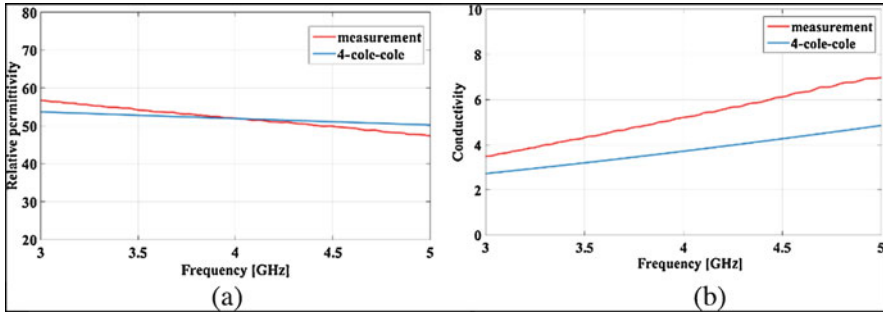


Fig. 40.3 Body tissue properties (a) Relative permittivity (b) Conductivity

frequency-dependent electric properties of human tissues. In our simulation, the surrounded tissue is muscle whose relative permittivity and conductivity from 3 to 5 GHz are calculated based on Gabriel's 4-Cole-Cole model. As shown in Fig. 40.3, with frequency growing, permittivity decreases while conductivity increases. At the center frequency 4 GHz, the theoretical ϵ_r is equal to 52 and s is equal to 3.6 S/m.

For measurement, a body tissue liquid is made up by mixing water and sugar. The relative permittivity of water is about 83 under room temperature and that of sugar is about 3. Conductivity of water is similar to that of body. By dissolving sugar into water, an imitation for body tissue could be created. The recipe is under our test about: 350 g sugar with 780 g water. Measurements of body tissue liquid are carried out at 20 °C grads by utilizing equipment Agilent 85070E. In Fig. 40.3, measurement results of the phantom are presented. The measured permittivity at center frequency is almost equal to the theoretical value but only its slope is a little larger. The maximal relative error is about 3%, which is not supposed to result in many differences between simulation and measurement. On the other hand, measured conductivity is larger than 4-Cole-Cole model within the whole band. It may be caused by that the water we used for testing is not distilled water which contains some unnecessary ions. Fortunately, conductivity only results in losses but attributes little at changing performances of antenna.

Antenna Results

Antennas are fabricated on 75-mil-thick Rogers TMM10 substrate, then cut into circular plate, and are shown in Fig. 40.4. To measure the electric characteristics of antennas, the coaxial cables are utilized to connect the antenna with the vector network analyzer (VNA). The conducting shield of coaxial is welded with the



Fig. 40.4 Fabricated antennas (a) Antennas without coaxial cables. (b) Antennas with coaxial cable

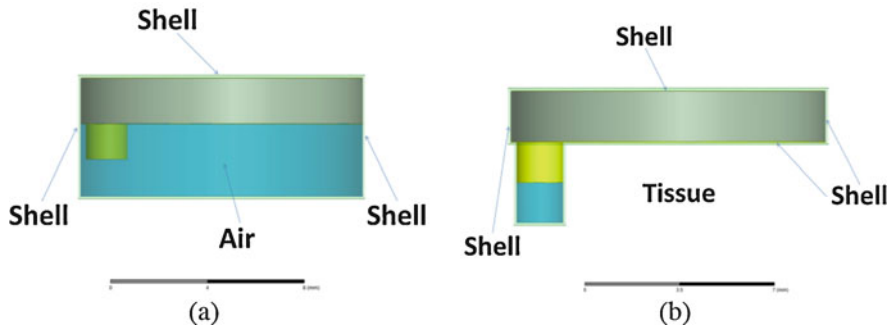


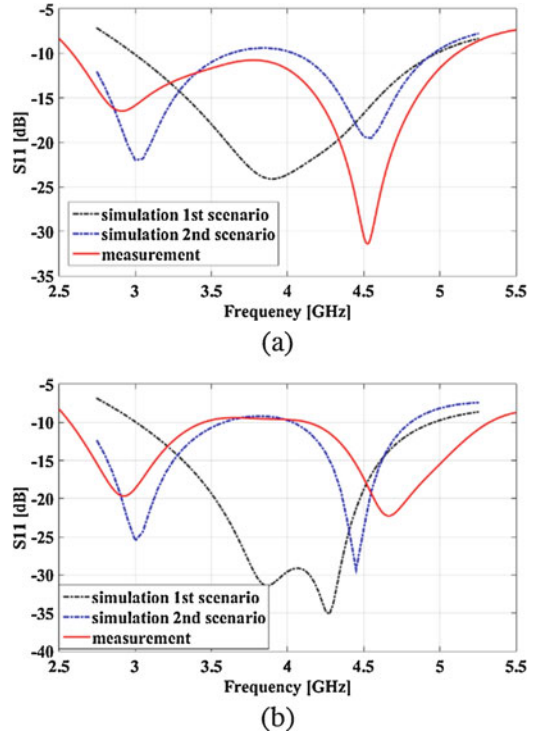
Fig. 40.5 Two different environment scenarios (a) in a capsule (b) coating for measurement

ground plane of antenna, and the inner conductor with the top layer. Figure 40.4a shows the fabricated antennas, and Fig. 40.4b is antennas with coaxial cables.

Because the high lossy characteristic of human body tissue can destroy the current distribution of antenna, a shell-isolating antenna from human tissue is very necessary. As mentioned the proposed antennas are used in a capsule. As shown in Fig. 40.5a, a shell surrounds the top and the side of antenna. As the capsule conceived in our plan, beneath antenna’s ground there should be something that has similar electrical properties like air. So antennas are simulated under this environment configuration. However, as shown in Fig. 40.4b, for testing no real shell are made and the tested antennas have a coating all around it, as shown in Fig. 40.5b. Beneath the ground and a thin isolation shell, there is nothing but human tissue instead of air. Both two environments are simulated, but the measurements are carried out only in the second scenario.

All simulation and measurement results are presented in Fig. 40.6. Impedance performances of both antennas are satisfied within the whole required band in every situation. Measurement results agree well with the simulation one, i.e., the second environment scenario. As illustrated, the lower bands of measurements

Fig. 40.6 S_{11} performances of two proposed antennas at simulation and measurement (a) first type (b) second type



are lower than simulation one while the upper bands are higher. This may be caused by differences between 4-Cole-Cole model and artificial liquid. As shown in Fig. 40.3, permittivity slope of the testing liquid is larger than that of 4-Cole-Cole model. Shorten factors enlarge at lower frequencies (<4 GHz) and on contrast decrease at higher frequencies (>4 GHz). It may consequently force the lower band lower and the higher band higher. However, this comparison can lead to that simulation and measurement is almost identical. And for scenario of capsule shell, i.e., first scenario, both antennas show very good impedance performances. At center frequency (4 GHz), S_{11} is deeper than -20 dB and -25 dB. Though there is no fabricated shell for testing, it can still be deduced that the proposed antennas can work well in a capsule.

As we can see from results, the EM-environment beneath the ground has a little influence on performance of the antenna: It shifts the two-resonating band apart, but fortunately the impedance performances are still lower than -10 dB within the whole band. It may be resulted that the ground copper is not larger than the radiation copper. As a result, EM-field of non-radiative field may not only be limited in the dielectric but also partly in the very close region beneath ground copper. The worst situation is the testing condition ($\epsilon_r > 50$ from 3 to 5 GHz). It means if in the future the air under the ground is substituted by crutching clapboard or microwave

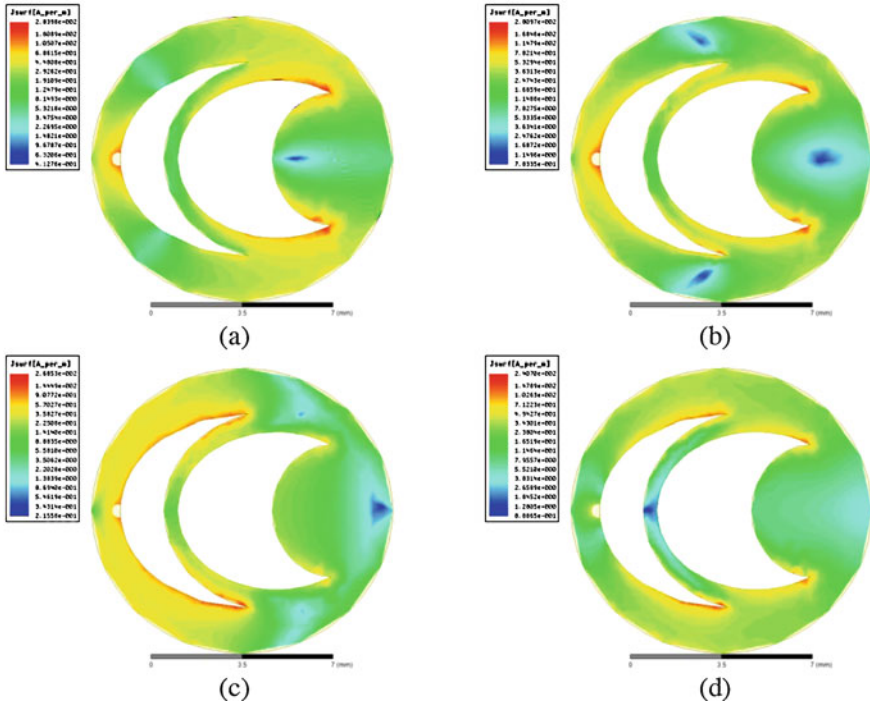


Fig. 4.07 Current configuration at 4GHz of second antenna type (a) phase = 0 (b) phase = 45 (c) phase = 90 (d) phase = 135

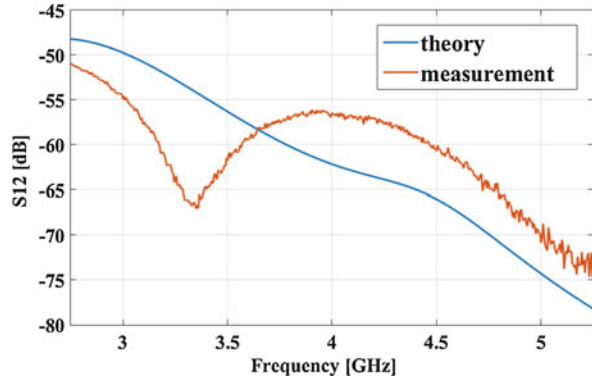
PCB-board, whose ϵ_r is smaller than 10, impedance performance will not change so much.

Figure 4.0.7 illustrates the current configuration upon the radiation part of second antenna type from phase = 0 to phase = 135. As expected before, current distributes along the curve of the two ellipses. Within a half duty cycle the current resonates from the probe to the two ellipses and then flow back. It means the energy is transmitted into tissue rather than attenuated within the dielectric.

Gain of an antenna could not be derived directly from its radiation pattern when the antenna is working within a lossy medium because in lossy medium EM-field will stimulate electric current within tissue and therefore there are no more far-fields. In this chapter [5], another method by applying path loss to evaluate the transmission budget between two antennas in lossy medium is proposed. A path loss equation is raised in the chapter and rewritten as follows:

$$\frac{1}{PL} = \frac{P_r}{P_t} = (1 - |S_{11}|^2) (1 - |S_{22}|^2) \cdot G_t G_r \cdot \frac{\lambda^2}{(4\pi r)^2} \cdot \exp(-\alpha r)$$

Fig. 40.8 Comparison between theoretical calculated path loss and measurement S_{12}



PL means path loss, P_r and P_t are transmitting and receiving power, respectively. G_t and G_r are the gain of the transmitting and receiving antennas according to the chapter. r is the distance of two antennas. α is the attenuation factor. This equation involves Friis Equation, mismatching of the input power at antenna feeding, antenna gains, and attenuation of EM-field in lossy medium. If G_t and G_r are set to 1, theoretical path loss can be derived. It means, when neglecting the so-called gain, an ideal path loss between two ideal point sources can be calculated. After measuring S_{12} , this theoretical value can be compared with the tested S_{12} . By doing that, an evaluation of antenna's transmission properties can be obtained.

Before measuring S_{12} , a proper distance should be ensured. Due to large attenuation in-body tissue, the distance between two antennas should not be too large; otherwise, the tested S_{12} will vanish within noises. And the distance should not be too small either, considering the near-field coupling. For our testing 40 mm is chosen, which is approximately four times the wavelength. The two antennas are placed like looking each other in a mirror. The radiation parts are parallel so that the polarization matches. In Fig. 40.8, comparison between measured S_{12} and theoretical path loss calculated from the former equation with $r = 40$ mm is illustrated. As illustrated, the trend of two lines is similar after 3.5 GHz and the S_{12} is even a little bit better. Between 3 and 3.5 GHz the measured result is a little bit worse. However, we can still conclude that the proposed antenna can work within the demanded frequency band, i.e., the energy is transmitted into body area rather than attenuated within the near field of the antenna.

40.4 Conclusion

To achieve high data rate and real-time video imaging transform from in-body to on-body devices, a novel type of implanted antenna for UWB body area communication is proposed. By using double elliptical rings and small elliptical branch, the wideband radiation and matching characteristics of antenna have been achieved. The

thick and high permittivity substrate also is used to extend the bandwidth and reduce the dimension of antenna further. The diameter of antenna is limited to be less than 10 mm to fit into the wireless endoscope capsule. Two antennas with different configurations are designed, the parameters of which are optimized in the muscle tissue. Operating frequencies of both antennas satisfy the requirement (3.1–4.8 GHz) according to the simulated and measurement results. The transmission coefficient between two same implanted antennas are also measured in the phantom to check the radiation characteristic of designed antennas, which shows that the measured result fits with the theoretically calculated one. In addition, we propose the receipt of phantom of muscle in the lower part of UWB band, and the measured relative permittivity and conductivity are shown in the chapter.

References

1. Fang, X., Ramzan, M., Wang, Q., Plettemeier, D.: Miniaturized antipodal Vivaldi antenna array for body area communication. In: 12th International Conference on Body Area Networks, Dalian, China, September 2017
2. Schantz, H.: *The Art and Science of Ultrawideband Antennas*, 2nd edn. Artech House Publishers (2015)
3. Alhargan, F., Judah, S.: Wide band confocal annular elliptic microstrip antenna. In: *Antennas and Propagation Society International Symposium, 1995. AP-S. Digest*, Newport Beach, CA, USA, June 1995
4. Gabriel, C.: *Compilation of the Dielectric Properties of Body Tissues at RF and Microwave Frequencies*. King's College, Department of Physics, London (1996)
5. Kurup, D., Vermeeren, G., Tanghe, E., Joseph, W., Martens, L.: In-to-out body antenna-independent path loss model for multilayered tissues and heterogeneous medium. *Sensors*. (2014)

Chapter 41

Motion Artifact Reduction in Electrocardiogram Using Adaptive Filtering Based on Skin-Potential Variation Monitoring



Shumei Dai, Dongyi Chen, Fan Xiong, and Zhenghao Chen

41.1 Introduction

Cardiovascular diseases have become more and more important in recent years. In the field of clinical and medical research, a standard commercial Ag/AgCl electrode is used to record ECG signal. This electrode contains an electrolyte gel, which can irritate the human skin, and the signal quality degrades over time due to the dehydration of the gel [1, 2]. For this reason, Ag/AgCl electrodes are not suitable for wearable health care devices which are intended for long-term continuous monitoring. Therefore, textile-based dry electrodes are alternatively used owing to their stable electrical properties. Textile electrodes are dry, free from gel, and can be readily converted into wearable medical garments, which make them preferable for long-term monitoring [3].

However, the biggest challenge of the fabric dry electrodes is that the collected ECG signals are greatly disturbed by motion artifacts. Most of the noise can be filtered out using common filtering techniques, but motion artifacts are difficult to filter out since they have the same frequency range as ECG signals. Accurate detection of a person's biopotential signals in movement state is always difficult and challenging [4]. SPV is a major composition of the motion artifacts [5].

The performance of adaptive filtering in noise suppression depends largely on the level of correlation between the reference signal and the ECG noise source [6]. The reference signal measures motion artifacts by means of various sensors (pressure sensors, accelerometers, and optical displacement sensors) [7–10]. A low correlation with motion artifacts were shown in indirectly measured reference

S. Dai · D. Chen (✉) · F. Xiong · Z. Chen
University of Electronic Science and Technology of China, School of Automation Engineering,
Chengdu, China
e-mail: dychen@uestc.edu.cn

signals, because they yield inaccurate estimates of the electrical characteristics of the skin/electrode interface. Ko et al. [11] designed an acquisition structure to measure the half-cell potential by using sol-gel foams wet electrodes, The half-cell potential signal was used to estimate motion artifacts, but wet electrodes were not suitable for long-term use. In general, these research works can effectively reduce motion artifacts by using adaptive filtering. However, the ECG signal collected by the textile electrodes and the motion artifact induced by skin-potential variation (SPV) were not taken into consideration.

In this chapter, a simple method was demonstrated to measure skin-potential variation (SPV). SPV signals were used as reference signals to reduce ECG motion artifacts with the adaptive filtering technique. To measure SPV signal, two additional textile electrodes were positioned adjacent to the ECG sensing electrodes and connected with a resistance. The skin deformation causes a potential difference between the two electrodes, and a voltage drop is generated across the resistance. This voltage drop signal is adaptively filtered as a reference signal input. This method can eliminate the need for placing different sensors on the body, and obtain SPV signal which is high similar with ECG signal by using two more textile electrodes to estimate motion artifacts with adaptive filtering.

41.2 Methodology and Measurement

The proposed method using textile electrodes acquired two types of physiological signals, ECG signals and SPV signals. Then formula derivation, circuit simulation, and experiments were carried on to demonstrate that motion artifacts can be effectively removed by the SPV signal.

Electrical Circuit Model

The equivalent circuit model for ECG signal is shown in Fig. 41.1a, b shows the equivalent circuit model for SPV signal [11]. Z_{si} is the impedance of skin, Z_{ei} is the impedance of skin–electrodes interface, Z_r is the resistance which connects two electrodes, and Z_{in} is the input impedance of the front-end.

In Fig. 41.1a:

$$\text{ECG} = V_1^+ \times \frac{Z_{in}}{Z_{s1} + Z_{e1} + Z_{in}} - V_1^- \times \frac{Z_{in}}{Z_{s2} + Z_{e2} + Z_{in}} \quad (41.1)$$

From Eq. (41.1), when the input impedance Z_{in} is large relatively to the interface impedance ($Z_{s1} + Z_{e1}$, $Z_{s2} + Z_{e2}$) and the impedance between the two lead electrodes is approximately equal ($Z_{s1} + Z_{e1}$, $Z_{s2} + Z_{e2}$), the equation is

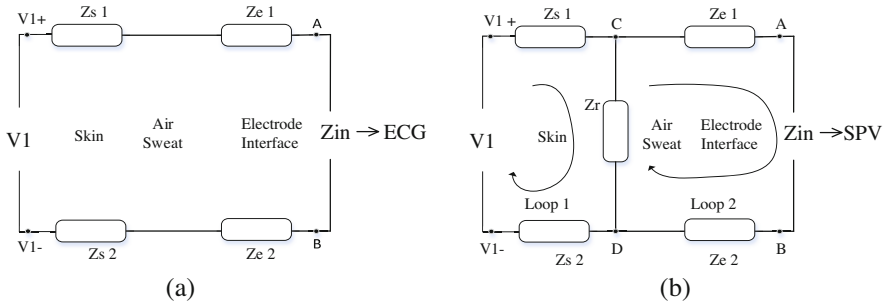


Fig. 41.1 Equivalent circuit model for (a) ECG signal; (b) SPV signal

approximately equal to $ECG = V_1^+ - V_1^-$. In conclusion, when the front-end input impedance is large relative to the interface impedance, the motion artifacts caused by the impedance change have little effect on the ECG.

In Fig. 41.1b:

$$C - D = (V_1^+ - V_1^-) \times \frac{Z_r}{Z_{s1} + Z_{s2} + Z_r} \cong 0 \quad \text{if } \frac{Z_r}{Z_{s1} + Z_{s2}} \cong 0 \quad (41.2)$$

In Eq. (41.2), when the impedance Z_r is smaller than the interface impedance $Z_{s1} + Z_{s2}$, the equation is close to 0.

$$SPV = C - D = Z_{in} \times \frac{C - D}{Z_{e1} + Z_{e2} + Z_{in} + Z_r} = \left(\frac{1}{1 + \frac{Z_{e1} + Z_{e2} + Z_r}{Z_{in}}} \right) \times (C - D) \quad (41.3)$$

In formula (41.3), C and D represent skin potentials which are in contact with the electrodes. When $\left(\frac{1}{1 + \frac{Z_{e1} + Z_{e2} + Z_r}{Z_{in}}} \right)$ approaches to 1, the SPV is approximate to $C - D$.

Circuit Simulation

First, by using a circuit simulation Software Multisim13.0, the ECG signal acquisition equivalent circuit model and SPV signal acquisition equivalent circuit model were built. Then the influence of impedance change was simulated. The R and the C component values used in the circuit were obtained from previous experiments. The feasibility of the proposed method was evaluated by changing the value of Z_r .

Fig. 41.2 Wearable chest strap

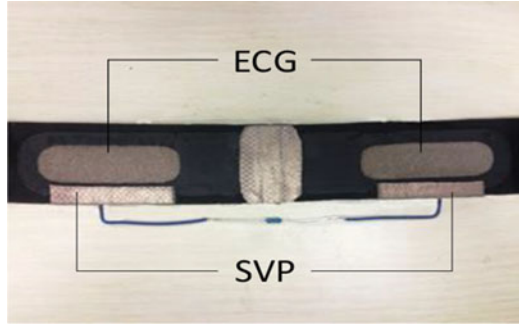
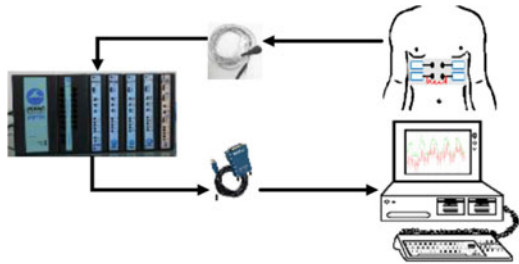


Fig. 41.3 Signal acquisition process



Experiment

The wearable chest strap is shown in Fig. 41.2; two pairs of textile electrodes are integrated on a wearable chest strap, one for ECG signal acquisition, and the other for SPV signal acquisition. Resistance (1, 22, 47, 100 k Ω) connects two textile electrodes which are used to obtain SPV signal connection. The experiment required six male volunteers (A–F) aged 20–25 years old to wear the wearable chest strap under the pressure of 2 N/cm², which was fixed at about 1 cm below the chest. The subjects performed stoop motions in an environment of 25 °. ECG signal and SPV signal were measured by BIOPAC data acquisition system (Model: MP36, BIOPAC Systems Inc., USA) with a sample rate of 2000 Hz and 10 s for each recording with the change of the resistance. Biological signals are finally analyzed and processed by a computer. The signal acquisition process is shown in Fig. 41.3.

41.3 Result and Discussion

Circuit Simulation Result

The simulation results are shown in Fig. 41.4 (red: ECG signal, green: SPV signal). As the resistance Z_r decreases, the amplitude of the SPV signal decreases. Obviously, the value of Z_r is very important. When Z_r is smaller than the interface

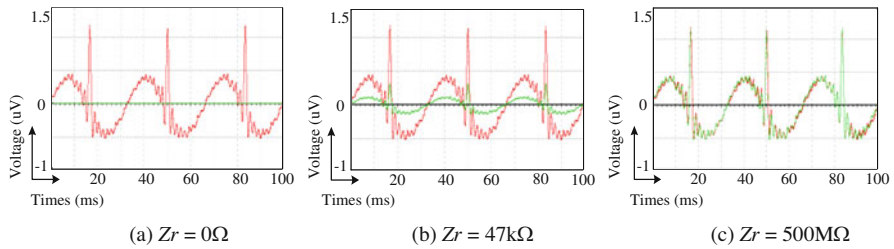


Fig. 41.4 Circuit simulation to evaluate the influence of Z_r . (a) $Z_r = 0 \Omega$, (b) $Z_r = 47 \text{ k}\Omega$, (c) $Z_r = 500 \text{ M}\Omega$

Table 41.1 The correlation of SPV signal and ECG signal in different resistance values of six males

Resistance value (kΩ)	Correlation of A	Correlation of B	Correlation of C	Correlation of D	Correlation of E	Correlation of F
1	0.3916	0.2665	0.0874	0.0915	0.0862	0.1282
22	0.5170	0.3483	0.2075	0.3291	0.1970	0.2366
47	0.5709	0.7563	0.8626	0.3890	0.2767	0.3684
100	0.4519	0.7088	0.8181	0.1431	0.1622	0.1164

impedance of $Z_{s1} + Z_{s2}$ and $Z_r/Z_{s1} + Z_{s2}$ is approximate to 0, so the SPV signal is close to 0. The effect is shown in Fig. 41.4a, b is the waveform diagram of the ECG signal and the SPV signal when Z_r is 47 kΩ. The SPV signal is superimposed with a weak ECG signal and needs to be removed by preprocessing. As shown in Fig. 41.4c, when Z_r is too large, the path is equivalent to broken circuit and the SPV signal approaches to the ECG signal.

Experimental Result

In the dynamic situation, Table 41.1 shows six volunteers' correlations between the SPV signal and the ECG signal in different value of resistance. When the value of resistance is equal to 47 kΩ, the SPV signal and the ECG signal have a highest correlation.

Adaptive filtering was conducted using a basic LMS (least mean square) error cancellation algorithm, and the SPV signal measured in four resistances are respectively input as adaptive filtering reference signal. The output of adaptive interference cancellation is shown in Fig. 41.5. It can be seen that the ECG signal and SPV signal in the 47 kΩ resistance have a high correlation, and the wave fluctuation of two signals is consistent. Table 41.2 shows the changes of SNR before and after the interference cancellation. As shown in Fig. 41.5 and Table 41.1, when the SPV signal measured in 47 kΩ resistance is used as a reference signal, the filtered QRS waveform is obvious and the SNR is improved.

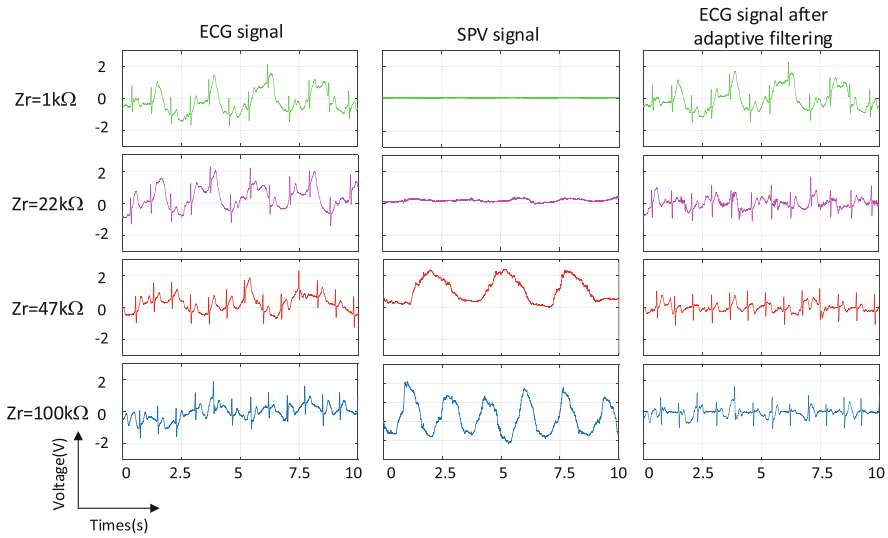


Fig. 41.5 ECG waveforms before and after adaptive filtering in different resistances

Table 41.2 The SNR changes of ECG signals with SPV interference in different resistance values

Resistance value (kΩ)	Before filtering SNR (dB)	After filtering SNR (dB)	SNRI (dB)
1	5.7453	5.8274	0.0821
22	5.7947	8.7272	2.9325
47	6.0317	11.7578	5.7261
100	5.5763	10.4293	4.8530

Independent component analysis is one of the recently developed techniques for the blind source separation (BSS). It is used to identify original signals from the observed linear combinations of the original signals. We deal with the ECG signals by using adaptive filtering algorithm and ICA algorithm, and the adaptive filtering reference signal is the SPV signal in 47 kΩ resistance. The output of filtering is shown in Fig. 41.6. Table 41.3 shows that adaptive filtering has higher SNR values and better noise suppression than ICA filtering.

The results demonstrate the feasibility of the method by using textile electrodes to measure the SPV signal as an adaptive filtering reference signal, and the results show the ability of adaptive filtering in suppression of motion artifacts in electrocardiograms recorded with textile electrodes.

Fig. 41.6 ECG waveforms after adaptive filtering of different resistances

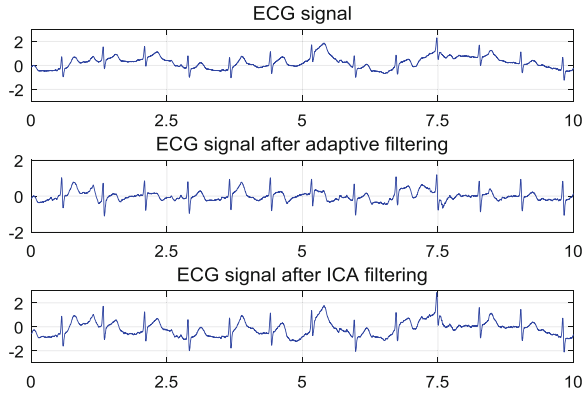


Table 41.3 The SNR changes of adaptive filtering and ICA filtering

Algorithm name	Before filtering SNR (dB)	After filtering SNR (dB)	SNRI (dB)
Adaptive filtering	6.0317	11.7578	5.7261
ICA filtering	6.0317	7.1343	1.1026

41.4 Conclusion

In this chapter, the SPV signal acquisition structure can effectively measure the skin-potential variation. The SPV signal is measured by textile electrodes and served as a reference signal for adaptive filtering. In this way, it can effectively remove the motion artifact caused by the skin-potential variation. Since two electrode pairs are distributed on the same substrate and the acquisition position of two signals is close, the motion artifact can be measured more accurately, ensuring the high correlation between ECG and SPV signals. Besides, using the electrode to collect the SPV signal doesn't require extra sensor components and improves the accuracy of the later diagnosis.

It can be found in the experiments that the correlation between the SPV signal and the ECG signal is deteriorated when large movements, such as running and jumping, are performed, which leads to insignificant signal characteristics after filtering. In the future, researchers should focus on removing motion artifacts under large-scale motions.

Acknowledgments This work is supported by National Natural Science Foundation of China (no. 61572110) and National Key Research & Development Plan of China (no. 2016YFB1001401).

References

1. Chi, Y.M., Jung, T.-P., Cauwenberghs, G.: Dry-contact and noncontact biopotential electrodes: methodological review. *IEEE Rev. Biomed. Eng.* **3**, 106–119 (2010)
2. Yao, S., Zhu, Y.: Nanomaterial-enabled dry electrodes for electrophysiological sensing: a review. *JOM.* **68**(4), 1145–1155 (2016)
3. Xu, P.J., Zhang, H., Tao, X.M.: Textile-structured electrodes for electrocardiogram. *Text. Prog.* **40**(4), 183–213 (2008)
4. Wiese, S.R., et al.: Electrocardiographic motion artifact versus electrode impedance. *IEEE Trans. Biomed. Eng.* **52**(1), 136–139 (2005)
5. Weihua, P., et al.: Skin-potential variation insensitive dry electrodes for ECG recording. *IEEE Trans. Biomed. Eng.* **64**(2), 463–470 (2017)
6. Lu, G., et al.: Removing ECG noise from surface EMG signals using adaptive filtering. *Neurosci. Lett.* **462**(1), 14–19 (2009)
7. Pengjun, X., Xiaoming, T., Shanyuan, W.: Measurement of wearable electrode and skin mechanical interaction using displacement and pressure sensors. In: 2011 4th International IEEE Conference on Biomedical Engineering and Informatics (BMEI), vol. 2, 2011
8. Tong, D.A.: Electrode systems and methods for reducing motion artifact. U.S. Patent No. 6,912,414, 28 Jun 2005
9. Tong, D.A., Bartels, K.A., Honeyager, K.S.: Adaptive reduction of motion artifact in the electrocardiogram. In: Proceedings of the Second Joint. IEEE Engineering in Medicine and Biology, 2002. 24th Annual Conference and the Annual Fall Meeting of the Biomedical Engineering Society EMBS/BMES Conference, 2002, vol. 2, 2002
10. Liu, Y., Pecht, M.G.: Reduction of skin stretch induced motion artifacts in electrocardiogram monitoring using adaptive filtering. In: Engineering in Medicine and Biology Society, 2006. EMBS'06. 28th Annual International Conference of the IEEE, IEEE, 2006
11. Byung-hoon, K. et al.: Motion artifact reduction in electrocardiogram using adaptive filtering based on half cell potential monitoring. In: 2012 Annual International Conference of the IEEE Engineering in Medicine and Biology Society (EMBC), 2012

Index

A

Accelerometer

- data stream, 116, 117
- sensor, 116, 119, 125
- signals, 120
- single hip-worn, 125
- time series, 120

Acoustical communications

- WBPLSec system model
 - air-gap acoustic channel, 94
 - data decomposition policy, 92
 - DSSS watermark signal, 93
 - narrow-band signal, 92
 - physical layer security mechanism, 94
 - spectrum, 93
 - SS watermark, 93
 - WAV, 94

Acoustical emanations, 92

Activity recognition

- anchors, 235
- five biaxial accelerometers, 233
- KNN method, 234, 240
- naive Bayes method, 234
- neural network, 234
- PIM, 235–236, 242
- RELIEFF method, 240
- SVM method, 240
- UWB, 234, 235, 237, 242
- wearable device, 233

Activity Shapelet/A-Shapelet

- accelerometer sensor, 119
- activity time series
 - average peak distance, 118
 - class shapelet representative, 119
 - distance metric, 119
 - shapelet extraction, 118

- CPU time/parallelization techniques, 117
- definition, 117
- library database, 118
- raw data, 117
- representative patterns, 119
- waveform, 116

Activity time series

- A-Shapelets, 119, 124
- DTW, 123
- Euclidean distance, 122
- extraction and selection, 117
- normalization, 119
- repetition periods, 120
- shapelet library database, 118

Acute COPD exacerbation, 267

Additive white Gaussian noise (AWGN), 80, 82–84, 411

Advanced driver assistance systems (ADASs), 132, 133, 141

Air-gap

- acoustical emanations, 92
- acoustic channel
 - experiments, 96–97
 - signals transmitted, 97, 98
 - spectrum, WBPLSec, 93
- acoustic covert channel, 92
- WBPLSec system model, 93–95

Amyotrophic lateral sclerosis, 339

Analog Front-Ends (AFE), 342, 343, 354, 356, 357, 359–361, 363

Analog-to-digital converter (ADC), 189, 294

- ANSYS High Frequency Structure Simulator (HFSS) software, 319
- Antenna, 318–321
- Antenna structure
- configuration and analysis, 433–439
 - cavity approach, 435–438
 - on-body simulation, 438–439
 - single low-UWB, 433–435
- design, 432
- Antiepileptic drugs (AED), 378
- Arm₁ and Arm₂, 175
- Artificial neural network (ANN), 326
- Augmented reality, *see* Brain computer interface (BCIs)
- Average Absolute Variation (AAV), 239–241
- B**
- Bagged decision tree model, 274
- Bandpass filter (BPF), 303
- Beats per minutes (BPM), 386, 387
- Bio-impedance (BImp), 301–307
- Bio-mechanical mobility modeling, 50, 51
- Biometal, 393
- BioPhone, 268, 269
- Biopotential acquisition, *see* Embedded platform
- BioWatch, 268, 269, 272, 278
- Bit error rate (BER), 51–52, 97–100, 256, 260, 262
- BLE 5
- broadcasting channels, 149
 - double data rate, 149
 - periodic advertisements, 149
 - PHY, 148
 - specification, 148
 - worst-case interference, 155
- Blood pressure (BP), *see* Pulse arrival time (PAT)
- Bluetooth
- canonical correlation analysis (CCA) based algorithm, 341
 - smart cushion, 327
 - Smart Safety Unit, 134
 - and Wi-Fi, 355
- Bluetooth Electroencephalogram (EEG)-headband, 133
- Bluetooth low energy (BLE), 382, 383
- analytical model, 149–150
 - BLE 5, 148
 - features, 148–149
 - healthcare and medical applications, 147
 - measurement devices, 151–153
 - precision mechanism, 65
 - ZigBee, 148
- Body area communication, 462
- Body area networks (BANs), 50, 171, 399, 439, 455
- Bose–Chaudhuri–Hocquenghem (BCH) codes, 79, 81, 256, 257, 260, 262
- Brain computer interface (BCIs)
- amyotrophic lateral sclerosis, 339
 - binary classifier, 341
 - classification techniques, 350
 - deficiency, 340
 - ERP and SSVEP, 340
 - firmware optimization, 349
 - locked-in syndrome, 339
 - microelectronics and wireless communication, 339
 - neurological/psychiatric disorders, 345
 - OpenBCI, 340
 - power consumption, 348–349
 - QR code recognition, 341
 - signal processing methods, 350
 - SSVEP, 346–348
 - stimulus presentation, 346
 - system description
 - acquisition and processing platform, 342–343
 - AR stimuli presentation, 343–344
 - CCA, 344–345
- C**
- Canonical correlation analysis (CCA), 341, 344–345
- Capsule endoscope
- BANs, 399
 - peak-formed electromagnetic fields, 401, 402
 - performance evaluation
 - estimation accuracy, 403–404
 - simulation environment, 402–403
 - scattered electromagnetic fields, 400–401
 - WCE, 399
- Cardiovascular diseases (CVD), 293
- Cavity approach, 435–438
- antenna parameter values, 435
 - directivity, 436–437
 - input impedance, 436
 - reflection coefficient, 436
 - wireless capsule endoscopy, 437–438
- Channel modeling
- in lossy tissue, 447
 - and mobility, 51
 - setup, 445

- Chip level postdetection integration (CLPDI), 97, 99, 100
 - Chronic obstructive pulmonary disease (COPD), 221, 267–269, 271, 280
 - Classification and regression tree (CART), 205
 - Coexistence state prediction, *see* Wireless body area network (WBAN)
 - Color light (CL) sensor, 246, 249, 251, 252
 - Commercial Off-The-Shelf (COTS) components, 354
 - Computational complexity, 197
 - COMSOL, 174, 175
 - Connected hospital, 157
 - Contact-based microphone, 222
 - Context-aware approach, 280
 - Context-aware mobile devices
 - acute COPD exacerbation, 267
 - BioPhone, 268, 269
 - BioWatch, 268, 269, 272, 278
 - context identification, 273–275
 - COPD (*see* Chronic obstructive pulmonary disease (COPD))
 - CPU and battery consumption, 279
 - data preprocessing, 272–273
 - design and data collection, 269–271
 - fusion mapping, 277
 - HeartSense, 268, 269
 - Kalman filter, 268
 - novel approach, 280
 - respiratory rate, 268, 275–278
 - SleepMonitor, 268, 269
 - smartphones, 268
 - smartwatches, 268
 - Continuous wave radar (CWR), 284–287, 289, 290
 - Control channel (CCH), 66
 - Convolutional Neural Networks (CNN), 133
 - Cough detection
 - cough classifier, 227–229
 - cough phases, 224
 - “Cough” vs. “Speech” vs. “None”, 224
 - majority voter, 229
 - privacy preservation, 229–230
 - sound event detector, 225–227
 - Covert channel, 91, 92, 94, 97
 - CWC-MOD-POW platforms, 152
 - Cyberonics, 377–378
 - Cybersecurity, 89, 90
 - Cyberspace, 89, 90
- D**
- Data channel (DCH), 66
 - DDD pacing mode (wireless-DDD), 421–422
 - Decision tree (DT), 124, 204, 205, 209–213, 215
 - Deep neural network, *see* Smart cushion
 - Degraded Gaussian Broadcast Channel (DGBCC), 410
 - Diastolic blood pressure (DBP), 297
 - Dielectric constant estimation method, 309
 - Dielectric properties of human tissues
 - 4-Cole–Cole expressions, 173
 - ionic conductivity, 174
 - permittivity, 173
 - quasi-static approximation, 174
 - Differential Phase-Shift Keying (DPSK), 256
 - Diffusion-based MC system
 - Boltzmann constant, 106
 - Brownian motion, 106
 - capacity C , 107
 - Fick’s diffusion, 107
 - Langevin equation, 106
 - mutual information, 107
 - physical system, 104, 105
 - Shannon capacity, 107
 - Direct sequence spread spectrum (DSSS), 93, 95, 96, 98, 99
 - Discrete Wavelet Transform (DWT), 360
 - Diversity
 - developed diversity antenna, 29
 - implant side diversity system, 30
 - MRC model, 30
 - polarization, 27, 28
 - transmit–receive, 31, 32
 - Driver monitoring, 133
 - Driving assistance service
 - applications, 132
 - IoT entities, 138
 - IoT environment, 138
 - modular architecture
 - Camera with Smart Bracelet, 141
 - GPS, 140
 - Smart Cushion with Smart Bracelet, 140
 - temperature sensor, 140
 - operations, 139
 - Driving operations recognition, *see* Smart cushion
 - Driving Right Leg (DgRL) circuit, 356
 - Dual chamber configuration, 420–421
 - Dual chamber leadless pacemaker system
 - functional block diagram, 423
 - pictorial representation, 423
 - RF pulse detection, 423
 - Dual-polarized implant antenna, 28, 32
 - Dynamic time warping (DTW), 116, 123, 129

E

- Effective Isotropic Radiated Power (EIRP), 261
- Electrical impedance tomography (EIT)
 - method, 309
- Electrocardiogram (ECG), 133, 171, 172, 283–290, 294–297, 299, 301–304, 370, 374, 465–471
 - and BImp electrode dots, 302
 - and CWR signals, 285, 287
 - equivalent circuit model, 466
 - Q-wave, 283
 - R-wave peak, 283
 - sensing electrodes, 466
 - SNR changes, 470, 471
 - and SPV signals, 469, 471
 - and UWB signal, 284
 - waveforms, 470, 471
- Electrode-skin impedance
 - CAD embroidery, 366
 - contact pressure, 369
 - conventional and embroidered electrodes, 370
 - conventional silver/silver chloride (Ag/AgCl) electrodes, 365, 371
 - e-textile electrodes, 366, 370
 - materials, 367–368
 - methods, 367–368
 - screen-printed electrodes, 366
 - SNRdB, 366, 368–369
 - surface electromyography, 365
 - values of impedance, 369
- Electroencephalography (EEG)
 - biosignal, 340
 - Emotiv NeuroHeadset, 341
 - hybrid system, 374
 - IFCN recommendations, 359
 - limited-channel, 378–379
 - radio transmissions, 161
 - seizure detection, 375
 - sensor density, 353
- Electromagnetic field (EMF)
 - RF EMF (*see* Radiofrequency electromagnetic field (RF EMF))
 - simulation model, 256
- Electromagnetic (EM) imaging method, 399–400
- Electromagnetic propagation simulation, 37–39
- Electromyography (EMG)
 - biosignal, 340
 - electrode–skin impedance (*see* Electrode-skin impedance)
 - input-referred noise, 359
 - SVM model, 361
- Electronic medical record (EMR), 90
- Embedded platform
 - AFEs, 354
 - application to EMG gesture recognition, 360–362
 - Bluetooth interface, 355, 356
 - Cortex M4 microcontroller, 355
 - EEG and EMG applications, 353
 - electrical characterization, 359–360
 - EMG acquired signal, 358
 - input-referred noise, 359
 - inverse filter signal reconstruction, 356–357
 - proposed system, 355
 - Sigma-Delta architecture, 354
 - signal acquisition, 356
 - Wi-Fi interface, 355, 356
- Embroidered electrode, 367–371
- Energy consumption, 50, 57, 60–61
- Energy/standard deviation (STD), 225–227
- Epileptic seizure, *see* Seizure detection
- Equivalent circuit model, 466
- ETSI SmartBAN network, 66, 67
- ETSI SmartBAN PHY
 - computer simulations, 81–84
 - frequency spectrum, 80
 - modulation and error controlling, 81
 - packet structure, 80–81
 - preamble detection, 80
- Euclidean distance, 122–123
- Event-related potential (ERP), 340

F

- Fabrication, 440
- Fast Fourier transform (FFT), 98, 99, 275–279, 303, 358, 360, 368
- Federal Communication Commission (FCC), 317, 318
- FFT based frequency domain approach, 275
- FFT-based method, 275
- Fick's diffusion, 107
- Fifth generation (5G), 17, 159, 317–321
 - antenna, 317–319
 - antenna 3D total realized gain pattern, 320
 - electromagnetic field radiation, 317
 - head modeling, 319
 - human body tissues, 317
 - international organizations, 318

- maximum value, power density, 321
- mobile devices, 317
- radiofrequency electromagnetic field
 - exposure assessment, 321
 - tissue electrical properties, 319
- Finite Difference Time-Domain (FDTD)
 - method, 258, 262
- Finite element method (FEM), 174, 182
- Finite impulse response (FIR) filter, 328–329
- Five number summary, 124
- Forward error correction (FEC), 148, 153
- Friis Equation, 462
- Future hospital, 157

G

- Galvanic coupling, 171, 173, 182
- Gastrointestinal (GI) tract, 431
- Gaussian frequency shift keying (GFSK), 52, 81, 148, 150
- Generic Attribute (GATT), 382
- Global Positioning System (GPS), 4, 58, 115, 133–135, 139, 140, 245, 250, 251
- Google Blockly, 383

H

- HAAR Mother Wavelet, 361
- HAR experimental evaluation
 - activity monitor device, 125
 - comparison with offline HAR, 126
 - participants and procedures, 125
 - results, 126
 - sensor independency, 129
 - subject-based analysis, 127–129
 - test duration effect, 127
 - training dataset effect, 126–127
- Head-mounted lightweight sensors, *see*
 - Indoor-outdoor (IO) detection
- Health-care system, 90
- Heart rate frequency (HRF), 303
- Heart rate variability (HRV), 133
- HeartSense, 268
- Heuristic method, 205
- Hidden Markov Model (HMM), 223, 326
- Hierarchical cough detection algorithm, 222
- High gain, 432, 435, 439
- Hospital technology, 157
- Hub, 49, 52, 66–68
- Human activity recognition (HAR)
 - application areas, 115
 - offline, 115, 116
 - online, 117

- real-time, 115
- sensor-based, 116
- Human body communication (HBC)
 - data decoding and displaying, 172
 - intra-body communication, 172
 - power consumption transmission, 171
 - 3D FEM multilayered cylindrical model, 173
 - transmitter (TX) and receiver (RX), 171
 - WBAN, 171
- Human-machine interactions (HMI), 339
- Human tissue layer model, 35–38, 44
- Hybrid wireless networks
 - light-based wireless systems, 161
 - radio-technology, 161
 - sensitive environments, 161

I

- Impedance cardiogram (ICG), 283
- Implantable cardioverter defibrillators (ICDs), 407
- Implantable medical devices (IMDs), 407
- Implant communications, 27, 32, 33
- Implanted antenna, 455–456, 462, 463
 - β -type Ti alloys, 393–394
 - CAD model, 395, 396
 - communication channel, 394
 - internal support and biological tissue replacement, 393
 - materials' characteristics, 394–395
 - metallic materials, 393
 - radiation pattern, 396
 - real-time monitoring/transmitting data, 394
 - space constraint, 394
 - 3D radiation pattern, 395
- Implant side diversity system
 - antenna development, polarization diversity, 28
 - communication performance, 30–31
 - implant communication, 27
 - living animal experiment, 29–30
 - UWB technology, 27, 28
- Implant synchronization, *see* Synchronization mechanism
- In-body antenna, 445–446
- In-body communication, 34, 44, 431
- Indoor energy harvesting
 - energy harvester module test, 191–192
 - experimental evaluation, 190–191
 - WE-safe, 187–190
- Indoor-outdoor (IO) detection
 - “CL” sensor, 246, 251, 252

- Indoor-outdoor (IO) detection (*cont.*)
 - data acquisition, 247
 - data analysis, 247–248
 - IMU sensor, 246, 251, 252
 - machine learning algorithms, 246
 - “P” sensor, 246, 251, 252
 - S-I and S-O environments, 247, 249, 250
 - “UV” sensor, 246, 251, 252
 - Industrial, scientific, and medical (ISM), 27, 66, 147, 148, 258, 395, 396
 - Inertial measurement unit (IMU), 246–249, 251, 252, 381
 - Information capacity, 106
 - Information leakage, 108–110
 - Information theoretic security (ITS), 108, 109, 409
 - Information transfer rate (ITR), 340
 - In-home pulmonary assessment
 - asthma, 221
 - COPD, 221
 - cough detection algorithm (*see* Cough detection)
 - hierarchical cough detection algorithm, 222
 - LPC, 229, 230
 - MFCC, 228
 - random forest, 228–230
 - speech obfuscation, 229
 - STD, 225–227
 - SVM, 223, 228, 229
 - Initial systolic time interval (ISTI), 283
 - Input, Output, Precondition, Effect (IOPE), 137, 139
 - Integer codes, 255–262
 - Inter-Beacon Interval (IBI)
 - alternating and non-alternating, 69–72
 - Control Channel Beacon discovery probability, 73–77
 - structure, SmartBAN, 66, 67
 - Inter-body communication model
 - COMSOL, 179
 - electric potential difference, 179
 - signal attenuation, 181
 - signal degradation, 182
 - transmission mechanisms, 180
 - Interference management method, 203
 - Interference ratio (SIR), 150
 - Interlink Electronics, 327
 - International Commission on Non-Ionizing Radiation Protection (ICNIRP), 318
 - International Workshop on Seizure Prediction (IWSP), 374
 - Internet of Things (IoT)
 - ADAS, 132
 - CNN, 133
 - domain model, 136–137
 - Driving Assistance Service, 132
 - low-power wireless communication, 147
 - medical and healthcare system, 79
 - metamodeling approach, 135
 - NIR, 133
 - opportunistic IoT service model, 137–138
 - sensors, 17
 - services, 131
 - smart objects, 132
 - SVM, 133
 - system architecture, 133–135
 - systems and components, 131
 - wireless sensor devices, 147
 - Intersecting tangent method, 301
 - Intra-body communication model
 - attenuation, 177
 - electrical potential distribution, 176
 - electric potential difference, 178, 179
 - frequencies, 177
 - model geometry and set up, 175
 - permittivity, 176
 - surface distance, 176
 - Inverse fast Fourier transform (IFFT), 35, 40–42, 44
 - IoT domain model, 136–137
- J**
- Jamming, 92, 94, 96–99, 410, 411
 - Java Virtual Machines (JVMs), 382
- K**
- Kalman filter, 268, 276–278, 280
 - Kinect2, 255–262
 - k*-Nearest Neighbors (KNN) method, 234, 240
- L**
- Laparotomy surgery, 29
 - Latency, 61–63, 283, 341, 347
 - Leadless cardiac pacemaker (LCP)
 - capacity and secrecy capacity region, 414, 415
 - cryptographic algorithms, 408
 - eavesdropper, 408
 - eavesdropping distance, 416, 417
 - ICDs, 407
 - IMDs, 407, 408
 - information rate R_1 vs. eve distance, 416
 - ITS, 409
 - MICS, 414
 - physical layer security methods, 409

- security and privacy, 408
 - signal-to-noise ratio, 409
 - subclavian vein, 407
 - system model
 - analysis of the strategies, 412–413
 - communication, 410
 - decoding, 411
 - DGBC, 410
 - encoding, 410–411
 - secrecy capacity, 411–412
 - Wyner model, 409
 - Leadless Pacemakers synchronization, *see*
 - Dual chamber leadless pacemaker system
 - Light-based wireless systems, 158, 161
 - Linear Predictive Coding (LPC), 229, 230
 - Linear support vector machine, 274
 - Line-of-sight (LOS), 4, 10, 51, 149, 150, 152, 153
 - Localization
 - RSS-based ranging, 450–452
 - Location-based services (LBSs), 3
 - Locked-in syndrome, 339
 - Longevity estimation, 423, 427
 - Long-Term Evolution (LTE-U), 147
 - Low-UWB band
 - geometry, 432
 - IEEE, 432
 - optimized parameters, 432, 433
 - WCE, 431
- M**
- Machine learning based HAR techniques, 127, 129
 - Machine learning based method, 203–215, 240
 - Machine learning processing, 195
 - Main Learning, 197
 - Majority voting, 225
 - MATLAB classification, 240
 - MATLAB Machine Learning Toolbox, 274
 - Maximum power point tracking (MPPT), 187, 190, 191
 - Mean Absolute Deviation (MAD), 239, 240
 - Mean absolute error (MAE), 275
 - Mean Crossing Rate (MCR), 239, 240
 - Medical implant communication (MICS) band, 414
 - Medium access control (MAC), 49–63, 65, 66, 77, 79, 80, 204
 - m-periodic MAC scheduling
 - joint throughput and channel aware, 56–57
 - scheduled access slot with repetition, 55–56
 - SmartBAN scheduling without repetition, 54–55
 - scheduled access mechanism, 50 (*See also* SmartBAN MAC scheduling)
 - Mel-Frequency Cepstral Coefficients (MFCC), 228
 - Metallic materials, 393
 - Metamodeling approach, 135
 - Method of method (MoM), 400
 - Microcontroller unit (MCU), 188
 - Micro wave
 - CT scan and MRI, 309
 - EIT method, 309
 - fat thickness
 - neural network, 313–314
 - proposed method, 311–313
 - measurement, 310–311
 - Microwave Studio (MS), 394
 - MIT Scratch, 383
 - Mixed condition approach, 223
 - Molecular communication (MC)
 - biological cells, 104
 - diffusion-based, 104–106
 - healthcare, 103
 - information capacity, 106–108
 - inter-disciplinary research, 103
 - secrecy capacity, 108–110, 113
 - security issues, 104
 - Motion artifacts reduction
 - cardiovascular diseases, 465
 - circuit simulation, 467–468
 - ECG, 466–467
 - fabric dry electrodes, 465
 - SPV, 465–466
 - Multi-layer model, 439, 440
 - Mutual information, 107
- N**
- Naive Bayes classifier (NBC), 204–206, 210–214
 - Naive Bayes method, 234
 - Near-infrared (NIR), 133
 - Neighbour WBAN discovery mechanism
 - BLE devices, 65
 - Control Channel Beacon discovery
 - probability, 73–76
 - discovery time
 - alternating IBI, 72
 - non-alternating IBI, 71
 - ETSI SmartBAN network, 66–67

- Neighbour WBAN discovery mechanism
(*cont.*)
 principles, 65
 probability of discovery
 alternating IBI, 70–71
 non-alternating IBI, 69–70
- Neural-net-based approach, 223
- Neural network (NN)
 calculation complexity, 199
 CVRR extraction, 198
 machine learning analysis, 195
 main learning, 197, 199
 performance evaluation, 197–198
 pre-learning, 197, 199
 preprocessing, 196–197
 simulation model and parameters, 198
 stress estimate, 200
 system model, 196
 wavelet transform, 196
- Non-contact measurement method, 309
- Nonparametric estimation method, 310
- nRF52840 Preview DK development kit, 151
- O**
- Obfuscation method, 229
- Offline HAR systems, 115, 116
- On board diagnostic (OBD), 325–326
- On-body antenna, 438–439, 441
- Open circuit voltage (OCV), 187
- OpenFDTD, 258
- Opportunistic IoT service model
 attributes, 137
 Driving Assistance Service (*see* Driving Assistance Service)
 IOPE, 137
- Optical wireless communications, 157, 161, 165
- Output discharge function (QOD), 188
- Over-the-air programming, 382, 383, 386
- P**
- Pacemaker therapy, 419
- Packet error rate (PER), 51, 56, 148–151, 153–155, 204, 207–209, 211–215
 interferer, 150
 LOS, 149, 153
 SER, 150
 SIR, 150
 SNR, 150
 ZigBee interference, 153
 ZigBee nodes, 154
- Packet reception rate (PRR), 49, 50, 56, 57, 59–62
- PAT extraction methods, 303, 305
- Path loss models
 for antennas, 450
 current frequency band, 443
 in-body antenna, 445–446
 measurement setup, 444, 447–448
 values, 449
 WCE, 443
- Peak detection method, 120–121, 275
- Peak-formed electromagnetic fields, 401, 402
- Pedestrian dead reckoning, 3
- Perfect Electric Conductor (PEC), 259
- Peripheral pulse transit time (PPTT), 293
- Personalized approach, 240
- Phantom
 permittivity and conductivity, 446–447
- Photoplethysmography (PPG)
 sensor array (*see* PPG-sensor array)
 signal, 301
- Physical layer (PHY), 49, 79, 84, 148, 151
See also ETSI SmartBAN PHY
- Physical-layer protocol data unit (PPDU), 52–55, 80, 81
- Physical layer security, 90–92, 94, 95, 101, 409
- Physical system, 105, 106
- Polarization diversity, 27, 28
- Position fixing, 3
- Position Independent Metrics (PIMs), 235–236
- Positioning
 GPS, 4
 hardware devices, on-field experimental tests, 9–10
 implementation, architecture, 9–10
 pedestrian dead reckoning, 3
 position fixing, 3
 process
 clock synchronization, 7
 TDOA positioning, 6
 time synchronization, 7–9
 system architecture, 6
 UWB (*see* Ultra-wide band (UWB))
- Power density (PD), 10, 18, 186, 188, 318, 321, 394
- Power line communication (PLC), 161, 168
- Power line interference (PLI), 345, 360
- Power spectral density (PSD), 346, 414
- PPG-sensor array
 beat-to-beat PWV, 297
 cuff-less BP monitoring, 293
 ECG, 294
 Finapres[®] NOVA system, 296

- outcomes, 297–299
 - PPTT, 293
 - PTT, 293–295
 - UART, 294
- Preamble detection
 - in ETSI SmartBAN PHY, 80–84
- Pre-ejection period (PEP)
 - CWR (*see* Continuous wave radar (CWR))
 - data analyzing, 286–287
 - Doppler echocardiography, 284
 - ECG, 283
 - experimental protocol, 285–286
 - ICG, 283
 - ISTI, 283
 - monitoring setup, 284–285
 - outcomes, 288–290
 - signal processing, 286–287
 - and UWB, 284
- Pre-Learning
 - CVRR, 197
 - effectiveness, 199
 - learning speed, 199, 200
 - medical knowledge, 200
 - three-layer NN, 197
- Preprocessing, 196–197
- Pressure sensor, 58, 134, 139, 140, 246, 326–328, 330, 333, 465
- Principal component analysis (PCA), 326, 375
- Printed circuit board (PCB), 187
- Private audio-based cough sensing, *see*
 - In-home pulmonary assessment
- Proof-of-concept evaluation
 - BLE Gateway tool, 386, 387
 - HTML/JavaScript web application, 386
 - libwabt.js library, 387
 - ModuleValue characteristic, 386
 - PPG sensor, 386
 - resource-constrained wearable sensor nodes, 388
 - size overhead, 387–388
- Proposed approaches, 233, 234, 242
- Pulse arrival time (PAT)
 - BImp (*see* Bio-impedance (BImp))
 - ECG and BImp electrode dots, 302
 - extraction methods, 305
 - outcomes, 304–305
 - PPG signal, 301
 - procedure, 302–303
 - PTT, 301
 - SBP, 302
 - signal processing, 303–304
- Pulse coupled neural network (PCNN), 133
- Pulse transit time (PTT), 293–295, 301

Q

- Quality rehabilitation, 195

R

- Radiofrequency electromagnetic field (RF EMF)
 - antenna, 318–319
 - communications and link coverage, 317
 - 5G, 317
 - head modeling, 319
 - outcomes, 319–321
 - PD, 318
- Radio frequency (RF), 419
- Radio-technology, 157
- Real-time HAR system
 - experimental evaluation (*see* HAR experimental evaluation)
 - implementation
 - labeling new activities, 124
 - training phase, 123–124
 - machine learning methods, 116
 - pattern matching (*see* A-Shapelet)
 - shapelet library creation, 119–121
 - time series/shapelets matching, 121–123
- Received signal strength indicator (RSSI), 151, 153, 203–204, 399
- Reconfigurable optical-radio access point, 163
- Reconfigurable optical-radio wireless body area network (RORWBAN)
 - data security, 165
 - energy efficiency/saving, 165
 - environmental/context/policy situation, 164
 - high reliability/high data throughput, 166
 - mobility and localization, 165
 - off-loading, 165
 - RF-restricted areas/coexistence, 165
 - single-technology, 164
- Reconfigurable optical-radio wireless network
 - future hospitals, 162
 - operating modes, 166–167
 - operating scenarios/applications
 - biosignals, 164
 - outside hospital, 166
 - reconfigurable optical-radio access point, 163
 - RORWBAN, 164
- RELIEFF method, 240
- Repetition periods, 120
- Root mean square (RMS), 208, 209, 211, 212, 239–241, 368
- Root mean square error (RMSE), 12–15
- R-R interval (RRI), 195, 196

S

- Secrecy capacity
 - Alice–Bob, 108, 113
 - Alice–Eve, 108, 113
 - closed-form mathematical expression, 110
 - diffusion-based channel, 109
 - diffusion-based MC system, 110
 - eavesdropper, 110
 - Eve’s distance, 110
 - information leakage, 108
 - information-theoretical security, 108
 - legitimate particles, 109
 - ligand–receptor binding, 113
 - strips, 112
 - transmit bandwidth, 112
 - 2D map, 110
- Security, 90
- Seizure detection
 - biosignals, 374
 - contribution, 374
 - EEG-based, 375–376
 - effectiveness, limited-channel EEG, 378–379
 - limitations, non-EEG, 377–378
 - non-EEG, 375
 - scalp electrodes, 374
 - setup and data collection, 376, 377
 - SUDEP, 373
- Semi-indoor (S-I) environment, 247, 249, 250
- Semi-outdoor (S-O) environment, 247, 249, 250
- Sensor data fusion, 131, 135
- Sensor distribution method, 328
- Shadowing, 21–22, 24, 60
- Shapelet library creation
 - extraction, 121
 - peak detection, 120–121
 - shapelet selection, 121
 - time series normalization, 119–120
- Signal acquisition process, 360, 468
- Signal processing, 91
 - application, 386
 - block diagram, 303
 - and data analyzing, 286
 - and statistical, 239
- Signal to interference plus noise ratio (SINR), 203, 204, 207–215
- Signal to interference ratio (SIR), 150
- Signal to noise ratio (SNR), 427
 - vs. probability of error, 427–428
 - receiver unit, 429
- Signal-to-noise ratios (SNRdB), 366, 368
- Simple moving average smoothing (SMA), 119
- Simulation-based human arm models
 - COMSOL, 174–175
 - inter-body communication model, 179–182
 - intra-body communication model, 175–179
- Single low-UWB, 433–435
 - directivity, 434, 435
 - Gain values, 434, 435
 - input impedance, 434
 - radiation patterns, 434
 - surface current distribution, 434
- Skin-potential variation (SPV), 465–466
- SleepMonitor, 268, 269
- Sliding time window, 329–330
- Small intestine, 399, 431, 438
- SmartBAN MAC scheduling
 - channel model, 51
 - energy consumption, 60–61
 - joint throughput and channel aware, 56–57
 - latency, packet, 61–62
 - mobility modeling, 51
 - performance assessment, 58
 - radio link modeling, 51–52
 - superframe format, 52–54
- Smart Body Area Network (SmartBAN)
 - ETSI SmartBAN network, 66, 67
 - mobility patterns, 50
 - PHY and MAC, 50
 - PRR performance, 49, 59–60
 - reference SmartBAN MAC scheduling, 58
- Smart Bracelet, 132–134, 139–141
- Smart cushion, 132–134, 139, 141
 - classification model construction, 330, 331
 - confusion matrix, classification results, 336
 - data collection, 331–333
 - data preprocessing, 333–334
 - data processing method
 - FIR filter, 328–329
 - PCA dimension reduction, 330
 - sliding time window, 329–330
 - data processing module, 327
 - distribution, traffic accidents statistics, 325, 326
 - driving data collection, 326
 - driving operations recognition experiment, 331
 - field of traffic safety, 337
 - hardware design, 327, 328
 - model construction, 334–336
 - OBD, 325–326
 - performance, classification model, 336
 - physiological characteristics, 337
 - proposed method, 327
 - traffic safety management, 325
 - vehicles and drivers, 325

Smartphone, 3, 6, 131–136, 139, 141, 148, 222, 223, 227, 230, 234, 235, 245, 251, 267–271, 273, 274, 279, 381–383, 385

Smart Safety Unit, 132–135, 138, 139, 141

Smartwatch, 133, 222, 223, 227, 230, 234, 267–270

Software development kit (SDK), 151

Sound event detector, 225–227

Specific Absorption Rate (SAR), 318

Sport

- LBSs, 3
- UWB positioning (*see* Ultra-wide band (UWB))

Standard Deviation (SD), 239

Start Frame Delimiter (SFD), 80–82, 84

Steady state visual evoked potential (SSVEP), 340, 346–348

Sternotomy wires

- description, 34
- IFFT and numerical results, 35, 40–42, 44
- location, on-body antennas, 34
- measurements, 35
- propagation path options, 37–39
- simplified layered human body tissue model, 35, 36
- simulations model, 35
- simulator, 34
- transmitter antenna, 34

Stress shielding, 393

Sudden unexpected death in epilepsy (SUDEP), 373

Supervised learning methods, 205

Support vector machines (SVM)

- algorithm, 355
- classifiers, 223
- posterior probabilistic model, 133
- posture detection, 204
- Viola–Jones algorithm, 133

Surface electromyography (sEMG), 365, 378

Symbol error rate (SER), 150

Synchronization mechanism

- ML non-coherent detector, 426
- timing diagram, 425

System on chip (SoC), 151, 152

Systolic blood pressure (SBP), 297–299, 302, 305, 306

T

Temporarily storing state list (TSSL), 210

Textile electrodes, 465

Throughput and channel aware scheduling, 50, 56–58, 60–61

Time domain approach, 278

Time of arrival (TOA)-based method, 399

Traditional cuff-based BP monitoring method, 293

Transmit–receive diversity, 31, 32

Transmitted RF pulse, 426

Transversal magnetic (TM), 400

U

Ultrasonic communications, 92

Ultra-wide band (UWB)

- adoption, WBANs, 18
- antenna design, 456–457
- bandwidth, UWB signals, 18
- body area environment, 457–458
- body locations, 4, 5
- EM-environment beneath, 460
- fabricated antennas, 458, 459
- five-a-side football, 4, 5
- four static UWB receivers, 4
- implant communications, 27, 28
- inside human body, 455
- measurements, 18
- on-body channel characteristics (*see* Sternotomy wires)
- on-body tag locations, evaluation, 11–12
- on-field tests, 4–5
- path loss equation, 461
- positioning system, 4
- RMSE, 12–15
- transmission power, 18
- UWB-IR transmission, 27
- wireless communications, 18

Universal asynchronous receiver-transmitter (UART), 294

UWB impulse radio (UWB-IR) transmission, 27

UWB off-body radio channel measurements

- absolute path loss values, 22–23
- antenna spots, 19, 20
- data processing, 20
- four-port VNA, 19
- human body effects, 24
- path loss (PLs) models, antenna sites, 21–22
- planar prototype antenna types, 19
- test person and anechoic chamber, 18–19

UWB signal-body interaction, 6, 9

V

- Vagus nerve stimulator (VNS), 378
- Vector network analyzer (VNA), 310, 311
 - equipment, 19
 - four-port, 19
 - frequency sweeping mode, 18, 24
 - sternotomy wires, 35
- Vehicle driving simulator, 332
- Vertical handover mechanism (VHO), 166, 167
- Virtual machine, *see* WebAssembly
- Visible light communications (VLC)
 - biosignals, 161
 - EEG signal, 161
 - medical environments, 161
 - PLC, 161
 - privacy and security, 161
 - solid-state lighting infrastructure, 160
 - uplink and downlink, 160
- Vivaldi directional antenna, 445, 446, 448, 449

W

- Watermark based blind physical layer security (WBPLSec)
 - acoustic air-gap channel, 96–97
 - acoustical communications, 91 (*See also* Acoustical communications)
 - BER, 97–99
 - evaluation, energy cost, 99, 100
 - implementation, 99
 - Nyquist–Shannon Sampling theorem, 95–96
- Watermarking, 92, 93, 95–97
- Waveguide penetration method, 309, 310
- Wearable chest strap, 468
- Wearable devices, 117, 118
- Wearables, *see* WebAssembly
- Wearable sensor node/network
 - effects, 185
 - environmental monitoring application, 185
 - hybrid wearable energy harvester, 186
 - low illumination, 186
 - piezoelectric, 186
 - reliable energy harvesting system, 186
 - WBAN, 185
- Wearable sensors, 3
- Wearable systems, *see* WebAssembly
- Wearable wireless networks (WWNs), 90–92
- WebAssembly
 - Contiki-OS, 382
 - implementation
 - BLE, 383
 - bluetooth low energy, 385–386
 - embedded systems, 384, 385
 - libwabt.js, 383
 - WAC, 383
 - JavaScript engines, 382
 - JVMs, 382
 - Python, 381
 - resource-constrained devices, 381
 - smartphones, 381
 - tablets, 381

- WebAssembly Binary Toolkit (WABT), 383
- WebAssembly in C (WAC), 383
- Weighted k-Nearest Neighbors (KNN), 274
- WE-safe energy harvesting
 - hardware implementation, 187–188
 - IoT sensor node, 188–190
- WE-safe IoT sensor node
 - current waveform, 190
 - duty-cycle adjustment, 188–189
 - energy harvester module test, 191
 - MCU, 188
 - power requirements, 188
 - solar panels' characteristic, 190
- Wireless body area networks (WBAN), 90, 339
 - authorities, 17
 - BCH codes, 257, 260, 262
 - cellular networks, 159
 - channel models, 33
 - classification, 159
 - close-range wireless network, 159
 - common MAC approach, 50
 - communication paths, 255
 - cyberspace, 90
 - D8PSK, 256, 260
 - DT, 205–206
 - 8-PSK or m-QAM, 256
 - electromagnetic simulation, 257–259
 - encoding scheme and simulation, 260
 - energy efficiency, 50
 - feature extraction, 204, 208–209, 213
 - human-centered wearable wireless network, 203
 - IEEE 802.15.6, standards, 79
 - integer codes, 255–262
 - LDPC codes, 262
 - level change (LC), 204
 - machine learning, 203–215
 - mobility patterns, 50
 - monitor wellbeing, 159
 - NBC, 206–207
 - neighbour network discovery (*see* Neighbour WBAN discovery mechanism)
 - performance evaluation, 210–215

- potential applications, 49
 - power-saving, 255
 - prediction algorithm, 209–210
 - problem description, 207–208
 - RF communications, 160
 - RRI, 195
 - sensor nodes, 49
 - SINR Square Integral (SSI), 204
 - smart healthcare applications, 147
 - in sports, 17
 - standardized protocols, 49
 - UWB technology, 18 (*See also* Ultra-wide band (UWB))
 - wireless characteristics, 18
 - WLAN technologies, 203
 - Wireless capsule endoscopy (WCE), 399, 431, 439, 443
 - Wireless coexistence, 148, 149
 - Wireless-DDD pacing mode, 424
 - Wireless local area networks (WLAN), 158, 159, 203
 - Wireless networks
 - hybrid networks, 161–162
 - VLC, 160–161
 - WBAN, 159–160
 - WLAN, 159
 - WWAN, 158–159
 - Wireless sensor networks (WSNs), 255
 - Wireless wide area networks (WWAN), 158–159
 - Wyner model, 409
- Z**
- Zero-crossing method, 275
 - ZigBee
 - interference, 152
 - interferers, 152